ULTRACOOL DEMOGRAPHY WITH A VOLUME-LIMITED CENSUS OF THE SOLAR NEIGHBORHOOD

A DISSERTATION SUBMITTED TO THE GRADUATE DIVISION OF THE UNIVERSITY OF HAWAIʻI AT MĀNOA IN PARTIAL FULFILLMENT OF THE REQUIREMENTS FOR THE DEGREE OF

DOCTOR OF PHILOSOPHY

IN

ASTRONOMY

DECEMBER 2018

By
William M. J. Best

Dissertation Committee:

Michael Liu, Chairperson
Eugene Magnier
Thierry Forveille
Daniel Huber
Jessica Lu
Mark Marley
Gary Huss

To my father, the original Dr. Best

Acknowledgements

Thank you to my advisors, Mike Liu and and Gene Magnier, who have given me so much guidance and support over the past seven years while keeping the bar high. Mike, thank you for taking a chance on me in 2010, giving me the opportunity to test the astronomical waters. Gene, thank you for helping me to think about data and statistics in useful and productive ways.

Thank you to my original committee. Mark Marley, Thierry Forveille, Jessica Lu, Kim Binsted, I've appreciated your questions and guidance. Gary Huss and Dan Huber, thank you for joining in the final hour to support me in getting my PhD finished.

Jonathan Williams, thank you for advising me through a fun 699 project, and many conversations since. I enjoyed working with you and appreciated your open door.

Many thanks to Trent Dupuy for help will all manner of things over the years, from emacs rectangles, to Keck aperture masking to parallax pipeline details.

Brendan Bowler, thanks for being my earliest peer mentor in astronomy. I'm glad we'll have a chance to work together again in Austin. Thanks to Eric Nielsen for a whole lot of advice and for helping me get my head around Bayesian analysis. Thanks to my collaborators at and beyond the IfA: Niall Deacon, Kimberly Aller, ZJ Zhang, Michael Kotson. I've enjoyed working with all of you. Thanks to my IfA cohort for much collaboration, laughs in the office, and survival through quals. Thanks especially to Kelly Lockhart for a lot of enjoyable office mate years. Thanks to my astro friends beyond the IfA: Daniella Bardalez Gagliuffi, Jonathan Gagné, Sarah Logsdon, Emily Martin, Joe Filippazzo. Here's to our future collaborations.

Thanks to Bill Unruh, Diane Tokumura, Faye Uyehara, Amy Miyashiro, Susan Lemn, Karl Uyehara, Chris Kaukali, Wayne Nakamoto, Lisa Araki, and all the staff at the IfA who keep the wheels turning for us.

Thank you to the University Research Council, the ARCS Foundation, and the Friends of the IfA for recognizing and rewarding my work.

Thanks to my daughter Hazel for giving me reasons to laugh and smile every day, and for helpful typing during the final stages of my thesis.

Finally, heartfelt love and thanks to Vivian Best for her incredible support during the past seven years. I'm looking forward to cooking with you again.

I thank Trevor Jim for the arduous task of converting and correcting the UH Thesis macros so that they would work properly with modern forms of Latex. And thanks to Kevin Jim for putting all the documentation and templates together for thesis work. Huge thanks to Jason Surace, Joe Jensen, Chris Dudley, Jeff Goldader, and the many others who created the initial versions of the macros.

The Pan-STARRS1 Surveys (PS1) have been made possible through contributions of the Institute for Astronomy, the University of Hawaii, the Pan-STARRS Project Office, the Max Planck Society and its participating institutes, the Max Planck Institute for Astronomy, Heidelberg and the Max Planck Institute for Extraterrestrial Physics, Garching, The Johns Hopkins University, Durham University, the University of Edinburgh, Queen's University Belfast, the Harvard-Smithsonian Center for Astrophysics, the Las Cumbres Observatory Global Telescope Network Incorporated, the National Central University of Taiwan, the Space Telescope Science Institute, the National Aeronautics and Space Administration under Grant No. NNX08AR22G issued through the Planetary Science Division of the NASA Science Mission Directorate, the National Science Foundation under Grant No. AST-1238877, the University of Maryland, Eotvos Lorand University (ELTE), and the Los Alamos National Laboratory. We thank the PS1 observing and processing staff for obtaining

the PS1 data, and Bill Sweeney, Heather Flewelling, and Mark Huber for assistance with accessing PS1 images.

UKIRT is owned by the University of Hawaii (UH) and operated by the UH Institute for Astronomy; operations are enabled through the cooperation of the East Asian Observatory. When some of the data reported here were acquired, UKIRT was supported by NASA and operated under an agreement among the University of Hawaii, the University of Arizona, and Lockheed Martin Advanced Technology Center; operations were enabled through the cooperation of the East Asian Observatory. When some other of the data reported here were acquired, UKIRT was operated by the Joint Astronomy Centre on behalf of the Science and Technology Facilities Council of the U.K. All UKIRT data reported here were obtained as part of the UKIRT Service Programme. This paper makes use of observations processed by the Cambridge Astronomy Survey Unit (CASU) at the Institute of Astronomy, University of Cambridge.

I thank Watson Varricatt and Tom Kerr at UKIRT, and Mike Irwin and Simon Hodgkin at CASU for their responsive and ongoing support of my observations and data reduction, and all the UKIRT staff for carrying out my service mode observations.

I thank John Rayner and Alan Tokunaga for making engineering time available for IRTF observations, and Katelyn Allers, Michael Kotson, Brian Cabreira, Bill Golisch, Dave Griep, Tony Matulonis, and Eric Volqardsen for assisting with these.

This work makes use of data products from the Two Micron All Sky Survey, which is a joint project of the University of Massachusetts and the Infrared Processing and Analysis Center/California Institute of Technology, funded by the National Aeronautics and Space Administration and the National Science Foundation. I have used data products from the Wide-field Infrared Survey Explorer, which is a joint project of the University of California, Los Angeles, and the Jet Propulsion Laboratory/California Institute of Technology, and NEOWISE, which is a project of the Jet Propulsion Laboratory/California Institute of Technology. *WISE* and NEOWISE are funded by the National Aeronautics and Space Administration. This work has made use of data from the European Space Agency (ESA)

mission *Gaia* (http://www.cosmos.esa.int/gaia), processed by the *Gaia* Data Processing and Analysis Consortium (DPAC, http://www.cosmos.esa.int/web/gaia/dpac/consortium). Funding for the DPAC has been provided by national institutions, in particular the institutions participating in the *Gaia* Multilateral Agreement.

This research has made use of NASA's Astrophysical Data System, the UKIDSS data products, the VISTA data products, the SpeX Prism Spectral Libraries, maintained by Adam Burgasser at http://pono.ucsd.edu/ adam/browndwarfs/spexprism, and the Database of Ultracool Parallaxes, maintained by Trent Dupuy at http://www.as.utexas.edu/ tdupuy/plx/Database_of_Ultracool_Parallaxes.html. This research has made extensive use of the SIMBAD and Vizier databases operated at CDS, Strasbourg, France. This work was greatly facilitated by many features of the TOPCAT software written by Mark Taylor (http://www.starlink.ac.uk/topcat/).

Finally, I recognize and acknowledge the cultural significance that the summit of Mauna Kea has always held within the indigenous Hawaiian community. I am most fortunate to have the opportunity to conduct observations from this mountain.

Abstract

As the lowest-mass objects created by star formation processes, brown dwarfs are essential to a complete understanding of the star and planet formation history of our galaxy. To this end, a complete volume-limited sample of brown dwarfs in the solar neighborhood is critical for testing formation theories. To create such a sample, we (1) searched for brown dwarfs missed in previous surveys to complete the census, and (2) measured precise trigonometric distances to define the sample. We conducted a wide-field (28,000 deg^2) search using the Pan-STARRS1 and *WISE* surveys, discovering the most L/T transition dwarfs of any search to date. We additionally discovered a binary brown dwarf with component masses $\approx$4 $M_{\rm Jup}$, the lowest-mass binary discovered to date, providing clear evidence that normal star-formation processes produce planetary-mass binaries. We measured parallaxes for 348 L and T dwarfs using the wide-field infrared camera WFCAM on the United Kingdom Infrared Telescope (UKIRT) to reach well beyond the red limit of *Gaia*, producing the largest single batch of parallaxes for brown dwarfs to date. We constructed a volume-limited sample of L0–T8 dwarfs out to 25 pc, covering two-thirds of the sky (declinations -30° to $+60^\circ$) and containing 350 members, four times more than the previous most complete sample of L and T dwarfs. Our volume-limited sample of brown dwarfs is the first beyond 8 pc defined entirely by parallaxes. We identified a distinct gap in the $J-K$ color at the L/T transition, implying a phase of rapid atmospheric evolution whose $T_{\rm eff}$ ($\approx$1300 K) is in tension with model predictions. Using synthetic populations tied to our volume-limited sample, we calculated the most precise brown dwarf space density and luminosity function to date, and we placed improved constraints on the substellar initial mass function and

formation history. Our volume-limited sample will continue to be a rich source of empirical constraints for studies of local brown dwarfs.

Table of Contents

List of Tables

List of Figures

Chapter 1

Introduction

Brown dwarfs are self-gravitating objects more massive than giant planets ($\gtrsim 13\ M_{\rm Jup}$; Basri 2000) but not massive enough to sustain hydrogen fusion in their cores and become stars ($\lesssim 70\ M_{\rm Jup}$; Dupuy & Liu 2017). Brown dwarfs therefore cool as they age, from late-M ($T_{\rm eff} \approx 2800$–2300 K) through L, T, and Y ($T_{\rm eff} \approx 200$–400 K) spectral types, and their atmospheres contain unique chemistry that evolves dramatically with declining temperature. This continuous cooling additionally means that brown dwarf luminosities and temperatures depend on both their ages and masses, with the result that a younger, less massive brown dwarf can have the same luminosity and temperature (and thus spectral type) as an older, more massive brown dwarf. The relationship between the observables (fluxes and spectra) and the underlying physical properties (masses, ages, metallicities, and gravities) of ultracool dwarfs is therefore challenging to disentangle, and evolutionary trends are difficult to identify.

Brown dwarf photospheres are dominated by molecules and dusty condensates that undergo significant chemical changes as they cool (e.g., Burrows et al. 2001). This is particularly true in the L/T transition (spectral types $\approx$ L8–T4), where the clouds that characterize L dwarfs fall below the photosphere via a process that is not yet understood (e.g., Burrows et al. 2006; Saumon & Marley 2008). State-of-the-art evolutionary and atmospheric models typically yield inaccurate luminosities and inconsistent temperatures for L/T objects with known masses and/or age determinations (e.g., Dupuy et al. 2009b,

2015b). A well-defined sample of L/T transition dwarfs with accurate luminosities would considerably improve our ability to test the models. However, the most significant deficiency in the local brown dwarf census to date is in the L/T transition because the near-infrared colors of L/T transition dwarfs are similar to those of background M dwarfs, making the L/T objects difficult to identify in wide-field searches.

The formation history of nearby brown dwarfs is also unsettled. They are thought to form like stars, via core collapse in molecular clouds, but it is unclear whether other mechanisms such as massive disk instability (Boss 1997) or ejection from young multiple systems (Reipurth & Clarke 2001) may contribute significantly to the field population (Chabrier et al. 2014). Precise values for the local ultracool mass function and binary fraction would help to ascertain the dominant formation mechanism(s), but these quantities are not well constrained (e.g., Marocco et al. 2015). It is also not currently possible to distinguish between a constant, declining, or largely stochastic birth rate (Burgasser 2004a; Deacon & Hambly 2006; Metchev et al. 2008; Day-Jones et al. 2013). Although ages for field objects cannot be directly observed, their kinematic distributions provide statistical measures of age (Wielen 1977; Faherty et al. 2009). However, no one has simultaneously studied the kinematics, space density, and mass function using a single well-defined sample to establish a formation timeline for the substellar field population.

Volume-limited samples have long been the gold standard for stellar population studies, as they are free of the selection biases inherent in surveys based on photometry and proper motion. Historically, completing these samples has required a major effort and taken many years. Gliese spent more than 35 years assembling his volume-limited catalog of stars, first out to 20 pc (Gliese 1957) and then to 25 pc (Gliese & Jahreiss 1991, containing 3,820 stars in 3,264 systems). But even in this landmark work, only 60% of the systems had trigonometric distances, and barely half of those had errors under 15%. The advent of *Gaia* has now revolutionized volume-limited studies of nearby stars, as *Gaia* DR2 (Gaia Collaboration et al. 2018) has produced 1.3 billion parallaxes within a few years of its launch, demonstrating the power of digital sky surveys that rapidly produce catalogs of

precise data. However, while *Gaia* DR2 includes parallaxes for essentially every star within 25 pc, *Gaia*'s ability to observe brown dwarfs is severely limited because most of the emission from brown dwarfs is in the infrared, beyond the reach of *Gaia*'s optical detectors.

Digital sky surveys in the red-optical or infrared, such as the Deep Near Infrared Survey of the Southern Sky (DENIS, Epchtein et al. 1999), the Sloan Digital Sky Survey (SDSS; York et al. 2000), the Two Micron All Sky Survey (2MASS; Skrutskie et al. 2006), the UKIRT Infrared Deep Sky Survey (UKIDSS; Lawrence et al. 2007), the Wide-Field Infrared Survey Explorer (*WISE*; Wright et al. 2010) and the Pan-STARRS1 3π Survey (PS1; Chambers et al. 2018) have similarly revolutionized brown dwarf studies, enabling most of the discoveries and providing a wealth of multi-band photometry. However, a volume-limited sample of brown dwarfs with depth comparable to stellar samples has not yet been established, and this has hindered our understanding of the field population. The most complete samples assembled to date are the 2MASS-based sample of Reid et al. (2008b), comprising 196 late-M, L, and T dwarfs out to 20 pc over 65% of the sky, but complete only for spectral types M9-L6 and using photometric distances for two-thirds of the members; and the full-sky 8 pc sample of Kirkpatrick et al. (2012), which contains only 33 L, T, and Y dwarfs. Two essential pieces were needed to enable the creation of a larger sample: a thorough search to find the missing nearby L/T transition dwarfs, and a campaign to measure enough parallaxes to robustly define a volume-limited sample. In this dissertation, I describe our completion of both of these missing pieces, leading to the first parallax-defined 25 pc volume-limited sample of L and T dwarfs.

Chapter 2

A Search for L/T Transition Dwarfs With Pan-STARRS1 and *WISE*. I. Discovery of Seven Nearby Objects Including Two Candidate Spectroscopic Variables

Note: This chapter originally appeared as Best et al. (2013), with co-authors Michael C. Liu, Eugene A. Magnier, Kimberly M. Aller, Niall R. Deacon, Trent J. Dupuy, Joshua Redstone, W. S. Burgett, K. C. Chambers, K. W. Hodapp, N. Kaiser, R.-P. Kudritzki, J. S. Morgan, P. A. Price, J. L. Tonry, and R. J. Wainscoat.

Abstract

We present initial results from a wide-field (30,000 deg^2) search for L/T transition brown dwarfs within 25 pc using the Pan-STARRS1 and *WISE* surveys. Previous large-area searches have been incomplete for L/T transition dwarfs, because these objects are faint in optical bands and have near-infrared colors that are difficult to distinguish from background stars. To overcome these obstacles, we have cross-matched the Pan-STARRS1 (optical) and *WISE* (mid-IR) catalogs to produce a unique multi-wavelength database for finding ultracool dwarfs. As part of our initial discoveries, we have identified seven brown dwarfs

in the L/T transition within $9-15$ pc of the Sun. The L9.5 dwarf PSO J140.2308+45.6487 and the T1.5 dwarf PSO J307.6784+07.8263 (both independently discovered by Mace et al. 2013a) show possible spectroscopic variability at the Y- and J-bands. Two more objects in our sample show evidence of photometric J-band variability, and two others are candidate unresolved binaries based on their spectra. We expect our full search to yield a well-defined, volume-limited sample of L/T transition dwarfs that will include many new targets for study of this complex regime. PSO J307.6784+07.8263 in particular may be an excellent candidate for in-depth study of variability, given its brightness ($J = 14.2$ mag) and proximity (11 pc).

2.1 Introduction

Over 1,200 brown dwarfs have been cataloged since the first unambiguous discovery less than twenty years ago (Nakajima et al. 1995). As a result, two new spectral types, L and T, have been created (Kirkpatrick et al. 1999; Burgasser et al. 2006a) to categorize these ultracool objects, and recent discoveries have identified the first brown dwarfs cooler than 400 K (Liu et al. 2011a; Luhman et al. 2011; Cushing et al. 2011; Kirkpatrick et al. 2012), spawning the creation of the Y spectral type. The main drivers of brown dwarf discoveries have been large-area digital surveys such as the Deep Near Infrared Survey of the Southern Sky (DENIS, Epchtein et al. 1999), the Sloan Digital Sky Survey (SDSS; York et al. 2000), the Two Micron All Sky Survey (2MASS; Skrutskie et al. 2006), and the UKIRT Infrared Deep Sky Survey (UKIDSS; Lawrence et al. 2007). Photometric searches using these surveys combined with spectroscopic follow-up have identified most of the known field brown dwarfs (e.g., Chiu et al. 2006; Cruz et al. 2007; Burningham et al. 2010a). More recently, the Pan-STARRS1 3π Survey (PS1; Kaiser et al. 2010), the Wide-Field Infrared Survey Explorer (*WISE*; Wright et al. 2010), and the VISTA Hemisphere Survey (VHS; PI McMahon, Cambridge, UK) have pushed brown dwarf searches to greater distances and cooler temperatures (e.g., Deacon et al. 2011; Kirkpatrick et al. 2011; Lodieu et al. 2012c).

Despite the overall success of past searches, it is expected that previous work has been less complete for L/T transition dwarfs (spectral types ≈L6–T5) because these objects are optically faint and have near-infrared colors that are difficult to distinguish from M and early-L dwarfs (e.g., Reid et al. 2008b). Past searches sensitive to L/T objects have also focused on modest areas of the sky. The most successful searches so far have been those of Chiu et al. (2006), who searched over 3,500 deg^2 using SDSS photometry (optical iz bands) to find 47 L6–T5 dwarfs; Metchev et al. (2008) and Geißler et al. (2011), who cross-matched SDSS DR1 (2,099 deg^2; Abazajian et al. 2003) with 2MASS (near-IR) photometry to identify 10 L6–T5 dwarfs (many of which showed spectral indications of binarity); and Day-Jones et al. (2013), who searched 495 deg^2 in UKIDSS and SDSS to find 15 L6–T5 dwarfs. Deacon et al. (2011, hereinafter D11) and Liu et al. (2011a; 2013, in prep) have combined Pan-STARRS1 and 2MASS photometry with proper motion to search three-quarters of the sky for T dwarfs. To date, however, there has been no large-area search specifically targeting nearby, bright L/T transition dwarfs.

Because of this slow progress in identifying the local L/T population, we do not yet have a well-constrained substellar mass function for the solar neighborhood. However, recent work indicates that the local space density has a minimum at the L/T transition (Day-Jones et al. 2013 and references therein). A natural explanation is that the L/T transition spans a fairly narrow temperature range ($\Delta T \approx 400$ K) compared to L0–L5 dwarfs ($\Delta T \approx 1000$ K; Golimowski et al. 2004; Stephens et al. 2009). Moreover, brown dwarfs cool as they age and evolve to later spectral types, resulting in a growing accumulation of late-T and Y dwarfs (Burgasser 2004a). Day-Jones et al. (2013) calculate errors of ∼17% and ∼40% for their estimates of the space density of L7–T0.5 and T1–T4.5 dwarfs, respectively. A larger sample of L/T objects will improve these estimates, allowing more accurate assessments of the local ultracool IMF.

L/T transition dwarfs are of further interest because their spectral features indicate significant variations in surface gravity, metallicity, and/or atmospheric clouds (Kirkpatrick 2005 and references therein). In particular, many changes in these spectral features are

thought to arise from the depletion of condensate clouds as brown dwarfs cool (e.g., Allard et al. 2001; Burrows et al. 2006; Saumon & Marley 2008), making L/T transition dwarfs ideal for case studies of cloud formation and gas chemistry in ultracool atmospheres. One notable example is the ~ 0.5 mag J-band brightening across the L/T transition as thick clouds dissipate to reveal lower, warmer layers of the photosphere, observed in isolated objects (Tinney et al. 2003; Dupuy & Liu 2012) as well as the components of L/T binaries (Liu et al. 2006; Looper et al. 2008a).

Another likely consequence of evolving and thinning clouds is photometric variability. Optical variability is known to be common in L dwarfs (Rockenfeller et al. 2006) and is typically periodic on timescales of several hours, consistent with rotation periods of brown dwarfs (Bailer-Jones 2004; Reiners & Basri 2008). However, detection of infrared variability has proven to be much more elusive (e.g., Enoch et al. 2003; Koen et al. 2005; Goldman et al. 2008). The first unambiguous detections of near-IR photometric variability in T dwarfs were in SIMP J013656.57+093347.3 (T2.5; Artigau et al. 2009, hereinafter SIMP 0136+0933) and 2MASS J21392676+0220226 (T1.5; Radigan et al. 2012, hereinafter 2MASS 2139+0220). Notably, both of these objects are members of the L/T transition. Apai et al. (2013) have subsequently detected J- and H-band spectral variability in these objects. Buenzli et al. (2012) discovered multiband infrared sinusoidal variability in the T6.5 dwarf 2MASS 2228−4310, along with a wavelength dependence of the variability phase, indicative of vertical cloud structure. Most recently, Khandrika et al. (2013) identified photometric J-band variability in two mid-L dwarfs and K-band variability in a T8 dwarf, while also confirming the J-band variability of 2MASS 2139+0220. These observations collectively suggest that variability is a normal feature of ultracool dwarfs. Khandrika et al. (2013) estimate a variability fraction of $35\% \pm 5\%$, and surprisingly find no strong evidence of a greater frequency for L/T transition objects.

Any search for brown dwarfs, especially those in the L/T transition, must also account for binaries. L+T binaries can have colors and composite spectra that mimic those of single L/T transition dwarfs (Burgasser 2007a) and can exaggerate the amplitude of the

J-band brightening (Liu et al. 2006; Dupuy & Liu 2012). Components of binary systems are valuable benchmarks, as they are coeval, equidistant, and have common metallicities. They are especially valuable in the L/T transition, where they can help to set tight constraints on the observed atmospheric transitions (Dupuy et al. 2009b; Liu et al. 2010). Compared to their stellar analogs, field brown dwarf binaries tend to have smaller separations (Allen et al. 2007) and mass ratios closer to unity (Allen 2007). This enables determination of their orbits and dynamical masses (e.g., Bouy et al. 2004; Liu et al. 2008; Dupuy et al. 2010; Konopacky et al. 2010), which breaks the mass/age degeneracy that plagues field brown dwarf analysis.

To increase the census of L/T transition dwarfs, we have begun a search using PS1 and *WISE*, leveraging the combined data of these optical and mid-infrared surveys. In order to construct a well-defined sample of L/T transition dwarfs, we have limited our search to candidates within 25 parsecs of the Sun, based on their photometric distances. Several past projects, including the Gliese catalog (Gliese & Jahreiss 1995) and the PMSU M dwarf survey (Reid et al. 2002a, and references therein), have searched this same volume of space for stars, so our project is well-matched to previous efforts. Our search will address a known deficiency in the solar neighborhood census, significantly improve the constraints on the local substellar mass and luminosity functions, and identify a well-defined, volume-limited sample of late L and early T dwarfs that can be used to better understand the evolution of brown dwarfs through the L/T transition.

In this paper, we present the first results of our ongoing search, namely the discovery of seven L/T transition dwarfs within 15 pc. Three objects are entirely new discoveries. The other four were identified independently by Mace et al. (2013a, hereinafter M13) in their search for T dwarfs in *WISE*, though without distance estimates. (Our spectroscopic confirmation preceded the publication of M13.) We explain our search process in Section 2.2. We describe our observations in Section 2.3, and our discoveries in Section 2.4. We discuss the properties of specific discoveries in Section 2.5, and summarize our findings in Section 2.6.

2.2 Search Method

We identified candidate L/T dwarfs through a series of quality, color, and magnitude cuts applied to our merged PS1+*WISE* database, followed by visual inspection of PS1, 2MASS, and *WISE* images. We then obtained and typed spectra of candidates using standard procedures described in Section 2.3.

The PS1 3π survey (Chambers et al., in prep) is obtaining multi-epoch imaging in five optical bands ($g_{\rm P1}, r_{\rm P1}, i_{\rm P1}, z_{\rm P1}, y_{\rm P1}$) with a 1.8-meter wide-field telescope on Haleakala, Maui, covering the entire sky north of declination $-30°$. Images are processed nightly through the Image Processing Pipeline (IPP; Magnier 2006, 2007; Magnier et al. 2008), with photometry on the AB magnitude scale (Tonry et al. 2012). Imaging began in May 2010 and should be completed by early 2014. The *WISE* All-Sky Release includes data taken between January and August 2010 (Cutri et al. 2012) in four mid-infrared bands: $W1$ (3.6 μm), $W2$ (4.5 μm), $W3$ (12 μm), and $W4$ (22 μm). We merged all PS1 detections through January 2012 with the *WISE* All-Sky catalog using a $3.0''$ matching radius. Because the two surveys are nearly contemporaneous, matching by position is effective for all but the highest proper motion objects. Matching the two surveys by position also eliminates transient objects (e.g., asteroids) in regions the surveys have only covered once. Candidates were selected from the full three-quarters of sky covered by the merged database.

To extract candidate L/T transition dwarfs from our PS1+*WISE* database, we applied the following quality-of-detection criteria (items shown in parentheses refer to flags within the database):

1. Detected in at least two separate $y_{\rm P1}$ frames (`y:nphot` $\geq$ `2`), to reject transients.

2. $\sigma_y < 0.2$ mag (`y:err` $<$ `0.2`), establishing S/N > 5 as the detection threshold for $y_{\rm P1}$.

3. "Good" or "poor" quality $y_{\rm P1}$ photometry, but not "bad", as defined in the PS1 DVO database (`y : flags = 256` or `y : flags = 512`), i.e., clear PSF identification, no saturated objects or cosmic rays.

4. $W1$ and $W2$ detections have S/N > 2 (`ph_qual = A, B,` or `C`).

5. $W1$ and $W2$ detections are not saturated (`w1sat` $= 0$ and `w2sat` $= 0$).

6. $W1$ and $W2$ detections are point sources (`ext_flg` $= 0$).

7. $W1$ and $W2$ detections are unlikely to be variable (`var_flg` ≤ 4).

We thus required that candidates have good detections in $y_{\rm P1}$, $W1$, and $W2$, but not necessarily in any other bands. We then applied the following color criteria, which are illustrated by Figures 2.1–2.3:

1. No more than one total detection in either $g_{\rm P1}$ or $r_{\rm P1}$ (`g:nphot` + `r:nphot` < 2), unless each band had only a single detection with $\sigma > 0.2$ mag. Among known L/T transition dwarfs, none are detected in $g_{\rm P1}$ and only one in $r_{\rm P1}$ — the nearby, unusually blue L6 dwarf SDSS J1416+1348 (Bowler et al. 2010). We therefore expect previously undiscovered L/T transition dwarfs to be too red to show up in $g_{\rm P1}$ and $r_{\rm P1}$ and this criterion rejects objects that are clearly detected in these bluer bands.

2. $i_{\rm P1} - z_{\rm P1} \geq 1.8$ mag (Figure 2.1), to exclude objects of spectral type mid-L and earlier. We applied this criterion only when the $i_{\rm P1}$ and $z_{\rm P1}$ photometry for an object met the same quality standards required for $y_{\rm P1}$ detections, i.e., $\sigma_i < 0.2$ mag and $\sigma_z < 0.2$ mag (`i:err` < 0.2 and `z:err` < 0.2) with at least two detections in both $i_{\rm P1}$ and $z_{\rm P1}$ (`i:nphot` ≥ 2 and `z:nphot` ≥ 2, to reject transient detections). Of the L/T transition dwarfs too faint to have been previously discovered in 2MASS and SDSS, even the brightest are likely to be near the detection limits of $i_{\rm P1}$ and $z_{\rm P1}$. (In fact, we do not detect any known T dwarfs in $i_{\rm P1}$.) So we only applied this cut when we had good quality photometry in both bands, and accepted objects with marginal or null detections in $i_{\rm P1}$ and $z_{\rm P1}$ as long as they passed the other cuts. We note that this criterion is somewhat more relaxed than the $i - z > 2.2$ mag and $\sigma_z < 0.12$ mag cuts used by Chiu et al. (2006) in their SDSS brown dwarf search.

3. $i_{\rm P1} - y_{\rm P1} \geq 2.8$ mag (Figure 2.1), also to exclude objects of spectral type mid-L and earlier. Again, we only applied this criterion if the $i_{\rm P1}$ photometry for an object met the same quality standards required for $y_{\rm P1}$ detections, i.e., $\sigma_i < 0.2$ mag (`i:err` < 0.2) and detection in $i_{\rm P1}$ in at least two separate frames (`i:nphot` ≥ 2).

4. $z_{\rm P1} - y_{\rm P1} \geq 0.6$ mag (Figure 2.2), to screen out early-M dwarfs. Similarly to the $i_{\rm P1} - z_{\rm P1}$ and $i_{\rm P1} - y_{\rm P1}$ cuts, we only applied this cut if the $z_{\rm P1}$ photometry for an object met the same quality standards required for $y_{\rm P1}$ detections, i.e., $\sigma_z < 0.2$ mag (`z:err` < 0.2) and detection in $z_{\rm P1}$ in at least two separate frames (`z:nphot` ≥ 2). This cut was also used by D11 in their PS1+2MASS T dwarf search.

5. $y_{\rm P1} - W1 \geq 3.0$ mag (Figure 2.3), to screen out early- and mid-M dwarfs. We expect this cut will have also rejected some late T dwarfs (SpT $\gtrsim$ T6), which have bluer $y_{\rm P1} - W1$ colors than L/T transition dwarfs.

6. $W1 - W2 \geq 0.4$ mag (Figure 2.3), to remove as many M and early-L dwarfs as possible. Kirkpatrick et al. (2011) and M13 used this same cut in their *WISE* search for nearby L and T dwarfs, but also restricted their search to bright objects with no 2MASS counterpart (i.e., objects which had moved more than 3" between 2MASS and *WISE*), criteria that we do not use here. Liu et al. (2011b) used a redder $W1 - W2 > 0.7$ mag cut to search only for T dwarfs.

7. $W2 - W3 \leq 2.5$ mag (Figure 2.2), to screen out extragalactic sources, as suggested by Figure 12 of Wright et al. (2010). Many of our candidates were not actually detected in $W3$, but *WISE* reports a lower magnitude limit for all non-detections, so we used the $W2 - W3$ value as an upper limit in those cases. Kirkpatrick et al. (2011) and M13 used $W1 - W2 > 0.96(W2 - W3) - 0.96$ mag for this purpose.

We then applied cuts based on spatial position:

1. We rejected all candidates within 3° of the Galactic plane.

2. To avoid objects in reddened star forming regions, we inspected the (RA, Dec) positions of candidates within 20° of the Galactic plane and rejected those that were clumped in tight groups.

3. We further rejected all remaining candidates in the highly reddened regions identified by Cruz et al. (2003), unless a candidate had a proper motion measured with S/N > 3 (based on 2MASS and PS1 astrometry).

We then reviewed the available images for each remaining candidate in all five PS1 filters (*g, r, i, z, y*), all three 2MASS filters (*J, H, K*), and *WISE* $W1$, $W2$, and $W3$. We rejected objects that were clearly artifacts (e.g., diffraction spikes or halos) in one or more bands or non-point sources such as galaxies.

As a final filter, we required objects to have sufficiently red $y-J$ colors to be in the L/T transition. We cross-matched our candidate list with the 2MASS, UKIDSS DR8 (Hambly et al. 2008; Lawrence et al. 2012), and VISTA DR1 (Cross et al. 2012) catalogs, and used J magnitudes from those catalogs when available with $\sigma_J < 0.1$ mag. The UKIDSS photometric system uses MKO standards (Tokunaga et al. 2002) and is described in Hewett et al. (2006). The VISTA filters are similar to those of UKIDSS, except that VISTA uses a K_s filter similar to that of 2MASS (Lodieu et al. 2012c)[1]. (A precise calibration of the VISTA photometric system has not yet been published.) For objects not found in any of these catalogs, we obtained our own photometry with UKIRT/WFCAM on the MKO system (as described in Section 2.3). We selected objects with $y_{\rm P1} - J_{2MASS} \geq 1.8$ mag (Figure 2.4) or $y_{\rm P1} - J_{MKO} \geq 1.9$ mag, removing bluer objects that were likely to be late-M and early-L dwarfs from our candidate list. This cut does permit objects bluer than the $2.2 < y_{\rm P1} - J_{2MASS} < 5.0$ mag cut used by D11, who searched exclusively for T dwarfs. Unlike D11, we did not apply a $J-H$ cut to our sample.

Because of the spectral changes endemic to L/T objects, $y_{\rm P1}$ absolute magnitudes are almost flat across the transition, from about L8 to T3 spectral types. Therefore, choosing

[1]For VISTA bandpass information, see http://casu.ast.cam.ac.uk/surveys-projects/vista/technical/filter-set.

a $y_{\rm P1}$-magnitude limit approximately creates a volume-limited sample, with only modest contamination by intrinsically brighter objects that lie beyond the search radius. For follow-up observations, we chose candidates with $y_{\rm P1} < 19.3$ mag to search the solar neighborhood for single L/T objects out to 25 pc, acknowledging that our search will also detect unresolved binaries out to larger distances.

2.3 Observations

We obtained follow-up near-IR imaging of our candidates using WFCAM (Casali et al. 2007) on the United Kingdom InfraRed Telescope (UKIRT) in queue mode. Over five nights spanning 2012 September 19–21 and 2012 December 13–14 UT, we observed a total of 308 candidates in different combinations of the Y, J, H and K bands (MKO system). Conditions were generally clear with seeing $\approx 0.6''$ on the September nights, while the December nights had many high clouds with seeing $\approx 0.8''$. Data were reduced and calibrated at the Cambridge Astronomical Survey Unit using the WFCAM survey pipeline (Irwin et al. 2004; Hodgkin et al. 2009).

We obtained low resolution near-IR spectra for our seven discoveries over eight nights in 2012 September, October and November and 2013 January with the NASA Infrared Telescope Facility (IRTF). We obtained additional spectra for PSO J307.6784+07.8263 (hereinafter PSO J307.6+07) on 2013 April 3–5, contemporaneously with the nearby M1V star 2MASS J20410101+0014278 (West et al. 2011, hereinafter 2MASS J2041+0014) for comparison. We used the facility spectrograph SpeX (Rayner et al. 2003) in prism ($R \sim 100$) and SXD ($R \sim 750$) modes with the $0.5''$ and $0.8''$ slits. Details of our observations are listed in Table 2.1. We observed a nearby A0V star contemporaneously with each science target for telluric calibration. All spectra were reduced using version 3.4 of the Spextool software package (Vacca et al. 2003; Cushing et al. 2004).

Initial spectral typing of candidates was accomplished using spectral indices from Burgasser et al. (2006a), with spectral types assigned using the polynomial fits from

Burgasser (2007a). The spectra were then visually compared to near-infrared spectra for L dwarf (Kirkpatrick et al. 2010) and T dwarf spectral standards (Burgasser et al. 2006a) for final assignment of spectral types. Following the procedure of Kirkpatrick et al. (2010), when comparing our candidate spectra with L dwarf standards, we first compared only the $0.9 - 1.4$ μm portions of the spectra to evaluate the goodness of fit. If the best match for a candidate was determined to be an L dwarf standard, then we compared the candidate spectrum to that of the standard over $1.4 - 2.4$ μm to determine if the candidate was unusually red or blue for its spectral type. When comparing candidates to T dwarf standards, we judged the goodness of fit for the entire $0.9 - 2.4$ μm window simultaneously.

2.4 Results

We present here seven bright initial L/T transition discoveries from our ongoing search. Our photometric distances place all seven within $9 - 15$ pc of the Sun, assuming they are single objects and not unresolved binaries. The astrometric, photometric, and spectral properties of these objects are listed in Tables 2.2 and 2.3. Near-IR SpeX prism spectra for these objects are shown in Figure 2.5.

Four of our seven new objects have been announced by M13 in their search for late-T and Y dwarfs in *WISE*; our discovery of all four was independent (our spectroscopic confirmation preceded publication of their paper). For the most part, we agree with the spectral indices and types published by M13, and we present additional photometry, photometric distances, astrometry, and spectral indices for the four objects, as well as higher-resolution SXD spectra for two of them. Specific objects are discussed in Section 2.5.

We used the $W2$ absolute magnitude vs. spectral type polynomial from Dupuy & Liu (2012)[2] to calculate photometric distances. The $W2$ polynomial was determined using objects of spectral types M5.5 to T9 and has an rms scatter about the fit of 0.35 mag (slightly lower than the rms scatter of 0.39 mag for the $W1$ polynomial). However, the

[2]Updated polynomials can be found in the Database of Ultracool Parallaxes maintained by Trent Dupuy at https://www.cfa.harvard.edu/~tdupuy/plx/Database_of_Ultracool_Parallaxes.html. Here we use the version posted on 2012 June 09.

scatter about the fit is smaller for later spectral types than for M dwarfs. Liu et al. (2011b) calculated an rms scatter of 0.18 mag for a $W2$ polynomial relationship using only objects with spectral types L5 and later. We adopted this rms to determine the uncertainty in the distance.

We combined 2MASS and PS1 astrometry to calculate proper motions for our discoveries and used our photometric distances to estimate tangential velocities. A comparison of these v_{tan} estimates to the $\sigma_{v_{tan}}$ vs. v_{tan} relations in Dupuy & Liu (2012, Figure 31) indicates that all seven discoveries are very likely to be members of the thin disk.

Figures 2.1–2.4 display $i_{\rm P1}$ through $W3$ colors of known ultracool dwarfs[3], overlaid with our seven discoveries. Compared with other early-T dwarfs, PSO J307.6+07 (T1.5) is unusually blue in $y_{\rm P1} - W1$ (by ~ 0.7 mag) and $y_{\rm P1}-J_{\rm 2MASS}$ (by ~ 0.3 mag), suggesting that its $y_{\rm P1}$ flux is unusually bright. In addition, the six objects that have spectral types L9−T1.5 are all bluer than typical late-L and early-T dwarfs by about half a magnitude in $y_{\rm P1}-J_{\rm 2MASS}$. We find no systematic reason why our search method would preferentially discover objects that are bluer in $y_{\rm P1}-J_{\rm 2MASS}$. It is possible that the previous searches that identified the known objects were biased toward finding objects with redder $y_{\rm P1}-J_{\rm 2MASS}$ colors (e.g., D11).

2.5 Discussion

2.5.1 Candidate Spectroscopic Variables

PSO J140.2308+45.6487 (hereinafter PSO J140.2+45), also known as WISE 0920+4538, and PSO J307.6+07, also known as WISE J2030+0749, are the second and third L/T transition dwarfs to be identified as candidate near-IR variables via spectroscopy, following SDSS J125453.90−012247.4 (Goldman et al. 2008). Spectra of PSO J140.2+45 taken on two different nights (Figure 2.6) show small but clear differences in the Y- and J-bands, while for PSO J307.6+07 (Figure 2.7) the difference in J-band is readily apparent.

[3]Compiled from DwarfArchives.org as of April 2011, Leggett et al. (2010), Burgasser et al. (2011b), and Gelino et al. (2011).

For comparison, Figure 2.8 shows SXD and prism spectra for PSO J339.0734+51.0978 (hereinafter PSO J339.0+51) taken ten nights apart with no clear variability.

For all three of these objects, we have normalized the pairs of spectra to the H-band peak (1.58 μm). These spectra are not absolutely calibrated, so we cannot determine with certainty the absolute changes in flux in each band; however, we note that each object's H- and K-bands show no significant change in spectral shape or in flux relative to the adjacent absorption bands. We calculated the differences in flux in the Y- and J-bands for each pair of spectra by first convolving our spectra in the wavelength intervals $0.95 - 1.13$ μm and $1.16 - 1.33$ μm with the UKIDSS Y ($0.97 - 1.07$ μm, Hewett et al. 2006) and J ($1.17 - 1.33$ μm, Tokunaga et al. 2002) filter profiles, respectively. We then integrated the convolved spectra over each interval, subtracted to get the differences in flux, and converted these flux differences and their uncertainties to magnitudes. In addition, we calculated the differences in magnitude in the narrow peaks of the Y-band ($1.06 - 1.10$ μm) and J-band ($1.27 - 1.30$ μm) using the same method.

Details of each candidate variable are described below; here we discuss briefly the possible causes of variability. Artigau et al. (2009) and Radigan et al. (2012) explain the J-band photometric variations in the early-T dwarfs SIMP 0136+0933 and 2MASS 2139+0220 as consequences of the clearing of atmospheric condensate clouds, the process thought to cause the observed J-band brightening in the L/T transition. The variations are seen only in the J-band because the condensates in question are primarily silicates that absorb most strongly at J-band wavelengths compared to other (gaseous) opacity sources (Ackerman & Marley 2001; Burrows et al. 2006). The clearing process is not well understood. Several scenarios have been proposed wherein condensate clouds thin gradually (reducing their opacities), rain out suddenly, or break up (e.g., Ackerman & Marley 2001; Knapp et al. 2004; Tsuji 2005; Burrows et al. 2006; Marley et al. 2010). Models using a mixture of thin and thick clouds may generate a better match to observed early-T dwarf spectra (Buenzli et al. 2012). Radigan et al. (2012) attempt a variety of model atmosphere fits to their observations of 2MASS 2139+0220 and find success combining models with different

condensate sedimentation efficiences, interpreted as heterogenous cloud formations. J-band variation over a period of several days could therefore be a sign of thinner and thicker clouds or even breaks in clouds, changing due to rotation and/or convective processes.

PSO J140.2308+45.6487 (WISE 092055.40+453856.3)

PSO J140.2+45 was first identified photometrically as a candidate L4–L5 brown dwarf (WISE 0920+4538) by Aberasturi et al. (2011) based on *WISE*/2MASS/SDSS photometry and measurable proper motion. Our spectra of PSO J140.2+45 taken two and a half months apart (Figure 2.6) indicate a marginal decrease of 0.05 ± 0.04 mag in the full Y-band, but a signficant decrease of 0.14 ± 0.03 mag in the Y-band peak. The decrease in J-band is also marginal: 0.05 ± 0.02 mag in the full band, and 0.03 ± 0.02 mag in the J-band peak. Visual classification of our SpeX spectrum for PSO J140.2+45 gives a spectral type L9.5, consistent with the L9.6 spectral type derived from the spectral indices. M13 classify this object as L9 and a weak binary candidate. Further observations are needed to confirm the near-IR variability of this object.

PSO J307.6784+07.8263 (WISE 203042.79+074934.7)

Figure 2.9 compares our SXD spectrum for PSO J307.6+07 with that of the T2 standard SDSS 1254−0122 (Leggett et al. 2000; Cushing et al. 2005; Burgasser et al. 2006a). No unusual spectral features are apparent in PSO J307.6+07 at this resolution ($R \sim 750$). The spectrum of PSO J307.6+07 is reasonably close to that of SDSS 1254−0122 but has slightly weaker methane absorption at $\sim$1.15 μm. The spectral indices have a mean classification of T0.9 $\pm$ 1.3. Given these estimates, we classify PSO J307.6+07 as a T1.5 dwarf. M13 identified this object as WISE 2030+0749 and assigned it the same spectral type.

Our spectra of PSO J307.6+07 taken six nights apart in 2012 September (Figure 2.7) show a decrease of 0.11 ± 0.02 mag in the full J-band, and 0.10 ± 0.02 mag in the J-band peak. The overlaid spectra also suggest an increase in the Y-band flux over the six-night

span, but we calculate this difference as only 0.02 ± 0.06 mag in the full Y-band, and 0.02 ± 0.05 mag in the Y-band peak.

Figure 2.10 shows spectra of PSO J307.6+07 obtained on three consecutive nights in 2013 April, along with the two 2012 September spectra from Figure 2.7. When examining the spectra of the comparison M1V star 2MASS J2041+0014 (presumably a non-variable source) from the same three April nights, we noticed a dimming at wavelengths $\lesssim 1.3\mu$m on April 3 compared to the two subsequent nights. This dimming may be due to the presence of a crescent Moon about 6° from the standard star during this night's observations. To correct for the dimming, we divided the April 4 spectrum of 2MASS J2041+0014 by its April 3 spectrum, and then multiplied this quotient into the April 3 spectrum of PSO J307.6+07. With this correction applied, the April data for PSO J307.6+07 show essentially no variation over the three nights. In the J-band, the April spectra also match well the 2012 September 20 spectrum, with only the September 26th SXD spectrum showing a clear difference in flux. However, in the Y-band, the April spectra all have noticeably lower flux than both of the September spectra.

Collectively, our data show significant spectrospcopic variation for PSO J307.6+07 in 2012 September, and no variation in 2013 April. The reason for this apparent contradiction is unclear. The long-term stability of near-IR spectrospcopic variations in L/T transition dwarfs is not well understood, so it is possible that the 2012 September observations simply occurred during an epoch of variability for PSO J307.6+07, while the 2013 April observations found the object in an epoch of constancy (or diminished variability). It is also possible that the detected variability is a result of an unrecognized oversight in the observations or data reduction. We note that the April data were obtained at higher airmass; care was taken during these observations to ensure the instrument slit was aligned with the parallactic angle, and the standard stars were observed at similar airmasses (within 0.1). We note as well that the September 26th spectrum is the only one obtained in SXD (cross-dispersed) mode. We have stitched the different orders together using the standard Spextool procedure *xcombspec* to create a single spectrum, and it is possible that this

procedure has scaled one or more orders to an incorrect flux. We consider this to be unlikely for three reasons: Cushing et al. (2005) showed that order stiching with *xcombspec* results in a mean color difference of $\langle \delta_{J-H} \rangle = 0.00 \pm 0.04$ mag, much smaller than the ΔJ we detected in PSO J307.6+07; we used the same stitching procedure to obtain the spectrum for PSO J339.0+51 (Figure 2.8), in which we find no significant variation; and we see similar spectral variation in PSO J140.2+45, where both spectra were obtained in prism mode. Overall, we cannot establish a decisive reason for the difference of the intra-night behavior between our 2012 Sept and 2013 April datasets, so we label PSO J307.6+07 a candidate spectroscopic variable. Further observations on multiple nights are needed to confirm or reject this object as a near-IR variable.

2.5.2 Candidate Photometric Variables

Since our seven discoveries are bright, they are all well detected in 2MASS. We can compare our MKO photometry to the 2MASS measurements as a simple two-epoch check for near-IR variability over a period of approximately ten years. (Note that we do not use our SpeX data to synthesize the conversions directly for each object, because the spectra and photometry were all obtained at different epochs.) We used the polynomial relations of Stephens & Leggett (2004, Table 4) to bring the two epochs of JHK photometry onto a common system. The UKIRT/WFCAM JHK filters were designed on the MKO photometric system, so we converted the 2MASS photometry for our discoveries to MKO. We find that the 2MASS and MKO JHK magnitudes of our objects are consistent within 0.1 mag, with two exceptions described below.

PSO J272.4689−04.8036 (WISE 180952.53−044812.5)

We assign a spectral type of T1 to PSO J272.4689−04.8036 (hereinafter PSO 272.4−04), although it is fainter in the H-band than the T1 standard SDSS J0151+1244 (Geballe et al. 2002; Burgasser et al. 2006a). M13 classify this object as a T0.5 (WISE 1809−0448). Its $J_{\rm MKO}$ magnitude, as converted from its 2MASS photometry, is 14.94 ± 0.06 mag, about

0.2 mag brighter than our UKIRT measurement of $J_{\rm MKO} = 15.15 \pm 0.01$ mag, a sign of potential J-band variability. The $K_{\rm MKO} = 13.99 \pm 0.06$ mag (converted from 2MASS) and VISTA $K_{\rm MKO} = 13.98 \pm 0.01$ mag measurements are consistent.

PSO J339.0734+51.0978 (WISE 223617.59+510551.9)

We find PSO J339.0734+51.0978 (hereinafter PSO J339.0+51) to be a good match to the T5 standard 2MASS J1503+2525 (Burgasser et al. 2003b, 2006a). Analysis of spectral indices gives a mean spectral type of T5.1 $\pm$ 0.1, so we assign a spectral type of T5, a half-type earlier than the T5.5 (WISE 2236+5105) assigned by M13. The $J_{\rm MKO}$ magnitude, converted from 2MASS, is 14.31 ± 0.04 mag, about 0.15 mag brighter than the UKIRT $J_{\rm MKO} = 14.46 \pm 0.01$ mag, so this object is another potential J-band variable. The H-band magnitudes of $H_{\rm MKO} = 14.53 \pm 0.05$ mag (converted from 2MASS) and UKIRT $H_{\rm MKO} = 14.62 \pm 0.02$ mag are consistent within 2σ. We do not have $K_{\rm MKO}$ photometry for PSO J339.0+51. We note that this object does not show any difference in spectra taken ten nights apart (Figure 2.8).

2.5.3 Candidate Binaries

We have examined our seven discoveries for unusual spectral features that might suggest unresolved binarity, by comparing their spectral indices to the index-index and index-spectral type plots in Burgasser et al. (2010a, hereinafter B10). We found evidence for binarity in two of our discoveries, described individually below. We performed spectral decomposition analysis on these two objects following the method described in Section 5.2 of Dupuy & Liu (2012). Briefly, we used the library of 178 IRTF/SpeX prism spectra presented in B10 to create summed spectra. For each template pairing we determined the scale factors needed to minimize the χ^2 of the difference with our observed spectrum. We then examined the resulting best pairing to determine the component spectral types, taking into account factors such as larger than average spectral type uncertainties in the best-match templates and the full range of properties implied when there were multiple

matches giving equally good fits. We estimated the flux ratios in standard near-infrared bandpasses using our χ^2 values and the weighting scheme described in Burgasser et al. (2010a). Our derived component spectral types and their corresponding uncertainties are listed in Table 2.4, and the best template pairing for each binary is shown in Figure 2.11. (Our analysis does not assess whether binary templates are better matches to our observed spectra than single-object templates.) For these template pairs, we calculate photometric distances by convolving absolute magnitudes for each component spectral type, determined using the same method as in Section 2.4.

PSO J103.0927+41.4601

Visually, the spectrum of PSO J103.0927+41.4601 (hereinafter PSO J103.0+41) appears to be a slightly earlier spectral type than the T0 standard SDSS J1207+0244 (Knapp et al. 2004; Burgasser et al. 2006a). The spectral indices, however, indicate a spectral type of T0.5 for PSO J103.0+41. Assuming this is a single object, we settle on a classification of T0, placing the object at a photometric distance of 14.2 ± 1.2 pc. However, the closest spectral match is in fact the L6+T2 binary SDSS 0423−0414AB (Geballe et al. 2002; Burgasser et al. 2005b; Dupuy & Liu 2012), and we find excellent agreement with a template pairing of L8+T2.5 (Figure 2.11, Table 2.4), which would indicate a distance of 20.1 ± 2.4 pc. PSO J103.0+41 also lies on the border of the binary regions in three of the B10 index-index plots. This object is therefore an appealing candidate for high-resolution imaging.

PSO J282.7576+59.5858

PSO J282.7576+59.5858 (hereinafter PSO J282.7+59) is not a good match to any of the T dwarf spectral standards. Its spectral indices average to L8.5, and our best visual J-band fit is L9, but the H- and K-band peaks have lower flux than the L9 standard 2MASS J0255−4700 (Martín et al. 1999b; Kirkpatrick et al. 2010). The shape of the H-band peak is almost flat with a slight increase toward longer wavelengths, a feature more typical of early L-dwarfs (see Figure 10 in Kirkpatrick et al. 2010). We tentatively classify

PSO J282.7+59 as an L9 for a single object (photometric distance 13.0 ± 1.1 pc), but the discordance in its spectral features suggests that we are looking at a blended spectrum. The best spectral match among known ultracool dwarfs is actually the suspected triple system DENIS-P 0205−1159 (Bouy et al. 2005). The spectral indices of PSO J282.7+59 do not place it in any of the binary regions of the B10 index-index plots, but B10 noted that their selection process was probably biased against systems with more than two components. We find the best match for binaries has a template pairing of L7+T4.5 (Figure 2.11, Table 2.4), at a distance of 17.9 ± 2.1 pc.

2.5.4 Our Discoveries in Other Surveys

All seven of the newly discovered objects are brighter than most known L/T transition dwarfs. This raises the question of why the objects were not discovered earlier. One reason is that several of the major surveys used in previous brown dwarf searches covered smaller fractions of the sky than PS1. Of our seven objects, only two are in regions covered by SDSS (PSO J103.0+41 and PSO J142.2+45) and only two lie within the UKIDSS search area (PSO J007.7921+57.8267 and PSO J142.2+45 again). Another reason is that we have searched close to the Galactic plane, using proper motion as well as colors to distinguish brown dwarf candidates from reddened background objects. Three of our seven discoveries have $|b| < 10°$, putting them in crowded regions commonly avoided in previous searches (e.g., Burgasser et al. 2004). Our combination of $y_{\rm P1}$ and $WISE$ photometry has also enabled us to discover objects whose JHK colors were excluded in near-infrared searches (e.g., Cruz et al. 2003).

2.6 Summary

We have discovered seven L/T transition dwarfs within $9 - 15$ pc of the Sun based on a search of the combined Pan-STARRS1 3π and *WISE* databases. We highlight several specific objects:

- PSO J140.2+45 (L9.5) and PSO J307.6+07 (T1.5) show changes in their J-band spectra taken on different nights. PSO J140.2+45 also shows a marginal change in Y-band flux. If confirmed by subsequent observations, these would be the third and fourth known near-infrared L/T transition variables, and PSO J307.6+07 would be the second brightest, following SIMP 0136+0933. PSO J307.6+07 also has unusually blue $y_{\rm P1} - W1$ and $y_{\rm P1} - J$ colors compared to previously known objects of similar spectral type.

- PSO J272.4−04 (T1) and PSO J339.0+51 (T5) have inconsistent 2MASS and UKIRT J magnitudes (by 0.2 and 0.15 mag, respectively), possibly signs of J-band variability.

- PSO J103.0+41 (T0) and PSO J282.7+59 (L9) show spectral evidence that they are not single objects, including similarity to previously known multiple systems. High resolution spatial and spectroscopic observations are needed to investigate the possible multiplicity of these objects.

These brown dwarfs are all relatively bright ($J < 15.5$) and easily close enough for accurate parallax measurements. All seven are excellent targets for observations studying the atmospheric processes endemic to the L/T transition.

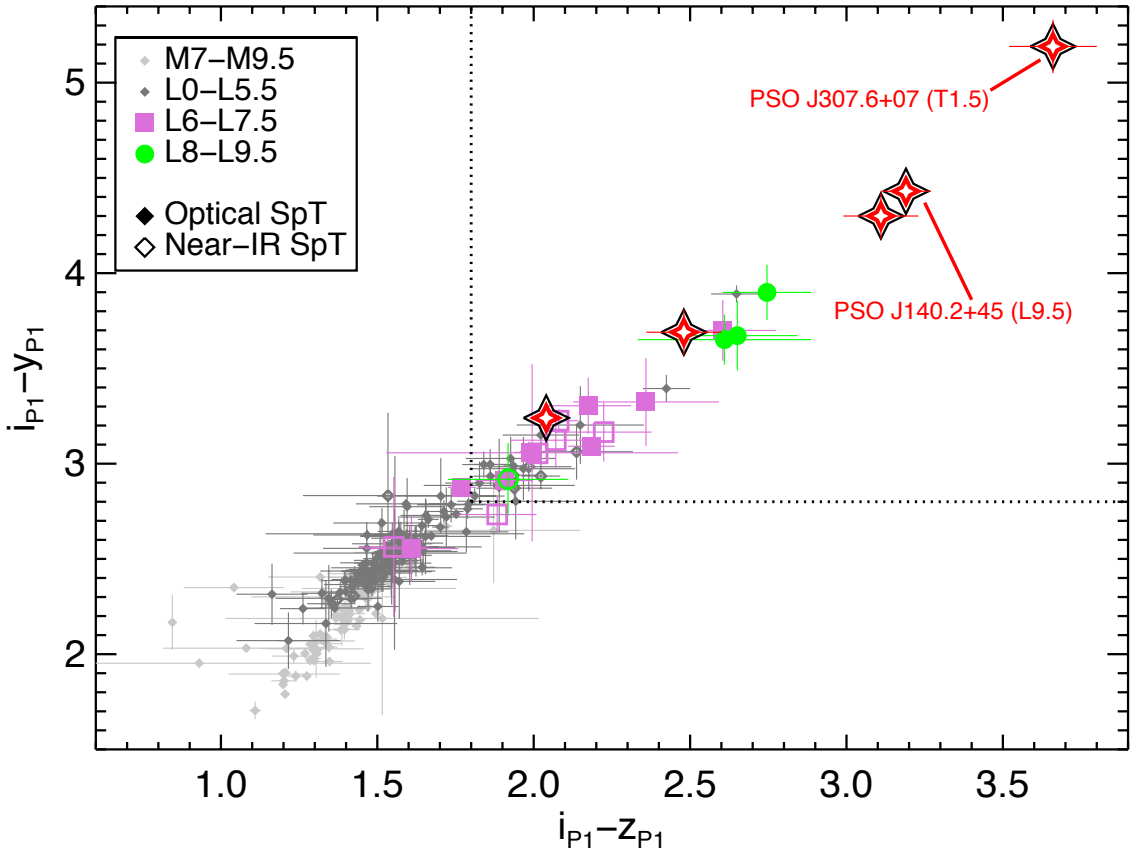

Figure 2.1 $i_{\rm P1} - z_{\rm P1}$ vs. $i_{\rm P1} - y_{\rm P1}$ diagram for known ultracool dwarfs. Late-L dwarfs are indicated with magenta squares (types L6–L7.5) and green circles (L8–L9.5); no known T dwarfs have $i_{\rm P1}$ detections in our PS1+*WISE* database. Objects with optical spectral types are plotted with filled symbols, and objects with near-infrared spectral types are plotted with open symbols. The dotted black lines indicate the color cuts used in our search; we selected objects above and to the right of the dotted lines, but only enforced each cut for objects which had $\sigma < 0.2$ mag and at least two detections in both bands. Our newly identified objects are marked with large red four-point stars, with the spectroscopic variable candidates labeled individually. (Two of our discoveries and many known L dwarfs were also not detected in $i_{\rm P1}$.) The new discoveries clearly extend the linear $i_{\rm P1} - z_{\rm P1}$ vs. $i_{\rm P1} - y_{\rm P1}$ locus to redder colors.

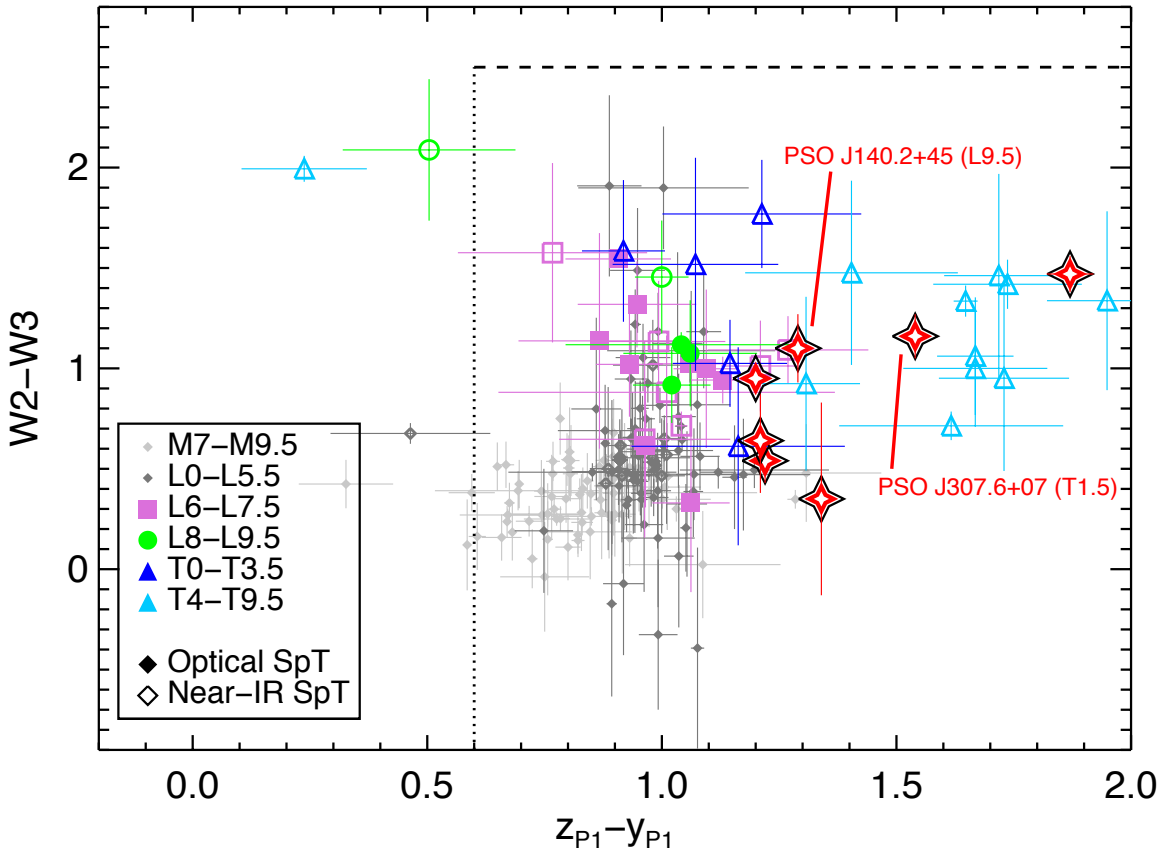

Figure 2.2 $W2-W3$ vs. $z_{\rm P1}-y_{\rm P1}$ diagram for known ultracool dwarfs, using the same colors and symbols as Figure 2.1; in addition, early-T dwarfs are indicated by dark blue triangles, and mid- and late-T dwarfs by light blue triangles. The vertical dotted line indicates our $z_{\rm P1}-y_{\rm P1}$ cut, which we applied only to objects with $\sigma_z < 0.2$ mag and at least two $z_{\rm P1}$ detections. The horizontal dashed line repesents our $W2-W3$ cut, which we applied to all objects in our search. We selected objects below and to the right of these lines.

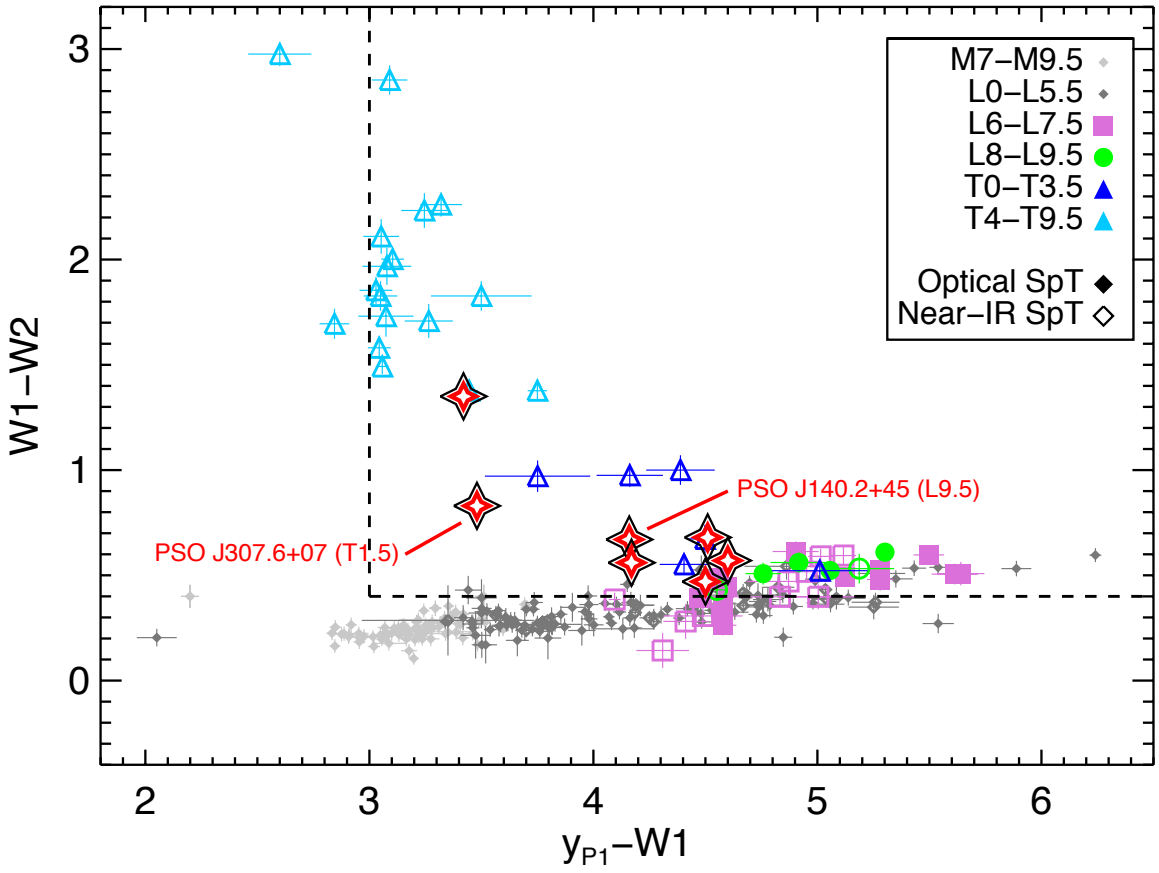

Figure 2.3 $W1 - W2$ vs. $y_{\rm P1} - W1$ diagram for known ultracool dwarfs, using the same colors, lines and symbols as Figures 2.1 and 2.2. We selected objects with colors above and to the right of the dashed lines. All of our discoveries lie in the typical region of this color space for late-L and early-T dwarfs, except that PSO J307.6+07 is fairly blue in $y_{\rm P1} - W1$ for an early-T dwarf.

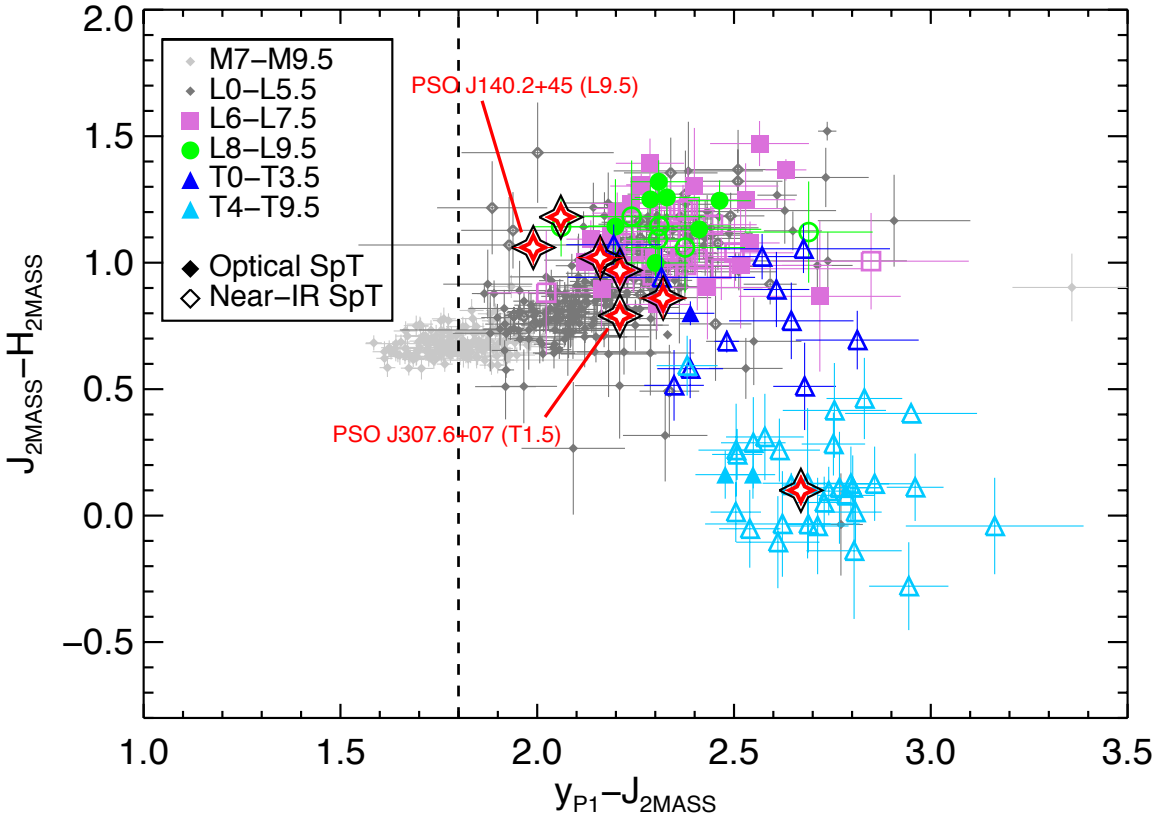

Figure 2.4 $J_{2\mathrm{MASS}} - H_{2\mathrm{MASS}}$ vs. $y_{\mathrm{P1}} - J_{2\mathrm{MASS}}$ diagram for known ultracool dwarfs, using the same colors, lines and symbols as Figures 2.1 and 2.2. We selected objects to the right of the dashed line. The red object at lower right is the T5 PSO J339.0+51; the other red objects have spectral types L9−T1. PSO J339.0+51 has typical $J_{2\mathrm{MASS}} - H_{2\mathrm{MASS}}$ and $y_{\mathrm{P1}} - J_{2\mathrm{MASS}}$ values for its spectral type, while all of our other new discoveries are blue in $y_{\mathrm{P1}} - J_{2\mathrm{MASS}}$ compared to known late-L and early-T dwarfs, possibly because previous searches have tended to find redder objects.

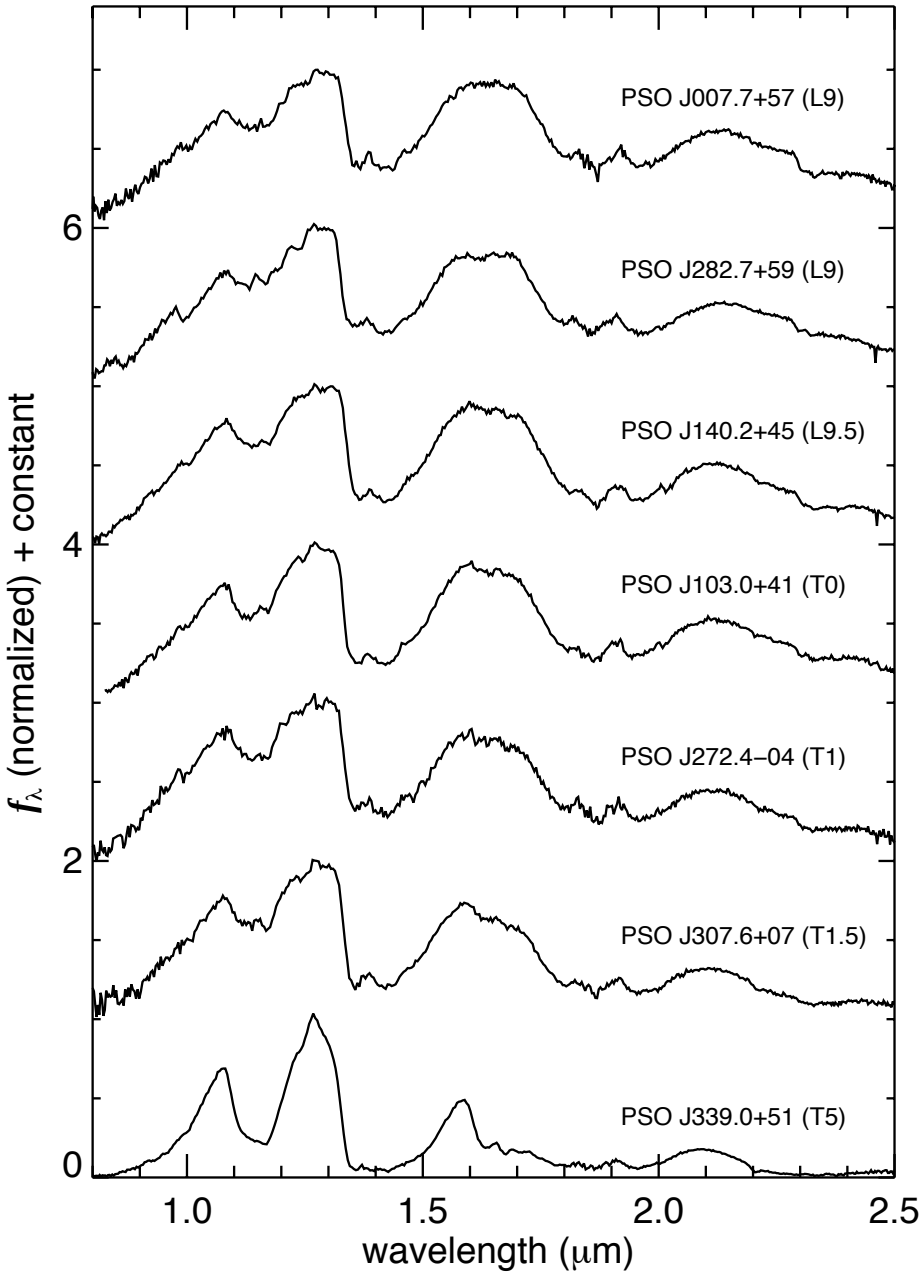

Figure 2.5 SpeX prism spectra for our seven objects, normalized at the J-band peak ($1.27\,\mu$m), arranged from earliest to latest spectral type and offset by a constant. Spectral typing was done by visual comparison with the near-infrared standards defined by Burgasser et al. (2006a) and Kirkpatrick et al. (2010).

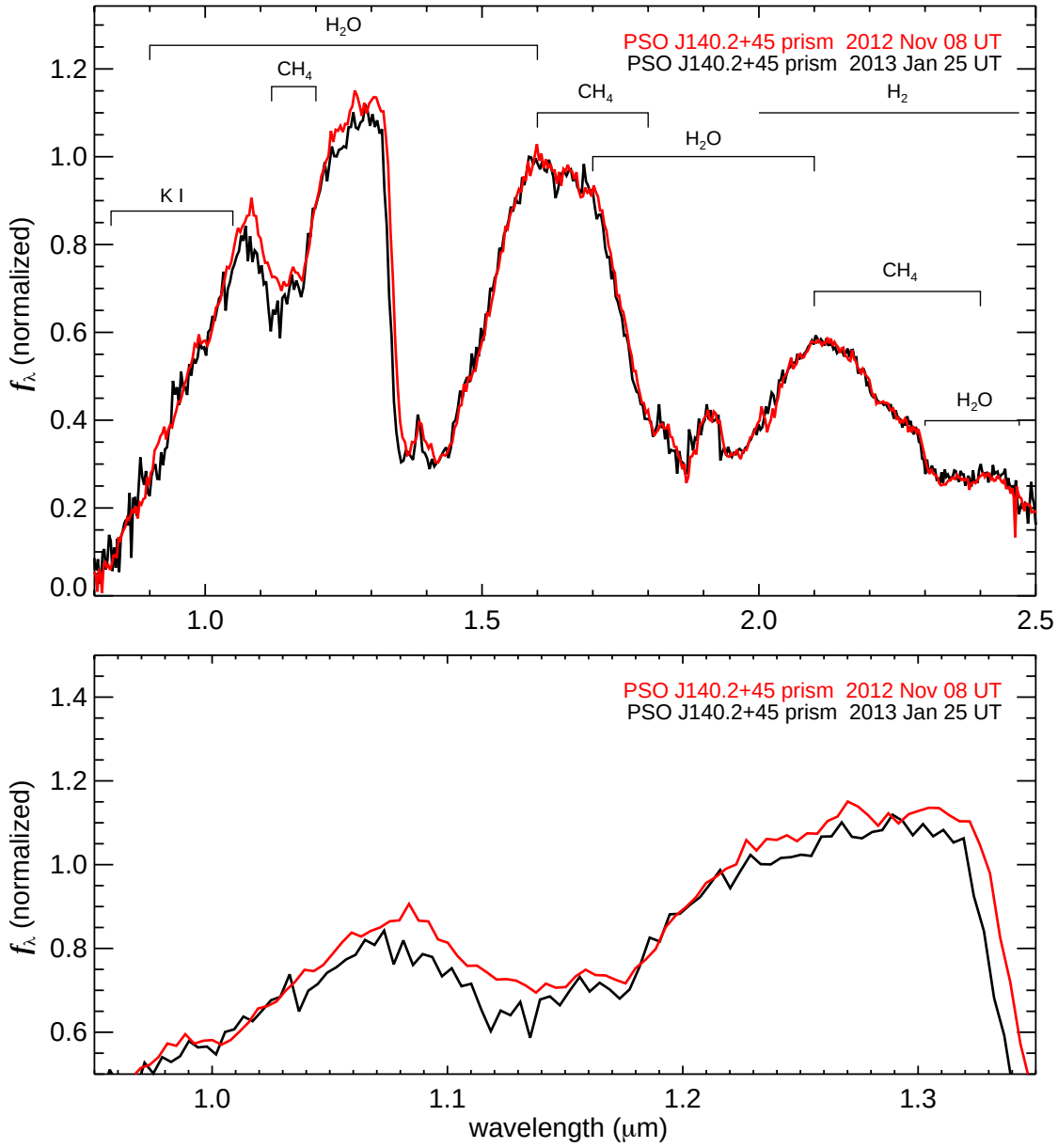

Figure 2.6 *Top:* Prism spectra ($R \sim 100$) for PSO J140.2+45 taken in November 2012 (black) and January 2013 (red), both with SpeX on IRTF. *Bottom:* Same as top window, but showing only the Y- and J-bands. The changes in flux in the Y-band peak ($1.06-1.10\ \mu$m) and marginally in the J-band ($1.16-1.33\ \mu$m) suggest variability similar to that previously detected in two other early-T dwarfs (Artigau et al. 2009; Radigan et al. 2012; Apai et al. 2013). The spectra have been normalized to the H-band peak ($1.58\,\mu$m) to highlight the Y- and J-band variations.

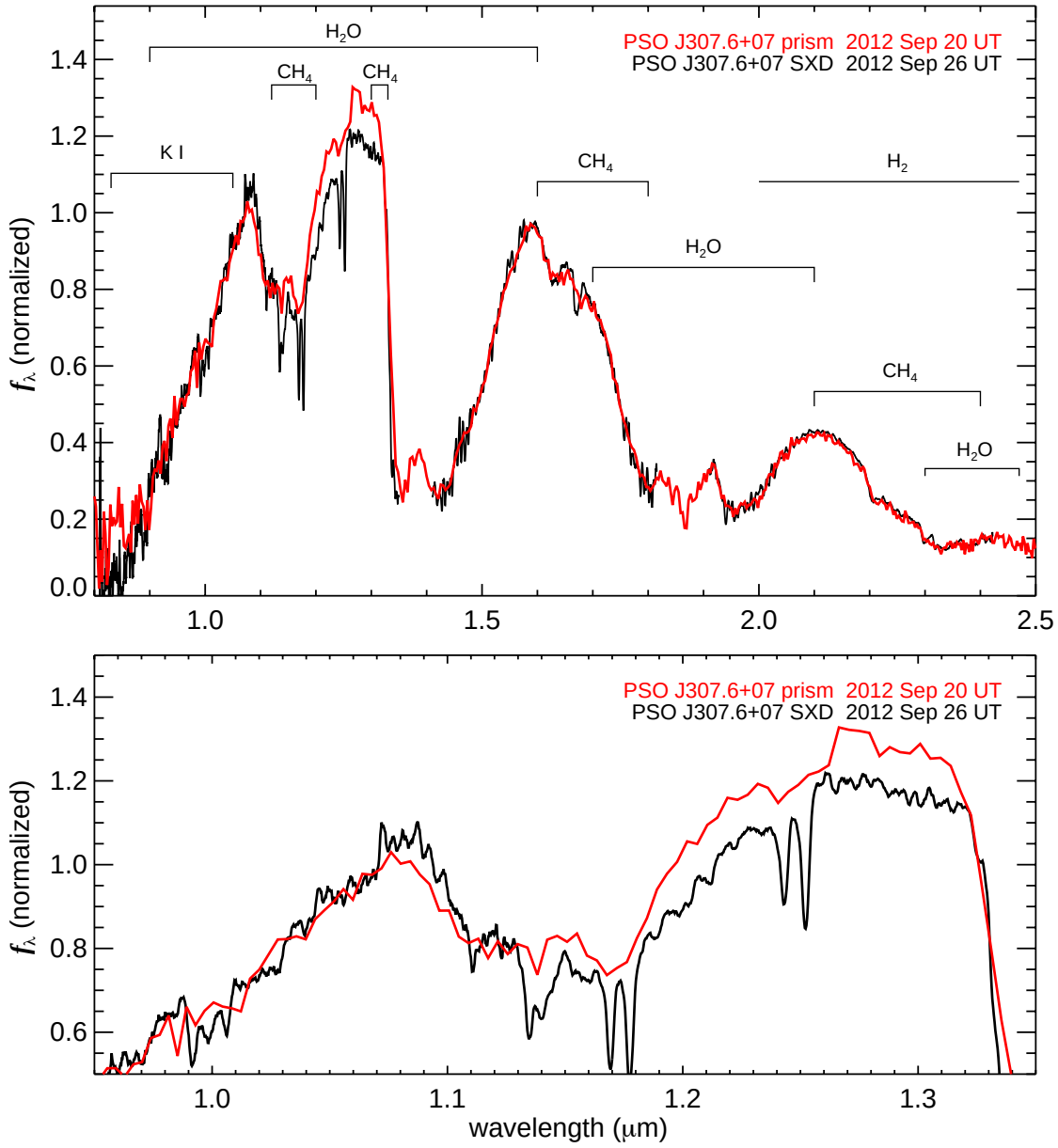

Figure 2.7 *Top:* Spectra for PSO J307.6+07 taken six nights apart, both with SpeX on IRTF. The prism spectrum (red) has $R \sim 100$ while the SXD spectrum (black) has $R \sim 750$ and is smoothed by an 8-pixel box. *Bottom:* Same as top window, but showing only the Y- and J-bands. The change in flux in the J-band ($1.16-1.33\ \mu$m) clearly suggests variability. The slight difference visible in the Y-band ($1.00-1.13\ \mu$m) flux is not statistically significant. The spectra have been normalized to the H-band peak ($1.58\,\mu$m) to highlight the J-band variation.

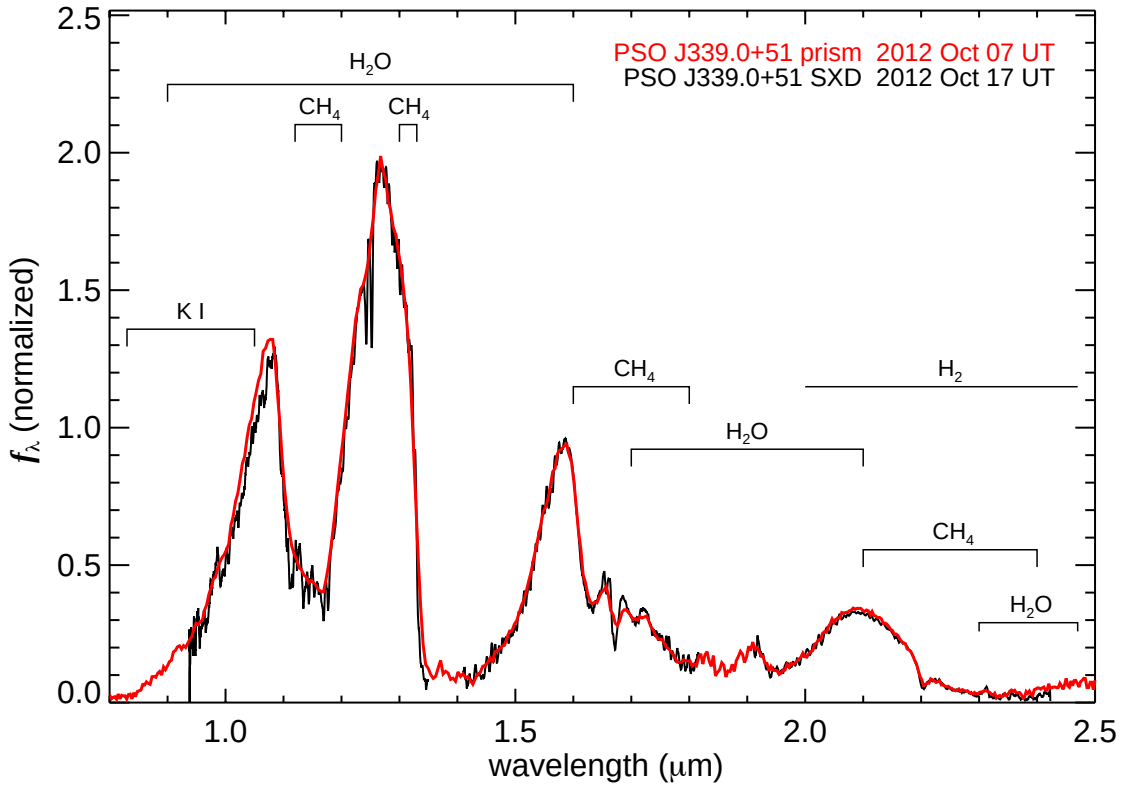

Figure 2.8 Spectra for PSO J339.0+51 taken ten nights apart, both with SpeX on IRTF. The prism spectrum (red) has $R \sim 100$ while the SXD spectrum (black) has $R \sim 750$ and is smoothed by an 8-pixel box. No clear sign of variability is seen between these two spectra; the slight difference visible in the Y-band ($1.00 - 1.13$ μm) flux is not statistically significant. As in Figures 2.6 and 2.7, these spectra have been normalized to the H-band peak.

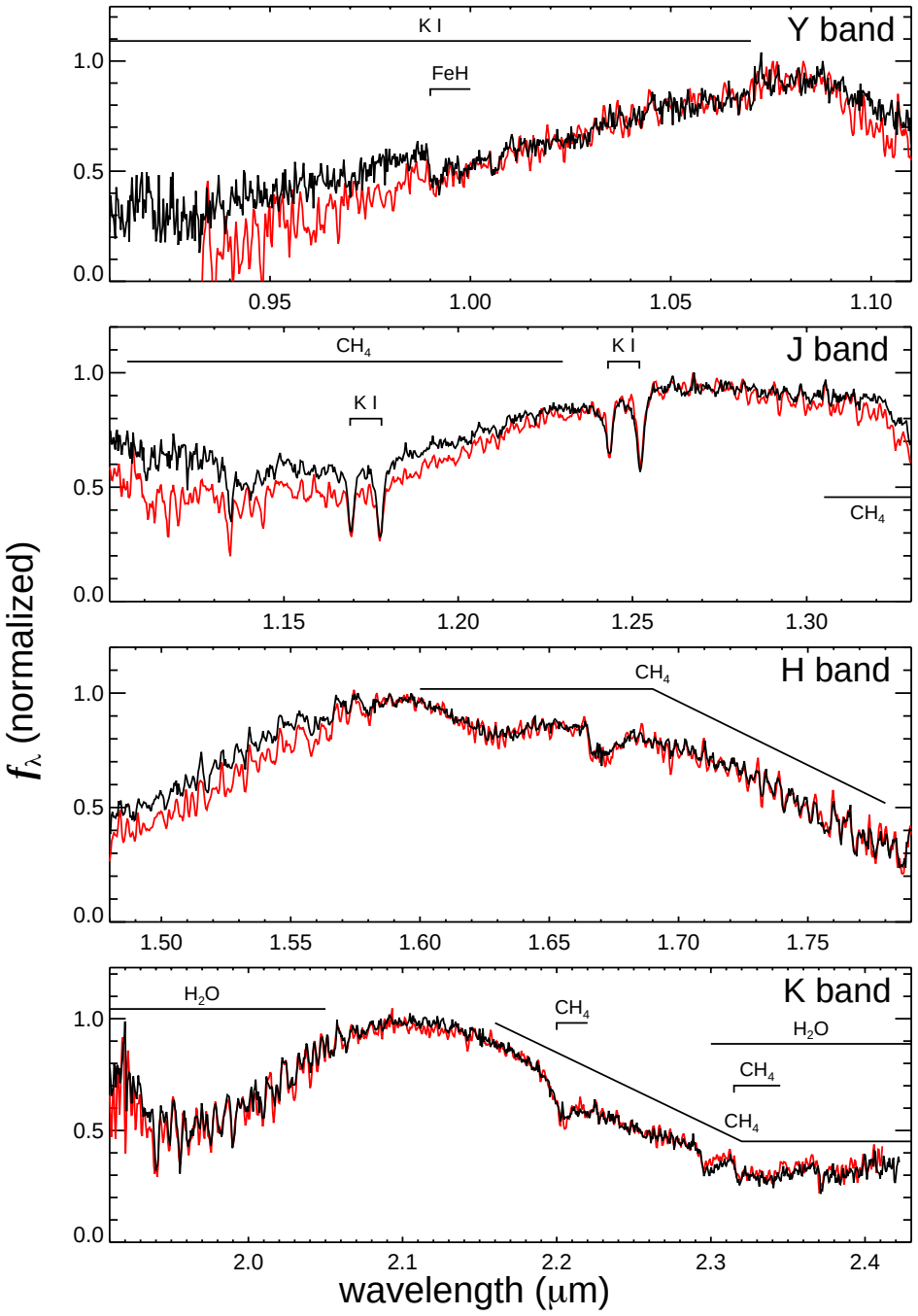

Figure 2.9 SpeX SXD spectra for PSO J307.6+07 (T1.5, black) and the T2 standard SDSS 1254−0122 (red, Cushing et al. 2005). The spectra are normalized to the peak value in each band and show the same prominent absorption features. The relative faintness of SDSS 1254−0122 in parts of the Y-, J- and H-bands is expected because PSO J307.6+07 is half a spectral type earlier.

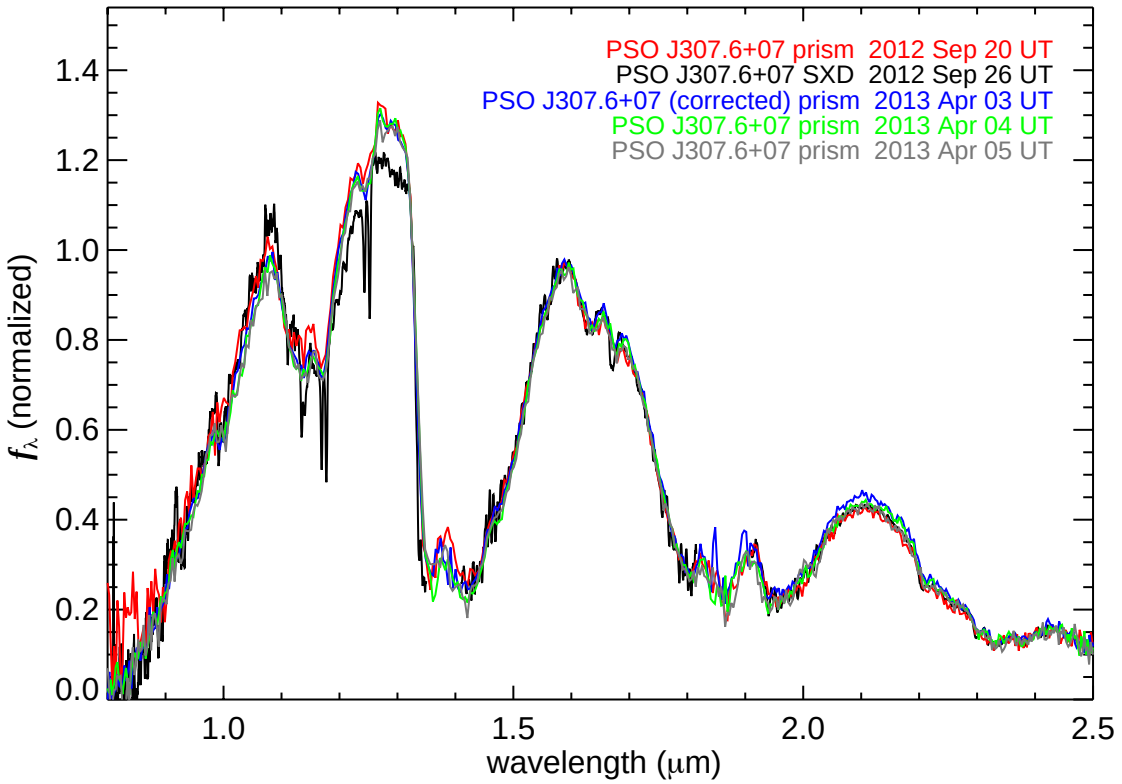

Figure 2.10 Spectra of PSO J307.6+07 taken in 2012 September (red and black, from Figure 2.7) and 2013 April (blue, green, and grey). The September 26 SXD spectrum (black) is smoothed by an 8-pixel box. The April 3 spectrum (blue) has been corrected for dimming seen in the comparison M1V star 2MASS J2041+0014 on that night. As in previous figures, these spectra have been normalized to the H-band peak. Unlike the September spectra, the April spectra show no variation. In the Y-band, both of the September spectra differ from the April spectra; in the J-band, only September 26 is different.

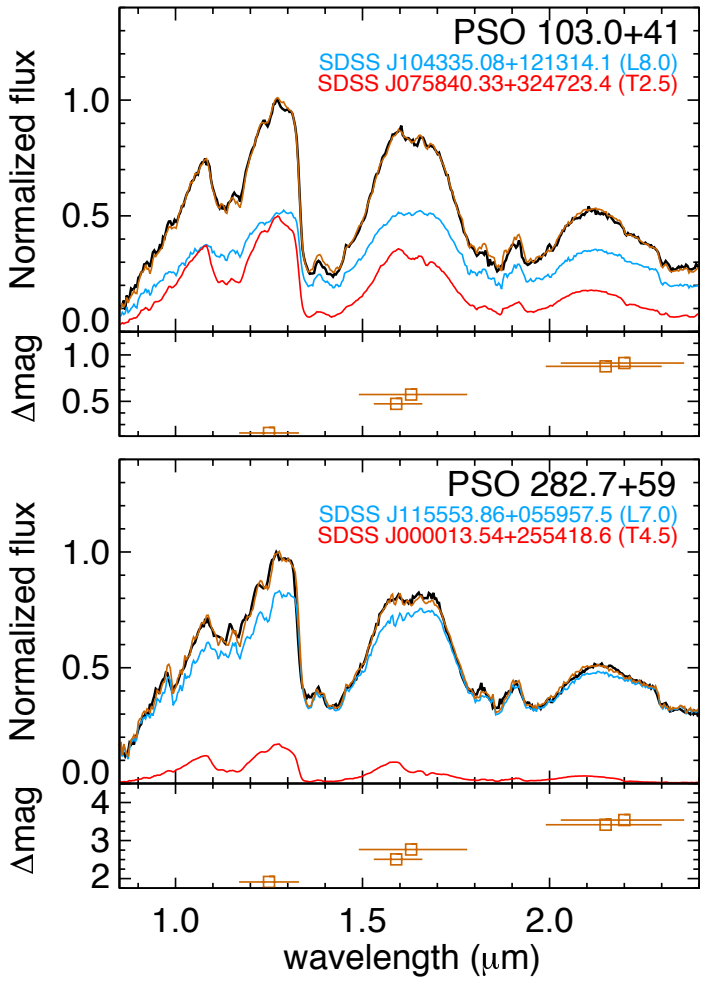

Figure 2.11 Best-matching template pairings for our candidate binaries PSO J103.0+41 (*top*) and PSO J282.7+59 (*bottom*). Observed spectra are shown in black, individual component templates in blue and red, and convolved templates in brown. The lower subpanels show the resulting flux ratios over standard NIR bandpasses computed from the best-matching template pairs (open brown squares).

Table 2.1. IRTF/SpeX Observations

Object	Date (UT)	Conditions	Seeing (arcsec)	Airmass	Mode	Slit (arcsec)	R ($\equiv \lambda/\Delta\lambda$)	$T_{\rm int}$ (s)	Standard
PSO J007.7921+57.8267	2012 Sep 24	Clear	0.9	1.27	prism	0.8×15	$\sim$100	200	HD 240290
PSO J103.0927+41.4601	2012 Sep 26	Clear	0.5	1.18	prism	0.5×15	$\sim$100	960	HD 39250
PSO J140.2308+45.6487	2012 Nov 8	Clear	0.8	1.32	prism	0.8×15	$\sim$100	720	HD 33654
PSO J140.2308+45.6487	2013 Jan 25	Clear	0.8	1.23	prism	0.8×15	$\sim$100	180	HD 79108
PSO J272.4689-04.8036	2012 Oct 14	Clear	1.1	1.28	prism	0.8×15	$\sim$100	720	HD 173591
PSO J282.7576+59.5858	2012 Sep 26	Clear	0.4	1.39	prism	0.8×15	$\sim$100	240	HD 240290
PSO J307.6784+07.8263	2012 Sep 20	Clear	0.6	1.15	prism	0.8×15	$\sim$100	80	HD 189920
PSO J307.6784+07.8263	2012 Sep 26	Clear	0.5	1.02	SXD	0.8×15	$\sim$750	1440	HD 189920
PSO J307.6784+07.8263	2013 Apr 03	Clear	1.0	1.43	prism	0.8×15	$\sim$100	180	HD 187170
PSO J307.6784+07.8263	2013 Apr 04	Clear	0.5	1.43	prism	0.8×15	$\sim$100	480	HD 187170
PSO J307.6784+07.8263	2013 Apr 05	Cloudy	0.8	1.50	prism	0.8×15	$\sim$100	320	HD 180150
PSO J339.0734+51.0978	2012 Oct 7	Cloudy	0.9	1.19	prism	0.8×15	$\sim$100	1200	HD 222749
PSO J339.0734+51.0978	2012 Oct 17	Cloudy	0.5	1.18	SXD	0.8×15	$\sim$750	1920	HD 209932

Table 2.1—Continued

Object	Date (UT)	Conditions	Seeing (arcsec)	Airmass	Mode	Slit (arcsec)	R ($\equiv \lambda/\Delta\lambda$)	$T_{\rm int}$ (s)	Standard

Table 2.2. Properties of New Discoveries

Property	PSO J007.7921+57.8267	PSO J103.0927+41.4601	PSO J140.2308+45.6487[a]	PSO J272.4689−04.8036[b]
		Astrometry		
PS1 R.A. (J2000)	7.7921°	103.0927°	140.2308°	272.4689°
	$00^{\rm h}31^{\rm m}10^{\rm s}.11$	$06^{\rm h}52^{\rm m}22^{\rm s}.25$	$09^{\rm h}20^{\rm m}55^{\rm s}.40$	$18^{\rm h}09^{\rm m}52^{\rm s}.53$
PS1 Dec. (J2000)	+57.8267°	+41.4601°	+45.6487°	−4.8036°
	+57°49′36.3″	+41°27′36.2″	+45°38′55.3″	−04°48′13.0″
PS1 epoch	2011.410	2011.400	2011.483	2011.020
Galactic longitude	120.2261°	174.8199°	174.3678°	23.8612°
Galactic latitude	−4.9385°	17.7353°	44.7239°	6.9942°
$\mu_\alpha \cos\delta$ (mas yr^{-1})	523 ± 17	-8 ± 6	-42 ± 23	-62 ± 18
μ_δ (mas yr^{-1})	-1 ± 16	-38 ± 6	-843 ± 23	-429 ± 17
2MASS designation	J00310928+5749364	J06522224+4127366	J09205549+4539058	J18095256-0448081
2MASS epoch	1998.983	1998.268	1999.139	1998.747
WISE designation	J003110.04+574936.3	J065222.24+412736.1	J092055.40+453856.3	J180952.53-044812.5
WISE epoch	2010.316	2010.233	2010.307	2010.224
		Photometry		
PS1 z (AB mag)	18.24 ± 0.01	18.85 ± 0.02	18.50 ± 0.01	18.80 ± 0.03
PS1 y (AB mag)	17.01 ± 0.01	17.64 ± 0.01	17.21 ± 0.01	17.46 ± 0.02
2MASS J (mag)	14.95 ± 0.04	15.48 ± 0.06	15.22 ± 0.05	15.14 ± 0.06

Table 2.2—Continued

Property	PSO J007.7921+57.8267	PSO J103.0927+41.4601	PSO J140.2308+45.6487[a]	PSO J272.4689−04.8036[b]
2MASS H (mag)	13.78 ± 0.04	14.46 ± 0.05	14.16 ± 0.05	14.28 ± 0.05
2MASS K_s (mag)	13.22 ± 0.03	13.89 ± 0.05	13.73 ± 0.05	13.96 ± 0.06
MKO Y (mag)	···	···	···	···
MKO J (mag)	14.79 ± 0.01[c]	15.36 ± 0.01[c]	15.04 ± 0.01[c]	15.15 ± 0.01[d]
MKO H (mag)	···	14.51 ± 0.03[c]	14.19 ± 0.02[c]	···
MKO K (mag)	···	13.95 ± 0.03[c]	13.77 ± 0.01[c]	13.98 ± 0.01[d,e]
WISE $W1$ (mag)	12.41 ± 0.02	13.13 ± 0.02	13.06 ± 0.02	13.29 ± 0.03
WISE $W2$ (mag)	11.84 ± 0.02	12.44 ± 0.03	12.39 ± 0.03	12.73 ± 0.03
WISE $W3$ (mag)	11.30 ± 0.10	11.80 ± 0.25	11.28 ± 0.17	12.38 ± 0.47
Spectral Indices				
H_2O-J	0.659 (L8.5)	0.588 (T0.4)	0.647 (L8.9)	0.657 (L8.6)
CH_4-J	0.835 (<T0)	0.709 (<T0)	0.875 (<T0)	0.773 (<T0)
H_2O-H	0.665 (L7.8)	0.575 (T0.6)	0.608 (L9.7)	0.630 (L9.0)
CH_4-H	1.047 (<T1)	0.981 (T1.1)	1.002 (<T1)	0.972 (T1.1)
CH_4-K	0.844 (L8.7)	0.778 (L9.9)	0.749 (T0.3)	0.719 (T0.7)
H_2O-K	0.687 (——)	0.658 (——)	0.631 (——)	0.644 (——)
Physical Properties				
Near-IR spectral type	L9	T0	L9.5	T1

Table 2.2—Continued

Property	PSO J007.7921+57.8267	PSO J103.0927+41.4601	PSO J140.2308+45.6487[a]	PSO J272.4689−04.8036[b]
Photometric distance (pc)	11.6 ± 1.0	14.2 ± 1.2	14.3 ± 1.2	15.0 ± 1.3
$v_{\rm tan}$ ($\rm km\,s^{-1}$)	29 ± 3	3 ± 1	57 ± 5	31 ± 3
Distinctive feature	——	Possible binary	J-band variable	Possible variable

[a]First identified photometrically by Aberasturi et al. (2011); also identified and spectrally typed by Mace et al. (2013a).

[b]Discovered independently by Mace et al. (2013a).

[c]Photometry obtained with UKIRT/WFCAM on 2012 December 13–14 UT.

[d]Photometry obtained from the VISTA VHS catalog (Cross et al. 2012).

[e]VISTA uses a K_s filter similar to 2MASS.

Table 2.3. Properties of New Discoveries

Property	PSO J282.7576+59.5858	PSO J307.6784+07.8263[a]	PSO J339.0734+51.0978[a]
		Astrometry	
PS1 R.A. (J2000)	282.7576°	307.6784°	339.0734°
	$18^{\rm h}51^{\rm m}01^{\rm s}.84$	$20^{\rm h}30^{\rm m}42^{\rm s}.81$	$22^{\rm h}36^{\rm m}17^{\rm s}.63$
PS1 Dec. (J2000)	+59.5858°	+7.8263°	+51.0978°
	+59°35′08.9″	+07°49′34.6″	+51°05′52.0″
PS1 epoch	2011.177	2010.757	2010.688
Galactic longitude	89.5093°	51.9998°	102.3625°
Galactic latitude	23.2059°	−17.9389°	−6.2959°
$\mu_\alpha \cos\delta$ (mas yr^{-1})	23 ± 19	659 ± 8	736 ± 14
μ_δ (mas yr^{-1})	412 ± 19	-113 ± 9	330 ± 8
2MASS designation	J18510178+5935040	J20304235+0749358	J22361685+5105487
2MASS epoch	1999.432	2000.442	2000.760
WISE designation	J185101.83+593508.6	J203042.79+074934.7	J223617.59+510551.9
WISE epoch	2010.344	2010.333	2010.498
		Photometry	
PS1 z (AB mag)	18.35 ± 0.01	17.97 ± 0.01	19.13 ± 0.05
PS1 y (AB mag)	17.15 ± 0.02	16.44 ± 0.01	17.25 ± 0.01
2MASS J (mag)	14.94 ± 0.04	14.23 ± 0.03	14.58 ± 0.04
2MASS H (mag)	13.97 ± 0.04	13.44 ± 0.03	14.49 ± 0.05
2MASS K_s (mag)	13.46 ± 0.05	13.32 ± 0.04	14.45 ± 0.09
MKO Y (mag)	...	15.22 ± 0.01[b]	15.66 ± 0.01[b]
MKO J (mag)	14.85 ± 0.01[b]	14.05 ± 0.01[b]	14.46 ± 0.01[b]
MKO H (mag)	14.03 ± 0.02[b]	13.48 ± 0.01[b]	14.62 ± 0.02[b]
MKO K (mag)	...	...	...
WISE $W1$ (mag)	12.65 ± 0.02	12.96 ± 0.03	13.84 ± 0.03
WISE $W2$ (mag)	12.18 ± 0.02	12.12 ± 0.03	12.48 ± 0.03
WISE $W3$ (mag)	11.23 ± 0.07	10.96 ± 0.11	11.02 ± 0.08

Table 2.3—Continued

Property	PSO J282.7576+59.5858	PSO J307.6784+07.8263[a]	PSO J339.0734+51.0978[a]
Spectral Indices			
H_2O-J	0.678 (L8.0)	0.625 (L9.4)	0.225 (T5.1)
CH_4-J	0.652 (T0.1)	0.698 (<T0)	0.405 (T5.0)
H_2O-H	0.650 (L8.3)	0.586 (T0.4)	0.335 (T5.1)
CH_4-H	1.016 (<T1)	0.878 (T1.7)	0.410 (T5.2)
CH_4-K	0.897 (L7.5)	0.548 (T2.2)	0.203 (T5.3)
H_2O-K	0.705 (——)	0.579 (——)	0.443 (——)
Physical Properties			
Near-IR spectral type	L9	T1.5	T5
Photometric distance (pc)	13.5 ± 1.1	10.9 ± 0.9	9.4 ± 0.8
$v_{\tan}$ ($\mathrm{km\,s^{-1}}$)	26 ± 3	35 ± 3	36 ± 3
Distinctive feature	Possible binary	J-band variable	Possible variable

[a]Discovered independently by Mace et al. (2013a).

[b]Photometry obtained with UKIRT/WFCAM on 2012 September 19–21 UT.

Table 2.4. Properties of Candidate Binaries

Property	PSO J103.0927+41.4601	PSO J282.7576+59.5858
Primary Spectral Type	L8±1	L7±1
Secondary Spectral Type	T2.5±0.5	T4.5±1
ΔJ (2MASS mag)	0.24 ± 0.05	2.53 ± 0.78
ΔH (2MASS mag)	0.57 ± 0.05	3.04 ± 1.03
ΔK (2MASS mag)	0.91 ± 0.08	2.31 ± 0.65
ΔJ (MKO mag)	0.18 ± 0.05	1.81 ± 0.37
ΔH (MKO mag)	0.58 ± 0.04	2.53 ± 0.77
ΔCH_4s (MKO mag)	0.48 ± 0.04	3.13 ± 1.08
ΔK (MKO mag)	0.95 ± 0.09	1.90 ± 0.41

Note. — These spectral types and flux ratios are estimated from spectral decomposition. They have not been directly measured.

Chapter 3

A Search for L/T Transition Dwarfs With Pan-STARRS1 and *WISE*. II. L/T Transition Atmospheres and Young Discoveries

Note: This chapter originally appeared as Best et al. (2015), with co-authors Michael C. Liu, Eugene A. Magnier, Niall R. Deacon, Kimberly M. Aller, Joshua Redstone, W. S. Burgett, K. C. Chambers, P. Draper, H. Flewelling, K. W. Hodapp, N. Kaiser, N. Metcalfe, J. L. Tonry, R. J. Wainscoat, and C. Waters.

Abstract

The evolution of brown dwarfs from L to T spectral types is one of the least understood aspects of the ultracool population, partly for lack of a large, well-defined, and well-characterized sample in the L/T transition. To improve the existing census, we have searched ≈28,000 deg^2 using the Pan-STARRS1 and *Wide-field Infrared Survey Explorer* surveys for L/T transition dwarfs within 25 pc. We present 130 ultracool dwarf discoveries with estimated distances $\approx 9-130$ pc, including 21 that were independently discovered by other authors and 3 that were previously identified as photometric candidates. Seventy-nine of our objects have near-IR spectral types of L6–T4.5, the most L/T transition dwarfs from any search to date, and we have increased the census of L9–T1.5 objects within 25 pc by

over 50%. The color distribution of our discoveries provides further evidence for the "L/T gap," a deficit of objects with $(J-K)_{\rm MKO} \approx 0.0$–$0.5$ mag in the L/T transition, and thus reinforces the idea that the transition from cloudy to clear photospheres occurs rapidly. Among our discoveries are 31 candidate binaries based on their low-resolution spectral features. Two of these candidates are common proper motion companions to nearby main sequence stars; if confirmed as binaries, these would be rare benchmark systems with the potential to stringently test ultracool evolutionary models. Our search also serendipitously identified 23 late-M and L dwarfs with spectroscopic signs of low gravity implying youth, including 10 with VL-G or INT-G gravity classifications and another 13 with indications of low gravity whose spectral types or modest spectral signal-to-noise ratio do not allow us to assign formal classifications. Finally, we identify 10 candidate members of nearby young moving groups (YMG) with spectral types L7–T4.5, including three showing spectroscopic signs of low gravity. If confirmed, any of these would be among the coolest known YMG members and would help to determine the effective temperature at which young brown dwarfs cross the L/T transition.

3.1 Introduction

Over the past 20 years some 1,500 brown dwarfs have been discovered in the field, yet fundamental questions about their formation, evolution, and atmospheres remain. Without sustained hydrogen fusion in their cores, brown dwarfs cool continuously, creating an observational degeneracy between their masses, ages and luminosities. Their photospheres are dominated by molecules and dusty condensates, and undergo significant chemical changes as they cool (e.g., Burrows et al. 2001). The relationship between the observable properties (fluxes and spectra) and the underlying physical properties (masses, ages, metallicities, and gravities) of ultracool dwarfs is therefore complex and challenging to disentangle, and evolutionary trends are difficult to identify.

This is particularly true in the L/T transition (spectral types $\approx$ L6–T4.5), where spectral features undergo significant changes and near-infrared colors become bluer by $\approx$2 magnitudes over a narrow range of effective temperature ($T_{\rm eff} \approx 1400 - 1200$ K; Golimowski et al. 2004; Stephens et al. 2009). These changes are thought to arise from the depletion of thick condensate clouds as brown dwarfs cool (e.g., Allard et al. 2001; Burrows et al. 2006; Saumon & Marley 2008). Several scenarios have been proposed wherein condensate clouds thin gradually, rain out suddenly, or break up (e.g., Ackerman & Marley 2001; Knapp et al. 2004; Tsuji 2005; Marley et al. 2010). The process is still not well understood, however, and state-of-the-art evolutionary and atmospheric models typically yield inaccurate luminosities and inconsistent temperatures for L/T objects with dynamical masses and/or age determinations (e.g., Dupuy et al. 2009b; Liu et al. 2010; Dupuy et al. 2014). Color-magnitude diagrams with accurate luminosities are still rather sparsely populated in the L/T transition (Dupuy & Liu 2012), hindering our ability to test the models.

A large and well-defined sample is a necessary starting point, but L/T transition dwarfs are known to be more elusive than those with higher and lower effective temperatures. At optical wavelengths, L/T transition dwarfs are faint. In the near-infrared, where they are brightest, their colors make them difficult to distinguish from low-mass stars (e.g., Reid et al. 2008b). The most productive previous searches so far each focused on $\lesssim$10% of the sky: Chiu et al. (2006) used the Sloan Digital Sky Survey (SDSS; York et al. 2000) to find 46 L6–T4.5 dwarfs over $\approx$3,500 deg^2, and Marocco et al. (2015) found 48 L6–T4.5 dwarfs in $\approx$4,000 deg^2 by cross-matching the UKIRT Infrared Deep Sky Survey (UKIDSS; Lawrence et al. 2007) Large Area Survey with SDSS. What has been missing is an all-sky search specifically targeting nearby, bright L/T transition dwarfs.

To address this deficiency, we have conducted an extensive search with these key features: (1) We used the new Pan-STARRS1 Survey (PS1; Kaiser et al. 2010) cross-matched with the Wide-Field Infrared Survey Explorer (*WISE*; Wright et al. 2010) All-sky Release, thereby exploiting the combined broad wavelength coverage of these optical and

mid-infrared surveys; (2) we searched ≈28,000 deg^2, nearly the full area of the PS1 3π survey; and (3) we searched to within 3° of the Galactic plane, whereas most previous searches stopped at $b = 10°$ or $b = 15°$ (e.g., Cruz et al. 2003; Scholz et al. 2011). In Best et al. (2013, hereinafter Paper I), we presented seven initial discoveries from our search, all bright L/T transition dwarfs within 15 pc. In this paper, we present the complete results of our search, including 79 total L/T transition dwarfs and 23 young or potentially young late-M and L dwarfs.

We describe our search in Section 3.2 and our observations in Section 3.3. In Section 3.4 we present the results of our search, including descriptions of interesting individual objects. In Section 3.5 we discuss implications of our discoveries for evolutionary models of the L/T transition. We discuss our young discoveries in more detail in Section 3.6 and summarize our findings in Section 3.7.

3.2 Search Method

3.2.1 Input Catalogs

The PS1 3π survey (K. C. Chambers et al., in preparation) has obtained an average of ≈12 epochs of imaging in five optical bands ($g_{\rm P1}, r_{\rm P1}, i_{\rm P1}, z_{\rm P1}, y_{\rm P1}$) with a 1.8-meter wide-field telescope on Haleakala, Maui, covering the entire sky north of −30° declination. Images were processed nightly through the Image Processing Pipeline (IPP; Magnier 2006, 2007; Magnier et al. 2008), with photometry on the AB magnitude scale (Tonry et al. 2012). Imaging began in May 2010 and concluded in March 2014. We conducted our search using PS1/IPP Processing Version 1 photometry, and constructed object names according to the PS1 convention using object coordinates as of January 2012. The *WISE* All-sky Source Catalog (Cutri et al. 2012) comprises data taken between January and August 2010 in four mid-infrared bands: $W1$ (3.6 μm), $W2$ (4.5 μm), $W3$ (12 μm), and $W4$ (22 μm).

3.2.2 Search Parameters

Our search is described in detail in Paper I. Briefly, we merged all PS1 detections through January 2012 with the *WISE* All-sky catalog using a 3.0″ matching radius. We removed objects within 3° of the Galactic plane and in the heavily reddened areas of the sky defined by Cruz et al. (2003), except for objects in these regions for which PS1 reported a proper motion with S/N > 3. We searched between $\delta = -30°$ (the southern limit of PS1) and $\delta = +70°$ (the northern limit of the NASA Infrared Telescope Facility (IRTF), which we used for spectroscopic follow-up). We identified candidate L/T dwarfs using a suite of quality and color cuts applied to our merged PS1+*WISE* database. After visually screening these candidates using images from PS1, *WISE*, and the Two Micron All Sky Survey (2MASS; Skrutskie et al. 2006), we obtained near-infrared photometry from 2MASS, UKIDSS, and our own observations (Section 3.3.1), and used this to apply a final screening based on colors and magnitudes. We summarize our photometric criteria here:

1. Detected in at least two separate $y_{\rm P1}$ frames with S/N > 5 in each.

2. Good quality photometry in $y_{\rm P1}$, no saturated objects or cosmic rays.

3. No more than one total detection in either $g_{\rm P1}$ or $r_{\rm P1}$.

4. $i_{\rm P1} - z_{\rm P1} \geq 1.8$ mag (only applied when the $i_{\rm P1}$ and $z_{\rm P1}$ photometry for an object met the same quality standards required for $y_{\rm P1}$).

5. $i_{\rm P1} - y_{\rm P1} \geq 2.8$ mag (only applied when $i_{\rm P1}$ photometry met the same quality standards required for $y_{\rm P1}$).

6. $z_{\rm P1} - y_{\rm P1} \geq 0.6$ mag (only applied when $z_{\rm P1}$ photometry met the same quality standards required for $y_{\rm P1}$).

7. $W1$ and $W2$ detections have S/N > 2 (for most candidates, PS1 establishes the sensitivity limit).

8. $W1$ and $W2$ detections are point sources, not saturated, and unlikely to be variable.

9. $y_{\rm P1} - W1 \geq 3.0$ mag.

10. $W1 - W2 \geq 0.4$ mag.

11. $W2 - W3 \leq 2.5$ mag.

12. $y_{\rm P1} - J_{2MASS} \geq 1.8$ mag or $y_{\rm P1} - J_{MKO} \geq 1.9$ mag.

We then obtained and classified near-IR spectra for 142 candidates using standard procedures described in Section 3.3. In Table 3.1 we present the PS1 and *WISE* photometry for the objects we observed spectroscopically, and Table 3.2 shows their near-infrared photometry. We did not re-observe objects also found by other concurrent PS1 searches for ultracool dwarfs (M. C. Liu et al., in preparation).

3.2.3 A *WISE* Photometric Criterion for L/T Transition Dwarfs Within 25 pc

Prior to obtaining spectra for our candidates, we used photometry to estimate distances. In Paper I, we noted that $y_{\rm P1}$ absolute magnitudes are roughly flat across the L/T transition, and we identified $y_{\rm P1} = 19.3$ mag as a limit for single objects expected to lie within 25 pc. We therefore used $y_{\rm P1} < 19.3$ mag to prioritize candidates for spectroscopic observations (though in the end, we did observe a few objects with $y_{\rm P1} > 19.3$ mag.) However, some of our first spectroscopic confirmations proved to be L/T transition dwarfs with spectrophotometric distances of $30 - 35$ pc and earlier L dwarfs at greater distances, so we sought a better criterion than the $y_{\rm P1}$ cutoff.

We examined the relationships between colors and magnitudes in the PS1, 2MASS, and *WISE* bands and the distances to ultracool dwarfs with known parallaxes from Dupuy & Liu (2012)[1]. We identified an inequality in the $W1$ vs. $W1 - W2$ color-magnitude diagram

[1]An updated list can be found in the Database of Ultracool Parallaxes maintained by Trent Dupuy at http://www.as.utexas.edu/ tdupuy/plx/Database_of_Ultracool_Parallaxes.html. Here we used the version posted on 2013-09-09.

that selects L/T transition dwarfs with $d < 25$ pc:

$$W1 \leq 2.833 \times (W1 - W2) + 12.667 \text{ mag} \tag{3.1}$$

This inequality excludes nearly all ultracool dwarfs with trigonometric distances beyond 25 pc for $0.5 \lesssim W1 - W2 \lesssim 1.2$ mag, equivalent to spectral types $\approx$ L8 $-$ T3.5 (Figure 3.1). For earlier and later spectral types, there is still contamination from distant objects, but the relationship helps.

Once we identified this inequality, we used it instead of $y_{\rm P1} < 19.3$ mag to prioritize candidates for spectroscopic follow-up. This increased our rate of success at confirming late-L and T dwarfs within 25 pc, but also meant that our final sample of 142 candidates was heterogeneously selected. If we had used the $W1$ vs. $W1 - W2$ inequality from the beginning of the search, we would have observed almost none of our discoveries with spectral types earlier than $\approx$L7.

3.3 Observations

3.3.1 Near-infrared Photometry

Following our initial PS1+*WISE* database search, our candidates all had red-optical ($y_{\rm P1}$, possibly $i_{\rm P1}$ and $z_{\rm P1}$) and mid-infrared ($W1$ and $W2$, possibly $W3$) photometry. Our red-optical and mid-IR photometry were drawn from single sources, so we sought a similarly homogenous set of near-IR photometry. The only near-IR survey covering our entire search area is 2MASS, but most of our candidates were too faint to have been well detected (S/N > 10) by 2MASS, and $\approx$30% were not detected at all. Thus, we obtained additional near-IR photometry in order to further vet our candidates prior to spectroscopic observations.

We therefore searched the UKIDSS Data Release 9 (DR9; Lawrence et al. 2013) and VISTA Hemisphere Survey (VHS; Cross et al. 2012) catalogs for JHK photometry of our

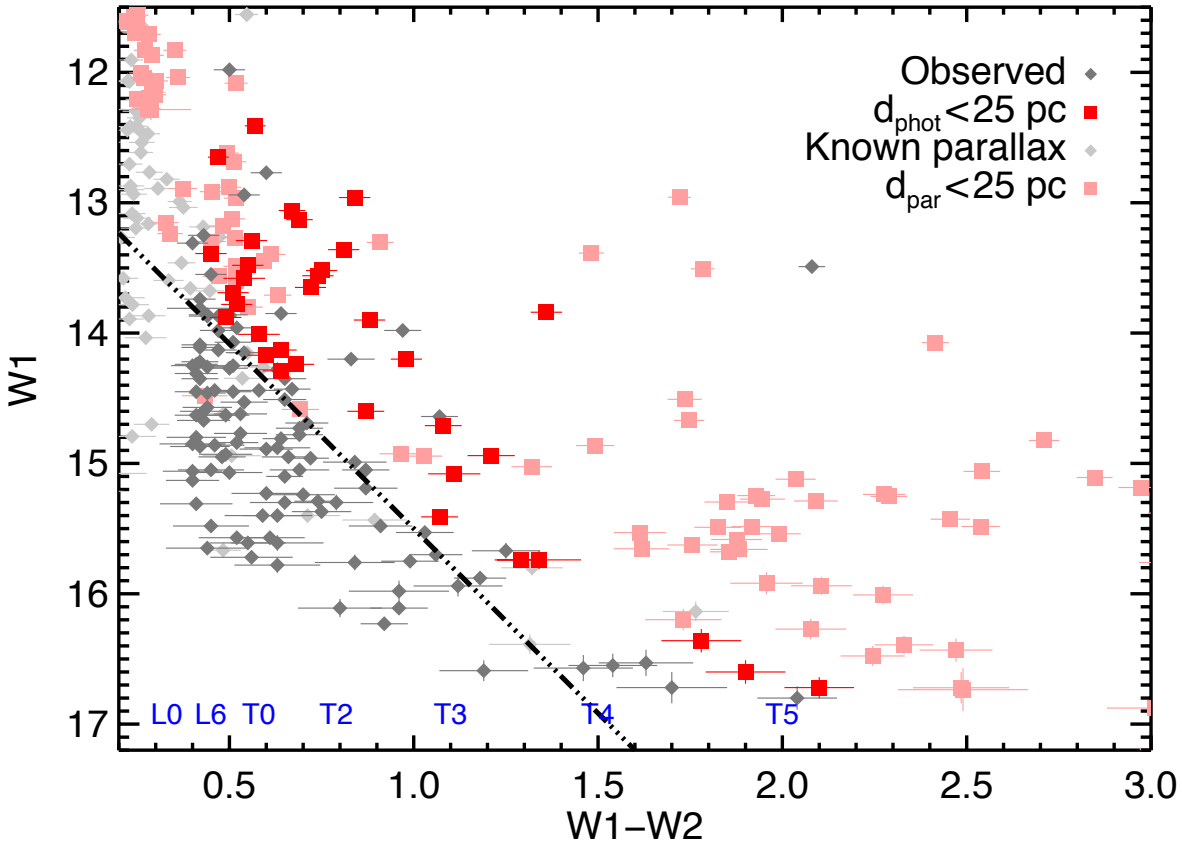

Figure 3.1 $W1$ vs. $W1-W2$ diagram for known ultracool dwarfs. Objects with known parallaxes (Dupuy & Liu 2012) and within 25 pc are shown as pink squares; those beyond 25 pc are light gray diamonds. Our new discoveries with photometric distances (Section 3.4) less than than 25 pc are plotted with red squares, and those with $d_{\rm phot} > 25$ pc are dark gray diamonds. Approximate spectral types for $W1-W2$ colors are indicated in blue along the bottom. The region above and to the right of the black dashed-dotted line, $W1 \leq 2.833 \times (W1-W2) + 12.667$ mag, includes 100% of our L/T transition discoveries with $d_{\rm phot} < 25$ pc but only 33% beyond 25 pc.

candidates on the Mauna Kea Observatories (MKO) filter system (Simons & Tokunaga 2002; Tokunaga et al. 2002). For objects not found in either survey, we obtained follow-up images using WFCAM (Casali et al. 2007) on the 3.8-meter United Kingdom InfraRed Telescope (UKIRT) as part of the UKIRT Service Programme. Observations took place on multiple nights spanning 2010 September to 2013 December. We obtained J band images for all observed targets, as well as H and K bands when time constraints permitted. Integrations were 5 sec $\times$ 5 dithers in J and H bands and 10 sec $\times$ 5 dithers in K band, sufficient to reach S/N>20 in most cases. Data were reduced and calibrated at the Cambridge Astronomical Survey Unit using the WFCAM survey pipeline (Irwin et al. 2004; Hodgkin et al. 2009).

For objects for which we did not obtain both H and K band images, we used our near-IR spectra (Section 3.3.2) to synthesize photometry in the missing band(s), using our measured J magnitudes to flux-calibrate the synthetic magnitudes. For nine candidates with existing 2MASS photometry for which we did not obtain UKIRT photometry, we synthesized MKO JHK photometry from the near-IR spectra using the corresponding 2MASS magnitudes to calibrate each synthetic magnitude. All observed and synthetic magnitudes are included in Table 3.2. Altogether we have MKO system JHK photometry for all but one of our 142 candidates.

3.3.2 Near-infrared Spectroscopy and Spectral Typing

We obtained low-resolution near-IR spectra for our candidates between 2012 July and 2014 January using the NASA Infrared Telescope Facility (IRTF). We used the facility spectrograph SpeX (Rayner et al. 2003) in prism mode with the $0.5''$ ($R \approx 120$) and $0.8''$ ($R \approx 75$) slits. We re-observed eight targets between 2015 January and June with the $0.5''$ slit to obtain higher S/N and assess possible low-gravity spectral signatures (Section 3.4.4). Details of our observations are listed in Table 3.3. Contemporaneously with each science target, we observed a nearby A0V star for telluric calibration. All spectra were reduced in the standard way using versions 3.4 and 4.0 of the Spextool software package (Vacca et al.

2003; Cushing et al. 2004). We aimed for S/N $\gtrsim$ 30, sufficient for accurate spectral typing based on overall morphology (i.e., visual comparison of JHK bands).

Spectral typing of our observed objects was performed by visually comparing our spectra to the near-infrared M and L dwarf standards of Kirkpatrick et al. (2010) and T dwarf standards of Burgasser et al. (2006a), substituting the T3 standard SDSS J1206+2813 suggested by Liu et al. (2010). When assigning M and L types we followed the procedure of Kirkpatrick et al. (2010), first comparing only the $0.9 - 1.4$ μm portions of the spectra to evaluate the goodness of fit, and subsequently determining if the object's $1.4 - 2.4$ μm flux was unusually red or blue for its spectral type. For T dwarfs, we compared our spectra to the standards over the entire $0.9 - 2.4$ μm window simultaneously. Our visual typing was able to identify spectra whose features clearly placed them in between consecutive spectral standards, so we assume a default uncertainty of $\pm$0.5 sub-types. In cases of larger uncertainty, we use ":" (e.g., spectral type L6:) to indicate an uncertainty of $\pm$1 sub-type, and "::" to indicate larger uncertainties.

We also determined spectral types for our discoveries using two index-based systems, which enable objective spectral typing based on specific spectral features. Allers & Liu (2013a, hereinafter AL13) developed a system of near-IR indices that are sensitive to spectral type while insensitive to differences in gravity. At least one index is defined for each spectral sub-type spanning M4–L7, so we calculated these indices for our discoveries in that range (M7–L7). Following Aller et al. (2016), we determined the spectral type uncertainties derived from each index by performing Monte Carlo simulations for each object to propagate the measurement errors of our reduced spectra and the rms uncertainties on index-spectral type conversions into the index calculations. We calculated a final index-based spectral type for each object equal to the weighted average of spectral types from all Monte Carlo runs, excluding those that fell outside the valid range for each index.

The second system of near-IR indices we used is that of Burgasser et al. (2006a, hereinafter B06), assigning spectral types based on each index using the polynomial fits from Burgasser (2007a). The indices were originally designed to classify T dwarfs, but the

polynomials for three of the five indices are valid for L dwarfs as well. We calculated a final B06 spectral type for each object as the mean of the individual index-based types, following the approach of Burgasser (2007a). For uncertainties, we use the standard deviations of the individual index-based types, which are typically $1.0 - 2.0$ subtypes for L dwarfs and $0.5 - 1.5$ subtypes for T dwarfs.

Neither of these index-based systems covers the full spectral type range of our objects, whereas visual typing was performed for every object. Therefore, we adopt the visually-assigned types as final spectral types for our discoveries.

3.4 Results

3.4.1 Ultracool Discoveries

Our search found 130 ultracool dwarfs, comprising 92% of our 142 spectroscopic targets. Of these, 106 are completely new discoveries. Twenty-one were independently discovered and published by other teams during our search, and 3 are previously identified photometric candidates for which we present the first spectroscopic confirmation. The SpeX prism spectra for 122 of our ultracool discoveries are presented in Figure 3.2, and their spectral types are listed in Table 3.4. The remaining eight discoveries are candidate members of the Scorpius-Centaurus Association and the Taurus star-forming region, and their spectra will be presented in a future paper (W. M. J. Best et al., in preparation). We include these eight objects in the summary figures of this paper in order to accurately characterize the overall results of our search. The objects previously published by other teams are listed in Table 3.5. Seven of our discoveries, all with photometric distances less than 15 pc, were initially presented in Paper I. We also identified 12 non-ultracool objects including a carbon star, an emission line galaxy, and background stars, which are detailed in Table 3.6.

Figure 3.3 shows the spectral type distribution of our ultracool discoveries. These include 79 L6–T4.5 dwarfs ($\approx$55% of our sample), giving us the largest number of L/T transition dwarfs identified by any search to date. Figure 3.4 compares the spectral type distributions

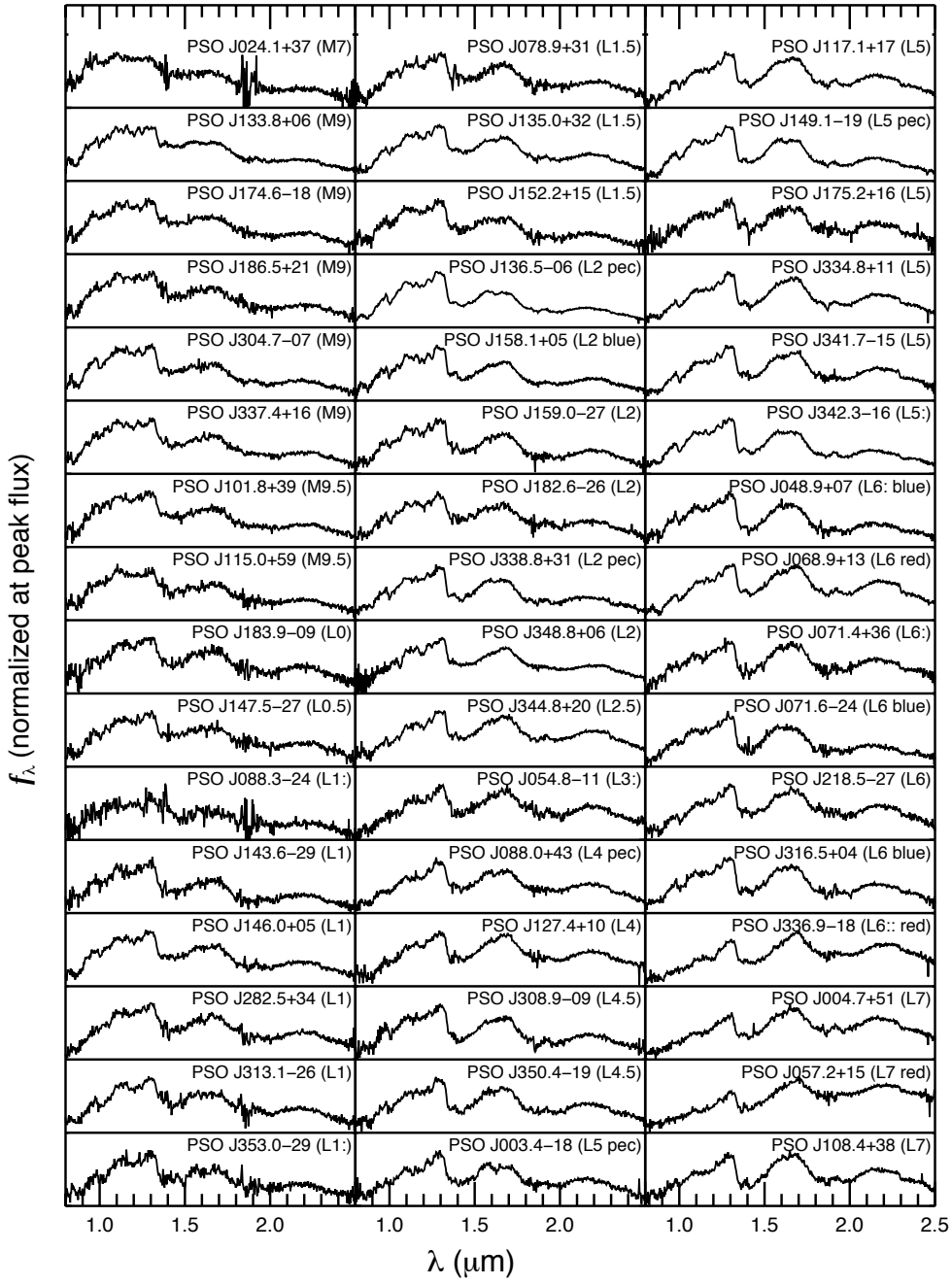

Figure 3.2 SpeX prism spectra for our discoveries, normalized at the peak flux value for each spectrum and arranged from earliest to latest spectral type. Spectra were typed by visual comparison with the near-infrared standards defined by Burgasser et al. (2006a) and Kirkpatrick et al. (2010).

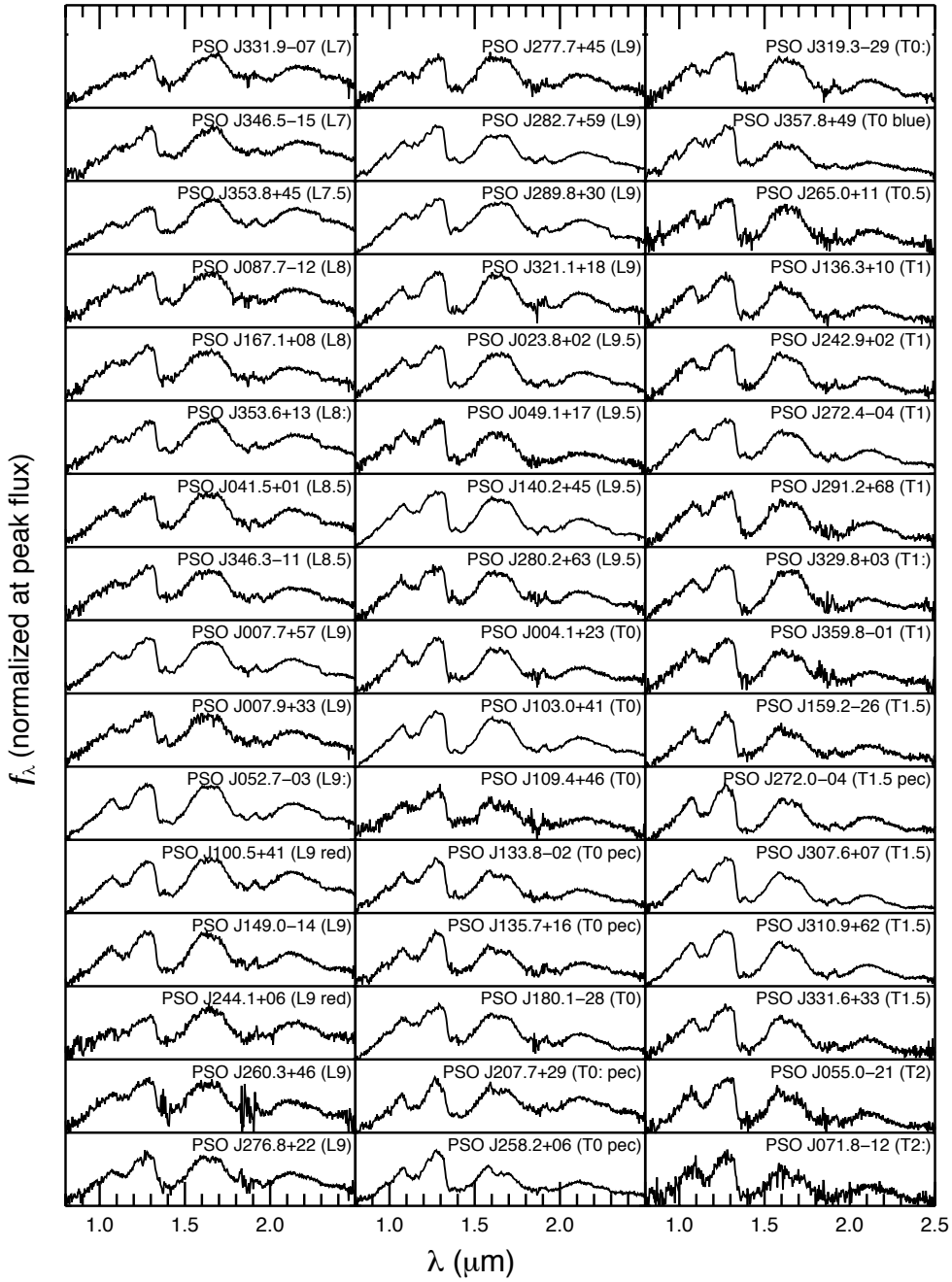

Figure 3.2 continued.

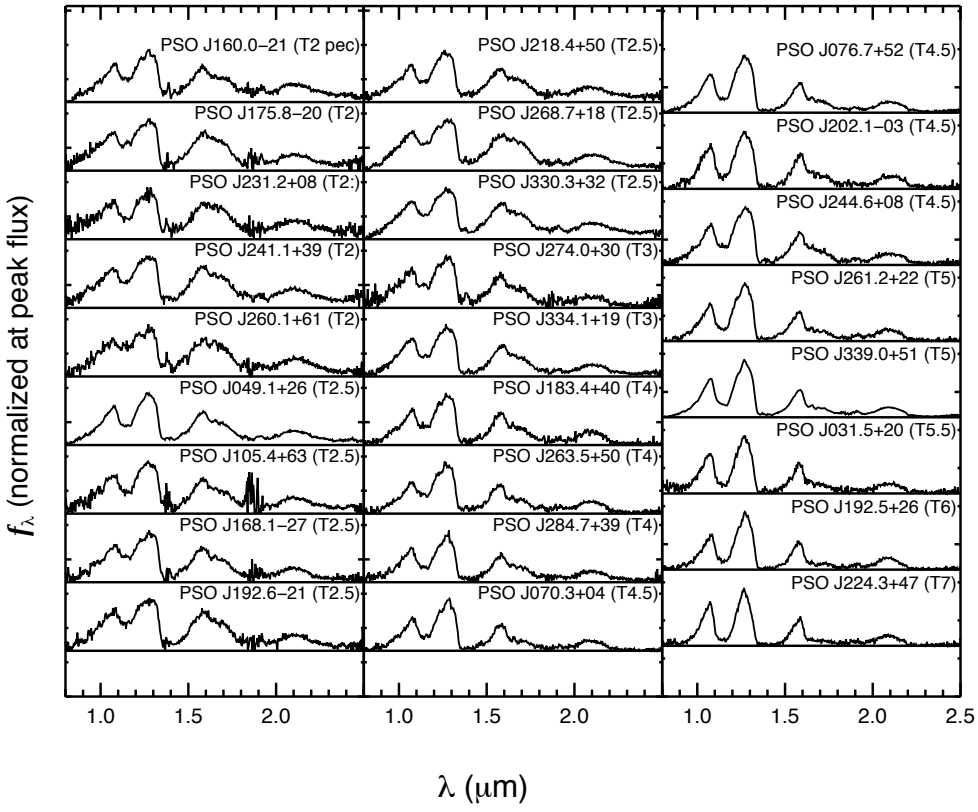

Figure 3.2 continued.

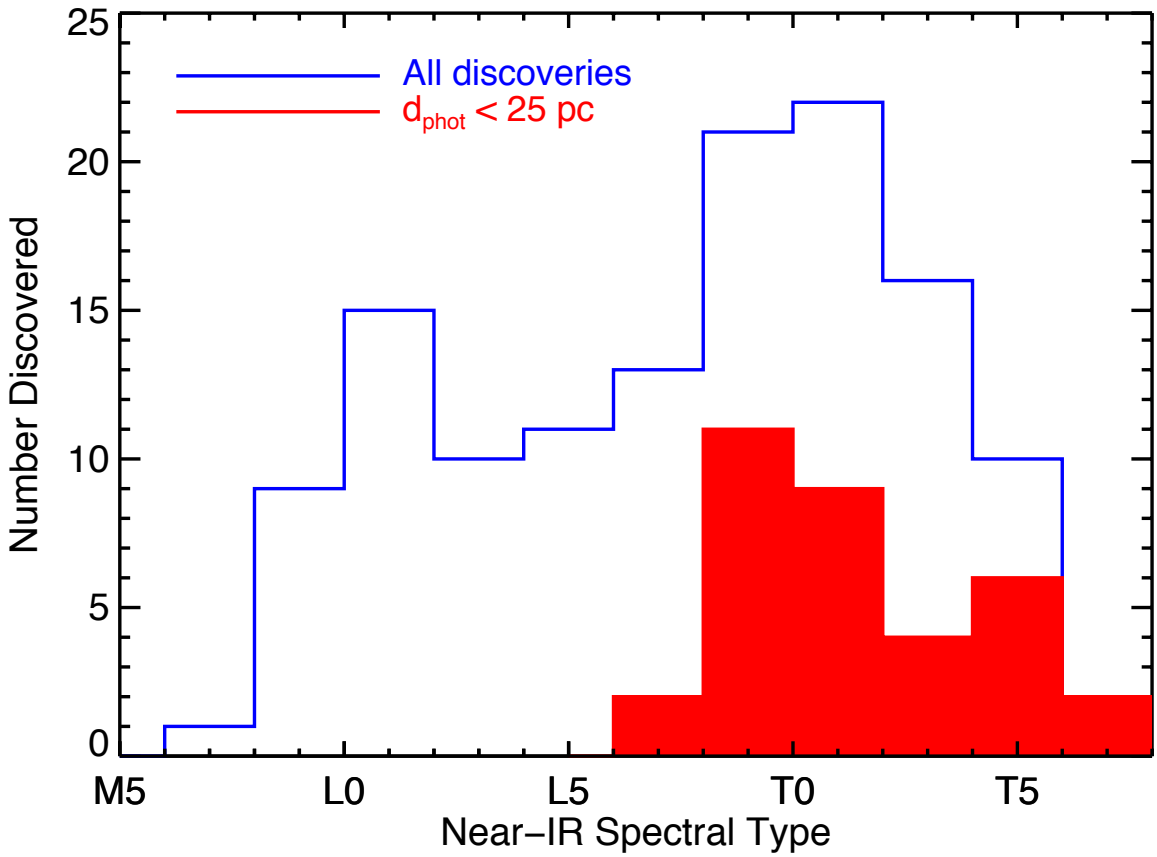

Figure 3.3 The spectral type distribution of our ultracool discoveries (blue open histogram), highlighting objects with W2 spectrophotometric distances less than 25 pc (solid red). We identified 79 objects with spectral types L6–T4.5, including 30 within 25 pc.

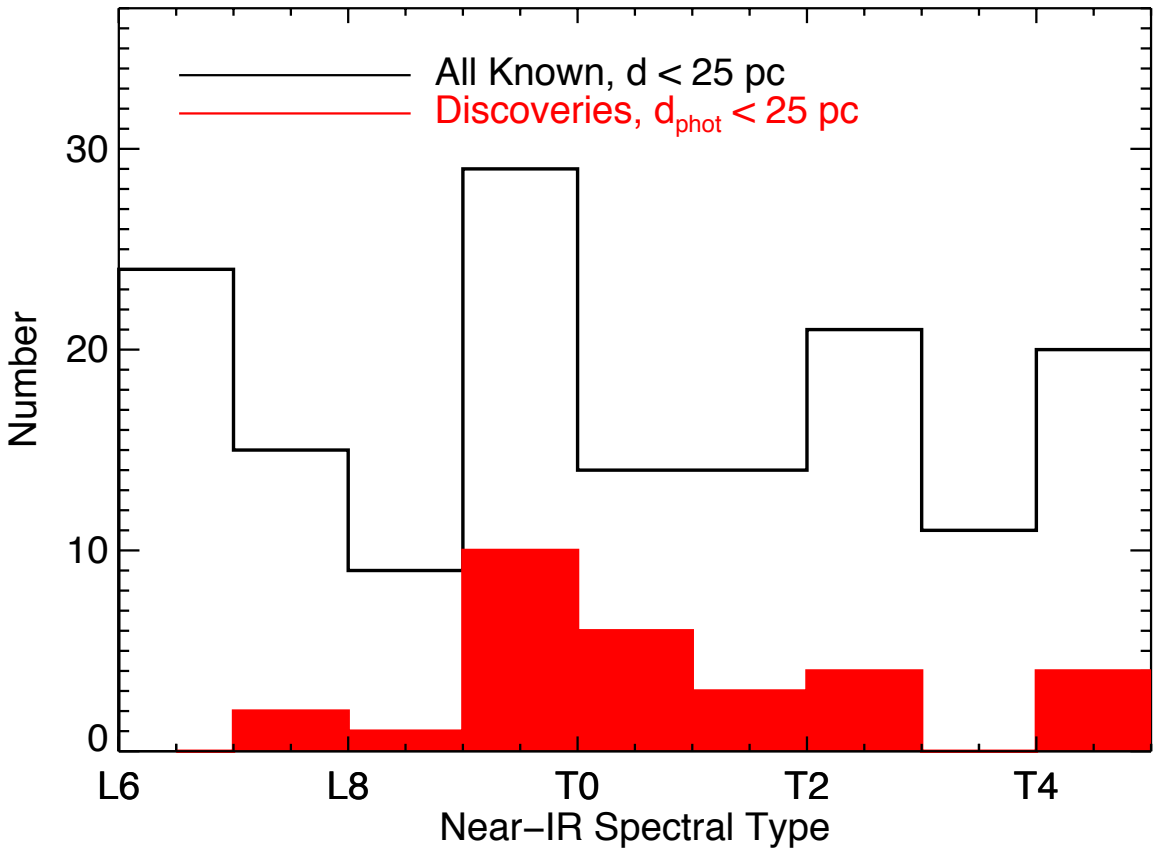

Figure 3.4 The near-infrared spectral type distribution of all known L/T transition dwarfs within 25 pc including our discoveries and previously published objects (black open histogram), compared with just our discoveries within 25 pc (solid red). In the middle of the L/T transition (L9–T1.5), our discoveries increase the census by over 50%.

within 25 pc of our 30 L/T transition discoveries and all known L/T transition dwarfs. Note that some previously published L/T transition dwarfs have spectral types based on optical spectra, while others have near-IR spectral types. For a fair comparison with our near-IR discoveries, we can only use near-IR spectral types for known objects because optical and near-IR types may not be the same for a given object (e.g., Kirkpatrick et al. 2010), and the optical spectral standards for L dwarfs do not include type L9 (Kirkpatrick et al. 1999). To obtain as complete a sample as possible of near-IR spectral types for known L/T transition dwarfs, we searched the literature and identified eight brown dwarfs within 25 pc with optical spectral types ≥L4 but no near-IR spectral types. Two of these have spectra in the SpeX Prism Library[2] which we used to determine near-IR spectral types (Table 3.7) following the visual method described in Section 3.3.2. Two more have optical spectral types L6 and L7, respectively, and we adopt these as the near-IR types for use in Figure 3.4. The remaining four all have optical spectral types of L5, so we do not include them in the known L/T transition sample. Figure 3.4 shows that our contribution is most significant for spectral types L9–T1.5, a range of particular interest for studies focused on photometric variability induced by clouds clearing in photospheres (Radigan et al. 2014). Our 19 L9–T1.5 discoveries have increased the 25 pc census by over 50%.

We note also that the $W1$ vs. $W1 - W2$ inequality we identified in Section 3.2.3 (Figure 3.1) preserves all of our L/T transition discoveries within 25 pc while excluding two-thirds of those farther away, and also excludes almost all of our discoveries having earlier spectral types (which all lie beyond 25 pc).

Eleven of our discoveries have spectral features we deemed unusual enough to assign the object's spectral type a "peculiar" designation. All of these objects were identified as candidate unresolved binaries, and we discuss them in Section 3.4.5.

[2]http://pono.ucsd.edu/~adam/browndwarfs/spexprism

3.4.2 Spectral Indices and Spectral Types

In Section 3.3.2, we described three methods we used to determine spectral types for our discoveries: visual comparison with field standards, and two index-based methods which applied to limited spectral type ranges. Because visual typing was the only method used for all objects, we adopted those types as the final spectral types for our discoveries. Here we describe the results of the index-based methods and compare our visual and index-based spectral types.

Allers & Liu (2013) Indices

Spectral types determined using the AL13 indices are presented in Table 3.8, along with our visual spectral types for these objects. Figure 3.5 compares our visual and index-derived spectral types. The final index spectral types are mostly consistent with our adopted visual spectral types, agreeing within the joint 1σ uncertainties in 49 out of 60 cases. Of the remaining 11 objects, only one (PSO J057.2+15, discussed below) has an index-derived spectral type more than 2σ different from the visual type, and none are candidate binaries (Section 3.4.5). Figure 3.5 shows an apparent tendency for visual spectral types to be slightly later ($\approx 0.5 - 1$ subtypes) than the AL13-based types, but the bias is within the uncertainties of both typing methods, and does not appear correlated with low-gravity objects or with possible binaries. Overall, our results generally support the effectiveness and insensitivity to gravity of the AL13 low-resolution spectral type indices.

We now discuss the objects whose index-derived spectral types are different from our adopted visual types by more than 1σ. The overall tendency here is for the AL13 index-based spectral types to be earlier than our visual types for unusually red objects.

PSO J004.7+51 (visual L7, index L5.4 $\pm$ 0.8) — The index-based spectral type is determined by only one index (H_2OD) and is too late-type for the other indices to apply. The spectrum is redder overall than the L7 standard, and this has probably affected the H_2OD index which measures the depth of the $\approx$1.9 μm water absorption band.

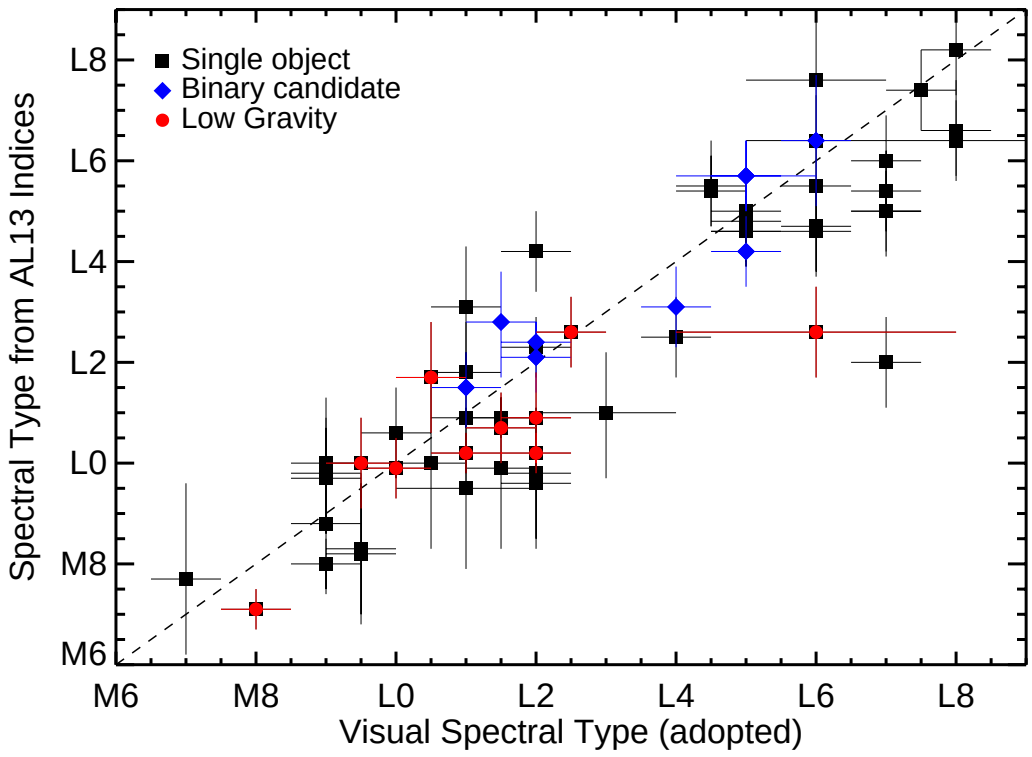

Figure 3.5 Comparison of our visual spectral types with spectral types calculated using the indices of Allers & Liu (2013a). Single objects are marked with black squares, binary candidates (Section 3.4.5) with blue diamonds, and objects having INT-G or VL-G gravity classifications (Section 3.4.4) with red circles. The dashed black line indicates equal spectral types. There is an overall tendency for our visual spectral types to be ≈1 sub-type later than the index-based types, but no other trend is apparent in the typing of binary candidates or low-gravity objects.

PSO J057.2+15 (visual L7 red, index L2.0 ± 0.9) — This late-L dwarf is very red. As with PSO J004.7+51, the index-based spectral type is determined by only the H_2OD index, and is 3.6σ different (joint uncertainties) from the visual L7 type. The ≈1.9 μm water absorption band measured by the H_2OD index is significantly shallower than for the L7 standard.

PSO J068.9+13 (Hya12) (visual L6 red, index L4.6 ± 0.8) — Another unusually red object, cool enough that only the H_2OD index is available to determine the spectral type. Visually, the J band is an excellent match to the L6 standard. The object was first identified photometrically by Hogan et al. (2008) and confirmed by Lodieu et al. (2014) as an L3.5 dwarf based on its optical spectrum. Lodieu et al. (2014) classify Hya12 as a candidate member of the Hyades based on it sky location, proper motion, and photometric distance. We tentatively assign this object a gravity classification of INT-G (Section 3.4.4), which would imply a younger age than the Hyades. A higher-S/N spectrum would confirm the youth of PSO J068.9+13, and parallax and radial velocity measurements are needed to assess its membership in the Hyades.

PSO J127.4+10 (visual L4, index L2.5 ± 0.8) — Also a redder object, with three indices contributing to the final index type, but with a good visual J band match to the L4 standard. We tentatively give this object a gravity classification of VL-G (Section 3.4.4), noting the triangular H band profile, but the lower S/N of the spectrum precludes a firm gravity determination.

PSO J143.6−29 (visual L1, index $L3.1^{+1.2}_{-1.3}$) — The S/N of this spectrum limits our ability to declare a firm spectral type and increases the uncertainties in the index-based type, but the J band matches the L1 standard quite well. This object is also discussed in Section 3.4.2.

PSO J159.0−27 (visual L2 blue, index L4.2 ± 0.8) — The object is atypically blue for an L2, which may increase the depth of the water absorption bands used by the indices to determine the spectral type. Visually it is a good match in J band to the L2 standard and

shows signs of low gravity. We tentatively assign this object a gravity classification of INT-G (Section 3.4.4).

PSO J218.5−27 (visual L6, index L3.9±0.8) — The modest S/N of this spectrum affects the indices (and results in the noise spikes in the H band peak). The J band spectrum is a good match to the L6 standard.

PSO J331.9−07 (visual L7, index L5.0±0.8) — This object is an excellent visual match to the L7 standard, and the index-based spectral type is determined by only one index (H_2OD).

PSO J336.9-18 (visual L6:: red, index L2.1 ± 0.7) — This extremely red L dwarf has a VL-G gravity class (Section 3.4.4). Visually, it is not a clear J band match to any field standard, but the shape of the J band peak and the depth of the ≈1.4 μm water absorption band are decent matches to the L6 standard. The index-based type depends on two indices. This object demonstrates the difficulty in assigning spectral types to unsually red L dwarfs.

PSO J346.5−15 (visual L7, index L5.0 ± 0.9) — This object is a good visual match to the L7 standard, albeit slightly blue, and the index-based spectral type is determined by only one index (H_2OD) in the fairly noisy spectrum.

PSO J348.8+06 (visual L2, index L0.2 ± 0.4) — We classify this object as VL-G (Section 3.4.4), as it shows many signs of low gravity in its spectra. The J band spectrum is a good match to the L2 standard.

Burgasser et al. (2006) Indices

We show spectral types calculated using the B06 indices for all of our L and T dwarf discoveries in Table 3.9, along with the adopted visual spectral types. Figure 3.6 compares our visual and B06 index-based spectral types. The spectral types from the two methods agree very well for T dwarfs (none differ by more than 1σ). 17 of the 70 L dwarfs have $>1\sigma$ differences in spectral type, even though the uncertainties on the L dwarf spectral types are larger. This larger scatter in L dwarf types is consistent with the smaller number of indices used as well as the wider variety of spectral features and colors seen in L dwarfs than in T

dwarfs (e.g., Kirkpatrick et al. 2010), and was previously noted by Burgasser et al. (2010a) who compared literature and B06 spectral types. The visual types appear to skew ≈1 sub-type earlier than the B06 types for early-L dwarfs and ≈1 sub-type later for late-L dwarfs. We see no significant correlation between low gravity and the differences in visual and B06 spectral types. The uncertainties in the index-based types are typically larger than the rms uncertainties of the Burgasser (2007a) polynomials but do not appear to be correlated with the S/N of our spectra. Overall, our results strongly support the effectiveness of the B06 indices for T dwarf classification, but B06 index-based spectral types for L dwarfs may differ visually determined ones by $\approx 0.5 - 1.0$ subtypes.

Below we comment on objects whose B06 index-derived spectral types differ from our adopted visual types by more than 1σ.

PSO J003.4−18 (2MASS J0013−1816) (visual L5 pec, index L8.0 ± 2.3) — We identify this object as a strong binary candidate in Section 3.4.5. Our visual L5 type was determined by the J band shape, but H and K bands have features typical of cooler dwarfs.

PSO J007.9+33 (visual L9, index L7.6±0.4) — We find a good fit to this object's J band profile with the L9 standard, but PSO J007.9+33 has slightly shallower water absorption bands at ≈1.15 μm and ≈1.4 μm which are suggestive of an earlier spectral type.

PSO J087.7−12 (visual L8, index L6.0 ± 1.1) — Low S/N likely affects the indices for this spectrum, which is a good visual fit to the L8 standard.

PSO J088.3−24 (visual L1:, index L6.8 ± 4.1) — This spectrum has only S/N ≈ 10. The overall early-L morphology is apparent, but more accurate typing by any method will require a higher S/N spectrum.

PSO J136.5-06 (visual L2 pec, index *L*6.6 ± 3.1) — This strong binary candidate (Section 3.4.5) shows multiple signs of an L+T blend, and consequently the individual indices gives spectral types ranging from L4.2 to T1.2.

PSO J143.6−29 (visual L1, index L3.0 ± 0.6) — This is the only object among our discoveries whose visual spectral type disagrees by more than 1σ with spectral types derived from both the AL13 (Section 3.4.2) and B10 indices. The index-based classifications are

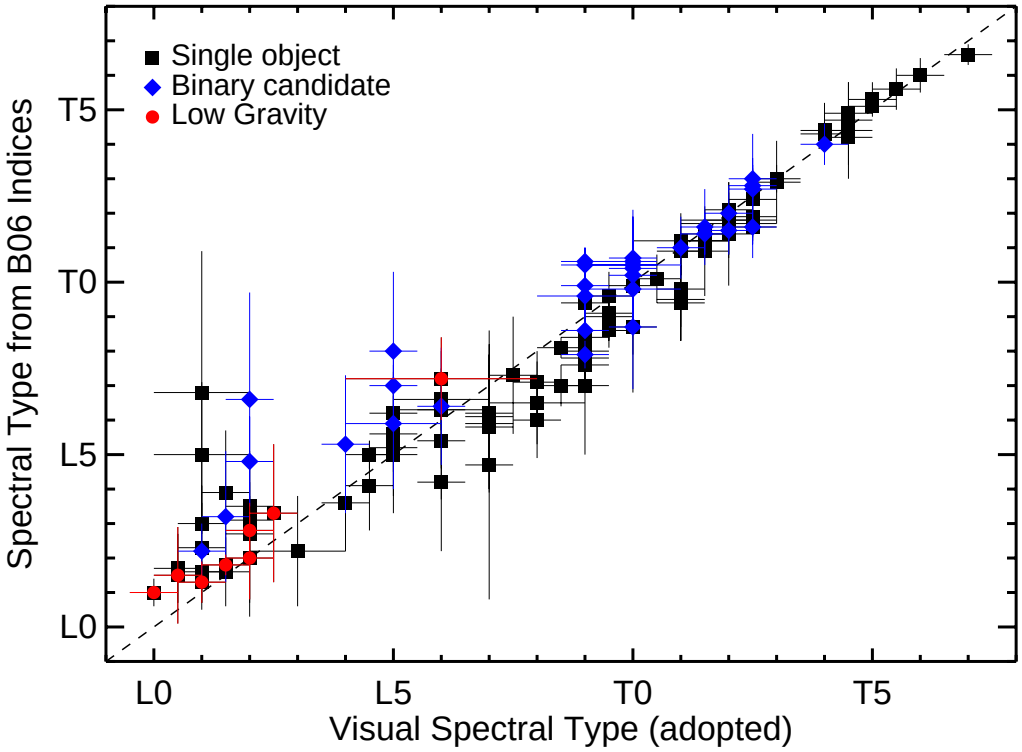

Figure 3.6 Comparison of our visual spectral types with spectral types calculated using the indices of Burgasser et al. (2006a), using the same symbols as Figure 3.5. Compared to the index-based spectral types, our visual spectral types are ≈1 sub-type earlier for early-L dwarfs, ≈1 sub-type later for late-L dwarfs, and in good agreement for T dwarfs. No other trend is apparent in the typing of low-gravity objects, but the objects with the largest discrepancy in types tend to be binary candidates. The two objects with visual L1 types and index-based types ≥L5 have spectra with S/N< 20, so their index-based types are not reliable.

L3.1 and L3.0, in close agreement, but this spectrum is noisy enough to make those types unreliable. We see a good J band match to the L1 standard.

PSO J149.0−14 (visual L9, index T0.5 ± 0.5) — This medium-ranked binary candidate (Section 3.4.5) shows an overall L9 morphology, but there are subtle signs of methane absorption that shift the index-based type to a T dwarf.

PSO J149.1−19 (visual L5, index L7.0 ± 0.6) — One of our strongest binary candidates (Section 3.4.5), this object's spectrum shows several L+T dwarf blend features along with a good J band fit to the L5 standard.

PSO J158.1+05 (visual L2 blue, index L3.5 ± 0.3) — The J-band spectrum is a good fit to the L2 standard, but the overall bluer spectral slope includes deeper water bands that point to a later index-based spectral type.

PSO J183.9−09 (visual L0, index L1.0 ± 0.4) — The spectral types differ by only 1.1σ, which is actually surprising given the very low S/N of this early-L spectrum.

PSO J244.1+06 (visual L9 red, index L7.8 ± 0.5) — The spectral types differ by only 1.2σ. This minor discrepancy may be due to the modest S/N of the spectrum and/or the object's unusually red color.

PSO J282.7+59 (WISE J1851+5935) (visual L9, index L7.9 ± 0.4) — This weak binary candidate (Section 3.4.5) was discussed in detail in Paper I, and was assigned a spectral type of L9 pec by Thompson et al. (2013). The object's blue color may contribute to the slightly earlier index-based spectral type.

PSO J321.1+18 (visual L9, index T0.6 ± 0.4) — This weak binary candidate (Section 3.4.5) features water absorption bands and an H band peak more similar to an early-T dwarf, which explains the T0.6 index-based type.

PSO J338.8+31 (visual L2 pec, index L4.8 ± 1.3) — The deeper water absorption bands of this strong binary candidate (Section 3.4.5) lead to a later index-based spectral type.

PSO J346.3−11 (visual L8.5, index L7.0 ± 0.6) — The J band shape is a clear fit to the L8 and L9 standards. Surprisingly, this object was assigned an earlier spectral type by the indices despite the depth of the water absorption bands and the slightly bluer color.

PSO J353.0−29 (visual L1:, index L5.0 ± 2.1) — This spectrum has only S/N ≈ 15. The overall early-L morphology is apparent, but more accurate typing by any method will require a higher S/N spectrum.

3.4.3 Colors and PS1 Photometry

Figures 3.7–3.11 show the colors of our discoveries and previously known ultracool dwarfs that we used to identify the candidate L/T transition dwarfs in our search (Section 3.2). Those color criteria were designed using PS1 photometry from January 2012 (Processing Version 1). Since then, ongoing PS1 observations and image processing have produced more detections and improved measurements. We have chosen to use PS1 data from March 2015 (Processing Version 2) to make Figures 3.7–3.11 because of the improved photometric precision and the increased number of detections, particularly valuable in $i_{\rm P1}$. WISE photometry is from the All-sky release (Cutri et al. 2012).

These figures demonstrate the success of our color criteria. In particular, Figure 3.7 shows the two colors at the core of our screening process, $y_{\rm P1} - W1$ and $W1 - W2$. Our $y_{\rm P1} - W1 \geq 3.0$ mag cut is very effective, removing only a few T dwarfs at the cool end of the L/T transition (spectral type ≈ T4–T5). Our $W1 - W2 \geq 0.4$ mag cut is similarly effective, excluding some L6–L7 dwarfs but also culling many more earlier-type objects. We also note that four of our discoveries now have $y_{\rm P1} - W1 < 3.0$ mag with the updated PS1 photometry; these objects have spectral types M7, T4, T4.5, and T5.5.

The updated PS1 photometry includes $i_{\rm P1}$ detections of 50 of our spectroscopic targets (compared with only 3 detections from the January 2012 PS1 photometry), nearly all of which have spectral types earlier than L6. The new $i_{\rm P1} - y_{\rm P1}$ and $i_{\rm P1} - z_{\rm P1}$ colors (Figure 3.8) would actually have culled most of these SpT < L6 objects from our candidate list, significantly increasing the efficiency of our search for L/T transition dwarfs (from 55% to ≈80%) but also eliminating most of our young discoveries (Section 3.4.4). $i_{\rm P1}$ detections of T dwarfs remain rare (≈10 in Processing Version 2), as these objects are optically extremely faint. Figure 3.9 shows the usefulness of $z_{\rm P1} - y_{\rm P1}$ for separating M

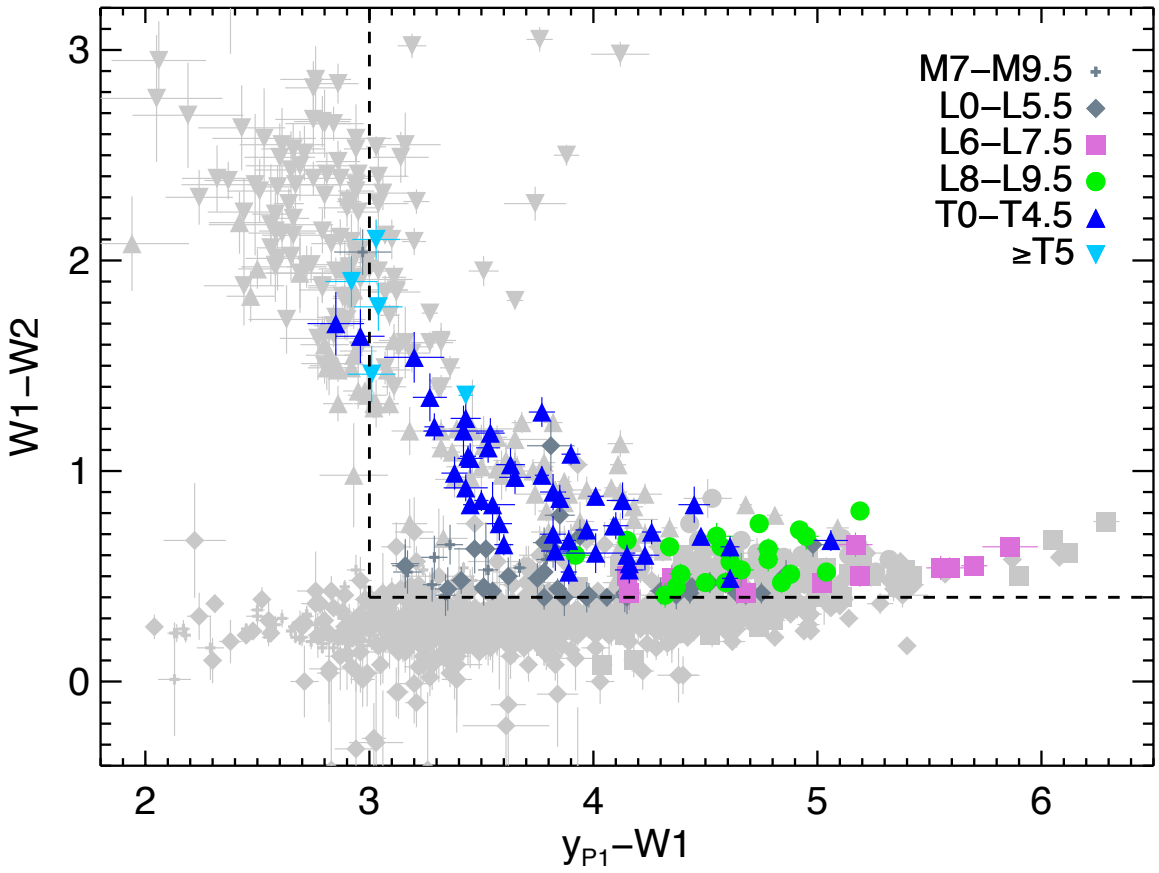

Figure 3.7 $W1-W2$ vs. $y_{\rm P1}-W1$ diagram showing our discoveries in dark gray and colors for spectral type bins (see legend at upper right), and previously known ultracool dwarfs in light gray using the same symbols as for our discoveries. We selected objects above and to the right of the dashed lines using $y_{\rm P1}$ photometry from 2012 January; this plot shows $y_{\rm P1}$ values as of 2015 March. Only 4 of our 130 discoveries would have been excluded from our search using the newer $y_{\rm P1}$ photometry.

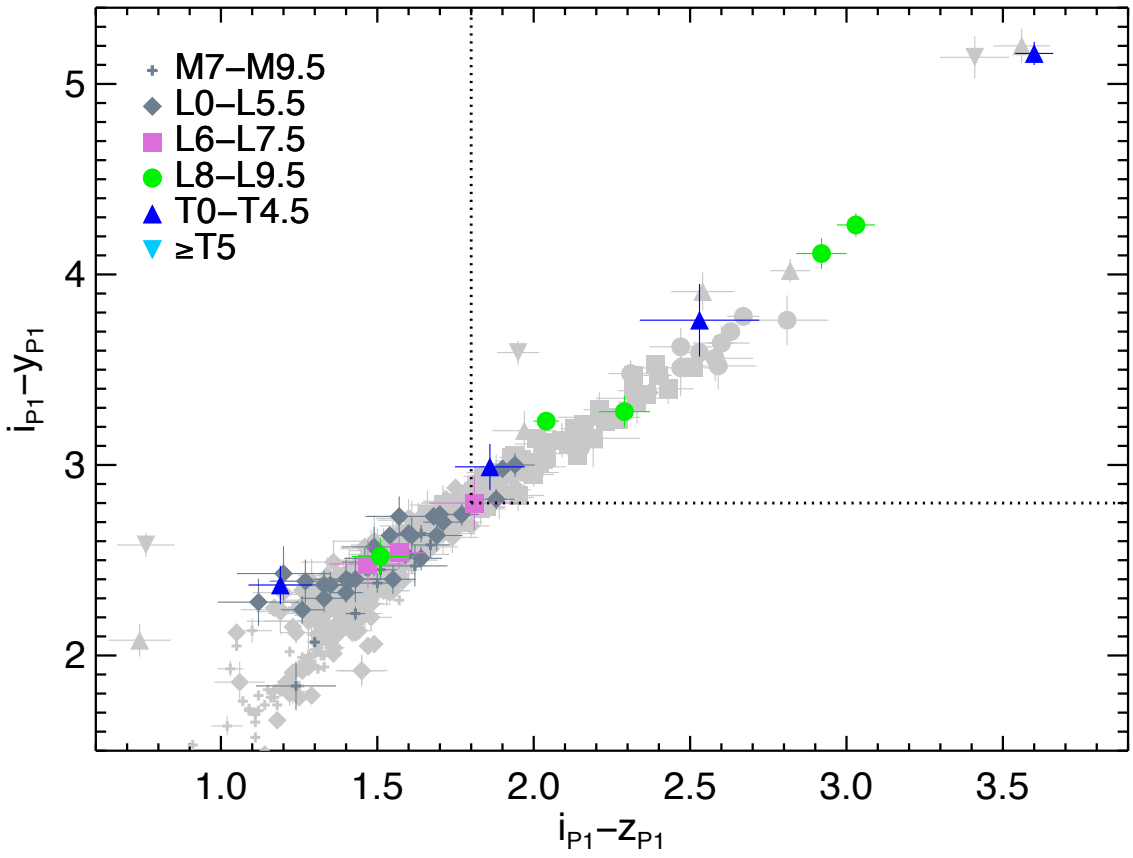

Figure 3.8 $i_{\rm P1} - y_{\rm P1}$ vs. $i_{\rm P1} - z_{\rm P1}$ diagram for our discoveries and known ultracool dwarfs, using PS1 photometry from 2015 March and the same symbols as in Figure 3.7. The dotted black lines indicate the color cuts used in our search; we selected objects above and to the right of the dotted lines, but only enforced each cut for objects having $\sigma < 0.2$ mag and at least two detections in both $i_{\rm P1}$ and $z_{\rm P1}$ in the 2012 January epoch of PS1 photometry. Most of our discoveries with spectral types less than L6 would have been culled from our search using the most recent PS1 photometry, which has many more detections in $i_{\rm P1}$ for our objects. This would have resulted in a significantly higher fraction (≈80%) of L/T transition discoveries, but far fewer discoveries of young objects.

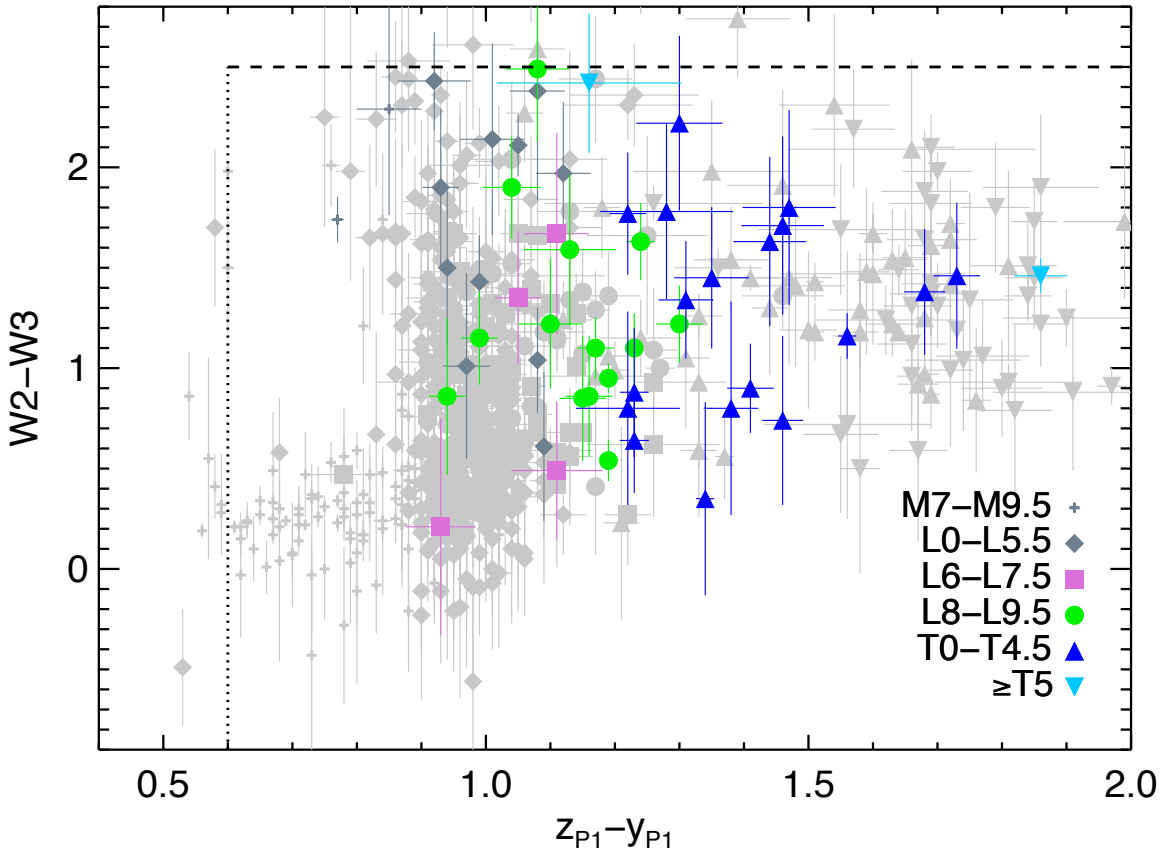

Figure 3.9 $W2-W3$ vs. $z_{\rm P1}-y_{\rm P1}$ diagram for our discoveries and known ultracool dwarfs, using PS1 photometry from 2015 March and the same symbols as in Figure 3.7. The vertical dotted line indicates our $z_{\rm P1}-y_{\rm P1}$ cut, which we applied only to objects with $\sigma_z < 0.2$ mag and having at least two $z_{\rm P1}$ detections in the 2012 January epoch of PS1 photometry. The horizontal dashed line represents our $W2-W3$ cut, which we applied to all objects in our search in order to exclude galaxies. We selected objects below and to the right of these lines.

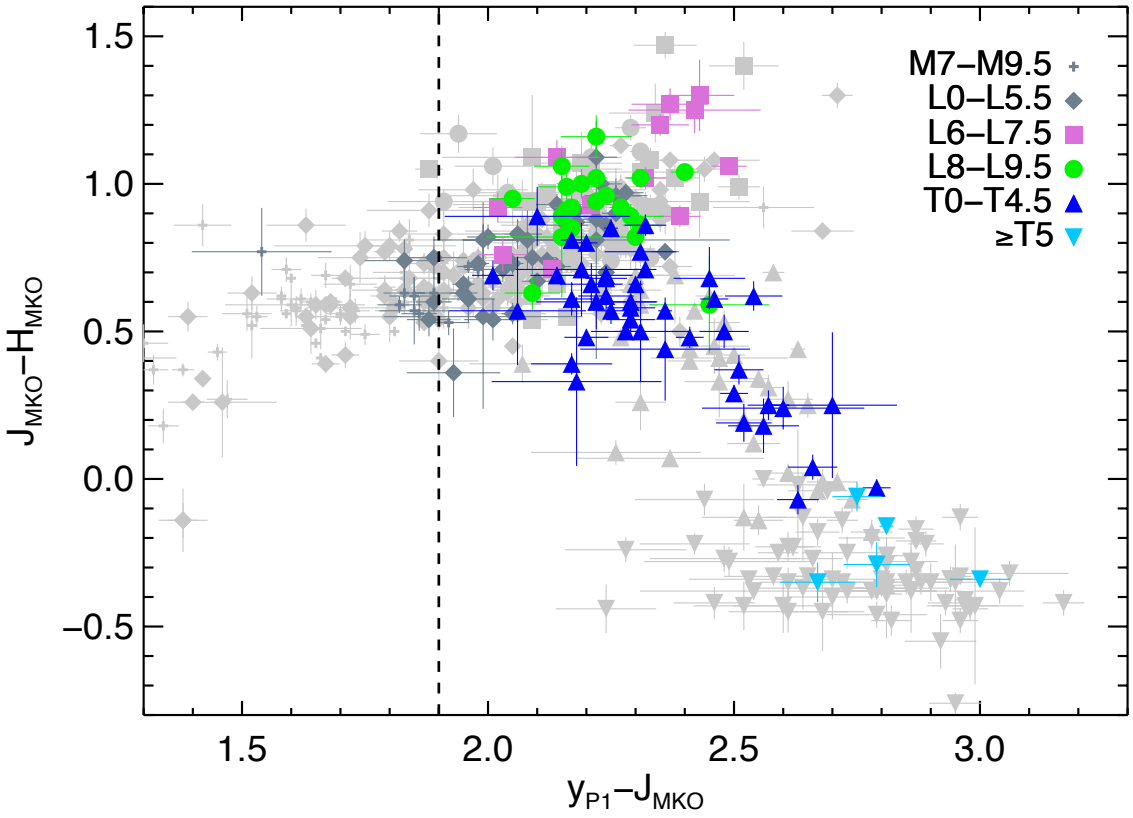

Figure 3.10 $J_{\rm MKO} - H_{\rm MKO}$ vs. $y_{\rm P1} - J_{\rm MKO}$ diagram for our discoveries and known ultracool dwarfs, using $y_{\rm P1}$ photometry from 2015 March and the same symbols as in Figure 3.7. We selected objects to the right of the dashed line using $y_{\rm P1}$ photometry from 2012 January. (We did not use $J - H$ color to screen targets in our search, but it has been used in many previous near-IR searches for T dwarfs.) The updated PS1 photometry has shifted eleven late-M and early-L dwarfs outside of our $y_{\rm P1} - J_{\rm MKO} \geq 1.9$ mag cut.

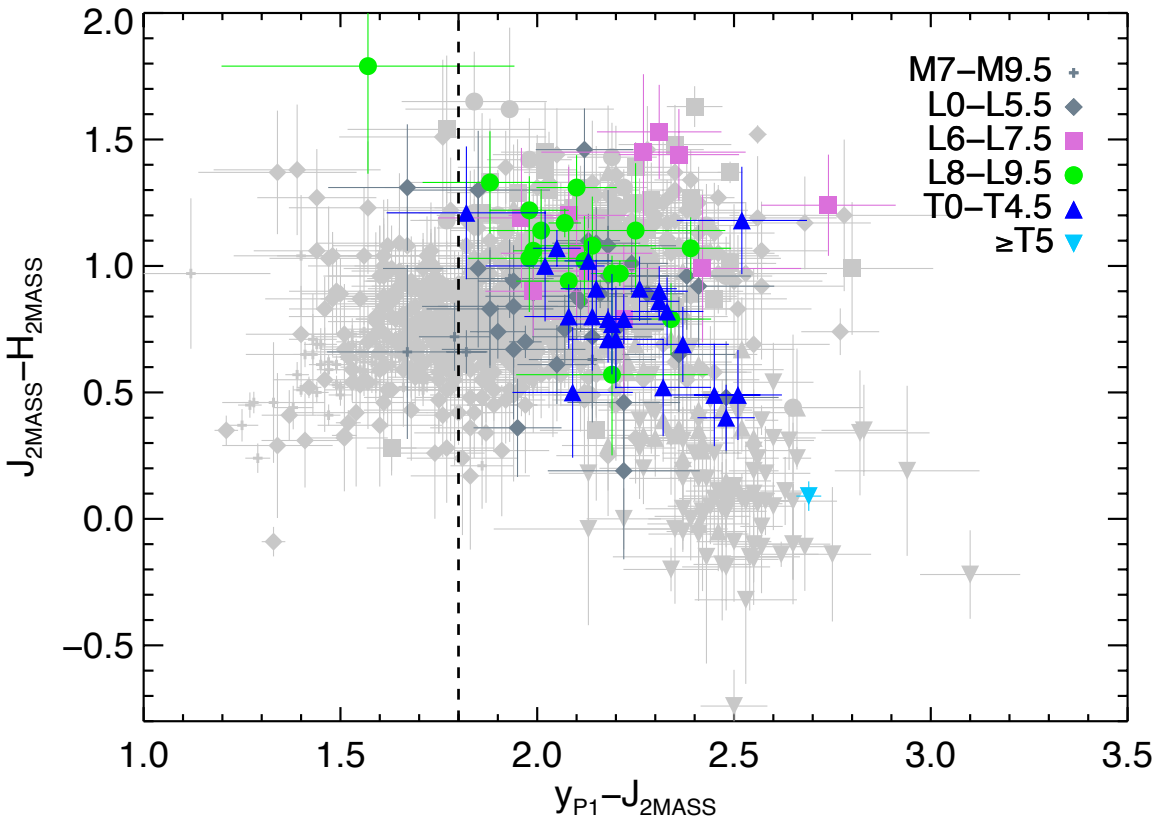

Figure 3.11 Same as Figure 3.10, but using 2MASS photometry for J and H bands instead of MKO. The updated PS1 photometry has revised the unusually blue $y_{\rm P1} - J_{\rm 2MASS}$ colors of discoveries we presented in Paper I, bringing them in line with other field objects.

dwarfs from L and T dwarfs, and similarly for $y_{\rm P1} - J_{\rm MKO}$ in Figure 3.10. The new $y_{\rm P1}$ photometry would also have rejected 11 of our late-M and early-L dwarf discoveries which now have $y_{\rm P1} - J_{\rm MKO} < 1.9$.

In Paper I, we reported unusually blue $y_{\rm P1} - J_{\rm 2MASS}$ colors for six of our bright nearby discoveries. We note that this color deviation has now disappeared. The updated $y_{\rm P1}$ photometry for these objects is slightly fainter, which brings the $y_{\rm P1} - J_{\rm 2MASS}$ colors of these discoveries into the locus of other field objects (Figure 3.11).

3.4.4 Low-Gravity Objects

Signatures of low gravity in the spectra of ultracool dwarfs are a reflection of the extended radii of young objects that are still contracting. AL13 identified a set of near-IR spectral indices at low ($R \approx 100$) and intermediate ($R \approx 1000$) spectral resolution to assess the surface gravity of M4–L7 dwarfs, and thereby to identify ultracool dwarfs younger than ≈200 Myr. Briefly, the low-resolution indices measure the depths of the $\rm FeH_z$ (0.99 μm), $\rm VO_z$ (1.06 μm), and K I$_{\rm J}$ (1.24 μm) absorption features relative to the continuum, as well as the shape of the H band continuum over $1.47 - 1.67$ μm. Based on these indices, an object is assigned a score of 0, 1, or 2, which correspond to classes of field gravity (FLD-G, ages $\gtrsim$ 200 Myr), intermediate gravity (INT-G, ages $\approx 50 - 200$ Myr), and very low gravity (VL-G, ages $\approx 10 - 30$ Myr), respectively. (Note that the age calibration of the these gravity classes is only notional, and more work is needed in this area.) The median value of the index scores is the final gravity score for the object.

We calculated low-resolution indices and gravity scores for our M and L dwarfs (through L7) using the approach described in Aller et al. (2016), performing Monte Carlo simulations for each object to propagate the measurement errors of our reduced spectra into the index calculations. Most of our spectra have $R \approx 75$, so the indices were computed using only a few resolution elements. We found that spectra with a mean S/N $\lesssim 30$ measured over the interval $1.20 - 1.31$ μm (encompassing the bulk of the J-band flux for L dwarfs) produced gravity scores with uncertainties too large to contain useful information, and we discarded

the scores for those objects. We visually inspected the remaining (higher S/N) spectra to confirm the gravity class, and flagged those with low enough S/N that we could not confirm the gravity class by eye.

Altogether, we classify 10 objects having low gravity (9 as VL-G, 1 as INT-G) and 9 more as FLD-G. Figure 3.12 plots the gravity classes derived from the four spectral indices for these objects against their spectral types. Our final gravity classifications are listed in Table 3.10, excluding six candidate members of the Scorpius-Centaurus Association and the Taurus star-forming region that will be presented in a future paper (Best et al., in prep). The remaining four, PSO J078.9+31 (L1.5 VL-G), PSO J336.9−18 (L6:: red VL-G), PSO J344.8+20 (L2.5 INT-G), and PSO J348.8+06 (L2 VL-G), appear to be young field objects, and their spectra are shown in Figure 3.13 along with field standards from Kirkpatrick et al. (2010) and VL-G standards from AL13 for comparison. Three of the objects (excluding PSO J336.9−18) show weak 0.99 μm FeH_z and strong 1.06 μm VO_z absorption features and a triangular H band shape, all signs of youth. PSO J336.9−18 is an L6 dwarf, too late-type for the FeH_z and VO_z features to yield reliable information about gravity (AL13), but featuring a triangular H-band shape and very red colors. While these are both recognized signatures of youth, AL13 caution that the triangular H-band shape can also appear in spectra of objects that have evidence of old age (based on kinematics). Therefore, while our classification of VL-G is formally correct for PSO J336.9−18, further evidence is needed to support the conclusion that the object is young.

We identify another 7 objects as potentially low-gravity based on their indices, but higher S/N spectra are needed to securely classify them. Among these is PSO J068.9+13 (L6 red, candidate INT-G), identified by Lodieu et al. (2014) as a candidate member of the Hyades (see discussion in Section 3.4.2). Figure 3.14 shows the gravity classes vs. spectral types for these 7 potentially low-gravity objects, and Figure 3.15 compares their spectra to the field and VL-G standards.

In Table 3.11, we list six more objects whose spectra show indications of youth, but for which the AL13 indices were not useful because of the spectral type of the object or the low

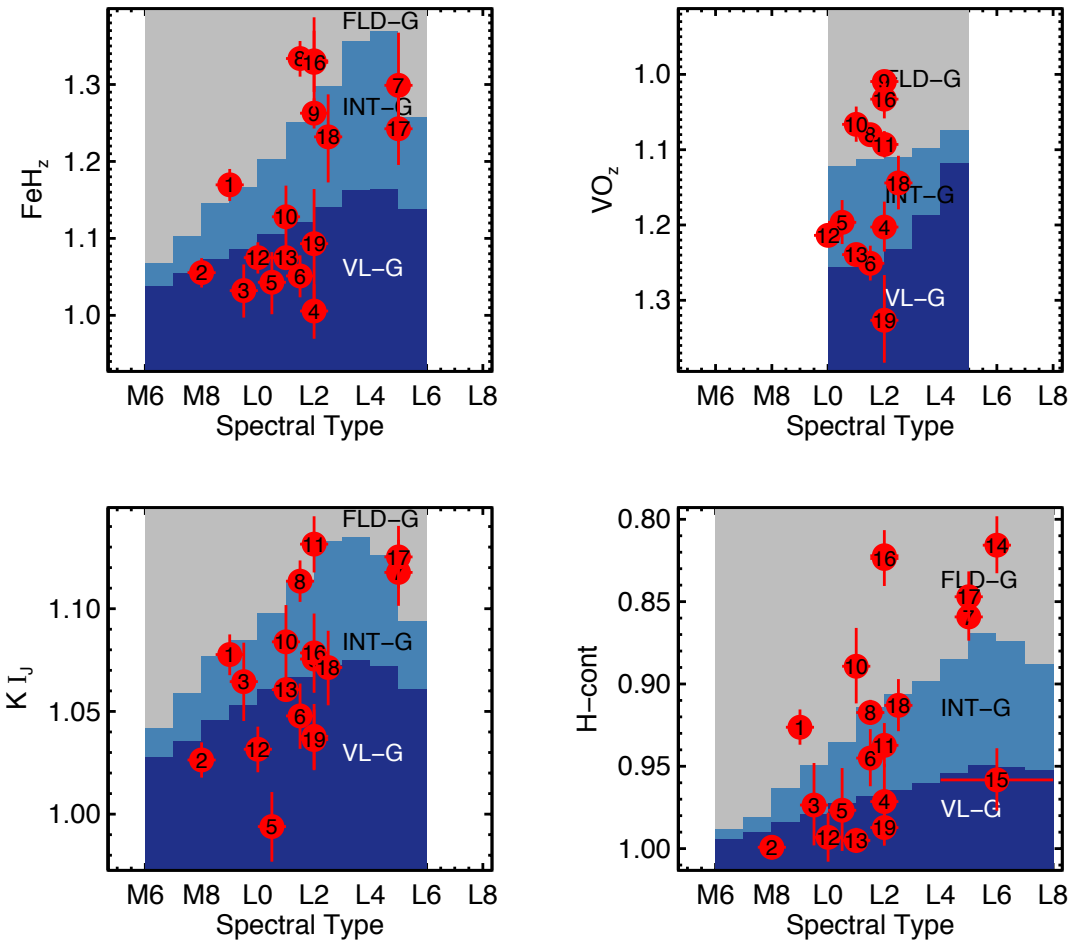

Figure 3.12 Values of the low-resolution gravity-sensitive spectral indices from Allers & Liu (2013a) for the objects whose gravity classes we confirm visually, including 9 FLD-G, 1 INT-G, and 9 VL-G objects. The index values are plotted in red, with values for the same object in different plots labelled with the same number. The gray, slate, and dark blue bars represent the ranges of index values corresponding to the FLD-G, INT-G, and VL-G gravity classes, respectively, and indicate the spectral types for which each index is valid for gravity classification. Given that our search targeted field L/T transition dwarfs and not young M and L dwarfs, discovering this many objects with low-gravity spectral signatures was unexpected.

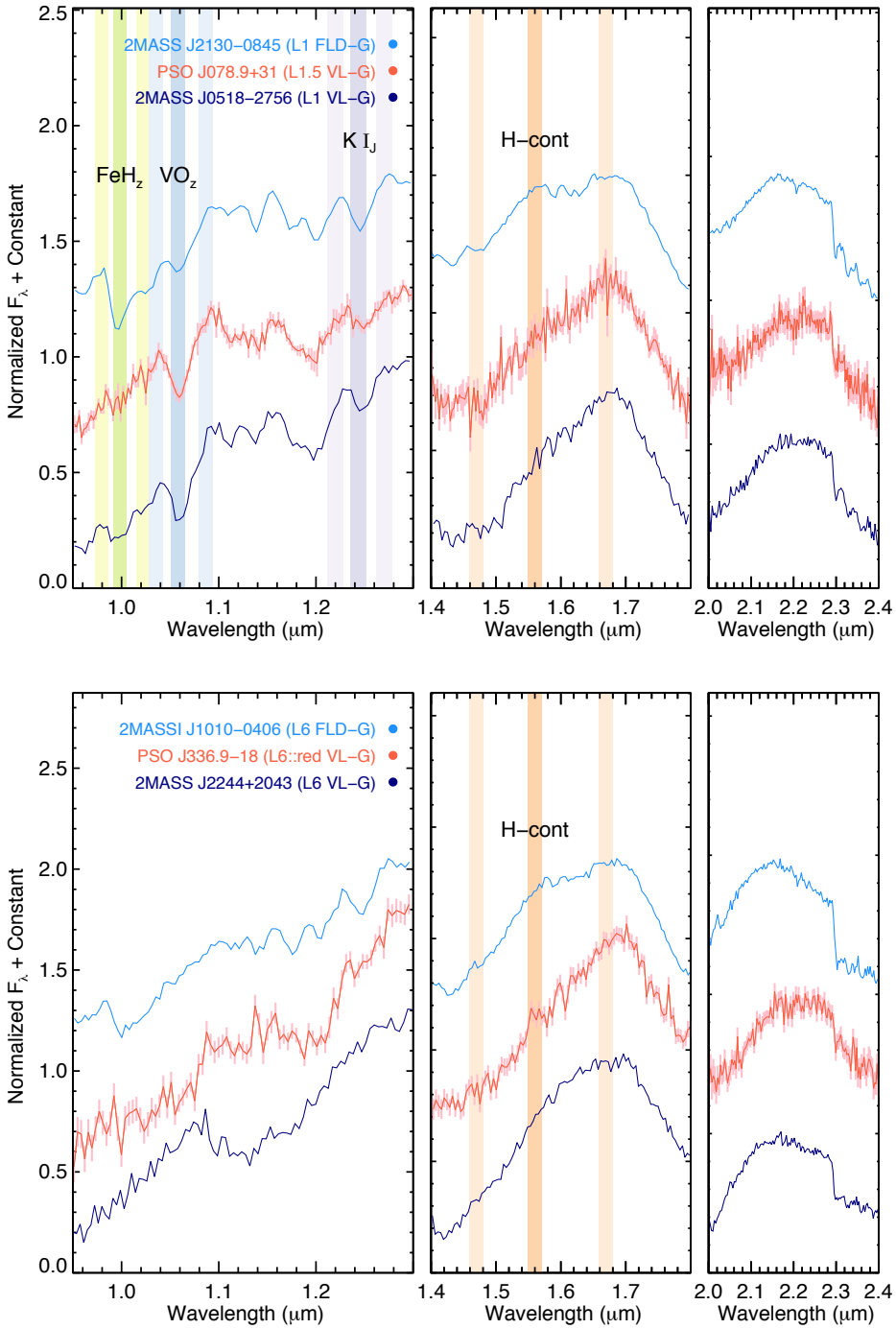

Figure 3.13 Plots showing our four newly identified field INT-G and VL-G objects (middle, with error bars) compared with field standards (top) from Kirkpatrick et al. (2010) and VL-G standards (bottom) from AL13 of the same spectral type (within 0.5 subtypes). The vertical colored bars show the spectral regions used to calculate the indicated indices, for visual comparison. Each plot shows only the indices that are valid for the object's spectral type.

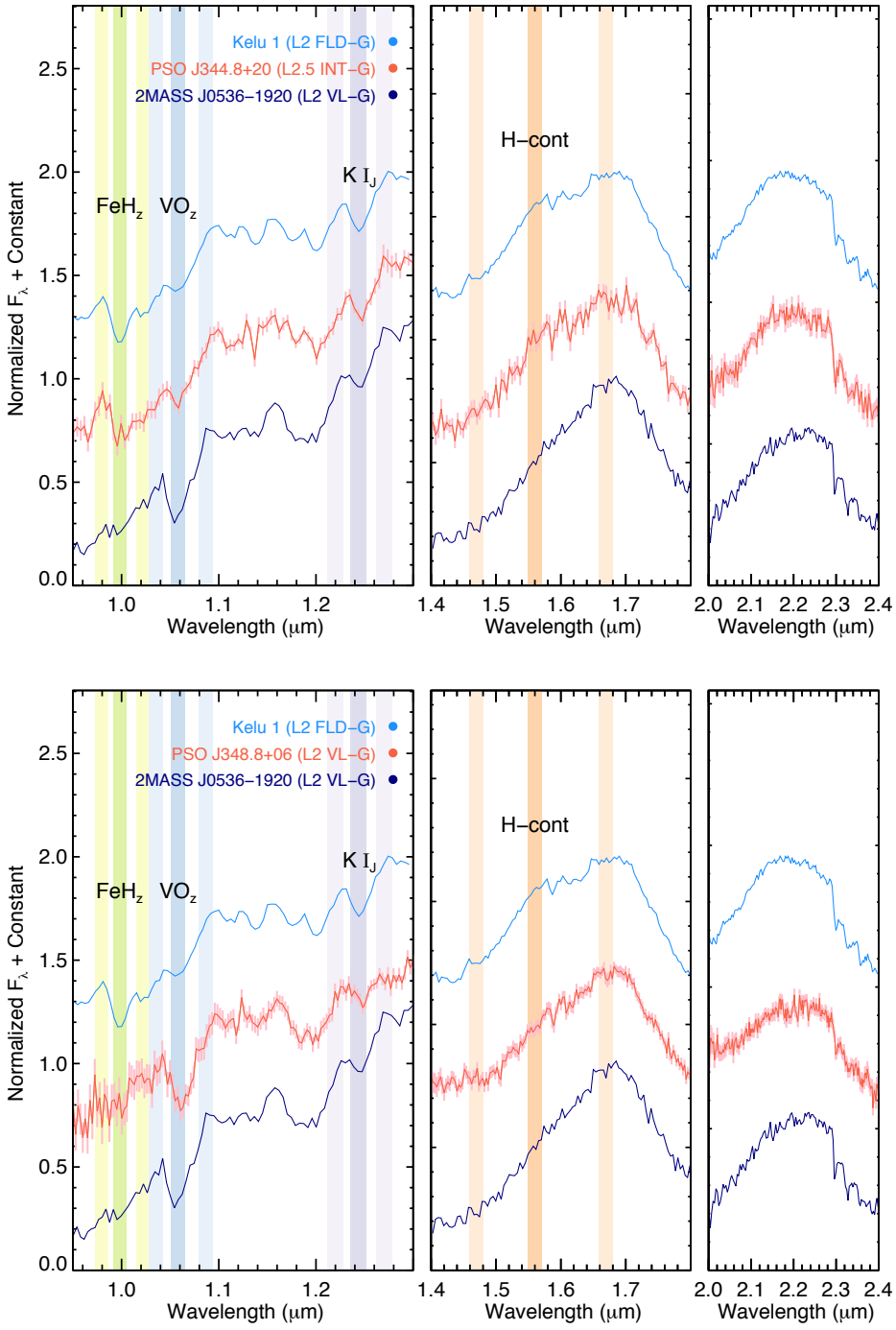

Figure 3.13 continued.

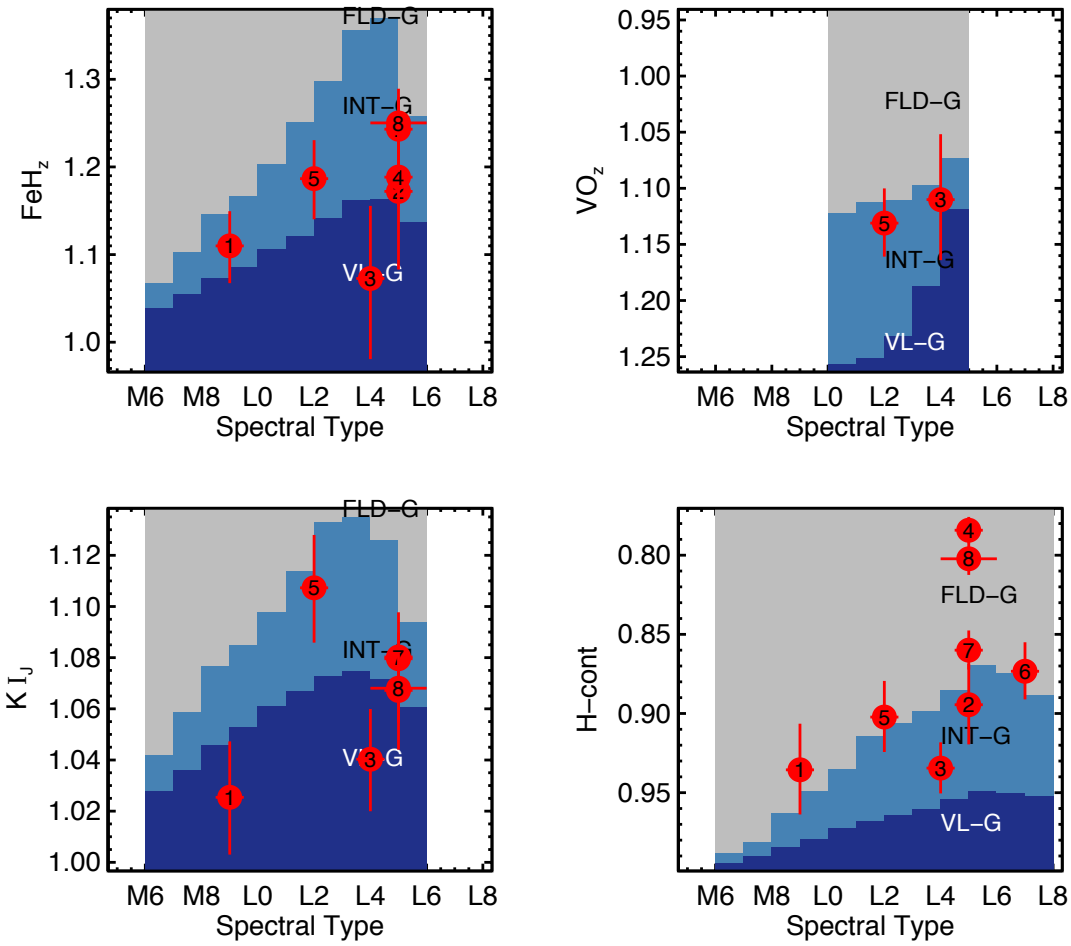

Figure 3.14 Same as Figure 3.12, but for objects whose index-based gravity classes we determine only tentatively due to modest S/N in the spectra.

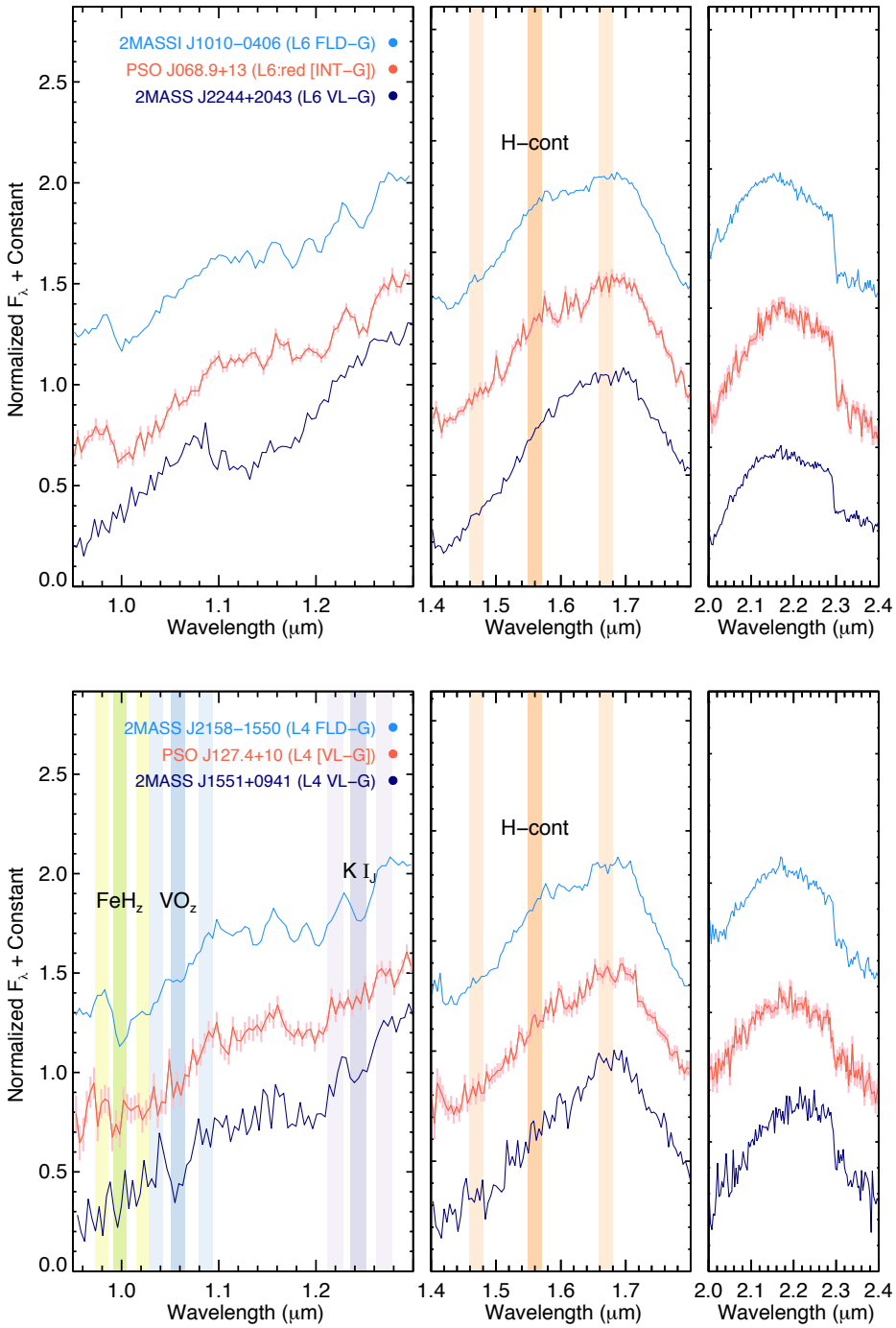

Figure 3.15 Same as Figure 3.13, but for objects whose index-based gravity classes we determine only tentatively (classes indicated in brackets as in Table 3.10) due to modest S/N in the spectra.

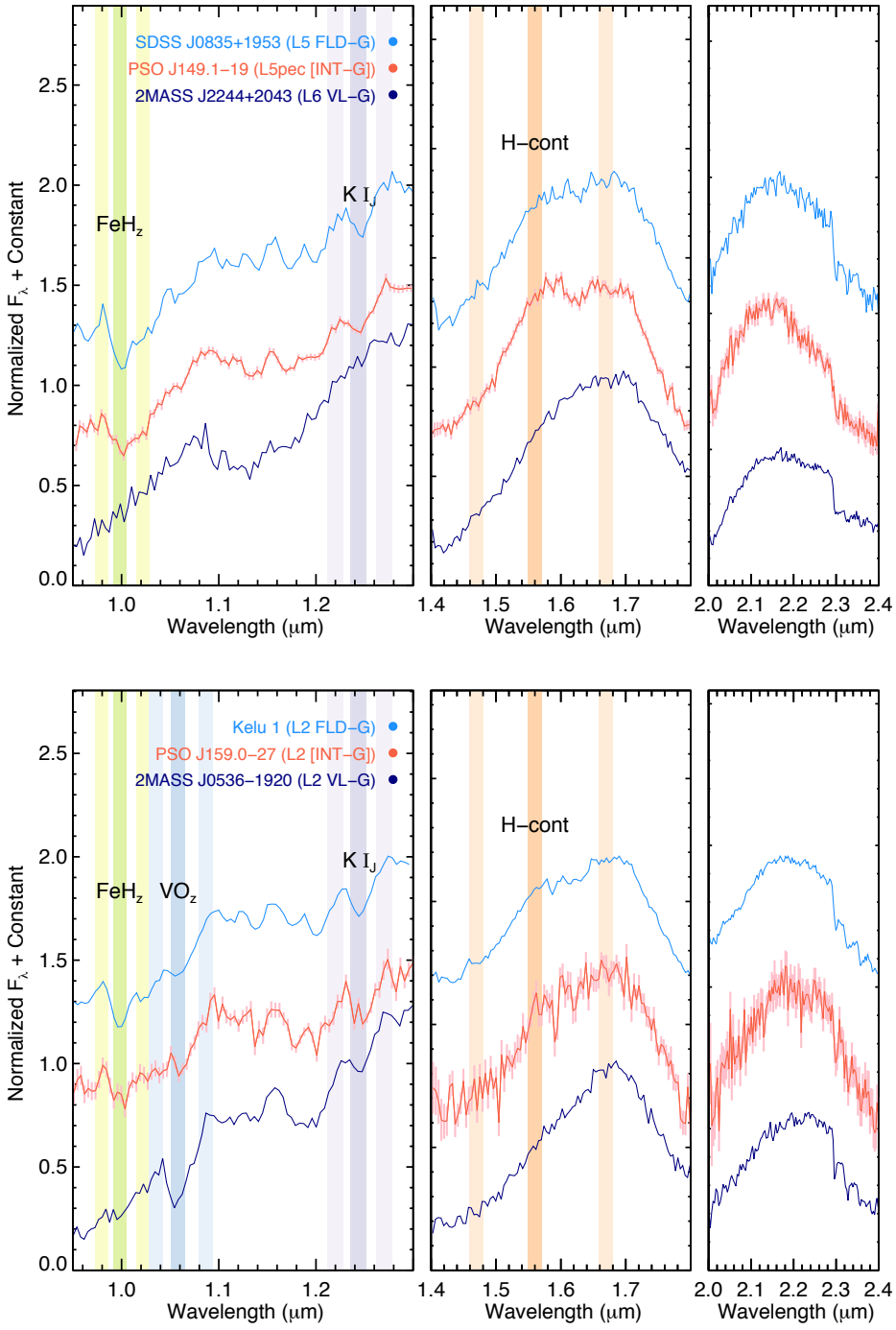

Figure 3.15 continued.

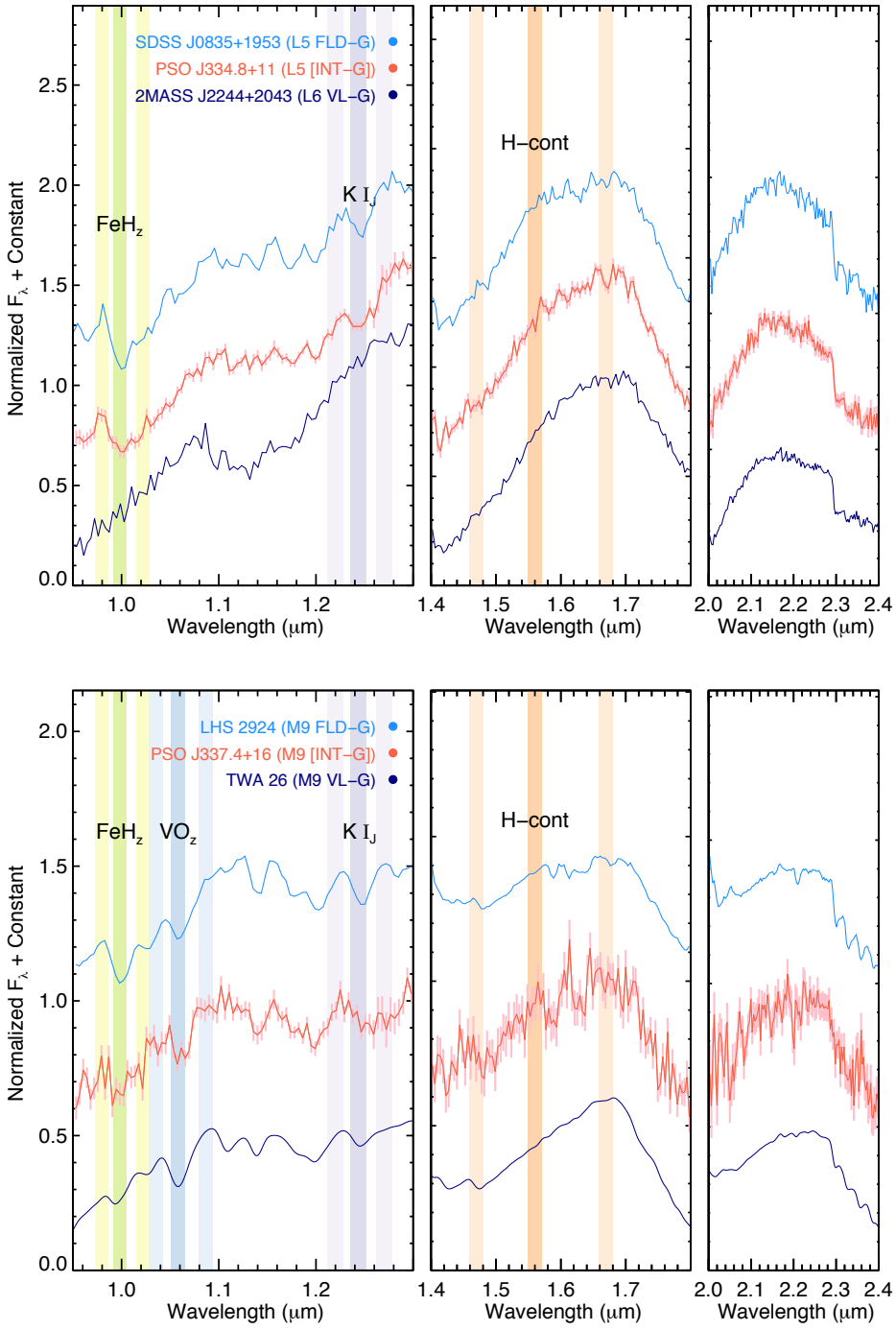

Figure 3.15 continued.

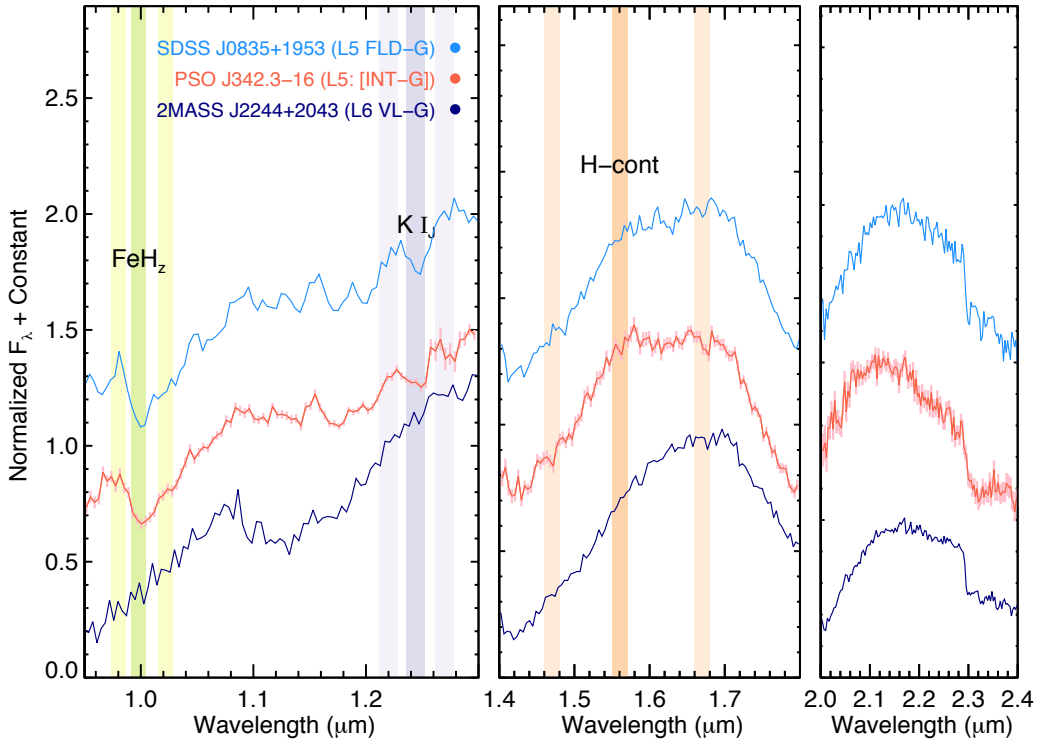

Figure 3.15 continued.

S/N (< 30) of our spectrum. These indications include the redder-than-normal colors and triangular H-band shape described above. Three are candidate members of young moving groups (Section 3.6.2), and three are field objects.

3.4.5 Candidate Binaries

Roughly $15-30\%$ of ultracool dwarfs are binaries (e.g., Basri & Reiners 2006; Liu et al. 2006; Burgasser 2007a). Binary systems are important benchmarks, as the binary components are equidistant, coeval, and have common metallicities. If resolved with high-resolution imaging, these systems can be monitored to determine their orbits and dynamical masses (e.g., Liu et al. 2008; Konopacky et al. 2010; Dupuy et al. 2010), breaking the mass/age degeneracy and providing stringent tests for atmospheric and evolutionary models (e.g., Dupuy et al. 2014, 2015b).

We have examined our discoveries for unusual spectral features that suggest unresolved binarity, using the spectral index criteria of Bardalez Gagliuffi et al. (2014, hereinafter BG14) for our M7–L7.5 dwarfs and Burgasser et al. (2010a, hereinafter B10) for our L8 and later dwarfs. We first ranked our discoveries by the number of index criteria satisfied, and then visually reviewed all spectra for peculiar features indicating blends (see descriptions of individual objects below). We rejected objects with J band ($1.20 - 1.31$ μm) S/N < 25, as several objects with S/N below this limit satisfied many index criteria but revealed no signs of spectral blends on visual inspection. We used the following scheme to identify strong, medium, and weak binary candidates. We ranked objects meeting at least 8 BG14 criteria or 4 B10 criteria as strong candidates. We ranked objects meeting at least 4 BG14 criteria or 3 B10 criteria, as well as objects having clear visual indications of blends plus at least 2 BG14 criteria or 1 B10 criterion, as medium candidates. We labeled other objects showing clear visual indications as weak candidates. This scheme is similar to those of BG14 and B10, but here we use three categories instead of two and we incorporate the results of visual inspection.

Overall, we identify 31 binary candidates (Table 3.12). We compare the spectra of our strong, medium, and weak binary candidates with those of field standards in Figures 3.16, 3.17, and 3.18, respectively. About 2/3 of these have spectral types L9–T2.5, broadly consistent with previous studies that suggested a higher observed frequency of binaries in the L/T transition (e.g., Liu et al. 2006; Burgasser 2007a). Allers & Liu (2013b) demonstrated that the AL13 indices' ability to identify low-gravity features is not affected by spectral blends. We find only one binary candidate (PSO J146.0+05) with mild hints of low gravity.

Below we briefly discuss individual binary candidates with notable spectral features.

Strong Binary Candidates

PSO J003.4−18 (2MASS J0013−1816) (L5 pec) — This object was independently discovered and typed by Baron et al. (2015) as an L1 dwarf and a common proper motion companion to the M3 dwarf NLTT 687. It satisfies 10 of the 12 BG14 criteria. The J band morphology of PSO J003.4−18 is closest to that of an L5 dwarf, but the deeply notched H band peak and a more subtle notch at ≈2.2 μm are both clear indications of methane. The peak in the J band at 1.3 μm and the overall blue color are further evidence of the presence of a T dwarf. Baron et al. (2015) used optical spectral indices to determine a spectral type, and their optical spectrum would be dominated by the primary and have very little flux from a T-type companion. PSO J003.4−18 is therefore very likely to be an early-L + early-T binary. As a companion to NLTT 687, it would also be a rare benchmark ultracool binary (Section 3.4.7).

PSO J049.1+26 (T2.5) — This object is a near-perfect spectral match to the T2+T7.5 binary 2MASS J12095613−1004008 (Burgasser et al. 2004; Liu et al. 2010). The J band shape fits the T2 standard best, but the H and K bands have the morphology of later-T dwarfs. This object satisfies 4 of the 6 B10 criteria.

PSO J071.6−24 (WISE J0446−2429) (L6 blue) — The J band morphology matches an L6 dwarf, but the peak in the J band at ≈1.3 μm suggests a later T dwarf, and the overall color and H and K band shapes match a T0 dwarf. Thompson et al. (2013) independently

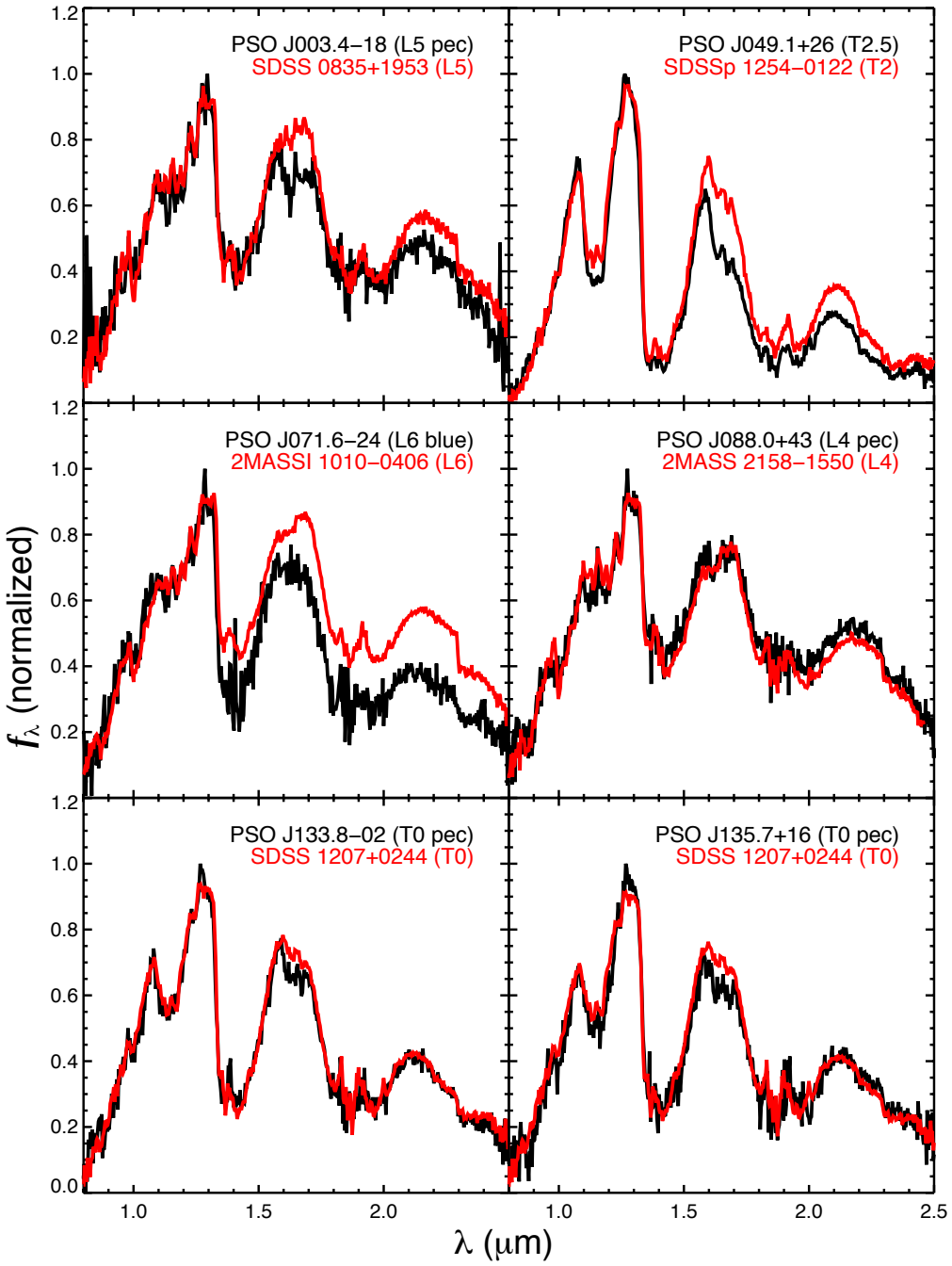

Figure 3.16 Plots comparing the spectra of our strong binary candidates (black) to the field standards of Kirkpatrick et al. (2010) and Burgasser et al. (2006a) (red). Distinctive features of these spectra are discussed in Section 3.4.5.

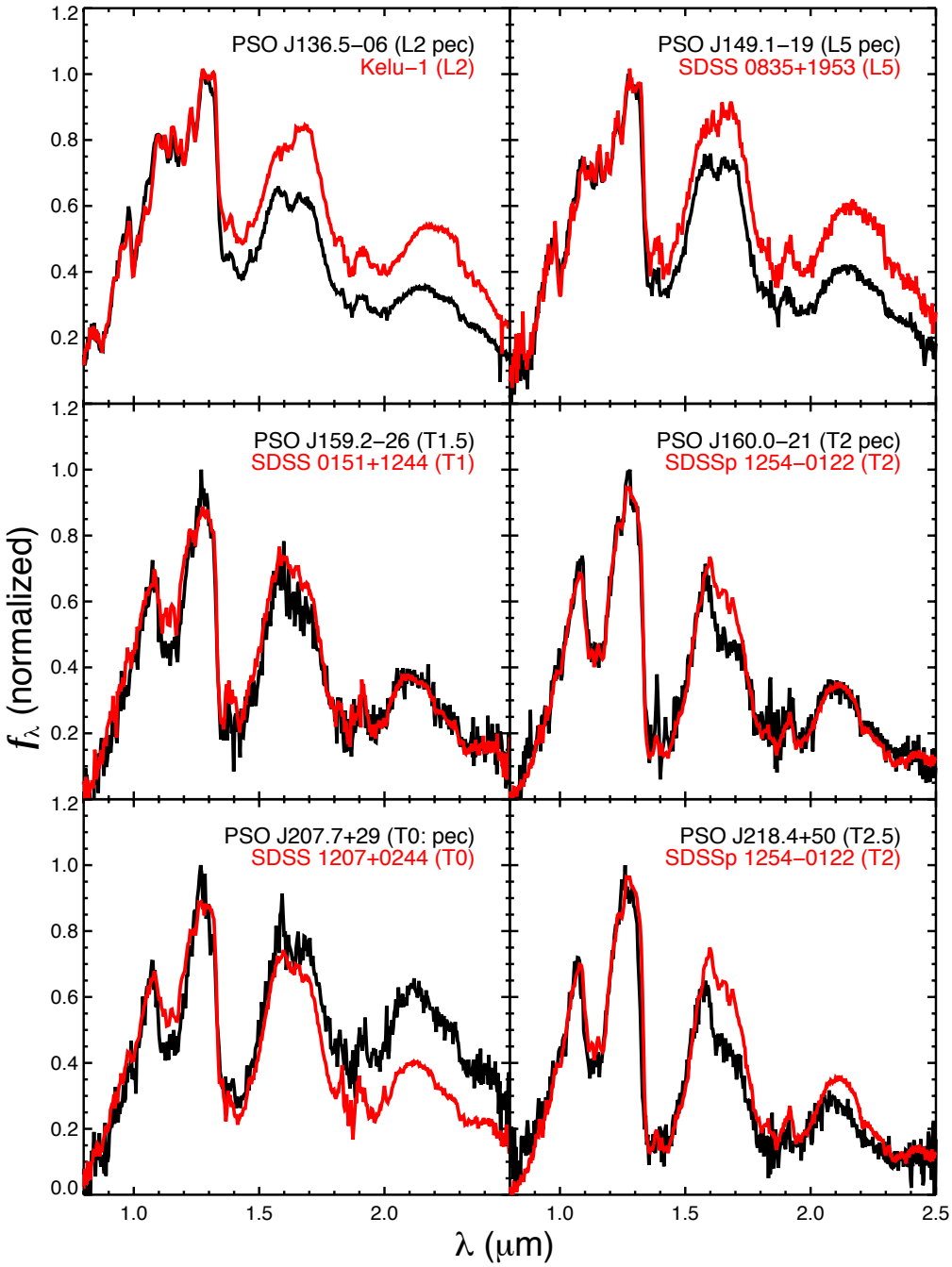

Figure 3.16 continued.

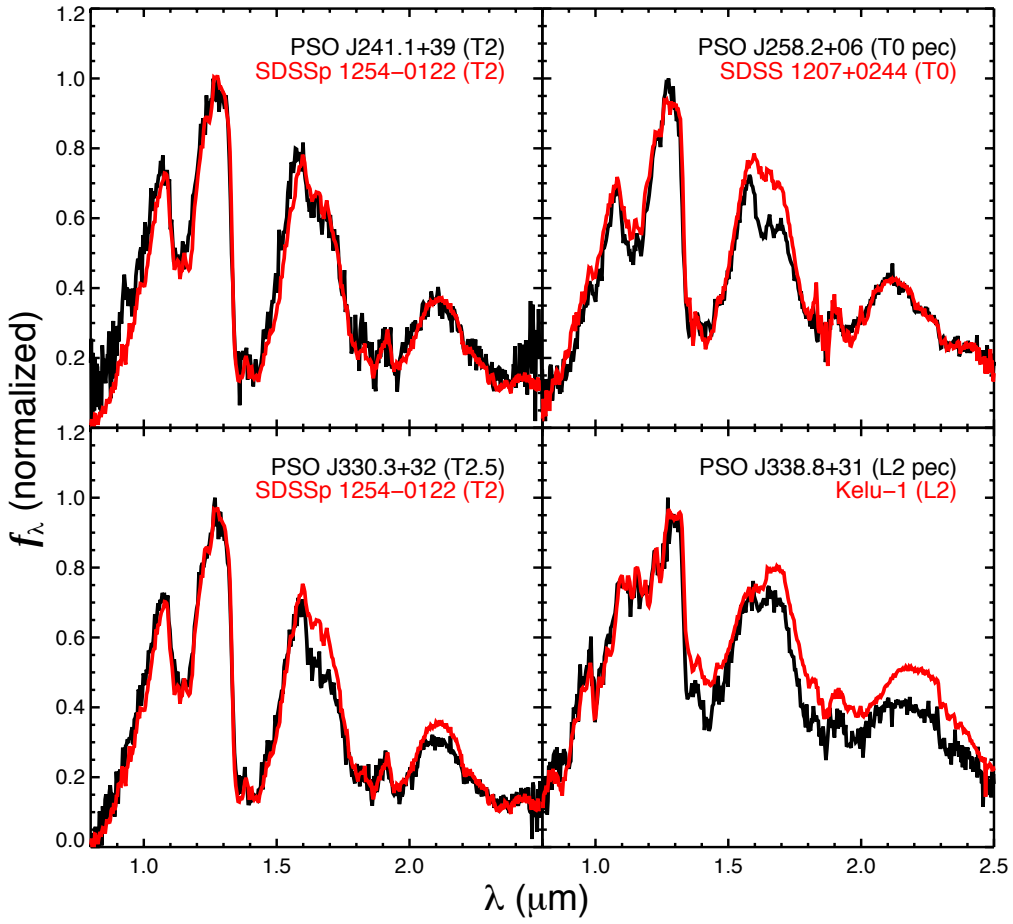

Figure 3.16 continued.

discovered this object and typed it L5 pec (blue), ascribing the unusual spectral features to thin large-grained clouds rather than a L+T blend. This object satisfies 8 of the 12 BG14 criteria.

PSO J088.0+43 (L4 pec) — The J band peak at ≈1.28 μm and the notched H band suggest a mid-T dwarf blended with a normal L4 dwarf. This object satisfies 9 of the 12 BG14 criteria.

PSO J133.8−02 (T0 pec) — The spectrum fits the overall shape of the T0 standard quite well, but the J and H band peaks (≈1.28 μm and ≈1.58 μm, respectively) suggest the additional presence of a later-T dwarf. This object satisfies 5 of the 6 B10 criteria.

PSO J135.7+16 (T0 pec) — The overall morphology is closest to that of a T0 dwarf, but the J and H bands have the shapes of a T2 dwarf. This object satisfies all 6 of the B10 criteria.

PSO J136.5−06 (L2 pec) — The J band shape matches the L2 spectral standard fairly well, but the deeper water absorption band at ≈1.4 μm and the blue color suggest a later-type object, and the notched H band peak and depression at at ≈2.2 μm both indicate the presence of methane. This object satisfies 9 of the 12 BG14 criteria.

PSO J149.1−19 (L5 pec) — The J band morphology is a clear match to L5, but the deeper water absorption band at ≈1.4 μm and the blue color indicate a later-type object. The notched H band peak and depression at ≈2.2 μm both point to methane and a T-dwarf companion. This object satisfies 10 of the 12 BG14 criteria.

PSO J159.2−26 (T1.5) — The K band shape is an excellent match to the T1 standard, but the J and H bands fit a T2 better. This object satisfies 4 of the 6 B10 criteria.

PSO J160.0−21 (T2 pec) — The overall slope of this spectrum matches that of the T2 standard, but the J band peak at ≈1.28 μm and the blue H band peak strongly suggest the presence of a late-T companion. This object satisfies all 6 of the B10 criteria.

PSO J207.7+29 (T0: pec) — This object has no good spectral matches among the L- and T-dwarf standards. The overall color is similar to an L9 dwarf, but the lower flux at

≈1.65 μm and ≈2.2 μm reveal the presence of methane, and the J band peak resembles a mid-T dwarf. This object satisfies all 6 of the B10 criteria.

PSO J218.4+50 (T2.5) — Similar to PSO J049.1+26, this object is a good spectral match to the known T2+T7.5 binary 2MASS J12095613−1004008 (Burgasser et al. 2004; Liu et al. 2010). The J band shape fits the T2 standard best but not well, and the H and K bands have the morphology of later-T dwarfs. This object satisfies 5 of the 6 B10 criteria.

PSO J241.1+39 (T2) — Overall and in the J band, this is a good match to the T2 standard, but the Y and H band peaks are bluer. This object satisfies 5 of the 6 B10 criteria.

PSO J258.2+06 (T0 pec) — The spectrum fits the overall color and K band shape of the T0 standard quite well, but the J and H band peaks resemble a later-T dwarf. This object satisfies all 6 of the B10 criteria.

PSO J330.3+32 (T2.5) — This object has unusually deep water absorption bands at ≈1.15 μm and ≈1.4 μm for a T2.5 dwarf, and satisfies 5 of the 6 B10 criteria. It is a common proper motion companion to the star Wolf 1154 (Section 3.4.7), and therefore would be a rare ultracool benchmark if confirmed as a binary binary.

PSO J338.8+31 (L2 pec) — The spectrum is a good match to the L2 standard in the J band, but the overall slope and K band shape are more like those of a T0, and H band notch indicates methane. This object satisfies 8 of the 12 BG14 criteria.

Medium Binary Candidates

PSO J004.1+23 (T0) — The overall morphology closely resembles a T0 dwarf, but the H band shows no clear sign of methane while the J band peak resembles that of a T2 dwarf. The spectrum is a good match to the L6+T2 binary SDSSp J042348.57-041403.5 (Geballe et al. 2002; Burgasser et al. 2005b). It meets 2 of the 6 B10 criteria.

PSO J100.5+41 (WISE J0642+4101) (L9 red) — This unusual object was independently identified by Mace et al. (2013a), who classify it as "extremely red" without assigning a spectral type. We type it as L9 based on its $1.2-1.3$ μm J band profile and the

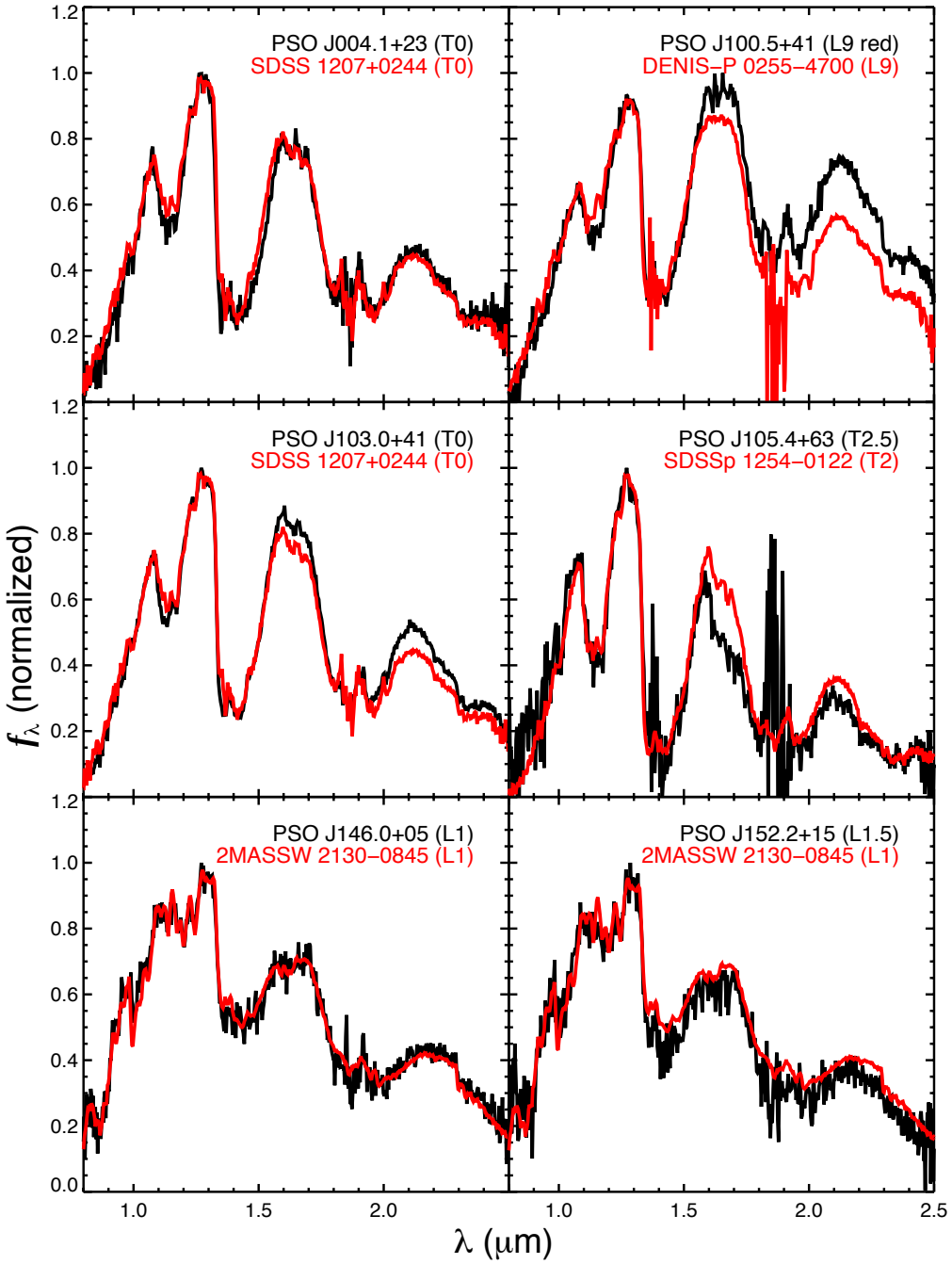

Figure 3.17 Same as Figure 3.16, but for our medium-ranked binary candidates. Distinctive features of these spectra are discussed in Section 3.4.5.

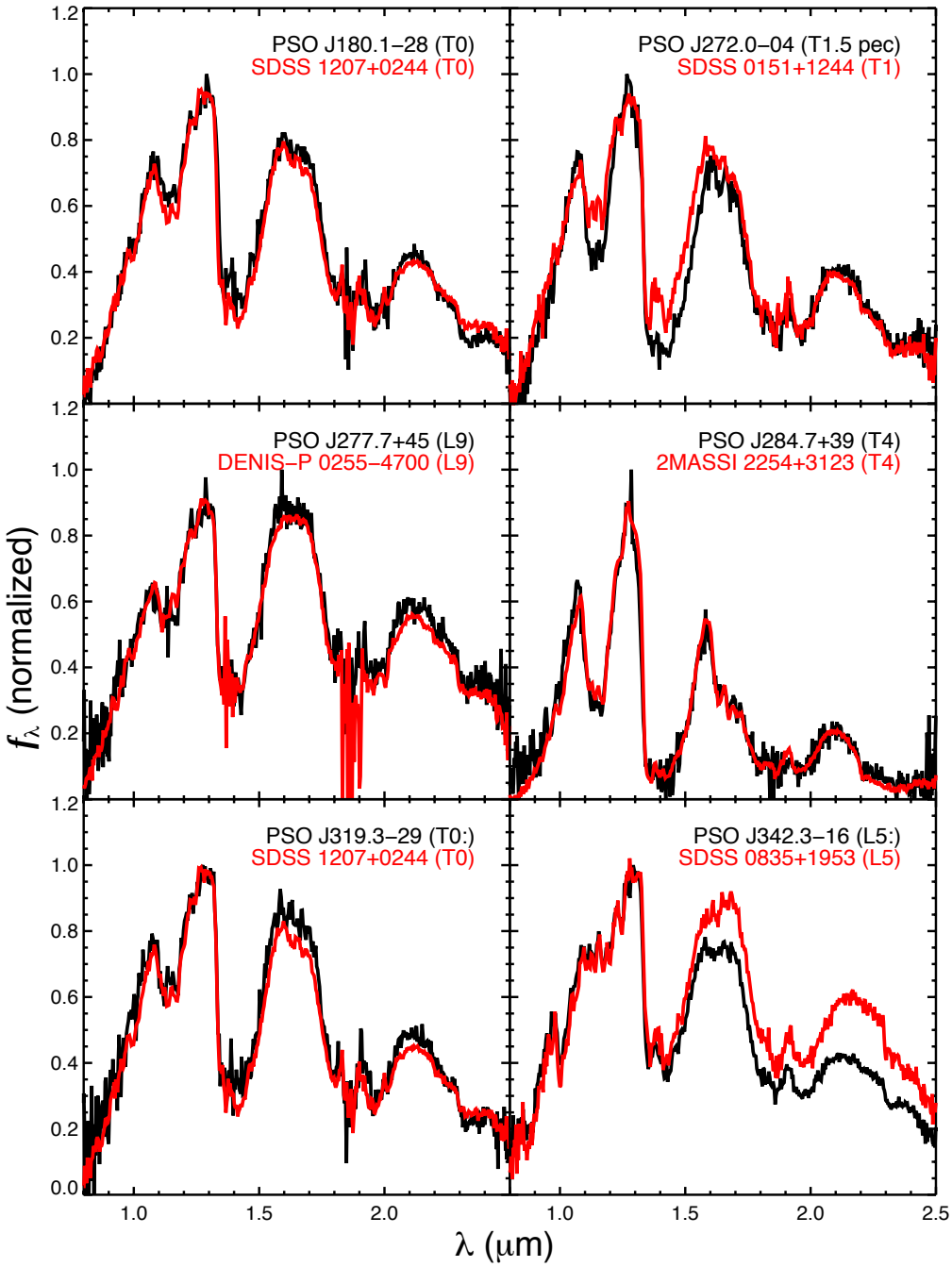

Figure 3.17 continued.

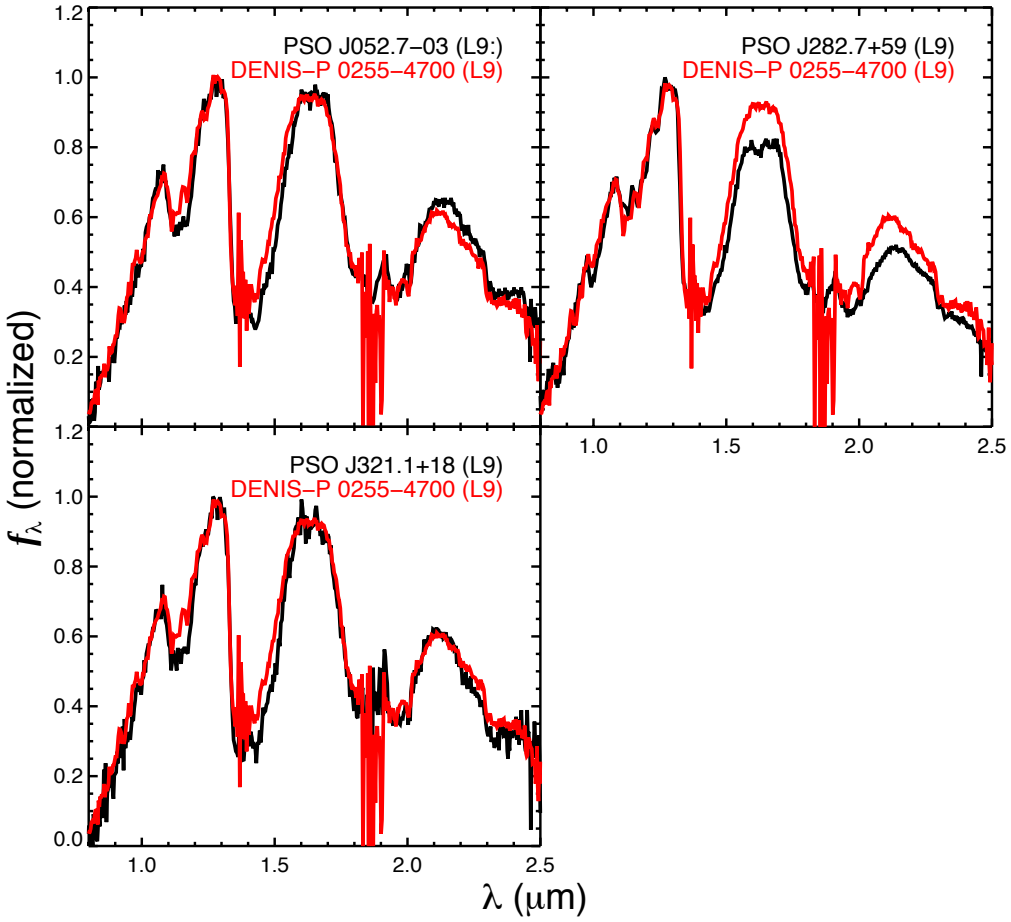

Figure 3.18 Same as Figure 3.16, but for our weak binary candidates. Distinctive features of these spectra are discussed in Section 3.4.5.

depth of its ≈1.4 μm water absorption band, and we concur with the very red color. The redness is most easily explained by large amounts of dusty condensates in the photosphere, but the object also satisfies 3 of the 6 B10 criteria.

PSO J103.0+41 (T0) — This object was identified by us as a candidate binary in Paper I, where it is discussed in detail. It is also a good match to the known L6+T2 binary SDSSp J042348.57-041403.5, and satisfies 2 of the 6 B10 criteria.

PSO J180.1−28 (T0) — This object matches the overall shape of the T0 standard fairly well but shows subtle signs of a companion later-T dwarf: the peak in the J band at 1.28 μm and the brighter peak in the K band. The J and H bands are also good matches to the L6+T2 binary SDSSp J042348.57-041403.5. PSO J180.1−28 meets 1 of the 6 B10 criteria.

PSO J272.0−04 (T1.5 pec) — The slope of this spectrum and the K band shape fall in between the T1 and T2 standards, but the depth of the ≈1.15 μm and ≈1.4 μm water absorption bands and the pointy J band peak suggest a later-type companion. This object satisfies 3 of the 6 B10 criteria.

PSO J277.7+45 (WISE J1830+4542) (L9) — This object, first identified by Kirkpatrick et al. (2011), fits the L9 standard in terms of overall color and morphology and J band shape, but there are signs of methane absorption at ≈1.65 μm and ≈2.2 μm. It meets 3 of the 6 B10 criteria.

PSO J284.7+39 (T4) — This spectrum is a good match to the T4 standard, except for the narrow profile of the J band, which suggests the additional presence of a later T-dwarf. (The spike at ≈1.29 μm is likely a noise artifact.) This object satisfies 2 of the 6 B10 criteria.

PSO J319.3−29 (T0:) — Clear indications of methane absorption at ≈1.65 μm and ≈2.2 μm point to a T dwarf, while the J band shape and ≈1.15 μm and ≈1.4 μm water absorption band depths are more like the L9 standard. This object meets 2 of the 6 B10 criteria.

PSO J342.3−16 (L5:) — The J band morphology matches L5, but the H and K band shapes and the bluer color indicate the additional presence of a T dwarf. This object satisfies 5 of the 12 BG14 criteria.

Weak Binary Candidates

PSO J052.7−035 (L9:) — The best match for the J band profile and adjacent water absorption bands is the T0 standard, but the H band shows no sign of methane absorption and the overall slope fits the L9 standard.

PSO J282.7+59 (WISE J1851+5935) (L9) — This object was identified as a candidate binary in Paper I, where it is discussed in detail. Thompson et al. (2013) type the object as L9 pec, and also describe it as a candidate late-L + early-T binary. Surprisingly, our spectrum meets none of the B06 criteria.

PSO J321.1+18 (L9) — The overall slope clearly fits L9, but there is methane absorption at ≈2.2 μm and the water absorption bands at ≈1.15 μm and ≈1.4 μm have early-T dwarf depth.

3.4.6 Proper Motions and Kinematics

The motion through space of (sub)stellar objects represents their kinematic histories, as younger objects tend to have smaller tangential velocities (e.g., Wielen 1977). We calculated the proper motions for our discoveries using the individual PS1 epochs (≈25–30 epochs per object, mostly in $z_{\rm P1}$ and $y_{\rm P1}$), along with their AllWISE reported positions. For the ≈70% of our sample also detected in the 2MASS Point Source Catalog, we included those positions as well (these objects have 2MASS photometry listed in Table 3.2). The inclusion of the 2MASS astrometry improved the precision of our proper motions in many cases despite the fact that the per-epoch precision for the 2MASS positions is larger (≈70 mas) than for the PS1 positions (≈25 mas), as 2MASS increased the time baseline for our calculations from $2-4$ years to $\gtrsim 10$ years.

Our proper motions are presented in Table 3.4. Proper motions for 17 of our discoveries were previously published by other authors (Table 3.5), in addition to 7 by us in Paper I. Figure 3.19 demonstrates the consistency of our proper motions with those in the literature as well as our improved precision (typically by a factor of $2-3$).

We calculated photometric distances for our discoveries, using $W2$ magnitudes and the spectral type polynomial from Dupuy & Liu (2012). We used these photometric distances along with our proper motions to determine tangential velocities ($v_{\rm tan}$) for our discoveries. These are also presented in Table 3.4, and we show the distribution of $v_{\rm tan}$ in Figure 3.20. The $v_{\rm tan}$ of our discoveries are overall $\approx$25% lower than those of the 20 pc volume-limited sample presented in Faherty et al. (2009), making them fully consistent with the younger thin disk population. One object in our sample, PSO J329.8+03, has a notably larger velocity ($v_{\rm tan} = 111 \pm 12$ km s^{-1}). We applied the analysis of Dupuy & Liu (2012, see their Figure 31) and found this $v_{\rm tan}$ gives PSO J329.8+03 a $\approx$10% chance of being a member of the thick disk. Older L dwarfs typically have bluer near-IR colors (Faherty et al. 2009), and while this age–color relationship has not been clearly established for early-T dwarfs, we note that PSO J329.8+03 has $(J-K)_{\rm MKO} = 1.26 \pm 0.03$ mag which is in fact redder than the mean $(J-K)_{\rm MKO} = 0.75 \pm 0.17$ mag for T1 dwarfs (Dupuy & Liu 2012). We consider PSO J329.8+03 to be a thin disk object along with the rest of our discoveries.

3.4.7 Comoving Companions

To identify if any of our discoveries were members of common proper motion systems, we cross-matched our discoveries with a large list of nearby stars from Lépine & Shara (2005), Salim & Gould (2003), Lépine & Gaidos (2011), Limoges et al. (2013), and Deacon & Hambly (2007). We searched for matches within 5 arcmin and identified eight possible pairs with proper motions differing by less than 5σ (where σ is the quadrature sum of the proper motion differences in each axis divided by the combined uncertainties in that axis). To test how many of these pairs were chance alignments of unrelated stars, we used the method of Lépine & Bongiorno (2007, see also Deacon et al. 2014). We offset the positions

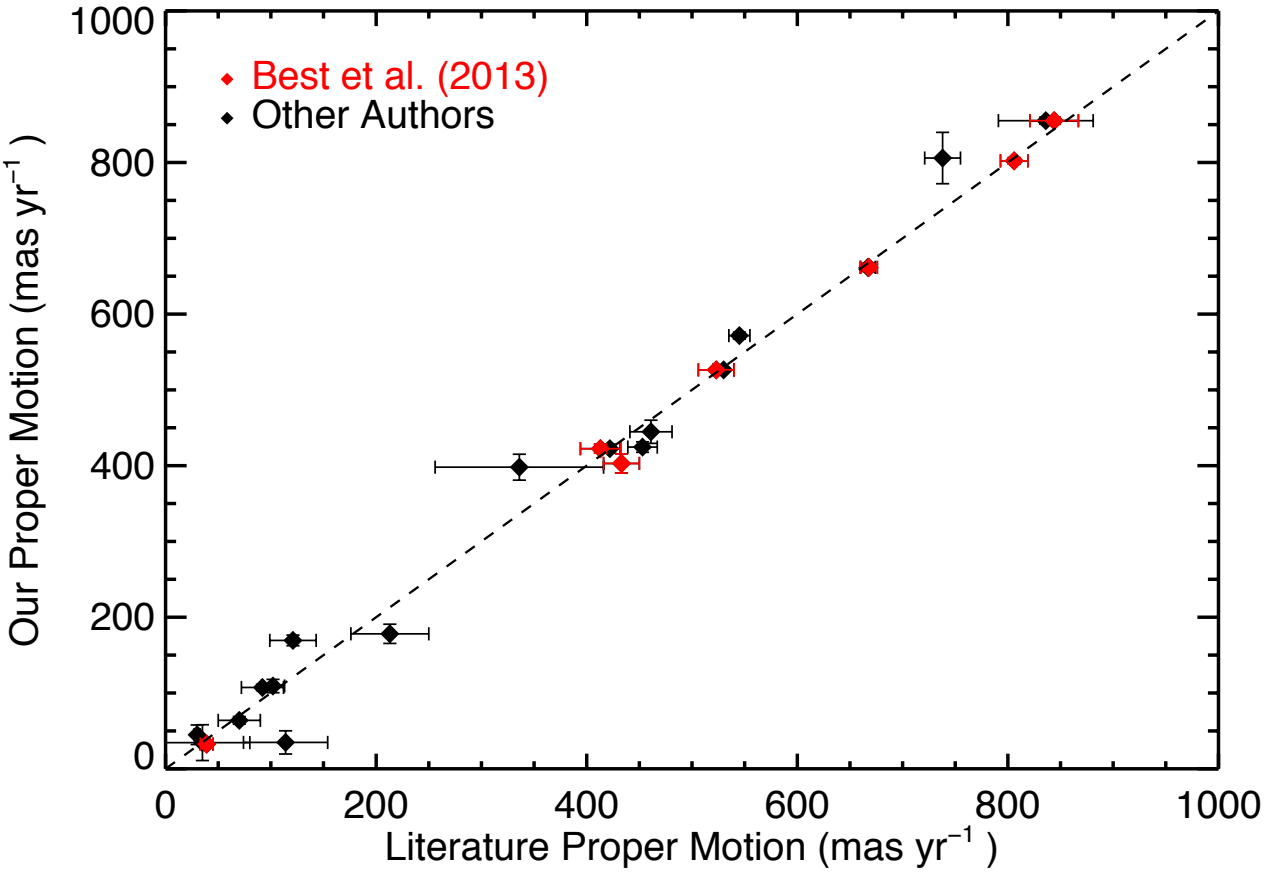

Figure 3.19 Comparison of our proper motions with previously published values from the literature. Objects plotted in red have proper motions in our Paper I, which we refine in this paper. Four objects have proper motions from Paper I as well as elsewhere in the literature, and we plot these as separate points. Our new proper motions are consistent with previous values and improve on the precision by a typical factor of $2-3$.

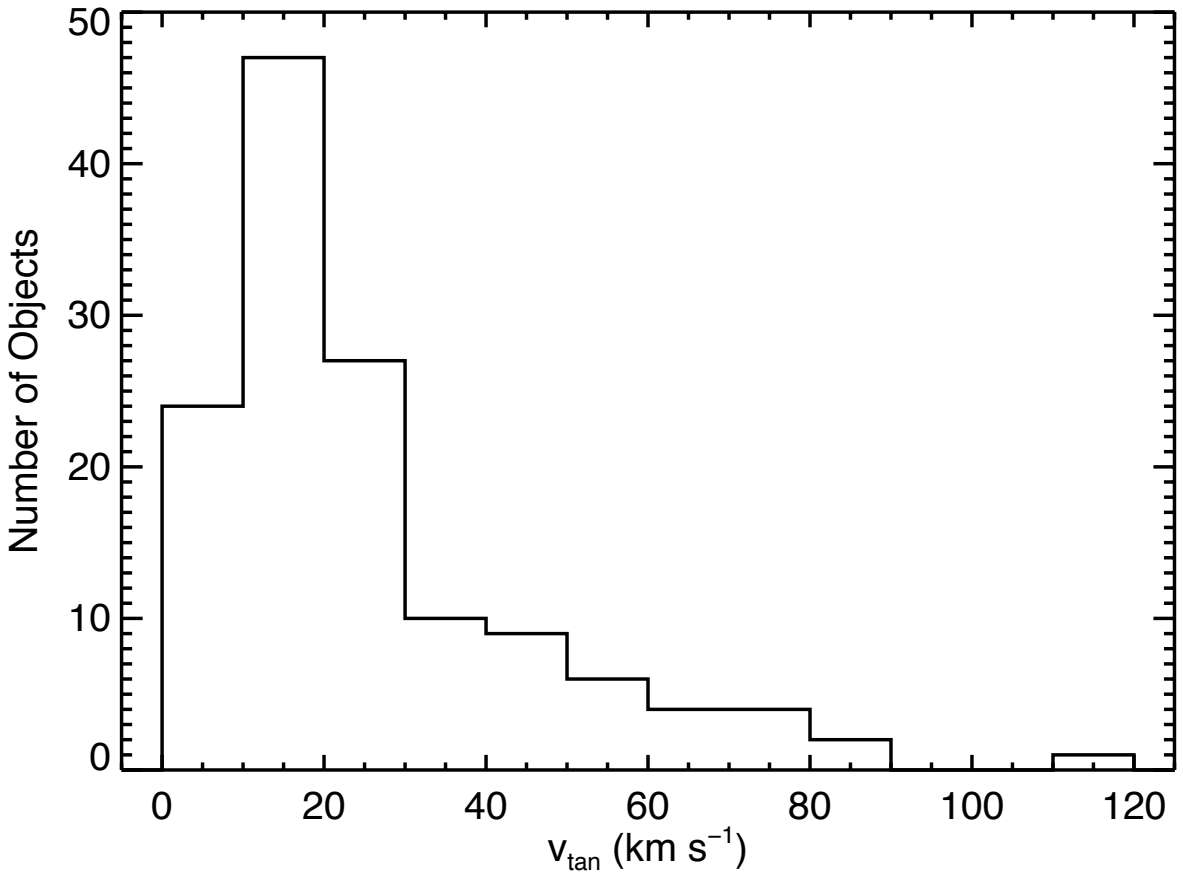

Figure 3.20 The distribution of tangential velocities for our discoveries. These $v_{\rm tan}$ indicate that our discoveries are all very likely to be members of the younger thin disk population.

in our input catalog by 2° and repeated our matching criteria, generating entirely coincident pairings. The results are shown in Figure 3.21. Three of our prospective pairs lie outside the area dominated by coincident pairs.

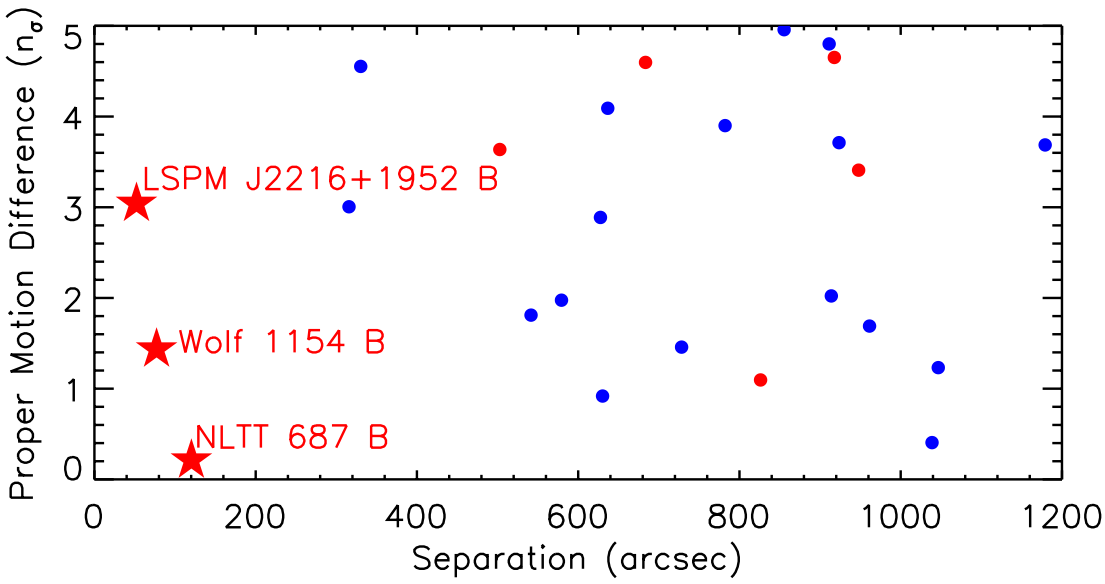

Figure 3.21 Our common proper motion systems (marked as red stars). The offset coincident pairings generated using the method of Lépine & Bongiorno (2007) are shown as blue dots. The remaining pairings (which are likely to be coincident) are shown as red dots.

Our three pairings are described in Table 3.13. One of the pairings, NLTT 687 and PSO J003.4−18, was previously discovered by Baron et al. (2015). Two of our secondaries, PSO J003.4−18 and PSO J334.1+19, are identified as candidate binaries (Section 3.4.5). If these are indeed binaries then these systems will be hierarchical triples. Such systems are useful benchmarks as the primaries can be used to constrain their ages and metallicities, allowing evolutionary models to estimate the masses, radii, and effective temperatures of the binary components. If the secondary can be resolved with high-resolution imaging into two components, their masses can be measured dynamically, providing a rigorous test of the evolutionary models. We also identify PSO J334.1+19 as a possible β Pictoris Moving Group member ($p = 77.8\%$, Section 3.6.2). Using the BANYAN II online tool (Gagné et al.

2014b) we found that its primary LSPM J2216+1952 is also a possible ($p = 58.2\%$) member of this moving group.

3.5 The Atmospheres of L/T Transition Dwarfs

The significant changes in the spectra and blueward shift in near-IR colors of brown dwarfs cooling through the L/T transition arise from the formation of methane and the depletion of photospheric condensate clouds. (e.g., Allard et al. 2001; Burrows et al. 2006; Saumon & Marley 2008). The process by which the clouds deplete is not well understood, and proposed scenarios involve the clouds gradually thinning, raining out suddenly, or breaking up (e.g., Ackerman & Marley 2001; Knapp et al. 2004; Tsuji 2005; Burrows et al. 2006; Marley et al. 2010). The manner in which clouds disappear from the photosphere may impact the cooling rate, and therefore the luminosities, of the brown dwarfs (Saumon & Marley 2008; Dupuy et al. 2015a). The colors of L/T transition objects can therefore shed light on the cloud dispersal process(es).

An accumulation of objects at a given color on the cooling sequence would indicate a long-live phase of evolution, with objects spending a longer time at the temperature corresponding to that color. The "hybrid" evolutionary models of Saumon & Marley (2008) predict a pile-up of objects in the L/T transition at $(J-K)_{\rm MKO} \approx 0.9-1.0$, as cloud clearing removes opacity from the photospheres of brown dwarfs and the cooling slows as entropy is released from deeper atmospheric layers. Dupuy & Liu (2012) found evidence of this type of pile-up and a subsequent gap (i.e., a short-lived evolutionary phase) in the distribution of near-IR colors of 36 L/T transition dwarfs (selected by absolute $H_{\rm MKO}$ magnitudes).

By combining our new discoveries with objects from the literature, we have built a larger sample of L/T transition dwarfs. We used parallaxes when available and photometric distances otherwise to construct a sample of 70 objects with spectral types L7–T5.5, volume-limited at 25 pc. In Figure 3.22, we show the distribution of $(J-K)_{\rm MKO}$ colors for this sample, computed in a Monte Carlo fashion accounting for errors in the photometry. This

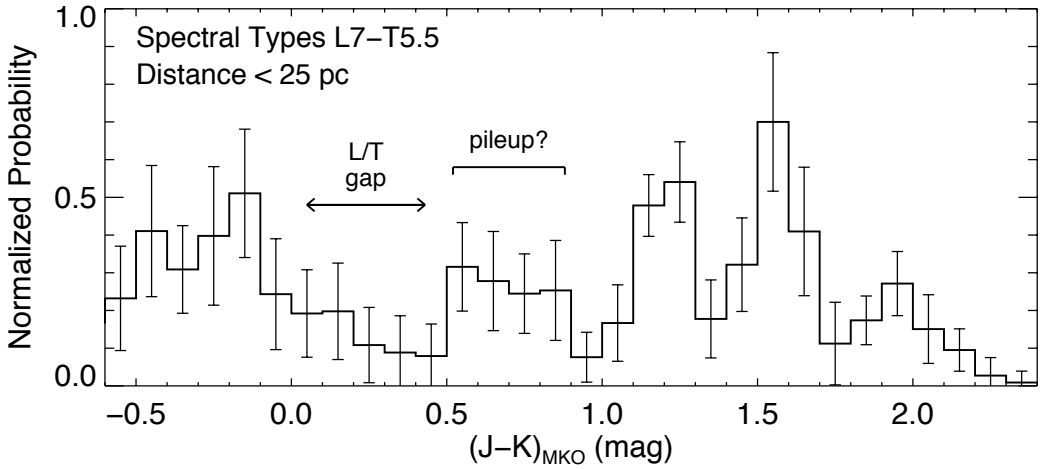

Figure 3.22 Distribution of $(J-K)_{\rm MKO}$ colors for 70 objects with spectral types L7–T5.5 and distances within 25 pc, including our discoveries and objects from the literature. The histogram was computed in a Monte Carlo fashion, accounting for errors in the photometry. The plotted uncertainties are the standard deviations for each color bin derived from the Monte Carlo simulations. The color distribution reveals signs of structure in the L/T transition, in particular the gap at $(J-K)_{\rm MKO} = 0.0 - 0.5$ mag first detected by Dupuy & Liu (2012), although the shape seen here is somewhat broader and shallower. We also detect a less prominent pileup just redward of the gap than Dupuy & Liu (2012), but see larger pileups at redder colors.

color distribution suggests pile-ups and gaps across the L/T transition. The most prominent gap is at $(J-K)_{\rm MKO} \approx -0.1 - 0.5$ mag, somewhat broader and shallower than the gap at $(J-K)_{\rm MKO} \approx 0.0 - 0.4$ mag detected by Dupuy & Liu (2012). We also find a less prominent pileup just redward of the gap than Dupuy & Liu (2012), but there may also be larger pileups at $(J-K)_{\rm MKO} \approx 1.2$ and 1.6 mag.

Our larger sample supports the existence of the "L/T gap", but also makes clear that a larger sample, ideally volume-limited and defined entirely by trigonometric distances, is needed to fully delineate the color evolution in the L/T transition.

3.6 Young Discoveries

3.6.1 Field Objects

Stars with ages $\lesssim$ 200 Myr are expected to be rare within 100 pc of the Sun, at most a few percent of the population for a uniform star-forming history. Our search was designed to identify field L/T transition dwarfs and generally avoided known star-forming regions, so we were surprised to find 23 of our 59 M7–L7 discoveries showing confirmed or possible spectral signatures of low gravity, i.e., youth (Section 3.4.4), and we explored why this happened.

Typically, young ultracool dwarfs are redder than older objects with the same spectral types in the photometric bands we used to select candidates (e.g., Gizis et al. 2012). They are also expected to be more luminous at longer wavelengths (i.e., in the mid-infrared WISE bands) due to both enhanced clouds and larger radii at younger ages. It is therefore natural to assume that our selection criteria, which screened out bluer and fainter objects, biased our candidates toward young brown dwarfs. To test this assumption, we assembled a set of FLD-G objects from our discoveries, AL13, and objects in the SpeX Prism Library[3]. We also gathered published objects with optical (β or γ; Cruz et al. 2009) or near-infrared (INT-G or VL-G; Allers & Liu 2013a) classifications of low gravity. Figure 3.23 compares the $W1$ magnitudes vs. $W1-W2$ colors for these sets of older and young objects. The two sets are drawn from multiple searches and sources, and we do not attempt to untangle the biases and selection effects. Nevertheless, Figure 3.23 suggests that our search criteria are indeed prone to selecting a disproportionately large number of young M and L dwarfs compared to the field population.

3.6.2 Young Moving Groups

Young moving groups (YMG) are associations of young stars (≈10–100 Myr) and brown dwarfs whose similar trajectories through space imply that the members originated in a common star-forming region (e.g., Zuckerman & Song 2004). YMG members are coeval, and

[3]http://pono.ucsd.edu/~adam/browndwarfs/spexprism

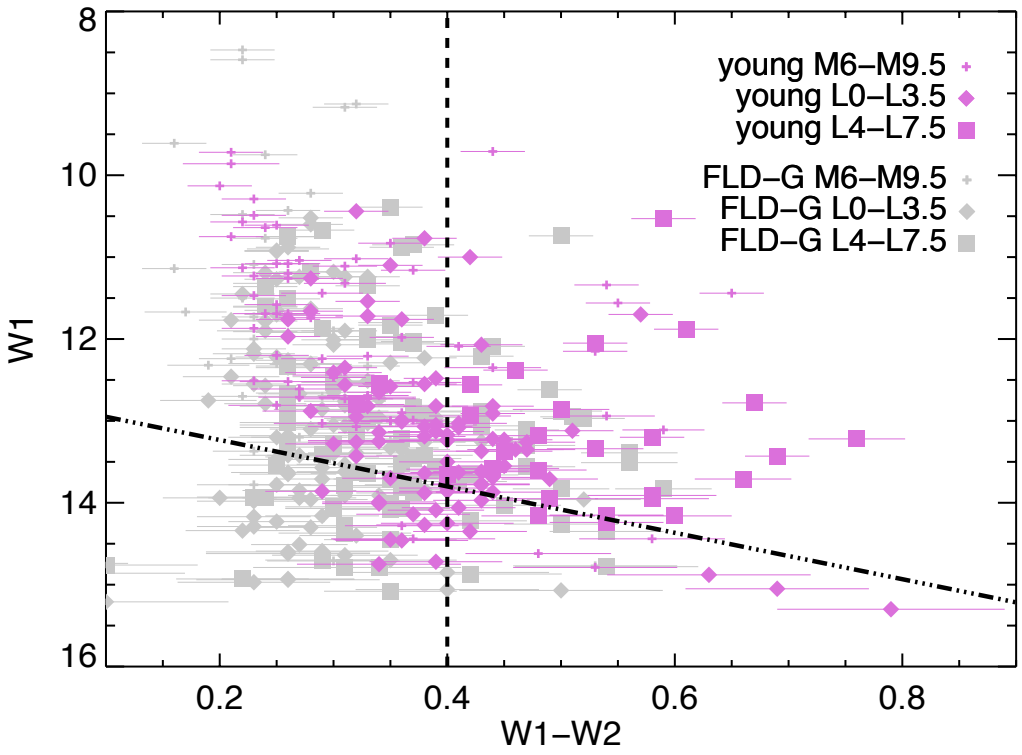

Figure 3.23 $W1$ vs. $W1 - W2$ photometry for confirmed young objects (magenta, with symbols according to spectral type — see legend at upper right) and FLD-G objects (light gray, same symbols) from AL13, this paper, and the SpeX Prism Library. The vertical dashed line marks the $W1 - W2 \geq 0.4$ mag selection criterion for our sample, while the diagonal dash-dot line shows the $W1$ vs. $W1 - W2$ line from Figure 3.1 that we used to identify candidates likely to be within 25 pc. The samples here are drawn from different searches and likely influenced by multiple biases, but there is clear indication that the two criteria select (above and to the right of the lines) a disproportionately large number of young M and L dwarfs compared to the field population.

therefore serve as both benchmarks for stellar and substellar atmospheres and as empirical laboratories for testing models of star formation. In addition, these young stars are prime targets for direct imaging searches for nearby exoplanets. Our search targeted field brown dwarfs without regard to age or space motion, but we investigated the possibility that we had serendipitously stumbled upon members of YMGs.

Candidates Selected With BANYAN II

We used the BANYAN II online tool (Malo et al. 2013; Gagné et al. 2014b) to calculate probabilities of membership in nearby YMGs for our discoveries. BANYAN II determines membership probabilities in a Bayesian fashion using sky position and proper motion, as well as radial velocity and distance when available. We computed photometric distances using $K_{\rm MKO}$ magnitudes (and the appropriate polynomial from Dupuy & Liu 2012) because the absolute magnitudes of young objects and field objects are most similar in this bandpass (Gagné et al. 2015c, M. C. Liu et al., in preparation). (We caution that photometric distances will not be accurate for objects that are unresolved equal-luminosity binaries.) Based on our sky positions, proper motions, and $K_{\rm MKO}$ photometric parallaxes, BANYAN II found that 10 of our discoveries have a $\gtrsim$70% probability of membership in a YMG (Table 3.14) and a corresponding false alarm rate of $\lesssim$10% (Gagné et al. 2014b).

Interestingly, our 10 candidates all have spectral types L7–T4.5, which would place any of them among the lowest-mass and coolest YMG members discovered to date. We estimated their masses assuming membership in their respective candidate YMGs, which have ages 149^{+51}_{-19} Myr for AB Doradus and 24 ± 3 Myr for β Pictoris (Bell et al. 2015), and 40 ± 10 Myr for Argus (Makarov & Urban 2000; Torres et al. 2008). We note that the Argus association lacks consensus in the literature about whether it is a real YMG, and if real its membership list is not yet well-defined (e.g., Bell et al. 2015). To estimate masses for our YMG candidates, we first calculated the $L_{\rm bol}$ for each object using our spectral types, the $K_{\rm MKO}$ bolometric corrections of Liu et al. (2010, their Table 6), and the $K_{\rm MKO}$-band photometric distance for each object. We then used the "hybrid" evolutionary models

of Saumon & Marley (2008) and our $L_{\rm bol}$ values to determine masses at the age of each candidate's YMG. Our final mass estimates are included in Table 3.14. We propagated the uncertainties on our spectral types, $K_{\rm MKO}$ magnitudes, bolometric corrections (Liu et al. 2010), distances, and ages into our mass determinations using Monte Carlo simulations and normal distributions for each uncertainty, and we quote 68th percentile confidence limits. Mass estimates for these objects, assuming they are YMG members, are ≈6–15 $M_{\rm Jup}$, spanning the deuterium-burning limit and comparable to the lowest-mass free-floating objects ever discovered (Liu et al. 2013; Gagné et al. 2015a).

We also repeat the warning of Shkolnik et al. (2012) and others that the spatial and kinematic locations of YMGs can be contaminated by unrelated field objects, so other indications of youth in a candidate are helpful for confirming membership. Unfortunately for our candidates, the AL13 gravity indices apply only to objects with spectral types ≤L7, and the spectra for our two L7 YMG candidates have S/N < 30 so we do not regard their indices as reliable. More generally, low-gravity spectral signatures in the L/T transition are not as well established as for earlier-type objects. The young (100 ± 30 Myr) T3.5 dwarf GU Psc b (Naud et al. 2014) has an unusually red $J - K_s$ color for its spectral type, but it is not known whether this is true for other young early-T dwarfs. We do not see unusually red near-IR colors in our T dwarf YMG candidates.

The most promising of our candidate YMG members is PSO J057.2+15.2 (L7), whose spectrum reveals the triangular H band profile typical of youth, and whose $(J-K)_{\rm 2MASS} = 2.28\pm0.25$ mag color is significantly redder than the average $(J-K)_{\rm 2MASS} = 1.77\pm0.22$ mag for L7 dwarfs (Schmidt et al. 2010). The BANYAN II online tool gives a 91.9% probability of membership in the β Pictoris Moving Group (βPMG; Zuckerman et al. 2001) based on proper motion and photometric distance. If confirmed, this object would provide a nearby (32 ± 4 pc) target for atmospheric studies with a well-constrained age. We estimate this object would have a mass of $8.1^{+1.8}_{-1.5}$ $M_{\rm Jup}$, firmly in the planetary regime, and comparable to the latest known βPMG member PSO J318.5338−22.8603 (spectral type L7 Liu et al. 2013).

Two other L dwarf candidates have unusually red near-IR colors for their spectral type, consistent with being low-gravity and thus young:

PSO J004.7+51 — The BANYAN II online tool gives this L7 dwarf a 79.9% probability of membership in the Argus Moving Group (ARG; Zuckerman et al. 2001). We estimate it would have a mass of $10.3^{+1.4}_{-1.2}$ $M_{\rm Jup}$.

PSO J100.5+41 (WISE 0642+4101) — The BANYAN II online tool gives this red L9 dwarf a 78.6% probability of membership in the AB Doradus Moving Group (ABDMG; Zuckerman et al. 2004). We estimate it would have a mass of 15^{+4}_{-3} $M_{\rm Jup}$.

BASS Catalog

We cross-matched our discoveries with the BASS catalog presented in Gagné et al. (2015b). The BASS catalog contains 252 ultracool candidate YMG members with spectral types ≥M5 selected in a Bayesian fashion by the full BANYAN II methodology (Malo et al. 2013; Gagné et al. 2014b), which incorporates 2MASS and *WISE* photometry in addition to the sky position, proper motion, radial velocity, and parallax used by the online tool. We found only one of our discoveries in BASS: the unusually red L dwarf PSO J100.5+41 (first identified as WISE 0642+4101 by Mace et al. 2013a). Gagné et al. (2015b) give this object a 38.4% probability of membership in ABDMG, more pessimistic than the 78.6% probability based on our data and the online tool. Gagné et al. (2015b) also present an LP-BASS catalog with 249 "low-priority" candidates; none of these are among our discoveries. We note that our search for L/T transition dwarfs targeted a somewhat different parameter space. The majority of our discoveries are near the Galactic plane ($|b| < 15°$), too faint (poor-quality or non-existent 2MASS photometry), or too blue (L/T transition objects have bluer $J-H$ colors than earlier-L dwarfs) to satisfy the criteria used to construct the BASS sample.

3.7 Summary

We have conducted a successful search for nearby L/T transition dwarfs using a merged Pan-STARRS1 3π + *WISE* database as our primary resource, supplemented by near-infrared photometry from 2MASS, UKIDSS, and our own observations. Our search has yielded 130 ultracool dwarfs over ≈28,000 deg^2 of sky. Of these, 79 objects have spectral types L6–T4.5, the largest number of L/T transition dwarfs discovered in any single search to date. Thirty of the L/T transition dwarfs have photometric distances less than 25 pc, and for spectral types L9–T1.5 we have increased the number of known objects within 25 pc by over 50%. We have analyzed the near-infrared colors of our L/T transition discoveries, and we find further evidence for the pile-up in the L/T transition first predicted by the "hybrid" evolutionary models of Saumon & Marley (2008) as well as a subsequent L/T gap first seen by Dupuy & Liu (2012).

We assigned spectral types to our discoveries by visual comparison with field spectral standards, and we compare these to types assigned using the index-based methods of Allers & Liu (2013a, M4–L7 dwarfs) and Burgasser et al. (2006a, L0–T8 dwarfs). We find that the Allers & Liu (2013a) method assigns spectral types generally in agreement with visually assigned types for most objects, but earlier (by ≈0.5–1 subtypes) for unusually red M and L dwarfs. The spectral types assigned by the indices of Burgasser et al. (2006a) are in good agreement with visual types for T dwarfs but may be different by ≈0.5–1.0 subtypes for L dwarfs.

Among the late-M to mid-L dwarfs in our sample, we found a total of 23 objects with spectral signatures of low gravity, indicating youth. Using the gravity-sensitive indices of Allers & Liu (2013a), we classify nine of these discoveries as VL-G and one as INT-G. We assign provisional VL-G and INT-G classifications to seven more objects based on spectra with modest S/N; higher S/N spectra are needed to clarify their gravity classes. These include the red L dwarf PSO J068.3126+52.4546 (Hya12), identified by Lodieu et al. (2014) as a candidate member of the Hyades. We identify a further 6 objects whose spectra have

clear visual suggestions of young age but no index classification due to low S/N or spectral types outside the applicable range of the indices. We conclude that our candidate selection criteria, designed to identify field L/T transition dwarfs, also favored the discovery of young M and L dwarfs because of their redder $y_{\rm P1} - W1$ and $W1 - W2$ colors.

Thirty-one of our discoveries are candidate binaries based on their low-resolution spectral features, making them prime targets for high-resolution imaging. Two of the candidate binaries are common proper motion companions to main sequence stars: PSO J003.4950−18.2802 (previously identified by Baron et al. 2015) and PSO J330.3214+32.3686. If confirmed as binaries, these objects would be ultracool binaries with ages and metallicities determined from their primaries, making them rare empirical test cases for evolutionary models.

We also identify 11 kinematic candidates for nearby young moving groups with spectral types L7–T4.5 using the BANYAN II online tool, including three that show possible spectral indications of youth. Eight of these have spectral types L9 or later, and if confirmed as YMG members they would provide an unprecedented opportunity to determine the effective temperatures and test evolutionary models of young L/T transition objects.

In conclusion, our discoveries include a large new set of L/T transition dwarfs that contribute significantly to the nearby census and shed light on the evolution of brown dwarf atmospheres in the L/T transition. They also include young late-M and L dwarfs, several of which are candidate very low mass brown dwarfs in nearby star-forming regions and young moving groups. If confirmed, these would be exceptional age-constrained benchmarks for understanding the properties of young cool atmospheres.

Table 3.1. Pan-STARRS1 and *WISE* All-sky Photometry

Pan-STARRS1 Name	$z_{\rm P1}$ (mag)	$y_{\rm P1}$ (mag)	*WISE* Name	$W1$ (mag)	$W2$ (mag)	$W3$ (mag)
PSO J003.4950−18.2802	20.08 ± 0.04	18.94 ± 0.07	J001358.81−181648.1	14.60 ± 0.04	14.17 ± 0.05	12.20 ± 0.35
PSO J004.1834+23.0741	20.27 ± 0.06	18.90 ± 0.03	J001643.96+230426.7	14.29 ± 0.03	13.65 ± 0.04	12.20 ± 0.35
PSO J004.7148+51.8918	20.06 ± 0.06	19.08 ± 0.07	J001851.51+515330.6	13.58 ± 0.04	13.04 ± 0.04	12.55 ± 0.34
PSO J007.7921+57.8267	18.18 ± 0.01	17.02 ± 0.01	J003110.04+574936.3	12.41 ± 0.02	11.84 ± 0.02	11.30 ± 0.10
PSO J007.9194+33.5961	19.62 ± 0.03	18.60 ± 0.02	J003140.64+333545.9	13.69 ± 0.03	13.18 ± 0.03	12.03 ± 0.23
PSO J010.2132+41.6091	19.99 ± 0.06	19.37 ± 0.04	J004051.14+413631.4	16.11 ± 0.07	15.31 ± 0.09	>12.97
PSO J023.8557+02.0884	19.62 ± 0.02	18.76 ± 0.02	J013525.37+020518.4	14.31 ± 0.03	13.90 ± 0.05	>12.04
PSO J024.1519+37.6443	20.46 ± 0.11	19.84 ± 0.08	J013636.31+373840.6	16.80 ± 0.09	14.76 ± 0.06	>12.72
PSO J031.5651+20.9097	20.99 ± 0.23	19.61 ± 0.05	J020615.62+205435.3	16.60 ± 0.09	14.70 ± 0.06	12.28 ± 0.34
PSO J041.5426+01.9456	20.10 ± 0.02	19.06 ± 0.03	J024610.23+015644.4	14.28 ± 0.03	13.65 ± 0.04	11.75 ± 0.25
PSO J048.9806+07.5414	20.11 ± 0.04	19.03 ± 0.05	J031555.29+073229.6	14.63 ± 0.04	14.14 ± 0.05	12.47 ± 0.50
PSO J049.1124+17.0885	20.24 ± 0.03	19.17 ± 0.04	J031626.95+170518.5	15.23 ± 0.05	14.63 ± 0.08	12.14 ± 0.35
PSO J049.1159+26.8409	20.09 ± 0.03	18.65 ± 0.02	J031627.78+265027.6	15.08 ± 0.05	13.97 ± 0.05	>12.47

Table 3.1—Continued

Pan-STARRS1 Name	z_{P1} (mag)	y_{P1} (mag)	*WISE* Name	$W1$ (mag)	$W2$ (mag)	$W3$ (mag)
PSO J052.7214−03.8409	19.78 ± 0.04	18.58 ± 0.02	J033053.14−035027.3	13.65 ± 0.03	12.93 ± 0.03	12.07 ± 0.30
PSO J053.3683+30.9663	18.64 ± 0.02	17.67 ± 0.02	J033328.27+305759.4	11.98 ± 0.03	11.48 ± 0.03	12.22 ± 0.42
PSO J054.8149−11.7792	19.98 ± 0.03	18.99 ± 0.06	J033915.57−114645.0	14.44 ± 0.03	13.98 ± 0.04	>12.81
PSO J055.0493−21.1704	20.59 ± 0.06	19.20 ± 0.04	J034011.81−211013.2	15.53 ± 0.05	14.50 ± 0.06	>12.50
PSO J057.2893+15.2433	20.76 ± 0.06	19.75 ± 0.11	J034909.44+151436.0	13.85 ± 0.03	13.21 ± 0.03	>12.07
PSO J060.3200+25.9645	20.05 ± 0.02	19.09 ± 0.03	J040116.80+255752.2	15.05 ± 0.04	14.36 ± 0.07	>12.39
PSO J068.3126+52.4546	20.50 ± 0.04	19.20 ± 0.04	J043315.02+522716.7	13.98 ± 0.03	13.01 ± 0.04	>11.71
PSO J068.9292+13.3958	20.22 ± 0.06	19.12 ± 0.03	J043542.99+132344.9	14.25 ± 0.03	13.74 ± 0.06	>11.88
PSO J070.3773+04.7333	20.69 ± 0.10	19.04 ± 0.04	J044130.52+044359.9	15.74 ± 0.07	14.40 ± 0.09	>12.35
PSO J071.4708+36.4930	19.94 ± 0.03	18.99 ± 0.03	J044552.98+362935.0	14.24 ± 0.03	13.83 ± 0.05	>12.51
PSO J071.6394−24.4991	19.51 ± 0.02	18.48 ± 0.03	J044633.45−242956.8	14.27 ± 0.03	13.77 ± 0.04	12.42 ± 0.33
PSO J071.8769−12.2713	20.37 ± 0.04	18.85 ± 0.04	J044730.40−121616.4	14.96 ± 0.03	14.24 ± 0.04	12.61 ± 0.42
PSO J076.1314+25.1940	20.72 ± 0.05	19.62 ± 0.08	J050431.53+251138.5	13.86 ± 0.03	13.42 ± 0.04	11.69 ± 0.24

Table 3.1—Continued

Pan-STARRS1 Name	z_{P1} (mag)	y_{P1} (mag)	*WISE* Name	$W1$ (mag)	$W2$ (mag)	$W3$ (mag)
PSO J076.7092+52.6087	20.00 ± 0.03	18.25 ± 0.02	J050650.20+523631.2	14.94 ± 0.04	13.73 ± 0.05	12.27 ± 0.36
PSO J077.1034+24.3810	20.21 ± 0.04	19.19 ± 0.06	J050824.82+242251.1	15.30 ± 0.06	14.51 ± 0.08	12.37 ± 0.47
PSO J078.9904+31.0171	19.76 ± 0.02	18.74 ± 0.03	J051557.68+310101.8	14.88 ± 0.04	14.25 ± 0.08	>12.26
PSO J085.3474+36.3037	19.99 ± 0.07	18.75 ± 0.03	J054123.39+361813.1	12.77 ± 0.03	12.17 ± 0.03	9.94 ± 0.06
PSO J087.7749−12.6537	19.71 ± 0.02	18.76 ± 0.03	J055105.96−123913.5	13.87 ± 0.03	13.40 ± 0.04	>11.98
PSO J088.0452+43.2123	19.69 ± 0.03	18.67 ± 0.02	J055210.83+431244.2	14.26 ± 0.03	13.82 ± 0.04	>12.10
PSO J088.3324−24.4439	19.83 ± 0.03	18.86 ± 0.03	J055319.77−242638.0	15.61 ± 0.05	15.06 ± 0.09	>12.96
PSO J100.5233+41.0320	19.74 ± 0.03	18.63 ± 0.02	J064205.58+410155.5	13.36 ± 0.03	12.55 ± 0.03	11.70 ± 0.31
PSO J101.8428+39.7462	19.71 ± 0.02	18.71 ± 0.03	J064722.28+394446.3	15.30 ± 0.05	14.65 ± 0.08	>12.23
PSO J103.0927+41.4601	18.88 ± 0.02	17.64 ± 0.01	J065222.24+412736.1	13.13 ± 0.02	12.44 ± 0.03	11.80 ± 0.25
PSO J105.4992+63.3581	19.47 ± 0.03	17.99 ± 0.01	J070159.79+632129.2	14.20 ± 0.03	13.22 ± 0.03	12.48 ± 0.42
PSO J108.4590+38.2086	20.15 ± 0.03	19.08 ± 0.04	J071350.14+381230.6	13.98 ± 0.03	13.51 ± 0.04	>12.69
PSO J109.4864+46.5278	20.65 ± 0.06	19.20 ± 0.06	J071756.71+463140.3	15.40 ± 0.05	14.77 ± 0.08	>12.54

Table 3.1—Continued

Pan-STARRS1 Name	z_{P1} (mag)	y_{P1} (mag)	*WISE* Name	$W1$ (mag)	$W2$ (mag)	$W3$ (mag)
PSO J115.0659+59.0473	19.62 ± 0.02	18.67 ± 0.02	J074015.81+590250.2	15.31 ± 0.04	14.90 ± 0.09	>12.78
PSO J117.1608+17.7259	19.38 ± 0.03	18.43 ± 0.02	J074838.58+174333.0	13.74 ± 0.03	13.32 ± 0.03	>12.55
PSO J127.4696+10.5777	20.23 ± 0.04	19.42 ± 0.04	J082952.73+103440.4	14.35 ± 0.03	13.70 ± 0.05	11.27 ± 0.24
PSO J133.8016−02.5658	19.53 ± 0.03	18.34 ± 0.01	J085512.39−023356.8	14.17 ± 0.03	13.57 ± 0.04	>12.69
PSO J133.8302+06.0160	19.11 ± 0.02	18.34 ± 0.02	J085519.22+060057.6	14.77 ± 0.04	14.24 ± 0.06	>11.87
PSO J135.0395+32.0845	18.78 ± 0.02	17.76 ± 0.02	J090009.49+320504.2	13.96 ± 0.03	13.44 ± 0.04	>11.97
PSO J135.7840+16.9932	19.87 ± 0.02	18.73 ± 0.04	J090308.17+165935.4	14.53 ± 0.04	13.99 ± 0.05	>12.35
PSO J136.3401+10.1151	20.53 ± 0.06	19.30 ± 0.04	J090521.62+100654.7	15.19 ± 0.05	14.32 ± 0.07	>12.40
PSO J136.5494−06.1944	17.89 ± 0.00	16.82 ± 0.01	J090611.85−061139.9	13.25 ± 0.03	12.82 ± 0.03	12.21 ± 0.37
PSO J140.2308+45.6487	18.49 ± 0.02	17.24 ± 0.01	J092055.40+453856.3	13.06 ± 0.02	12.39 ± 0.03	11.28 ± 0.17
PSO J143.6774−29.8356	19.33 ± 0.03	18.38 ± 0.02	J093442.54−295007.7	14.95 ± 0.04	14.47 ± 0.05	12.57 ± 0.39
PSO J146.0144+05.1319	19.67 ± 0.02	18.75 ± 0.03	J094403.46+050755.2	15.07 ± 0.04	14.57 ± 0.08	>12.63
PSO J147.5092−27.6337	19.98 ± 0.04	18.91 ± 0.03	J095002.19−273801.3	15.48 ± 0.05	15.03 ± 0.09	>12.63

Table 3.1—Continued

Pan-STARRS1 Name	z_{P1} (mag)	y_{P1} (mag)	*WISE* Name	$W1$ (mag)	$W2$ (mag)	$W3$ (mag)
PSO J149.0341−14.7857	19.51 ± 0.02	18.36 ± 0.02	J095608.17−144708.2	13.52 ± 0.03	12.77 ± 0.03	11.14 ± 0.19
PSO J149.1907−19.1730	18.48 ± 0.01	17.37 ± 0.01	J095645.75−191022.3	13.31 ± 0.03	12.91 ± 0.03	11.87 ± 0.26
PSO J152.2977+15.9912	19.59 ± 0.03	18.61 ± 0.04	J100911.47+155928.4	15.05 ± 0.04	14.60 ± 0.08	>12.10
PSO J158.1597+05.2231	19.61 ± 0.05	18.75 ± 0.04	J103238.32+051323.2	14.85 ± 0.04	14.45 ± 0.08	>12.32
PSO J159.0433−27.6357	18.99 ± 0.03	18.04 ± 0.02	J103610.38−273808.3	14.46 ± 0.03	14.02 ± 0.04	12.52 ± 0.38
PSO J159.2399−26.3885	20.44 ± 0.10	19.04 ± 0.05	J103657.59−262319.0	14.69 ± 0.03	13.98 ± 0.05	>12.88
PSO J160.0416−21.3281	20.35 ± 0.04	19.03 ± 0.03	J104010.00−211940.9	15.05 ± 0.04	14.18 ± 0.05	>12.63
PSO J167.1132+08.6331	19.74 ± 0.02	18.74 ± 0.03	J110827.18+083759.5	14.13 ± 0.03	13.66 ± 0.04	>12.62
PSO J168.1800−27.2264	···	19.16 ± 0.14	J111243.25−271336.1	15.76 ± 0.06	14.92 ± 0.09	12.57 ± 0.42
PSO J174.6630−18.6530	19.04 ± 0.02	18.20 ± 0.02	J113839.14−183910.8	14.86 ± 0.04	14.40 ± 0.07	>12.48
PSO J175.2003+16.1403	20.41 ± 0.07	18.94 ± 0.03	J114048.05+160825.1	14.63 ± 0.03	14.22 ± 0.05	>12.29
PSO J175.8169−20.4072	20.52 ± 0.07	19.23 ± 0.04	J114316.04−202425.7	15.67 ± 0.06	14.42 ± 0.07	12.20 ± 0.43
PSO J180.1475−28.6160	19.73 ± 0.06	18.21 ± 0.02	J120035.41−283657.6	14.24 ± 0.03	13.56 ± 0.04	>12.40

Table 3.1—Continued

Pan-STARRS1 Name	z_{P1} (mag)	y_{P1} (mag)	*WISE* Name	$W1$ (mag)	$W2$ (mag)	$W3$ (mag)
PSO J182.6569−26.6197	19.62 ± 0.03	18.66 ± 0.03	J121037.66−263710.6	14.93 ± 0.04	14.44 ± 0.06	>12.30
PSO J183.4547+40.7901	21.17 ± 0.18	19.79 ± 0.07	J121349.14+404724.6	16.72 ± 0.12	15.02 ± 0.09	12.56 ± 0.39
PSO J183.9318−09.7914	19.45 ± 0.02	18.51 ± 0.02	J121543.62−094729.1	14.45 ± 0.03	14.04 ± 0.05	>12.60
PSO J186.5342+21.8364	19.71 ± 0.04	18.94 ± 0.09	J122608.20+215010.8	15.57 ± 0.05	15.05 ± 0.09	12.76 ± 0.52
PSO J192.5647+26.4796	···	19.60 ± 0.12	J125015.56+262846.9	16.36 ± 0.09	14.58 ± 0.06	>12.84
PSO J192.6717−21.8250	20.68 ± 0.09	19.09 ± 0.05	J125041.21−214930.1	15.75 ± 0.05	14.76 ± 0.06	>12.66
PSO J202.1635−03.7660	21.43 ± 0.15	19.58 ± 0.04	J132839.25−034558.2	15.74 ± 0.05	14.45 ± 0.05	>12.82
PSO J202.5764−26.1469	···	18.70 ± 0.12	J133018.38−260848.4	15.65 ± 0.05	15.21 ± 0.10	>12.89
PSO J207.7496+29.4240	20.81 ± 0.06	19.79 ± 0.13	J135059.90+292526.7	14.43 ± 0.03	13.76 ± 0.04	12.96 ± 0.48
PSO J218.4532+50.7231	20.68 ± 0.13	19.40 ± 0.04	J143348.76+504322.8	15.88 ± 0.05	14.70 ± 0.05	>13.05
PSO J218.5616−27.8952	19.75 ± 0.03	18.76 ± 0.04	J143414.79−275342.6	14.07 ± 0.03	13.56 ± 0.04	>12.05
PSO J224.3820+47.4057	···	19.72 ± 0.13	J145731.67+472420.1	16.72 ± 0.08	14.62 ± 0.05	12.66 ± 0.28
PSO J228.6775−29.7088	19.85 ± 0.05	18.77 ± 0.03	J151442.58−294231.9	14.95 ± 0.04	14.29 ± 0.06	>12.53

Table 3.1—Continued

Pan-STARRS1 Name	z_{P1} (mag)	y_{P1} (mag)	*WISE* Name	$W1$ (mag)	$W2$ (mag)	$W3$ (mag)
PSO J229.2354−26.6738	20.30 ± 0.09	19.01 ± 0.03	J151656.50−264025.3	14.80 ± 0.04	14.39 ± 0.07	>12.59
PSO J231.2588+08.5622	20.96 ± 0.05	19.49 ± 0.05	J152502.10+083343.8	15.29 ± 0.04	14.55 ± 0.05	>12.70
PSO J231.7900−26.4494	19.18 ± 0.03	18.09 ± 0.02	J152709.58−262657.7	14.25 ± 0.03	13.85 ± 0.05	>12.48
PSO J231.8943−29.0599	18.75 ± 0.02	17.81 ± 0.01	J152734.62−290335.7	13.87 ± 0.03	13.43 ± 0.04	11.32 ± 0.15
PSO J237.1471−23.1489	17.39 ± 0.01	16.62 ± 0.01	J154835.30−230855.4	12.94 ± 0.03	12.40 ± 0.03	10.66 ± 0.11
PSO J239.7016−23.2664	19.28 ± 0.02	18.28 ± 0.03	J155848.37−231559.1	14.44 ± 0.04	13.86 ± 0.05	>12.38
PSO J241.1376+39.0369	20.91 ± 0.09	19.74 ± 0.15	J160432.99+390212.9	16.11 ± 0.05	15.15 ± 0.06	>12.99
PSO J242.9129+02.4856	20.61 ± 0.04	19.52 ± 0.08	J161139.11+022908.1	15.48 ± 0.05	14.57 ± 0.07	>12.12
PSO J244.1180+06.3598	20.93 ± 0.07	19.77 ± 0.07	J161628.34+062135.2	14.78 ± 0.04	14.09 ± 0.05	>12.36
PSO J244.6801+08.7185	21.14 ± 0.20	19.56 ± 0.05	J161843.22+084306.9	16.53 ± 0.10	14.90 ± 0.08	>12.53
PSO J249.4774−10.8754	18.64 ± 0.02	18.25 ± 0.02	J163754.58−105231.6	13.81 ± 0.04	13.39 ± 0.08	10.91 ± 0.16
PSO J255.6623+10.7542	20.57 ± 0.07	19.96 ± 0.10	J170238.96+104515.2	14.64 ± 0.03	13.57 ± 0.04	11.13 ± 0.12
PSO J258.2413+06.7612	19.73 ± 0.02	18.50 ± 0.02	J171257.92+064540.3	13.88 ± 0.03	13.39 ± 0.03	>12.04

Table 3.1—Continued

Pan-STARRS1 Name	$z_{\rm P1}$ (mag)	$y_{\rm P1}$ (mag)	*WISE* Name	$W1$ (mag)	$W2$ (mag)	$W3$ (mag)
PSO J260.1623+61.7636	21.10 ± 0.09	19.66 ± 0.11	J172038.99+614548.9	16.23 ± 0.04	15.31 ± 0.05	>14.07
PSO J260.3363+46.6739	19.99 ± 0.03	18.79 ± 0.09	J172120.70+464026.1	14.45 ± 0.03	13.94 ± 0.04	12.72 ± 0.32
PSO J261.2881+22.9269	21.42 ± 0.20	19.64 ± 0.08	J172509.16+225536.8	16.57 ± 0.10	15.11 ± 0.09	>12.64
PSO J263.5879+50.3975	20.59 ± 0.08	18.89 ± 0.03	J173421.02+502349.9	15.41 ± 0.03	14.34 ± 0.04	>13.48
PSO J265.0759+11.4855	20.82 ± 0.09	19.73 ± 0.18	J174018.21+112907.5	15.57 ± 0.05	14.96 ± 0.08	>12.84
PSO J268.7928+18.0557	19.68 ± 0.06	18.15 ± 0.02	J175510.28+180320.2	14.60 ± 0.03	13.73 ± 0.04	12.36 ± 0.31
PSO J272.0887−04.9943	20.87 ± 0.10	19.51 ± 0.07	J180821.29−045940.1	14.99 ± 0.05	14.15 ± 0.07	12.37 ± 0.43
PSO J272.4689−04.8036	18.79 ± 0.03	17.46 ± 0.01	J180952.53−044812.5	13.29 ± 0.03	12.73 ± 0.03	12.38 ± 0.47
PSO J274.0908+30.5470	21.12 ± 0.18	19.79 ± 0.07	J181621.86+303248.9	16.55 ± 0.09	15.01 ± 0.08	>13.04
PSO J276.0671−01.9863	20.50 ± 0.04	19.77 ± 0.08	J182416.10−015910.8	14.20 ± 0.04	13.37 ± 0.05	>11.85
PSO J276.8234+22.4380	19.91 ± 0.04	18.86 ± 0.02	J182717.60+222616.9	14.01 ± 0.04	13.43 ± 0.04	>12.09
PSO J277.7441+45.7160	20.55 ± 0.06	19.34 ± 0.10	J183058.56+454257.4	14.81 ± 0.03	14.17 ± 0.04	>13.17
PSO J280.2973+63.2600	19.66 ± 0.02	18.56 ± 0.04	J184111.36+631535.6	14.13 ± 0.03	13.49 ± 0.03	12.39 ± 0.15

Table 3.1—Continued

Pan-STARRS1 Name	z_{P1} (mag)	y_{P1} (mag)	*WISE* Name	$W1$ (mag)	$W2$ (mag)	$W3$ (mag)
PSO J282.5878+34.7691	20.14 ± 0.08	19.32 ± 0.07	J185021.04+344609.7	15.13 ± 0.04	14.73 ± 0.06	>13.12
PSO J282.7576+59.5858	18.35 ± 0.01	17.15 ± 0.01	J185101.83+593508.6	12.65 ± 0.02	12.18 ± 0.02	11.23 ± 0.07
PSO J284.7214+39.3189	21.45 ± 0.21	19.90 ± 0.06	J185853.08+391908.0	16.59 ± 0.08	15.40 ± 0.09	>13.24
PSO J289.8149+30.7664	19.10 ± 0.04	17.74 ± 0.02	J191915.54+304558.4	13.39 ± 0.03	12.94 ± 0.03	11.72 ± 0.19
PSO J291.2688+68.5310	20.16 ± 0.05	18.65 ± 0.05	J192504.54+683151.7	15.10 ± 0.03	14.45 ± 0.04	13.65 ± 0.53
PSO J296.0820+35.7035	19.74 ± 0.11	19.07 ± 0.04	J194419.69+354212.5	14.67 ± 0.04	14.24 ± 0.06	12.01 ± 0.20
PSO J303.7105+31.9331	20.12 ± 0.08	19.68 ± 0.12	J201450.36+315600.2	13.49 ± 0.03	11.41 ± 0.02	10.46 ± 0.24
PSO J304.7573−07.2350	19.59 ± 0.03	18.70 ± 0.04	J201901.74−071405.3	15.40 ± 0.05	14.81 ± 0.09	>12.54
PSO J307.6784+07.8263	17.99 ± 0.01	16.46 ± 0.01	J203042.79+074934.7	12.96 ± 0.03	12.12 ± 0.03	10.96 ± 0.11
PSO J308.9834−09.7312	20.94 ± 0.10	19.76 ± 0.13	J203556.02−094352.3	15.94 ± 0.08	14.82 ± 0.09	>12.35
PSO J310.9853+62.3470	19.29 ± 0.04	17.92 ± 0.02	J204356.42+622048.9	13.90 ± 0.03	13.02 ± 0.03	12.12 ± 0.22
PSO J313.1577−26.0050	20.36 ± 0.05	19.18 ± 0.05	J205237.87−260018.0	15.61 ± 0.06	14.98 ± 0.11	12.60 ± 0.53
PSO J316.5156+04.1173	20.13 ± 0.06	19.14 ± 0.05	J210603.72+040702.4	14.87 ± 0.04	14.45 ± 0.07	>12.01

Table 3.1—Continued

Pan-STARRS1 Name	z_{P1} (mag)	y_{P1} (mag)	*WISE* Name	$W1$ (mag)	$W2$ (mag)	$W3$ (mag)
PSO J319.3102−29.6682	18.90 ± 0.02	17.66 ± 0.02	J211714.44−294005.2	13.56 ± 0.03	12.82 ± 0.03	11.94 ± 0.32
PSO J321.1619+18.8243	20.50 ± 0.05	19.41 ± 0.07	J212438.82+184927.5	14.73 ± 0.04	14.04 ± 0.05	12.45 ± 0.37
PSO J329.8288+03.0840	20.52 ± 0.20	19.25 ± 0.10	J215918.90+030502.8	14.89 ± 0.04	14.29 ± 0.06	>12.56
PSO J330.3214+32.3686	19.90 ± 0.03	18.63 ± 0.04	J220117.10+322206.9	14.71 ± 0.03	13.63 ± 0.04	12.29 ± 0.29
PSO J331.6058+33.0207	20.30 ± 0.06	18.93 ± 0.04	J220625.35+330114.6	15.37 ± 0.04	14.62 ± 0.07	12.82 ± 0.48
PSO J331.9397−07.0570	20.71 ± 0.09	19.77 ± 0.07	J220745.53−070325.1	14.51 ± 0.03	13.86 ± 0.05	>12.18
PSO J334.1193+19.8800	20.79 ± 0.06	19.18 ± 0.07	J221628.62+195248.1	15.70 ± 0.04	14.64 ± 0.06	12.93 ± 0.44
PSO J334.8034+11.2278	19.95 ± 0.03	18.92 ± 0.05	J221912.81+111340.1	14.11 ± 0.03	13.69 ± 0.04	12.68 ± 0.46
PSO J336.9036−18.9148	20.71 ± 0.07	19.81 ± 0.08	J222736.87−185453.1	14.15 ± 0.03	13.61 ± 0.04	>12.70
PSO J337.4314+16.4215	19.91 ± 0.03	18.91 ± 0.02	J222943.60+162516.5	15.72 ± 0.05	15.16 ± 0.10	>12.69
PSO J338.8587+31.4729	20.13 ± 0.04	19.14 ± 0.05	J223526.08+312822.3	15.06 ± 0.04	14.66 ± 0.07	>12.62
PSO J339.0734+51.0978	19.15 ± 0.06	17.27 ± 0.01	J223617.59+510551.9	13.84 ± 0.03	12.48 ± 0.03	11.02 ± 0.08
PSO J341.7509−15.1075	19.72 ± 0.03	18.73 ± 0.03	J224700.20−150626.8	14.22 ± 0.03	13.80 ± 0.04	>12.75

Table 3.1—Continued

Pan-STARRS1 Name	z_{P1} (mag)	y_{P1} (mag)	*WISE* Name	$W1$ (mag)	$W2$ (mag)	$W3$ (mag)
PSO J342.3797−16.4665	19.29 ± 0.04	18.27 ± 0.02	J224931.09−162759.4	14.09 ± 0.03	13.67 ± 0.04	>12.08
PSO J342.9795−09.6000	21.22 ± 0.17	20.04 ± 0.14	J225154.99−093600.5	15.98 ± 0.08	15.02 ± 0.11	>12.54
PSO J344.8146+20.1917	20.31 ± 0.11	18.99 ± 0.04	J225915.51+201129.9	14.35 ± 0.03	13.93 ± 0.04	>12.33
PSO J346.3203−11.1654	20.37 ± 0.05	19.29 ± 0.05	J230516.86−110955.2	14.62 ± 0.04	14.09 ± 0.06	>12.24
PSO J346.5281−15.9406	20.15 ± 0.08	19.28 ± 0.09	J230606.72−155626.1	13.86 ± 0.03	13.36 ± 0.04	>12.09
PSO J348.8808+06.2873	19.09 ± 0.01	18.06 ± 0.02	J231531.39+061714.2	13.55 ± 0.03	13.10 ± 0.03	11.67 ± 0.23
PSO J350.4673−19.0783	20.02 ± 0.05	19.08 ± 0.05	J232152.15−190441.6	14.57 ± 0.03	14.13 ± 0.06	>12.61
PSO J353.0517−29.8947	20.33 ± 0.05	19.24 ± 0.08	J233212.40−295341.5	15.78 ± 0.06	15.15 ± 0.10	>12.84
PSO J353.6355+13.2209	19.79 ± 0.03	18.88 ± 0.02	J233432.53+131315.3	13.78 ± 0.03	13.26 ± 0.03	12.40 ± 0.39
PSO J353.8627+45.1946	20.13 ± 0.03	19.15 ± 0.07	J233527.07+451140.9	13.48 ± 0.03	12.93 ± 0.03	12.72 ± 0.54
PSO J357.8314+49.6330	20.04 ± 0.04	18.73 ± 0.03	J235119.56+493758.9	14.84 ± 0.03	14.32 ± 0.05	12.55 ± 0.30
PSO J359.8867−01.8651	20.31 ± 0.06	19.06 ± 0.03	J235932.81−015154.1	15.24 ± 0.05	14.54 ± 0.07	>12.64

Note. — Pan-STARRS1 photometry is quoted as of March 2015. The photometric selections described in this paper were done using Pan-STARRS1 photometry from January 2012. *WISE* photometry is from the *WISE* All-sky Release.

Table 3.2. Near-infrared Photometry

Name	2MASS Photometry			MKO Photometry			
	J_{2MASS} (mag)	H_{2MASS} (mag)	K_{2MASS} (mag)	J_{MKO} (mag)	H_{MKO} (mag)	K_{MKO} (mag)	Ref.[a]
PSO J003.4−18	16.54 ± 0.14	15.89 ± 0.18	15.04 ± 0.13	16.68 ± 0.27	15.87 ± 0.30	$[15.18 \pm 0.28]$	1
PSO J004.1+23	>16.41	15.70 ± 0.14	>14.97	16.58 ± 0.03	15.72 ± 0.02	$[15.24 \pm 0.05]$	1
PSO J004.7+51	16.82 ± 0.15	15.29 ± 0.11	14.64 ± 0.07	16.70 ± 0.05	15.40 ± 0.11	$[14.51 \pm 0.07]$	1
PSO J007.7+57	14.95 ± 0.04	13.78 ± 0.04	13.22 ± 0.03	14.80 ± 0.01	13.86 ± 0.01	$[13.21 \pm 0.03]$	1
PSO J007.9+33	16.45 ± 0.13	15.43 ± 0.12	14.49 ± 0.08	16.40 ± 0.03	$[15.47 \pm 0.08]$	$[14.69 \pm 0.08]$	1
PSO J010.2+41	···	···	···	18.27 ± 0.14	$[17.34 \pm 0.20]$	$[16.78 \pm 0.22]$	1
PSO J023.8+02	16.62 ± 0.13	15.48 ± 0.10	15.12 ± 0.12	16.48 ± 0.15	15.66 ± 0.14	14.99 ± 0.12	2
PSO J024.1+37	···	···	···	18.23 ± 0.11	17.46 ± 0.10	$[17.14 \pm 0.16]$	1
PSO J031.5+20	···	···	···	16.73 ± 0.03	17.02 ± 0.07	$[16.79 \pm 0.31]$	1
PSO J041.5+01	>16.88	15.87 ± 0.16	15.01 ± 0.13	16.91 ± 0.04	15.85 ± 0.04	$[15.10 \pm 0.08]$	1
PSO J048.9+07	17.02 ± 0.21	15.83 ± 0.18	15.43 ± 0.20	16.95 ± 0.04	16.19 ± 0.04	$[15.65 \pm 0.10]$	1

Table 3.2—Continued

Name	2MASS Photometry			MKO Photometry			Ref.[a]
	J_{2MASS} (mag)	H_{2MASS} (mag)	K_{2MASS} (mag)	J_{MKO} (mag)	H_{MKO} (mag)	K_{MKO} (mag)	
PSO J049.1+17	16.96 ± 0.24	16.39 ± 0.21	15.75 ± 0.24	17.06 ± 0.04	16.43 ± 0.04	$[15.96 \pm 0.11]$	1
PSO J049.1+26	16.59 ± 0.15	15.59 ± 0.16	>15.16	16.11 ± 0.02	15.82 ± 0.02	$[15.50 \pm 0.05]$	1
PSO J052.7−03	16.47 ± 0.10	15.16 ± 0.08	14.72 ± 0.09	16.26 ± 0.02	15.24 ± 0.02	$[14.58 \pm 0.04]$	1
PSO J053.3+30	15.13 ± 0.04	13.70 ± 0.03	12.96 ± 0.03	15.09 ± 0.00	13.75 ± 0.00	12.94 ± 0.00	2
PSO J054.8−11	16.79 ± 0.15	15.83 ± 0.13	15.06 ± 0.14	16.71 ± 0.05	15.75 ± 0.03	$[14.97 \pm 0.10]$	1
PSO J055.0−21	···	···	···	16.95 ± 0.05	16.29 ± 0.05	$[16.12 \pm 0.16]$	1
PSO J057.2+15	17.29 ± 0.22	16.30 ± 0.19	15.01 ± 0.11	17.29 ± 0.06	16.04 ± 0.05	14.90 ± 0.02	1
PSO J060.3+25	16.81 ± 0.17	15.73 ± 0.14	15.36 ± 0.17	16.93 ± 0.04	16.10 ± 0.03	$[15.53 \pm 0.07]$	1
PSO J068.3+52	16.88 ± 0.15	15.41 ± 0.09	14.86 ± 0.11	16.63 ± 0.05	15.65 ± 0.06	14.70 ± 0.01	1
PSO J068.9+13	16.73 ± 0.16	15.77 ± 0.14	14.80 ± 0.12	16.89 ± 0.03	15.80 ± 0.02	14.99 ± 0.01	1
PSO J070.3+04	···	···	···	16.39 ± 0.03	16.46 ± 0.04	$[16.38 \pm 0.22]$	1

Table 3.2—Continued

Name	2MASS Photometry			MKO Photometry			Ref.[a]
	J_{2MASS} (mag)	H_{2MASS} (mag)	K_{2MASS} (mag)	J_{MKO} (mag)	H_{MKO} (mag)	K_{MKO} (mag)	
PSO J071.4+36	16.83 ± 0.19	15.78 ± 0.17	15.03 ± 0.15	16.72 ± 0.03	15.79 ± 0.02	$[14.94 \pm 0.09]$	1
PSO J071.6−24	16.43 ± 0.12	15.53 ± 0.13	15.14 ± 0.16	16.29 ± 0.02	15.58 ± 0.02	15.13 ± 0.02	1
PSO J071.8−12	16.48 ± 0.11	15.99 ± 0.17	15.55 ± 0.22	16.69 ± 0.04	16.07 ± 0.04	$[15.66 \pm 0.16]$	1
PSO J076.1+25	17.12 ± 0.20	15.27 ± 0.09	14.46 ± 0.08	17.02 ± 0.04	15.38 ± 0.02	14.41 ± 0.02	1
PSO J076.7+52	15.75 ± 0.07	15.35 ± 0.11	15.60 ± 0.20	15.44 ± 0.02	15.47 ± 0.02	15.60 ± 0.03	1
PSO J077.1+24	16.93 ± 0.14	16.47 ± 0.25	15.82 ± 0.22	17.06 ± 0.04	16.31 ± 0.04	15.59 ± 0.03	1
PSO J078.9+31	···	···	···	16.67 ± 0.03	15.96 ± 0.03	15.30 ± 0.03	1
PSO J085.3+36	>15.86	>14.55	14.34 ± 0.07	16.10 ± 0.01	14.70 ± 0.00	13.80 ± 0.00	2
PSO J087.7−12	16.63 ± 0.13	15.69 ± 0.15	14.71 ± 0.13	16.52 ± 0.04	15.52 ± 0.03	$[14.71 \pm 0.08]$	1
PSO J088.0+43	16.37 ± 0.09	15.48 ± 0.08	14.87 ± 0.08	16.29 ± 0.02	15.52 ± 0.02	14.80 ± 0.03	1
PSO J088.3−24	···	···	···	16.84 ± 0.09	16.48 ± 0.12	$[15.62 \pm 0.26]$	1

Table 3.2—Continued

Name	2MASS Photometry			MKO Photometry			Ref.[a]
	J_{2MASS} (mag)	H_{2MASS} (mag)	K_{2MASS} (mag)	J_{MKO} (mag)	H_{MKO} (mag)	K_{MKO} (mag)	
PSO J100.5+41	16.16 ± 0.10	15.09 ± 0.07	14.28 ± 0.06	16.15 ± 0.02	15.11 ± 0.01	14.31 ± 0.01	1
PSO J101.8+39	···	···	···	16.83 ± 0.03	16.20 ± 0.04	15.61 ± 0.02	1
PSO J103.0+41	15.48 ± 0.06	14.46 ± 0.05	13.89 ± 0.05	15.36 ± 0.01	14.51 ± 0.03	13.95 ± 0.03	1
PSO J105.4+63	15.79 ± 0.06	15.08 ± 0.07	14.88 ± 0.11	[[15.66 ± 0.10]]	[[15.16 ± 0.14]]	[[14.89 ± 0.19]]	1
PSO J108.4+38	16.92 ± 0.15	15.72 ± 0.12	14.92 ± 0.10	16.68 ± 0.03	15.66 ± 0.02	14.84 ± 0.01	1
PSO J109.4+46	···	···	···	17.06 ± 0.04	16.45 ± 0.04	15.86 ± 0.03	1
PSO J115.0+59	16.51 ± 0.16	15.88 ± 0.19	>16.32	16.76 ± 0.04	16.13 ± 0.04	15.56 ± 0.03	1
PSO J117.1+17	16.27 ± 0.11	15.18 ± 0.09	14.42 ± 0.09	16.16 ± 0.02	15.26 ± 0.02	14.50 ± 0.01	1
PSO J127.4+10	···	···	···	17.07 ± 0.03	16.11 ± 0.02	15.25 ± 0.02	1
PSO J133.8−02	16.10 ± 0.07	15.31 ± 0.07	14.96 ± 0.13	16.00 ± 0.02	15.29 ± 0.02	[14.77 ± 0.06]	1
PSO J133.8+06	16.31 ± 0.12	15.43 ± 0.13	15.03 ± 0.12	16.34 ± 0.01	[15.68 ± 0.04]	[15.19 ± 0.05]	2

Table 3.2—Continued

Name	2MASS Photometry			MKO Photometry			Ref.[a]
	J_{2MASS} (mag)	H_{2MASS} (mag)	K_{2MASS} (mag)	J_{MKO} (mag)	H_{MKO} (mag)	K_{MKO} (mag)	
PSO J135.0+32	15.84 ± 0.07	15.10 ± 0.08	14.50 ± 0.09	15.76 ± 0.02	15.03 ± 0.01	14.41 ± 0.03	1
PSO J135.7+16	16.49 ± 0.11	15.78 ± 0.16	15.49 ± 0.19	16.40 ± 0.02	15.80 ± 0.02	15.26 ± 0.02	1
PSO J136.3+10	...	...	...	17.08 ± 0.02	16.39 ± 0.02	16.07 ± 0.02	2
PSO J136.5−06	14.83 ± 0.04	14.13 ± 0.05	13.66 ± 0.04	14.75 ± 0.02	14.19 ± 0.03	13.70 ± 0.02	1
PSO J140.2+45	15.22 ± 0.05	14.16 ± 0.05	13.73 ± 0.05	15.04 ± 0.01	14.19 ± 0.02	13.77 ± 0.01	1
PSO J143.6−29	16.41 ± 0.11	16.05 ± 0.16	15.21 ± 0.16	16.47 ± 0.03	15.87 ± 0.02	15.33 ± 0.02	1
PSO J146.0+05	16.81 ± 0.16	15.98 ± 0.17	15.63 ± 0.23	16.74 ± 0.02	16.11 ± 0.02	15.55 ± 0.02	2
PSO J147.5−27	16.89 ± 0.18	16.22 ± 0.21	15.46 ± 0.19	[[16.84 ± 0.20]]	[[16.29 ± 0.24]]	[[15.43 ± 0.23]]	1
PSO J149.0−14	16.28 ± 0.10	15.06 ± 0.09	14.22 ± 0.06	15.99 ± 0.02	15.07 ± 0.01	14.46 ± 0.02	1
PSO J149.1−19	15.21 ± 0.04	14.32 ± 0.04	13.85 ± 0.05	15.13 ± 0.01	14.43 ± 0.02	13.90 ± 0.01	1
PSO J152.2+15	16.89 ± 0.20	15.58 ± 0.15	15.45 ± 0.17	16.68 ± 0.04	16.14 ± 0.04	[15.53 ± 0.11]	1

Table 3.2—Continued

Name	2MASS Photometry			MKO Photometry			Ref.[a]
	J_{2MASS} (mag)	H_{2MASS} (mag)	K_{2MASS} (mag)	J_{MKO} (mag)	H_{MKO} (mag)	K_{MKO} (mag)	
PSO J158.1+05	···	···	···	16.62 ± 0.01	15.95 ± 0.02	15.35 ± 0.01	2
PSO J159.0−27	15.92 ± 0.10	15.31 ± 0.12	14.62 ± 0.10	16.02 ± 0.02	15.36 ± 0.01	$[14.72 \pm 0.07]$	1
PSO J159.2−26	16.81 ± 0.17	16.01 ± 0.13	15.30 ± 0.17	16.71 ± 0.03	16.03 ± 0.03	15.51 ± 0.03	1
PSO J160.0−21	16.58 ± 0.12	16.06 ± 0.15	15.47 ± 0.18	16.49 ± 0.02	16.01 ± 0.03	$[15.55 \pm 0.10]$	1
PSO J167.1+08	16.58 ± 0.16	15.50 ± 0.11	15.03 ± 0.16	16.56 ± 0.01	15.65 ± 0.01	14.99 ± 0.01	2
PSO J168.1−27	···	···	···	17.14 ± 0.02	16.75 ± 0.03	16.71 ± 0.07	3
PSO J174.6−18	16.35 ± 0.09	15.63 ± 0.10	15.18 ± 0.17	16.29 ± 0.05	15.67 ± 0.04	$[15.13 \pm 0.11]$	1
PSO J175.2+16	16.86 ± 0.15	16.14 ± 0.24	15.23 ± 0.13	16.82 ± 0.02	15.95 ± 0.01	15.24 ± 0.01	2
PSO J175.8−20	···	···	···	16.74 ± 0.17	16.30 ± 0.04	$[15.99 \pm 0.20]$	1
PSO J180.1−28	15.98 ± 0.09	15.07 ± 0.07	14.68 ± 0.10	15.96 ± 0.02	15.15 ± 0.01	$[14.75 \pm 0.05]$	1
PSO J182.6−26	16.48 ± 0.12	15.73 ± 0.12	15.20 ± 0.16	16.72 ± 0.05	16.11 ± 0.06	$[15.28 \pm 0.09]$	1

Table 3.2—Continued

Name	2MASS Photometry			MKO Photometry			Ref.[a]
	J_{2MASS} (mag)	H_{2MASS} (mag)	K_{2MASS} (mag)	J_{MKO} (mag)	H_{MKO} (mag)	K_{MKO} (mag)	
PSO J183.4+40	···	···	···	17.05 ± 0.04	16.86 ± 0.05	$[16.76 \pm 0.27]$	1
PSO J183.9−09	16.33 ± 0.13	15.45 ± 0.11	14.85 ± 0.14	16.31 ± 0.01	15.57 ± 0.01	$[14.95 \pm 0.10]$	3
PSO J186.5+21	17.07 ± 0.20	16.41 ± 0.28	15.39 ± 0.18	16.92 ± 0.02	16.33 ± 0.02	15.79 ± 0.02	2
PSO J192.5+26	···	···	···	16.40 ± 0.01	16.74 ± 0.02	16.79 ± 0.05	2
PSO J192.6−21	···	···	···	16.84 ± 0.04	16.30 ± 0.04	$[16.22 \pm 0.17]$	1
PSO J202.1−03	···	···	···	16.94 ± 0.03	16.69 ± 0.04	$[16.70 \pm 0.26]$	1
PSO J202.5−26	16.67 ± 0.12	16.19 ± 0.14	15.45 ± 0.19	16.73 ± 0.08	16.24 ± 0.04	$[16.28 \pm 0.34]$	1
PSO J207.7+29	16.97 ± 0.15	15.79 ± 0.15	15.41 ± 0.14	17.18 ± 0.02	16.41 ± 0.02	15.50 ± 0.02	2
PSO J218.4+50	···	···	···	16.91 ± 0.03	16.54 ± 0.04	$[16.16 \pm 0.15]$	1
PSO J218.5−27	16.58 ± 0.12	15.60 ± 0.12	14.83 ± 0.11	16.32 ± 0.03	15.43 ± 0.02	$[14.59 \pm 0.08]$	1
PSO J224.3+47	···	···	···	17.08 ± 0.03	17.43 ± 0.06	$[17.09 \pm 0.26]$	1

Table 3.2—Continued

Name	2MASS Photometry			MKO Photometry			Ref.[a]
	J_{2MASS} (mag)	H_{2MASS} (mag)	K_{2MASS} (mag)	J_{MKO} (mag)	H_{MKO} (mag)	K_{MKO} (mag)	
PSO J228.6−29	16.79 ± 0.19	15.95 ± 0.15	15.31 ± 0.16	16.72 ± 0.05	16.18 ± 0.05	$[15.37 \pm 0.11]$	1
PSO J229.2−26	16.46 ± 0.13	15.98 ± 0.18	15.18 ± 0.15	16.76 ± 0.03	15.85 ± 0.02	$[15.14 \pm 0.08]$	1
PSO J231.2+08	···	···	···	17.19 ± 0.02	16.71 ± 0.02	16.31 ± 0.03	2
PSO J231.7−26	15.96 ± 0.08	15.21 ± 0.11	14.62 ± 0.10	15.98 ± 0.02	15.25 ± 0.03	$[14.64 \pm 0.05]$	1
PSO J231.8−29	15.77 ± 0.09	14.83 ± 0.07	14.33 ± 0.08	$[[15.72 \pm 0.09]]$	$[[14.91 \pm 0.08]]$	$[[14.29 \pm 0.08]]$	1
PSO J237.1−23	14.79 ± 0.05	14.13 ± 0.07	13.60 ± 0.05	$[[14.73 \pm 0.06]]$	$[[14.19 \pm 0.07]]$	$[[13.57 \pm 0.06]]$	1
PSO J239.7−23	16.30 ± 0.11	15.35 ± 0.11	15.00 ± 0.13	16.25 ± 0.02	15.54 ± 0.02	$[15.02 \pm 0.07]$	1
PSO J241.1+39	···	···	···	17.71 ± 0.13	$[17.13 \pm 0.15]$	16.71 ± 0.07	1
PSO J242.9+02	···	···	···	17.11 ± 0.13	16.40 ± 0.09	$[16.07 \pm 0.16]$	1
PSO J244.1+06	···	···	···	17.51 ± 0.06	16.35 ± 0.04	$[15.54 \pm 0.10]$	1
PSO J244.6+08	···	···	···	16.84 ± 0.03	16.80 ± 0.03	$[16.80 \pm 0.18]$	1

Table 3.2—Continued

Name	2MASS Photometry			MKO Photometry			Ref.[a]
	J_{2MASS} (mag)	H_{2MASS} (mag)	K_{2MASS} (mag)	J_{MKO} (mag)	H_{MKO} (mag)	K_{MKO} (mag)	
PSO J249.4−10	16.43 ± 0.15	>14.74	>14.16	16.53 ± 0.03	15.69 ± 0.02	$[14.90 \pm 0.07]$	1
PSO J255.6+10	···	···	···	18.34 ± 0.09	17.27 ± 0.05	$[16.20 \pm 0.24]$	1
PSO J258.2+06	16.16 ± 0.09	15.34 ± 0.10	14.78 ± 0.11	16.03 ± 0.02	15.42 ± 0.02	14.76 ± 0.02	1
PSO J260.1+61	···	···	···	···	···	···	···
PSO J260.3+46	16.86 ± 0.15	15.83 ± 0.15	15.23 ± 0.13	16.79 ± 0.02	15.84 ± 0.02	$[15.24 \pm 0.09]$	1
PSO J261.2+22	···	···	···	16.83 ± 0.03	16.89 ± 0.04	$[16.86 \pm 0.20]$	1
PSO J263.5+50	16.34 ± 0.11	15.85 ± 0.14	>15.37	$[[16.15 \pm 0.13]]$	$[[15.90 \pm 0.21]]$	$[[15.82 \pm 0.24]]$[c]	1
PSO J265.0+11	···	···	···	17.48 ± 0.08	16.59 ± 0.06	$[16.38 \pm 0.15]$	1
PSO J268.7+18	16.02 ± 0.09	15.22 ± 0.09	14.68 ± 0.13	15.82 ± 0.02	15.32 ± 0.02	15.24 ± 0.02	1
PSO J272.0−04	···	···	···	16.90 ± 0.03	$[16.28 \pm 0.05]$	$[15.74 \pm 0.06]$	1
PSO J272.4−04	15.14 ± 0.05	14.28 ± 0.05	13.96 ± 0.06	15.15 ± 0.01	$[14.49 \pm 0.04]$	13.98 ± 0.01	1

Table 3.2—Continued

Name	2MASS Photometry			MKO Photometry			Ref.[a]
	J_{2MASS} (mag)	H_{2MASS} (mag)	K_{2MASS} (mag)	J_{MKO} (mag)	H_{MKO} (mag)	K_{MKO} (mag)	
PSO J274.0+30	···	···	···	17.53 ± 0.07	16.93 ± 0.06	$[17.33 \pm 0.31]$	1
PSO J276.0−01	>16.39	>15.84	15.03 ± 0.16	17.60 ± 0.08	16.21 ± 0.04	$[15.48 \pm 0.10]$	1
PSO J276.8+22	16.91 ± 0.17	15.58 ± 0.11	14.87 ± 0.08	16.48 ± 0.03	15.62 ± 0.02	$[14.82 \pm 0.07]$	1
PSO J277.7+45	···	···	···	17.22 ± 0.04	16.23 ± 0.03	$[15.55 \pm 0.08]$	1
PSO J280.2+63	16.13 ± 0.10	15.34 ± 0.10	14.83 ± 0.12	$[[16.02 \pm 0.12]]$	$[[15.43 \pm 0.11]]$	$[[14.82 \pm 0.13]]$	1
PSO J282.5+34	17.25 ± 0.24	16.26 ± 0.20	15.40 ± 0.20	17.10 ± 0.03	16.28 ± 0.03	$[15.68 \pm 0.08]$	1
PSO J282.7+59	14.94 ± 0.04	13.97 ± 0.03	13.46 ± 0.04	14.85 ± 0.01	14.03 ± 0.02	$[13.40 \pm 0.02]$	1
PSO J284.7+39	···	···	···	17.41 ± 0.04	17.17 ± 0.06	$[17.03 \pm 0.19]$	1
PSO J289.8+30	15.57 ± 0.05	14.60 ± 0.05	13.95 ± 0.05	15.52 ± 0.02	14.56 ± 0.01	$[13.95 \pm 0.03]$	1
PSO J291.2+68	16.61 ± 0.15	16.11 ± 0.21	15.49 ± 0.23	$[[16.52 \pm 0.17]]$	$[[16.19 \pm 0.23]]$	$[[15.52 \pm 0.25]]$	1
PSO J296.0+35	16.42 ± 0.11	15.88 ± 0.15	15.20 ± 0.15	16.47 ± 0.03	15.94 ± 0.03	$[15.76 \pm 0.13]$	1

Table 3.2—Continued

Name	2MASS Photometry			MKO Photometry			Ref.[a]
	J_{2MASS} (mag)	H_{2MASS} (mag)	K_{2MASS} (mag)	J_{MKO} (mag)	H_{MKO} (mag)	K_{MKO} (mag)	
PSO J303.7+31	16.07 ± 0.09	15.22 ± 0.09	15.24 ± 0.16	[[16.06 ± 0.15]]	[[15.28 ± 0.19]]	[[15.24 ± 0.32]]	1
PSO J304.7−07	16.81 ± 0.17	15.97 ± 0.16	15.37 ± 0.19	16.77 ± 0.03	16.24 ± 0.03	[15.70 ± 0.10]	1
PSO J307.6+07	14.23 ± 0.03	13.44 ± 0.03	13.32 ± 0.04	14.05 ± 0.01	13.48 ± 0.01	[13.37 ± 0.04]	1
PSO J308.9−09	···	···	···	17.67 ± 0.08	16.86 ± 0.06	[16.33 ± 0.12]	1
PSO J310.9+62	15.60 ± 0.07	14.70 ± 0.07	14.42 ± 0.07	[[15.46 ± 0.07]]	[[14.78 ± 0.08]]	[[14.44 ± 0.09]]	1
PSO J313.1−26	···	···	···	17.24 ± 0.06	16.49 ± 0.04	[15.92 ± 0.11]	1
PSO J316.5+04	16.81 ± 0.20	16.02 ± 0.22	15.59 ± 0.24	17.01 ± 0.04	16.09 ± 0.03	[15.49 ± 0.07]	1
PSO J319.3−29	15.60 ± 0.06	14.53 ± 0.04	14.15 ± 0.07	15.45 ± 0.02	14.65 ± 0.01	[14.17 ± 0.08]	1
PSO J321.1+18	17.03 ± 0.22	15.89 ± 0.15	15.36 ± 0.17	16.99 ± 0.03	16.10 ± 0.03	[15.42 ± 0.05]	1
PSO J329.8+03	···	···	···	16.98 ± 0.02	16.29 ± 0.02	15.72 ± 0.02	2
PSO J330.3+32	16.35 ± 0.09	15.44 ± 0.09	>15.23	16.13 ± 0.04	15.63 ± 0.04	[15.34 ± 0.09]	1

Table 3.2—Continued

Name	2MASS Photometry			MKO Photometry			Ref.[a]
	J_{2MASS} (mag)	H_{2MASS} (mag)	K_{2MASS} (mag)	J_{MKO} (mag)	H_{MKO} (mag)	K_{MKO} (mag)	
PSO J331.6+33	16.58 ± 0.11	15.89 ± 0.10	>17.23	16.66 ± 0.03	16.08 ± 0.03	$[15.75 \pm 0.15]$	1
PSO J331.9−07	17.41 ± 0.25	15.96 ± 0.18	15.66 ± 0.25	17.54 ± 0.05	16.45 ± 0.03	$[15.50 \pm 0.07]$	1
PSO J334.1+19	···	···	···	16.59 ± 0.06	16.41 ± 0.07	$[16.28 \pm 0.14]$	1
PSO J334.8+11	16.74 ± 0.12	15.28 ± 0.11	14.82 ± 0.10	16.58 ± 0.02	15.61 ± 0.02	$[14.90 \pm 0.05]$	1
PSO J336.9−18	17.00 ± 0.16	15.76 ± 0.12	15.24 ± 0.14	17.37 ± 0.05	16.10 ± 0.02	$[15.14 \pm 0.07]$	1
PSO J337.4+16	···	···	···	17.02 ± 0.03	16.46 ± 0.05	$[15.85 \pm 0.08]$	1
PSO J338.8+31	···	···	···	17.05 ± 0.03	16.19 ± 0.03	$[15.75 \pm 0.07]$	1
PSO J339.0+51	14.58 ± 0.03	14.49 ± 0.05	14.45 ± 0.09	14.46 ± 0.01	14.62 ± 0.02	$[14.57 \pm 0.03]$	1
PSO J341.7−15	16.41 ± 0.09	15.40 ± 0.09	14.83 ± 0.11	16.43 ± 0.02	15.55 ± 0.02	$[14.78 \pm 0.05]$	1
PSO J342.3−16	16.12 ± 0.08	15.26 ± 0.09	14.83 ± 0.11	16.09 ± 0.02	15.37 ± 0.02	$[14.83 \pm 0.04]$	1
PSO J342.9−09	···	···	···	18.85 ± 0.14	17.98 ± 0.10	$[17.31 \pm 0.39]$	1

Table 3.2—Continued

Name	2MASS Photometry			MKO Photometry			Ref.[a]
	J_{2MASS} (mag)	H_{2MASS} (mag)	K_{2MASS} (mag)	J_{MKO} (mag)	H_{MKO} (mag)	K_{MKO} (mag)	
PSO J344.8+20	16.58 ± 0.19	15.66 ± 0.15	14.85 ± 0.12	16.76 ± 0.03	15.76 ± 0.03	$[15.00 \pm 0.05]$	1
PSO J346.3−11	17.71 ± 0.37	15.92 ± 0.21	15.40 ± 0.19	17.13 ± 0.03	16.24 ± 0.03	$[15.51 \pm 0.07]$	1
PSO J346.5−15	16.69 ± 0.15	15.25 ± 0.10	14.78 ± 0.12	16.56 ± 0.02	15.50 ± 0.02	$[14.63 \pm 0.06]$	1
PSO J348.8+06	15.86 ± 0.08	14.76 ± 0.07	14.07 ± 0.06	15.75 ± 0.01	14.89 ± 0.01	14.11 ± 0.01	2
PSO J350.4−19	17.15 ± 0.18	15.85 ± 0.15	15.15 ± 0.13	16.86 ± 0.03	15.93 ± 0.02	$[15.31 \pm 0.07]$	1
PSO J353.0−29	17.03 ± 0.18	16.84 ± 0.30	15.69 ± 0.23	17.42 ± 0.04	16.68 ± 0.06	$[16.20 \pm 0.15]$	1
PSO J353.6+13	>16.65	15.78 ± 0.15	14.76 ± 0.10	16.60 ± 0.01	15.58 ± 0.01	14.66 ± 0.01	2
PSO J353.8+45[b]	16.70 ± 0.19	>15.26	>14.46	16.83 ± 0.03	15.63 ± 0.02	$[14.65 \pm 0.05]$	1
PSO J357.8+49	16.54 ± 0.13	15.77 ± 0.15	15.15 ± 0.13	16.48 ± 0.02	15.91 ± 0.04	15.50 ± 0.04	1
PSO J359.8−01	17.24 ± 0.20	16.03 ± 0.17	16.09 ± 0.27	17.05 ± 0.03	16.36 ± 0.04	$[15.97 \pm 0.11]$	1

Note. — All 2MASS photometry is from the 2MASS Point Source Catalog (Cutri et al. 2003) except where noted. For MKO photometry, H and K band magnitudes enclosed in single brackets were synthesized using observed J band magnitudes and our low-resolution spectra. MKO magnitudes enclosed in double brackets were synthesized using the 2MASS magnitudes for the corresponding filters and our low-resolution spectra.

[a]References for MKO photometry: (1) this work, (2) UKIDSS DR9 (Lawrence et al. 2013), (3) VISTA Hemisphere Survey (Cross et al. 2012).

[b]2MASS photometry from 2MASS Point Source Reject Table (Skrutskie et al. 2006).

[c]Calibrated using the 2MASS H magnitude because the 2MASS K magnitude is an upper limit.

Table 3.3. IRTF/SpeX Observations

Object	Date (UT)	Slit (")	$t_{\rm int}$ (s)	A0 V Standard
PSO J003.4−18	2012 Dec 1	0.8	720	HD 3604
PSO J004.1+23	2012 Dec 1	0.8	720	HD 9711
PSO J004.7+51	2013 Sep 22	0.8	540	HD 19844
PSO J007.7+57	2012 Sep 24	0.8	200	HD 240290
PSO J007.9+33	2013 Sep 22	0.8	540	HD 15240
PSO J010.2+41	2012 Oct 28	0.8	2880	HD 219290
PSO J023.8+02	2012 Nov 8	0.8	720	HD 18571
PSO J024.1+37	2012 Oct 25	0.8	2880	HD 12381
PSO J031.5+20	2013 Jul 12	0.8	960	HD 6313
PSO J041.5+01	2013 Jan 26	0.8	960	HD 18571
PSO J048.9+07	2013 Jan 26	0.8	720	HD 18571
PSO J049.1+17	2013 Jan 26	0.8	960	HD 18571
PSO J049.1+26	2012 Nov 8	0.8	720	HD 18571
PSO J052.7−03	2012 Nov 8	0.8	720	HD 18571
PSO J053.3+30	2012 Sep 26	0.5	720	HD 22859
PSO J054.8−11	2013 Jan 26	0.8	840	HD 27700
PSO J055.0−21	2013 Jan 26	0.8	1080	HD 27166
PSO J057.2+15	2014 Jan 18	0.8	1440	HD 25175
PSO J068.3+52	2013 Jan 26	0.8	960	HD 31064
PSO J068.9+13	2012 Nov 7	0.8	720	HD 27761
PSO J070.3+04	2013 Jan 25	0.8	1200	HD 31411

Table 3.3—Continued

Object	Date (UT)	Slit (")	$t_{\rm int}$ (s)	A0 V Standard
PSO J071.4+36	2013 Apr 4	0.8	600	HD 35656
PSO J071.6−24	2013 Jan 26	0.8	600	HD 46996
PSO J071.8−12	2013 Jan 26	0.8	840	HD 27700
PSO J076.1+25	2014 Jan 17	0.8	720	HD 35036
PSO J076.7+52	2013 Jan 25	0.8	720	HD 33654
PSO J078.9+31	2013 Jan 26	0.8	540	HD 38245
	2015 Jan 28	0.5	1080	HD 31411
PSO J078.9+31	2013 Jan 26	0.8	540	HD 38245
PSO J085.3+36	2013 Jan 26	0.8	360	HD 38245
PSO J087.7−12	2013 Jan 25	0.8	960	HD 44442
PSO J088.0+43	2013 Apr 4	0.8	480	HD 39250
PSO J088.3−24	2013 Apr 17	0.8	720	HD 43070
PSO J100.5+41	2013 Jan 25	0.8	720	HD 50931
PSO J101.8+39	2013 Jan 25	0.8	960	HD 63586
PSO J103.0+41	2012 Sep 26	0.5	960	HD 39250
PSO J105.4+63	2012 Oct 25	0.8	180	HD 33654
PSO J108.4+38	2013 Apr 4	0.8	480	HD 56248
PSO J109.4+46	2013 Apr 4	0.8	960	HD 63586
PSO J115.0+59	2013 Apr 4	0.8	840	HD 56385
PSO J117.1+17	2013 Jan 25	0.8	360	HD 79752
PSO J127.4+10	2014 Jan 17	0.8	960	HD 79108

Table 3.3—Continued

Object	Date (UT)	Slit (")	$t_{\rm int}$ (s)	A0 V Standard
PSO J133.8−02	2013 Apr 4	0.8	480	HD 89911
PSO J133.8+06	2013 Apr 14	0.8	1440	HD 74721
	2015 Jan 20	0.5	1440	HD 74721
PSO J135.0+32	2013 Jan 25	0.8	360	HD 79108
	2015 May 29	0.5	2760	HD 79108
PSO J135.7+16	2013 Apr 17	0.8	840	GSC 1407-00828
PSO J136.3+10	2013 May 15	0.8	960	HD 79108
PSO J136.5−06	2012 Nov 8	0.8	720	HD 58056
PSO J140.2+45	2012 Nov 8	0.8	720	HD 33654
PSO J143.6−29	2013 Apr 5	0.8	600	HD 87727
PSO J146.0+05	2013 Apr 17	0.8	2160	HD 93346, HD 97516
PSO J147.5−27	2013 Apr 17	0.8	1920	HD 87727
PSO J149.0−14	2013 Apr 5	0.8	960	HD 87727
PSO J149.1−19	2013 Nov 23	0.8	360	HD 90723
PSO J152.2+15	2013 Apr 18	0.8	720	HD 97516
PSO J158.1+05	2013 Apr 18	0.8	720	HD 89239
	2015 Jan 20	0.5	2160	HD 89239
PSO J159.0−27	2013 Apr 17	0.5	1200	HD 81694
PSO J159.2−26	2013 Apr 5	0.8	1440	HD 98949
PSO J160.0−21	2013 Apr 4	0.8	960	HD 98201
PSO J167.1+08	2013 Apr 4	0.8	960	HD 108140

Table 3.3—Continued

Object	Date (UT)	Slit (")	$t_{\rm int}$ (s)	A0 V Standard
PSO J168.1−27	2014 Jan 17	0.8	960	HD 93185
PSO J174.6−18	2013 Apr 5	0.8	960	HD 101122
PSO J175.2+16	2013 Apr 5	0.8	1320	HD 112304
PSO J175.8−20	2014 Jan 17	0.8	720	HD 105764
PSO J180.1−28	2013 Apr 3	0.8	720	HD 89911
PSO J182.6−26	2013 Apr 17	0.8	2160	HD 125509
PSO J183.4+40	2013 Jul 13	0.8	1320	HD 109055
PSO J183.9−09	2013 Apr 5	0.8	720	HD 112304
PSO J186.5+21	2013 Apr 4	0.8	1200	HD 109691
PSO J192.5+26	2013 Jul 12	0.8	960	HD 111744
PSO J192.6−21	2013 Apr 4	0.8	960	HD 110902
PSO J202.1−03	2013 Jul 12	0.8	1200	HD 122749
PSO J202.5−26	2013 Apr 19	0.8	960	HD 126458
PSO J207.7+29	2013 Jul 12	0.8	1680	HD 122945
PSO J218.4+50	2013 Jul 12	0.8	1680	HD 179933
PSO J218.5−27	2013 Jul 14	0.8	720	HD 125438
PSO J224.3+47	2013 Jul 13	0.8	1200	HD 128039
PSO J231.2+08	2012 Jul 7	0.8	960	7 Ser
PSO J241.1+39	2012 Aug 10	0.8	1920	26 Ser
PSO J242.9+02	2012 Jul 8	0.8	1200	q Her
PSO J244.1+06	2012 Jul 8	0.8	1500	q Her

Table 3.3—Continued

Object	Date (UT)	Slit (")	$t_{\rm int}$ (s)	A0 V Standard
PSO J244.6+08	2012 Jul 7	0.8	1200	q Her
PSO J249.4−10	2013 Apr 16	0.8	960	HD 157170
PSO J255.6+10	2012 Oct 6	0.8	3720	HD 160512
PSO J258.2+06	2013 Apr 5	0.8	720	HD 161289
PSO J260.1+61	2012 Oct 15	0.8	2640	BD+60 2651
PSO J260.3+46	2012 Oct 7	0.8	1920	HD 179933
PSO J261.2+22	2013 Jul 12	0.8	960	HD 165029
PSO J263.5+50	2012 Sep 26	0.8	600	HD 199217
PSO J265.0+11	2012 Jul 6	0.8	2160	HD 171149
PSO J268.7+18	2012 Oct 15	0.8	720	HD 165029
PSO J272.0−04	2013 Jul 13	0.8	1440	HD 173591
PSO J272.4−04	2012 Oct 14	0.8	720	HD 173591
PSO J274.0+30	2012 Jul 7	0.8	1440	HD 165029
PSO J276.0−01	2013 Jul 13	0.8	2160	HD 165029
PSO J276.8+22	2012 Oct 17	0.8	960	HD 332937
PSO J277.7+45	2012 Sep 20	0.5	1200	HD 199217
PSO J280.2+63	2012 Oct 19	0.8	960	HD 179933
PSO J282.5+34	2012 Oct 17	0.8	1440	HD 332937
PSO J282.7+59	2012 Sep 26	0.8	240	HD 240290
PSO J284.7+39	2012 Sep 20	0.8	960	HD 197291
PSO J289.8+30	2012 Oct 6	0.8	720	HD 199217

Table 3.3—Continued

Object	Date (UT)	Slit (")	$t_{\rm int}$ (s)	A0 V Standard
PSO J291.2+68	2012 Oct 19	0.8	720	HD 179933
PSO J296.0+35	2012 Oct 25	0.8	720	HD 191225
PSO J303.7+31	2012 Aug 10	0.8	3600	HD 192243
PSO J304.7−07	2012 Nov 8	0.8	1200	HD 196442
PSO J307.6+07	2012 Sep 20	0.8	80	HD 189920
PSO J308.9−09	2012 Sep 20	0.8	1200	HD 189920
PSO J310.9+62	2012 Oct 6	0.8	720	HD 222749
PSO J313.1−26	2012 Oct 6	0.8	1920	HD 202941
PSO J316.5+04	2012 Oct 28	0.8	1920	HD 210501
PSO J319.3−29	2012 Sep 20	0.8	150	HD 195062
PSO J321.1+18	2012 Oct 6	0.8	1920	HD 209932
PSO J329.8+03	2012 Oct 17	0.8	960	HD 210501
PSO J330.3+32	2012 Aug 10	0.8	480	HD 210501
PSO J331.6+33	2012 Sep 20	0.8	960	BD+39 4890
PSO J331.9−07	2012 Oct 6	0.8	2160	HD 219833
PSO J334.1+19	2012 Aug 10	0.8	600	HD 210501
PSO J334.8+11	2012 Nov 7	0.8	720	HD 210501
PSO J336.9−18	2013 Jul 13	0.8	960	HD 202025
PSO J337.4+16	2012 Nov 8	0.8	1200	HD 210501
PSO J338.8+31	2012 Nov 7	0.8	720	HD 210501
PSO J339.0+51	2012 Oct 7	0.8	1200	HD 222749

Table 3.3—Continued

Object	Date (UT)	Slit (")	$t_{\rm int}$ (s)	A0 V Standard
PSO J341.7−15	2012 Oct 19	0.8	960	HD 213030
PSO J342.3−16	2012 Nov 7	0.8	720	HD 219833
PSO J342.9−09	2012 Sep 20	0.8	960	HD 216807
PSO J344.8+20	2012 Nov 8	0.5	720	HD 210501
PSO J346.3−11	2012 Nov 8	0.5	960	HD 215833
PSO J346.5−15	2012 Nov 8	0.5	720	HD 219545
PSO J348.8+06	2012 Sep 20	0.8	360	HD 216807
	2015 Jun 28	0.5	70	HD 210501
PSO J350.4−19	2012 Nov 8	0.5	960	HD 219545
PSO J353.0−29	2012 Sep 20	0.8	2160	HD 215298
PSO J353.6+13	2012 Nov 8	0.5	720	HD 7215
PSO J353.8+45	2012 Nov 8	0.5	960	HD 222749
PSO J357.8+49	2012 Nov 8	0.5	720	HD 222749
PSO J359.8−01	2012 Dec 1	0.8	840	HD 222749

Note. — All observations performed in prism mode with the 0.8×15 arcsec ($R \approx 75$) or 0.5×15 arcsec ($R \approx 120$) slit. Observations for PSO J007.7+57, PSO J103.0+41, PSO J140.2+45, PSO J272.4-04, PSO J282.7+59, PSO J307.6+07, and PSO J339.0+51 were originally presented in Best et al. (2013).

Table 3.4. Visual Spectral Types and Kinematics

Name	SpT (visual)	$d_{\rm phot}$[a] (pc)	$\mu_\alpha \cos\delta$[b] (mas yr^{-1})	μ_δ[b] (mas yr^{-1})	$v_{\rm tan}$ (km s^{-1})	Discovery References
PSO J003.4−18	L5 pec	46.1 ± 5.6	-31 ± 12	-175 ± 13	39 ± 6	1
PSO J004.1+23	T0	24.7 ± 2.5	398 ± 13	36 ± 15	47 ± 5	2
PSO J004.7+51	L7	23.4 ± 2.8	293 ± 4	-12 ± 7	33 ± 4	2
PSO J007.7+57	L9	11.6 ± 1.4	526 ± 2	-12 ± 4	29 ± 3	3,4
PSO J007.9+33	L9	21.4 ± 2.6	-19 ± 5	-10 ± 6	2 ± 1	2
PSO J023.8+02	L9.5	28.8 ± 3.0	87 ± 11	-470 ± 12	65 ± 7	2
PSO J024.1+37	M7	134.8 ± 22.6	-6 ± 10	-7 ± 15	6 ± 8	2
PSO J031.5+20	T5.5	24.7 ± 2.3	286 ± 34	88 ± 28	35 ± 5	2
PSO J041.5+01	L8.5	27.7 ± 3.4	28 ± 13	-50 ± 12	8 ± 2	2
PSO J048.9+07	L6: (blue)	41.9 ± 5.1	52 ± 21	53 ± 22	15 ± 5	2
PSO J049.1+17	L9.5	40.3 ± 4.3	221 ± 22	-68 ± 24	44 ± 6	2
PSO J049.1+26	T2.5	23.5 ± 2.4	204 ± 15	-25 ± 19	23 ± 3	2

Table 3.4—Continued

Name	SpT (visual)	$d_{\rm phot}$[a] (pc)	$\mu_\alpha \cos\delta$[b] (mas yr^{-1})	μ_δ[b] (mas yr^{-1})	$v_{\rm tan}$ (km s^{-1})	Discovery References
PSO J052.7−03	L9:	19.1 ± 2.3	-140 ± 7	60 ± 7	14 ± 2	2
PSO J054.8−11	L3:	50.3 ± 6.1	16 ± 11	-73 ± 11	18 ± 3	2
PSO J055.0−21	T2	31.3 ± 3.3	230 ± 11	-155 ± 16	41 ± 5	2
PSO J057.2+15	L7 (red)	25.2 ± 3.0	68 ± 11	-127 ± 12	17 ± 3	2
PSO J068.9+13	L6 (red)	34.9 ± 4.3	108 ± 9	-14 ± 10	18 ± 3	5,6
PSO J070.3+04	T4.5	23.9 ± 2.3	186 ± 7	-68 ± 8	22 ± 2	2
PSO J071.4+36	L6:	36.3 ± 4.4	-16 ± 13	-154 ± 18	27 ± 4	2
PSO J071.6−24	L6 (blue)	35.3 ± 4.3	-199 ± 13	398 ± 16	74 ± 9	3
PSO J071.8−12	T2:	27.7 ± 2.9	20 ± 19	-89 ± 19	12 ± 3	2
PSO J076.7+52	T4.5	17.6 ± 1.6	57 ± 4	-196 ± 7	17 ± 2	2
PSO J078.9+31	L1.5	65.7 ± 11.2	25 ± 4	-58 ± 4	20 ± 4	2
PSO J087.7−12	L8	25.5 ± 3.1	-144 ± 11	-39 ± 9	18 ± 3	2

Table 3.4—Continued

Name	SpT (visual)	$d_{\rm phot}$[a] (pc)	$\mu_\alpha \cos\delta$[b] (mas yr^{-1})	μ_δ[b] (mas yr^{-1})	$v_{\rm tan}$ (km s^{-1})	Discovery References
PSO J088.0+43	L4 pec	42.8 ± 5.2	2 ± 4	-80 ± 6	16 ± 2	2
PSO J088.3−24	L1:	100.5 ± 17.1	16 ± 7	-21 ± 6	13 ± 4	2
PSO J100.5+41	L9 (red)	16.1 ± 1.9	12 ± 4	-372 ± 6	28 ± 3	7
PSO J101.8+39	M9.5	97.2 ± 16.5	1 ± 7	-23 ± 9	11 ± 5	2
PSO J103.0+41	T0	14.2 ± 1.4	3 ± 3	-32 ± 5	2 ± 0	4
PSO J105.4+63	T2.5	16.7 ± 1.7	-14 ± 2	-264 ± 5	21 ± 2	7
PSO J108.4+38	L7	29.1 ± 3.5	-36 ± 9	-60 ± 11	10 ± 2	2
PSO J109.4+46	T0	41.5 ± 4.5	39 ± 8	-29 ± 12	10 ± 2	2
PSO J115.0+59	M9.5	108.8 ± 18.6	-17 ± 36	-34 ± 16	20 ± 12	2
PSO J117.1+17	L5	31.3 ± 3.8	-63 ± 5	8 ± 6	9 ± 1	8,9
PSO J127.4+10	L4	40.4 ± 4.9	0 ± 7	-45 ± 8	9 ± 2	2
PSO J133.8−02	T0 pec	23.8 ± 2.4	-157 ± 6	101 ± 7	21 ± 2	2

Table 3.4—Continued

Name	SpT (visual)	$d_{\rm phot}$[a] (pc)	$\mu_\alpha \cos\delta$[b] (mas yr^{-1})	μ_δ[b] (mas yr^{-1})	$v_{\rm tan}$ (km s^{-1})	Discovery References
PSO J133.8+06	M9	84.9 ± 14.3	-12 ± 11	-37 ± 11	16 ± 5	2
PSO J135.0+32	L1.5	45.2 ± 7.5	-91 ± 5	-11 ± 5	20 ± 3	2
PSO J135.7+16	T0 pec	29.0 ± 3.0	25 ± 14	-24 ± 17	5 ± 2	8,82
PSO J136.3+10	T1	31.2 ± 3.3	-8 ± 11	-118 ± 8	18 ± 2	10
PSO J136.5−06	L2 pec	32.4 ± 5.4	34 ± 5	-17 ± 4	6 ± 1	2
PSO J140.2+45	L9.5	14.3 ± 1.5	-77 ± 4	-852 ± 5	58 ± 6	17,4
PSO J143.6−29	L1	76.4 ± 12.8	-11 ± 12	-65 ± 14	24 ± 6	2
PSO J146.0+05	L1	80.2 ± 13.6	19 ± 18	-35 ± 22	15 ± 8	2
PSO J147.5−27	L0.5	104.4 ± 17.8	-8 ± 15	-17 ± 19	9 ± 9	2
PSO J149.0−14	L9	17.7 ± 2.1	96 ± 5	-148 ± 6	15 ± 2	2
PSO J149.1−19	L5 pec	25.8 ± 3.1	-100 ± 4	27 ± 5	13 ± 2	2
PSO J152.2+15	L1.5	77.3 ± 13.1	-200 ± 17	-51 ± 34	76 ± 15	2

Table 3.4—Continued

Name	SpT (visual)	$d_{\rm phot}$[a] (pc)	$\mu_\alpha \cos\delta$[b] (mas yr^{-1})	μ_δ[b] (mas yr^{-1})	$v_{\rm tan}$ (km s^{-1})	Discovery References
PSO J158.1+05	L2 (blue)	68.6 ± 11.6	-186 ± 5	-120 ± 6	72 ± 12	2
PSO J159.0−27	L2 (blue)	56.4 ± 9.4	-55 ± 5	-244 ± 5	67 ± 11	2
PSO J159.2−26	T1.5	25.7 ± 2.7	-12 ± 14	12 ± 15	2 ± 2	2
PSO J160.0−21	T2 pec	27.0 ± 2.8	-231 ± 16	-49 ± 14	30 ± 4	2
PSO J167.1+08	L8	28.8 ± 3.5	-246 ± 17	-313 ± 17	54 ± 7	2
PSO J168.1−27	T2.5	36.5 ± 4.0	-273 ± 121	104 ± 39	51 ± 20	2
PSO J174.6−18	M9	91.3 ± 15.4	-77 ± 11	102 ± 12	56 ± 11	2
PSO J175.2+16	L5	47.2 ± 5.8	-13 ± 19	-35 ± 22	8 ± 5	2
PSO J175.8−20	T2	30.2 ± 3.2	-38 ± 9	-137 ± 8	20 ± 2	2
PSO J180.1−28	T0	23.8 ± 2.4	-545 ± 6	-39 ± 7	62 ± 6	2
PSO J182.6−26	L2	68.3 ± 11.5	-82 ± 12	-10 ± 14	27 ± 6	2
PSO J183.4+40	T4	33.4 ± 3.6	-118 ± 7	-82 ± 10	23 ± 3	2

Table 3.4—Continued

Name	SpT (visual)	$d_{\rm phot}$[a] (pc)	$\mu_\alpha \cos\delta$[b] (mas yr^{-1})	μ_δ[b] (mas yr^{-1})	$v_{\rm tan}$ (km s^{-1})	Discovery References
PSO J183.9−09	L0	69.5 ± 11.6	-69 ± 11	-24 ± 13	24 ± 5	2
PSO J186.5+21	M9	123.3 ± 21.1	-23 ± 22	-26 ± 25	20 ± 14	12,2
PSO J192.5+26	T6	22.1 ± 2.0	-514 ± 35	-621 ± 33	85 ± 9	7
PSO J192.6−21	T2.5	33.9 ± 3.6	-162 ± 10	-88 ± 11	30 ± 4	2
PSO J202.1−03	T4.5	24.6 ± 2.2	-168 ± 13	2 ± 15	20 ± 2	2
PSO J207.7+29	T0: pec	25.9 ± 2.7	-156 ± 12	-68 ± 16	21 ± 3	2
PSO J218.4+50	T2.5	32.9 ± 3.4	36 ± 8	-156 ± 15	25 ± 4	2
PSO J218.5−27	L6	32.2 ± 3.9	-75 ± 8	-9 ± 11	12 ± 2	2
PSO J224.3+47	T7	19.9 ± 1.8	100 ± 41	-67 ± 61	11 ± 5	2
PSO J231.2+08	T2:	32.0 ± 3.3	24 ± 8	-77 ± 9	12 ± 2	10
PSO J241.1+39	T2	42.2 ± 4.4	132 ± 9	11 ± 9	27 ± 3	2
PSO J242.9+02	T1	35.1 ± 3.7	65 ± 7	93 ± 7	19 ± 2	2

Table 3.4—Continued

Name	SpT (visual)	$d_{\rm phot}$ [a] (pc)	$\mu_\alpha \cos\delta$ [b] ($\rm mas\,yr^{-1}$)	μ_δ [b] ($\rm mas\,yr^{-1}$)	$v_{\rm tan}$ ($\rm km\,s^{-1}$)	Discovery References
PSO J244.1+06	L9 (red)	32.6 ± 4.0	-88 ± 8	-46 ± 9	15 ± 2	2
PSO J244.6+08	T4.5	30.2 ± 2.9	37 ± 20	-31 ± 31	7 ± 4	2
PSO J258.2+06	T0 pec	21.9 ± 2.2	-186 ± 8	-113 ± 7	23 ± 2	2
PSO J260.1+61	T2	45.4 ± 4.7	-2 ± 68	192 ± 134	41 ± 29	2
PSO J260.3+46	L9	30.4 ± 3.7	54 ± 9	-265 ± 15	39 ± 5	2
PSO J261.2+22	T5	31.6 ± 3.1	-43 ± 12	0 ± 15	6 ± 2	2
PSO J263.5+50	T4	24.5 ± 2.5	-19 ± 8	293 ± 15	34 ± 4	7
PSO J265.0+11	T0.5	43.4 ± 4.7	13 ± 61	52 ± 45	11 ± 10	2
PSO J268.7+18	T2.5	21.1 ± 2.2	-424 ± 7	10 ± 9	43 ± 4	7
PSO J272.0−04	T1.5 pec	27.8 ± 3.0	11 ± 43	-37 ± 64	5 ± 8	2
PSO J272.4−04	T1	15.0 ± 1.5	-46 ± 4	-400 ± 13	29 ± 3	7,4
PSO J274.0+30	T3	36.4 ± 3.9	-33 ± 30	-127 ± 33	23 ± 6	2

Table 3.4—Continued

Name	SpT (visual)	$d_{\rm phot}$[a] (pc)	$\mu_\alpha \cos\delta$[b] (mas yr^{-1})	μ_δ[b] (mas yr^{-1})	$v_{\rm tan}$ (km s^{-1})	Discovery References
PSO J276.8+22	L9	24.1 ± 2.9	58 ± 8	10 ± 9	7 ± 1	2
PSO J277.7+45	L9	33.8 ± 4.1	105 ± 6	133 ± 7	27 ± 3	13
PSO J280.2+63	L9.5	23.8 ± 2.4	-54 ± 3	125 ± 12	15 ± 2	2
PSO J282.5+34	L1	86.1 ± 14.5	44 ± 17	-10 ± 21	19 ± 8	2
PSO J282.7+59	L9	13.5 ± 1.6	32 ± 3	421 ± 6	27 ± 3	3,4
PSO J284.7+39	T4	39.9 ± 4.4	-5 ± 49	63 ± 32	12 ± 6	2
PSO J289.8+30	L9	19.2 ± 2.3	386 ± 4	421 ± 5	52 ± 6	3
PSO J291.2+68	T1	33.2 ± 3.4	-237 ± 10	-88 ± 22	40 ± 4	2
PSO J304.7−07	M9	110.4 ± 18.8	-49 ± 16	71 ± 18	45 ± 12	2
PSO J307.6+07	T1.5	10.9 ± 1.1	652 ± 5	-113 ± 6	34 ± 3	7,14,4
PSO J308.9−09	L4.5	65.0 ± 8.2	-15 ± 12	2 ± 12	5 ± 4	2
PSO J310.9+62	T1.5	16.5 ± 1.7	298 ± 2	515 ± 5	47 ± 5	7

Table 3.4—Continued

Name	SpT (visual)	$d_{\rm phot}$[a] (pc)	$\mu_\alpha \cos\delta$[b] (mas yr^{-1})	μ_δ[b] (mas yr^{-1})	$v_{\rm tan}$ (km s^{-1})	Discovery References
PSO J313.1−26	L1	96.9 ± 16.8	182 ± 6	5 ± 5	84 ± 15	2
PSO J316.5+04	L6 (blue)	48.3 ± 6.0	34 ± 20	-60 ± 20	16 ± 5	2
PSO J319.3−29	T0:	16.9 ± 1.7	148 ± 4	-162 ± 4	18 ± 2	2
PSO J321.1+18	L9	31.8 ± 3.9	249 ± 18	100 ± 22	40 ± 6	2
PSO J329.8+03	T1:	30.7 ± 3.2	94 ± 22	-751 ± 20	110 ± 12	2
PSO J330.3+32	T2.5	20.1 ± 2.1	105 ± 8	64 ± 9	12 ± 1	2
PSO J331.6+33	T1.5	34.4 ± 3.7	176 ± 9	16 ± 11	29 ± 3	2
PSO J331.9−07	L7	34.1 ± 4.1	74 ± 19	-78 ± 22	17 ± 4	2
PSO J334.1+19	T3	30.7 ± 3.2	119 ± 11	-60 ± 9	19 ± 3	2
PSO J334.8+11	L5	37.0 ± 4.5	-25 ± 7	-72 ± 6	13 ± 2	2
PSO J336.9−18	L6:: (red)	32.9 ± 4.0	23 ± 13	-9 ± 13	4 ± 2	2
PSO J337.4+16	M9	129.4 ± 22.2	25 ± 6	-18 ± 5	19 ± 5	2

Table 3.4—Continued

Name	SpT (visual)	$d_{\rm phot}$[a] (pc)	$\mu_\alpha \cos\delta$[b] (mas yr^{-1})	μ_δ[b] (mas yr^{-1})	$v_{\rm tan}$ (km s^{-1})	Discovery References
PSO J338.8+31	L2 pec	75.5 ± 12.7	42 ± 6	-6 ± 6	15 ± 3	2
PSO J339.0+51	T5	9.4 ± 0.8	732 ± 4	328 ± 5	36 ± 3	7,4
PSO J341.7−15	L5	39.0 ± 4.7	47 ± 5	58 ± 6	14 ± 2	2
PSO J342.3−16	L5:	36.7 ± 4.4	377 ± 6	143 ± 6	70 ± 9	2
PSO J344.8+20	L2.5	51.5 ± 6.2	54 ± 10	-29 ± 10	15 ± 3	2
PSO J346.3−11	L8.5	33.8 ± 4.2	131 ± 33	15 ± 33	21 ± 6	2
PSO J346.5−15	L7	27.1 ± 3.3	120 ± 6	14 ± 6	16 ± 2	2
PSO J348.8+06	L2	36.8 ± 6.1	59 ± 5	-30 ± 5	12 ± 2	2
PSO J350.4−19	L4.5	47.2 ± 5.8	72 ± 12	-37 ± 14	18 ± 4	2
PSO J353.0−29	L1:	104.8 ± 18.1	-97 ± 24	3 ± 25	48 ± 15	2
PSO J353.6+13	L8:	24.0 ± 2.9	46 ± 9	-2 ± 8	5 ± 1	2
PSO J353.8+45	L7.5	21.4 ± 2.6	-84 ± 4	-66 ± 5	11 ± 1	3

Table 3.4—Continued

Name	SpT (visual)	$d_{\rm phot}$ [a] (pc)	$\mu_\alpha \cos\delta$ [b] (mas yr^{-1})	μ_δ [b] (mas yr^{-1})	$v_{\rm tan}$ (km s^{-1})	Discovery References
PSO J357.8+49	T0 (blue)	33.7 ± 3.5	-345 ± 7	-184 ± 12	62 ± 7	2
PSO J359.8−01	T1	34.5 ± 3.7	-2 ± 31	-149 ± 28	24 ± 5	2

Note. — Uncertainties for these visual spectral types are ±0.5 subtypes, except for those listed with : (±1.0 subtype) or :: ($\geq$ ±1.5 subtypes).

[a]Photometric distances calculated using $W2$ magnitudes and the polynomial from Dupuy & Liu (2012).

[b]Proper motions calculated using PS1 astrometry, as well as 2MASS astrometry when available.

[c]Photometric candidate.

References. — Discovery References: (1) Baron et al. (2015), (2) this paper, (3) Thompson et al. (2013), (4) Best et al. (2013) (Paper I), (5) Hogan et al. (2008), (6) Lodieu et al. (2014), (7) Mace et al. (2013a), (8) Zhang et al. (2009), (9) Bardalez Gagliuffi et al. (2014), (10) Marocco et al. (2015), (11) Aberasturi et al. (2011), (12) Zhang et al. (2010), (13) Kirkpatrick et al. (2011), (14) Bihain et al. (2013). Objects first published by other authors (and independently discovered by us) are detailed in Table 3.5.

Table 3.5. Spectral Types and Proper Motions of Previously Discovered Objects

Previous Observations					This Paper			
Name	References	SpT	$\mu_\alpha \cos\delta$ (mas yr^{-1})	μ_δ (mas yr^{-1})	Name	SpT (visual)	$\mu_\alpha \cos\delta$ (mas yr^{-1})	μ_δ (mas yr^{-1})
Spectroscopically Confirmed Objects								
2MASS J00135882−1816462	Baron et al. (2015)	L1	-20 ± 41	-212 ± 37	PSO J003.4−18	L5 pec	-31 ± 12	-175 ± 13
WISE J003110.04+574936.3	Thompson et al. (2013)	L8	530 ± 10	-10 ± 10	PSO J007.7+57	L9	526 ± 2	-12 ± 4
	Best et al. (2013) (Paper I)	L9	523 ± 17	-1 ± 16				
Hya12	Hogan et al. (2008)	L[a]	112.04 ± 7[b]	-17.86 ± 7[b]	PSO J068.9+13	L6 (red)	108 ± 9	-14 ± 10
	Lodieu et al. (2014)	L3.5	101 ± 11	-15 ± 11				
WISE J044633.45−242956.8	Thompson et al. (2013)	L5 pec (blue)	-210 ± 20	410 ± 20	PSO J071.6−24	L6 (blue)	-199 ± 13	398 ± 16
WISE J064205.58+410155.5	Mace et al. (2013a)	extremely red	···	···	PSO J100.5+41	L9 (red)	12 ± 4	-372 ± 6
PSO J103.0927+41.4601	Best et al. (2013) (Paper I)	T0	-8 ± 6	-38 ± 6	PSO J103.0+41	T0	3 ± 3	-32 ± 5
WISE J070159.79+632129.2	Mace et al. (2013a)	T3	···	···	PSO J105.4+63	T2.5	-14 ± 2	-264 ± 5
SDSS J074838.61+174332.9	Zhang et al. (2009)	L7[a]	-70 ± 20	-10 ± 20	PSO J117.1+17	L5	-63 ± 5	8 ± 6
	Bardalez Gagliuffi et al. (2014)	L6	···	···				
ULAS J090521.61+100654.9	Marocco et al. (2015)	T0	···	···	PSO J136.3+10	T1	-8 ± 11	-118 ± 8
WISE J092055.40+453856.3	Aberasturi et al. (2011)	L4-5[a]	-75 ± 10	-833 ± 45	PSO J140.2+45	L9.5	-77 ± 4	-852 ± 5
	Mace et al. (2013a)	L9 sb?	···	···				
	Best et al. (2013) (Paper I)	L9.5	-42 ± 23	-843 ± 23				
WISE J125015.56+262846.9	Mace et al. (2013a)	T6.5	···	···	PSO J192.5+26	T6	-514 ± 35	-621 ± 33

Table 3.5—Continued

Previous Observations					This Paper			
Name	References	SpT	$\mu_\alpha \cos\delta$ (mas yr^{-1})	μ_δ (mas yr^{-1})	Name	SpT (visual)	$\mu_\alpha \cos\delta$ (mas yr^{-1})	μ_δ (mas yr^{-1})
	Cardoso et al. (2015)	T6.5[c]	-456 ± 18	-580 ± 26				
ULAS J152502.10+083344.0	Marocco et al. (2015)	T2	···	···	PSO J231.2+08	T2:	24 ± 8	-77 ± 9
WISE J173421.02+502349.9	Mace et al. (2013a)	T4	···	···	PSO J263.5+50	T4	-19 ± 8	293 ± 15

Table 3.5—Continued

Previous Observations					This Paper			
Name	References	SpT	$\mu_\alpha \cos\delta$ (mas yr^{-1})	μ_δ (mas yr^{-1})	Name	SpT (visual)	$\mu_\alpha \cos\delta$ (mas yr^{-1})	μ_δ (mas yr^{-1})
WISE J175510.28+180320.2	Mace et al. (2013a)	T2	···	···	PSO J268.7+18	T2.5	-424 ± 7	10 ± 9
	Luhman & Sheppard (2014)	T2	-453 ± 14	-8 ± 14				
WISE J180952.53−044812.5	Mace et al. (2013a)	T0.5	···	···	PSO J272.4−04	T1	-46 ± 4	-400 ± 13
	Best et al. (2013) (Paper I)	T1	-62 ± 18	-429 ± 17				
WISEPA J183058.57+454257.9	Kirkpatrick et al. (2011)	L9	56 ± 22	107 ± 22	PSO J277.7+45	L9	105 ± 6	133 ± 7
WISE J185101.83+593508.6	Thompson et al. (2013)	L9 pec	40 ± 10	420 ± 10	PSO J282.7+59	L9	32 ± 3	421 ± 6
	Best et al. (2013) (Paper I)	L9	23 ± 19	412 ± 19				
WISE J191915.54+304558.4	Thompson et al. (2013)	L6	370 ± 10	400 ± 10	PSO J289.8+30	L9	386 ± 4	421 ± 5
WISE J203042.79+074934.7	Mace et al. (2013a)	T1.5	···	···	PSO J307.6+07	T1.5	652 ± 5	-113 ± 6
	Bihain et al. (2013)	T1.5	653 ± 6	-138 ± 16				
	Best et al. (2013) (Paper I)	T1.5	659 ± 8	-113 ± 9				
WISE J204356.42+622048.9	Mace et al. (2013a)	T1.5	···	···	PSO J310.9+62	T1.5	298 ± 2	515 ± 5
WISE J223617.59+510551.9	Mace et al. (2013a)	T5.5	···	···	PSO J339.0+51	T5	732 ± 4	328 ± 5
	Best et al. (2013) (Paper I)	T5	736 ± 14	330 ± 8				
WISE J233527.07+451140.9	Thompson et al. (2013)	L9 pec (v. red)	-70 ± 20	-60 ± 20	PSO J353.8+45	L7.5	-84 ± 4	-66 ± 5
Photometric Candidates Confirmed By Our Spectroscopy								
SDSS J090308.17+165935.5	Zhang et al. (2009)	L6[a]	90 ± 40	-70 ± 40	PSO J135.7+16	T0 pec	25 ± 14	-24 ± 17

Table 3.5—Continued

Previous Observations					This Paper			
Name	References	SpT	$\mu_\alpha \cos\delta$ (mas yr^{-1})	μ_δ (mas yr^{-1})	Name	SpT (visual)	$\mu_\alpha \cos\delta$ (mas yr^{-1})	μ_δ (mas yr^{-1})
SDSS J110827.31+083801.8	Zhang et al. (2009)	L8.5[a]	-200 ± 80	-270 ± 80	PSO J167.1+08	L8	-246 ± 17	-313 ± 17
SDSS J122608.20+215010.9	Zhang et al. (2010)	L0[a]	-21 ± 45	-28 ± 45	PSO J186.5+21	M9	-23 ± 22	-26 ± 25

Note. — Uncertainties for our visual spectral types are ±0.5 subtypes, except for those listed with : (±1.0 subtype) or :: (≥ ±1.5 subtypes).

[a]Based on photometry only.

[b]Hogan et al. (2008) report typical proper motion errors of ±7 mas yr^{-1}.

[c]Derived from CH_4s–CH_4l photometry.

Table 3.6. Non-ultracool Interlopers

Name	Probable Type[a]	Description[b]
PSO J010.2+41	carbon star	Carbon star in the direction of NGC 205
PSO J249.4−10	RBO	Nondescript continuum broadly peaked in J band
PSO J255.6+10	galaxy	Flat continuum with strong emission features at ≈1.05 μm, ≈1.75 μm, and ≈2.05 μm
PSO J342.9−09	unknown	Nondescript continuum, flux decreases with wavelength (low S/N)
PSO J276.0−01	RBO	Nondescript continuum broadly peaked in H band, wide absorption feature at ≈1.8 μm. $b = 5.1°$
PSO J202.5−26	K2 V	Good match to the SpeX Spectral Library K2 V standard HD 3765 (Rayner et al. 2009)
PSO J053.3+30	RBO	Nondescript continuum sharply peaked in H band
PSO J068.3+52	RBO	Sharp peaks in J, H, and K bands. $b = 3.1°$
PSO J076.1+25	RBO	Nondescript continuum sharply peaked in H band. $b = -9.7°$
PSO J085.3+36	RBO	Nondescript continuum sharply peaked in H band. $b = 3.1°$
PSO J303.7+31	RBO	Nondescript continuum broadly peaked in J band. $b = -1.6°$
PSO J296.0+35	K5 V	Good match to the SpeX Spectral Library K5 V standard HD 36003 (Rayner et al. 2009)

[a]RBO = Reddened background object (likely a giant or supergiant star).

[b]Five of these objects lie within 10° of the galactic plane. Their galactic latitudes (b) are indicated.

Table 3.7. New Near-infrared Spectral Types

Object Name	Opt SpT	Opt Ref	NIR SpT
2MASS J09153413+0422045	L6[a]	Reid et al. (2008b)	L5
2MASSW J1239272+551537	L5	Kirkpatrick et al. (2000)	L5

[a]Binary brown dwarf (Reid et al. 2006a); both components have spectral type L6.

Table 3.8. Index-based Spectral Types from Allers & Liu (2013a) for M7–L8 Objects

Name	Index-derived Spectral Types					Adopted SpT (visual)[b]
	H_2O	H_2OD	H_2O–1	H_2O–2	SpT[a] (avg.)	
M Dwarfs						
PSO J024.1+37[c]	···	···	···	···	···	M7
PSO J101.8+39	$M7.6^{+2.1}_{-1.9}$	···	$M6.6^{+1.5}_{-1.5}$	$M9.3^{+1.6}_{-1.6}$	$M8.2^{+1.4}_{-1.2}$	M9.5
PSO J115.0+59	$M9.0^{+2.2}_{-2.3}$	···	$M7.9^{+1.4}_{-1.4}$	$M7.3^{+1.9}_{-1.8}$	$M8.3^{+1.5}_{-1.5}$	M9.5
PSO J133.8+06	$M8.0^{+0.7}_{-0.7}$	···	$M6.5^{+1.2}_{-1.2}$	$M8.2^{+0.7}_{-0.7}$	$M8.0^{+0.5}_{-0.5}$	M9
PSO J174.6−18	$L0.1^{+1.4}_{-1.4}$	···	$M8.3^{+1.3}_{-1.4}$	$M9.5^{+1.6}_{-1.8}$	$M9.7^{+1.0}_{-1.0}$	M9
PSO J186.5+21	$L0.8^{+1.9}_{-2.0}$	···	$M6.9^{+1.5}_{-1.5}$	$M9.4^{+1.7}_{-1.9}$	$L0.0^{+1.3}_{-1.4}$	M9
PSO J304.7−07	···	···	$L0.4^{+1.3}_{-1.3}$	$M8.4^{+1.7}_{-1.7}$	$M8.8^{+1.4}_{-1.4}$	M9
PSO J337.4+16	$L1.1^{+1.7}_{-1.8}$	···	$M8.5^{+1.3}_{-1.3}$	$M8.1^{+1.5}_{-1.5}$	$M9.8^{+1.1}_{-1.2}$	M9
L Dwarfs						
PSO J003.4−18	···	$L4.7^{+0.9}_{-0.9}$	$L3.2^{+1.2}_{-1.2}$	···	$L4.2^{+0.7}_{-0.7}$	L5 pec
PSO J004.7+51	···	$L5.4^{+0.8}_{-0.8}$	···	···	$L5.4^{+0.8}_{-0.8}$	L7
PSO J048.9+07	···	$L7.6^{+1.3}_{-1.2}$	···	···	$L7.6^{+1.3}_{-1.2}$	L6: (blue)
PSO J054.8−11	$L0.9^{+1.6}_{-1.7}$	$L2.7^{+1.1}_{-1.2}$	$M8.1^{+1.4}_{-1.5}$	···	$L1.0^{+1.2}_{-1.3}$	L3:
PSO J057.2+15	···	$L2.0^{+0.9}_{-0.9}$	···	···	$L2.0^{+0.9}_{-0.9}$	L7 (red)

Table 3.8—Continued

Name	Index-derived Spectral Types					Adopted SpT (visual)[b]
	H_2O	H_2OD	H_2O–1	H_2O–2	SpT[a] (avg.)	
PSO J068.9+13	···	$L4.6^{+0.8}_{-0.8}$	···	···	$L4.6^{+0.8}_{-0.8}$	L6 (red)
PSO J071.4+36	···	$L6.4^{+0.9}_{-0.9}$	···	···	$L6.4^{+0.9}_{-0.9}$	L6:
PSO J071.6−24	···	$L6.4^{+1.3}_{-1.3}$	···	···	$L6.4^{+1.3}_{-1.3}$	L6 (blue)
PSO J078.9+31	$L1.6^{+1.0}_{-1.0}$	···	$L1.6^{+1.1}_{-1.1}$	$M9.0^{+1.0}_{-1.0}$	$L0.7^{+0.7}_{-0.7}$	L1.5
PSO J087.7−12	···	$L6.6^{+1.0}_{-0.9}$	···	···	$L6.6^{+1.0}_{-0.9}$	L8
PSO J088.0+43	$L3.3^{+0.9}_{-1.1}$	$L3.8^{+0.9}_{-1.0}$	$L1.5^{+1.2}_{-1.2}$	···	$L3.2^{+0.7}_{-0.8}$	L4 pec
PSO J088.3−24[c]	···	···	···	···	···	L1:
PSO J108.4+38	···	$L6.0^{+0.9}_{-0.9}$	···	···	$L6.0^{+0.9}_{-0.9}$	L7
PSO J117.1+17	···	$L5.3^{+0.8}_{-0.8}$	$L3.2^{+1.2}_{-1.2}$	···	$L4.6^{+0.7}_{-0.7}$	L5
PSO J127.4+10	$L2.5^{+1.0}_{-1.1}$	$L3.6^{+0.9}_{-0.8}$	$L0.1^{+1.3}_{-1.3}$	···	$L2.5^{+0.8}_{-0.8}$	L4
PSO J135.0+32	$L1.5^{+0.6}_{-0.6}$	$L0.2^{+0.8}_{-0.8}$	$L0.7^{+1.1}_{-1.1}$	$L0.4^{+0.6}_{-0.6}$	$L0.9^{+0.4}_{-0.4}$	L1.5
PSO J136.5−06	$L3.5^{+0.5}_{-0.6}$	$L3.5^{+0.8}_{-0.8}$	$L2.3^{+1.1}_{-1.1}$	$L0.0^{+0.7}_{-0.7}$	$L2.4^{+0.4}_{-0.4}$	L2 pec
PSO J143.6−29	···	$L3.5^{+1.7}_{-1.8}$	$L2.4^{+1.4}_{-1.4}$	···	$L3.1^{+1.2}_{-1.3}$	L1
PSO J146.0+05	$L1.6^{+1.2}_{-1.3}$	$L2.8^{+1.1}_{-1.2}$	$L1.2^{+1.2}_{-1.2}$	$L0.7^{+1.1}_{-1.3}$	$L1.5^{+0.7}_{-0.8}$	L1
PSO J147.5−27	$L0.1^{+1.8}_{-1.9}$	···	$M9.7^{+1.3}_{-1.4}$	···	$L0.0^{+1.6}_{-1.7}$	L0.5
PSO J149.1−19	···	$L6.2^{+0.8}_{-0.8}$	$L4.6^{+1.1}_{-1.1}$	···	$L5.7^{+0.7}_{-0.7}$	L5 pec
PSO J152.2+15	$L3.2^{+0.9}_{-1.5}$	$L3.3^{+1.3}_{-1.4}$	$L1.8^{+1.3}_{-1.3}$	$L0.9^{+1.2}_{-1.6}$	$L2.2^{+1.0}_{-1.1}$	L1.5
PSO J158.1+05	$L2.3^{+0.7}_{-0.7}$	$L1.9^{+0.9}_{-0.9}$	$L2.8^{+1.1}_{-1.1}$	$L1.0^{+0.9}_{-0.9}$	$L1.9^{+0.5}_{-0.5}$	L2
PSO J159.0−27	···	$L4.7^{+1.1}_{-1.1}$	$L3.0^{+1.2}_{-1.2}$	···	$L4.2^{+0.8}_{-0.8}$	L2 (blue)

Table 3.8—Continued

Name	Index-derived Spectral Types					Adopted SpT (visual)[b]
	H_2O	H_2OD	H_2O–1	H_2O–2	SpT[a] (avg.)	
PSO J167.1+08	···	$L8.2^{+1.0}_{-0.9}$	···	···	$L8.2^{+1.0}_{-0.9}$	L8
PSO J175.2+16	···	$L6.3^{+1.1}_{-1.1}$	$L1.7^{+1.4}_{-1.4}$	···	$L4.8^{+0.9}_{-0.8}$	L5
PSO J182.6−26	$L2.9^{+1.1}_{-1.5}$	$L2.6^{+1.2}_{-1.3}$	$M9.7^{+1.3}_{-1.3}$	···	$L2.3^{+1.0}_{-1.2}$	L3:
PSO J183.9−09	$L0.8^{+1.5}_{-1.5}$	$L3.5^{+1.2}_{-1.3}$	$M7.7^{+1.4}_{-1.5}$	$M9.8^{+1.5}_{-1.7}$	$L0.6^{+0.9}_{-0.9}$	L0
PSO J218.5−27	···	$L4.7^{+0.9}_{-1.0}$	$L2.1^{+1.2}_{-1.2}$	···	$L3.9^{+0.8}_{-0.8}$	L6
PSO J282.5+34	$L2.1^{+1.3}_{-1.4}$	$L2.3^{+1.1}_{-1.2}$	$M8.8^{+1.3}_{-1.3}$	$L1.5^{+0.8}_{-1.1}$	$L1.7^{+0.8}_{-0.9}$	L1
PSO J308.9−09	···	$L6.9^{+1.1}_{-1.1}$	$L2.6^{+1.2}_{-1.2}$	···	$L5.5^{+0.9}_{-0.8}$	L4.5
PSO J313.1−26	$L0.6^{+1.7}_{-1.8}$	$L2.3^{+1.3}_{-1.4}$	$M9.7^{+1.4}_{-1.4}$	$L0.9^{+1.1}_{-1.5}$	$L0.8^{+1.0}_{-1.1}$	L1
PSO J316.5+04	···	$L5.5^{+0.9}_{-0.9}$	···	···	$L5.5^{+0.9}_{-0.9}$	L6 (blue)
PSO J331.9−07	···	$L5.0^{+0.8}_{-0.8}$	···	···	$L5.0^{+0.8}_{-0.8}$	L7
PSO J334.8+11	···	$L5.2^{+0.8}_{-0.8}$	$L3.4^{+1.1}_{-1.1}$	···	$L4.6^{+0.7}_{-0.7}$	L5
PSO J336.9−18	···	$L2.6^{+0.9}_{-0.9}$	$L1.0^{+1.2}_{-1.2}$	···	$L2.1^{+0.7}_{-0.7}$	L6:: (red)
PSO J338.8+31	···	$L5.2^{+0.9}_{-0.9}$	$L4.7^{+1.1}_{-1.1}$	$L0.1^{+1.1}_{-1.1}$	$L2.1^{+0.7}_{-0.7}$	L2 pec
PSO J341.7−15	···	$L6.0^{+0.8}_{-0.8}$	$L2.8^{+1.1}_{-1.1}$	···	$L5.0^{+0.7}_{-0.7}$	L5
PSO J342.3−16	···	$L6.3^{+0.8}_{-0.8}$	$L4.6^{+1.1}_{-1.1}$	···	$L5.7^{+0.7}_{-0.7}$	L5: pec
PSO J344.8+20	$L2.7^{+0.9}_{-1.0}$	$L2.8^{+0.9}_{-0.8}$	$L1.9^{+1.2}_{-1.2}$	···	$L2.6^{+0.7}_{-0.7}$	L2.5
PSO J346.5−15	···	$L5.0^{+0.9}_{-0.9}$	···	···	$L5.0^{+0.9}_{-0.9}$	L7
PSO J348.8+06	$L0.8^{+0.6}_{-0.7}$	···	$M9.7^{+1.2}_{-1.2}$	$M9.2^{+0.7}_{-0.6}$	$L0.2^{+0.4}_{-0.4}$	L2
PSO J350.4−19	···	$L5.7^{+0.9}_{-0.9}$	$L4.7^{+1.2}_{-1.2}$	···	$L5.4^{+0.7}_{-0.7}$	L4.5

Table 3.8—Continued

Name	Index-derived Spectral Types					Adopted SpT (visual)[b]
	H_2O	H_2OD	H_2O–1	H_2O–2	SpT[a] (avg.)	
PSO J353.0−29	···	$L1.9^{+1.7}_{-1.6}$	$M9.5^{+1.6}_{-1.6}$	···	$L0.8^{+1.4}_{-1.5}$	L1:
PSO J353.6+13	···	$L6.4^{+0.8}_{-0.8}$	···	···	$L6.4^{+0.8}_{-0.8}$	L8:
PSO J353.8+45	···	$L7.4^{+0.8}_{-0.8}$	···	···	$L7.4^{+0.8}_{-0.8}$	L7.5

Note. — None of these indices are valid for spectral types later than L8, so objects with those spectral types are not listed here.

[a]Calculated as the weighted average of the spectral types from Monte Carlo simulations for all indices, excluding those that fell outside the valid range for each index.

[b]Spectral types determined by visual comparison with spectral standards, which we adopt as the final spectral types for our discoveries. Uncertainties for these visual spectral types are ±0.5 subtypes, except for those listed with : (±1.0 subtype) or :: (≥ ±1.5 subtypes).

[c]No indices yielded spectral types within the valid range of any index for this object, so no average spectral type was derived.

Table 3.9. Index-based Spectral Types from Burgasser et al. (2006a) for L0–T7 Objects

Name	Index Values (Derived Spectral Types)[a]						Adopted SpT (visual)[b]
	H_2O-J	CH_4-J	H_2O-H	CH_4-H	CH_4-K	SpT (avg.)	
L Dwarfs							
PSO J003.4−18	0.693 (L7.5)	0.780 (<T0)	0.703 (L6.4)	0.934 (T1.3)	0.924 (L6.8)	L8.0±2.3	L5 pec
PSO J004.7+51	0.667 (L8.3)	0.783 (<T0)	0.721 (L5.7)	1.136 (<T1)	1.007 (L4.2)	L6.1±2.1	L7
PSO J007.7+57	0.659 (L8.5)	0.834 (<T0)	0.665 (L7.8)	1.047 (<T1)	0.844 (L8.7)	L8.4±0.5	L9
PSO J007.9+33	0.697 (L7.4)	0.747 (<T0)	0.658 (L8.1)	1.009 (<T1)	0.899 (L7.5)	L7.6±0.4	L9
PSO J023.8+02	0.662 (L8.4)	0.742 (<T0)	0.625 (L9.2)	1.069 (<T1)	0.870 (L8.2)	L8.6±0.5	L9.5
PSO J041.5+01	0.680 (L7.9)	0.866 (<T0)	0.646 (L8.5)	0.998 (T1.0)	0.875 (L8.0)	L8.1±0.3	L8.5
PSO J048.9+07	0.794 (L4.4)	0.905 (<T0)	0.674 (L7.5)	1.029 (<T1)	0.914 (L7.1)	L6.3±1.7	L6: (blue)
PSO J049.1+17	0.635 (L9.2)	0.751 (<T0)	0.611 (L9.6)	0.996 (T1.0)	0.869 (L8.2)	L9.0±0.7	L9.5

Table 3.9—Continued

Name	Index Values (Derived Spectral Types)[a]						Adopted SpT (visual)[b]
	H_2O-J	CH_4-J	H_2O-H	CH_4-H	CH_4-K	SpT (avg.)	
PSO J052.7−03	0.600 (T0.1)	0.747 (<T0)	0.590 (T0.2)	1.081 (<T1)	0.862 (L8.3)	L9.6±1.1	L9:
PSO J054.8−11	0.823 (L3.5)	0.963 (<T0)	0.798 (L2.7)	1.147 (<T1)	1.092 (L0.5)	L2.2±1.6	L3:
PSO J057.2+15	0.671 (L8.2)	1.015 (<T0)	0.729 (L5.4)	1.155 (<T1)	1.092 (L0.5)	L4.7±3.9	L7 (red)
PSO J068.9+13	0.760 (L5.5)	0.966 (<T1)	0.735 (L5.2)	1.110 (<T2)	1.063 (L1.9)	L4.2±2.0	L6 (red)
PSO J071.4+36	0.725 (L6.5)	0.861 (<T0)	0.674 (L7.5)	1.098 (<T1)	0.962 (L5.7)	L6.6±0.9	L6:
PSO J071.6−24	0.746 (L5.9)	0.792 (<T0)	0.742 (L4.9)	0.982 (T1.1)	0.864 (L8.3)	L6.4±1.7	L6 (blue)
PSO J078.9+31	0.894 (L1.6)	0.899 (<T0)	0.814 (L2.0)	1.132 (<T1)	1.112 (<L0)	L1.8±0.3	L1.5
PSO J087.7−12	0.719 (L6.7)	0.861 (<T0)	0.745 (L4.8)	1.064 (<T1)	0.935 (L6.5)	L6.0±1.1	L8
PSO J088.0+43	0.703 (L7.2)	0.827 (<T0)	0.731 (L5.4)	1.002 (<T1)	1.029 (L3.3)	L5.3±2.0	L4 pec
PSO J088.3−24	0.821 (L3.6)	0.935 (<T0)	0.730 (L5.4)	0.934 (T1.3)	1.182 (<L0)	L6.8±4.1	L1:
PSO J100.5+41	0.561 (T1.0)	0.754 (<T0)	0.598 (L10.0)	1.044 (<T1)	0.841 (L8.8)	L9.9±1.1	L9 (red)

Table 3.9—Continued

Name	Index Values (Derived Spectral Types)[a]						Adopted SpT (visual)[b]
	H_2O-J	CH_4-J	H_2O-H	CH_4-H	CH_4-K	SpT (avg.)	
PSO J108.4+38	0.722 (L6.6)	0.859 (<T0)	0.672 (L7.6)	1.107 (<T1)	1.002 (L4.3)	L6.2±1.7	L7
PSO J117.1+17	0.720 (L6.7)	0.838 (<T0)	0.700 (L6.5)	1.065 (<T1)	0.974 (L5.3)	L6.2±0.8	L5
PSO J127.4+10	0.830 (L3.3)	0.904 (<T0)	0.739 (L5.0)	1.136 (<T1)	1.053 (L2.3)	L3.6±1.4	L4
PSO J135.0+32	0.932 (L0.7)	0.908 (<T0)	0.825 (L1.6)	1.035 (<T1)	1.045 (L2.6)	L1.6±1.0	L1.5
PSO J136.5−06	0.792 (L4.5)	0.834 (<T0)	0.747 (L4.7)	0.961 (T1.2)	0.946 (L6.2)	L6.6±3.1	L2 pec
PSO J140.2+45	0.647 (L8.8)	0.874 (<T0)	0.608 (L9.7)	1.001 (<T1)	0.749 (T0.3)	L9.6±0.7	L9.5
PSO J143.6−29	0.849 (L2.8)	0.865 (<T0)	0.771 (L3.7)	1.076 (<T1)	1.047 (L2.5)	L3.0±0.6	L1
PSO J146.0+05	0.905 (L1.3)	0.851 (<T0)	0.800 (L2.6)	1.001 (<T1)	1.043 (L2.7)	L2.2±0.8	L1
PSO J147.5−27	0.919 (L1.0)	0.886 (<T0)	0.905 (<L0)	1.037 (<T1)	1.052 (L2.4)	L1.7±1.0	L0.5
PSO J149.0−14	0.581 (T0.6)	0.708 (<T0)	0.562 (T1.0)	1.014 (<T1)	0.770 (T0.0)	T0.5±0.5	L9
PSO J149.1−19	0.733 (L6.3)	0.766 (<T0)	0.679 (L7.3)	0.997 (T1.0)	0.907 (L7.3)	L7.0±0.6	L5 pec

Table 3.9—Continued

Name	Index Values (Derived Spectral Types)[a]						Adopted SpT (visual)[b]
	H_2O-J	CH_4-J	H_2O-H	CH_4-H	CH_4-K	SpT (avg.)	
PSO J152.2+15	0.872 (L2.1)	0.871 (<T0)	0.815 (L2.0)	1.025 (<T1)	0.971 (L5.4)	L3.2±1.9	L1.5
PSO J135.0+32	0.932 (L0.7)	0.908 (<T0)	0.825 (L1.6)	1.035 (<T1)	1.045 (L2.6)	L1.6±1.0	L1.5
PSO J159.0−27	0.850 (L2.7)	0.906 (<T0)	0.740 (L5.0)	1.127 (<T1)	1.087 (L0.7)	L2.8±2.1	L2 (blue)
PSO J167.1+08	0.707 (L7.1)	0.769 (<T0)	0.710 (L6.2)	1.046 (<T1)	0.882 (L7.9)	L7.1±0.9	L8
PSO J175.2+16	0.792 (L4.5)	0.840 (<T0)	0.726 (L5.6)	1.092 (<T1)	0.963 (L5.7)	L5.2±0.7	L5
PSO J182.6−26	0.862 (L2.4)	0.842 (<T0)	0.801 (L2.5)	1.074 (<T1)	1.001 (L4.4)	L3.1±1.1	L2
PSO J183.9−09	0.926 (L0.8)	0.907 (<T0)	0.828 (L1.4)	1.066 (<T1)	1.085 (L0.8)	L1.0±0.4	L0
PSO J218.5−27	0.754 (L5.7)	0.948 (<T0)	0.688 (L7.0)	1.119 (<T1)	1.021 (L3.6)	L5.4±1.7	L6
PSO J244.1+06	0.667 (L8.3)	0.796 (<T0)	0.662 (L7.9)	1.120 (<T1)	0.907 (L7.3)	L7.8±0.5	L9 (red)
PSO J260.3+46	0.709 (L7.0)	0.744 (<T0)	0.659 (L8.0)	1.011 (<T1)	0.825 (L9.1)	L8.0±1.0	L9
PSO J276.8+22	0.580 (T0.6)	0.738 (<T0)	0.618 (L9.4)	1.014 (<T1)	0.870 (L8.2)	L9.4±1.2	L9

Table 3.9—Continued

Name	Index Values (Derived Spectral Types)[a]						Adopted SpT (visual)[b]
	H_2O-J	CH_4-J	H_2O-H	CH_4-H	CH_4-K	SpT (avg.)	
PSO J277.7+45	0.659 (L8.5)	0.770 (<T0)	0.639 (L8.7)	0.979 (T1.1)	0.848 (L8.6)	L8.6±0.1	L9
PSO J280.2+63	0.667 (L8.3)	0.766 (<T0)	0.616 (L9.5)	0.996 (T1.0)	0.796 (L9.6)	L9.1±0.7	L9.5
PSO J282.5+34	0.931 (L0.7)	0.951 (<T0)	0.801 (L2.5)	1.114 (<T1)	1.070 (L1.5)	L1.6±0.9	L1
PSO J282.7+59	0.678 (L8.0)	0.653 (T0.0)	0.650 (L8.3)	1.016 (<T1)	0.897 (L7.5)	L7.9±0.4	L9
PSO J289.8+30	0.696 (L7.4)	0.809 (<T0)	0.744 (L4.8)	1.044 (<T1)	0.838 (L8.8)	L7.0±2.0	L9
PSO J308.9−09	0.852 (L2.7)	0.916 (<T0)	0.734 (L5.2)	1.089 (<T1)	0.998 (L4.5)	L4.1±1.3	L4.5
PSO J313.1−26	0.946 (L0.4)	0.909 (<T0)	0.806 (L2.3)	1.013 (<T1)	1.011 (L4.0)	L2.3±1.8	L1
PSO J316.5+04	0.748 (L5.9)	0.789 (<T0)	0.681 (L7.3)	1.057 (<T1)	0.957 (L5.9)	L6.3±0.8	L6 (blue)
PSO J321.1+18	0.567 (T0.9)	0.710 (<T0)	0.569 (T0.8)	1.048 (<T1)	0.761 (T0.1)	T0.6±0.4	L9
PSO J331.9−07	0.706 (L7.1)	0.872 (<T0)	0.700 (L6.5)	1.121 (<T1)	1.019 (L3.7)	L5.8±1.8	L7
PSO J334.8+11	0.733 (L6.3)	0.854 (<T0)	0.687 (L7.0)	1.102 (<T1)	1.021 (L3.6)	L5.6±1.8	L5

Table 3.9—Continued

Name	Index Values (Derived Spectral Types)[a]						Adopted SpT (visual)[b]
	H_2O-J	CH_4-J	H_2O-H	CH_4-H	CH_4-K	SpT (avg.)	
PSO J336.9−18	0.676 (L8.0)	0.957 (<T0)	0.705 (L6.3)	1.229 (<T1)	1.123 (<L0)	L7.2±1.2	L6:: (red)
PSO J338.8+31	0.827 (L3.4)	0.820 (<T0)	0.736 (L5.2)	1.005 (<T1)	0.957 (L5.9)	L4.8±1.3	L2 pec
PSO J341.7−15	0.742 (L6.0)	0.833 (<T0)	0.712 (L6.1)	1.074 (<T1)	1.035 (L3.0)	L5.0±1.7	L5
PSO J342.3−16	0.804 (L4.1)	0.834 (<T0)	0.720 (L5.8)	1.004 (<T1)	0.884 (L7.8)	L5.9±1.9	L5:
PSO J344.8+20	0.797 (L4.3)	0.912 (<T0)	0.752 (L4.5)	1.112 (<T1)	1.082 (L1.0)	L3.3±2.0	L2.5
PSO J346.3−11	0.690 (L7.6)	0.833 (<T0)	0.705 (L6.3)	1.035 (<T1)	0.912 (L7.1)	L7.0±0.6	L8.5
PSO J346.5−15	0.701 (L7.3)	0.857 (<T0)	0.693 (L6.8)	1.140 (<T1)	1.023 (L3.5)	L5.9±2.0	L7
PSO J348.8+06	0.879 (L2.0)	0.960 (<T0)	0.785 (L3.2)	1.138 (<T1)	1.083 (L0.9)	L2.0±1.2	L2
PSO J350.4−19	0.790 (L4.6)	0.823 (<T0)	0.729 (L5.4)	1.071 (<T1)	0.981 (L5.1)	L5.0±0.4	L4.5
PSO J353.0−29	0.981 (<L0)	0.987 (<T0)	0.701 (L6.5)	1.008 (<T1)	1.024 (L3.5)	L5.0±2.1	L1:
PSO J353.6+13	0.693 (L7.5)	0.836 (<T0)	0.693 (L6.8)	1.079 (<T1)	0.981 (L5.1)	L6.5±1.2	L8:

Table 3.9—Continued

Name	Index Values (Derived Spectral Types)[a]						Adopted SpT (visual)[b]
	H_2O-J	CH_4-J	H_2O-H	CH_4-H	CH_4-K	SpT (avg.)	
PSO J353.8+45	0.656 (L8.6)	0.831 (<T0)	0.663 (L7.9)	1.128 (<T1)	0.974 (L5.3)	L7.3±1.7	L7.5
T Dwarfs							
PSO J004.1+23	0.549 (T1.3)	0.628 (T0.7)	0.546 (T1.4)	1.011 (<T1)	0.796 (L9.6)	T0.7±0.8	T0
PSO J031.5+20	0.150 (T5.9)	0.320 (T6.2)	0.302 (T5.6)	0.363 (T5.5)	0.258 (T4.6)	T5.6±0.6	T5.5
PSO J049.1+26	0.387 (T3.8)	0.537 (T2.7)	0.468 (T3.1)	0.728 (T2.9)	0.537 (T2.3)	T3.0±0.6	T2.5
PSO J055.0−21	0.518 (T1.9)	0.733 (<T0)	0.501 (T2.5)	0.842 (T2.0)	0.572 (T2.1)	T2.1±0.2	T2
PSO J070.3+04	0.292 (T4.6)	0.574 (T2.0)	0.343 (T5.0)	0.449 (T4.9)	0.195 (T5.4)	T4.4±1.4	T4.5
PSO J071.8−12	0.469 (T2.7)	0.729 (<T0)	0.534 (T1.7)	0.768 (T2.5)	0.745 (T0.3)	T1.8±1.1	T2:
PSO J076.7+52	0.253 (T4.9)	0.454 (T4.2)	0.336 (T5.1)	0.499 (T4.5)	0.260 (T4.6)	T4.7±0.3	T4.5

Table 3.9—Continued

Name	Index Values (Derived Spectral Types)[a]						Adopted SpT (visual)[b]
	H_2O-J	CH_4-J	H_2O-H	CH_4-H	CH_4-K	SpT (avg.)	
PSO J103.0+41	0.588 (T0.4)	0.708 (<T0)	0.576 (T0.6)	0.982 (T1.1)	0.778 (L9.9)	T0.5±0.5	T0
PSO J105.4+63	0.435 (T3.2)	0.660 (<T0)	0.462 (T3.2)	0.732 (T2.8)	0.586 (T2.0)	T2.8±0.6	T2.5
PSO J109.4+46	0.651 (L8.7)	0.750 (<T0)	0.540 (T1.6)	0.895 (T1.6)	0.888 (L7.7)	L9.9±2.0	T0
PSO J133.8−02	0.588 (T0.4)	0.673 (<T0)	0.627 (L9.1)	0.882 (T1.7)	0.798 (L9.6)	T0.2±1.1	T0 pec
PSO J135.7+16	0.548 (T1.3)	0.714 (<T0)	0.588 (T0.3)	0.897 (T1.6)	0.852 (L8.6)	T0.4±1.4	T0 pec
PSO J136.3+10	0.613 (L9.8)	0.667 (<T0)	0.559 (T1.1)	0.861 (T1.8)	0.675 (T1.2)	T1.0±0.9	T1
PSO J159.2−26	0.502 (T2.2)	0.619 (T0.9)	0.568 (T0.8)	0.862 (T1.8)	0.693 (T1.0)	T1.4±0.6	T1.5
PSO J160.0−21	0.456 (T2.9)	0.595 (T1.5)	0.550 (T1.3)	0.750 (T2.7)	0.647 (T1.4)	T2.0±0.8	T2 pec
PSO J168.1−27	0.547 (T1.3)	0.667 (<T0)	0.517 (T2.1)	0.753 (T2.7)	0.391 (T3.4)	T2.4±0.9	T2.5
PSO J175.8−20	0.573 (T0.7)	0.580 (T1.8)	0.521 (T2.0)	0.838 (T2.0)	0.551 (T2.2)	T1.8±0.6	T2
PSO J180.1−28	0.711 (L7.0)	0.874 (<T0)	0.646 (L8.5)	0.976 (T1.1)	0.733 (T0.5)	L8.7±1.8	T0

Table 3.9—Continued

Name	Index Values (Derived Spectral Types)[a]						Adopted SpT (visual)[b]
	H_2O-J	CH_4-J	H_2O-H	CH_4-H	CH_4-K	SpT (avg.)	
PSO J183.4+40	0.387 (T3.8)	0.472 (T3.9)	0.385 (T4.5)	0.595 (T3.9)	0.195 (T5.4)	T4.3±0.7	T4
PSO J192.5+26	0.148 (T5.9)	0.383 (T5.3)	0.269 (T6.1)	0.241 (T6.5)	0.104 (≥T7)	T6.0±0.5	T6
PSO J192.6−21	0.556 (T1.1)	0.708 (<T0)	0.523 (T2.0)	0.783 (T2.4)	0.547 (T2.2)	T1.9±0.6	T2.5
PSO J202.1−03	0.218 (T5.2)	0.492 (T3.6)	0.280 (T5.9)	0.492 (T4.6)	0.219 (T5.1)	T4.9±0.9	T4.5
PSO J207.7+29	0.497 (T2.3)	0.656 (<T0)	0.614 (L9.5)	0.923 (T1.4)	0.840 (L8.8)	T0.5±1.6	T0: pec
PSO J218.4+50	0.440 (T3.2)	0.420 (T4.8)	0.584 (T0.4)	0.723 (T2.9)	0.552 (T2.2)	T2.7±1.6	T2.5
PSO J224.3+47	0.109 (T6.5)	0.265 (T6.9)	0.256 (T6.3)	0.238 (T6.5)	0.106 (≥T7)	T6.6±0.3	T7
PSO J231.2+08	0.468 (T2.8)	0.638 (T0.4)	0.517 (T2.1)	0.910 (T1.5)	0.636 (T1.5)	T1.7±0.9	T2:
PSO J241.1+39	0.523 (T1.8)	0.630 (T0.6)	0.572 (T0.8)	0.807 (T2.2)	0.602 (T1.8)	T1.5±0.7	T2
PSO J242.9+02	0.585 (T0.4)	0.716 (<T0)	0.594 (T0.1)	0.923 (T1.4)	0.648 (T1.4)	T0.9±0.7	T1
PSO J244.6+08	0.341 (T4.2)	0.528 (T2.9)	0.355 (T4.9)	0.571 (T4.0)	0.246 (T4.7)	T4.2±0.8	T4.5

Table 3.9—Continued

Name	Index Values (Derived Spectral Types)[a]						Adopted SpT (visual)[b]
	H_2O-J	CH_4-J	H_2O-H	CH_4-H	CH_4-K	SpT (avg.)	
PSO J258.2+06	0.532 (T1.6)	0.639 (T0.4)	0.636 (L8.8)	0.820 (T2.1)	0.773 (L9.9)	T0.6±1.3	T0 pec
PSO J260.1+61	0.636 (L9.2)	0.505 (T3.3)	0.561 (T1.0)	0.941 (T1.3)	0.588 (T1.9)	T1.4±1.5	T2
PSO J261.2+22	0.212 (T5.2)	0.342 (T5.9)	0.376 (T4.6)	0.418 (T5.1)	0.168 (T5.8)	T5.3±0.5	T5
PSO J263.5+50	0.380 (T3.9)	0.392 (T5.2)	0.456 (T3.3)	0.523 (T4.4)	0.216 (T5.1)	T4.4±0.8	T4
PSO J265.0+11	0.607 (L9.9)	0.685 (<T0)	0.567 (T0.9)	1.053 (<T1)	0.802 (L9.5)	T0.1±0.7	T0.5
PSO J268.7+18	0.552 (T1.2)	0.679 (<T0)	0.547 (T1.4)	0.887 (T1.7)	0.552 (T2.2)	T1.6±0.4	T2.5
PSO J272.0−04	0.471 (T2.7)	0.640 (T0.4)	0.513 (T2.2)	1.013 (<T1)	0.700 (T0.9)	T1.6±1.1	T1.5 pec
PSO J272.4−04	0.657 (L8.6)	0.772 (<T0)	0.630 (L9.0)	0.972 (T1.1)	0.720 (T0.7)	L9.4±1.1	T1
PSO J274.0+30	0.452 (T3.0)	0.527 (T2.9)	0.504 (T2.4)	0.651 (T3.5)	0.401 (T3.3)	T3.0±0.4	T3
PSO J284.7+39	0.318 (T4.4)	0.417 (T4.8)	0.428 (T3.8)	0.641 (T3.5)	0.396 (T3.3)	T4.0±0.6	T4
PSO J291.2+68	0.660 (L8.5)	0.795 (<T0)	0.621 (L9.3)	1.023 (<T1)	0.708 (T0.8)	L9.5±1.2	T1

Table 3.9—Continued

Name	Index Values (Derived Spectral Types)[a]						Adopted SpT (visual)[b]
	H_2O-J	CH_4-J	H_2O-H	CH_4-H	CH_4-K	SpT (avg.)	
PSO J307.6+07	0.625 (L9.4)	0.698 (<T0)	0.586 (T0.4)	0.878 (T1.7)	0.548 (T2.2)	T0.9±1.3	T1.5
PSO J310.9+62	0.567 (T0.9)	0.600 (T1.4)	0.565 (T0.9)	0.897 (T1.6)	0.649 (T1.4)	T1.2±0.3	T1.5
PSO J319.3−29	0.669 (L8.2)	0.772 (<T0)	0.619 (L9.3)	0.955 (T1.2)	0.744 (T0.4)	L9.8±1.3	T0:
PSO J329.8+03	0.556 (T1.1)	0.642 (T0.3)	0.508 (T2.3)	1.102 (<T1)	0.689 (T1.0)	T1.2±0.8	T1:
PSO J330.3+32	0.496 (T2.3)	0.649 (T0.1)	0.541 (T1.5)	0.763 (T2.6)	0.628 (T1.6)	T1.6±0.9	T2.5
PSO J331.6+33	0.588 (T0.4)	0.684 (<T0)	0.531 (T1.8)	0.915 (T1.5)	0.572 (T2.1)	T1.4±0.7	T1.5
PSO J334.1+19	0.425 (T3.4)	0.619 (T0.9)	0.406 (T4.2)	0.708 (T3.0)	0.425 (T3.1)	T2.9±1.2	T3
PSO J339.0+51	0.225 (T5.1)	0.405 (T5.0)	0.336 (T5.1)	0.411 (T5.2)	0.203 (T5.3)	T5.1±0.1	T5
PSO J357.8+49	0.707 (L7.1)	0.735 (<T0)	0.677 (L7.4)	0.945 (T1.3)	0.833 (L8.9)	L8.7±1.9	T0 (blue)
PSO J359.8−01	0.643 (L9.0)	0.777 (<T0)	0.628 (L9.1)	0.952 (T1.2)	0.767 (T0.0)	L9.8±1.1	T1

[a]Spectral types were calculated using the polynomials defined in Burgasser (2007a).

[b]Spectral types determined by visual comparison with spectral standards, which we adopt as the final spectral types for our discoveries. Uncertainties for these visual spectral types are ±0.5 subtypes, except for those listed with : (±1.0 subtype) or :: (≥ ±1.5 subtypes).

Table 3.10. Low-Resolution Gravity Indices from Allers & Liu (2013a)

Name	FeH_z	VO_z	KI_J	H-cont	Index Scores[a]	Gravity Score[b]	Gravity Class[c]	SpT (visual)
				M dwarfs				
PSO J133.8+06	$1.170^{+0.021}_{-0.021}$	$1.080^{+0.014}_{-0.014}$	$1.078^{+0.010}_{-0.010}$	$0.926^{+0.011}_{-0.011}$	0n10 (0n?0)	$0.0^{+1.0}_{-0.0}$	FLD-G[d]	M9
PSO J337.4+16	$1.110^{+0.040}_{-0.042}$	$1.103^{+0.027}_{-0.028}$	$1.026^{+0.022}_{-0.022}$	$0.936^{+0.028}_{-0.029}$	1n20 (1n20)	$1.0^{+1.0}_{-0.0}$	[INT-G]	M9
				L dwarfs				
PSO J068.9+13	$1.355^{+0.043}_{-0.045}$	$1.037^{+0.019}_{-0.019}$	$1.120^{+0.015}_{-0.015}$	$0.884^{+0.012}_{-0.013}$	nnn1 (nnn?)	$1.0^{+0.0}_{-1.0}$	[INT-G]	L6 (red)
PSO J078.9+31	$1.051^{+0.027}_{-0.028}$	$1.251^{+0.023}_{-0.023}$	$1.048^{+0.016}_{-0.016}$	$0.945^{+0.017}_{-0.018}$	2221 (222?)	$2.0^{+0.0}_{-0.5}$	VL-G	L1.5
PSO J117.1+17	$1.299^{+0.068}_{-0.074}$	$0.951^{+0.026}_{-0.027}$	$1.118^{+0.016}_{-0.016}$	$0.859^{+0.014}_{-0.015}$	0n00 (0n00)	$0.0^{+0.0}_{-0.0}$	FLD-G	L5
PSO J127.4+10	$1.073^{+0.083}_{-0.092}$	$1.110^{+0.054}_{-0.058}$	$1.040^{+0.020}_{-0.020}$	$0.934^{+0.016}_{-0.016}$	2121 (202?)	$1.5^{+0.5}_{-0.0}$	[VL-G]	L4
PSO J135.0+32	$1.334^{+0.023}_{-0.023}$	$1.080^{+0.011}_{-0.011}$	$1.113^{+0.010}_{-0.010}$	$0.917^{+0.008}_{-0.008}$	0011 (00??)	$0.5^{+0.0}_{-0.0}$	FLD-G	L1.5

Table 3.10—Continued

Name	FeH_z	VO_z	KI_J	H-cont	Index Scores[a]	Gravity Score[b]	Gravity Class[c]	SpT (visual)
PSO J136.5−06	$1.263^{+0.019}_{-0.020}$	$1.009^{+0.009}_{-0.009}$	$1.076^{+0.006}_{-0.006}$	$0.822^{+0.006}_{-0.006}$	1010 (10?0)	$0.5^{+0.0}_{-0.0}$	FLD-G	L2 pec[e]
PSO J146.0+05	$1.128^{+0.040}_{-0.043}$	$1.066^{+0.023}_{-0.024}$	$1.084^{+0.018}_{-0.018}$	$0.889^{+0.023}_{-0.023}$	1010 (10?0)	$0.5^{+0.5}_{-0.0}$	FLD-G[d]	L1[e]
PSO J149.1−19	$1.188^{+0.032}_{-0.034}$	$1.020^{+0.015}_{-0.015}$	$1.080^{+0.009}_{-0.009}$	$0.784^{+0.008}_{-0.008}$	1n10 (1n?0)	$1.0^{+0.0}_{-0.0}$	[INT-G]	L5 pec[e]
PSO J158.1+05	$1.331^{+0.039}_{-0.040}$	$1.093^{+0.017}_{-0.018}$	$1.131^{+0.014}_{-0.014}$	$0.937^{+0.013}_{-0.014}$	0011 (00??)	$0.5^{+0.5}_{-0.5}$	FLD-G[d]	L2
PSO J159.0−27	$1.187^{+0.044}_{-0.046}$	$1.131^{+0.030}_{-0.031}$	$1.107^{+0.021}_{-0.021}$	$0.902^{+0.022}_{-0.023}$	1110 (11?0)	$1.0^{+0.0}_{-0.5}$	[INT-G]	L2 (blue)
PSO J316.5+04	$1.173^{+0.046}_{-0.049}$	$0.948^{+0.023}_{-0.024}$	$1.090^{+0.018}_{-0.018}$	$0.816^{+0.017}_{-0.018}$	nnn0 (nnn0)	$0.0^{+0.0}_{-0.0}$	FLD-G	L6 (blue)
PSO J331.9−07	$1.038^{+0.058}_{-0.062}$	$0.983^{+0.033}_{-0.035}$	$1.052^{+0.018}_{-0.019}$	$0.873^{+0.018}_{-0.018}$	nnn0 (nnn0)	$0.0^{+1.0}_{-0.0}$	[FLD-G][d]	L7
PSO J334.8+11	$1.243^{+0.046}_{-0.049}$	$0.998^{+0.022}_{-0.022}$	$1.080^{+0.017}_{-0.018}$	$0.860^{+0.012}_{-0.012}$	1n10 (1n?0)	$1.0^{+0.0}_{-1.0}$	[INT-G]	L5
PSO J336.9−18	$1.005^{+0.062}_{-0.067}$	$1.112^{+0.047}_{-0.048}$	$1.005^{+0.022}_{-0.023}$	$0.958^{+0.019}_{-0.019}$	nnn2 (nnn2)	$2.0^{+0.0}_{-1.0}$	VL-G	L6:: (red)
PSO J338.8+31	$1.329^{+0.059}_{-0.062}$	$1.033^{+0.026}_{-0.026}$	$1.079^{+0.019}_{-0.019}$	$0.824^{+0.017}_{-0.017}$	0010 (00?0)	$0.0^{+0.5}_{-0.0}$	FLD-G	L2 pec[e]
PSO J341.7−15	$1.242^{+0.044}_{-0.047}$	$1.009^{+0.025}_{-0.025}$	$1.125^{+0.015}_{-0.015}$	$0.847^{+0.015}_{-0.015}$	1n00 (1n00)	$0.0^{+0.0}_{-0.0}$	FLD-G	L5
PSO J342.3−16	$1.250^{+0.029}_{-0.030}$	$1.000^{+0.014}_{-0.014}$	$1.068^{+0.013}_{-0.014}$	$0.802^{+0.010}_{-0.010}$	1n10 (1n?0)	$1.0^{+0.0}_{-1.0}$	[INT-G]	L5: pec[e]
PSO J344.8+20	$1.232^{+0.055}_{-0.059}$	$1.144^{+0.035}_{-0.036}$	$1.071^{+0.018}_{-0.018}$	$0.913^{+0.016}_{-0.016}$	1121 (112?)	$1.0^{+0.0}_{-0.0}$	INT-G	L2.5

Table 3.10—Continued

Name	FeH_z	VO_z	KI_J	H-cont	Index Scores[a]	Gravity Score[b]	Gravity Class[c]	SpT (visual)
PSO J348.8+06	$1.093^{+0.071}_{-0.078}$	$1.326^{+0.056}_{-0.060}$	$1.036^{+0.015}_{-0.015}$	$0.987^{+0.011}_{-0.011}$	2222 (2222)	$2.0^{+0.0}_{-0.0}$	VL-G	L2

Note. — This table includes M7–L7 discoveries for which our spectrum has high enough S/N to extract useful measurements of the AL13 gravity indices, corroborated by visual inspection. No AL13 index is valid for spectral types later than L7, so objects with those spectral types are not included.

[a]Scores in parentheses were determined using the original AL13 classification scheme, in which objects with index values corresponding to INT-G but within 1σ of the FLD-G value are classified with a score of "?".

[b]The overall gravity classification value and the 68% confidence limits calculated as described in Aller et al. (2016).

[c]Gravity classes in brackets are based on lower-S/N spectra and could not be confirmed visually, and therefore should be considered tentative. Higher-S/N spectra are needed to clarify the gravity.

[d]Although this object is classified as FLD-G under the AL13 system, we note that within the uncertainties in our gravity score, this object shows signs of intermediate gravity. A higher resolution spectrum is needed to more accurately classify the gravity of this object.

[e]Strong or medium candidate binary (see text). The spectral type may therefore be based on a composite spectrum.

Table 3.11. Other Objects Showing Low Gravity Spectral Features

Name	SpT (visual)	Reason for No Gravity Class[a]	Youth[b]
PSO J004.7+51	L7	Low S/N	Red
PSO J054.8−11	L3:	Low S/N	H band; Red
PSO J057.2+15	L7 (red)	Low S/N	H band; Red
PSO J100.5+41[c]	L9 (red)	SpT > L7	Red
PSO J244.1+06	L9 (red)	SpT > L7; Low S/N	Red
PSO J353.8+45	L7.5	SpT > L7	Red

[a] "SpT > L7": None of the AL13 spectral indices are defined for spectral types later than L7. "Low S/N": Spectra with J band S/N < 30 produced AL13 gravity scores with uncertainties too large to yield useful results.

[b] "Red": Redder-than-normal near-IR colors for the spectral type. "H band": Triangular H band profile.

[c] Previously identified by Mace et al. (2013a) as an "extremely red" L dwarf, WISE 0642+4101, and by Gagné et al. (2014b) as a candidate member of the AB Dor young moving group (Section 3.6.2).

Table 3.12. Candidate Binaries

Name	SpT (Visual)	BG14[a] Criteria	B10[b] Criteria	Visual Signs[c]
		Strong Candidates		
PSO J003.4−18	L5 pec	10	···	Y
PSO J049.1+26	T2.5	···	4	Y
PSO J071.6−24	L6 (blue)	8	···	Y
PSO J088.0+43	L4 pec	9	···	Y
PSO J133.8−02	T0 pec	···	5	Y
PSO J135.7+16	T0 pec	···	6	Y
PSO J136.5−06	L2 pec	9	···	Y
PSO J149.1−19	L5 pec	10	···	Y
PSO J159.2−26	T1.5	···	4	Y
PSO J160.0−21	T2 pec	···	6	Y
PSO J207.7+29	T0: pec	···	6	Y
PSO J218.4+50	T2.5	···	5	Y
PSO J241.1+39	T2	···	5	Y
PSO J258.2+06	T0 pec	···	6	Y
PSO J330.3+32	T2.5	···	5	N
PSO J338.8+31	L2 pec	8	···	Y
		Medium Candidates		

Table 3.12—Continued

Name	SpT (Visual)	BG14[a] Criteria	B10[b] Criteria	Visual Signs[c]
PSO J004.1+23	T0	···	2	Y
PSO J100.5+41	L9 (red)	···	3	N
PSO J103.0+41	T0	···	2	Y
PSO J105.4+63	T2.5	···	3	N
PSO J146.0+05	L1	4	···	N
PSO J152.2+15	L1.5	5	···	N
PSO J180.1−28	T0	···	1	Y
PSO J272.0−04	T1.5 pec	···	3	Y
PSO J277.7+45	L9	···	3	Y
PSO J284.7+39	T4	···	2	Y
PSO J319.3−29	T0:	···	2	Y
PSO J342.3−16	L5:	5	···	Y
Weak Candidates				
PSO J052.7−03	L9:	···		Y
PSO J282.7+59	L9	···		Y
PSO J321.1+18	L9	···		Y

Note. — Our spectra for all binary candidates listed above have S/N $\geq$ 25 averaged over the J band (1.20 − 1.31 μm).

[a]Number of index based-criteria (out of 12) for binarity from Bardalez Gagliuffi et al. (2014) satisfied by this object's spectrum. These indices apply only to M7–L7 dwarfs (we included our L7.5 discoveries).

[b]Number of index based-criteria (out of 6) for binarity from Burgasser et al. (2010a) satisfied by this object's spectrum. These indices apply only to L8, L9, and T dwarfs.

[c]See text (Section 3.4.5) for descriptions.

Table 3.13. Common Proper Motion Pairings

Name	$\mu_\alpha \cos\delta$ (mas yr^{-1})	μ_δ (mas yr^{-1})	Dist. (pc)	SpT	r (arcsec)	r (AU)
NLTT 687[a]	-33 ± 5	-173 ± 5[b]	42^{+26}_{-16}[c]	M3[c]	120.3	5053
PSO J003.4950−18.2802	-31 ± 12	-175 ± 13	46.1 ± 5.6	L5 pec		
Wolf 1154	121.0 ± 4.1	62.0 ± 4.0[d]	$27.5^{+11.9}_{-6.3}$[e]	M1[f]	77.1	2313
PSO J330.3214+32.3686	105 ± 8	65 ± 9	20.1 ± 2.1	T2.5		
LSPM J2216+1952	146 ± 8	-96 ± 8[g]	$30.0^{+11.2}_{-8.2}$[h]	M4	52.2	1566
PSO J334.1193+19.8800	120 ± 8	-72 ± 9	30.7 ± 3.2	T3		

[a]This pairing was previously discovered by Baron et al. (2015).

[b]Salim & Gould (2003)

[c]Baron et al. (2015)

[d]Høg et al. (2000)

[e]Lépine & Gaidos (2011)

[f]Estimated from $V - J$ and the color-SpT relation of Lépine & Gaidos (2011).

[g]Lépine & Shara (2005)

[h]Estimated using the distance relations of Lépine (2005).

Table 3.14. Candidate Members of Young Moving Groups

Name	SpT (visual)	$d_{\rm phot}$[a] (pc)	$\mu_\alpha \cos\delta$ (mas yr^{-1})	μ_δ (mas yr^{-1})	Youth[b]	BANYAN II YMG	BANYAN II Prob. (%)	$\log(L_{\rm bol}/L_\odot)$ (dex)	Mass[c] ($M_{\rm Jup}$)
PSO J004.7148+51.8918	L7	26.4 ± 3.7	293 ± 4	-12 ± 7	Red	Argus	79.9	$-4.36^{+0.12}_{-0.14}$	$10.3^{+1.4}_{-1.2}$
PSO J007.7921+57.8267	L9	11.2 ± 1.5	526 ± 2	-12 ± 4	···	Argus	98.7	$-4.54^{+0.12}_{-0.13}$	$8.8^{+1.3}_{-1.1}$
PSO J057.2893+15.2433	L7 (red)	31.5 ± 4.4	68 ± 11	-127 ± 12	H band; Red	β Pictoris	92.0	$-4.36^{+0.12}_{-0.13}$	$8.1^{+1.8}_{-1.5}$
PSO J071.8769−12.2713	T2:	25.9 ± 3.1	20 ± 19	-89 ± 19	···	β Pictoris	86.4	$-4.69^{+0.13}_{-0.14}$	6.1 ± 0.7
PSO J076.7092+52.6087	T4.5	18.1 ± 4.4	57 ± 4	-196 ± 7	···	Argus	71.4	-4.8 ± 0.2	$7.0^{+1.5}_{-1.2}$
PSO J100.5233+41.0320[d]	L9 (red)	18.5 ± 2.6	12 ± 4	-372 ± 6	Red	AB Doradus	78.6	$-4.54^{+0.12}_{-0.13}$	15^{+4}_{-3}
PSO J272.4689−04.8036	T1	13.1 ± 1.3	-46 ± 4	-400 ± 13	···	AB Doradus	93.8	-4.65 ± 0.09	14 ± 2
PSO J319.3102−29.6682	T0:	15.6 ± 1.6	148 ± 4	-162 ± 4	···	β Pictoris	97.1	$-4.60^{+0.10}_{-0.11}$	$6.5^{+0.7}_{-0.6}$
PSO J331.6058+33.0207	T1.5	28.3 ± 3.4	176 ± 9	16 ± 11	···	Argus	74.6	$-4.67^{+0.12}_{-0.13}$	$8.0^{+1.2}_{-1.0}$
PSO J334.1193+19.8800	T3	30.9 ± 3.6	119 ± 11	-60 ± 9	···	β Pictoris	84.4	$-4.73^{+0.12}_{-0.13}$	$5.9^{+0.7}_{-0.6}$

[a] Photometric distances calculated using $K_{\rm MKO}$ magnitudes and the polynomial from Dupuy & Liu (2012).

[b] "Red": Redder-than-normal near-IR colors for the spectral type. "H band": Triangular H band profile.

[c] Mass estimates derived assuming the objects are members of the given YMGs. We used $L_{\rm bol}$ and the "hybrid" evolutionary models of Saumon & Marley (2008), following the method described in Section 3.6.2.

[d] Previously identified by Gagné et al. (2014b, 2015b) as a candidate member of the AB Doradus Moving Group. First discovered as WISE 0642+4101 (Mace et al. 2013a).

Chapter 4

A Search for L/T Transition Dwarfs With Pan-STARRS1 and *WISE*. III. Young L Dwarf Discoveries and Proper Motion Catalogs in Taurus and Scorpius-Centaurus

Note: This chapter originally appeared as Best et al. (2017b), with co-authors Michael C. Liu, Eugene A. Magnier, Brendan P. Bowler, Kimberly M. Aller, Zhoujian Zhang, Michael C. Kotson, W. S. Burgett, K. C. Chambers, P. Draper, H. Flewelling, K. W. Hodapp, N. Kaiser, N. Metcalfe, R. J. Wainscoat, and C. Waters.

Abstract

We present the discovery of eight young M7–L2 dwarfs in the Taurus star-forming region and the Scorpius-Centaurus OB Association, serendipitously found during a wide-field search for L/T transition dwarfs using Pan-STARRS1 (optical) and *WISE* (mid-infrared) photometry. We identify PSO J060.3200+25.9644 (near-infrared spectral type L1) and PSO J077.1033+24.3809 (L2) as new members of Taurus based on their VL-G gravity classifications, the consistency of their photometry and proper motions with previously known Taurus objects, and the low probability of contamination by field objects.

PSO J077.1033+24.3809 is the coolest substellar member of Taurus found to date. Both Taurus objects are among the lowest mass free-floating objects ever discovered, with estimated masses ≈6 $M_{\rm Jup}$, and provide further evidence that isolated planetary-mass objects can form as part of normal star-formation processes. PSO J060.3200+25.9644 (a.k.a. DANCe J040116.80+255752.2) was previously identified as a likely member of the Pleiades (age ≈ 125 Myr) based on photometry and astrometry, but its VL-G gravity classification and near-infrared photometry imply a much younger age and thus point to Taurus membership. We have also discovered six M7–L1 dwarfs in outlying regions of Scorpius-Centaurus with photometry, proper motions, and low-gravity spectral signatures consistent with membership. These objects have estimated masses ≈15–36 $M_{\rm Jup}$. The M7 dwarf, PSO J237.1470−23.1489, shows excess mid-infrared flux implying the presence of a circumstellar disk. Finally, we present catalogs of Pan-STARRS1 proper motions for low-mass members of Taurus and Upper Scorpius with median precisions of ≈3 mas yr^{-1}, including 67 objects with no previous proper motion and 359 measurements that improve on literature values.

4.1 Introduction

Brown dwarfs with ages $\lesssim$ 100 Myr are valuable laboratories for testing both the youngest substellar evolutionary models and the lowest-gravity (therefore lowest-mass) atmospheric models. For instance, brown dwarfs with $T_{\rm eff} \lesssim 1400$ K and ages $\lesssim$ 20 Myr will have masses $\lesssim$ 10 $M_{\rm Jup}$ (e.g., Chabrier et al. 2000), firmly in the planetary regime ($\lesssim$ 13 $M_{\rm Jup}$). These young, very low mass brown dwarfs therefore serve as vital templates for understanding directly imaged planets.

Star-forming regions and young open clusters offer the opportunity to identify multiple young brown dwarfs in small areas of the sky, at the age when these objects are brightest. Planetary-mass objects in star-forming regions have been discovered both as companions to stars (e.g., Luhman et al. 2006; Lafreniere et al. 2008) and as free-floating objects (e.g.,

Luhman et al. 2009; Weights et al. 2009). Wide-field, red-sensitive surveys such as the Pan-STARRS1 3π Survey (PS1; Kaiser et al. 2010, K. Chambers et al., 2017, in prep), the Two Micron All Sky Survey (2MASS; Skrutskie et al. 2006), the UKIRT Infrared Deep Sky Survey (UKIDSS; Lawrence et al. 2007), and the Wide-Field Infrared Survey Explorer (*WISE*; Wright et al. 2010) have the ability to detect free-floating very low mass brown dwarfs in nearby star-forming regions (e.g., Lodieu 2013; Esplin et al. 2014), although interstellar reddening at optical and near-infrared wavelengths can make brown dwarfs difficult to distinguish from background giant stars. More discoveries of these objects would improve our understanding of the early evolution of low mass brown dwarfs and giant planets.

At a distance of ≈145 pc and an age of ≈1–2 Myr (Kraus & Hillenbrand 2009a), the Taurus-Auriga molecular cloud (hereinafter Taurus) is one of the closest star-forming regions to the Sun. A comprehensive review of Taurus and its observational history can be found in Kenyon et al. (2008). Taurus has been searched extensively for substellar members from optical to mid-infrared wavelengths (e.g., Luhman 2006; Slesnick et al. 2006; Guieu et al. 2006; Luhman et al. 2009; Quanz et al. 2010; Rebull et al. 2010). Esplin et al. (2014) cataloged 74 members with spectral types M6–L0, which at the young age of Taurus span the full brown dwarf mass regime from the stellar/sub-stellar boundary down to planetary masses ($\lesssim$13 $M_{\rm Jup}$). The coolest known substellar objects in Taurus to date are the free-floating ≈4–7 $M_{\rm Jup}$ 2MASS J04373705+2331080 (hereinafter 2MASS J0437+2331), discovered and classified as L0 by Luhman et al. (2009), and the planetary-mass companion 2MASS J04414489+2301513 Bb (Todorov et al. 2010), with a near-IR spectral type of L1$\pm$1 on the Allers & Liu (2013a) system and an estimated mass of $\approx 10 \pm 2$ $M_{\rm Jup}$ Bowler & Hillenbrand (2015).

The Scorpius-Centaurus Association (hereinafter Sco-Cen) is the nearest OB association to the Sun. The Sco-Cen complex, reviewed in detail by Preibisch & Mamajek (2008), has a distance similar to Taurus but an older age (≈10–20 Myr). With no significant ongoing star formation, Sco-Cen is much less affected by interstellar reddening, but any planetary-

mass objects will also have cooled and become fainter than equivalent-mass objects in Taurus. The Upper Scorpius subgroup in particular has been the target of many searches for ultracool dwarfs (e.g., Martín et al. 2004; Lodieu et al. 2006, 2011; Slesnick et al. 2006, 2008; Dawson et al. 2014). Lodieu et al. (2008) have probed the deepest into the substellar regime, spectroscopically confirming over 20 M8–L2 dwarfs in Upper Scorpius with masses down to $\approx$15 $M_{\rm Jup}$.

Here we present the discovery of two early-L dwarfs in Taurus and six M7–L1 dwarfs in Sco-Cen, serendipitously identified in a wide-field search for L/T transition dwarfs in the Pan-STARRS1 and *WISE* catalogs. In Section 4.2 we explain how these objects were initially identified, and we describe follow-up observations in Section 4.3. We detail the observed features of our discoveries in Section 4.4. We discuss their membership in Taurus (Section 4.5) or Sco-Cen (Section 4.6), and provide estimated masses and comparisons with model spectra. We summarize our discoveries in Section 4.7.

4.2 Photometric Selection

We conducted a search over $\approx$28,000 deg^2 for L/T transition dwarfs in the field using a merged catalog of PS1 and *WISE* photometry. The search is described in detail in Best et al. (2013, hereinafter Paper I), and the full spectroscopic follow-up results are presented in Best et al. (2015, hereinafter Paper II), including our discovery of 130 ultracool dwarfs. Among these discoveries were 23 late-M and L dwarfs with spectroscopic signs of low gravity, implying youth. This was a surprisingly large number given that we were searching for objects with field ages and cooler spectral types ($\approx$L6–T5) and that objects with ages $\lesssim$ 200 Myr should comprise at most a few percent of the local population in a galaxy $\gtrsim$10 Gyr old. In Paper II, we determined that our search could find late-M and L dwarfs with $W1-W2$ colors redder than average for their spectral types, bringing younger objects into our sample.

Our search also specifically avoided the heavily reddened areas of the sky defined in Cruz et al. (2003), which include Taurus and Sco-Cen. The eight discoveries described in this paper lie just outside these reddened regions, with one exception: PSO J060.3200+25.9644 (hereinafter PSO J060.3+25) lies $\approx 2^\circ$ inside the Cruz et al. (2003) Taurus boundaries, but we pursued follow-up observations because its spectral energy distribution (SED) from $z_{\rm P1}$ through $W2$ (0.9–4.6 μm) strongly suggested an unreddened ultracool object.

The PS1 $z_{\rm P1}$ and $y_{\rm P1}$, *WISE*, 2MASS, and MKO photometry for our discoveries was originally presented in Paper II. In Table 4.1, we update the earlier version of PS1 photometry from Paper II with photometry from the PS1 Data Release 1 (DR1; Chambers et al., 2017, in prep; Magnier et al., 2017, in prep) and include $i_{\rm P1}$ magnitudes. The photometry used in both Paper II and this work is the mean PSF photometry from individually calibrated images; the DR1 photometry in this work includes many more epochs. We also replace the WISE All-Sky photometry (Cutri et al. 2012) used in Paper II with AllWISE magnitudes (Cutri et al. 2014). For reference, we reproduce the 2MASS and MKO photometry here in Table 4.2. We also include photometry for the previously-identified Taurus L dwarf 2MASS J0437+2331.

4.3 Near-Infrared Spectroscopy

We obtained near-infrared spectra for our candidates between 2013 January and 2015 May using the NASA Infrared Telescope Facility (IRTF). We used the facility spectrograph SpeX (Rayner et al. 2003) in prism mode with the $0.5''$ ($R \approx 120$) and $0.8''$ ($R \approx 75$) slits. Details of our observations are listed in Table 4.3. For each science target we observed a nearby A0V star contemporaneously for telluric calibration. All spectra were reduced in standard fashion using versions 3.4 and 4.0 of the Spextool software package (Vacca et al. 2003; Cushing et al. 2004). These observations were part of a large program (Paper II) in which our desired S/N was $\gtrsim$30, sufficient for accurate spectral typing based on overall spectral morphology but not necessarily for robust analysis of specific features. We therefore observed PSO J060.3+25

and PSO J077.1033+24.3809 (hereinafter PSO J077.1+24) a second time to achieve higher S/N, and for each object we combined the first and second epochs using the Spextool *xcombspec* routine to obtain a single higher-S/N spectrum, which we present in this paper.

While comparing the spectra of our discoveries to spectral standards, we noticed a small wavelength offset in the spectrum of the field L0 standard 2MASS J03454316+2540233 (hereinafter 2MASS J0345+2540) from Burgasser & McElwain (2006). The offset is large enough to affect calculations of the Allers & Liu (2013a) gravity-sensitive spectral indices that we used to analyze our discoveries (Section 4.4.2). We therefore used IRTF/SpeX to obtain a new spectrum of 2MASS J0345+2540 with more accurate wavelength calibration, which we used for our analysis. Appendix C presents this new spectrum and provides details of the observations.

4.4 Results

4.4.1 Ultracool Discoveries

The SpeX prism spectra for our eight young ultracool discoveries are presented in Figure 4.1, and their spectral types are listed in Table 4.4. We show their locations in the sky in Figure 4.2. PSO J060.3+25 was previously identified by Sarro et al. (2014) and Bouy et al. (2015) as a likely very low-mass member of the Pleiades cluster, based on photometry and astrometry. PSO J237.1471−23.1489 (hereinafter PSO J237.1−23) was identified by Lodieu (2013) as a photometric and astrometric candidate member of Upper Sco. We independently discovered these objects and present here spectral confirmation of their ultracool nature. We also find that PSO J060.3+25 is more likely to be a Taurus member than a Pleiad (Section 4.5.1). The other six objects are new discoveries.

In Figures 4.3 and 4.4 we compare the colors of our discoveries with those of previously known late-M and early-L dwarfs. Our discoveries in Taurus and Sco-Cen have red $W1-W2$ colors compared with field objects of similar spectral types, which led to the fortuitous discovery of these young M7–L2 dwarfs even though our search was designed to find L/T

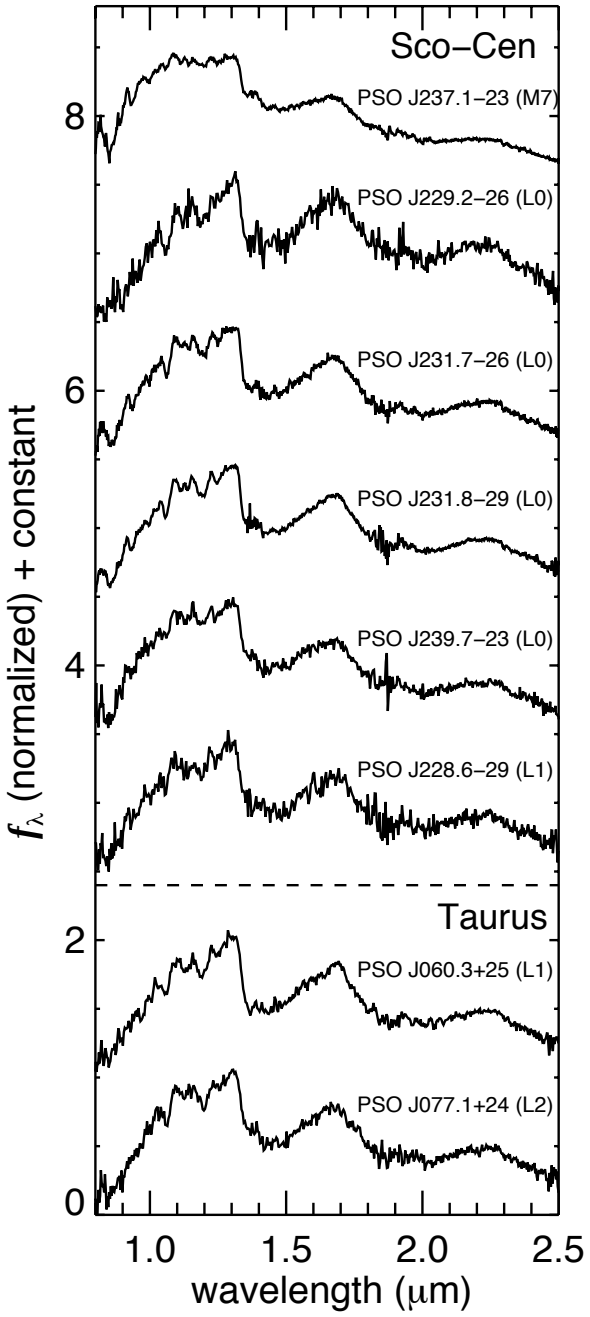

Figure 4.1 SpeX prism spectra for our eight discoveries, normalized at the J-band peak ($1.27\,\mu$m), arranged from earliest to latest spectral type, and offset by a constant. Our two Taurus discoveries are at the bottom.

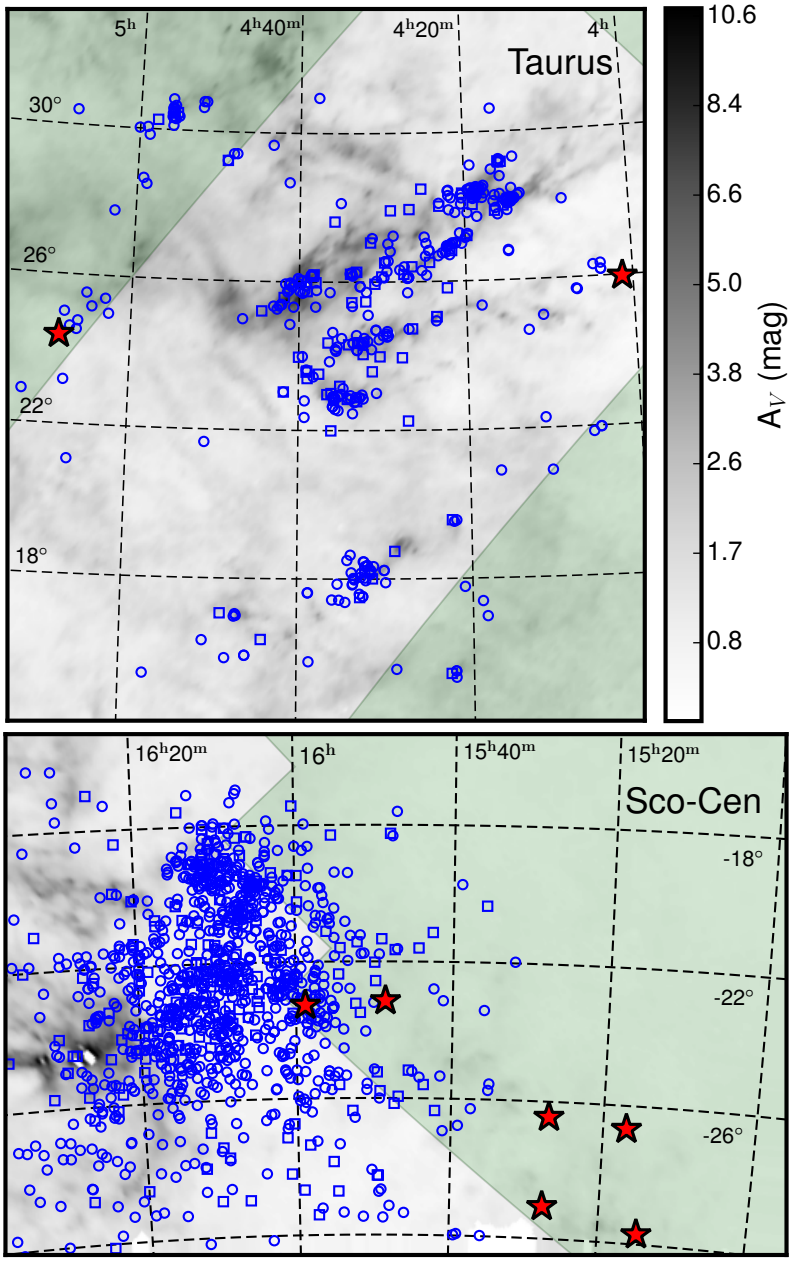

Figure 4.2 *Top*: The locations in Taurus of our discoveries (red stars) and known stars (blue circles) and ultracool dwarfs (SpT $\geq$ M6, blue squares) from Esplin et al. (2014). The grayscale background shows visual extinction (scale at right) from the reddening map of Schlafly et al. (2014). The green shading marks the regions included in our search (Paper II), i.e., outside of reddened regions identified by Cruz et al. (2003). Our two discoveries lie on the outskirts of Taurus in regions of low extinction. *Bottom*: The portion of Sco-Cen surveyed by PS1 (north of $-30°$) shown in the same format, with known members of Upper Sco from Luhman & Mamajek (2012), Dawson et al. (2014), and Rizzuto et al. (2015). The two leftmost discoveries are in Upper Sco, while the other four appear to be members of Upper Centaurus-Lupus. The knot of high extinction near (16^h30^m, $-24°$) is the ρ Ophiuchi star-forming region.

transition dwarfs (spectral types ≈ L6–T4). The $y_{P1} - W1$, $y_{P1} - J_{MKO}$ and $(J - H)_{MKO}$ colors of our discoveries are normal compared with field objects of similar spectral types.

4.4.2 Spectral Indices and Spectral Types

We used three methods to assign spectral types for our discoveries: visual comparison with low-gravity field standards and two index-based methods. Table 4.4 gives the spectral types calculated from the index-based system of Allers & Liu (2013a, hereinafter AL13). The AL13 indices were designed to assign near-infrared spectral types consistent with optical spectral types, independent of surface gravity. Since all of our discoveries show clear spectral signs of low gravity (Section 4.4.3), we adopted the AL13 index-based types as our final spectral types, rounded to the nearest subtype and assigned an uncertainty of 1 subtype (following AL13). For confirmation, we visually compared our spectra to the VL-G standards of AL13. All of our visually-determined types are within 1 subtype of the adopted index-based types.

In Table 4.5, we list the spectral types determined using the index-based system of Burgasser et al. (2006a, hereinafter B06), compared with our adopted AL13 spectral types. The B06 and AL13 spectral types are consistent within their 2σ uncertainties, although the B06 types are mostly 1–3 subtypes later. This is probably a consequence of the fact that the B06 indices are not defined for spectral types earlier than L0, so the B06 spectral types are averages only of L types.

4.4.3 Low-Gravity Signatures

Low-gravity signatures in ultracool dwarf spectra are a well-established indication of ages $\lesssim$200 Myr (e.g., Kirkpatrick et al. 2008; Allers & Liu 2013a). We used the AL13 system based on gravity-sensitive near-IR spectral indices to assess whether our spectra display signs of low gravity. In this system, an object is assigned a score of 0 for field gravity (FLD-G, ages $\gtrsim$ 200 Myr), 1 for intermediate gravity (INT-G, ages $\approx 50 - 200$ Myr), or 2 for very low gravity (VL-G, ages $\approx 10 - 30$ Myr). We calculated indices and gravity scores for

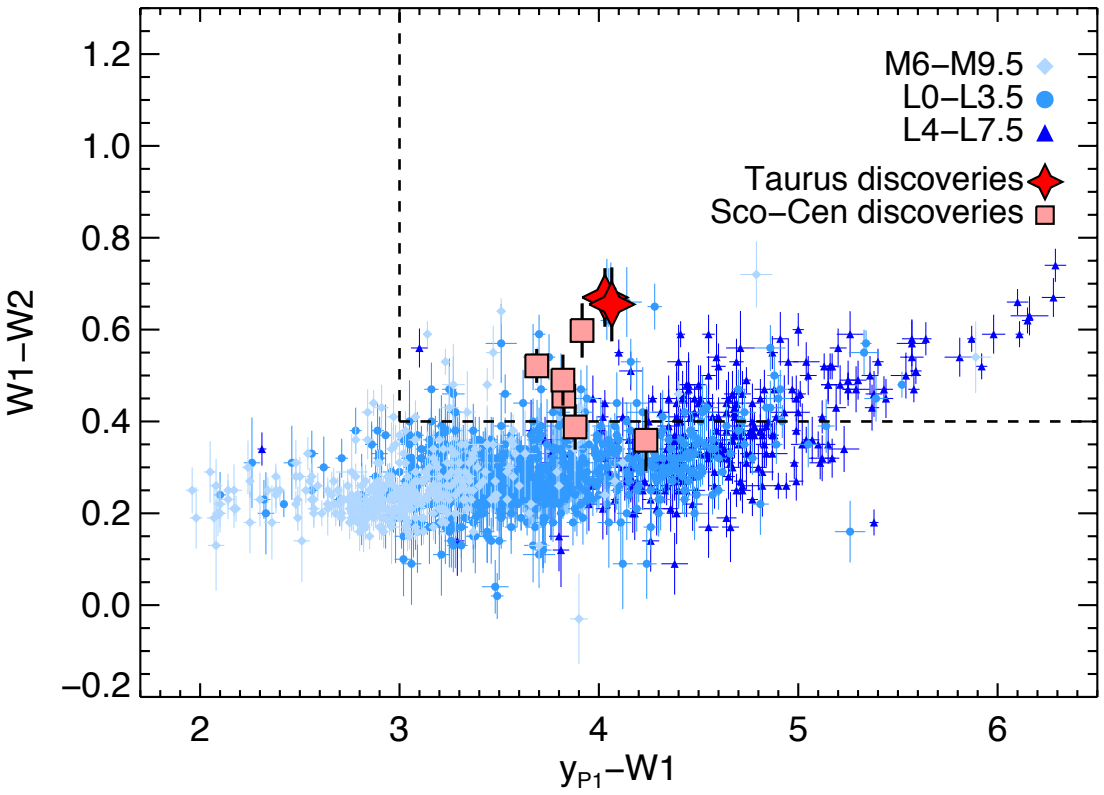

Figure 4.3 $W1-W2$ vs. $y_{\rm P1}-W1$ (AllWISE) diagram featuring our discoveries in Taurus (red stars) and Sco-Cen (pink triangles), plotted over previously known ultracool dwarfs in shades of blue (cooler spectral types have darker shades). The black dashed lines represent the color cuts we used in our search (Paper II), for which we used WISE All-Sky photometry. We chose objects above and to the right of the dashed lines. (The two Sco-Cen discoveries with AllWISE $W1-W2 < 0.4$ mag were included in our search because they have WISE All-Sky $W1-W2 > 0.4$ mag.) Our young M7–L2 discoveries have somewhat redder $W1-W2$ colors than field objects of the same spectral types, which explains why our search for L/T transition dwarfs found these earlier-type objects.

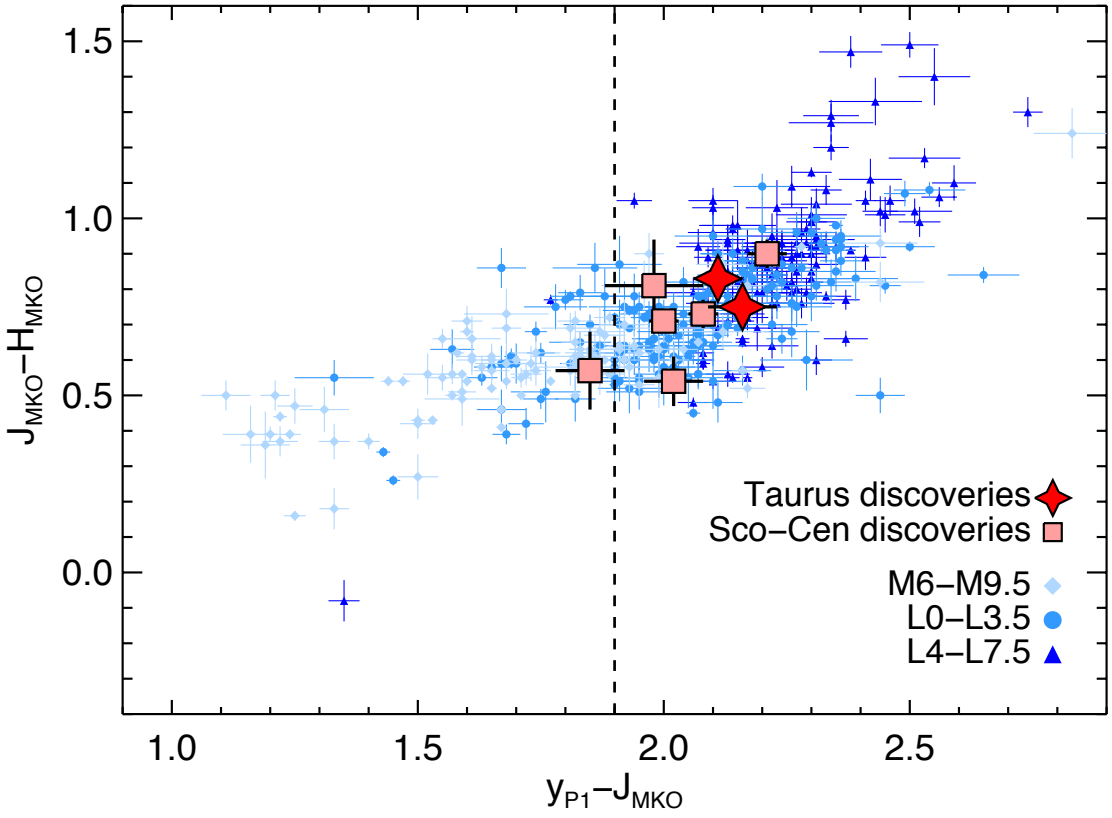

Figure 4.4 $(J-H)_{\rm MKO}$ vs. $y_{\rm P1}-J_{\rm MKO}$ diagram for our discoveries, using the same format as Figure 4.3. We chose objects in our search to the right of the dashed line (using an earlier, preliminary version of $y_{\rm P1}$ photometry); $J-H$ was not used to select objects. Our discoveries have normal $y_{\rm P1}-J_{\rm MKO}$ and $(J-H)_{\rm MKO}$ colors compared with field objects of the same spectral types.

our discoveries following Aller et al. (2016), who adapt AL13 to incorporate Monte Carlo assessment of the uncertainties in the indices and gravity classes. We also visually examined the gravity-sensitive features in our spectra as a check on the gravity scores.

We classify six of our discoveries as VL-G: PSO J060.3+25, PSO J077.1+24, PSO J231.7899−26.4494 (hereinafter PSO J231.7−26), PSO J231.8942−29.0600 (hereinafter PSO J231.8−29), PSO J237.1−23, and PSO J239.7016−23.2664 (hereinafter PSO J239.7−23). Table 4.6 lists their indices and gravity scores. Figure 4.5 compares the spectra of these six VL-G objects with field standards from Kirkpatrick et al. (2010) and VL-G standards from AL13 having the same spectral types. For the L0 field standard 2MASS J0345+2540, we use our new SpeX prism spectrum (Appendix C). All six of our spectra display weak 0.99 μm FeH and 1.25 μm K I absorption, and a triangular H band shape, all signs of youth. PSO J060.3+25, PSO J077.1+24, PSO J231.7−26, and PSO J231.8−29 also show strong 1.06 μm VO absorption, which AL13 identify as an additional sign of youth for L0–L4 dwarfs.

For the other two objects, PSO J228.6773−29.7088 (hereinafter PSO J228.6−29) and PSO J229.2354−26.6738 (hereinafter PSO J229.2−26), the S/N of our spectra was too low ($\lesssim$30) to yield robust gravity scores from the AL13 indices. Figure 4.6 shows these spectra, again compared with the appropriate field and VL-G standards. In spite of the measurement uncertainties, visual inspection confirms that both objects have weak 0.99 μm FeH and 1.25 μm K I absorption, strong 1.06 μm VO absorption, and triangular H band shapes, so we regard them as strong candidate VL-G objects.

4.4.4 Proper Motions

Proper motions are key to establishing membership in star-forming regions and clusters whose bulk motion through space is well defined. We use proper motions from PS1 Processing Version 3.2 (PV3.2), the version used for the photometry and mean positions in PS1 DR1. (PS1 proper motions will be part of a future public release.) PV3.2 astrometry is calibrated to the *Gaia* DR1 (Gaia Collaboration et al. 2016a) astrometric reference

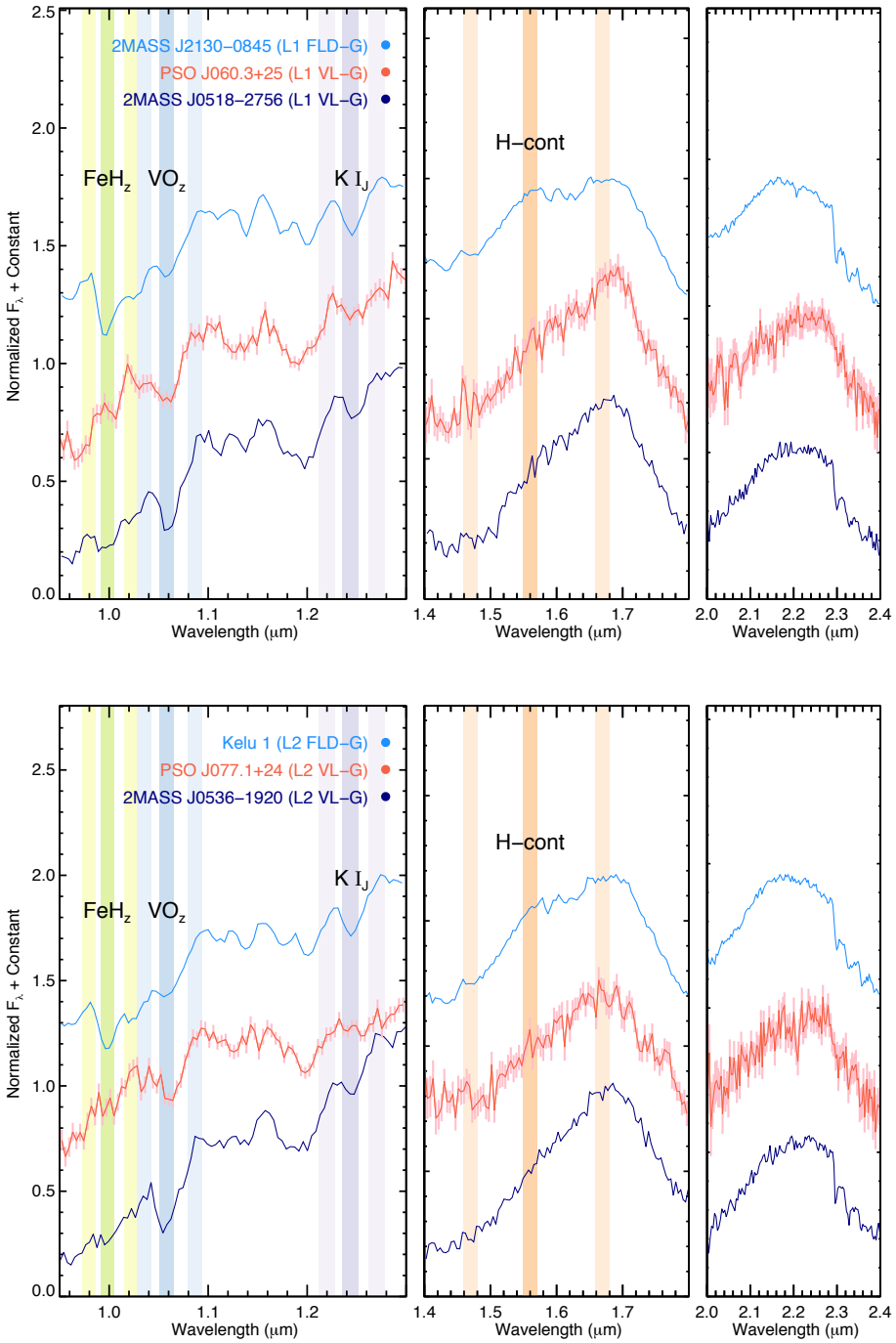

Figure 4.5 Our six VL-G discoveries (middle/red, with error bars), compared with field standards (top/light blue) from Kirkpatrick et al. (2010) and VL-G standards (bottom/dark blue) from AL13 of the same spectral type. The vertical colored bands show the wavelength intervals used to calculate the labeled spectral indices. For all six objects, the FeH$_z$, K I$_J$, and H-cont features are more similar to the VL-G standards, and the VO$_z$ absorption also indicates VL-G for the L dwarfs. (VO$_z$ is not a valid gravity indicator for M dwarfs.)

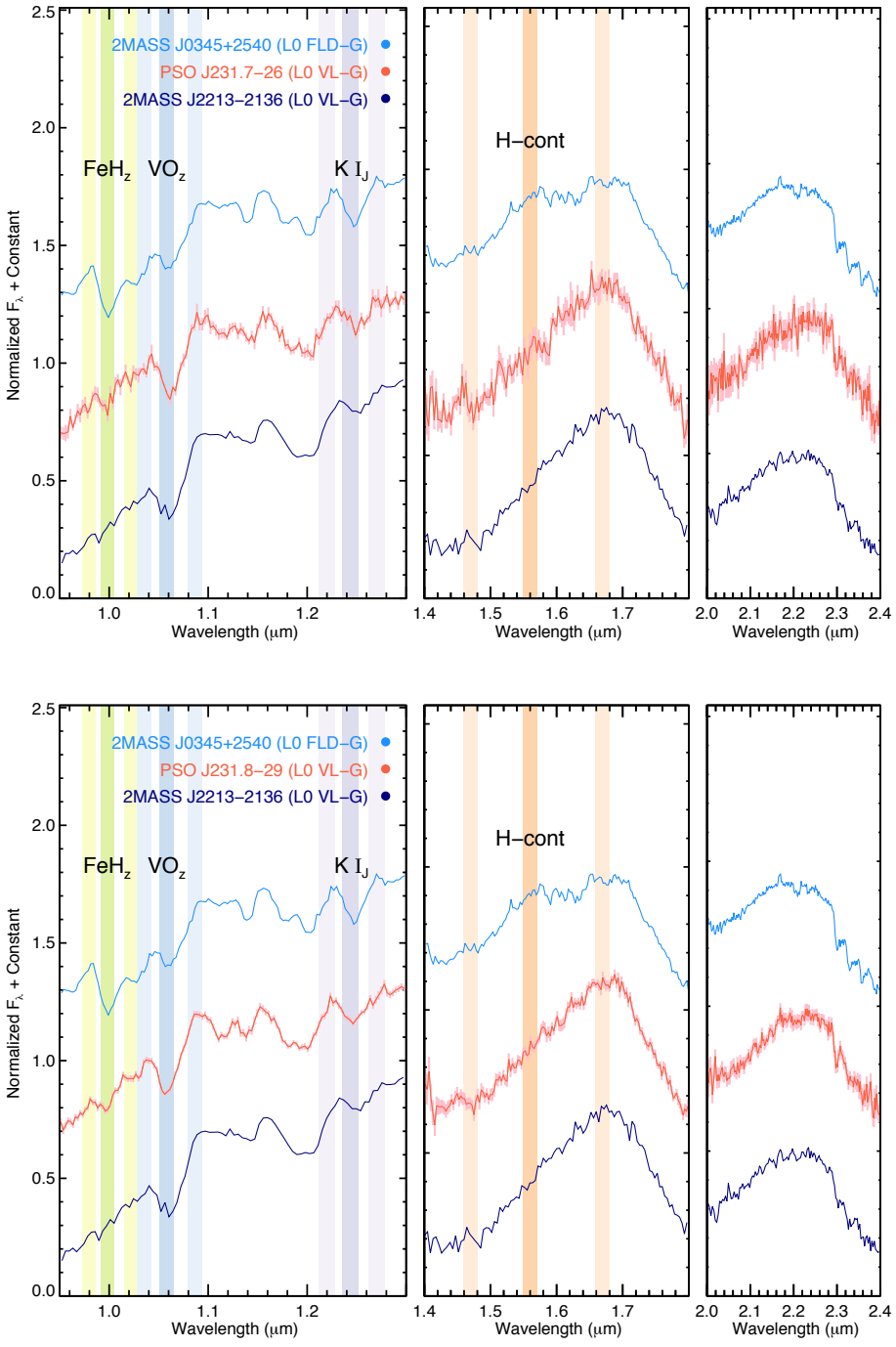

Figure 4.5 continued.

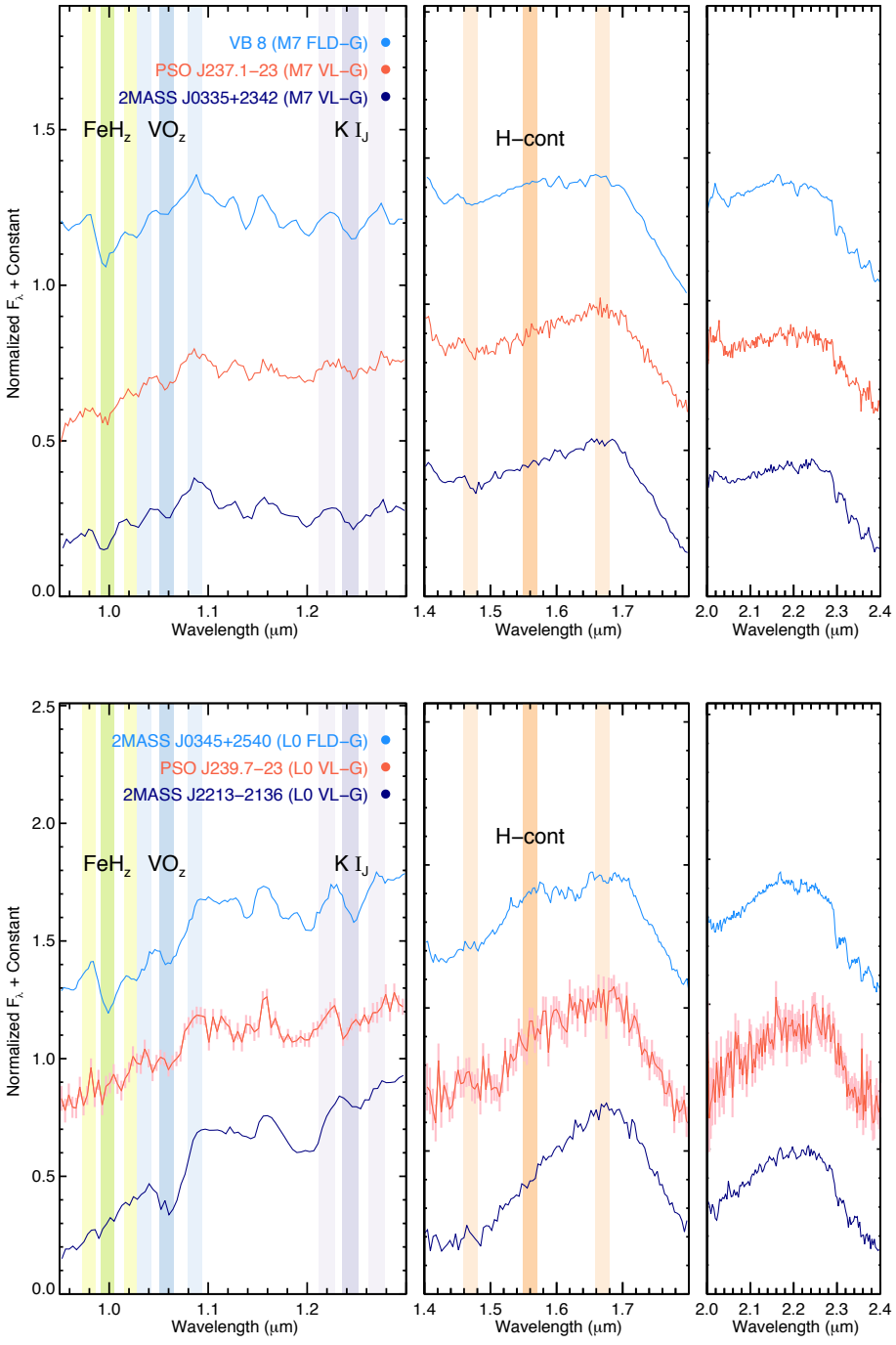

Figure 4.5 continued.

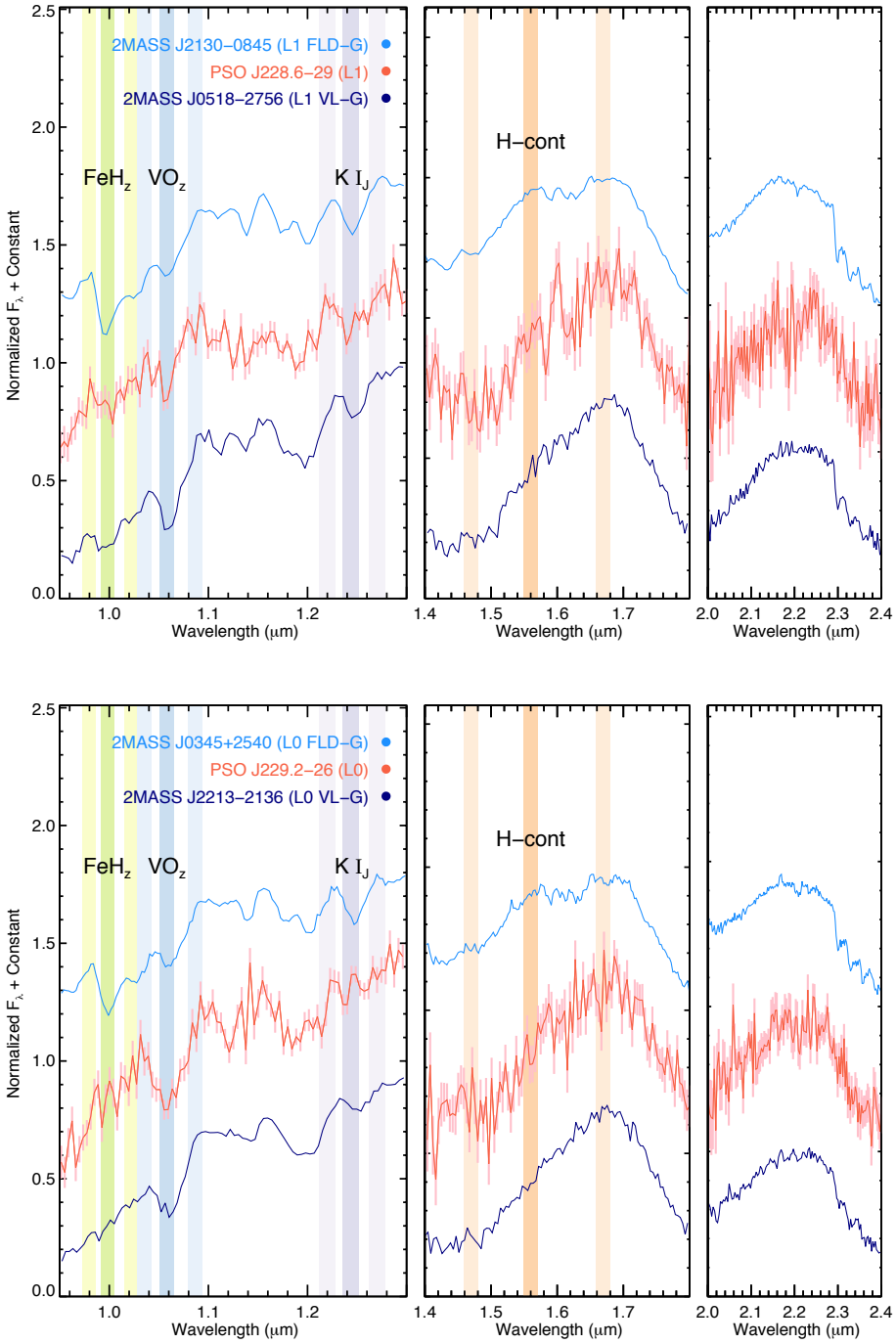

Figure 4.6 Same as Figure 4.5, but showing the two objects (PSO J228.6−29 and PSO J229.2−26) for which we did not calculate gravity classes due to low S/N. These two spectra nevertheless show FeH$_z$, VO$_z$, K I$_J$, and H-cont features resembling those of the VL-G standards.

frame. We present the proper motions for our discoveries in Table 4.7, and we discuss their consistency with members of Taurus and Sco-Cen in Sections 4.5 and 4.6. We present catalogs of proper motions for low-mass members of Taurus and Upper Sco in Appendices A and B, along with a brief summary of the method used to calculate PS1 proper motions.

4.4.5 No Candidate Binaries

As in Paper II, we used the spectral index criteria of Bardalez Gagliuffi et al. (2014, hereinafter BG14) and visual inspection to search for spectral features indicating that our discoveries may be unresolved binaries. PSO J228.6−29 satisfies only one of the twelve BG14 criteria, and our other seven discoveries meet none of the BG14 criteria. Similarly, we found no evidence of spectral blends via visual inspection. None of these objects appear to be candidate unresolved binaries.

In addition, we investigated whether any of our discoveries could be members of wide binary or multiple systems. We searched for nearby known members of the star-forming regions in which our discoveries reside, using the catalogs of Esplin et al. (2014) for Taurus and Luhman & Mamajek (2012) for Upper Scorpius. As several of our Sco-Cen discoveries lie outside the classical boundaries of Upper Scorpius (Section 4.6), we also searched across all catalogs in *Vizier*[1] for objects near these discoveries. We found no known members of Taurus or Sco-Cen within $70''$ (corresponding to a projected separation $\approx 10,000$ AU) of our discoveries. At wider separations, it is still possible for a pair of low-mass stars and/or brown dwarfs to be physically bound (Dhital et al. 2010; Deacon et al. 2014). However, such a binary is likely to have formed through capture in the natal cluster rather than as an initially bound system (Kouwenhoven et al. 2010). Thus, we conclude that all of our discoveries are likely to be free-floating brown dwarfs that formed as single objects.

[1] http://vizier.u-strasbg.fr/viz-bin/VizieR

4.5 Taurus Discoveries

Two of our discoveries, PSO J060.3+25 (L1) and PSO J077.1+24 (L2), reside at the projected outer edges of the nearby Taurus star-forming region. Figure 4.2 shows their sky locations in Taurus. In Section 4.5.1 we present confirmation that they are bona fide members of Taurus. We also estimate their masses (Section 4.5.2) and assess whether they have circumstellar disks (Section 4.5.3).

We first explore why these objects were not identified in previous studies of Taurus, a region that has been repeatedly searched for ultracool dwarfs. Our objects lie $\approx 8^\circ$ ($\approx$20 pc) from the projected center of Taurus, on opposite sides from each other. Many searches surveyed smaller and/or more central regions of Taurus that did not include our objects (e.g., Guieu et al. 2006; Luhman et al. 2009; Quanz et al. 2010; Rebull et al. 2010). Our objects also lie just outside the footprint of Spitzer images analyzed by Esplin et al. (2014). Our objects are very faint, especially at optical wavelengths, so previous searches using i-band photometry (e.g., Slesnick et al. 2006) were not able to detect them. Similarly, both objects lie within the area searched by Esplin et al. (2014) using WISE photometry, but are fainter than the $W1 \leq 14$ mag limit used in that search. Luhman (2006) would have detected PSO J077.1+24 in 2MASS photometry, but its $(J-H)_{\rm 2MASS} = 0.46 \pm 0.28$ mag color is bluer than the $(J-H)_{\rm 2MASS} \geq 0.6$ mag cut used in that search.[2] PSO J060.3+25 lies just outside the Luhman (2006) search area but would also have been excluded due to its relatively blue $(H-K_S)_{\rm 2MASS}$ color (also having a large error). We note also that Luhman (2006) used previously known low-mass members of Taurus as templates to define color cuts, and many of those members are reddened by local extinction. Our discoveries do not appear to be reddened, as discussed in Sections 4.5.1 and 4.5.1.

[2]We note the large error on this color is due to this object being near the detection limit of 2MASS. Our deeper MKO photometry (Table 2) shows this object has $(J-H)_{\rm MKO} = 0.75 \pm 0.06$ mag.

4.5.1 Evidence for Membership

Youth

Both PSO J060.3+25 and PSO J077.1+24 have VL-G gravity classes (Section 4.4.3). While more work is needed to calibrate the ages of VL-G objects (Allers & Liu 2013a), the classification suggests an age $\lesssim 30$ Myr, much younger than the field population.

Photometry

Figure 4.7 compares the photometry of PSO J060.3+25 and PSO J077.1+24 to that of known Taurus members from Esplin et al. (2014). The J vs. $J - K_S$ (2MASS) and $y_{\rm P1}$ vs. $y_{\rm P1} - W1$ color-magnitude diagrams for Taurus make evident the significant reddening in this region of the sky. We calculated reddening vectors for these color-magnitude diagrams using the $y_{\rm P1}$ coefficient from Schlafly & Finkbeiner (2011, their Table 6, $R_V = 3.1$) and the $J/K_S/W1$ coefficients from Davenport et al. (2014, their Table 3). We include these reddening vectors, scaled to an extinction of $A_V = 5$ mag, in Figure 4.7. Our two discoveries sit at the faint end of the unreddened cluster sequence, consistent with their projected locations on the unobscured outskirts of the region. While some young early-L dwarfs have unusually red $(J - K_S)_{\rm 2MASS}$ colors for their spectral types (e.g., Gagné et al. 2015c), we note that the $(J - K_S)_{\rm 2MASS}$ colors of our Taurus discoveries (1.45 ± 0.24 mag for PSO J060.3+25, 1.11 ± 0.26 mag for PSO J077.1+24) are consistent with those of older field dwarfs with the same spectral types (Schmidt et al. 2010; Faherty et al. 2013). However, both PSO J060.3+25 and PSO J077.1+24 have $W1 - W2$ colors (Figure 4.3) that are 3σ redder than those of field early-L dwarfs, a common sign of low gravity (Gizis et al. 2012).

Proper Motions

To assess the kinematic consistency of our discoveries with previously known members of Taurus, we created a list of proper motions for the Taurus stars and brown dwarfs from Esplin et al. (2014) that are not saturated in PS1. We obtained the proper motions from PS1

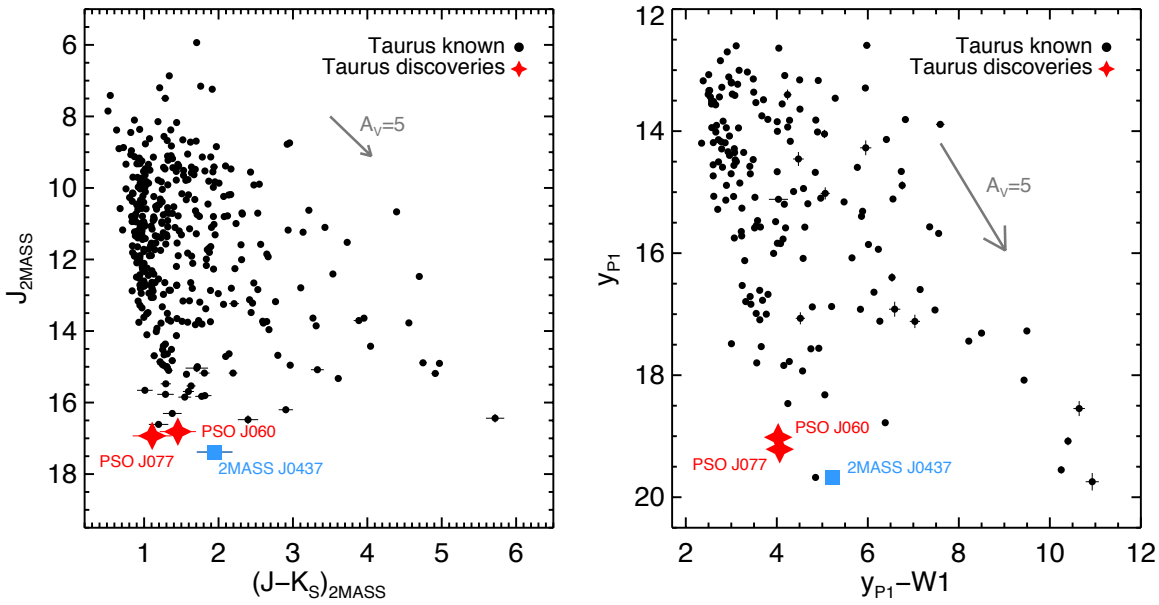

Figure 4.7 Comparison of the photometry of our discoveries in the Taurus star-forming region (red stars) to known Taurus members from Esplin et al. (2014) (black circles). We also highlight the known Taurus L1 dwarf 2MASS J0437+2331 (Section 4.5.1, blue square) and indicate reddening vectors equivalent to an extinction of $A_V = 5$ mag with gray arrows. *Left*: J vs. $J - K_S$ (2MASS) diagram. *Right*: $y_{\rm P1}$ vs. $y_{\rm P1} - W1$ diagram for Taurus objects not saturated in PS1. Both plots show an unreddened cluster sequence on the left, with many objects significantly reddened by the Taurus molecular cloud. Our two discoveries lie at the faint end of the cluster sequence and are minimally affected by extinction, consistent with their locations on the outer edges of Taurus.

Processing Version 3.2 (PV3.2), the same source as the proper motions of our discoveries (Section 4.4.4). We discuss our complete list of proper motions in detail in Appendix A. Figure 4.8 compares the proper motions of PSO J060.3+25 and PSO J077.1+24 with all reliable PS1 Taurus proper motions. We calculated a weighted mean proper motion for the known Taurus members of ($\mu_\alpha \cos\delta = 7.6 \pm 0.2,\ \mu_\delta = -17.4 \pm 0.2$ mas yr^{-1}), with a weighted rms of 4.9 mas yr^{-1} in R.A. and 6.4 mas yr^{-1} in Dec.

PSO J077.1+24 has a proper motion of ($14.1 \pm 12.5, -27.1 \pm 12.1$ mas yr^{-1}), consistent with the mean Taurus proper motion. Because the Taurus region has a number of distinct subgroups, we also compared the proper motion of PSO J077.1+24 to that of the closest subgroup on the sky identified by Luhman et al. (2009), L1544. This subgroup has a median proper motion of ($0.9 \pm 1, -17.6 \pm 1$ mas yr^{-1}; Luhman et al. 2009), consistent with PSO J077.1+24.

For PSO J060.3+25, we adopt the proper motion ($14.3 \pm 3.1, -26.4 \pm 3.2$ mas yr^{-1}) from Bouy et al. (2015). Our PS1 proper motion of ($19.0 \pm 8.2, -38.1 \pm 8.2$ mas yr^{-1}) is consistent, but the Bouy et al. (2015) measurement is more precise. The adopted proper motion is very similar to PSO J077.1+24 and consistent with our mean Taurus proper motion. The closest Taurus subgroup on the sky to PSO J060.3+25 identified by Luhman et al. (2009), B209 ($\approx 4^\circ$ away), has a mean proper motion of ($6.9 \pm 1, -22.3 \pm 1$ mas yr^{-1}; Luhman et al. 2009), consistent within 1.8σ in R.A. and 1.0σ in Dec.

PSO J060.3+25 (a.k.a. DANCe J040116.80+255752.2) was also previously identified by Sarro et al. (2014) and Bouy et al. (2015) as a high-probability (93%) member of the Pleiades cluster, based on $zYJHK_S$ photometry and astrometry. The Pleiades lie at a mean distance of 136.2 ± 1.2 pc (Melis et al. 2014), commensurate with the $\approx$145 pc distance to Taurus. The projected center of the Pleiades lies $\approx 3.5^\circ$ away from PSO J060.3+25, or $\approx$8 pc at the distance of the Pleiades, so it is possible that PSO J060.3+25 falls within the 9.5 ± 0.5 pc tidal radius of the Pleiades (Danilov & Loktin 2015). The mean proper motion for low-mass brown dwarfs ($0.012 - 0.025\ M_\odot$) in the Pleiades is ($21.6, -47.6$ mas yr^{-1}) with a dispersion of $\sigma_\mu = 7.5 \pm 6.1$ mas yr^{-1} (Zapatero Osorio et al. 2014b), so the proper motion

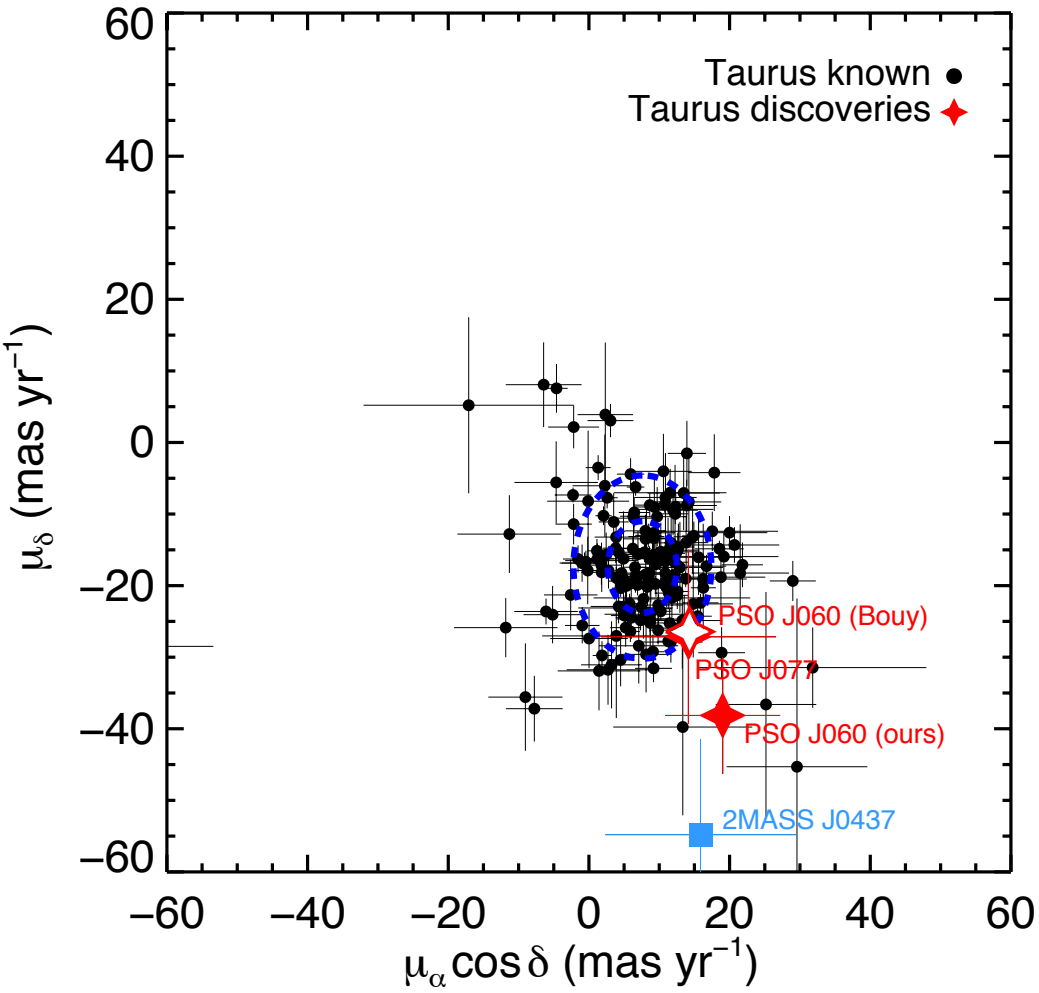

Figure 4.8 Vector-point diagram showing the proper motions of our discoveries in the Taurus star-forming region (red stars) and those of known Taurus members from Esplin et al. (2014) that are not saturated in PS1 and have reliable PS1 proper motion fits (black circles). We also include the only previously known L dwarf in Taurus, 2MASS J0437+2331 (Luhman et al. 2009), which we classify as L1. We adopt the proper motion for PSO J060.3+25 from Bouy et al. (2015), shown with an open red star. Note that the PS1 proper motion for PSO J077.1+24 and the Bouy et al. (2015) proper motion for PSO J060.3+25 are very similar and their symbols coincide in the figure. Both of these adopted proper motions are consistent with the mean Taurus proper motion, while the PS1 proper motion for 2MASS J0437+2331 is $\approx 2\sigma$ discrepant in μ_δ.

of PSO J060.3+25 is intermediate between the bulk motions of Taurus and the Pleiades, and consistent within 2σ with both groups. Our VL-G classification for PSO J060.3+25 suggests a younger age ($\lesssim$ 30 Myr) than for the Pleiades ($\approx$125 Myr; Stauffer et al. 1998b), although the age range of VL-G objects has not been firmly established (e.g., Liu et al. 2016). We note that Allers & Liu (2013b) classified several Pleiades members as VL-G, but they used spectra with mostly lower resolution ($R \approx 50$) and S/N ($\lesssim$20) than the prism spectra we present here for our discoveries, so we regard those classifications as provisional. In Figure 4.9 we also compare the J and K-band photometry of known Taurus members and our discoveries, as a function of spectral type, to known VLM members of the Pleiades. The published spectral types for the Pleiades members are derived from multiple sources and methods and are therefore heterogenous, but classification of these objects using the AL13 system shows a consistent result (Allers & Liu 2013b). Figure 4.9 shows that our discoveries have J magnitudes more consistent with the younger, brighter members of Taurus. We therefore find it more likely that PSO J060.3+25 is a member of the 1–2 Myr old Taurus region. A radial velocity measurement would help to further assess the Taurus membership of PSO J060.3+25.

Likelihood of Field Contamination

We investigated the possibility that PSO J060.3+25 or PSO J077.1+24 could be a foreground or background field object in the direction of Taurus by estimating the number of such contaminating field objects from our search. For this estimate, we generously defined the boundaries of the Taurus region to be $4^{\rm h}00^{\rm m} \leq \alpha \leq 5^{\rm h}15^{\rm m}$ and $14^\circ \leq \delta \leq 32^\circ$ (see Figure 4.2), covering 309.4 deg^2. Our search covered the entire sky between declinations -30° and $+70^\circ$ except for locations within 3° of the Galactic plane (Paper II), an area totaling 28,070 deg^2. (We noted in Section 4.2 that our search also avoided reddened regions identified by Cruz et al. 2003, but PSO J060.3+25 actually lies within one of these reddened regions, so we include those regions in this estimate.)

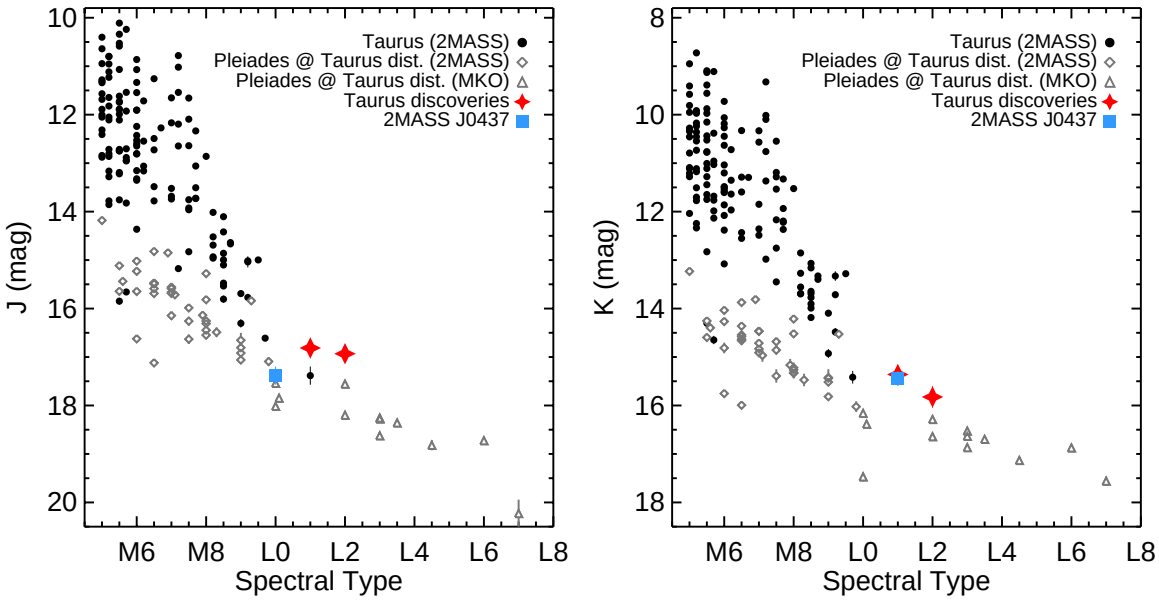

Figure 4.9 J (*left*) and K (*right*) apparent magnitudes as a function of spectral type for our discoveries in the Taurus star-forming region (red stars) compared with known members of Taurus (Esplin et al. 2014, black circles) and the Pleiades (grey open symbols). Pleiades magnitudes have been adjusted by +0.136 mag to place the objects at the distance of Taurus (145 pc). We use 2MASS photometry (Skrutskie et al. 2006, diamonds) for the brighter Pleiades members, and MKO photometry from the UKIDSS Galactic Clusters Survey (Lawrence et al. 2012, triangles) for members too faint to be detected by 2MASS. We also highlight the previously coolest known member of Taurus, 2MASS J0437+2331 (blue square), which we classify as L1 on the AL13 system. Our discoveries lie $\gtrsim$1 mag above the Pleiades sequence but are consistent with an extension of the Taurus sequence, supporting membership in the younger Taurus region. References for Pleiades spectral types: Bihain et al. (2006, 2010); Festin (1998); Martín et al. (1996, 1998a,b, 2000); Pinfield et al. (2003); Stauffer et al. (1998a,b); Steele & Jameson (1995); Zapatero Osorio et al. (1997, 2014c).

We found a total of fourteen VL-G L0–L2 dwarfs in our search, including two previously known objects and three discoveries that we consider to be strong VL-G candidates. We would therefore expect our search to find 0.15 VL-G L0–L2 dwarfs in an arbitrary Taurus-sized area of sky.

In addition, we assessed the likelihood that an early-L dwarf observed in the direction of Taurus would have a proper motion consistent with members of Taurus (as do PSO J060.3+25 and PSO J077.1+24). We used the Besançon Galactic model[3] (Robin et al. 2003) to generate a synthetic population of field M dwarfs in a volume spanning our Taurus boundaries between 50 pc and 240 pc. We assigned uncertainties to the synthetic proper motions using an astrometric error vs. K_S relationship derived from our Taurus proper motions (Section 4.5.1). Assuming that early-L dwarfs have the same kinematics as M dwarfs in the field, we used Monte Carlo trials to determine that $20.3 \pm 0.2\%$ of early-L dwarfs in the direction of Taurus will have proper motions within 3σ of the mean Taurus $\mu_\alpha \cos\delta$ and μ_δ.

We would therefore expect our search to find $(3.13 \pm 0.03) \times 10^{-2}$ VL-G dwarfs within our Taurus boundaries having proper motions consistent with Taurus membership. Poisson statistics give us a probability of 96.9% that neither PSO J060.3+25 nor PSO J077.1+24 is an interloping field object in the direction of Taurus, and a negligible 5×10^{-4} probability that both objects are contaminants.

Comparison with 2MASS J04373705+2331080

Prior to our discoveries, 2MASS J0437+2331 was the only known free-floating L dwarf member of Taurus, discovered and classified as L0 by Luhman et al. (2009). We used the SpeX Prism spectrum for 2MASS J0437+2331 from Bowler et al. (2014) to assign a near-infrared spectral type of L1 $\pm$ 1, based on a calculated type of L0.9 $\pm$ 0.9 using the AL13 indices (Section 4.4.2).

[3]http://model.obs-besancon.fr

Luhman et al. (2009) claimed membership in Taurus for 2MASS J0437+2331 based on weaker Na I and K I absorption features in its red-optical spectrum, which are recognized signs of youth (Kirkpatrick et al. 2006), along with its central projected location in Taurus. Similarly to two of our Sco-Cen discoveries, the spectrum for 2MASS J0437+2331 does not have a high enough S/N for us to confidently assign a gravity class, but Figure 4.12 shows that it more closely resembles the L1 VL-G standard than the field standard, confirming its young age. Figure 4.7 shows that the $y_{P1}JK_SW1$ photometry of 2MASS J0437+2331 is also similar to that of PSO J060.3+25 and PSO J077.1+24, and consistent with being a slightly reddened member of Taurus. 2MASS J0437+2331 has a proper motion of $(15.9 \pm 13.5, -54.8 \pm 13.4$ mas yr$^{-1})$, consistent with our mean motion of Taurus in R.A. but nearly 2σ different in Dec. We note that 2MASS J0437+2331 satisfies all the criteria for our search (Section 4.2), except that it lies well within the excluded reddened region of Cruz et al. (2003).

We compare the spectrum of 2MASS J0437+2331 to those of PSO J060.3+25 and PSO J077.1+24 in Figures 4.10 and 4.11, along with the appropriate field (Kirkpatrick et al. 2010) and VL-G (AL13) standards. Interestingly, the near-IR spectrum of 2MASS J0437+2331 is notably redder than those of our discoveries, and its position in the color-magnitude diagrams in Figure 4.7 is consistent with an extinction of $A_V \approx 2-4$ mag. This redness was also noted by Alves de Oliveira et al. (2013), who calculated an extinction of $A_V = 2.1-3.3$ mag for 2MASS J0437+2331 based on 2MASS photometry and comparison to the near-IR spectra of other young M and L dwarfs. However, Luhman et al. (2009) found an extinction of $A_J = 0$ mag for 2MASS J0437+2331 using an optical spectrum, which is more sensitive to dust-induced reddening than longer near-IR wavelengths. Our near-IR spectrum also closely resembles the L2 VL-G standard in color. It therefore appears that the red near-IR colors of 2MASS J0437+2331 are photospheric in nature.

Overall, we find supporting evidence that 2MASS J0437+2331 is a member of Taurus, and we find the photometric and spectral qualities of PSO J060.3+25 and PSO J077.1+24 to be very similar to those of 2MASS J0437+2331. The only notable difference is the redder

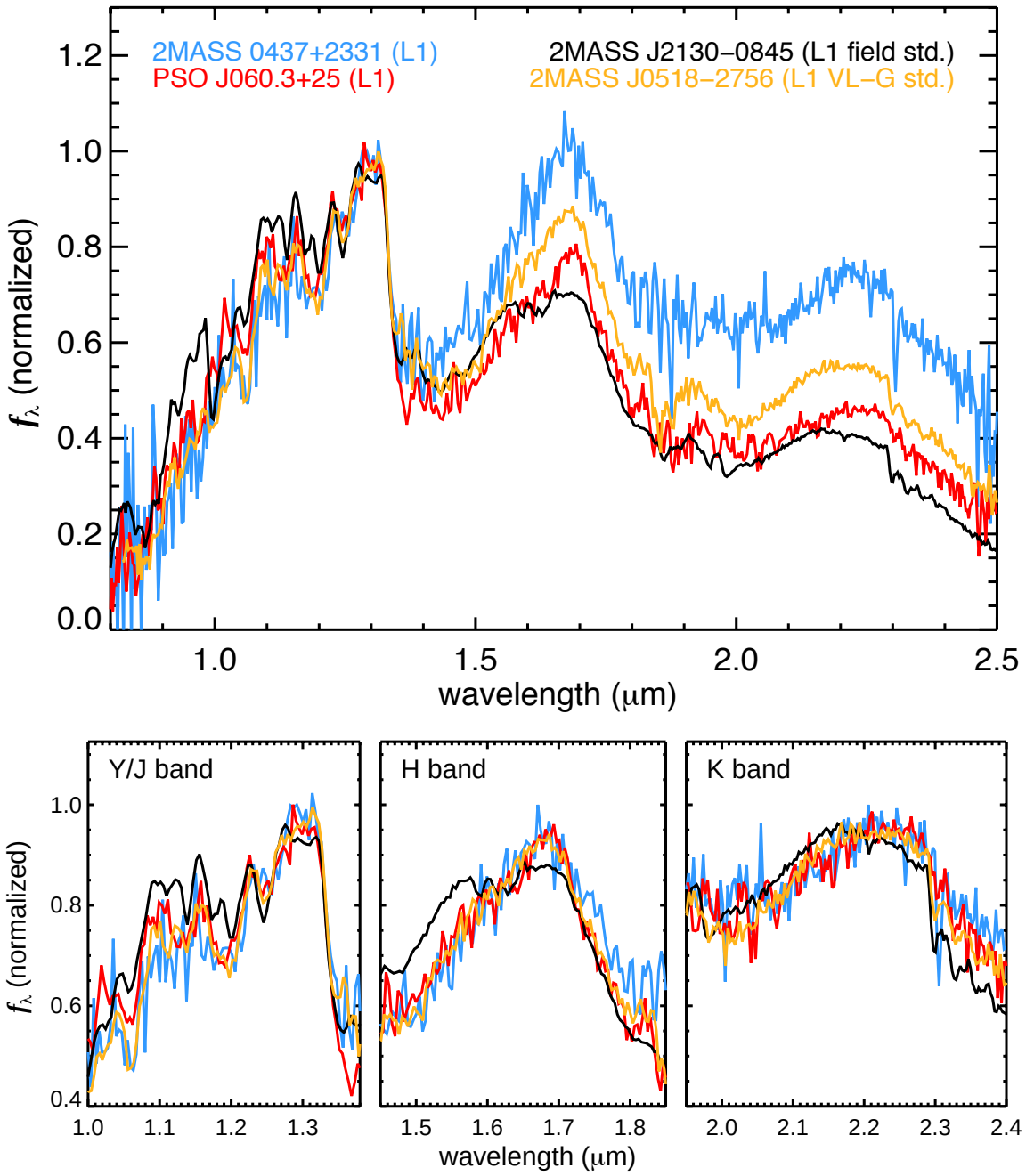

Figure 4.10 *Top*: The SpeX Prism spectrum of 2MASS J0437+2331 (blue) from Bowler et al. (2014), overplotted with PSO J060.3+25 (red) along with the field (black; Kirkpatrick et al. 2010) and VL-G (orange; Allers & Liu 2013a) standards of the same spectral type (L1) as PSO J060.3+25. All four spectra are normalized at the *J*-band peak. 2MASS J0437+2331 is notably redder than PSO J060.3+25 as well the L1 VL-G standard, while PSO J060.3+25 has colors similar to those of the field standard. *Bottom*: The same four spectra plotted separately for Y/J, H, and K bands, normalized separately for each band to compare the spectral shapes in each band. The two young Taurus objects and the L1 VL-G standard have similar shapes in all bands, distinct from the older field standard.

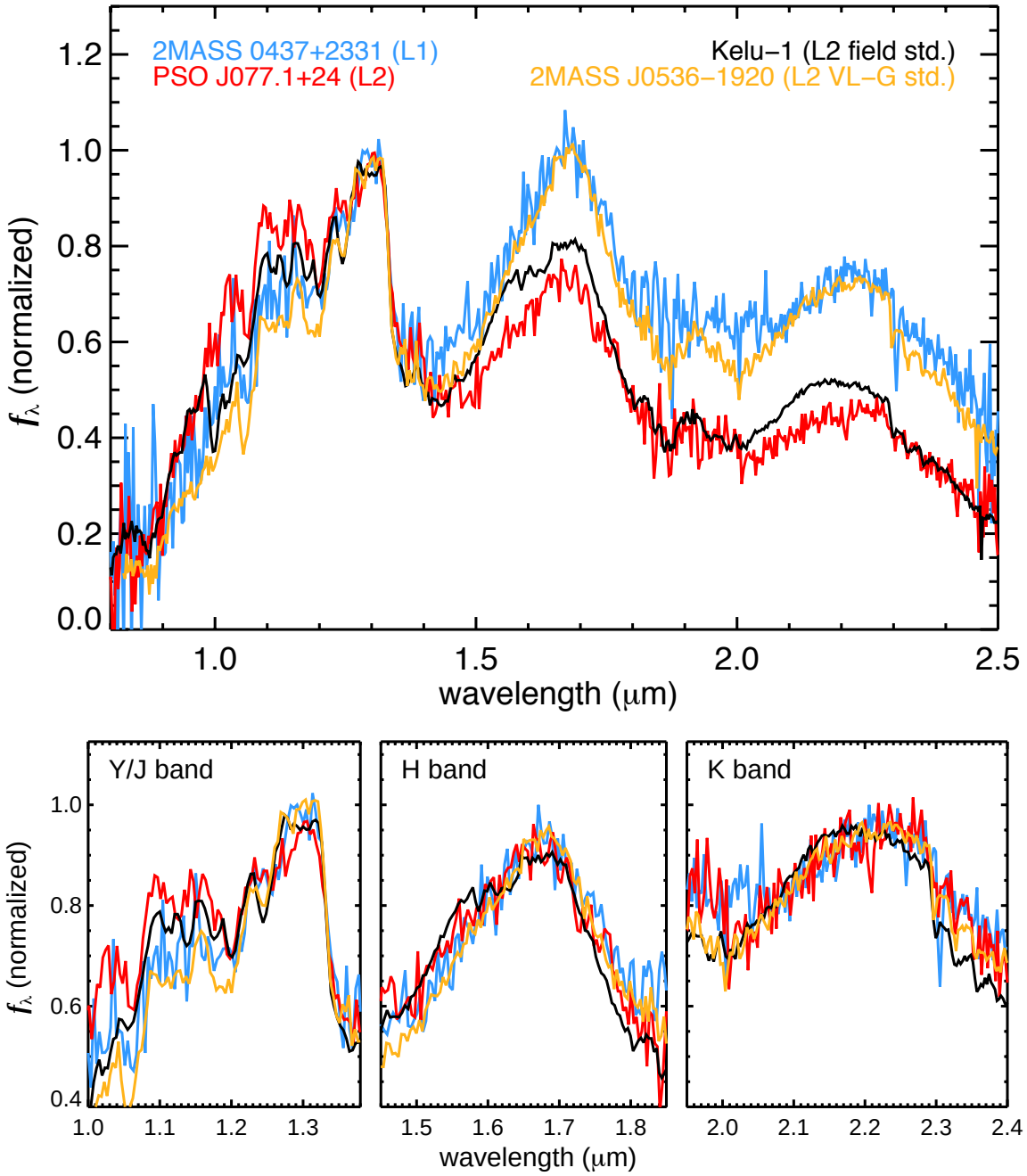

Figure 4.11 The SpeX Prism spectrum of 2MASS J0437+2331 (blue) from Bowler et al. (2014), overplotted with PSO J077.1+24 (red) along with the field (black; Kirkpatrick et al. 2010) and VL-G (orange; Allers & Liu 2013a) standards of the same spectral type (L2) as PSO J077.1+24, using the same format as Figure 4.10. 2MASS J0437+2331 is significantly redder than PSO J077.1+24 but has similar colors to the L2 VL-G standard, while PSO J077.1+24 has colors more similar to those of the field standard.

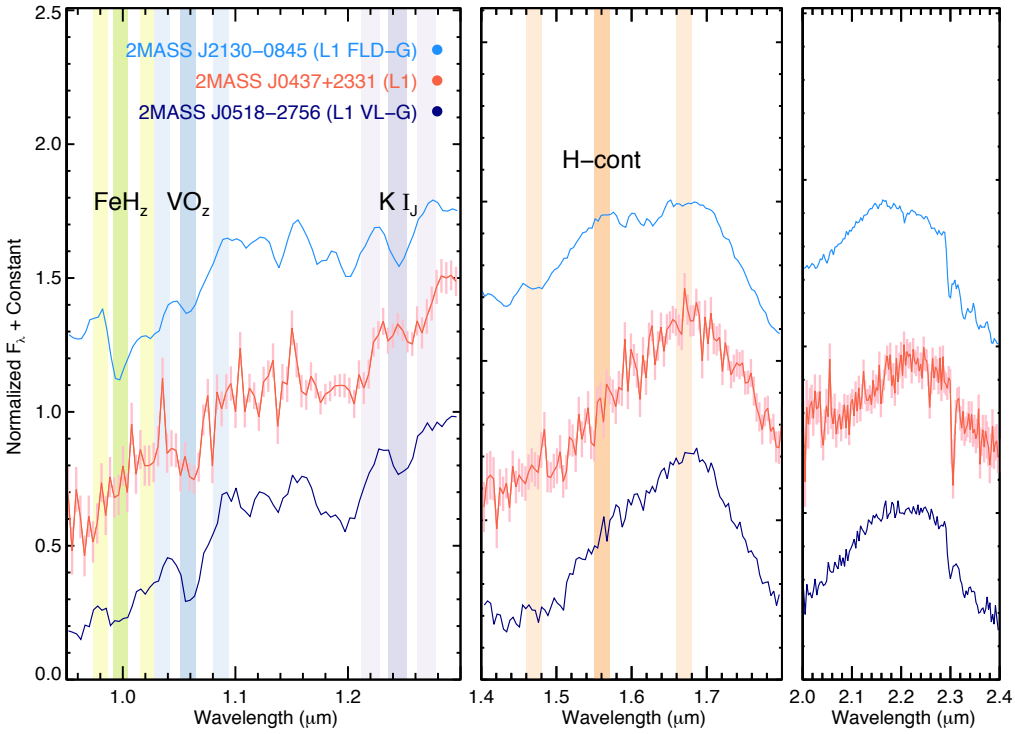

Figure 4.12 Same as Figure 4.5 but showing the SpeX Prism spectrum for 2MASS J0437+2331 (Luhman et al. 2009; Bowler et al. 2014). We did not determine a gravity class for 2MASS J0437+2331 due to low spectral S/N, but its FeH_z, VO_z, K I$_J$, and H-cont features do resemble those of the L1 VL-G standard (Allers & Liu 2013a).

overall near-infrared spectral slope of 2MASS J0437+2331, which does not appear to be due to interstellar extinction (Luhman et al. 2009).

Membership in Taurus

Because of the locations of PSO J060.3+25 and PSO J077.1+24 on Taurus color-magnitude diagrams, their plausibly consistent proper motions, their VL-G gravity classifications, their photometric and spectral similarity to the known Taurus L1 dwarf 2MASS J0437+2331, and the low probability of contamination by field objects, we consider PSO J060.3+25 and PSO J077.1+24 to be bona fide members of Taurus. Their near-infrared colors, consistent with those of field early-L dwarfs but bluer than 2MASS J0437+2331, confirm that the near-infrared redness observed in some low-gravity early-L dwarfs (e.g., Gizis et al. 2012; Faherty et al. 2013; see also Aller et al. 2016) is not a universal feature even for very young (1–2 Myr) L1 and L2 dwarfs.

4.5.2 Luminosities and Masses

To estimate the masses of our Taurus discoveries, we assumed a distance of 145 ± 15 pc and an age of 1–2 Myr (Kraus & Hillenbrand 2009a). We first calculated bolometric luminosities for each object using our spectral types, the $K_{\rm MKO}$ bolometric corrections of Liu et al. (2010, their Table 6), and the distance to Taurus. We then used the Lyon/DUSTY evolutionary models[4] (Chabrier et al. 2000) and our $L_{\rm bol}$ values to interpolate masses at the age of Taurus. We propagated the uncertainties on our spectral types ($\pm$1 subtype), $K_{\rm MKO}$ magnitudes, bolometric correction, distance, and age into our mass determinations using Monte Carlo simulations, and we quote 68% confidence limits. We used normal distributions for each uncertainty except for age, for which we used a uniform distribution spanning 1–2 Myr to avoid unreasonably young ages. We estimate masses of $6.0^{+0.9}_{-0.8}$ $M_{\rm Jup}$ for PSO J060.3+25 and $5.9^{+0.9}_{-0.8}$ $M_{\rm Jup}$ for PSO J077.1+24 (Table 4.7). We also applied this method to 2MASS J0437+2331 using $K_{\rm MKO} = 15.20 \pm 0.02$ mag from the UKIDSS Galactic

[4]The more recent BHAC15 models (Baraffe et al. 2015) do not extend to masses below $0.01 M_{\odot}$ ($\approx 10 M_{\rm Jup}$).

Clusters Survey (Lawrence et al. 2007, 2013). We estimate $\log(L_{\rm bol}/L_{\odot}) = -3.17^{+0.9}_{-1.0}$ dex and a mass of $7.1^{+1.1}_{-1.0}$ $M_{\rm Jup}$ for 2MASS J0437+2331, consistent with the masses of our discoveries and the 4–7 $M_{\rm Jup}$ estimate of Luhman et al. (2009).

With no evidence of companionship to any nearby star or of unresolved binarity (Section 4.4.5), our discoveries are among the lowest mass free-floating substellar objects ever discovered, similar to 2MASS J0437+2331, the young β Pictoris Moving Group L dwarf PSO J318.5338−22.8603 (8.3 ± 0.5 $M_{\rm Jup}$; Liu et al. 2013; Allers et al. 2016), the young TW Hydrae Associaton L dwarfs 2MASS J11193254−1137466 (4.3–7.6 $M_{\rm Jup}$; Kellogg et al. 2016) and WISEA J114724.10−204021.3 (5–13 $M_{\rm Jup}$; Schneider et al. 2016b), the AB Doradus Moving Group T dwarf SDSS J111010.01+011613.1 (≈10–12 $M_{\rm Jup}$; Gagné et al. 2015a), and the field Y dwarf WISE J085510.83−071442.5 (3–10 $M_{\rm Jup}$; Luhman 2014; Leggett et al. 2015). They provide significant evidence that free-floating planetary-mass objects can form as part of normal star-formation processes.

For comparison, we also converted spectral types into effective temperatures, and then used the DUSTY models and our $T_{\rm eff}$ values to estimate masses. No empirically calibrated conversion of spectral type to $T_{\rm eff}$ has been determined for very young L dwarfs, so we extrapolated the scale of Luhman et al. (2003, 2008), arriving at 2000 K for the L1 dwarf and 1800 K for the L2 dwarf. We assumed an error of ±100 K for each object. With this distance-independent approach, we estimate masses of $7.1^{+1.4}_{-1.1}$ $M_{\rm Jup}$ for PSO J060.3+25 and $5.2^{+0.9}_{-0.8}$ $M_{\rm Jup}$ for PSO J077.1+24. If instead we use the field dwarf (i.e., not young) SpT-to-$T_{\rm eff}$ conversion of Stephens et al. (2009, Eq. 3), we find temperatures of 2112 ± 100 K for the L1 dwarf and 1971 ± 100 K for the L2 dwarf, resulting in masses of $8.6^{+2.0}_{-1.6}$ $M_{\rm Jup}$ for PSO J060.3+25 and $6.8^{+1.3}_{-1.1}$ $M_{\rm Jup}$ for PSO J077.1+24.

We note also that a recent study by Daemgen et al. (2015) identified evidence suggesting an older sub-population of Taurus with an age of ≈20 Myr. If confirmed, and our discoveries are in fact members of this sub-population, the older age would lead to a factor of ≈3 increase in our mass estimates.

4.5.3 Evidence for Circumstellar Disks

Many low-mass stellar members of Taurus are known to host circumstellar disks (e.g., Andrews et al. 2013; Esplin et al. 2014). We searched for evidence of elevated fluxes at mid-infrared wavelengths that would indicate the presence of circumstellar disks around our Taurus discoveries. We fit the BT-Settl grid of synthetic spectra from Baraffe et al. (2015) to our 0.85–2.45 μm prism spectra of PSO J060.3+25, PSO J077.1+24, and 2MASS J0437+2331 following the method of Bowler et al. (2011). In summary, the models are smoothed to the resolving power of the data and resampled to the same wavelength grid. The 1.60–1.65 μm and 1.8–1.95 μm regions are ignored to avoid incomplete methane line lists and low S/N portions of our spectra. The spectra are flux-calibrated to each object's J-band photometry. A scale factor, equal to the square of the object's radius divided by its distance, is calculated by minimizing the χ^2 value following Cushing et al. (2008). Assuming a distance of 145 ± 15 pc to Taurus allows us to simultaneously infer the radius at each grid point.

The results of the fits are shown in Figure 4.13. The best-fit synthetic spectra ($T_{\rm eff}$=1800 K, log g=5.5 dex [cgs] for both of our discoveries and $T_{\rm eff}$=1600 K, log g=5.5 dex for 2MASS J0437+2331) offer relatively poor fits to the data, largely failing to reproduce the observed H and K-band spectral shapes. The best-fit models have field-age surface gravities, contrary to the VL-G classes indicated by the observed spectra, so we include synthetic spectra with the same $T_{\rm eff}$ as the best-fit models but with log g=3.5 dex (roughly the gravity expected for VL-G objects) in Figure 4.13 for comparison. The inferred radii for our discoveries are all $\geq$2 $R_{\rm Jup}$, consistent with expectations for very young objects still undergoing gravitational contraction (e.g., Burrows et al. 1997). Synthetic photometry of the best fitting models is generally consistent with the observed photometry from Pan-STARRS, UKIRT, and the $W1$ (3.4 μm) filter from WISE, but is significantly lower for the $W2$ (4.6 μm) channel at the 7–9σ level. This may represent evidence of thermal excess from a disk around both objects, but we note that the observed $W2$ photometry is much more consistent with the log g=3.5 dex model spectra. The discrepancy at $W2$ is therefore

likely to be a consequence of the poor model fits, or possibly a result of a systematic error in the model atmospheres, for example from imperfect opacity sources.

The Taurus objects have photometric upper limits in WISE for the $W3$ (12 μm) and $W4$ (22 μm) bands, with one exception. PSO J060.3+25 has a reported 2.6σ detection in $W4$ that is significantly brighter than the synthetic model photometry. We visually inspected the WISE images of this object and could not confirm that the $W4$ detection is distinct from noise. A clear excess at 22 μm would indicate the presence of a disk, but this marginal detection requires confirmation by deeper imaging.

We note that Luhman et al. (2009) also found no excess at mid-IR wavelengths in *Spitzer* photometry that would indicate the presence of a disk around 2MASS J0437+2331.

4.6 Scorpius-Centaurus Discoveries

The Scorpius-Centaurus Association is the nearest OB association to the Sun. We have discovered six new late-M and early-L members of Sco-Cen. Using the boundaries defined by de Zeeuw et al. (1999), PSO J237.1−23 (M7) and PSO J239.7−23 (L0) lie within the Upper Scorpius subgroup (hereinafter Upper Sco), while PSO J228.6−29 (L1), PSO J229.2−26 (L0), PSO J231.7−26 (L0), and PSO J231.8−29 (L0) sit on the northern outskirts of the Upper Centaurus Lupus subgroup (hereinafter UCL). Figure 4.2 shows the sky locations of our discoveries. Upper Sco and UCL are among the reddened regions on the sky identified by Cruz et al. (2003) that we excluded from our search, and our discoveries lie just outside the excluded areas.

Like Taurus, the Upper Sco region has been searched multiple times for brown dwarfs. Unlike in Taurus, more than a dozen L0–L2 dwarfs have previously been confirmed in Upper Sco, in particular by Lodieu et al. (2008) using early release data from the UKIDSS Galactic Clusters Survey (GCS). Our discoveries were not found by that search, nor by Lodieu et al. (2006, 2011), because of incomplete coverage of the region by the early version of GCS. They also remained undetected by searches using optical data as part of the selection

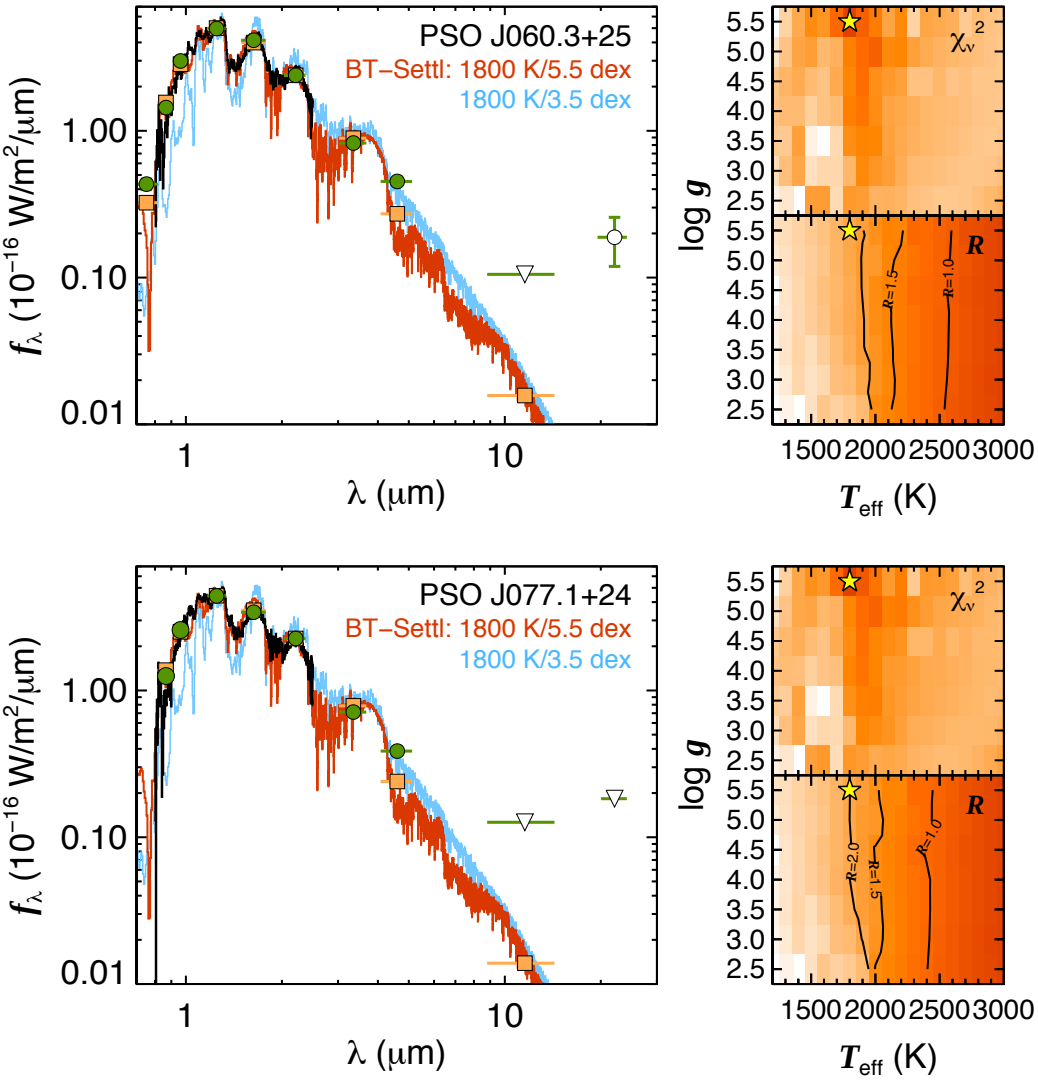

Figure 4.13 Best-fit BT-Settl model spectra (Baraffe et al. 2015) for our two Taurus discoveries and 2MASS J0437+2331. For each object, the left-hand plot includes our prism spectrum (black), the best-fit model spectrum (red), and the synthetic spectrum with the same $T_{\rm eff}$ as the best-fit model but with $\log g = 3.5$ (roughly that expected for VL-G objects) in blue. In addition, we plot observed PS1/MKO/AllWISE photometry (green circles), and synthetic photometry for the best-fit model (orange squares). Upper limits for $W3$ (12 μm) and $W4$ (22 μm) are plotted with open triangles; the $W4$ detection for PSO J060.3+25 (open circle) is marginal at 2.6σ. The right-hand plots show the χ^2 surface for the model ($T_{\rm eff}$, $\log g$) fits (*top*) and the inferred radius in units of $R_{\rm Jup}$ (*bottom*). The best-fit models match the observed spectra fairly poorly, particular in the H and K-band morphology. The observed excess flux relative to the best-fit models at $W2$ (4.6 μm) in all three objects may indicate the presence of a disk, but the excess is not seen relative to the low-gravity model spectra, and may therefore be the result of a systematic error in the model atmospheres.

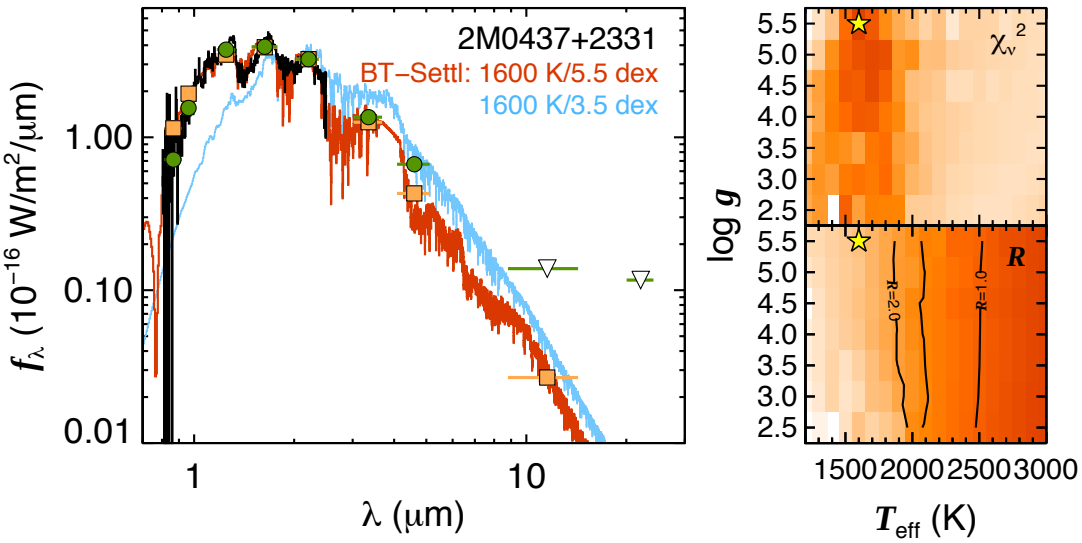

Figure 4.13 continued.

process (Martín et al. 2004; Slesnick et al. 2006, 2008). The objects were detected in GCS Data Release 8 and later versions, but were only observed in H and K bands, and so were not included in the search of Dawson et al. (2011, 2013) who required Z and J photometry in their selection process. PSO J237.1−23 was identified as a candidate member of Upper Sco by Lodieu (2013) as part of their "HK-only sample", but PSO J239.7−23 is too faint to qualify for this sample. Searches for young ultracool dwarfs have not focused on UCL, so our four discoveries lie outside regions targeted by previous efforts.

In this Section we follow the structure of Section 4.5, presenting the evidence that our discoveries are members of Sco-Cen (Section 4.6.1), estimating their masses (Section 4.6.2), and comparing their SEDs to model atmospheres to look for evidence of circumstellar disks (Section 4.6.3).

4.6.1 Evidence for Membership

Youth

Four of our six Sco-Cen discoveries have VL-G gravity classes, suggesting ages $\lesssim 30$ Myr. The other two, PSO J228.6−29 and PSO J229.2−26, have lower-S/N spectra that do not permit robust calculation of the AL13 gravity-sensitive indices but nevertheless show clear visual indications of low gravity (Section 4.4.3).

Photometry

Figure 4.14 demonstrates the consistency of our six discoveries' photometry with that of known Upper Sco members from Luhman & Mamajek (2012, hereinafter LM12), Dawson et al. (2014), and Rizzuto et al. (2015), and with photometric/astrometric candidates from unreddened regions in the UKIDSS GCS Data Release 10 (Lodieu 2013, their Table A1). The LM12 catalog contains a handful of objects that are reddened by interstellar extinction, and we include reddening vectors (Section 4.5.1) scaled to an extinction of $A_V = 2$ mag in Figure 4.14. Most of our discoveries lie along the unreddened cluster sequence of the Upper Sco J vs. $J-K$ and $y_{\rm P1}$ vs. $y_{\rm P1}-W1$ color-magnitude diagrams, fully consistent with the reddening-free sample of Lodieu (2013). PSO J237.1−23 is redder than the cluster sequence in $y_{\rm P1}-W1$, likely evidence for a circumstellar disk (Section 4.6.3). As with PSO J060.3+25 and PSO J077.1+24 in Taurus, the Sco-Cen objects have $(J-K_S)_{\rm 2MASS}$ colors that are consistent with field L0–L1 dwarfs but have $W1-W2$ colors that are 1–3σ redder than the field population (Gizis et al. 2012; Faherty et al. 2013).

Proper Motion

We compare the proper motions of our Sco-Cen discoveries to the proper motions of several literature sources in Figure 4.15. Pecaut et al. (2012) calculated proper motions for F-type stars in Upper Sco and UCL, and Lodieu (2013) calculated proper motions for a list of unreddened photometric/astrometric members and candidates in UKIDSS

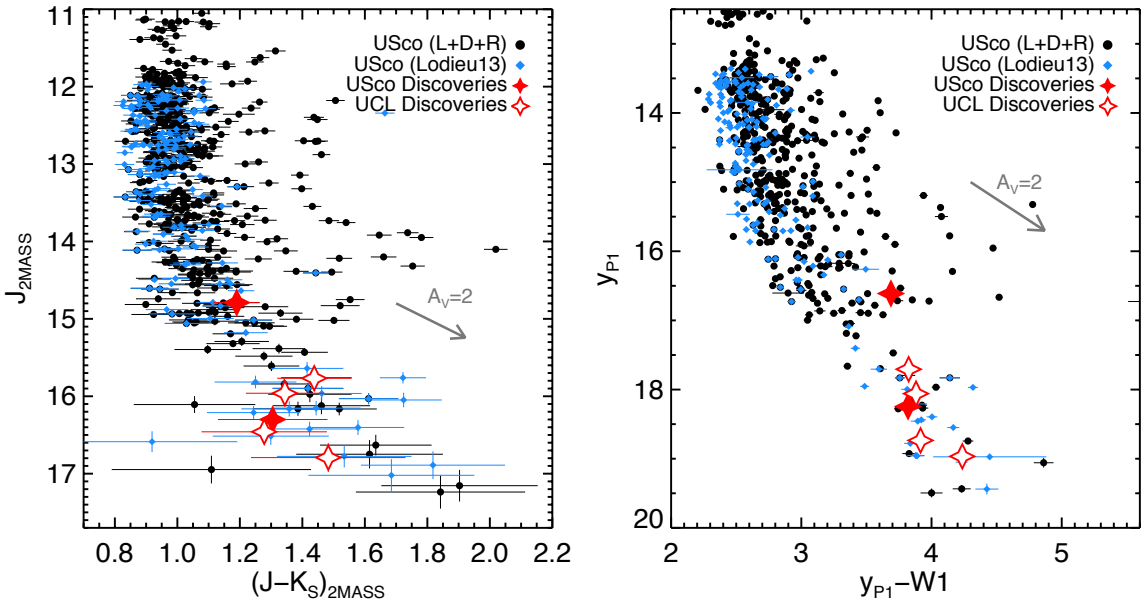

Figure 4.14 Comparison of the photometry of our discoveries in Upper Sco (USco, filled red stars) and Upper Centaurus Lupus (UCL, open red stars) to known members of Upper Sco from Luhman & Mamajek (2012), Dawson et al. (2014), and Rizzuto et al. (2015) (black circles, labeled "L+D+R" in the legend) and known and candidate Upper Sco members from UKIDSS GCS (Lodieu 2013, blue diamonds). *Left*: J vs. $J-K$ (MKO) diagram. *Right*: $y_{\rm P1}$ vs. $y_{\rm P1}-W1$ diagram for non-saturated objects in PS1. We include reddening vectors (gray arrows) scaled to an extinction of $A_V = 2$ mag. All six of our discoveries have photometry lying along the cluster sequences. The brighter Upper Sco discovery, PSO J237.1−23, has a redder $y_{\rm P1}-W1$ color suggesting the presence of a circumstellar disk (Section 4.6.3).

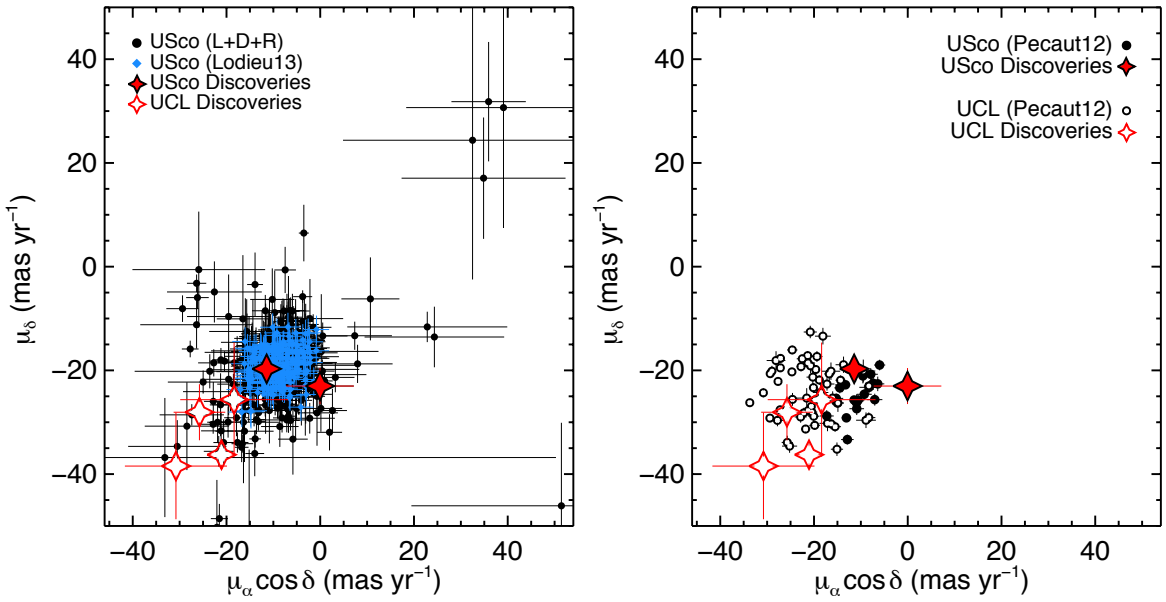

Figure 4.15 Vector-point diagrams comparing the proper motions of our discoveries in Upper Scorpius (USco, filled red stars) and Upper Centaurus Lupus (UCL, open red stars) to those of Sco-Cen objects from the literature. *Left*: We show our proper motions for objects in the Upper Sco lists of LM12, Dawson et al. (2014), and Rizzuto et al. (2015) (black circles, labeled "L+D+R" in the legend) that are not saturated in PS1 and have reliable proper motion fits, and the proper motions of known and candidate Upper Sco members from UKIDSS GCS (Lodieu 2013, blue diamonds). *Right*: Proper motions of F-type stars in Upper Sco (black filled circles) and UCL (black open circles) from Pecaut et al. (2012). All six of our Sco-Cen discoveries have proper motions consistent with all literature sources.

GCS. LM12 do not quote proper motions for their catalog of Upper Sco members, so we obtained PS1 Processing Version 3.2 (PV3.2) proper motions for these objects as well as those from Dawson et al. (2014) and Rizzuto et al. (2015). From these PS1 proper motions we calculated a weighted mean proper motion for known Upper Sco members of ($\mu_\alpha \cos\delta = -8.5 \pm 0.1$, $\mu_\delta = -19.6 \pm 0.1$ mas yr^{-1}), with a weighted rms of 4.3 mas yr^{-1} in R.A. and 5.6 mas yr^{-1} in Dec. Our complete list of PS1 proper motions for objects from this combined catalog that are not saturated in PS1 is described in Appendix B. Figure 4.15 demonstrates the consistency of the proper motions of our discoveries with all literature sources.

Likelihood of Field Contamination

We estimated the likelihood that any of our Sco-Cen discoveries could be interloping foreground or background field objects, using the same approach as in Section 4.5.1. Upper Sco and UCL are distinct regions with different ages and bulk proper motions (Pecaut et al. 2012), so we considered them separately.

We defined the boundaries of Upper Sco to be $343^\circ \leq l \leq 360^\circ$ and $10^\circ \leq b \leq 30^\circ$ (Figure 4.2). The portion of this region surveyed by PS1 (i.e., north of $\delta = -30^\circ$) covers 281.0 deg^2. We found that $28.42 \pm 0.11\%$ of a synthetic population (Besançon Galactic model) of field M dwarfs in the direction of Upper Sco will have proper motions within 3σ of the mean Upper Sco $\mu_\alpha \cos\delta$ and μ_δ (Section 4.6.1). We estimate that our search would find $(3.99 \pm 0.02) \times 10^{-2}$ field VL-G dwarfs within the projected boundaries of Upper Sco having proper motions consistent with Upper Sco membership. We find a probability of 96.1% that both PSO J237.1−23 and PSO J239.7−23 are members of Upper Sco.

For UCL, we used the data for F stars from Pecaut et al. (2012) to calculate a weighted mean proper motion of ($\mu_\alpha \cos\delta = -23.0 \pm 0.1$, $\mu_\delta = -23.8 \pm 0.1$ mas yr^{-1}) with a weighted rms of 5.7 mas yr^{-1} in R.A. and 4.9 mas yr^{-1} in Dec. Only 0.51% of our synthetic M dwarf population have proper motions consistent within 3σ with the mean UCL motion. PSO J228.6−29, PSO J229.2−26, PSO J231.7−26, and PSO J231.8−29 all have proper motions consistent with UCL, so the probability that any of them is a field interloper is negligible based on proper motions alone.

Membership in Scorpius-Centaurus

All six of our discoveries in the direction of Sco-Cen have VL-G gravity classifications or clear spectral indications of low gravity. Their positions in color-magnitude diagrams, proper motions, and very low probability of contamination by field objects confirm that they are members of Sco-Cen.

4.6.2 Luminosities and Masses

We calculated bolometric luminosities and estimated the masses of our Sco-Cen discoveries using the method described in Section 4.5.2. We adopted a distance of 145 ± 15 pc (de Zeeuw et al. 1999; Preibisch & Zinnecker 1999) and an age of 11 ± 2 Myr (Pecaut et al. 2012) for Upper Sco. The mean distance to UCL is 140 ± 2 pc (de Zeeuw et al. 1999). de Bruijne (1999) found a substantial depth of 50 ± 20 pc for UCL, but all four of our UCL discoveries have photometry consistent with members of Upper Sco (Figure 4.14), so we used the same distance uncertainty as Upper Sco and adopted a UCL distance of 140 ± 15 pc, along with an age of 16 ± 1 Myr (Pecaut et al. 2012). We used normal distributions for the age and distance uncertainties in our Monte Carlo simulations. Our luminosity and mass estimates for our Sco-Cen discoveries are listed in Table 4.7. The masses span $15 - 36$ $M_{\rm Jup}$, near the low-mass end of the brown dwarf regime and comparable to the lowest mass members known in these regions (Lodieu et al. 2011; Aller et al. 2013).

4.6.3 A Candidate Circumstellar Disk

At ages $\gtrsim$10 Myr, our discoveries in Sco-Cen are less likely to harbor circumstellar disks than are the $\approx$1–2 Myr Taurus objects (e.g., Mathews et al. 2012). However, LM12 have demonstrated that $\approx$25% of M5–L0 objects in Upper Sco have disks detectable at mid-infrared wavelengths. They developed color vs. spectral type relationships to identify stars and brown dwarfs with candidate circumstellar disks, using colors including $K_S - W2$, $K_S - W3$, and $K_S - W4$. Our L dwarf discoveries were not detected in $W3$ or $W4$, and LM12 caution that the $K_S - W2$ colors do not reliably discriminate between excess flux from a disk and rapidly reddening photospheres beyond spectral type M8.5. We nevertheless checked the $K_S - W2$ colors of our L dwarfs (including the Taurus discoveries), and none are redder than the typical colors of Upper Sco M9–L1 dwarfs (LM12), so we cannot identify any candidate disk hosts among these objects.

PSO J237.1−23, the lone M dwarf (M7) among our discoveries, has significantly mid-infrared redder colors than those of late-M dwarfs lacking disks, strongly suggesting the

presence of a circumstellar disk. The $K_S - W2$ and $K_S - W3$ colors both satisfy the LM12 criteria by $\gtrsim 5\sigma$. PSO J237.1−23 also has a marginal $W4$ detection at 8.75 ± 0.45 mag, which if real would give the object a $K_S - W4$ color over 3.5 mag redder than the LM12 limit for disk-hosting M7 dwarfs. We therefore consider PSO J237.1−23 to be a clear candidate circumstellar disk host, joining over a dozen other candidates in Upper Sco with spectral types M7 or later (LM12).

We also looked for evidence of excess mid-infrared fluxes using the method described in Section 4.5.3, fitting the BT-Settl model spectra (Baraffe et al. 2015) to the prism spectra of our Sco-Cen discoveries. The results are shown in Figure 4.16. As with our Taurus discoveries, the best-fit synthetic spectra for our Sco-Cen objects have field-age gravities inconsistent with the low-gravity features in the observed spectra, fit the emprical JHK-band morphologies fairly poorly, and have radii $\geq 2\ R_{\rm Jup}$ (consistent with models). Synthetic photometry from the models is generally consistent with the observed photometry. The significantly lower synthetic flux at $W2$ seen in our Taurus discoveries (Figure 4.13) is present here for two of the six Sco-Cen objects, although again this is likely to be an consequence of poor model fits. Our disk candidate, PSO J237.1−23, does show an excess in observed flux relative to the best-fit and low-gravity models at all four *WISE* bands, although the model synthetic fluxes are higher than observations in the optical bands, indicating that the fit has failed to correctly capture the observed SED.

4.7 Summary

As part of a wide-field search for L/T transition dwarfs using the Pan-STARRS1 and *WISE* surveys, we have serendipitously discovered eight young late-M and early-L dwarfs in the nearby Taurus and Scorpius-Centaurus star-forming regions. PSO J060.3+25 (spectral type L1) and PSO J077.1+24 (L2) are members of Taurus. Both have VL-G gravity classifications indicating ages $\lesssim 30$ Myr, photometry consistent with previously known ultracool members of Taurus, and proper motions consistent with the Taurus population. We estimate the

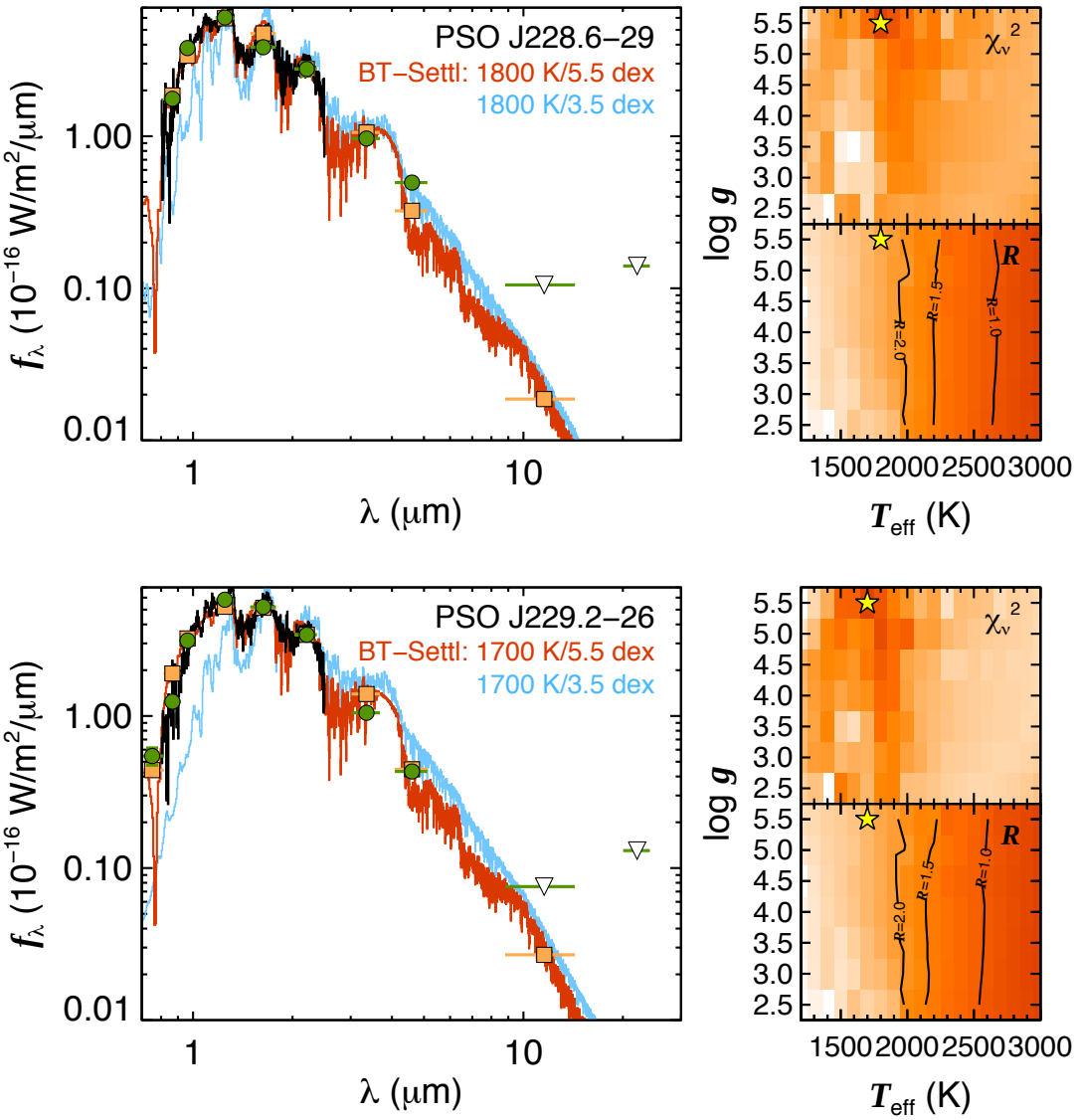

Figure 4.16 Same as Figure 4.13, but showing the best-fit BT-Settl model spectra (Baraffe et al. 2015) to our Sco-Cen discoveries. The best-fit models again match the observed spectra fairly poorly, particularly in the H and K-band morphology. The observed excess flux at $W2$ (4.6 μm) seen in Figure 4.13 is seen here in three of the six objects, but the excess again disappears in two cases (PSO J228.6−29 and PSO J239.7−23) when compared to the low-gravity models expected for VL-G objects. However, PSO J237.1−23 does show a clear excess in flux relative to the models at all four *WISE* bands ($\geq$ 3.4 μm), implying the presence of a circumstellar disk.

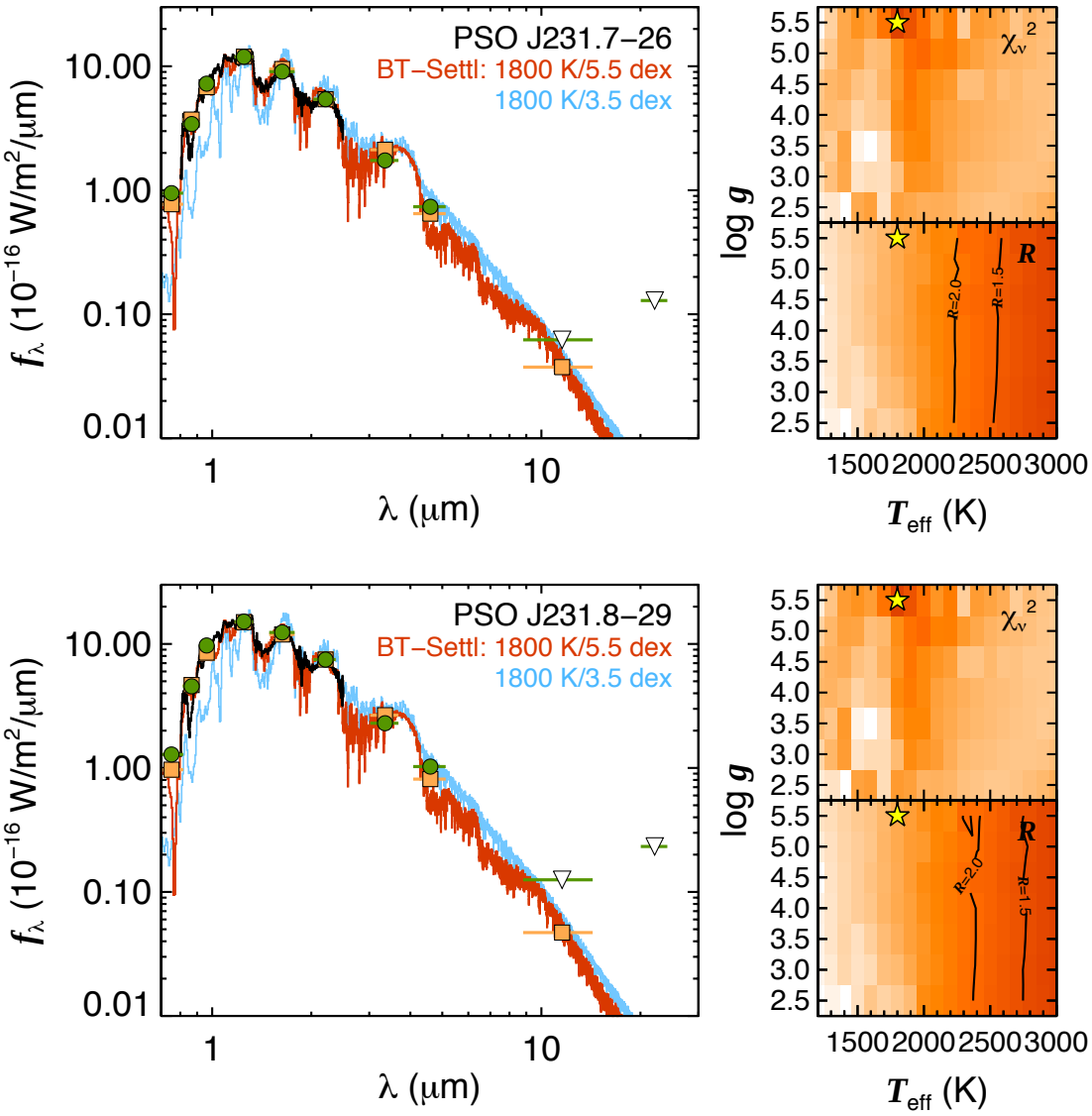

Figure 4.16 continued.

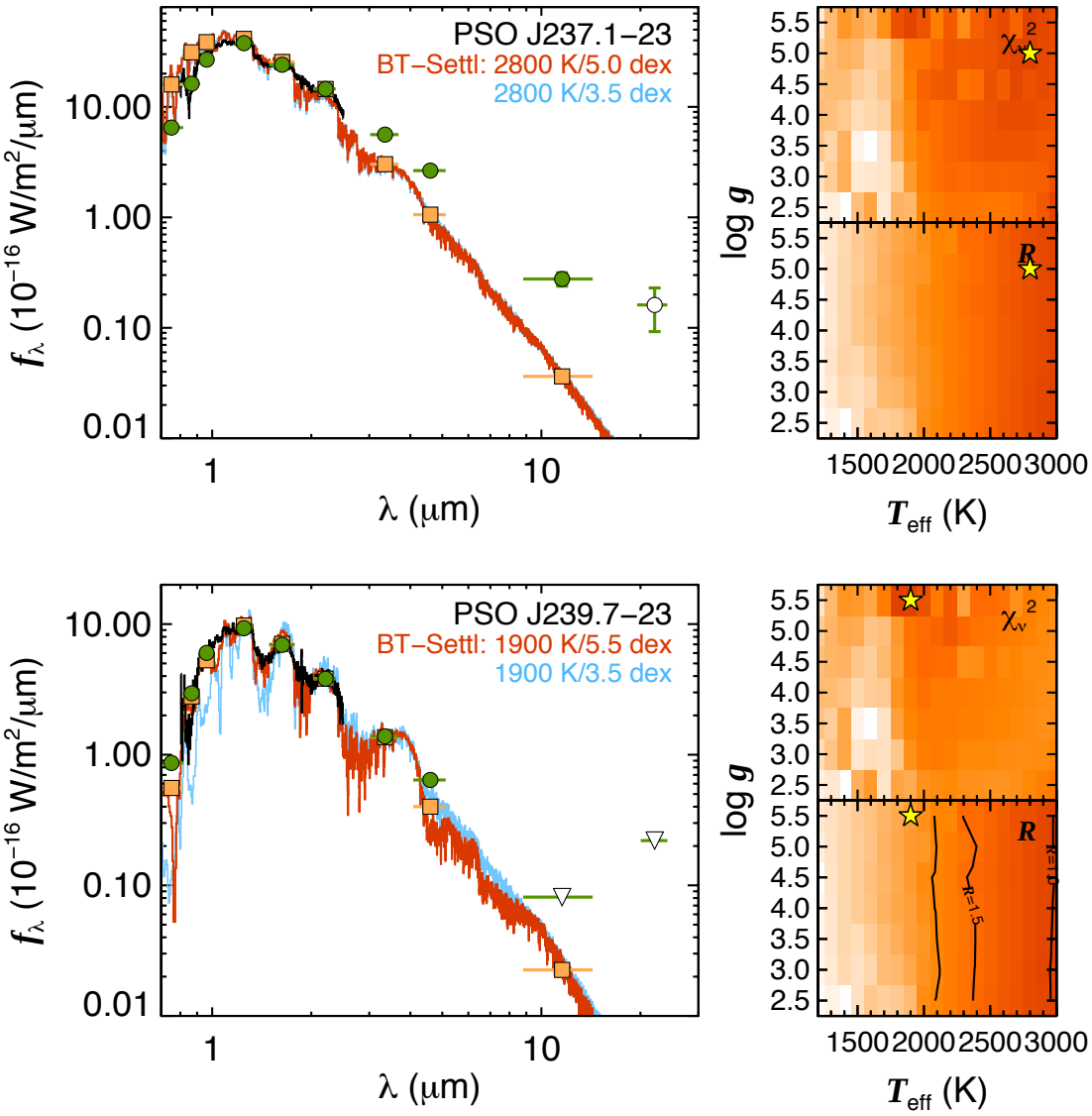

Figure 4.16 continued.

probability that neither object is a foreground (or background) field dwarf to be 97%. The spectral and photometric properties of our two discoveries are also similar to the only previously known free-floating L dwarf in Taurus, 2MASS J0437+2331 (Luhman et al. 2009). At the young (≈1–2 Myr) age of Taurus, PSO J060.3+25 and PSO J077.1+24 have estimated masses of ≈6 $M_{\rm Jup}$, and they join 2MASS J0437+2331 (≈7 $M_{\rm Jup}$, spectral type L1) as the lowest-mass isolated known members of Taurus. PSO J077.1+24 is additionally the coolest known free-floating object discovered in Taurus to date.

PSO J060.3+25 was previously identified by Sarro et al. (2014) and Bouy et al. (2015) as DANCe J040116.80+255752.2, a likely ultracool member of the Pleiades (age ≈ 125 Myr) based on its photometry and astrometry. Our spectrum confirms the late spectral type of PSO J060.3+25, but its VL-G gravity class implies an age ($\lesssim$30 Myr) consistent with the much younger Taurus star-forming region, and its near-infrared photometry is more consistent with other VLM members of Taurus.

The other six M7–L1 dwarf discoveries lie on the outskirts of the Upper Scorpius and Upper Centaurus-Lupus associations (ages ≈ 11–16 Myr), with estimated masses $\approx 15 - 36$ $M_{\rm Jup}$. Four have VL-G gravity classifications; our spectra for the other two did not have enough S/N for confident gravity classification, but visual inspection finds they have clear spectral signatures of low gravity. The photometry and proper motions of all six objects are fully consistent with membership in Scorpius-Centaurus. Lodieu (2013) previously identified PSO J237.1−23 as an astrometric and photometric candidate member of Upper Sco, which we confirm with our independent discovery and spectroscopy.

We found no spectral indications that any of our discoveries have unresolved companions, nor did we find any comoving objects nearby. The Taurus objects represent strong evidence that normal star formation processes can produce isolated objects with masses as low as ≈6 $M_{\rm Jup}$.

The $J - K$ colors of all seven young L dwarf discoveries are consistent with those of older field L0–L2 dwarfs. This contrasts with the redder $J - K$ colors of some previously discovered young early-L dwarfs, and confirms that near-infrared redness is not a universal

feature of very young (1–2 Myr) brown dwarfs. Our discoveries do have $W1 - W2$ colors that are redder than those of early-L field objects, which we identify as the primary reason we discovered these objects during a search for L/T transition dwarfs.

We fit BT-Settl synthetic spectra (Baraffe et al. 2015) to our observed spectra and found that the best-fit models reproduce our spectra relatively poorly in the near-infrared. At 4.6 μm (*WISE* $W2$ band), all three Taurus objects and two Sco-Cen objects show a significant observed excess flux over the model predictions. These elevated fluxes are suggestive of the presence of a circumstellar disk but may also indicate a source of systematic error in the model atmospheres. The M7 dwarf PSO J237.1−23 shows strong excess fluxes at $W2$, $W3$, and possibly at $W4$, making it a likely host for a circumstellar disk.

Our discovery of these eight young brown dwarfs in well-searched regions of the sky, while looking for older objects with cooler spectral types, has a few important implications:

- The combination of PS1 and *WISE* photometry is a powerful tool for identifying young ultracool dwarfs (see also Paper II).
- Unusually red $W1 - W2$ colors in late-M and early-L dwarfs may indicate the objects are young (Figure 4.3), providing leverage for searches for young M/L dwarfs.
- There are likely to be more young planetary-mass brown dwarfs that could be discovered with focused searches in even well-studied star-forming regions.

Table 4.1. Pan-STARRS1 and AllWISE Photometry

Name	i_{P1} (mag)	z_{P1} (mag)	y_{P1} (mag)	AllWISE Name	$W1$ (mag)	$W2$ (mag)	$W3$ (mag)	$W4$ (mag)
Taurus Discoveries								
PSO J060.3200+25.9644	21.61 ± 0.04	20.06 ± 0.02	19.02 ± 0.02	J040116.80+255752.0	14.99 ± 0.04	14.32 ± 0.05	>11.98	8.58 ± 0.39
PSO J077.1033+24.3809	21.62 ± 0.10	20.18 ± 0.05	19.21 ± 0.06	J050824.81+242251.3	15.15 ± 0.05	14.49 ± 0.07	>11.78	>8.61
Taurus (previously known)								
2MASS J04373705+2331080[a]	···	20.75 ± 0.03	19.67 ± 0.10	J043737.06+233107.3	14.45 ± 0.03	13.90 ± 0.05	>11.68	>9.10
Scorpius-Centaurus Discoveries								
PSO J228.6773−29.7088	21.41 ± 0.04	19.87 ± 0.05	18.74 ± 0.03	J151442.59−294231.9	14.82 ± 0.03	14.22 ± 0.05	>11.83	>8.90
PSO J229.2353−26.6737	21.36 ± 0.05	20.14 ± 0.04	18.97 ± 0.02	J151656.49−264025.3	14.73 ± 0.04	14.37 ± 0.06	>12.34	>8.98
PSO J231.7899−26.4494	20.73 ± 0.04	19.10 ± 0.02	18.06 ± 0.02	J152709.57−262658.0	14.18 ± 0.03	13.79 ± 0.04	>12.55	>8.99
PSO J231.8942−29.0600	20.40 ± 0.06	18.81 ± 0.02	17.71 ± 0.01	J152734.62−290335.8	13.88 ± 0.03	13.43 ± 0.03	>11.79	>8.35
PSO J237.1470−23.1489	18.69 ± 0.01	17.41 ± 0.01	16.61 ± 0.01	J154835.30−230855.5	12.92 ± 0.03	12.40 ± 0.03	10.93 ± 0.15	8.75 ± 0.45
PSO J239.7015−23.2665	20.88 ± 0.05	19.26 ± 0.01	18.24 ± 0.02	J155848.37−231559.1	14.43 ± 0.03	13.94 ± 0.05	>12.26	>8.41

Note. — Pan-STARRS1 photometry is mean PSF magnitudes from Pan-STARRS1 Data Release 1.

[a]Discovered by Luhman et al. (2009). Also known as PSO J069.4044+23.5186.

Table 4.2. Near-Infrared Photometry

Name	2MASS Photometry				MKO Photometry		
	2MASS Name	J_{2MASS} (mag)	H_{2MASS} (mag)	$K_{S,2MASS}$ (mag)	J_{MKO} (mag)	H_{MKO} (mag)	K_{MKO} (mag)
Taurus Discoveries							
PSO J060.3+25	J04011678+2557527	16.81 ± 0.17	15.73 ± 0.14	15.36 ± 0.17	16.93 ± 0.04	16.10 ± 0.03	[15.53 ± 0.07]
PSO J077.1+24	J05082480+2422518	16.93 ± 0.14	16.47 ± 0.25	15.82 ± 0.22	17.06 ± 0.04	16.31 ± 0.04	15.59 ± 0.03
Taurus (previously known)							
2MASS J0437+2331	J04373705+2331080	17.38 ± 0.19	16.13 ± 0.15	15.44 ± 0.15	17.24 ± 0.02[a]	16.16 ± 0.01[a]	15.20 ± 0.02[b]
Scorpius-Centaurus Discoveries							
PSO J228.6−29	J15144258−2942315	16.79 ± 0.19	15.95 ± 0.15	15.31 ± 0.16	16.72 ± 0.05	16.18 ± 0.05	[15.37 ± 0.11]
PSO J229.2−26	J15165651−2640251	16.46 ± 0.13	15.98 ± 0.18	15.18 ± 0.15	16.76 ± 0.03	15.85 ± 0.02	[15.14 ± 0.08]
PSO J231.7−26	J15270961−2626574	15.96 ± 0.08	15.21 ± 0.11	14.62 ± 0.10	15.98 ± 0.02	15.25 ± 0.03	[14.64 ± 0.05]
PSO J231.8−29	J15273464−2903354	15.77 ± 0.09	14.83 ± 0.07	14.33 ± 0.08	[[15.72 ± 0.09]]	[[14.91 ± 0.08]]	[[14.29 ± 0.08]]
PSO J237.1−23	J15483530−2308557	14.79 ± 0.05	14.13 ± 0.07	13.60 ± 0.05	[[14.73 ± 0.06]]	[[14.19 ± 0.07]]	[[13.57 ± 0.06]]
PSO J239.7−23	J15584839−2315589	16.30 ± 0.11	15.35 ± 0.11	15.00 ± 0.13	16.25 ± 0.02	15.54 ± 0.02	[15.02 ± 0.07]

Note. — All 2MASS photometry is from the 2MASS Point Source Catalog (Cutri et al. 2003). MKO photometry was obtained using UKIRT/WFCAM (Best et al. 2015) unless enclosed in brackets or otherwise indicated. H_{MKO} and K_{MKO} magnitudes enclosed in single brackets were synthesized using our observed J_{MKO} magnitudes and our low-resolution spectra (Section 4.3). MKO magnitudes enclosed in double brackets were synthesized using the 2MASS magnitudes for the corresponding filters and our low-resolution spectra.

[a]From the UKIDSS Galactic Plane Survey (DR6; Lucas et al. 2012).

[b]From the UKIDSS Galactic Clusters Survey (DR9; Lawrence et al. 2013).

Table 4.3. IRTF/SpeX Observations

Object	Date (UT)	Slit (")	R ($\lambda/\Delta\lambda$)	$t_{\rm int}$ (s)	S/N[a]	A0 V Standard
PSO J060.3+25[b]	2013 Jan 25	0.8	75	1920	37	HD 27761
	2013 Nov 23	0.8	75	960		HD 31069
PSO J077.1+24[b]	2013 Jan 26	0.8	75	840	34	HD 34977
	2013 Nov 23	0.8	75	1320		HD 38245
PSO J228.6−29	2013 Apr 18	0.8	75	720	24	HD 146880
PSO J229.2−26	2013 Apr 17	0.8	75	2880	26	HD 143822
PSO J231.7−26	2015 May 18	0.5	120	1440	49	HD 133466
PSO J231.8−29	2015 May 29	0.5	120	3600	84	HD 146606
PSO J237.1−23	2015 May 18	0.5	120	720	79	HD 133466
PSO J239.7−23	2013 Apr 18	0.8	75	720	33	HD 147013

[a]Mean J-band (1.20–1.31 μm) S/N per resolution element.

[b]We present a combined spectrum and S/N from the two observations (Section 4.3).

Table 4.4. Index-based Spectral Types from Allers & Liu (2013a)

Name	Index-derived Spectral Types					Visual SpT[b]	Adopted SpT[c]
	H_2O	H_2OD	H_2O–1	H_2O–2	Avg. SpT[a]		
Taurus Discoveries							
PSO J060.3+25	$L1.3^{+1.4}_{-1.4}$	···	$L0.8^{+1.2}_{-1.2}$	$L0.5^{+1.1}_{-1.2}$	$L0.9^{+0.9}_{-0.9}$	L0.5	L1
PSO J077.1+24	$L2.0^{+1.2}_{-1.2}$	···	$L0.1^{+1.2}_{-1.2}$	$L1.5^{+0.8}_{-1.0}$	$L1.7^{+0.9}_{-0.9}$	L1	L2
Taurus (previously known)							
2MASS J0437+2331[d]	$L1.5^{+1.3}_{-1.4}$	···	$L0.1^{+1.3}_{-1.3}$	$L0.0^{+1.2}_{-1.2}$	$L0.9^{+0.9}_{-0.9}$	L1.5	L1
Scorpius-Centaurus Discoveries							
PSO J228.6−29	$L1.4^{+1.9}_{-2.2}$	$L1.7^{+1.4}_{-1.4}$	$L1.1^{+1.4}_{-1.4}$	$M9.5^{+1.7}_{-1.9}$	$L0.8^{+1.1}_{-1.3}$	L0.5	L1
PSO J229.2−26	···	···	$M9.8^{+1.3}_{-1.3}$	···	$M9.8^{+1.3}_{-1.3}$	L0	L0
PSO J231.7−26	$M9.9^{+0.9}_{-0.9}$	···	$M9.6^{+1.1}_{-1.2}$	$L0.0^{+0.9}_{-0.9}$	$M9.9^{+0.6}_{-0.6}$	L0	L0
PSO J231.8−29	$L0.3^{+0.6}_{-0.6}$	···	$L1.0^{+1.1}_{-1.1}$	$M9.9^{+0.6}_{-0.6}$	$L0.2^{+0.4}_{-0.4}$	L0	L0
PSO J237.1−23	$M7.1^{+0.5}_{-0.6}$	···	$M7.3^{+1.2}_{-1.2}$	$M7.1^{+0.6}_{-0.6}$	$M7.1^{+0.4}_{-0.4}$	M7.5	M7
PSO J239.7−23	$L0.1^{+1.2}_{-1.2}$	···	$M9.5^{+1.3}_{-1.3}$	$L0.1^{+1.3}_{-1.4}$	$L0.0^{+0.9}_{-0.9}$	M9	L0

[a]Calculated as the weighted average of the spectral types from Monte Carlo trials for all indices, excluding those that fell outside the valid range for each index.

[b]Spectral types determined by visual comparison with the VL-G spectral standards proposed by Allers & Liu (2013a). Uncertainties for these visual spectral types are ±1 subtype for all objects.

[c]The index-based average spectral types rounded to the nearest subtype, which we adopt as the final spectral types for our discoveries with uncertainties of ±1 subtype.

[d]Classified as L0 by Luhman et al. (2009) using an optical spectrum.

Table 4.5. Index-Based Spectral Types from Burgasser et al. (2006a) for L dwarfs

Name	Index Values (Derived Spectral Types)[a]						Adopted SpT[b]
	H_2O-J	CH_4-J	H_2O-H	CH_4-H	CH_4-K	Avg. SpT	
Taurus Discoveries							
PSO J060.3+25	0.867 (L2.3)	0.933 (<T0)	0.780 (L3.4)	1.118 (<T1)	1.122 (<L0)	L2.8±0.8	L1
PSO J077.1+24	0.946 (L0.4)	0.924 (<T0)	0.803 (L2.5)	1.167 (<T1)	1.137 (<L0)	L1.5±1.4	L2
Taurus (previously known)							
2MASS J0437+2331[d]	0.810 (L3.9)	0.942 (<T0)	0.788 (L3.1)	1.190 (<T1)	1.147 (<L0)	L3.5±0.6	L1
Scorpius-Centaurus Discoveries							
PSO J228.6−29	0.852 (L2.7)	0.837 (<T0)	0.735 (L5.2)	1.126 (<T1)	1.146 (<L0)	L3.9±1.8	L1
PSO J229.2−26	0.918 (L1.0)	0.969 (<T0)	0.755 (L4.4)	1.119 (<T1)	1.111 (<L0)	L2.7±2.4	L0
PSO J231.7−26	0.920 (L1.0)	0.927 (<T0)	0.841 (L1.0)	1.167 (<T1)	1.135 (<L0)	L1.0±0.5[c]	L0
PSO J231.8−29	0.923 (L0.9)	0.905 (<T0)	0.821 (L1.7)	1.150 (<T1)	1.136 (<L0)	L1.3±0.6	L0
PSO J237.1−23	0.978 (<L0)	0.918 (<T0)	0.929 (<L0)	1.053 (<T1)	1.026 (<L0)	···	M7
PSO J239.7−23	0.971 (L0.0)	0.913 (<T0)	0.810 (L2.2)	1.071 (<T1)	1.106 (<L0)	L1.1±1.5	L0

[a]Spectral types calculated using the polynomials defined in Burgasser (2007a).

[b]For description see Section 4.4.2 and Table 4.4.

[c]The two contributing index-based spectral types are both L1.0, so we adopt an uncertainty of 0.5 subtypes.

[d]Classified as L0 by Luhman et al. (2009) using an optical spectrum.

Table 4.6. Low-Resolution Gravity Indices from Allers & Liu (2013a)

Name	FeH_z	VO_z	KI_J	H-cont	Index Scores[a]	Gravity Score[b]	Gravity Class	Adopted SpT
				Taurus Discoveries				
PSO J060.3+25	$1.006^{+0.035}_{-0.036}$	$1.203^{+0.032}_{-0.034}$	$1.038^{+0.016}_{-0.016}$	$0.971^{+0.022}_{-0.023}$	2122 (2122)	$2.0^{+0.0}_{-0.5}$	VL-G	L1
PSO J077.1+24	$1.043^{+0.039}_{-0.042}$	$1.196^{+0.029}_{-0.030}$	$0.994^{+0.017}_{-0.017}$	$0.977^{+0.025}_{-0.026}$	2122 (2122)	$2.0^{+0.0}_{-0.5}$	VL-G	L2
				Scorpius-Centaurus Discoveries				
PSO J231.7−26	$1.075^{+0.020}_{-0.021}$	$1.214^{+0.015}_{-0.015}$	$1.032^{+0.011}_{-0.011}$	$0.993^{+0.015}_{-0.015}$	2n22 (2n22)	$2.0^{+0.0}_{-0.0}$	VL-G	L0
PSO J231.8−29	$1.075^{+0.011}_{-0.011}$	$1.239^{+0.009}_{-0.009}$	$1.061^{+0.006}_{-0.006}$	$0.995^{+0.008}_{-0.008}$	2122 (2122)	$2.0^{+0.0}_{-0.0}$	VL-G	L0
PSO J237.1−23	$1.056^{+0.019}_{-0.019}$	$1.045^{+0.014}_{-0.014}$	$1.026^{+0.009}_{-0.009}$	$0.999^{+0.007}_{-0.007}$	2n22 (2n22)	$2.0^{+0.0}_{-0.0}$	VL-G	M7
PSO J239.7−23	$1.032^{+0.034}_{-0.035}$	$1.101^{+0.025}_{-0.025}$	$1.065^{+0.019}_{-0.019}$	$0.974^{+0.025}_{-0.026}$	2n12 (2n12)	$2.0^{+0.0}_{-1.0}$	VL-G	L0

Note. — This table includes the discoveries for which our spectrum has high enough S/N to extract reliable measurements of the AL13 gravity indices, corroborated by visual inspection. Our spectra for PSO J228.6−29 and PSO J229.2−26 and the 2MASS J0437+2331 spectrum from Bowler et al. (2014) did not yield reliable gravity scores, but do show visual indications of low gravity (Sections 4.4.3 and 4.5.1).

[a]Scores in parentheses were determined using the original AL13 classification scheme, in which objects with index values corresponding to INT-G but within 1σ of the FLD-G value are classified with a score of "?".

[b]The overall gravity score and the 68% confidence limits were calculated as described in Aller et al. (2016).

Table 4.7. Proper Motions, Luminosities, and Masses

Name	SpT	$\mu_\alpha \cos\delta$[a] (mas yr^{-1})	μ_δ[a] (mas yr^{-1})	χ^2_ν	$N_{\rm ep}$	Δt (yr)	$\log(L_{\rm bol}/L_\odot)$ (dex)	Mass[b] ($M_{\rm Jup}$)
Taurus (age = 1.5 ± 0.5 Myr, distance = 145 ± 15 pc)								
PSO J060.3+25	L1	19.0 ± 8.2	-38.1 ± 8.2	0.8	43	17.2	$-3.32^{+0.09}_{-0.10}$	$6.0^{+0.9}_{-0.8}$
		14.3 ± 3.1[c]	-26.4 ± 3.2[c]		29[c]	12.9[c]		
PSO J077.1+24	L2	14.1 ± 12.5	-27.1 ± 12.1	0.6	27	16.0	$-3.34^{+0.09}_{-0.10}$	$5.9^{+0.9}_{-0.8}$
2MASS J0437+2331	L1	15.9 ± 13.5	-54.8 ± 13.4	0.5	16	15.0	$-3.17^{+0.09}_{-0.10}$	$7.1^{+1.1}_{-1.0}$
Upper Centaurus-Lupus (age = 16 ± 1 Myr, distance = 140 ± 15 pc)								
PSO J228.6−29	L1	-18.4 ± 11.5	-25.6 ± 11.0	1.3	18	15.4	$-3.29^{+0.10}_{-0.10}$	$15.1^{+0.6}_{-0.6}$
PSO J229.2−26	L0	-30.8 ± 10.9	-38.4 ± 10.3	0.9	29	15.3	$-3.18^{+0.09}_{-0.11}$	$15.7^{+1.6}_{-1.5}$
PSO J231.7−26	L0	-25.8 ± 5.5	-28.1 ± 5.4	1.0	35	16.2	$-2.93^{+0.10}_{-0.10}$	20^{+4}_{-4}
PSO J231.8−29	L0	-21.1 ± 2.8	-36.3 ± 2.3	0.5	36	16.5	$-2.82^{+0.10}_{-0.11}$	25^{+8}_{-6}
Upper Scorpius (age = 11 ± 2 Myr, distance = 145 ± 15 pc)								
PSO J237.1−23	M7	-11.4 ± 2.8	-19.7 ± 2.8	2.1	34	16.6	$-2.43^{+0.10}_{-0.11}$	36^{+15}_{-10}
PSO J239.7−23	L0	-0.1 ± 7.2	-23.0 ± 3.5	0.6	38	15.7	$-3.10^{+0.09}_{-0.10}$	$16.2^{+1.4}_{-1.2}$

[a]Proper motions from Pan-STARRS1 Processing Version 3.2, calculated using PS1, 2MASS, and *Gaia* DR1 astrometry (Section 4.4.4).

[b]Masses estimated using $L_{\rm bol}$ and the Lyon/DUSTY evolutionary models (Chabrier et al. 2000) as described in Sections 4.5 and 4.6.

[c]From Bouy et al. (2015). We adopt this proper motion for our analysis in Section 4.5.

Chapter 5

The Young L Dwarf 2MASS J11193254−1137466 is a Planetary-mass Binary

Note: This chapter originally appeared as Best et al. (2017a), with co-authors Michael C. Liu, Trent J. Dupuy, and Eugene A. Magnier.

Abstract

We have discovered that the extremely red, low-gravity L7 dwarf 2MASS J11193254−1137466 is a 0.14″ (3.6 au) binary using Keck laser guide star adaptive optics imaging. 2MASS J11193254−1137466 has previously been identified as a likely member of the TW Hydrae Association (TWA). Using our updated photometric distance and proper motion, a kinematic analysis based on the BANYAN II model gives an 82% probability of TWA membership. At TWA's 10 ± 3 Myr age and using hot-start evolutionary models, 2MASS J11193254−1137466AB is a pair of $3.7^{+1.2}_{-0.9}$ $M_{\rm Jup}$ brown dwarfs, making it the lowest-mass binary discovered to date. We estimate an orbital period of 90^{+80}_{-50} years. One component is marginally brighter in K band but fainter in J band, making this a probable flux-reversal binary, the first discovered with such a young age. We also imaged the spectrally similar TWA L7 dwarf WISEA J114724.10−204021.3 with Keck and found no sign of binarity. Our evolutionary model-derived $T_{\rm eff}$ estimate for WISEA J114724.10−204021.3 is ≈230 K higher than for 2MASS J11193254−1137466AB,

at odds with the spectral similarity of the two objects. This discrepancy suggests that WISEA J114724.10−204021.3 may actually be a tight binary with masses and temperatures very similar to 2MASS J11193254−1137466AB, or further supporting the idea that near-infrared spectra of young ultracool dwarfs are shaped by factors other than temperature and gravity. 2MASS J11193254−1137466AB will be an essential benchmark for testing evolutionary and atmospheric models in the young planetary-mass regime.

5.1 Introduction

Brown dwarfs with masses $\lesssim$15 $M_{\rm Jup}$ and ages $\lesssim$100 Myr lie at a nexus of astronomical interest. They represent the lowest-mass and youngest products of star formation, and as such offer rare empirical tests for evolutionary and atmospheric models. They are also the best field analogs to directly-imaged giant exoplanets, which are far more difficult to directly observe due to the glare of their host stars.

Brown dwarfs cool continuously as they age, and the resulting mass-age-luminosity degeneracy makes their physical properties challenging to infer without constraints on at least two of those three parameters. The atmospheres of young brown dwarfs exhibit clear spectral signatures of low gravity (Cruz et al. 2009; Allers & Liu 2013a), but the age calibration for these signatures lacks precision better than ≈100 Myr (e.g., Liu et al. 2016). Some of the lowest-mass objects have been identified as members of nearby young moving groups (e.g., Gagné et al. 2014b), which provide much tighter age constraints and thus more precise mass estimates from evolutionary models than for ordinary field objects. Young binaries with small separations are even more useful as benchmarks, as their orbits can yield model-independent dynamical masses, providing exacting tests for models (e.g., Dupuy et al. 2009c; Dupuy & Liu 2017).

2MASS J11193254−1137466 (a.k.a. TWA 42; hereinafter 2MASS J1119−1137) was discovered by Kellogg et al. (2015, hereinafter K15) in a search for L and T dwarfs with unusual photometry. 2MASS J1119−1137 is an L7 dwarf with extremely red optical and

near-IR colors along with spectral signatures of low gravity indicating youth (K15; Kellogg et al. 2016, hereinafter K16). K16 identified 2MASS J1119−1137 as a candidate member of the TW Hydrae Association (TWA; Webb et al. 1999), whose age implies a mass of only 4.3–7.6 $M_{\rm Jup}$ for this object. 2MASS J1119−1137 would be one of the two lowest-mass isolated members of TWA, comparable only to the L7 dwarf WISEA J114724.10−204021.3 (hereinafter WISEA J1147−2040; 6.6 ± 1.9 $M_{\rm Jup}$; Schneider et al. 2016b; Faherty et al. 2016), and among the lowest-mass free-floating brown dwarfs known.

We are conducting a high angular-resolution imaging survey of nearby brown dwarfs to identify binaries. In this Letter we show that 2MASS J1119−1137 is a nearly equal-flux binary with component masses in the planetary regime.

5.2 Observations

We observed 2MASS J1119−1137 on 2016 November 25 UT using the laser guide star adaptive optics (LGS AO) system at the Keck II Telescope (van Dam et al. 2006; Wizinowich et al. 2006). We used the facility infrared camera NIRC2 in its narrow field-of-view configuration, using the $R = 13.5$ mag field star USNO-B1.0 0783-0249513 (Monet et al. 2003) located $35''$ from 2MASS J1119−1137 for tip-tilt correction. Skies were mostly clear, with K-band seeing of $1.6''$ measured contemporaneously at UKIRT. We obtained three dithered images at K band in which 2MASS J1119−1137 appeared to be an equal-flux binary. We observed 2MASS J1119−1137 again on 2017 March 18 UT in $YJHK$ bands using the same configuration, under clear skies with seeing $\approx 0.5''$ as measured by the differential image motion monitor (DIMM) at the Canada-France-Hawaii Telescope (CFHT). Details are in Table 5.1.

In addition, we observed WISEA J1147−2040 on 2016 May 18 UT with a similar configuration using the $R = 17.4$ mag field star USNO-B1.0 0693-0264226 (Monet et al. 2003) located $66''$ away for tip-tilt correction, under clear skies with seeing $\approx 0.5''$ from DIMM. The target appeared to be a single object at $0.11''$ resolution.

We reduced and analyzed our data using the methods described in, e.g., Liu et al. (2008) and Dupuy & Liu (2017). Briefly, we calibrated our images using flat fields and dark frames, performed sky subtraction, and registered and stacked images to form a final mosaic for each epoch and filter (Figure 5.1). We measured the relative astrometry and flux ratios of the binary by fitting a PSF model to the individual images, applying the NIRC2 pixel scale, orientation, and distortion correction from Service et al. (2016). For images in which the components were well separated (all but Y band), we used the StarFinder software package (Diolaiti et al. 2000) to simultaneously solve for an empirical PSF and binary parameters. For Y band, we used an analytical PSF of two elliptical three-component Gaussians. We applied additional corrections for differential aberration and atmospheric refraction. We used the rms of the measurements from individual images as the uncertainties on the separation, position angle (PA), and Δmag of the binary components (Table 5.1), adding the errors in plate scale (0.4%) and orientation (0.02°) from Service et al. (2016) in quadrature.

The NIRC2 J, H, and K filters we used are from the Mauna Kea Observatories (MKO) photometric system (Simons & Tokunaga 2002; Tokunaga et al. 2002), and the NIRC2 Y-band filter is described in Liu et al. (2012). The unresolved photometry reported in K16 is from the VISTA Hemisphere Survey (VHS; PI: McMahon, Cambridge, UK), which uses MKO J and H filters but a non-MKO K_S filter. We used the IRTF/SpeX spectrum from K15 to calculate a synthetic $K_{MKO} = 14.658 \pm 0.066$ mag for 2MASS J1119−1137, flux-calibrated with K16's K_S magnitude. The VISTA and NIRC2 Y filters are similar enough that no conversion was necessary.

We split the unresolved 2MASS J1119−1137 YJH photometry from K16 and our synthetic K magnitude into resolved photometry using our measured flux ratios (Table 5.2). K-band flux decreases monotonically with spectral type (e.g., Dupuy & Liu 2012), and the northeast component of 2MASS J1119−1137 is slightly brighter in K, so we designate this object as the "A" component. We note a 0.098 ± 0.014 mag difference between the K-band flux ratios measured at the two epochs. This may indicate variability in one or both

Table 5.1. Keck LGS AO Observations

Object	Date (UT)	Filter	N	$t_{\rm int}$ (s)	Airmass	FWHM[a] (mas)	Strehl Ratio[a]	Separation (mas)	Position Angle (deg)	Δmag
2MASS J1119−1137	2016 Nov 25	$K_{\rm MKO}$	3	60	1.26	94 ± 3	0.148 ± 0.015	137.8 ± 1.7	239.2 ± 0.5	0.125 ± 0.010
	2017 Mar 18	$K_{\rm MKO}$	6	60	1.17	59 ± 2	0.41 ± 0.04	138.10 ± 0.10	239.08 ± 0.07	0.027 ± 0.010
		$H_{\rm MKO}$	6	60	1.17	51.3 ± 0.5	0.212 ± 0.011	138.08 ± 0.23	238.95 ± 0.07	0.008 ± 0.007
		$J_{\rm MKO}$	6	120	1.17	62 ± 9	0.062 ± 0.010	137.54 ± 0.27	238.72 ± 0.17	-0.097 ± 0.004
		$Y_{\rm NIRC2}$	5	120	1.18	70 ± 27	0.036 ± 0.008	136.7 ± 3.5	238.4 ± 0.7	-0.094 ± 0.063
WISEA J1147−2040	2016 May 03	$K_{\rm MKO}$	4	60	1.33	108 ± 11	0.088 ± 0.025	...	...	...

[a]FWHM and Strehl ratios were calculated from each image's fitted PSF, except for the Y-band data for which we isolated the brighter object by rotating the image 180° about the fainter object and subtracting. The tabulated uncertainties are the rms of measurements from individual images.

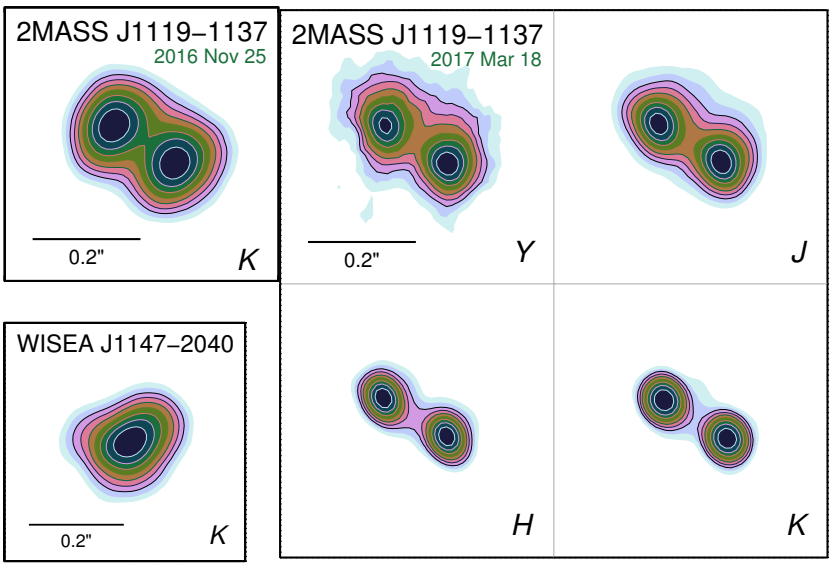

Figure 5.1 Our Keck LGS AO images of 2MASS J1119−1137 (*top left and 2×2 grid at right*) and WISEA J1147−2040 (*bottom left*). North is up and east to the left, with filters indicated at lower right and contours marking logarithmic intervals from 100% to 10% of the peak. The northeast component (2MASS J1119−1137A) is marginally brighter in K while the southwest component is brighter in Y and J, making this system a possible flux-reversal binary.

components, or systematic errors unaccounted in our uncertainties. We use the 2017 March K-band flux ratio for our analysis, as photometry in all other bands was measured that night, and because of the better image quality.

We also identified a faint source in our JHK images from 2017 March, lying $3.79 \pm 0.02''$ from 2MASS J1119−1137A at PA $= 76.47 \pm 0.13$ deg. It was not well detected but appears to be a point source. Images from the DSS, 2MASS, SDSS, AllWISE, and Pan-STARRS1 surveys indicate no object at this location. We measure flux ratios of 4.8 mag in J, 5.0 mag in H, and 5.7 mag in K, relative to 2MASS J1119−1137A. At the same distance as 2MASS J1119−1137, this source's $J = 22.9$ mag would be consistent with known Y0 dwarfs, but its $(J-K)_{\rm MKO} = 1.8$ mag color is $\gtrsim$3 mag too red (Leggett et al. 2017). It is almost certainly a background object. Its $(J-K)_{\rm MKO}$ color suggests an L dwarf, evolved star, or galaxy.

Table 5.2. Properties of 2MASS J1119−1137AB

Property	A Component (northeast)	B Component (southwest)	References
	Observed		
R.A.[a](deg)	169.88521		1
Decl.[a](deg)	−11.62990		1
$\mu_\alpha \cos\delta$ (mas yr^{-1})	-154.0 ± 4.0		1
μ_δ (mas yr^{-1})	-107.9 ± 1.8		1
Radial velocity (km s^{-1})	8.5 ± 3.3		2
SpT	L7 VL-G		3,4,5
Y (mag)	19.045 ± 0.093		2
J (mag)	17.330 ± 0.029		2
H (mag)	15.884 ± 0.017		2
K (mag)	14.658 ± 0.066[b]		3
Y (mag)	19.84 ± 0.10	19.75 ± 0.10	3
J (mag)	18.13 ± 0.03	18.04 ± 0.03	3
H (mag)	16.59 ± 0.02	16.60 ± 0.02	3
K (mag)	15.40 ± 0.07	15.43 ± 0.07	3
$Y - J$ (mag)	1.71 ± 0.10	1.71 ± 0.10	3
$J - H$ (mag)	1.54 ± 0.03	1.43 ± 0.03	3
$J - K$ (mag)	2.73 ± 0.07	2.61 ± 0.07	3
$\Delta(J - K)$ (mag)	0.125 ± 0.011		3

Table 5.2—Continued

Property	A Component (northeast)	B Component (southwest)	References
	Estimated		
$d_{\rm phot}$ (pc)	26.4 ± 6.9		3,8
$m - M$ (mag)	2.11 ± 0.56		3
$v_{\rm tan}$ (km s^{-1})	23.6 ± 6.1		3
Projected separation (au)	3.6 ± 0.9		3
Semi-major axis (au)	$3.9^{+1.9}_{-1.4}$		3
Orbital Period (year)	90^{+80}_{-50}		3
log ($L_{\rm bol}/L_{\odot}$) (unresolved)	$-4.44^{+0.21}_{-0.27}$		3,6
log ($L_{\rm bol}/L_{\odot}$) (resolved)	$-4.73^{+0.21}_{-0.27}$	$-4.74^{+0.21}_{-0.27}$	3
	Model-derived (Lyon/DUSTY) assuming TWA membership		
Age (Myr)	10 ± 3 Myr		7
Mass ($M_{\rm Jup}$)	$3.7^{+1.2}_{-0.9}$	$3.7^{+1.2}_{-0.9}$	3
$T_{\rm eff}$ (K)	1013^{+122}_{-109}	1006^{+122}_{-109}	3
	Model-derived (Lyon/DUSTY) assuming young field (VL-G)		
Age (Myr)	$10 - 100$ Myr		8

Table 5.2—Continued

Property	A Component (northeast)	B Component (southwest)	References
Mass ($M_{\rm Jup}$)	$9.2^{+2.3}_{-1.9}$	$9.0^{+2.4}_{-1.9}$	3
$T_{\rm eff}$ (K)	1065^{+133}_{-118}	1059^{+133}_{-118}	3

Note. — JHK photometry is on the MKO system. Y photometry is from similar filters on VISTA (integrated light) and Keck/NIRC2 (resolved); no conversion was performed.

[a]Epoch 54858.45 (MJD).

[b]Synthetic photometry based on the SpeX prism spectrum (K15) and VHS $K_{\rm S}$ photometry (K16).

References. — (1) Best et al. (2018), (2) K16, (3) this work, (4) K15, (5) Gagné et al. (2017), (6) Faherty et al. (2016), (7) Bell et al. (2015), (8) Liu et al. (2016).

5.3 Results

5.3.1 2MASS J1119−1137AB Is Comoving

Our JHK-band astrometry from 2017 March has a mean separation of 137.88 ± 0.34 mas and PA $238.91 \pm 0.20°$, with uncertainties estimated as in Section 5.2. The change in separation from 2016 November is 0.7 ± 1.5 mas, consistent with no change. Using the proper motion and photometric distance of 2MASS J1119−1137 (Section 5.3.3), if 2MASS J1119−1137B were a stationary background object, the separation would have decreased by 91.7 ± 9.8 mas in 2017 March, inconsistent by 9.4σ from our observation (Figure 5.2). In addition, images from DSS, 2MASS, SDSS, and Pan-STARRS1 showed no objects that could appear as a false close companion given the proper motion. We therefore conclude that 2MASS J1119−1137AB is a gravitationally bound binary.

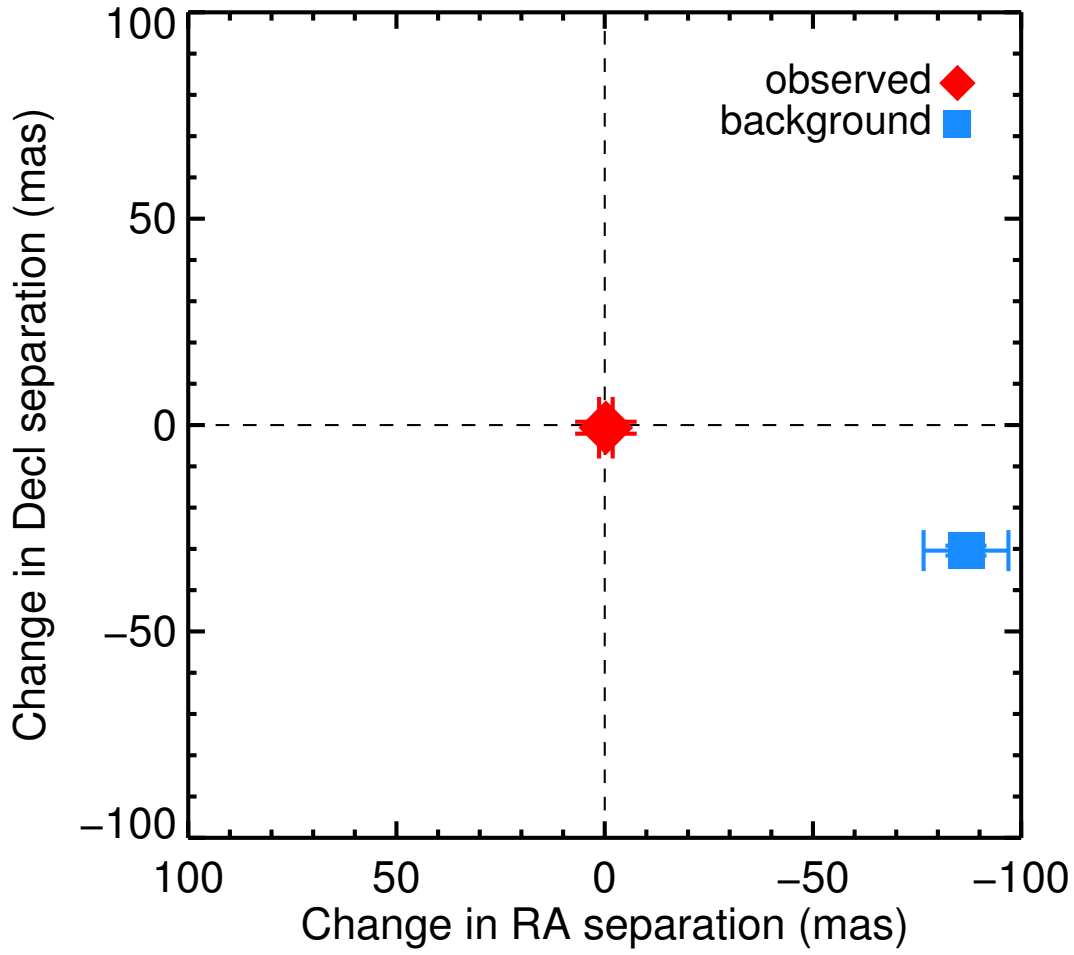

Figure 5.2
Change in position of 2MASS J1119−1137B with respect to 2MASS J1119−1137A between 2016 November 25 and 2017 March 18 (red diamond), compared with the change expected due to parallax and proper motion of 2MASS J1119−1137A if 2MASS J1119−1137B were a stationary background object (blue square). The error for the background position is dominated by the uncertainty on our photometric distance. The observed positions of 2MASS J1119−1137B are consistent with no change, while the background position differs by 9.4σ, confirming that 2MASS J1119−1137AB is a binary.

5.3.2 Spectral Type and Gravity Classification

We used the IRTF/SpeX prism spectrum for 2MASS J1119−1137 and the method of Allers & Liu (2013a) to determine a spectral type of L7, concurring with previous work (K15, Faherty et al. 2016; Gagné et al. 2017). A higher-resolution J-band spectrum (K16) shows weakened K I absorption lines having equivalent widths consistent with VL-G classification for L7 dwarfs (Allers & Liu 2013a; Gagné et al. 2017). We therefore adopt L7 VL-G as the unresolved spectral type. The extremely red $(J-K)_{\rm MKO}$ colors of 2MASS J1119−1137AB are consistent with other low-gravity late-L dwarfs (Figure 5.3). Both the $(J-K)_{\rm MKO}$ colors and $K_{\rm MKO}$ magnitudes for the two components are similar, and the integrated-light spectrum shows no peculiarities that would suggest a blend of two objects with different spectral types. We conclude that both 2MASS J1119−1137A and 2MASS J1119−1137B have spectral types L7 VL-G.

5.3.3 Distance

We used the spectral-type-to-$M_{K_{\rm MKO}}$ relation for VL-G dwarfs from Liu et al. (2016) and our resolved photometry to estimate photometric distances of 26.3 ± 6.8 pc and 26.6 ± 6.9 pc for 2MASS J1119−1137A and 2MASS J1119−1137B, respectively. We adopt 26.4 ± 6.9 pc as the distance to the system, giving the binary a projected separation of 3.6 ± 0.9 au. Our distance is consistent with K16's kinematic distance of 28.9 ± 3.6 pc assuming membership in TWA.

5.3.4 TWA Membership

K16 identified 2MASS J1119−1137 as a candidate TWA member, using the BANYAN II online tool (Malo et al. 2013; Gagné et al. 2014b) to calculate an 88% membership probability with a contamination probability of 0.003% based on 2MASS J1119−1137's sky position, proper motion, radial velocity, and youth. Faherty et al. (2016) analyzed moving group membership using four different tools and found >90% probabilities for TWA in three cases; LACEwING (Riedel et al. 2017) found a contrasting probability of 16%. Gagné

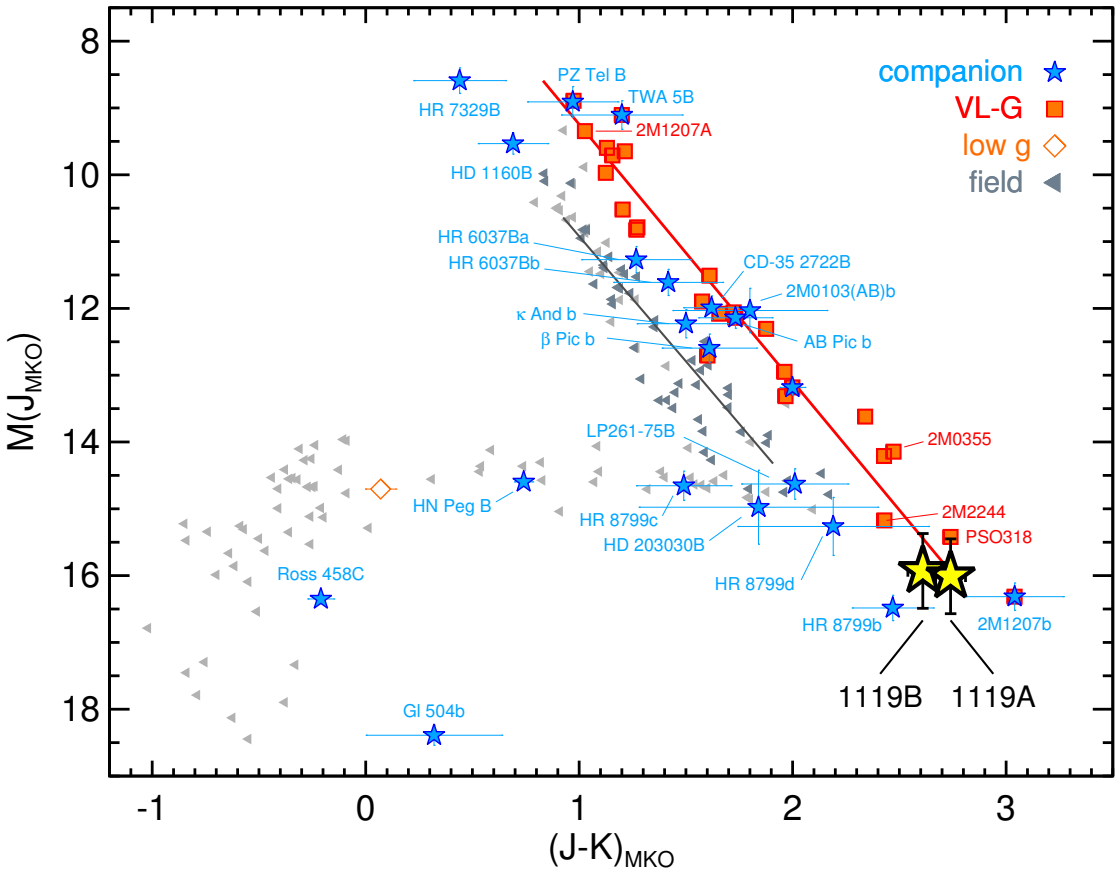

Figure 5.3 $J_{\rm MKO}$ vs. $(J-K)_{\rm MKO}$ color-magnitude diagram for ultracool dwarfs having parallaxes (adapted from Liu et al. 2016). Gray triangles indicate field brown dwarfs, red squares indicate late-M and L dwarfs with VL-G classifications, and blue stars indicate companions. Gray and red lines show linear fits for the FLD-G and VL-G dwarfs, respectively. 2MASS J1119−1137AB (yellow stars, using our photometric distance) lies among the faintest and reddest planetary-mass L dwarfs. The $M_{J_{\rm MKO}}$ errors for 2MASS J1119−1137AB are dominated by the $d_{\rm phot}$; we measure $\Delta J_{\rm MKO} = -0.097 \pm 0.004$ mag. The relative positions of 2MASS J1119−1137AB imply that 2MASS J1119−1137B has begun the transition from a red L dwarf to a bluer T dwarf.

et al. (2017) used the full BANYAN II analysis (including photometry) to calculate a 97% probability of membership. Liu et al. (2016) found that objects lacking parallaxes that have full BANYAN II probabilities $\gtrsim$80% tend to have memberships confirmed by subsequent parallax measurements for the well-established moving groups, including TWA.

We reassessed the moving group membership of 2MASS J1119−1137 using the BANYAN II online tool. For position and proper motion, we adopted the values from Best et al. (2018), which are calculated from 2MASS (Skrutskie et al. 2006) and Pan-STARRS1 3π (Chambers et al. 2018; Magnier et al. 2018) astrometry and calibrated to the *Gaia* DR1 reference frame (Gaia Collaboration et al. 2016a; Lindegren et al. 2016). Our μ_δ differs by 35.5 mas yr^{-1} (2σ) from K16's value but is consistent with measurements by K15 and Gagné et al. (2017).

Using only our astrometry and the radial velocity from K16 as inputs to BANYAN II, we obtained a TWA membership probability of 73%. The decrease from K16's 88% probability is due almost entirely to the difference in μ_δ. When we included our photometric distance, the probability of TWA membership increased to 82%.

Based on our BANYAN II results and the VL-G spectrum, 2MASS J1119−1137 is a very likely member of TWA. We note that a comparison in UVW and XYZ of 2MASS J1119−1137 to known members of moving groups using $\tilde{\chi}^2$ as a rubric (see Equation 1 of Liu et al. 2016) supports membership in TWA, β Pictoris (0% probability from BANYAN II), and Tucana-Horologium (0%), and especially the AB Doradus (4%) moving group. A precise trigonometric distance, now underway by us at CFHT, is needed to firmly establish the membership.

5.3.5 Physical Properties

As a TWA member, 2MASS J1119−1137 would share the age of 10 ± 3 Myr derived from the stellar members (Bell et al. 2015). We estimated the components' masses and effective temperatures using bolometric luminosities and the Lyon/DUSTY hot-start evolutionary models (Chabrier et al. 2000). To obtain $L_{\rm bol}$, we adjusted the integrated-light value from

Faherty et al. (2016) to our new photometric distance, and decomposed this into individual $L_{\rm bol}$ values using the binary's $K_{\rm MKO}$ flux ratio. Using these $L_{\rm bol}$ and the assumed age, we then interpolated a mass and effective temperature from the DUSTY models for each component. We propagated the uncertainties on distance, flux ratio, and age into our calculations via Monte Carlo trials using normal distributions for each uncertainty, and we quote the resulting median and 68% confidence limits (Table 5.2). We estimate masses of $3.7^{+1.2}_{-0.9}$ $M_{\rm Jup}$ for both components. We did not use the more recent BHAC15 models (Baraffe et al. 2015) as they do not include masses below 0.01 $M_{\odot}$.

If 2MASS J1119−1137 is not a TWA member, its VL-G classification still constrains its age to ≈10–100 Myr (Liu et al. 2016). Our estimated masses and effective temperatures for this age range (uniformly distributed for error propagation) are shown in Table 5.2.

Using our masses, we considered the effect of 2MASS J1119−1137AB's orbital motion on the radial velocity measured by K16. For an edge-on circular orbit with components at quadrature, we found a difference in radial velocities of $1.3^{+0.4}_{-0.3}$ km s^{-1} for TWA masses or $2.0^{+0.6}_{-0.4}$ km s^{-1} for field-VL-G masses. The $R \sim 6000$ (50 km s^{-1}) spectrum of K16 would not resolve such orbital motion, so the radial velocity from K16 remains valid.

5.4 Discussion

Assuming 2MASS J1119−1137 is a member of TWA, its total mass is $7.4^{+2.5}_{-1.9}$ $M_{\rm Jup}$, making it the lowest-mass binary discovered to date. The individual masses of 2MASS J1119−1137A and 2MASS J1119−1137B also place them among the lowest-mass free-floating brown dwarfs, including WISEA J1147−2040 and the Y dwarfs (Dupuy & Kraus 2013; Leggett et al. 2017). Even if 2MASS J1119−1137AB is actually a young field object, its total mass of $18.2^{+4.7}_{-3.8}$ $M_{\rm Jup}$ would still be among the lowest-mass binaries, surpassed only by the young binary DENIS-P J035726.9-441730 (14–15 $M_{\rm Jup}$; Bouy et al. 2003; Gagné et al. 2014b) and possibly by the T9+Y0 binaries CFBDSIR J145829+101343 (≈18–45 $M_{\rm Jup}$; Liu et al. 2011a) and WISE J014656.66+423410.0 (Dupuy et al. 2015a). As

an extremely low mass young binary, 2MASS J1119−1137AB will be a crucial benchmark for tests of evolutionary and atmospheric models.

The isolation of 2MASS J1119−1137AB strongly suggests that it is a product of normal star-formation processes, which therefore must be capable of making binaries with $\lesssim$5 $M_{\rm Jup}$ components. 2MASS J1119−1137AB could be a fragment of a higher-order system that was ejected via dynamical interactions (Reipurth & Mikkola 2015), although the lack of any confirmed member of TWA within 10° (projected separation ≈ 5 pc) of 2MASS J1119−1137 makes this scenario unlikely. Formation of very low mass binaries in extended massive disks around Sun-like stars followed by ejection into the field has been proposed by, e.g., Stamatellos & Whitworth (2009), but disks of this type have not been observed.

Binary brown dwarfs can be monitored to map their orbits, which yield dynamical masses that stringently test evolutionary models. We estimated 2MASS J1119−1137AB's orbital period using Kepler's Third Law. We first used the projected separation and a conversion factor from Dupuy & Liu (2011, Table 6, assuming moderate discovery bias for very low mass visual binaries) to estimate a semi-major axis of $3.9^{+1.9}_{-1.4}$ au. Our model-derived masses assuming TWA membership give an orbital period of 90^{+80}_{-50} years. A dynamical mass can be determined once ≈1/3 of an orbit has been observed (e.g., Dupuy & Liu 2017), so 2MASS J1119−1137AB would yield a dynamical mass in ≈15–55 years. Assuming a field VL-G age, we estimate an orbital period of 60^{+50}_{-30} years, yielding a mass in ≈10–35 years.

The integrated-light spectrum and photometry of 2MASS J1119−1137 are notably similar to those of the young L7 dwarf WISEA J1147−2040 (Gagné et al. 2017), implying similar temperatures and gravity. However, using the $L_{\rm bol}$ for WISEA J1147−2040 from Faherty et al. (2016) and the method from Section 5.3.5, we estimate a $T_{\rm eff}$ of 1242^{+73}_{-69} K, which is ≈230 K higher than our estimates for 2MASS J1119−1137A and 2MASS J1119−1137B. This discrepancy is particularly surprising given that both objects are very likely members of TWA and therefore should have the same age and composition. The simplest resolution is that WISEA J1147−2040 is also an equal-

flux binary, unresolved in our images, with component temperatures very similar to those of 2MASS J1119−1137AB. Using the method from Section 5.3.3 we calculated $d_{\rm phot} = 27.3 \pm 6.9$ pc for a hypothetical equal-flux binary WISEA J1147−2040, leading to a maximum projected separation of 2.9 ± 0.8 au to remain unresolved in our images. Another possibility is that 2MASS J1119−1137AB is not a member of TWA and is older; our VL-G-age temperature estimates are only ≈50 K higher, but would then agree with the WISEA J1147−2040 estimate within uncertainties. A third intriguing possibility is that the low-resolution spectra of young red L dwarfs are driven at least partially by factors other than temperature and gravity (Allers & Liu 2013a; Liu et al. 2016), allowing coeval objects with differing masses and effective temperatures to have similar spectra.

Figure 5.3 compares the $J_{\rm MKO}$ vs. $(J-K)_{\rm MKO}$ position of 2MASS J1119−1137AB to the ultracool dwarf population, highlighting other low-gravity objects and substellar companions. 2MASS J1119−1137AB lies among other planetary-mass objects at the faint red end of the L dwarf sequence. 2MASS J1119−1137B is brighter in J band and slightly fainter in K band, making the system a probable flux-reversal binary. (The K magnitudes for the two components are formally consistent within uncertainties, but 2MASS J1119−1137B is fainter in all nine of our individual K-band images.) The flux-reversal phenomenon is a hallmark of field-age L/T transition binaries (e.g., Gizis et al. 2003; Liu et al. 2006; Dupuy et al. 2015b), thought to occur when the cooler component reaches a temperature at which the clouds that suppress near-IR flux in L dwarfs begin to clear, reducing the J-band opacity relative to the warmer component (e.g., Burrows et al. 2006). The slightly bluer $(J-K)_{\rm MKO}$ color of 2MASS J1119−1137B implies that it is cooler than its primary. In field-age brown dwarfs this transition to bluer $J-K$ colors is typically seen at warmer temperatures (≈1400 K; e.g., Stephens et al. 2009). The potential flux-reversal of 2MASS J1119−1137AB suggests that it is beginning the transition at $T_{\rm eff} \approx 1000 \pm 100$ K, an even lower temperature than the ≈1100−1200 K found for other low (but somewhat higher) mass L dwarfs (e.g. Metchev & Hillenbrand 2006; Barman et al. 2011; Liu et al. 2013), implying a possible systematic correlation between mass and L/T transition temperature.

Precise photometry and resolved spectroscopy of 2MASS J1119−1137AB with the Hubble and James Webb Space Telescopes will enable differential studies of the atmospheres of young planetary-mass objects and may yield insights into the L/T transition at young ages.

Chapter 6

Photometry and Proper Motions of M, L, and T Dwarfs from the Pan-STARRS1 3π Survey

Note: This chapter originally appeared as Best et al. (2018), with co-authors Eugene A. Magnier, Michael C. Liu, Kimberly M. Aller, Zhoujian Zhang, W. S. Burgett, K. C. Chambers, P. Draper, H. Flewelling, N. Kaiser, R.-P. Kudritzki, N. Metcalfe, J. L. Tonry, R. J. Wainscoat, and C. Waters.

Abstract

We present a catalog of 9888 M, L and T dwarfs detected in the Pan-STARRS1 3π Survey (PS1), covering three-quarters of the sky. Our catalog contains nearly all known objects of spectral types L0–T2 in the PS1 field, with objects as early as M0 and as late as T9, and includes PS1, 2MASS, and AllWISE photometry. We have rigorously vetted the association of PS1 measurements to previously identified objects, in particular to detections in the 2MASS and AllWISE surveys. We analyze the different types of photometry reported by PS1 and use two types in our catalog in order to maximize both depth and accuracy. We systematically assess the quality of the photometry to ensure that the faintest detections in our catalog are real. Using parallaxes from the literature, we construct empirical SEDs for field ultracool dwarfs spanning $0.5 - 12$ μm. We determine typical colors of M0–T9 dwarfs and highlight the distinctive colors of subdwarfs and young objects. Our catalog

includes 494 L dwarfs detected in $r_{\rm P1}$, the largest sample of L dwarfs detected at such blue wavelengths. We combine astrometry from PS1 (a multi-epoch survey), 2MASS, and *Gaia* DR1 to calculate new proper motions for our catalog. We achieve a median precision of 2.9 mas yr^{-1}, a factor of $\approx$3$-$10 improvement over previous large catalogs. Our method enables us to merge the PS1 epochs of fast-moving objects ($\mu \gtrsim 200$ mas yr^{-1}) whose detections are split among more than one object in the PS1 database. Our catalog contains proper motions for 2405 M6–T9 dwarfs and includes the largest set of homogeneous proper motions for L and T dwarfs published to date, 406 objects for which there were no previous measurements, and 1176 objects for which we improve upon previous literature values. We analyze the kinematics of ultracool dwarfs in our catalog and find evidence that bluer but otherwise generic late-M and L field dwarfs (i.e., not subdwarfs) tend to have tangential velocities higher than those of typical field objects. With the public release of the PS1 data, this survey will continue to be an essential tool for characterizing the ultracool dwarf population.

6.1 Introduction

Ultracool dwarfs (spectral types M6 and later) are the lowest-mass members of the stellar population, encompassing the coolest stars, brown dwarfs, and planetary-mass objects. The discovery of brown dwarfs over 20 years ago launched an understanding of the complex properties and evolution of ultracool atmospheres (e.g., Burrows et al. 2006), and allowed us to constrain the low-mass end of the stellar mass and luminosity functions in the solar neighborhood (Marocco et al. 2015, and references therein). In addition, the youngest ($\approx$10–100 Myr) ultracool dwarfs in the field appear to be our best analogs to directly imaged giant planets (e.g., Liu et al. 2013), and they are far easier to observe without the drowning glare of host stars. The major drivers for ultracool discoveries, which now include $\approx$2,000 L and T dwarfs and many thousands of late-M dwarfs, have been wide-field imaging surveys such as the Deep Near Infrared Survey of the Southern Sky (DENIS, Epchtein et al. 1999),

Sloan Digital Sky Survey (SDSS; York et al. 2000), Two Micron All Sky Survey (2MASS; Skrutskie et al. 2006), UKIRT Infrared Deep Sky Survey (UKIDSS; Lawrence et al. 2007), and Wide-Field Infrared Survey Explorer (*WISE*; Wright et al. 2010).

Large photometric samples obtained from these imaging surveys have provided much of our fundamental knowledge about ultracool dwarfs. Samples of L dwarfs have revealed a surprising diversity of near-IR colors (e.g. Leggett et al. 2002b; Knapp et al. 2004; Gizis et al. 2012) which are believed to be caused by variations in surface gravity and/or dusty clouds (e.g. Kirkpatrick et al. 2008; Allers & Liu 2013a) or thermochemical instabilities (Tremblin et al. 2016). Objects transitioning from L to T spectral types undergo a dramatic shift to bluer near-IR colors thought to be driven by the clearing of clouds and the formation of methane (e.g., Burgasser et al. 2002; Chiu et al. 2006; Saumon & Marley 2008). UKIDSS and *WISE* have illustrated the diversity of late-T and Y dwarf near- and mid-IR colors (e.g., Burningham et al. 2010a; Kirkpatrick et al. 2011; Mace et al. 2013a), and *WISE* has enabled the discovery of the coolest known substellar objects (e.g., Cushing et al. 2011; Kirkpatrick et al. 2012; Luhman 2014). Large samples have revealed the mass and luminosity functions of the local ultracool population (e.g., Allen et al. 2005; Cruz et al. 2007; Burningham et al. 2010a). Measurements of the space density of brown dwarfs (e.g. Metchev et al. 2008; Reid et al. 2008b) have identified a relative paucity of L/T transition dwarfs, indicating that this evolutionary phase is short-lived and constraining the birth history of substellar objects (e.g., Day-Jones et al. 2013; Marocco et al. 2015). The surveys have also enhanced brown dwarf searches in star-forming regions (e.g., Lodieu et al. 2009; Martín et al. 2010), important for determination of the substellar initial mass function. Photometric samples encompassing more than one survey have enabled us to determine ultracool colors across a broad range of wavelengths (e.g., Schmidt et al. 2015; Skrzypek et al. 2015) and to measure bolometric luminosities that yield effective temperatures and constraints on atmospheric and evolutionary models (e.g. Leggett et al. 2002b; Golimowski et al. 2004).

Similarly, large samples of proper motions have contributed significantly to our discovery and understanding of the ultracool population. Proper motions have enabled searches to

distinguish ultracool dwarfs from distant luminous red objects such as giants and galaxies (e.g., Kirkpatrick et al. 2000; Lépine & Shara 2005; Theissen et al. 2016, 2017) and to determine whether individual discoveries are members of star-forming regions (e.g., Lodieu et al. 2007a, 2012a). Proper motions have helped to find objects in crowded areas of the sky such as the Galactic plane (e.g., Luhman 2013; Smith et al. 2014b) and to identify ultracool dwarfs with atypical colors that were missed by color cuts used in photometry-only searches (e.g., Kirkpatrick et al. 2010). Several studies have found clear evidence for dynamically cold (slow-moving) and hot (fast-moving) populations of ultracool dwarfs that are consistent with thin disk and thick disk/halo populations (e.g., Faherty et al. 2009; Schmidt et al. 2010; Dupuy & Liu 2012), implying that ultracool dwarfs form in the same manner as hotter stars. Searches for high proper motion objects, often using surveys with shorter time baselines, have identified rare fast-moving objects that are typically members of the older, low-metallicity populations (e.g., Jameson et al. 2008; Smith et al. 2014a; Kirkpatrick et al. 2014) or very nearby, previously overlooked objects (e.g., Luhman & Sheppard 2014; Luhman 2014; Schneider et al. 2016a; Kirkpatrick et al. 2016). Proper motions measured from the large surveys have enabled us to identify the substellar members of nearby young moving groups (e.g., Gagné et al. 2015b,c; Faherty et al. 2016; Liu et al. 2016), a population crucial to our understanding of brown dwarf evolution over their first few hundred million years. Proper motions from large catalogs have also identified wide comoving companions to higher-mass stars whose ages and metallicities can more easily be determined (e.g., Zhang et al. 2013; Luhman et al. 2012; Burningham et al. 2013; Smith et al. 2014b), making the ultracool companions important benchmarks for constraining atmospheric and evolutionary models.

The Panoramic Survey Telescope And Rapid Response System (Pan-STARRS1) is a large multi-epoch, multi-wavelength, optical imaging survey using a 1.8 m wide-field telescope on Haleakala, Maui (Kaiser et al. 2010). Pan-STARRS1 uses a 1.4 gigapixel camera (GPC1) with a $0\farcs258$ pixel scale. The Pan-STARRS1 3π Survey (PS1; K. C. Chambers et al., 2017, in prep) observed the entire sky north of $\delta = -30^\circ$ (three-quarters

of the sky) in five filters ($g_{\rm P1}r_{\rm P1}i_{\rm P1}z_{\rm P1}y_{\rm P1}$) over four years (2010 May – 2014 March), imaging ≈12 times in each filter and achieving a median angular resolution of ≈1.″1 with a floor of ≈0.″7 (E. A. Magnier et al. 2017, in prep). PS1 images are ∼1 mag deeper in z-band than the most comparable optical survey to date (SDSS), and the novel $y_{\rm P1}$ filter (0.918−1.001 μm) extends further toward the near-infrared than previous optical surveys. This long-wavelength sensitivity allows PS1 to better detect and characterize red objects such as ultracool dwarfs. In addition, the multi-epoch astrometry of PS1 enables precise measurement of proper motions and parallaxes that help to distinguish faint, nearby ultracool dwarfs from reddened background stars and galaxies.

Significant ultracool discoveries from PS1 include many wide ultracool companions to main sequence (Deacon et al. 2012a,b, 2014) and young stars (Aller et al. 2013), L/T transition dwarfs that are difficult to identify with near-IR photometry alone (Deacon et al. 2011; Best et al. 2013, 2015), new low-mass members of the Hyades (Goldman et al. 2013) and Praesepe (Wang et al. 2014a), and new brown dwarf members of nearby young moving groups (Liu et al. 2013; Aller et al. 2016). PS1 has also enabled studies with large samples of more massive stars, including fiducial sequences of Galactic star clusters (Bernard et al. 2014), proper motions and wide binaries in the *Kepler* field (Deacon et al. 2016, who also present SEDs for spectral types B9V through M9V in the PS1 photometric system), and photometric distances and reddening for all stars detected by PS1 (Green et al. 2014; Schlafly et al. 2014). PS1 can detect ultracool dwarfs at larger distances than SDSS and 2MASS, so its optical photometry helps to create a rich multi-color catalog that will enable even bigger searches based solely on photometry, a precursor to science with the Large Synoptic Survey Telescope (LSST; Ivezić et al. 2008). In addition, the proper motions and parallaxes in PS1 should be fertile ground for identifying more ultracool dwarfs that have eluded detection due to their locations in crowded areas of the sky (e.g., Liu et al. 2011b), or are too red and faint to be measured by *Gaia* (Gaia Collaboration et al. 2016a).

In this paper, we present a comprehensive catalog of ultracool dwarfs observed by PS1, including photometry, proper motions, spectral types, gravity classifications, and

multiplicity. Section 6.2 describes the contents and assembly of our catalog. The PS1 photometry and proper motions are discussed in detail in Sections 6.3 and 6.4, respectively. We briefly describe a binary M7 dwarf newly identified by PS1 in Section 6.5. We summarize our catalog and its features in Section 6.6.

6.2 Catalog

Our catalog of ultracool dwarfs in Pan-STARRS1 contains photometry and proper motions from PS1 for 9888 M, L, and T dwarfs, along with photometry from 2MASS, AllWISE, and *Gaia* DR1 whenever available. The catalog includes all L and T dwarfs published as of 2015 December that have photometry in at least one of the five PS1 bands ($g_{\rm P1}r_{\rm P1}i_{\rm P1}z_{\rm P1}y_{\rm P1}$). The catalog does not contain all known M dwarfs, but does include a large sample in order to accurately represent the colors and kinematics of M dwarfs in PS1.

We describe the construction of our catalog in Section 6.2.1. In Sections 6.2.2 and 6.2.3, we provide more details about our selection of L+T and M dwarfs, respectively. In Section 6.2.4, we discuss the spectral types used in our catalog. We describe our identification of young objects in Section 6.2.5 and our treatment of binaries in Section 6.2.6. In Section 6.2.7 we assess the completeness of our catalog.

6.2.1 Construction

To create our catalog, we compiled a list of late-M, L and T dwarfs from DwarfArchives,[1] M dwarfs from West et al. (2008), and numerous literature sources from 2012–2017. We included positions, proper motions, spectral types, and photometry from 2MASS (Cutri et al. 2003), AllWISE (Cutri et al. 2014), and *Gaia* DR1 (Lindegren et al. 2016) when available. We also tracked objects identified as binaries and those with spectroscopic or other indications of youth. The catalog includes new discoveries through 2015 December and a handful of updates to photometry, astrometry, and spectral types from 2016 and 2017.

[1]Hosted at http://DwarfArchives.org. Last updated 2013-05-29.

In order to ensure that every object in our catalog is a bona fide M, L, or T dwarf, we included only published objects with spectroscopic classification. We have therefore excluded objects with only photometric spectral types (e.g., based on optical or near-infrared colors or methane imaging). Our catalog also does not include close substellar companions to main sequence stars detected by high-angular resolution imaging and/or radial velocity because these objects are not resolved by PS1.

We cross-matched our list with the full PS1 Processing Version 3.3 database (PV3.3, 2017 March) by position using a 3" matching radius, retaining the closest object matched in PS1. PV3.3 includes an update to the 2016 December public data release (PS1 DR1) that reduced the astrometric errors but did not affect photometry (E. A. Magnier et al. 2017, in prep). In order to maximize the number of accurate matches, we used PS1 positions published in the literature (from earlier processing versions) or AllWISE positions (nearly contemporaneous with PS1) whenever possible for the objects in our list. If neither of those were available, we used the most recent positions reported in the literature; frequently these came from 2MASS, SDSS, or UKIDSS. When these objects had reported proper motions, we used the proper motions to project expected PS1 coordinates and adopted those for our cross-match.

To ensure that our catalog contains only secure PS1 measurements of real astrophysical objects, we applied photometric quality cuts described in detail in Section 6.3.1. Briefly, we required our PS1 matches to have photometric errors less than 0.2 mag in at least one PS1 band, with detections at two or more epochs in that band, and we excluded objects likely to be saturated in all bands. In addition, we excluded any sources flagged as having poor PSF fits (`psf_qf` $<$ `0.85`), and we verified that none of our PS1 matches were marked as quasars, transients, periodic variables, or solar system objects. Any object without a PS1 match within 3" of the expected coordinates was removed from our catalog.

To check for incorrect matches, we calculated colors using the 2MASS, AllWISE, and PS1 photometry for our matches (Section 6.3.4). We sorted our list into bins of one spectral sub-type, and inspected every object with a $g_{\rm P1} - y_{\rm P1}$, $r_{\rm P1} - i_{\rm P1}$, $r_{\rm P1} - z_{\rm P1}$, $r_{\rm P1} - y_{\rm P1}$,

$i_{\rm P1} - z_{\rm P1}$, $i_{\rm P1} - y_{\rm P1}$, $z_{\rm P1} - y_{\rm P1}$, $y_{\rm P1} - J_{\rm 2MASS}$, or $y_{\rm P1} - W1$ color differing from the mean for its spectral type by more than 3 times the rms color for that spectral type bin. We also inspected every T dwarf with a reported $g_{\rm P1}$, $r_{\rm P1}$, or $i_{\rm P1}$ detection. In addition, because the cool temperatures of M, L, and T dwarfs necessitate reddish PS1 (optical) colors, we inspected all objects having a secure detection in a bluer band but not in a redder band (e.g., some nearby M dwarfs were saturated in $i_{\rm P1}$, $z_{\rm P1}$, and $y_{\rm P1}$, but not in $g_{\rm P1}$ or $r_{\rm P1}$). To inspect an object, we examined stacked images from PS1, 2MASS, and AllWISE, and searched in all three surveys within a 60" radius around the PS1 position for other possible matches. We discarded PS1 matches for which an image artifact, a nearby brighter star, or a blue or extended background object had clearly contaminated the detection (i.e., the source of contamination is within the visible PSF of the object from our list). In cases where contamination affected some but not all of the PS1 bands, we retained the object in our catalog and rejected photometry only from the contaminated bands. (All $g_{\rm P1}$ and $r_{\rm P1}$ detections of T dwarfs were discarded in this manner.) We corrected a match when the images and colors clearly pointed to a different PS1 source, but we did not make corrections in ambiguous cases in order to minimize rejection of objects with naturally-occurring unusual photometry.

For most outliers we found nothing to indicate the object was anything other than an object with unusual colors. Many red outliers were young objects in star-forming regions and/or with low gravity spectral classifications, both associated with redder-than-typical colors for L dwarfs (e.g., Faherty et al. 2013). We discovered a few cases in which the 2MASS or AllWISE photometry was for a different nearby object, often a brighter source with which the ultracool object was blended. In the case of blends we rejected the 2MASS or AllWISE photometry; otherwise we adopted the photometry of the correct ultracool object.

6.2.2 L and T Dwarfs

Although ultracool dwarfs are normally brightest in the near-infrared, the depth and red-optical sensitivity of Pan-STARRS1 have allowed PS1 to detect 1617 L and T dwarfs, including spectral types as late as T9. Barring unintentional omissions, our catalog contains all spectroscopically confirmed L and T dwarfs published through 2015 December and meeting our detection standards in PS1. The L and T dwarfs in our catalog are primarily drawn from DwarfArchives and Mace (2014), supplemented by other literature sources. The final catalog includes 1265 L dwarfs and 352 T dwarfs.

6.2.3 M Dwarfs

M dwarfs comprise the majority of the stars in our galaxy, so a clear understanding of M dwarf properties is essential for characterizing the local stellar population and constraining models of star formation and evolution. In addition, M dwarfs provide context for the photometric and kinematic properties of L and T dwarfs, and more massive brown dwarfs younger than $\sim$200 Myr will have late-M spectral types. Compiling a complete list of known M dwarfs would require an effort far beyond what is needed to accurately characterize the PS1 photometry and proper motions of the nearby field population. Instead, we built a representative sample of the field population from two sub-samples.

The first sub-sample comprises objects with well-studied and/or potentially distinctive photometry and kinematics from the recent literature, and contains 463 M6–M9 dwarfs. These objects were included in order to sample the diversity of colors and kinematics in late-M dwarfs. We included M dwarfs from the proper motion and parallax compilations of Faherty et al. (2009, 2012) and Dupuy & Liu (2012), the young object list from Allers & Liu (2013a), the young moving group members and non-members from Gagné et al. (2015c), the catalog of SpeX spectra from Bardalez Gagliuffi et al. (2014), and wide ultracool companions to main sequence stars from Deacon et al. (2014).

The second sub-sample is a large set of M dwarfs with high-quality photometry, representative of the generic field population. We cross-matched all M0–M9 dwarfs listed in

the catalog of West et al. (2008) with PS1, 2MASS, and AllWISE, using a matching radius of $5''$. We required sources to have photometric errors < 0.05 mag in at least five of the eight total PS1 and 2MASS bands ($grizyJHK$), and at least two detections in individual exposures in each PS1 band. To avoid saturated objects, we rejected any sources brighter than the limits listed in Section 6.3.1 or flagged by PS1 for poor PSF fits (`psf_qf` < 0.85). We then removed objects with non-zero confusion, saturation, extendedness, or de-blending flags in either 2MASS or AllWISE. These cuts are more stringent than for the late-M, L, and T dwarfs in our catalog in order to ensure a very clean field M dwarf sample with high-quality photometry. This sub-sample contains 7808 M dwarfs from West et al. (2008), bringing the total for M dwarfs in our catalog to 8271.

6.2.4 Spectral Types

For the objects in our catalog, we use spectral types from the literature. These spectral types were determined by a variety of methods, based on visual or numerical analysis of red-optical ($\approx 0.65 - 1$ μm) or near-infrared ($\approx 1 - 2.5$ μm) spectra. In cases where an object has both an optical and a near-IR spectral type, we adopt the optical type for M and L dwarfs and the near-IR type for T dwarfs. The spectral types for the M dwarfs drawn from West et al. (2008) were all derived from optical spectra.

There are seven objects in our catalog with an optical L type and a near-IR T type. For these we use the T spectral type (all T0–T1). All seven objects show clear methane absorption at 1.6 μm and/or 2.2 μm in their near-IR spectra, a hallmark of T dwarfs. We note that these objects are all confirmed binaries (by high-resolution imaging) or candidate binaries (based on peculiar spectra) with components spanning the L/T transition. The spectral types are therefore based on unresolved spectral blends, explaining the disagreement between the optical and near-IR types.

We show the distribution of all spectral types in our catalog in Figure 6.1. The earliest type in our catalog is M0 (by construction), and the latest spectral type detected by PS1 is T9. Our catalog contains more than 20 objects of each spectral sub-type through T7,

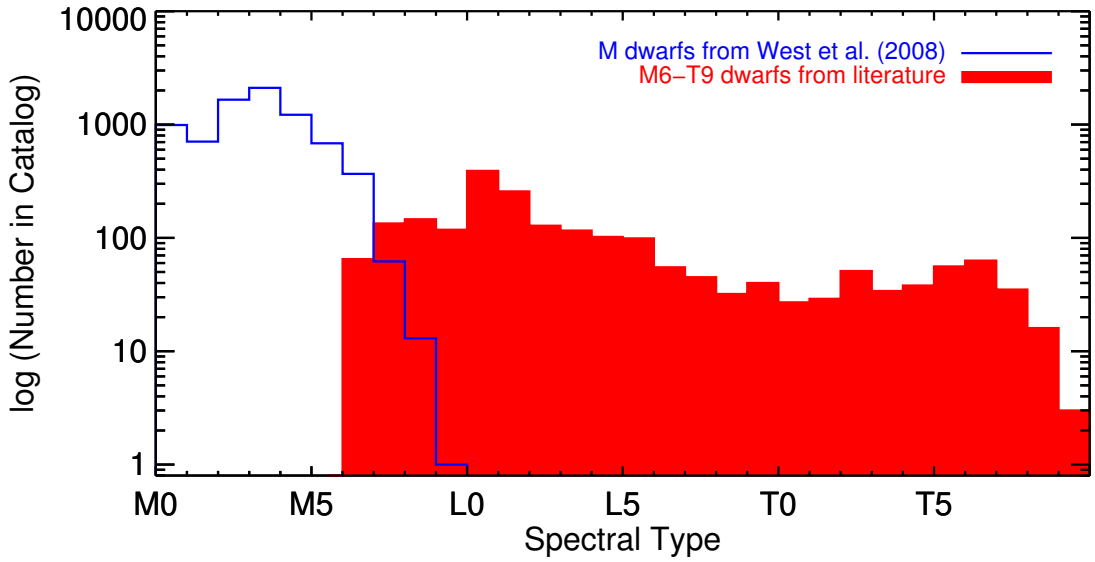

Figure 6.1 The distribution of spectral types in our catalog. The late-M, L, and T dwarfs compiled from the literature are shown in solid red, while the M dwarfs from West et al. (2008) are shown with a blue outline. The catalog robustly samples the temperature range of all but the coolest brown dwarfs, and includes objects with spectral types as late as T9.

robustly sampling the ultracool dwarf population for all but the coolest objects. We compare the distribution of L and T dwarfs in our catalog to all L and T dwarfs in the PS1 field (north of $\delta = -30°$) in Figure 6.2. The known objects not present in our catalog are mostly later-T dwarfs too faint to be detected by PS1. These have chiefly been discovered by deeper near-IR searches over narrower fields (e.g., Albert et al. 2011; Burningham et al. 2013) or by searches for late-T and Y dwarfs using *WISE* (e.g., Kirkpatrick et al. 2011). The ≈30 L dwarfs not detected by PS1 are mostly unresolved companions to higher-mass stars or discoveries from deep imaging of star-forming regions.

6.2.5 Young Objects

Our catalog includes many young objects (ages $\lesssim$ 200 Myr), which are known to have distinctive colors and kinematics (e.g., Kirkpatrick et al. 2008; Faherty et al. 2009). We identify young objects primarily by low-gravity classifications reported in

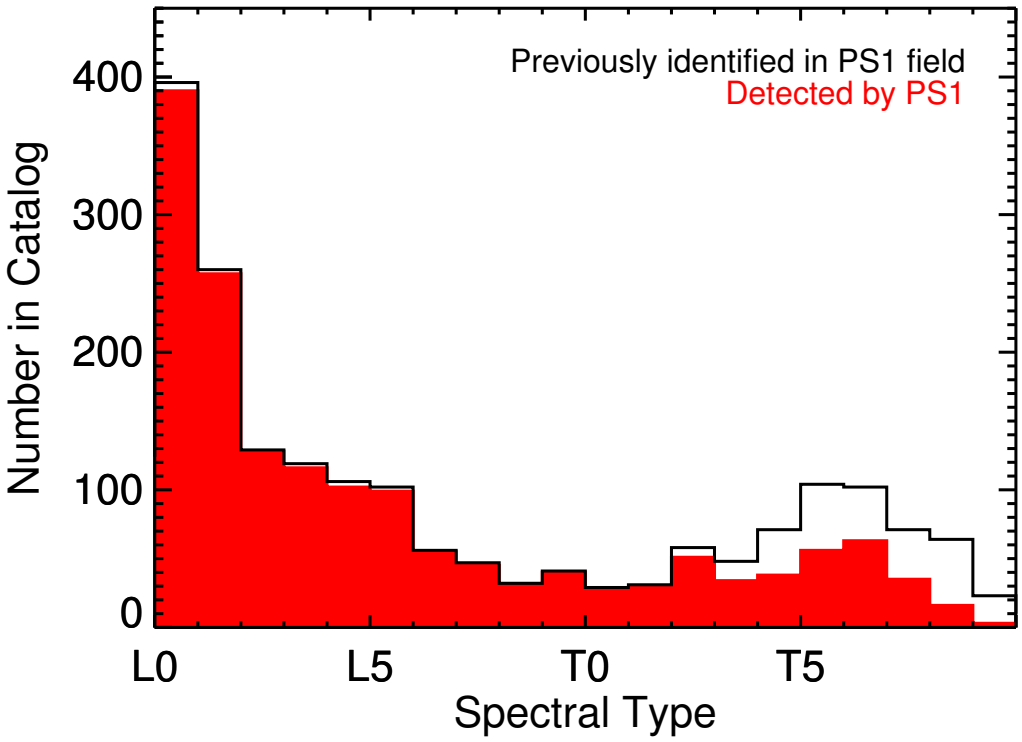

Figure 6.2 The distribution of L and T spectral types in our catalog, compared to previously identified L and T dwarfs in the PS1 field. PS1 has detected nearly all previously known L dwarfs; the handful of non-detections are mostly faint objects in star-forming regions or unresolved companions to higher-mass stars. The T dwarfs (mostly later-type) not detected by PS1 have primarily been discovered by deeper near-IR searches over narrower fields or in the mid-IR using the *WISE* survey.

the literature: β, γ, and δ classes based on optical (Kirkpatrick 2005; Cruz et al. 2009) or near-IR (Gagné et al. 2015c) spectra, and INT-G and VL-G based on near-IR spectra (Allers & Liu 2013a). We also identify any object in a star-forming region as young. In addition, we include objects in our young sample that lack formal low-gravity classifications but have other evidence for youth: NLTT 13728, LP 423-31, and 2MASS J19303829−1335083 (Shkolnik et al. 2009), LSPM J1314+1320 (Schlieder et al. 2014), 2MASS J17081563+2557474 (Kellogg et al. 2015), and 2MASS J22344161+4041387 (Allers et al. 2009) show spectroscopic signs of low gravity; SDSSp J111010.01+011613.1 (Gagné et al. 2015a) and WISEA J114724.10−204021.3 (Schneider et al. 2016b) are members of young moving groups; and LP 261-75B (Reid & Walkowicz 2006) and Gl 417BC (Kirkpatrick et al. 2001a) are wide companions to young stars.

6.2.6 Binaries

Our catalog naturally includes ultracool binaries with separations wide enough to be resolved in PS1, as well as many that are unresolved. In our catalog, we assigned the term "binary" only to pairs that are unresolved in PS1 but confirmed by high-resolution imaging or radial velocity measurements. We treat these as single objects, reporting their blended photometry. We note that peculiar spectral features have been used to identify candidate unresolved binaries (Burgasser et al. 2010a; Bardalez Gagliuffi et al. 2014), but this technique has not been demonstrated to robustly distinguish actual blends from single objects with unusual atmospheric properties. Given our conservative approach, we expect our catalog to contain some unidentified binaries. Our catalog identifies a total of 81 unresolved binaries and two unresolved triple systems among the 2080 late-M, L, and T dwarfs from the literature. This binary fraction of only 4% is less than the $\approx$ 20% estimated by population studies (e.g., Marocco et al. 2015), implying that our catalog indeed contains unrecognized binaries. This is not surprising given that many ultracool dwarfs have not yet been targeted with high-resolution imaging.

The $\approx 1\farcs1$ angular resolution of PS1 allows it to resolve binaries that were not resolved in either 2MASS ($\approx 2\farcs5$ Skrutskie et al. 2006) or AllWISE ($\approx 6''$ for the W1 and W2 bands Wright et al. 2010). However, the literature contains fewer than twenty binaries with separations wider than $1''$ for which both components are ultracool dwarfs. Most of these binaries do not appear in our catalog because they are too far south for PS1 ($\delta < -30°$) or because both components are M dwarfs (for which our catalog is not complete). Our catalog contains a single instance of a binary resolved in PS1 and 2MASS, but not in AllWISE: UScoCTIO 108 and UScoCTIO 108b (Béjar et al. 2008). For this pair, we report the AllWISE photometry (blended) only for the primary (treating it as an unresolved binary), and no AllWISE photometry for the secondary.

Our catalog also contains three ultracool binaries that are resolved in PS1, 2MASS, and AllWISE. We report the photometry and proper motion for each component individually. One pair, LP 704-48 and SDSS J000649.16−085246.3 (itself an unresolved binary), is well-separated at $27\farcs4$ (Burgasser et al. 2012). Another pair, the blue L6 dwarf SDSS J141624.08+134826.7 and the T7.5 dwarf ULAS J141623.94+134836.3, has a separation of $9''$ (Burningham et al. 2010b) and is well resolved in PS1. ULAS J141623.94+134836.3 was not detected in 2MASS despite lying well outside the PSF of the brighter L6 primary; we include synthetic 2MASS photometry from Dupuy & Liu (2012) in our catalog. ULAS J141623.94+134836.3 appears barely resolved in AllWISE images, and we include pipeline-deblended AllWISE photometry for each component in our catalog. Finally, VHS J125601.92−125723.9AB (also an unresolved binary; Stone et al. 2016) and its companion VHS J125601.92-125723.9 b (separation $8\farcs1$; Gauza et al. 2015) are well-resolved in both PS1 and 2MASS. They appear partially resolved in AllWISE images. We include in our catalog the deblended photometry from AllWISE for the primary and the decontaminated photometry for the wide companion (removing a diffraction spike) from Gauza et al. (2015).

We also note two previously known binaries in our catalog with separations $\approx 1''$ that appear resolved in PS1 images, but are each represented by only a single object in the PS1

database: DENIS-P J220002.05−303832.9 and 2MASS J17072343−0558249. These cases result from the algorithm by which the PS1 database assembles multiple detections over the four years of PS1 observations into individual objects (see Section 6.4.1 and E. A. Magnier et al., 2017, in prep, for more details). Close binaries may be combined into a single object in the database, especially if the binary's proper motion over the PS1 survey period is comparable in amplitude and direction to the binary's separation. We have not attempted to de-blend these objects in our catalog, and we mark both as binaries (unresolved) in our catalog. More ≈1" binaries such as these are sure to appear in the PS1 database as single objects; we describe our discovery of one such binary in Section 6.5.

6.2.7 Completeness

Our catalog is a combination of discoveries from many searches for M, L, and T dwarfs, conducted using a variety of methods and therefore containing a variety of biases. Our selection of a representative sample of M dwarfs means that our catalog will be far from complete for this spectral type, especially for types M0–M5 for which our photometric quality cuts include only bright objects. While we have included all previously identified L and T dwarfs observed by PS1, there are some L and T dwarfs beyond the detection limit or angular resolution of PS1 (Figure 6.2), and there are sure to be undiscovered objects remaining in the PS1 field.

We assess the completeness of our catalog for spectral types M6–T9 by examining the number of objects as a function of distance, shown in Figure 6.3. We use trigonometric parallax distances when available from the literature. For the remaining objects we use photometric distances calculated from $W2$ magnitudes and the spectral type-absolute magnitude polynomial from Dupuy & Liu (2012). Photometric distances for unresolved binaries will be systematically too small, so we exclude known binaries from our assessment. Figure 6.3 also compares the cumulative distributions of late-M, L, and T dwarf distances to distributions from a simple Galactic thin disk model for space density $\rho = \rho_0 \exp[-Z/H_0]$, where ρ_0 is the space density at the Galactic plane, Z is the distance from the plane and

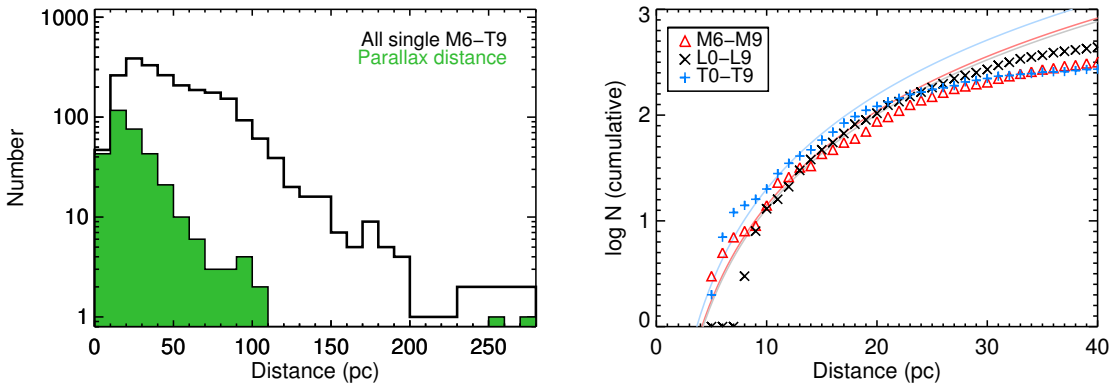

Figure 6.3 *Left*: Distribution of the distances of single M6–T9 dwarfs in our catalog (black outline). Where available, we use a parallax distance from the literature (solid green). For other objects we use $W2$-based photometric distances. *Right*: Cumulative distribution of these distances for M (red triangles), L (black ×), and T (blue +) dwarfs, using a format similar to Figure 5 in Faherty et al. (2009). The curves indicate density distributions from a simple Galactic thin disk model with a scale height of 300 pc, normalized at 10 pc. We use light red, grey, and blue curves for M, L, and T dwarfs, respectively. Our catalog is not consistent with the expected density distribution beyond 10 pc for late-M and T dwarfs, or 20 pc for L dwarfs, implying that our catalog is incomplete beyond these distances.

$H_0 = 300$ pc is the scale height (Bochanski et al. 2010). We integrate this model over the PS1 survey area to account for varying lines of sight relative to the galactic plane. We normalize this model distribution with the cumulative numbers of known late-M, L, and T dwarfs at 10 pc. The numbers of objects begin to deviate from our model distributions at ≈10 pc for late-M and T dwarfs and ≈20 pc for L dwarfs, implying that our catalog is not volume-complete beyond these distances.

6.3 Photometry

We present the PS1, 2MASS, and AllWISE photometry for our catalog in Table 6.1. PS1 photometry is on the AB magnitude scale (Tonry et al. 2012), calibrated using the procedures outlined in Schlafly et al. (2012) and Magnier et al. (2013). 2MASS, AllWISE, and *Gaia* photometry are calibrated on the Vega magnitude scale (Cohen et al. 2003; Wright et al. 2010; Carrasco et al. 2016, respectively).

The full table contains 51 columns, and is available for download in electronic form in the online journal. Table 6.1 is arranged in two parts: (1) the late-M, L, and T dwarfs compiled from the literature, followed by (2) the M dwarfs from West et al. (2008). For reference, Table 6.1 includes spectral types (with notation for subdwarfs), and indicates whether an object has been classified as a low-gravity object based on its optical or near-IR spectrum, identified as a young object (due to low gravity or other reasons), or confirmed as a binary. Table 6.2 shows a sample of the rows and columns of Table 6.1 for guidance regarding format and content.

Table 6.1. Photometry of M, L, and T Dwarfs in the Pan-STARRS1 3π Survey

Column	Label	Description
1	Name	Name used in the object's discovery or spectral confirmation paper
2	Spectral Type: Opt	Optical spectral type[a,b]
3	Spectral Type: NIR	Near-infrared spectral type[a,b]
4	Spectral Type: Adopted	Adopted spectral type[a,b]
5	Gravity: Opt	Low-gravity classification from an optical spectrum[b]
6	Gravity: NIR	Low-gravity classification from a near-infrared spectrum[b]
7	Binary	"Y" or "triple" for known binary or triple systems not resolved in PS1
8	Young	"Y" for known young objects[c]
9	Pan-STARRS1 Name	PS1 Designation;[d] rrr.rrrr+dd.dddd (J2000)
10	$g_{\rm P1}$	PS1 g magnitude
11	$\rm err_{g_{P1}}$	Error in PS1 g magnitude
12	N_g	Number of measurements used in the $g_{\rm P1}$ photometry
13	$\rm S_g$	Source of the $g_{\rm P1}$ photometry: chip (C), recalculated chip[e](R), or forced warp (W)
14	$r_{\rm P1}$	PS1 r magnitude
15	$\rm err_{r_{P1}}$	Error in PS1 r magnitude
16	N_r	Number of measurements used in the $r_{\rm P1}$ photometry
17	$\rm S_r$	Source of the $r_{\rm P1}$ photometry: chip (C), recalculated chip[e](R), or forced warp (W)
18	$i_{\rm P1}$	PS1 i magnitude
19	$\rm err_{i_{P1}}$	Error in PS1 i magnitude
20	N_i	Number of measurements used in the $i_{\rm P1}$ photometry
21	$\rm S_i$	Source of the $i_{\rm P1}$ photometry: chip (C), recalculated chip[e](R), or forced warp (W)
22	$z_{\rm P1}$	PS1 z magnitude

Table 6.1—Continued

Column	Label	Description
23	$\mathrm{err}_{z_{\mathrm{P1}}}$	Error in PS1 z magnitude
24	N_z	Number of measurements used in the z_{P1} photometry
25	S_z	Source of the z_{P1} photometry: chip (C), recalculated chip$^{\mathrm{e}}$(R), or forced warp (W)
26	y_{P1}	PS1 y magnitude
27	$\mathrm{err}_{y_{\mathrm{P1}}}$	Error in PS1 y magnitude
28	N_y	Number of measurements used in the y_{P1} photometry
29	S_y	Source of the y_{P1} photometry: chip (C), recalculated chip$^{\mathrm{e}}$(R), or forced warp (W)
30	2MASS Name	2MASS catalog designation
31	J	J magnitude or upper limit (2MASS)
32	err_J	Error in J magnitude
33	H	H magnitude or upper limit (2MASS)
34	err_H	Error in H magnitude
35	K_S	K_S magnitude or upper limit (2MASS)
36	err_{K_S}	Error in K_S magnitude
37	2MASS Clfg	2MASS contamination and confusion flags: three-character string corresponding to JHK bands.

Table 6.1—Continued

Column	Label	Description
38	AllWISE Name	AllWISE catalog designation
39	$W1$	$W1$ magnitude or upper limit (AllWISE)
40	err_{W1}	Error in $W1$ magnitude
41	$W2$	$W2$ magnitude or upper limit (AllWISE)
42	err_{W2}	Error in $W2$ magnitude
43	$W3$	$W3$ magnitude or upper limit (AllWISE)
44	err_{W3}	Error in $W3$ magnitude
45	$W4$	$W4$ magnitude or upper limit (AllWISE)
46	err_{W4}	Error in $W4$ magnitude
47	AllWISE cc_flags	AllWISE contamination and confusion flags: four-character string corresponding to W1W2W3W4 bands.
48	AllWISE neighbor	Number of other AllWISE objects detected within $8''$ of the AllWISE position.
49	G	*Gaia* DR1 G magnitude
50	err_{G}	Error in *Gaia* DR1 G magnitude
51	References	References: Discovery, Spectral Type, Gravity, Binarity, 2MASS photometry, AllWISE photometry

[a]Spectral types taken from the literature (Section 6.2.4). When both optical and near-IR types are available, we adopt the optical type for M and L dwarfs and the near-IR type for T dwarfs. Most spectral types have an uncertainty of ±0.5 subtypes; ":" = ±1 subtype; "::" = ±2 or more subtypes. "sd" = subdwarf; "esd" = extreme subdwarf (Gizis 1997).

[b]β, γ, and δ indicate classes of increasingly low gravity based on optical (Kirkpatrick 2005; Cruz et al. 2009) or near-infrared (Gagné et al. 2015c) spectra. FLD-G indicates near-infrared spectral signatures of field-age gravity, INT-G indicates intermediate gravity, and VL-G indicates very low gravity (Allers & Liu 2013a).

[c]Young objects identified by low-gravity classifications or other spectroscopic evidence for youth, membership in star-forming regions or young moving groups, or companionship to a young star (Section 6.2.5).

[d]Pan-STARRS names are from the 3π Survey, Processing Version 3.3 (PV3.3). Photometry listed here is from PV3.3 and supersedes values in previous publications.

[e]Chip photometry recalculated by combining the measurements for an object that is split into two or more "partial objects" in PS1 (Sections 6.3.1 and 6.4.1).

[f]Although classified as FLD-G, the spectrum shows hints of intermediate gravity (as described in Aller et al. 2016).

[g]Photometry rejected for this band after visual inspection of stack images found no detection at the PS1 coordinates.

[h]Photometry rejected for this band after visual inspection of stack images found obvious contamination by a background object.

[i]Photometry rejected for this band after visual inspection of stack images found an image processing artifact at the PS1 coordinates.

[j]Photometry rejected for this band after visual inspection of stack images found obvious contamination from a nearby bright star.

[k]UScoCTIO 108 and UScoCTIO 108b (Béjar et al. 2008) are not resolved in AllWISE. For this binary, we report AllWISE photometry (blended) only for the primary, and no AllWISE photometry for the secondary.

Note. — This table is available in its entirety in machine-readable form in the online journal. A sample of the rows and columns is shown in Table 6.2.

6.3.1 PS1 Photometry

Chip and Forced Warp Photometry

Our catalog uses two types of PSF photometry from the PS1 database, known as "chip" and "forced warp." These types are described in detail in E. A. Magnier et al. (2017, in prep), and we explain them briefly here.

During PS1 data processing, each raw image was individually detrended and calibrated to create a "chip" image, and each detected object on a chip was fitted with a PSF model to determine its photometry and astrometry. The chip pixels were geometrically transformed onto a grid with uniform $0.25''\,\mathrm{pixel}^{-1}$ scale representing pre-defined sky coordinates (R.A. and Decl.), creating "warp" images. The warps for each filter matching the same portions of the sky were then summed together, forming "stack" images. Detections in the warps and stacks were again fit with PSFs to measure photometry and astrometry.

Chip photometry is the mean measurement from all chips in which an object was detected, and is likely to be the most accurate photometry for a well-detected object due to the individual calibration of each chip. Stack photometry is measured from the single fit to a stack detection. Stack photometry will generally be less accurate because individual images forming a stack were taken in varying conditions and at different locations on the Pan-STARRS1 detector, creating poorly-defined PSFs. However, the stacks can identify objects too faint to be detected in individual images, as long as the objects do not move significantly over the 4-year time baseline of the survey. To take advantage of the greater depth of the stacks without sacrificing too much of the calibration of the chip images, the PS1 data pipeline fit a model PSF on every warp image at the location of each object detected in a stack. The warp photometry reported by PS1 is the mean of the fluxes from the forced PSF fits at a given location, excluding cases where the warp pixels were excessively masked. Warp photometry will not have the full accuracy of the chip measurements, but achieves the depth of the stack photometry with more accuracy than the stack image alone.

Table 6.2. Sample of columns in Table 6.1

Discovery Name	Spectral Type[a,b]			Binary	Young[c]	Pan-STARRS1								References (Disc; SpT; Grav; Bin;) (2MASS; AllWISE)
	Opt	NIR	Adopted			z_{P1} (mag)	$\mathrm{err}_{z_{P1}}$ (mag)	N_z	S_z	y_{P1} (mag)	$\mathrm{err}_{y_{P1}}$ (mag)	N_y	S_y	
SDSS J000013.54+255418.6	T5	T4.5	T4.5	···	···	19.17	0.01	10	C	17.42	0.01	11	C	175; 247,51; –; –; 88; –
SDSS J000112.18+153535.5	···	L3.7 INT-G	L3.7 INT-G	···	Y	18.85	0.02	7	C	17.81	0.01	10	C	175; 124; 124; –; 88; 89
WISEA J000131.93−084126.9	···	L1 pec (blue)	L1 pec (blue)	···	···	18.57	0.01	12	C	17.57	0.01	10	C	218; 218; –; –; 88; 89
SDSS J000250.98+245413.8	···	L5.5	L5.5	···	···	20.30	0.04	9	W	19.31	0.03	16	W	74; 74; –; –; 88; 89
2MASSI J0003422−282241	M7.5	M7: FLD-G	M7.5	···	···	15.43	0.01	6	C	14.67	0.01	6	C	83; 83,11; 11; –; 88; 89
2MASS J00044144−2058298	M8	···	M8	···	···	14.94	0.01	5	C	14.06	0.01	7	C	160; 161; –; –; 88; 89
2MASS J00054844−2157196	M9	···	M9	···	···	15.69	0.01	10	C	14.84	0.01	8	C	270; 268; –; –; 88; 89

References. — (1) This work, (2) Aberasturi et al. (2014), (3) Aganze et al. (2016), (4) Albert et al. (2011), (5) Allen et al. (2007), (6) Allen et al. (2012), (7) Aller et al. (2013), (8) Aller et al. (2016), (9) Allers et al. (2009), (10) Allers et al. (2010), (11) Allers & Liu (2013a), (12) Allers & Liu (2013b), (13) Alves de Oliveira et al. (2013), (14) Artigau et al. (2006), (15) Artigau et al. (2011), (16) Bardalez Gagliuffi et al. (2014), (17) Bardalez Gagliuffi et al. (2015), (18) Baron et al. (2015), (19) Barrado Y Navascués et al. (2002), (20) Basri et al. (2000), (21) Beamín et al. (2013), (22) Becklin & Zuckerman (1988), (23) Béjar et al. (2008), (24) Bessell (1991), (25) Best et al. (2013), (26) Best et al. (2015), (27) Best et al. (2017a), (28) Best et al. (2017b), (29) Bihain et al. (2010), (30) Bihain et al. (2013), (31) Boeshaar (1976), (32) Boudreault & Lodieu (2013), (33) Bouvier et al. (2008), (34) Bouy et al. (2003), (35) Bowler et al. (2010), (36) Bryja et al. (1992), (37) Bryja et al. (1994), (38) Burgasser et al. (1999), (39) Burgasser et al. (2000a), (40) Burgasser et al. (2000b), (41) Burgasser et al. (2002), (42) Burgasser et al. (2003a), (43) Burgasser et al. (2003e), (44) Burgasser et al. (2003c), (45) Burgasser et al. (2003b), (46) Burgasser et al. (2003d), (47) Burgasser (2004b), (48) Burgasser et al. (2004), (49) Burgasser et al. (2005b), (50) Burgasser et al. (2005a), (51) Burgasser et al. (2006a), (52) Burgasser & Kirkpatrick (2006), (53) Burgasser et al. (2006b), (54) Burgasser & McElwain (2006), (55) Burgasser (2007b), (56) Burgasser et al. (2007), (57) Burgasser et al. (2008a), (58) Burgasser et al. (2008b), (59) Burgasser et al. (2009b), (60) Burgasser et al. (2009a), (61) Burgasser et al. (2010b), (62) Burgasser et al. (2010a), (63) Burgasser et al. (2011a), (64) Burgasser et al. (2012), (65) Burgasser et al. (2015a), (66) Burgasser et al. (2016), (67) Burningham et al. (2010a), (68) Burningham et al. (2010b), (69) Burningham et al. (2011), (70) Burningham et al. (2013), (71) Castro & Gizis (2012), (72) Castro et al. (2013), (73) Castro & Gizis (2016), (74) Chiu et al. (2006), (75) Chiu et al. (2008), (76) Close et al. (2002a), (77) Close et al. (2002b), (78) Close et al. (2003), (79) Crifo et al. (2005), (80) Cruz & Reid (2002), (81) Cruz et al. (2003), (82) Cruz et al. (2004), (83) Cruz et al. (2007), (84) Cruz et al. (2009), (85) Cushing & Vacca (2006), (86) Cushing et al. (2011), (87) Cushing et al. (2014), (88) Cutri et al. (2003), (89) Cutri et al. (2014), (90) Dahn et al. (1986), (91) Dahn et al. (2002), (92) Dahn et al. (2008), (93) Dawson et al. (2014), (94) Day-Jones et al. (2013), (95) Deacon et al. (2005), (96) Deacon & Hambly (2007), (97) Deacon et al. (2009), (98) Deacon et al. (2011), (99) Deacon et al. (2012a), (100) Deacon et al. (2012b), (101) Deacon et al. (2014), (102) Deacon et al. (2017a), (103) Deacon et al. (2017b), (104) Delfosse et al. (1997), (105) Delfosse et al. (1999), (106) Delorme et al. (2008), (107) Dobbie et al. (2002), (108) Dupuy et al. (2009a), (109) Dupuy et al. (2010), (110) Dupuy & Liu (2012), (111) Dupuy et al. (2015b), (112) Dupuy et al. (2016), (113) Dupuy & Liu (2017), (114) Faherty et al. (2009), (115) Faherty et al. (2010), (116) Faherty et al. (2012), (117) Faherty et al. (2013), (118) Faherty et al. (2016), (119) Fan et al. (2000), (120) Folkes et al. (2012), (121) Forveille et al. (2005), (122) Freed et al. (2003), (123) Gagné et al. (2014a), (124) Gagné et al. (2015c), (125) Gagné et al. (2017), (126) Gauza et al. (2012), (127) Gauza et al. (2015), (128) Geballe et al. (2002), (129) Geißler et al. (2011), (130) Gelino et al. (2011), (131) Gelino et al. (2014), (132) Giampapa & Liebert (1986), (133) Giclas et al. (1967), (134) Gillon et al. (2016), (135) Gilmore et al. (1985), (136) Gizis (1997), (137) Gizis & Reid (1997), (138) Gizis et al. (2000a), (139) Gizis et al. (2000b), (140) Gizis et al. (2001), (141) Gizis (2002), (142) Gizis et al. (2003), (143) Gizis et al. (2011b), (144) Gizis et al. (2011a), (145) Gizis et al. (2012), (146) Gizis et al. (2013), (147) Gizis et al. (2015a), (148) Goldman et al. (2010), (149) Gomes et al. (2013), (150) Hall (2002), (151) Hawley et al. (2002), (152) Henry & Kirkpatrick (1990), (153) Henry et al. (2004), (154) Henry et al. (2006), (155) Huelamo et al. (2015), (156) Irwin et al. (1991), (157) Kellogg et al. (2015), (158) Kendall et al. (2003), (159) Kendall et al. (2004), (160) Kendall et al. (2007a), (161) Kendall et al. (2007b), (162) Kirkpatrick et al. (1991), (163) Kirkpatrick et al. (1993), (164) Kirkpatrick et al. (1994), (165) Kirkpatrick et al. (1995), (166) Kirkpatrick et al. (1997b), (167) Kirkpatrick et al. (1997a), (168) Kirkpatrick et al. (1999), (169) Kirkpatrick et al. (2000), (170) Kirkpatrick et al. (2001b), (171) Kirkpatrick et al. (2008), (172) Kirkpatrick et al. (2010), (173) Kirkpatrick et al. (2011), (174) Kirkpatrick et al. (2014), (175) Knapp et al. (2004), (176) Koerner et al. (1999), (177) Kraus & Hillenbrand (2009b), (178) Lachapelle et al. (2015), (179) Law et al. (2006), (180) Leggett (1992), (181) Leggett et al. (1996), (182) Leggett et al. (2000), (183) Leinert et al. (1994), (184) Lépine et al. (2002b), (185) Lépine et al. (2002a), (186) Lépine et al. (2003a), (187) Lépine et al. (2003b), (188) Lépine et al. (2003c), (189) Lépine & Shara (2005), (190) Lépine et al. (2009), (191) Liebert et al. (1979), (192) Liebert et al. (2003), (193) Liebert & Gizis (2006), (194) Liu et al. (2002b), (195) Liu & Leggett (2005), (196) Liu et al. (2006), (197) Liu et al. (2010), (198) Liu et al. (2011b), (199) Liu et al. (2013), (200) Liu et al. (2016), (201) Lodieu et al. (2002), (202) Lodieu et al. (2005), (203) Lodieu et al. (2007b), (204) Lodieu et al. (2008), (205) Lodieu et al. (2010), (206) Lodieu et al. (2012c), (207) Lodieu et al. (2012b), (208) Lodieu (2013), (209) Lodieu et al. (2014), (210) Looper et al. (2007), (211) Looper et al. (2008b), (212) Looper (2011), (213) Loutrel et al. (2011), (214) Lucas et al. (2010), (215) Luhman et al. (2007), (216) Luhman et al. (2009), (217) Luhman et al. (2012), (218) Luhman & Sheppard (2014), (219) Luyten (1979), (220) Mace et al. (2013a), (221) Manjavacas et al. (2013), (222) Marocco et al. (2013), (223) Marocco et al. (2015), (224) Marshall (2008), (225) Martín et al. (1994), (226) Martín et al. (1998b), (227) Martín et al. (1999b), (228) Martín et al. (1999a), (229) Martín et al. (2000), (230) Martín et al. (2010), (231) Matsuoka et al. (2011), (232) McCarthy et al. (1964), (233) McCaughrean et al. (2002), (234) McElwain & Burgasser (2006), (235) McGovern et al. (2004), (236) Metchev et al. (2008), (237) Mohanty & Basri (2003), (238) Montagnier et al. (2006), (239) Mugrauer et al. (2006), (240) Murphy et al. (2015), (241) Murray et al. (2011), (242) Muzic et al. (2012), (243) Phan-Bao et al. (2001), (244) Phan-Bao & Bessell (2006), (245) Phan-Bao et al. (2006), (246) Phan-Bao et al. (2008), (247) Pineda et al. (2016), (248) Pinfield et al. (2008), (249) Pokorny et al. (2004), (250) Probst & Liebert (1983), (251) Radigan et al. (2008), (252) Radigan et al. (2013), (253) Rebolo et al. (1998), (254) Reid & Gilmore (1981), (255) Reid et al. (1995), (256) Reid et al. (2000), (257) Reid et al. (2001), (258) Reid & Cruz (2002), (259) Reid et al. (2002b), (260) Reid et al. (2003a), (261) Reid et al. (2003b), (262) Reid (2003), (263) Reid et al. (2004), (264) Reid & Gizis (2005), (265) Reid et al. (2006b), (266) Reid et al. (2006a), (267) Reid et al. (2007), (268) Reid et al. (2008b), (269) Reiners & Basri (2006), (270) Reylé & Robin (2004), (271) Rice et al. (2010), (272) Rodono et al. (1980), (273) Rodriguez et al. (2013), (274) Ruiz et al. (1997), (275) Ruiz et al. (2001), (276) Sahlmann et al. (2015a), (277) Salim et al. (2003), (278) Sarro et al. (2014), (279) Schmidt et al. (2007), (280) Schmidt et al. (2010), (281) Schmidt et al. (2015), (282) Schneider et al. (1991), (283) Schneider et al. (2002), (284) Schneider et al. (2011), (285) Schneider et al. (2014), (286) Schneider et al. (2016a), (287) Schneider et al. (2016b), (288) Scholz et al. (2001), (289) Scholz & Meusinger (2002), (290) Scholz et al. (2004a), (291) Scholz et al. (2004b), (292) Scholz et al. (2009), (293) Scholz (2010a), (294) Scholz (2010b), (295) Scholz et al. (2011), (296) Scholz et al. (2012), (297) Scholz (2014), (298) Scholz et al. (2014), (299) Schweitzer et al. (1999), (300) Seifahrt et al. (2010), (301) Sheppard & Cushing (2009), (302) Shkolnik et al. (2009), (303) Siegler et al. (2003), (304) Siegler et al. (2005), (305) Siegler et al. (2007), (306) Silvestri et al. (2007), (307) Sivarani et al. (2009), (308) Skrutskie et al. (2006), (309) Stern et al. (2007), (310) Stone et al. (2016), (311) Strauss et al. (1999), (312) Stumpf et al. (2009), (313) Stumpf et al. (2010), (314) Stumpf et al. (2011), (315) Thompson et al. (2013), (316) Thorstensen & Kirkpatrick (2003), (317) Tinney (1993a), (318) Tinney (1993b), (319) Tinney et al. (1993), (320) Tinney (1996), (321) Tinney et al. (1998), (322) Tinney et al. (2005), (323) Tsvetanov et al. (2000), (324) van Biesbroeck (1961), (325) West et al. (2008), (326) Wilson et al. (2001), (327) Wilson et al. (2003), (328) Wright et al. (2013), (329) Zapatero Osorio et al. (1999), (330) Zapatero Osorio et al. (2000), (331) Zhang et al. (2009), (332) Zhang et al. (2010), (333) Zhang et al. (2013).

Note. — Table 6.1 is published in its entirety in machine readable format in the online journal. A portion is shown here for guidance regarding its form and content. The full table contains 51 columns and 9888 rows.

Warp photometry is therefore most useful, at least in theory, for slow-moving objects with magnitudes comparable to or fainter than the chip detection limit.

To quantify where PS1 chip and warp photometry differ significantly, we examined the photometry of a large sample of well-detected objects in PS1 chip images. For each of the five PS1 bands, we extracted the chip and warp magnitudes for all objects having at least three chip detections in a 4 deg^2 patch of sky (centered at $\alpha = 80°$, $\delta = 5°$) at moderate galactic latitude ($\approx -18°$) and away from regions of significant reddening. This gave us a sample of more than 60,000 objects in each band, $\gtrsim$99% having proper motions less than 100 mas yr^{-1}. Figure 6.4 plots the differences between y_{P1} chip and warp magnitudes for each object, normalized by the quadrature sum of the chip and warp errors, as a function of magnitude. For brighter unsaturated objects ($y_{\mathrm{P1}} \approx 13 - 19$ mag), the difference between chip and warp magnitudes is nearly always less than 2σ. For objects fainter than $y_{\mathrm{P1}} \approx 19$ mag, however, the chip photometry becomes significantly brighter for many objects, due to a flux overestimation bias for objects near the chip detection threshold. This well-known bias is discussed in depth in the context of 2MASS in Cutri et al. (2006) and Kellogg et al. (2015), and is important for detections with S/N $\lesssim 10$. Briefly, because the chips have brighter detection limits than the warps, mean chip photometry may not include the fainter measurements that are present in the warp photometry. For example, an object near the chip detection limit may have 10 forced warp measurements but only three chip detections due to noise at the detection threshold. Those chip detections will be the three brightest measurements of the object, so the mean chip magnitude will be brighter than the mean warp magnitude. Warp photometry is therefore more likely to be accurate for faint objects near the chip detection limits in each band. We list the magnitudes at which the flux overestimation bias becomes significant for chip photometry in each PS1 band in Table 6.3, based on visual inspection of Figure 6.4 and analogous plots for the other PS1 bands. We note that for even fainter objects, flux overestimation bias will also impact the warp photometry, but for those objects there is no deeper PS1 photometry available.

Table 6.3. Flux overestimation bias thresholds for PS1 chip photometry

Band	Threshold (mag)
$g_{\rm P1}$	21.0
$r_{\rm P1}$	21.0
$i_{\rm P1}$	20.5
$z_{\rm P1}$	20.0
$y_{\rm P1}$	19.0

Note. — PS1 chip magnitudes fainter than these thresholds may be significantly affected by flux overestimation bias. For slow-moving objects (<100 mas yr^{-1}), warp photometry is more likely to be accurate.

Objects that moved significantly over the four years of PS1 observations will be smeared on the stack images. This smearing will also impact the warp photometry, because the warp PSF fits are applied at the same location on each warp but a moving object will not be centered at that location in every warp. To assess the impact of proper motion on warp photometry, we examined the difference between chip and warp magnitudes for objects brighter than the faint thresholds in Table 6.3, sorted into bins of PS1-measured proper motion. We determined that nearly all objects for which chip and warp photometry are $>2\sigma$ different have proper motions exceeding 100 mas yr^{-1} (Figure 6.4), so we do not use warp photometry for objects moving faster than 100 mas yr^{-1}.

PS1 Photometry Reported in Our Catalog

For each object and PS1 band ($g_{\rm P1}r_{\rm P1}i_{\rm P1}z_{\rm P1}y_{\rm P1}$) in our catalog, we report a single magnitude, either chip or warp. By default, we use the chip photometry for objects with

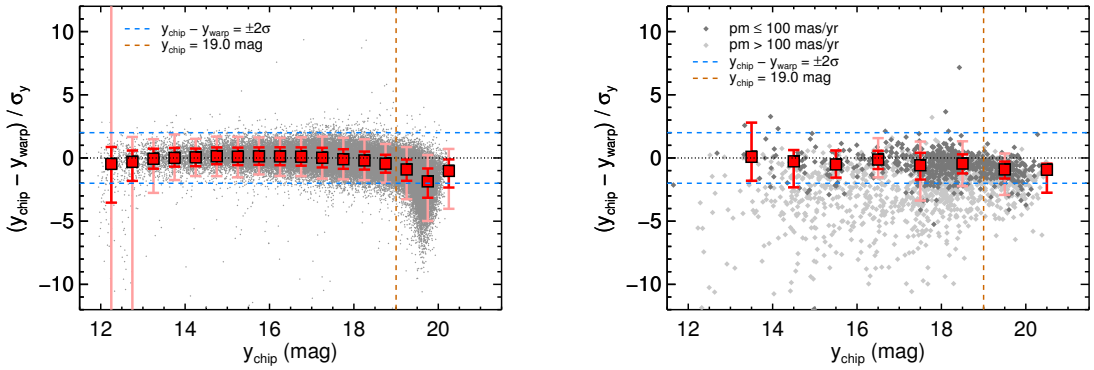

Figure 6.4 *Left*: Differences in $y_{\rm P1}$ chip and warp mean magnitudes (gray dots) for objects in an arbitrary 4 deg^2 patch of sky, normalized by the uncertainties. Over 99% of these objects have proper motions less than 100 mas yr^{-1}. The red boxes show the median differences for objects in bins of 0.5 mag; the dark and light red error bars indicate 68% and 95% confidence limits, respectively. For reference, the blue dashed lines mark $y_{\rm chip} - y_{\rm warp}$ differences of $\pm 2\sigma$, and the dotted black line indicates no difference. For objects of moderate brightness, the differences between chip and warp magnitudes are nearly always less than 2σ significance. At the bright end, saturation causes significant scatter in magnitudes. At the faint end, many chip magnitudes become significantly brighter due to flux overestimation bias. The vertical brown dashed line at $y = 19$ mag marks the onset of this bias. *Right*: The same plot for objects from our ultracool catalog. Those having proper motions less than 100 mas yr^{-1} are plotted in dark grey, with faster moving objects in light grey. The red boxes indicate the median $y_{\rm chip} - y_{\rm warp}$ differences only for the slower ($\mu \leq 100$ mas yr^{-1}) objects. Warp photometry is significantly fainter than chip photometry for most of the faster moving objects because an object is not at the same force-fit position in all warps. We use chip photometry in our catalog as our default, but use warp photometry for objects with $y_{\rm chip} > 19.0$ mag and proper motion < 100 mas yr^{-1}. Analogous plots for the other four PS1 bands show similar results.

chip errors < 0.2 mag and detected in at least two chip exposures. We use the warp photometry only in specific cases, when either:

1. Chip photometry is fainter than the thresholds listed in Table 6.3, to avoid flux overestimation bias in the chip photometry.

2. Chip photometry is either not measured or of insufficient quality (i.e., fewer than two detections or error ≥ 0.2 mag).

However, because warp photometry degrades for faster-moving objects, we only use warp photometry when both of the following are true:

1. A proper motion of $\mu > 100$ mas yr^{-1} with $\frac{\mu}{\sigma_\mu} > 3$ has not been measured in PS1 or the literature, to avoid fast-moving objects.

2. A proper motion with $\mu - \sigma_\mu > 100$ mas yr^{-1} has not been measured in PS1 or the literature, to avoid most fast-moving objects with poorly-measured proper motions.

Finally, we only use warp photometry with errors < 0.2 mag that are calculated from at least two successful warp fits, the same standards we use for chip photometry.

On the bright end, we rejected any photometry with $g_{\rm P1} < 14.5$ mag, $r_{\rm P1} < 14.5$ mag, $i_{\rm P1} < 14.5$ mag, $z_{\rm P1} < 13.5$ mag, or $y_{\rm P1} < 12.5$ mag to avoid saturation.

For many objects in our catalog we use chip photometry for some bands and warp for others, depending on the values and quality of the chip photometry. If neither the chip nor the warp photometry meet our quality standards in a given band, we report no photometry for that band. Objects with no chip or warp photometry of sufficient quality in any of the five PS1 bands do not appear in our catalog.

The photometric errors reported in the PS1 database are formal errors that do not include systematics. Given the sensitivity of the Pan-STARRS1 camera and the multiple epochs of photometry, these formal errors can be very small, less than 0.0005 mag in some cases. A full assessment of the systematic errors for PV3.3 has not yet been completed, but a calibration of the first 1.5 years of PS1 photometry performed by Schlafly et al. (2012)

found per-image zeropoints had rms scatter ≈ 10 mmag in all five PS1 filters, so we adopt this value (0.01 mag) as a floor for our catalog.

False Warp Detections of Faint Objects

While inspecting the PS1 colors of our catalog objects, we discovered a few dozen instances where very faint objects near the stack detection limit (e.g., $g_{\rm P1} \gtrsim 23$ mag) had warp photometry with implausibly small errors (as small as 0.01 mag) despite only two or three warps contributing to the mean photometry. In particular, we found T dwarfs with high-S/N warp photometry reported for $g_{\rm P1}$ and $r_{\rm P1}$. T dwarfs are much too faint in these visual bands to be detected by PS1. We confirmed that the $g_{\rm P1}$ and $r_{\rm P1}$ stack images showed no objects at the locations of these false detections.

We traced the source of these false high-S/N detections to the method used to calculate PS1 photometry errors. This method is described in detail in E. A. Magnier et al. (2017, in prep); here we give a brief summary. Each individual photometry measurement (chip, warp, or stack) includes a measurement uncertainty, which naturally is large for faint objects. Mean chip and warp magnitudes are computed using an iterative reweighting process to reject outliers, and the errors for the mean photometry are calculated by bootstrap resampling of the non-outlier measurements. Bootstrapping uses the individual measurements but not their uncertainties, instead sampling the outlier-cleaned photometry measurements to determine the error. For well-detected objects with multiple measurements, bootstrapping is demonstrated to calculate errors consistent with standard errors on the mean photometry while effectively clipping outliers such as transient image artifacts (E. A. Magnier et al., 2017, in prep). However, in cases where photometry was measured only a few times for an object, and those measurements are very similar (a statistical possibility even for objects at the detection limit), the bootstrapping process will produce a very small error, even if the individual measurements had large uncertainties. The false $g_{\rm P1}$ and $r_{\rm P1}$ warp detections in our catalog were the result of $\approx$2–3 low-S/N forced

warp measurements of background noise that happened to find similar values, resulting in errors < 0.2 mag (from bootstrapping) on the mean warp photometry.

To systematically identify and remove these false detections from our catalog, we extracted the individual warp flux measurements used to calculate the mean PS1 warp photometry for each object in our catalog, along with the formal uncertainties for the measurements. For each object and band, we calculated a weighted-mean warp magnitude (using inverse variance weighting) and the standard error on this weighted mean. If the reported warp error in PS1 (from bootstrapping) was less than 0.2 mag but our calculated standard error was greater than 0.2 mag, we discarded the warp photometry for that object and band. This procedure removed 12% of the PS1-reported warp measurements for the late-M, L, and T dwarfs from the literature that passed our original criteria for inclusion in the catalog (i.e., slow-moving objects with secure proper motion measurements, Section 6.3.1), affecting 255 objects in at least one band and demonstrating that false detections in the warps can be a significant source of contamination at the faint end. Specifically, we discarded 129 out of 199 measurements in $g_{\rm P1}$, 123 out of 410 in $r_{\rm P1}$, 27 out of 601 in $i_{\rm P1}$, 19 out of 677 in $r_{\rm P1}$, and 0 out of 698 in $y_{\rm P1}$, consistent with the red nature of the objects in our sample (nearly all have strong $y_{\rm P1}$ detections). If the reported warp error in PS1 and the standard error were both less than 0.2 mag, we retained the PS1-reported photometry and error for our catalog. We used our calculated standard errors only to assess the reliability of small warp photometry errors reported by PS1, and do not include them in our catalog.

Fast-Moving Objects

As discussed in detail in Section 6.4.1, we found that objects with proper motions $\gtrsim 200$ mas yr^{-1} were often split into two or more distinct "partial objects" in the PS1 database. In these cases we use the photometry from the partial object with the chip photometry in the most PS1 bands, giving preference to the redder bands if no partial object had photometry in all bands. In a few dozen cases where a chosen partial object had

no photometry or photometry of insufficient quality in a PS1 band, we used photometry recalculated by combining the measurements from the partial objects into a single object (Section 6.4.1) for that band.

6.3.2 2MASS and AllWISE Photometry

Our catalog contains photometry from 2MASS and AllWISE for all objects matched to PS1 detections (Section 6.2.1). We include 2MASS and AllWISE photometry with nonzero contamination and confusion flags for completeness' sake, and note that some of this potentially contaminated photometry has been used in previous studies. We include columns for the 2MASS and AllWISE contamination and confusion flags in Table 6.1, and refer readers to the Explanatory Supplements[2,3] for these surveys for details.

In addition, because the large $\approx 6''$ beam of WISE makes blending with nearby objects a frequent issue, we include a column in Table 6.1 indicating whether each object has an AllWISE neighbor within $8''$ of the AllWISE position. The AllWISE catalog includes deblended photometry for objects with overlapping PSFs, but the deblending may not be completely successful when objects are within $8''$ of each other (Theissen et al. 2016, see their Figure 6).

While we include photometry with non-zero contamination and confusion flags and potential contamination from neighbors in our catalog, we exclude such photometry from our analysis of colors and SEDs in Section 6.3.4.

6.3.3 *Gaia* DR1 Photometry

To obtain *Gaia* DR1 G-band photometry, we cross-matched our catalog (PS1 coordinates) with *Gaia* DR1 using a $2''$ matching radius. We found matches for 7772 objects including 284 L dwarfs. As *Gaia* DR1 is preliminary and does not cover the entire PS1 survey area, we do not evaluate the DR1 G-band photometry for M, L, and T dwarfs here, but we include it in our catalog for reference. We rejected *Gaia* photometry for objects in our

[2]http://www.ipac.caltech.edu/2mass/releases/allsky/doc/sec2_2a.html
[3]http://wise2.ipac.caltech.edu/docs/release/allwise/expsup/sec2_1a.html

catalog for which we had identified contamination to $g_{\rm P1}$, $r_{\rm P1}$, or $i_{\rm P1}$ photometry by a bluer object (Section 6.2.1), but performed no other quality inspection of the *Gaia*-PS1 matches. Many G magnitudes have reported errors less than 0.01 mag, but as *Gaia*'s systematic photometric uncertainties are not yet fully understood (Gaia Collaboration et al. 2016b), we adopt a minimum error of 0.01 mag.

6.3.4 Colors and SEDs

We show multiple colors from our catalog in Figures 6.5–6.8, spanning $g_{\rm P1}$ through $W3$. We show 11 colors using at least one PS1 band, and four more ($(J-K_S)_{\rm 2MASS}$, $J_{\rm 2MASS}-W1$, $W1-W2$, and $W2-W3$) that have been used in many previous studies. To create these figures, we have extracted all objects known to be young, subdwarfs, or binaries, and used these to form a sample of "unusual" objects. The remaining objects are our "normal field" sample. Figure 6.5 shows colors as a function of spectral type for the normal field sample, and Figure 6.6 shows the same colors for the unusual sample. In Figures 6.7 and 6.8, we use the same format to show colors vs. colors for the normal field and unusual samples, respectively.

For the figures and analysis presented in this section, we only use 2MASS and AllWISE photometry with errors less than 0.2 mag, the same standard we use for PS1 photometry (Section 6.3.1). (Note that Table 6.1 includes 2MASS and AllWISE photometry with larger errors.) In addition, we exclude any 2MASS or AllWISE magnitude with a non-zero contamination flag, and we exclude all AllWISE magnitudes for each object that has an AllWISE neighbor within $8''$ (Section 6.3.2).

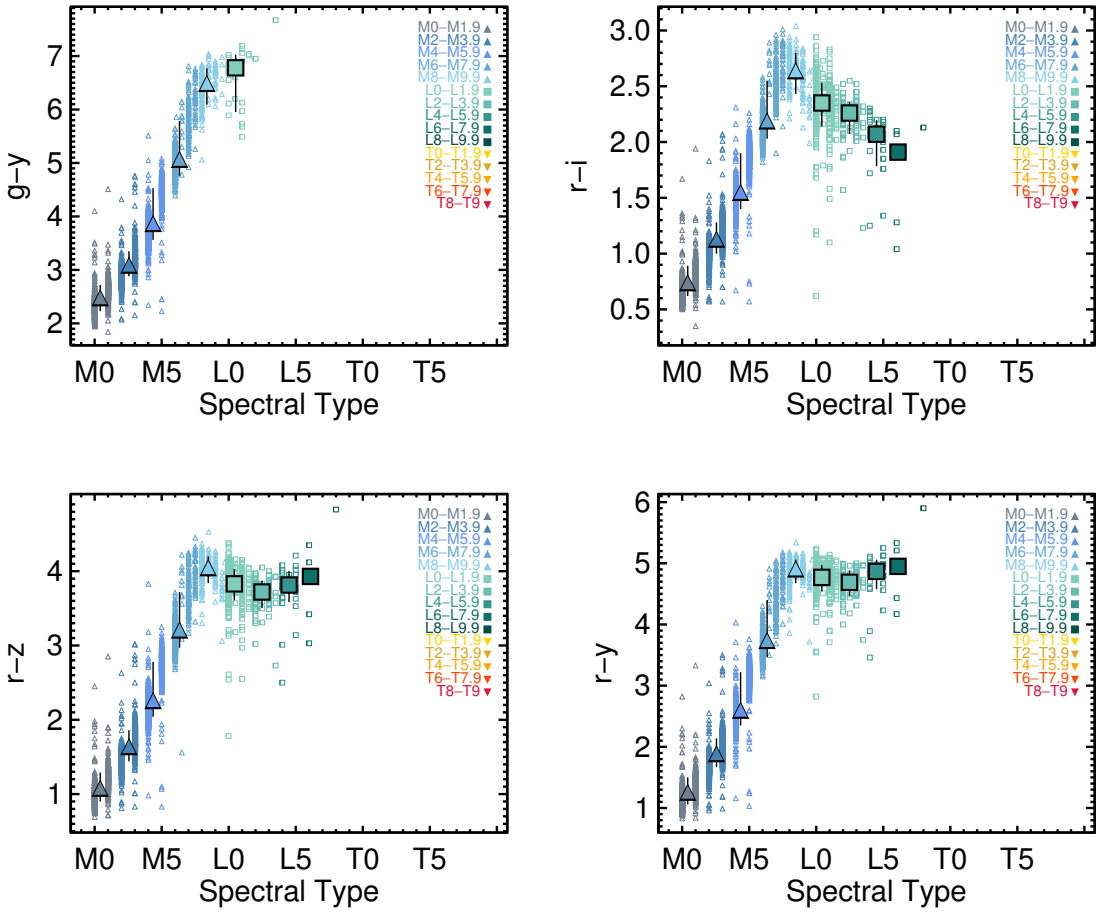

Figure 6.5 Color vs. spectral type plots for the M, L, and T dwarfs in our PS1-detected catalog, excluding objects known to be binaries, subdwarfs, or young. We use only photometry with errors < 0.2 mag. For objects having both optical and near-IR spectral types, we use the optical type for M and L dwarfs and the near-IR type for T dwarfs. Colors of individual objects are shown with small open symbols, while median colors and 68% confidence limits for bins of two spectral subtypes are shown with large filled symbols (see legend in each figure). Median symbols are plotted for bins with at least three objects, and confidence limits for bins with at least seven objects. Most PS1 colors plateau through the L dwarfs but become redder for T dwarfs (when detected); $r_{\rm P1} - i_{\rm P1}$ and $y_{\rm P1} - W1$ are notable exceptions.

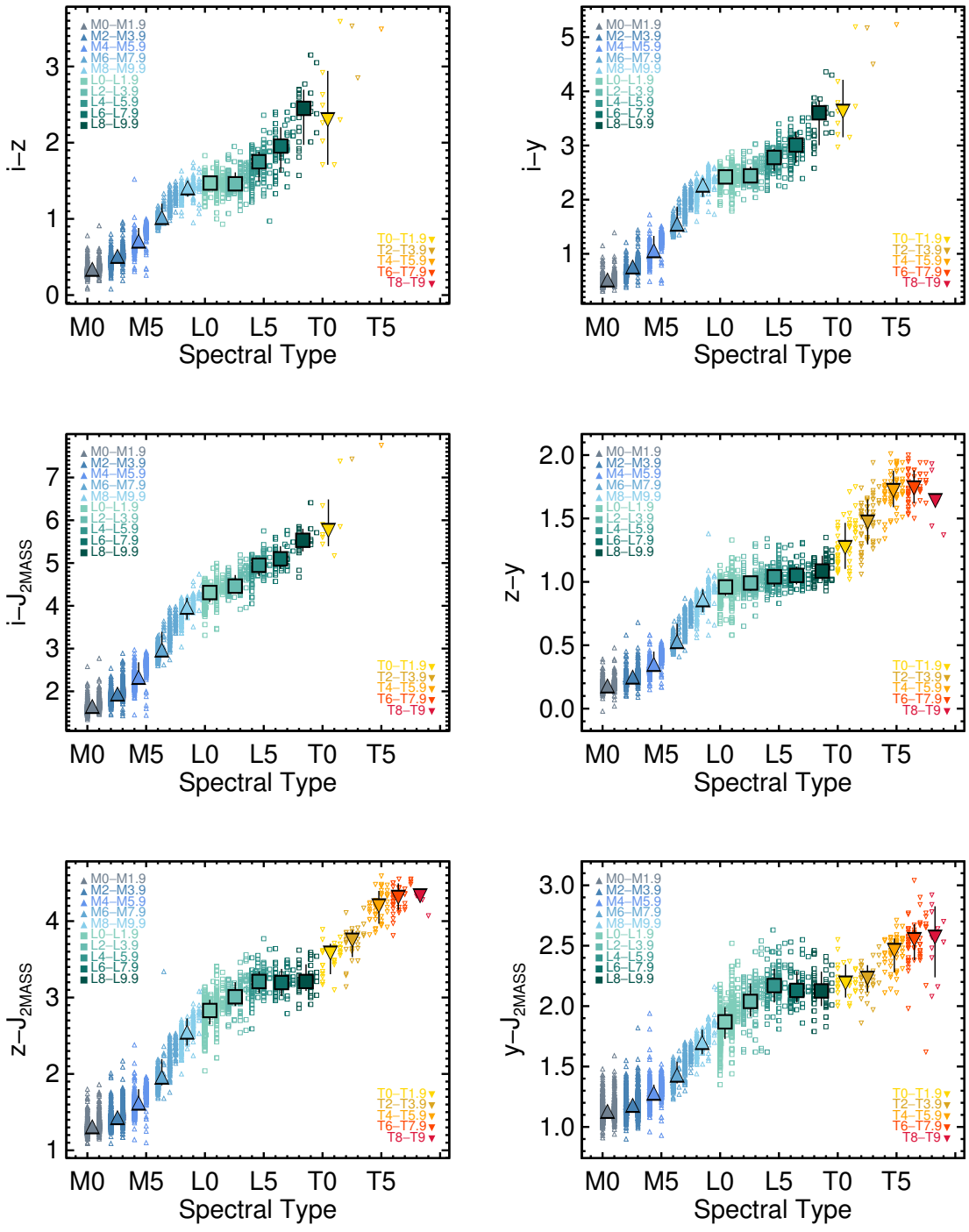

Figure 6.5 continued.

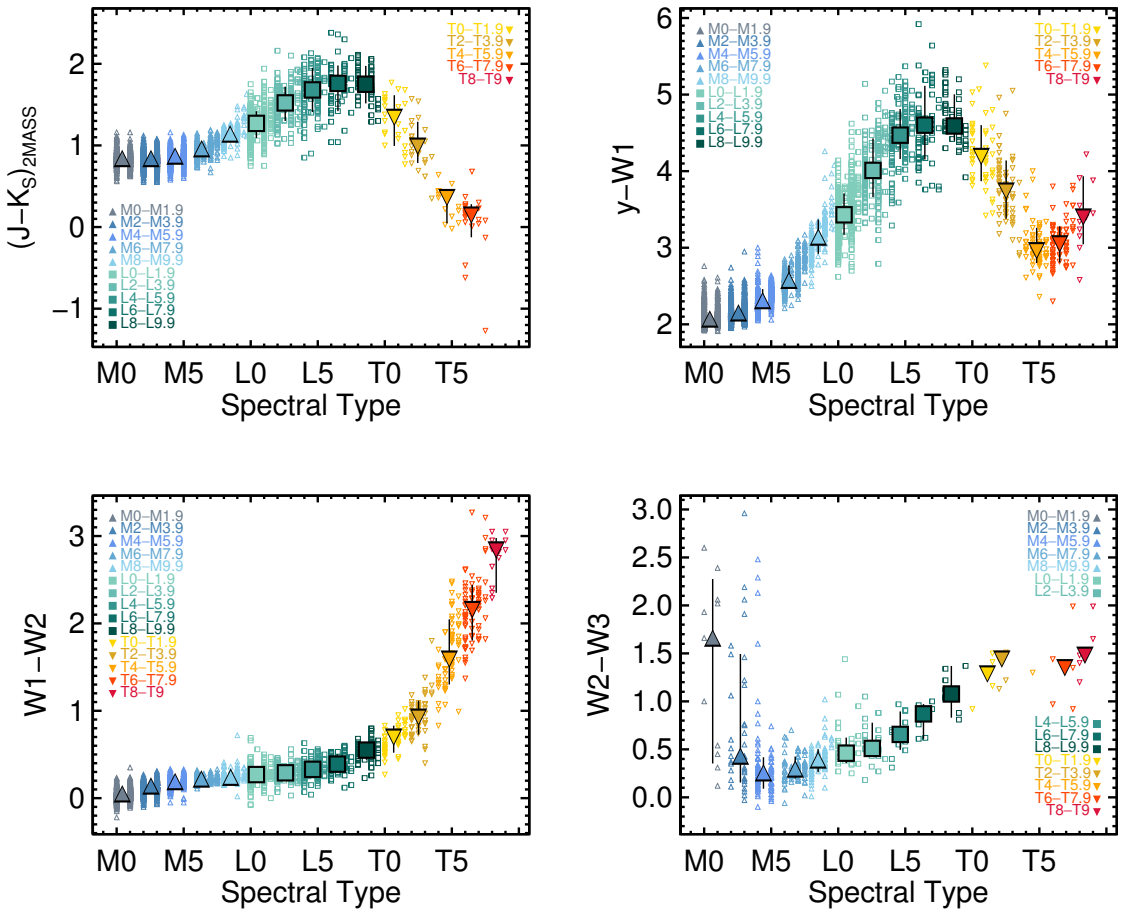

Figure 6.5 continued.

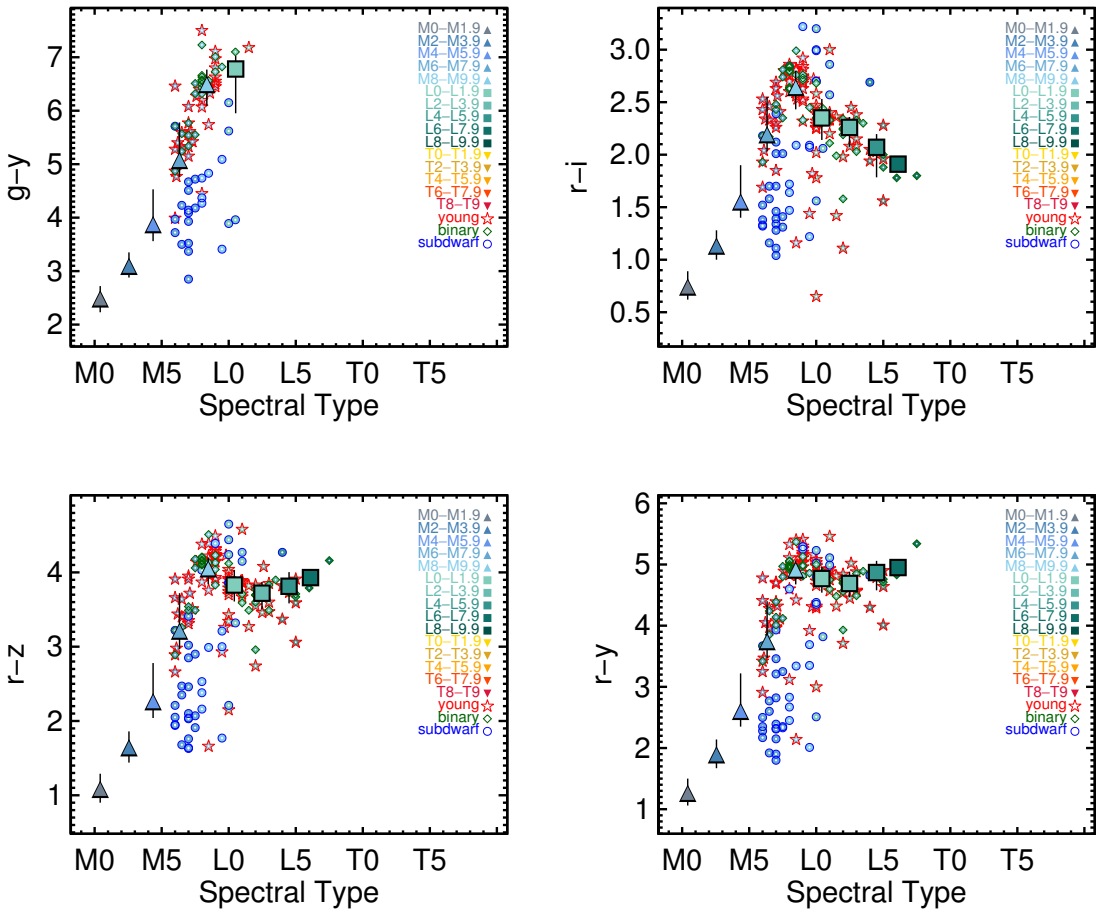

Figure 6.6 Color vs. spectral type plots for known young objects (outlined with red stars), binaries (green diamonds), and subdwarfs (blue circles) in our PS1-detected catalog. Interiors of the symbols use the same color scheme as in Figure 6.5 (see legends). Median colors and 68% confidence limits for normal field objects from Figure 6.5 are overplotted for reference. Typically the young objects have field-like or redder colors while the subdwarfs have bluer-than-field colors, but the $r_{\rm P1} - i_{\rm P1}$, $r_{\rm P1} - z_{\rm P1}$, and $r_{\rm P1} - y_{\rm P1}$ vs. SpT plots show a number of exceptions to both of these norms.

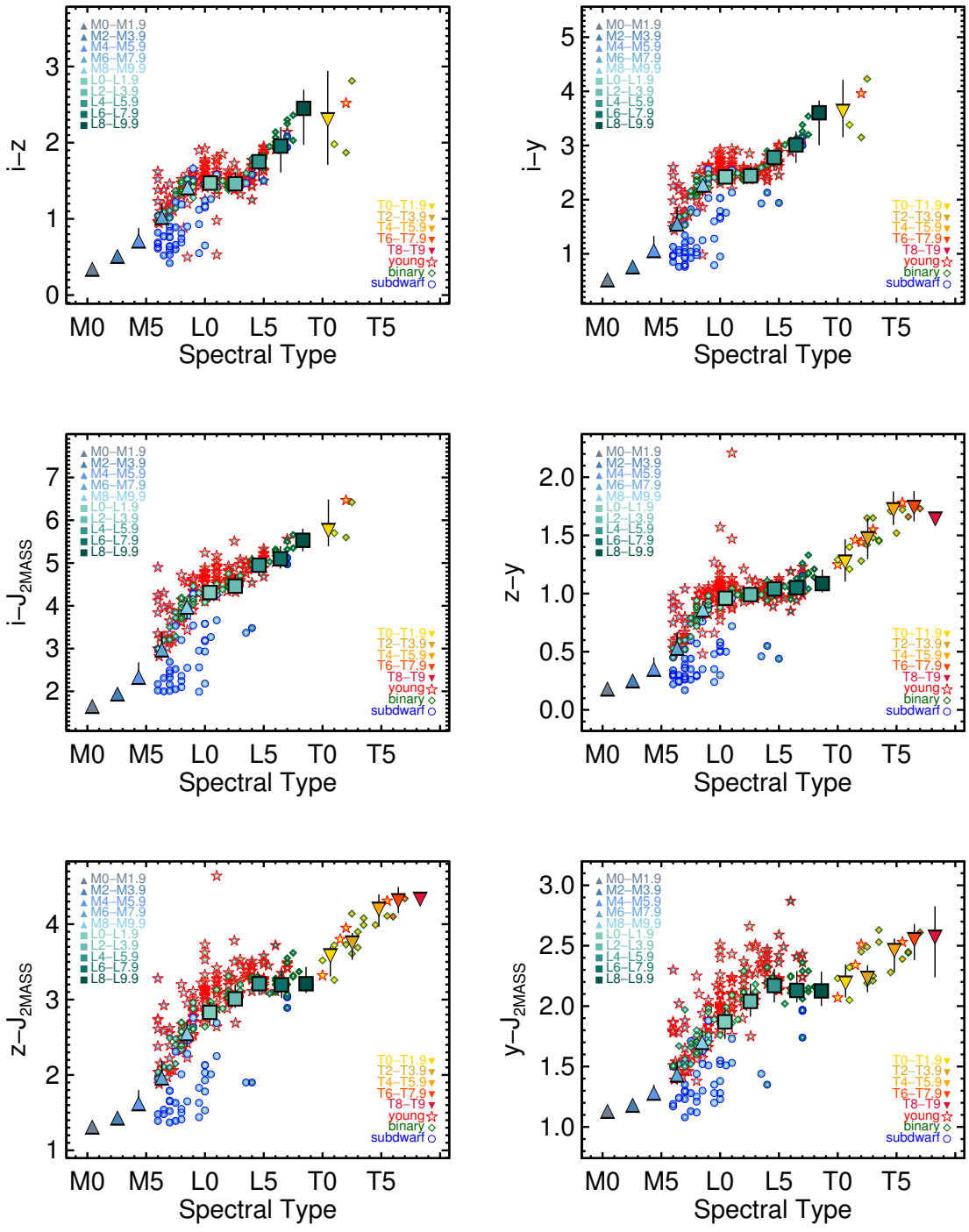

Figure 6.6 continued.

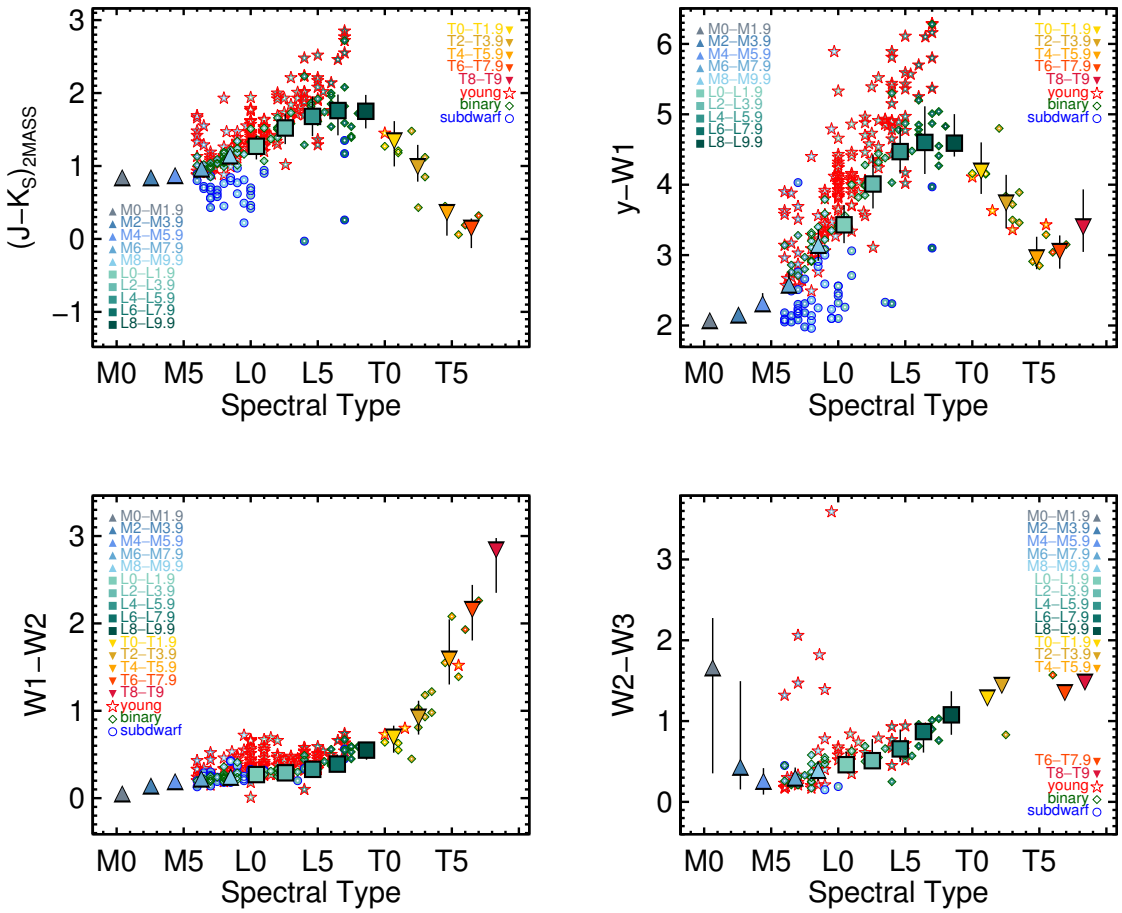

Figure 6.6 continued.

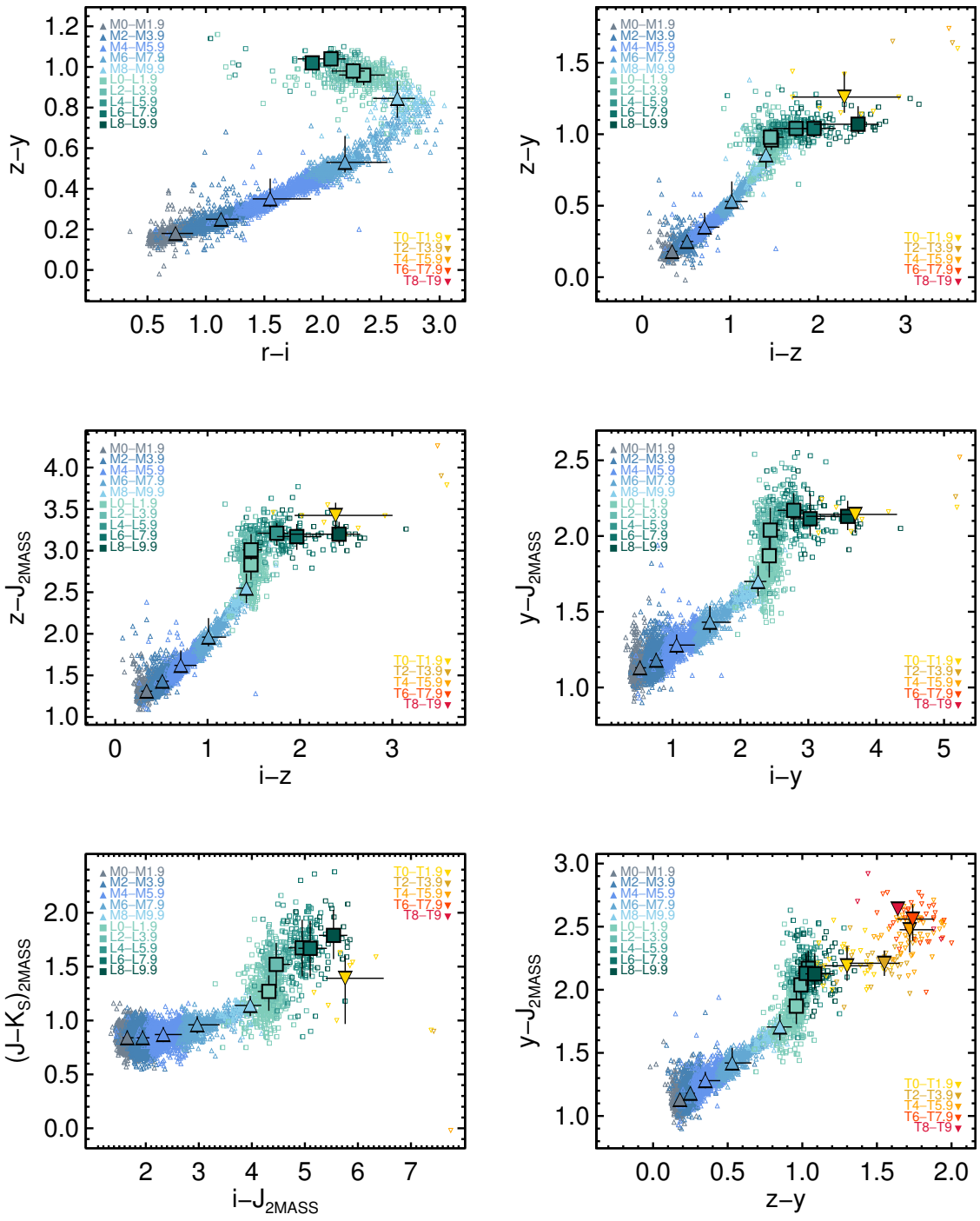

Figure 6.7 Color-color plots for the M, L, and T dwarfs in our PS1-detected catalog, using the same format as in Figure 6.5. The L dwarf color plateau is especially evident for $z_{\rm P1}-y_{\rm P1}$ and $z_{\rm P1}-J_{\rm 2MASS}$.

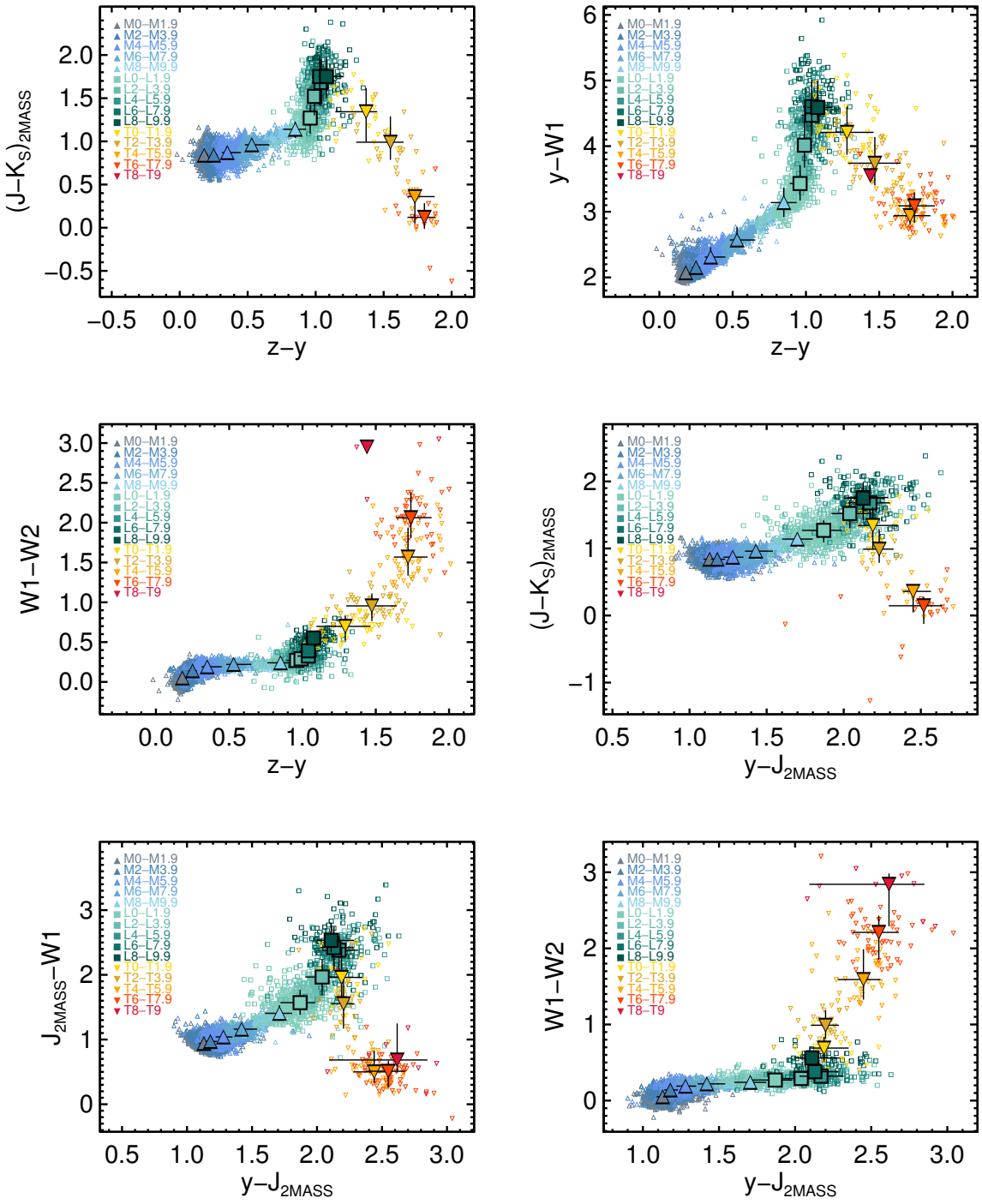

Figure 6.7 continued.

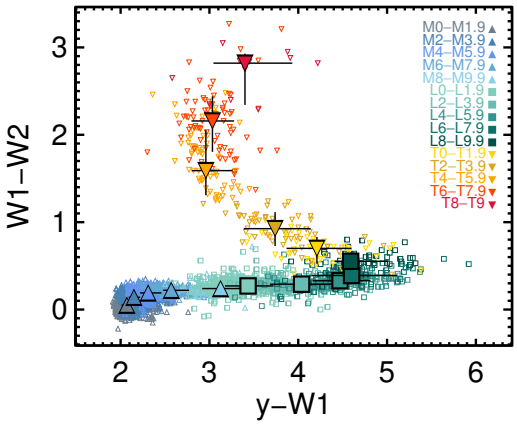

Figure 6.7 continued.

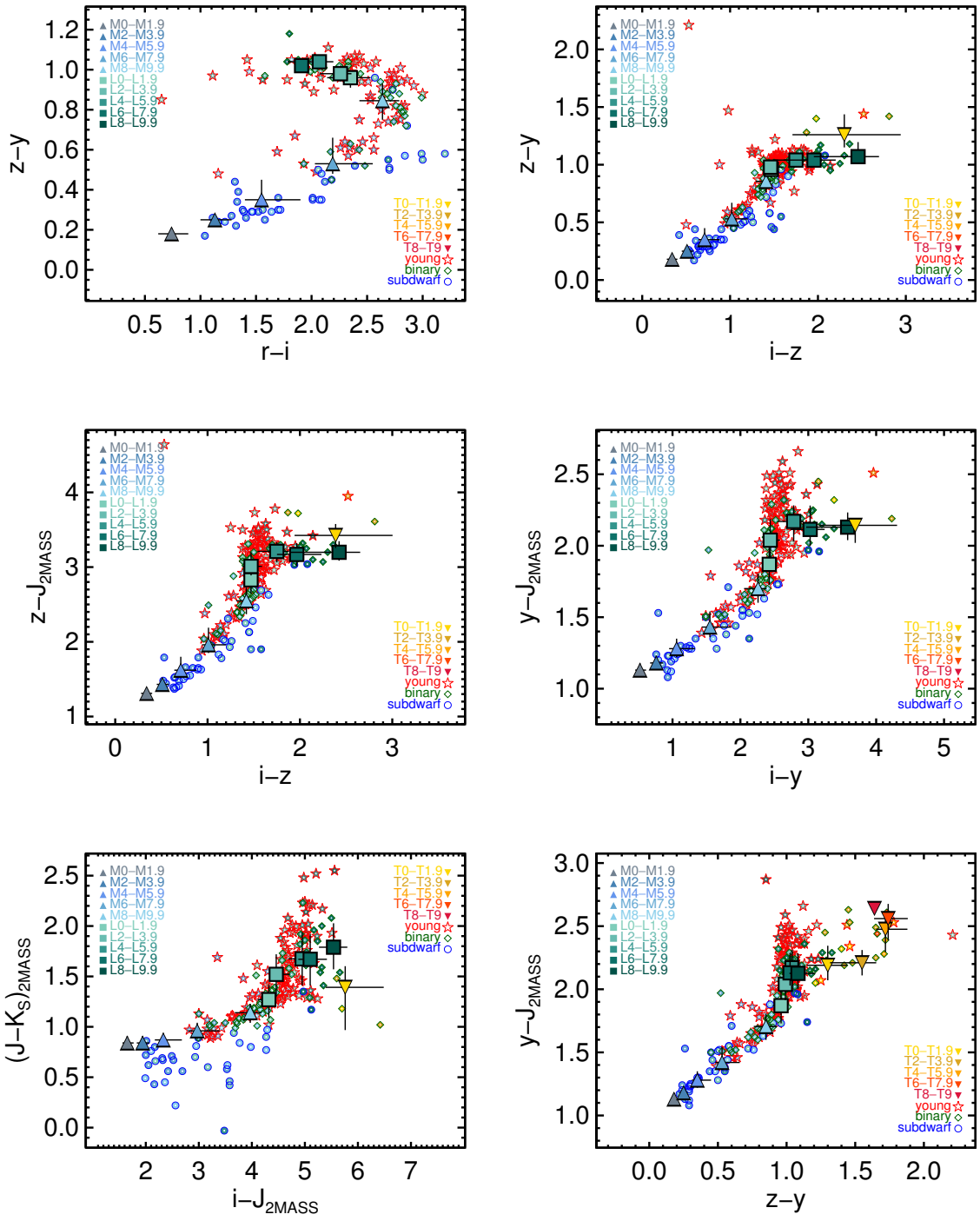

Figure 6.8 Color-color plots for known young objects, binaries, and subdwarfs in our PS1-detected catalog, using the same format as in Figure 6.6. Median colors and 68% confidence limits for normal field objects from Figure 6.7 are overplotted for reference.

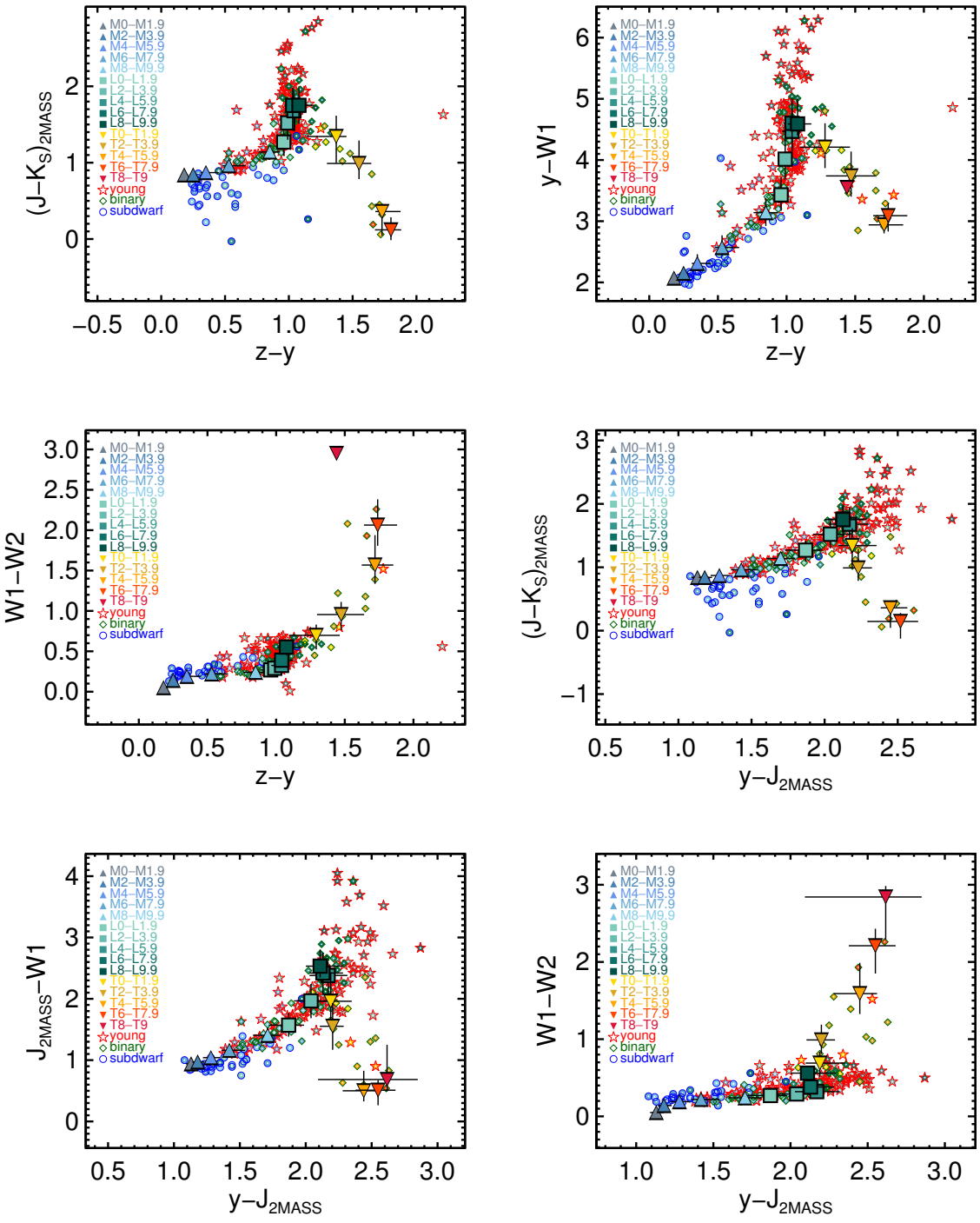

Figure 6.8 continued.

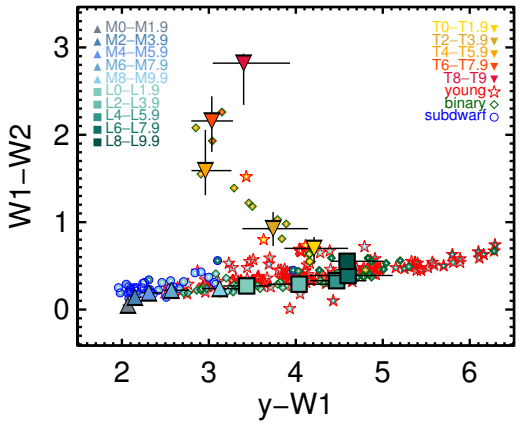

Figure 6.8 continued.

Our catalog contains 494 L dwarfs with $r_{\rm P1}$ detections, including 433 in the normal field sample. With these we present the largest set of r-band colors of L dwarfs to date, a tenfold increase over the sample presented by Liebert & Gizis (2006) and the compilation of Koen (2013). Most PS1 colors become redder through the M dwarfs, plateau for the L dwarfs and become redder again for T dwarfs (when detected), but the L dwarfs show a different behavior with $r_{\rm P1}$. $r_{\rm P1} - i_{\rm P1}$ features a blueward turn at spectral type ≈M8, becoming ≈0.8 mag bluer by spectral type L5 where the objects become too faint for $r_{\rm P1}$ detection, robustly confirming previous findings using much smaller samples (Hawley et al. 2002; Liebert & Gizis 2006). We see similar but less pronounced trends for $r_{\rm P1} - z_{\rm P1}$ and $r_{\rm P1} - y_{\rm P1}$. Liebert & Gizis (2006) explain these unusual blueward trends as a consequence of decreasing TiO absorption, which strongly suppresses r-band flux in M7-M8 dwarfs but weakens in later spectral types as Ti-bearing dust grains form. The resulting reduction in $r_{\rm P1}$ opacity largely cancels out the drop in flux expected from cooler objects, while the flux in $i_{\rm P1}$, $z_{\rm P1}$, and $y_{\rm P1}$ continues to decrease. In addition, K I absorption doublets centered in the $i_{\rm P1}$-band (7665 Å and 7699 Å) increase in strength through the L types (Kirkpatrick et al. 1999), enhancing the trend toward bluer $r_{\rm P1} - i_{\rm P1}$ colors. We note that another color, $y_{\rm P1} - W1$, also takes a blueward turn, peaking at spectral type ≈L7 and becoming more than 1.5 mag bluer through spectral type T5. This trend arises from the appearance of the methane fundamental band at 3.3 μm in late-L dwarfs (Noll et al. 2000), which broadens to a deep trough spanning $3.1 - 4.0$ μm by mid-T spectral types (Kirkpatrick 2005).

We also note in Figure 6.5 that early-M dwarfs have few detections and redder colors in $W2 - W3$. M dwarfs are relatively faint in $W3$, and the early-M dwarfs in our catalog are more distant than other spectral types, so most were not detected in $W3$. In contrast, all were detected with errors ≤ 0.05 mag in $W2$. The few early-M dwarfs that have $W3$ detections are the brightest ones in that band in our catalog, so the observed colors are redder than the overall population. The source of the $W3$ emission for the reddest objects is most likely to be debris disks or contamination from background objects, and we note that the $W2 - W3$ colors are consistent with those of other debris disks (e.g., Theissen & West

2014). We therefore do not interpret the $W2-W3$ colors in our catalog as representative of stellar photospheres for spectral types earlier than M5.

We use the photometry from our catalog to calculate median colors of field M0–T9 dwarfs spanning ≈0.55 to 12 μm. As with Figures 6.5 and 6.7, we have excluded all known binaries, young objects, and subdwarfs from these calculations in order to produce colors representative of the normal field population. Tables 6.4 and 6.5 presents these colors in single steps of adjacent filter pairs from $g_{\rm P1}$ to $W3$ (excluding spectral types M0–M4 for $W2-W3$, as explained in the preceding paragraph). Table 6.6 presents five additional colors previously used to study ultracool dwarfs: $i_{\rm P1}-y_{\rm P1}$, $i_{\rm P1}-J_{\rm 2MASS}$, $z_{\rm P1}-J_{\rm 2MASS}$, $(J-K_S)_{\rm 2MASS}$, and $y_{\rm P1}-W1$. For both tables, we list the median colors and 68% confidence limits for single spectral subtypes, along with the number of objects used to determine each color.

Table 6.4. Median $g_{\rm P1}$ through $J_{\rm 2MASS}$ colors of M0–T9 dwarfs

SpT	$g_{\rm P1} - r_{\rm P1}$			$r_{\rm P1} - i_{\rm P1}$			$i_{\rm P1} - z_{\rm P1}$			$z_{\rm P1} - y_{\rm P1}$			$y_{\rm P1} - J_{\rm 2MASS}$		
	Median (mag)	68% (mag)	N	Median (mag)	68% (mag)	N	Median (mag)	68% (mag)	N	Median (mag)	68% (mag)	N	Median (mag)	68% (mag)	N
M0–M0.9	1.19	$^{+0.04}_{-0.05}$	991	0.67	$^{+0.08}_{-0.08}$	991	0.31	$^{+0.04}_{-0.04}$	991	0.17	$^{+0.02}_{-0.02}$	991	1.12	$^{+0.04}_{-0.04}$	991
M1–M1.9	1.22	$^{+0.04}_{-0.04}$	707	0.85	$^{+0.08}_{-0.08}$	707	0.39	$^{+0.03}_{-0.04}$	707	0.20	$^{+0.02}_{-0.02}$	707	1.14	$^{+0.05}_{-0.04}$	707
M2–M2.9	1.21	$^{+0.04}_{-0.04}$	1657	1.02	$^{+0.07}_{-0.07}$	1657	0.46	$^{+0.03}_{-0.03}$	1657	0.23	$^{+0.02}_{-0.02}$	1657	1.16	$^{+0.05}_{-0.04}$	1657
M3–M3.9	1.21	$^{+0.04}_{-0.05}$	2107	1.22	$^{+0.09}_{-0.08}$	2107	0.55	$^{+0.05}_{-0.04}$	2107	0.27	$^{+0.02}_{-0.03}$	2107	1.20	$^{+0.04}_{-0.05}$	2106
M4–M4.9	1.23	$^{+0.05}_{-0.06}$	1220	1.46	$^{+0.12}_{-0.08}$	1220	0.67	$^{+0.06}_{-0.04}$	1220	0.32	$^{+0.04}_{-0.02}$	1220	1.25	$^{+0.04}_{-0.05}$	1220
M5–M5.9	1.31	$^{+0.04}_{-0.05}$	683	1.88	$^{+0.10}_{-0.08}$	683	0.87	$^{+0.04}_{-0.04}$	683	0.44	$^{+0.03}_{-0.03}$	683	1.34	$^{+0.05}_{-0.04}$	683
M6–M6.9	1.33	$^{+0.06}_{-0.07}$	399	2.13	$^{+0.15}_{-0.12}$	388	0.98	$^{+0.07}_{-0.05}$	387	0.51	$^{+0.05}_{-0.03}$	387	1.40	$^{+0.07}_{-0.05}$	391
M7–M7.9	1.40	$^{+0.09}_{-0.11}$	155	2.55	$^{+0.23}_{-0.16}$	154	1.21	$^{+0.13}_{-0.09}$	157	0.67	$^{+0.09}_{-0.07}$	157	1.54	$^{+0.08}_{-0.08}$	154
M8–M8.9	1.53	$^{+0.16}_{-0.13}$	90	2.69	$^{+0.12}_{-0.20}$	108	1.38	$^{+0.07}_{-0.10}$	119	0.81	$^{+0.07}_{-0.09}$	120	1.66	$^{+0.08}_{-0.08}$	108
M9–M9.9	1.79	$^{+0.16}_{-0.29}$	35	2.58	$^{+0.11}_{-0.23}$	59	1.44	$^{+0.05}_{-0.06}$	85	0.92	$^{+0.05}_{-0.07}$	85	1.77	$^{+0.09}_{-0.06}$	61
L0–L0.9	1.85	$^{+0.14}_{-0.29}$	16	2.35	$^{+0.21}_{-0.21}$	202	1.47	$^{+0.05}_{-0.05}$	344	0.95	$^{+0.04}_{-0.07}$	347	1.82	$^{+0.13}_{-0.13}$	307
L1–L1.9	2.00	$^{+0.24}_{-1.13}$	11	2.35	$^{+0.13}_{-0.22}$	113	1.48	$^{+0.09}_{-0.07}$	225	0.97	$^{+0.04}_{-0.05}$	232	1.94	$^{+0.11}_{-0.13}$	176
L2–L2.9	2.30	···	1	2.27	$^{+0.08}_{-0.20}$	50	1.45	$^{+0.08}_{-0.08}$	107	0.97	$^{+0.04}_{-0.05}$	109	2.00	$^{+0.13}_{-0.11}$	90
L3–L3.9	2.70	···	1	2.23	$^{+0.14}_{-0.17}$	31	1.49	$^{+0.16}_{-0.12}$	97	1.01	$^{+0.05}_{-0.07}$	101	2.12	$^{+0.09}_{-0.15}$	78
L4–L4.9	···	···	0	2.11	$^{+0.16}_{-0.15}$	17	1.63	$^{+0.20}_{-0.17}$	68	1.02	$^{+0.05}_{-0.08}$	84	2.15	$^{+0.13}_{-0.14}$	54
L5–L5.9	···	···	0	2.00	$^{+0.16}_{-0.25}$	13	1.77	$^{+0.15}_{-0.20}$	64	1.05	$^{+0.07}_{-0.06}$	83	2.18	$^{+0.15}_{-0.10}$	55
L6–L6.9	···	···	0	1.91	···	5	1.89	$^{+0.25}_{-0.33}$	34	1.05	$^{+0.05}_{-0.07}$	45	2.09	$^{+0.19}_{-0.07}$	32
L7–L7.9	···	···	0	···	···	0	2.10	$^{+0.22}_{-0.33}$	16	1.02	$^{+0.12}_{-0.05}$	27	2.19	$^{+0.23}_{-0.10}$	21
L8–L8.9	···	···	0	2.13	···	1	2.45	$^{+0.23}_{-0.55}$	17	1.05	$^{+0.11}_{-0.04}$	28	2.14	$^{+0.17}_{-0.12}$	22
L9–L9.9	···	···	0	···	···	0	2.45	$^{+0.70}_{-0.41}$	8	1.16	$^{+0.06}_{-0.15}$	40	2.11	$^{+0.15}_{-0.11}$	28

Table 6.4—Continued

SpT	$g_{P1} - r_{P1}$			$r_{P1} - i_{P1}$			$i_{P1} - z_{P1}$			$z_{P1} - y_{P1}$			$y_{P1} - J_{2MASS}$		
	Median (mag)	68% (mag)	N	Median (mag)	68% (mag)	N	Median (mag)	68% (mag)	N	Median (mag)	68% (mag)	N	Median (mag)	68% (mag)	N
T0–T0.9	···	···	0	···	···	0	2.38	···	6	1.21	$^{+0.20}_{-0.11}$	24	2.21	$^{+0.18}_{-0.13}$	13
T1–T1.9	···	···	0	···	···	0	2.30	···	3	1.39	$^{+0.12}_{-0.26}$	25	2.19	$^{+0.12}_{-0.13}$	14
T2–T2.9	···	···	0	···	···	0	3.53	···	1	1.45	$^{+0.14}_{-0.22}$	39	2.22	$^{+0.07}_{-0.12}$	22
T3–T3.9	···	···	0	···	···	0	2.85	···	1	1.55	$^{+0.17}_{-0.23}$	23	2.24	$^{+0.19}_{-0.07}$	11
T4–T4.9	···	···	0	···	···	0	···	···	0	1.71	$^{+0.08}_{-0.19}$	30	2.43	$^{+0.11}_{-0.17}$	21
T5–T5.9	···	···	0	···	···	0	3.49	···	1	1.74	$^{+0.19}_{-0.11}$	32	2.49	$^{+0.07}_{-0.20}$	30
T6–T6.9	···	···	0	···	···	0	···	···	0	1.74	$^{+0.15}_{-0.13}$	32	2.54	$^{+0.09}_{-0.16}$	38
T7–T7.9	···	···	0	···	···	0	···	···	0	1.80	$^{+0.05}_{-0.09}$	15	2.56	$^{+0.19}_{-0.16}$	21
T8–T8.9	···	···	0	···	···	0	···	···	0	1.76	···	4	2.57	$^{+0.27}_{-0.43}$	9
T9–T9.9	···	···	0	···	···	0	···	···	0	1.37	···	1	2.61	···	2

Note. — For each spectral type and color, this table lists the median color and 68% confidence limits followed by the number of objects (N) used to determine the median. Confidence intervals were calculated only when $N \geq 7$.

Table 6.5. Median $J_{2\mathrm{MASS}}$ through $W3$ colors of M0–T9 dwarfs

SpT	$(J-H)_{2\mathrm{MASS}}$			$(H-K_S)_{2\mathrm{MASS}}$			$K_{S,2\mathrm{MASS}}-W1$			$W1-W2$			$W2-W3$		
	Median (mag)	68% (mag)	N	Median (mag)	68% (mag)	N	Median (mag)	68% (mag)	N	Median (mag)	68% (mag)	N	Median (mag)	68% (mag)	N
M0–M0.9	0.66	$^{+0.05}_{-0.06}$	991	0.18	$^{+0.06}_{-0.06}$	991	0.10	$^{+0.05}_{-0.06}$	969	0.02	$^{+0.06}_{-0.05}$	969	···	···	0
M1–M1.9	0.64	$^{+0.06}_{-0.05}$	707	0.21	$^{+0.05}_{-0.07}$	707	0.11	$^{+0.07}_{-0.06}$	700	0.07	$^{+0.05}_{-0.06}$	700	···	···	0
M2–M2.9	0.62	$^{+0.06}_{-0.07}$	1657	0.22	$^{+0.06}_{-0.06}$	1657	0.12	$^{+0.06}_{-0.05}$	1633	0.12	$^{+0.05}_{-0.06}$	1633	···	···	0
M3–M3.9	0.60	$^{+0.06}_{-0.06}$	2106	0.24	$^{+0.05}_{-0.06}$	2107	0.14	$^{+0.05}_{-0.06}$	2079	0.16	$^{+0.03}_{-0.05}$	2079	···	···	0
M4–M4.9	0.59	$^{+0.05}_{-0.05}$	1220	0.26	$^{+0.06}_{-0.05}$	1220	0.16	$^{+0.05}_{-0.05}$	1198	0.18	$^{+0.03}_{-0.03}$	1198	···	···	0
M5–M5.9	0.59	$^{+0.06}_{-0.05}$	683	0.31	$^{+0.06}_{-0.06}$	683	0.19	$^{+0.05}_{-0.06}$	676	0.21	$^{+0.03}_{-0.03}$	676	0.21	$^{+0.16}_{-0.14}$	44
M6–M6.9	0.60	$^{+0.06}_{-0.05}$	401	0.33	$^{+0.05}_{-0.05}$	402	0.20	$^{+0.05}_{-0.04}$	388	0.22	$^{+0.03}_{-0.03}$	388	0.25	$^{+0.12}_{-0.07}$	40
M7–M7.9	0.63	$^{+0.04}_{-0.05}$	157	0.39	$^{+0.04}_{-0.05}$	158	0.22	$^{+0.04}_{-0.03}$	147	0.23	$^{+0.02}_{-0.03}$	141	0.32	$^{+0.10}_{-0.08}$	60
M8–M8.9	0.68	$^{+0.04}_{-0.05}$	111	0.43	$^{+0.05}_{-0.04}$	112	0.26	$^{+0.04}_{-0.05}$	99	0.23	$^{+0.04}_{-0.04}$	97	0.35	$^{+0.11}_{-0.11}$	52
M9–M9.9	0.72	$^{+0.08}_{-0.06}$	60	0.48	$^{+0.06}_{-0.06}$	64	0.31	$^{+0.07}_{-0.04}$	56	0.26	$^{+0.05}_{-0.04}$	63	0.44	$^{+0.18}_{-0.12}$	35
L0–L0.9	0.76	$^{+0.12}_{-0.13}$	277	0.48	$^{+0.13}_{-0.13}$	281	0.32	$^{+0.09}_{-0.09}$	263	0.27	$^{+0.07}_{-0.05}$	311	0.51	$^{+0.22}_{-0.13}$	21
L1–L1.9	0.80	$^{+0.10}_{-0.15}$	166	0.51	$^{+0.11}_{-0.10}$	168	0.35	$^{+0.11}_{-0.07}$	152	0.26	$^{+0.06}_{-0.04}$	189	0.46	$^{+0.15}_{-0.11}$	16
L2–L2.9	0.91	$^{+0.10}_{-0.14}$	89	0.59	$^{+0.12}_{-0.11}$	92	0.42	$^{+0.12}_{-0.10}$	82	0.29	$^{+0.06}_{-0.04}$	96	0.55	$^{+0.21}_{-0.14}$	14
L3–L3.9	0.95	$^{+0.13}_{-0.22}$	77	0.64	$^{+0.13}_{-0.09}$	78	0.52	$^{+0.12}_{-0.19}$	73	0.30	$^{+0.06}_{-0.07}$	90	0.50	$^{+0.32}_{-0.10}$	11
L4–L4.9	1.06	$^{+0.14}_{-0.21}$	51	0.64	$^{+0.11}_{-0.20}$	53	0.61	$^{+0.16}_{-0.12}$	50	0.32	$^{+0.06}_{-0.08}$	71	0.64	$^{+0.06}_{-0.29}$	8
L5–L5.9	1.06	$^{+0.16}_{-0.20}$	54	0.67	$^{+0.11}_{-0.15}$	55	0.67	$^{+0.20}_{-0.09}$	50	0.33	$^{+0.11}_{-0.08}$	74	0.65	$^{+0.26}_{-0.09}$	8
L6–L6.9	0.99	$^{+0.22}_{-0.11}$	30	0.65	$^{+0.27}_{-0.24}$	34	0.71	$^{+0.14}_{-0.18}$	35	0.38	$^{+0.10}_{-0.09}$	43	0.76	···	5
L7–L7.9	1.12	$^{+0.28}_{-0.20}$	18	0.73	$^{+0.10}_{-0.17}$	20	0.73	$^{+0.16}_{-0.08}$	17	0.42	$^{+0.12}_{-0.11}$	23	0.96	···	2
L8–L8.9	1.13	$^{+0.17}_{-0.13}$	23	0.65	$^{+0.19}_{-0.08}$	28	0.85	$^{+0.08}_{-0.13}$	26	0.53	$^{+0.08}_{-0.09}$	27	1.12	···	5
L9–L9.9	1.07	$^{+0.14}_{-0.13}$	27	0.58	$^{+0.15}_{-0.10}$	27	0.78	$^{+0.13}_{-0.11}$	22	0.57	$^{+0.10}_{-0.13}$	32	0.88	···	3

Table 6.5—Continued

SpT	$(J-H)_{2MASS}$			$(H-K_S)_{2MASS}$			$K_{S,2MASS}-W1$			$W1-W2$			$W2-W3$		
	Median (mag)	68% (mag)	N	Median (mag)	68% (mag)	N	Median (mag)	68% (mag)	N	Median (mag)	68% (mag)	N	Median (mag)	68% (mag)	N
T0–T0.9	0.93	$^{+0.12}_{-0.18}$	12	0.56	$^{+0.04}_{-0.19}$	12	0.78	$^{+0.15}_{-0.26}$	13	0.58	$^{+0.13}_{-0.09}$	21	0.92	···	1
T1–T1.9	0.86	$^{+0.17}_{-0.08}$	12	0.33	$^{+0.28}_{-0.18}$	12	0.63	$^{+0.19}_{-0.20}$	13	0.72	$^{+0.16}_{-0.10}$	25	1.41	···	3
T2–T2.9	0.80	$^{+0.21}_{-0.11}$	16	0.25	$^{+0.29}_{-0.22}$	17	0.57	$^{+0.21}_{-0.29}$	16	0.91	$^{+0.14}_{-0.18}$	39	1.44	···	5
T3–T3.9	0.59	$^{+0.12}_{-0.29}$	7	0.17	$^{+0.43}_{-0.13}$	7	0.56	$^{+0.13}_{-0.26}$	8	1.07	$^{+0.19}_{-0.37}$	19	···	···	0
T4–T4.9	0.32	$^{+0.09}_{-0.16}$	11	0.11	$^{+0.11}_{-0.06}$	9	0.19	$^{+0.07}_{-0.20}$	7	1.35	$^{+0.25}_{-0.17}$	26	1.30	···	1
T5–T5.9	0.18	$^{+0.35}_{-0.10}$	10	0.03	···	6	0.15	···	3	1.85	$^{+0.36}_{-0.32}$	40	···	···	0
T6–T6.9	0.05	$^{+0.18}_{-0.17}$	20	0.06	$^{+0.17}_{-0.21}$	14	0.37	$^{+0.24}_{-0.32}$	14	2.08	$^{+0.30}_{-0.36}$	47	1.21	···	2
T7–T7.9	0.08	$^{+0.12}_{-0.24}$	12	0.01	$^{+0.21}_{-0.09}$	7	0.33	···	5	2.26	$^{+0.29}_{-0.34}$	27	1.35	···	3
T8–T8.9	0.09	···	1	···	···	0	···	···	0	2.79	$^{+0.15}_{-0.44}$	10	1.40	···	3
T9–T9.9	0.24	···	1	···	···	0	···	···	0	2.95	···	3	1.82	···	2

Note. — For each spectral type and color, this table lists the median color and 68% confidence limits followed by the number of objects (N) used to determine the median. Confidence intervals were calculated only when $N \geq 7$.

Table 6.6. More Median Colors

SpT	$i_{P1} - y_{P1}$			$i_{P1} - J_{2MASS}$			$z_{P1} - J_{2MASS}$			$(J - K_S)_{2MASS}$			$y_{P1} - W1$		
	Median (mag)	68% (mag)	N	Median (mag)	68% (mag)	N	Median (mag)	68% (mag)	N	Median (mag)	68% (mag)	N	Median (mag)	68% (mag)	N
M0–M0.9	0.48	$^{+0.05}_{-0.05}$	991	1.61	$^{+0.07}_{-0.08}$	991	1.29	$^{+0.05}_{-0.05}$	991	0.84	$^{+0.06}_{-0.07}$	991	2.05	$^{+0.06}_{-0.06}$	969
M1–M1.9	0.59	$^{+0.05}_{-0.05}$	707	1.74	$^{+0.07}_{-0.08}$	707	1.34	$^{+0.05}_{-0.04}$	707	0.85	$^{+0.06}_{-0.07}$	707	2.10	$^{+0.06}_{-0.05}$	700
M2–M2.9	0.69	$^{+0.05}_{-0.04}$	1657	1.85	$^{+0.07}_{-0.06}$	1657	1.39	$^{+0.05}_{-0.05}$	1657	0.84	$^{+0.07}_{-0.08}$	1657	2.12	$^{+0.06}_{-0.05}$	1633
M3–M3.9	0.82	$^{+0.06}_{-0.06}$	2107	2.02	$^{+0.09}_{-0.09}$	2106	1.46	$^{+0.06}_{-0.05}$	2106	0.84	$^{+0.06}_{-0.07}$	2106	2.17	$^{+0.06}_{-0.06}$	2079
M4–M4.9	0.99	$^{+0.09}_{-0.06}$	1220	2.24	$^{+0.13}_{-0.09}$	1220	1.57	$^{+0.07}_{-0.06}$	1220	0.86	$^{+0.06}_{-0.07}$	1220	2.26	$^{+0.07}_{-0.07}$	1198
M5–M5.9	1.31	$^{+0.07}_{-0.07}$	683	2.66	$^{+0.09}_{-0.11}$	683	1.78	$^{+0.07}_{-0.07}$	683	0.91	$^{+0.06}_{-0.07}$	683	2.44	$^{+0.06}_{-0.07}$	676
M6–M6.9	1.48	$^{+0.13}_{-0.07}$	389	2.89	$^{+0.17}_{-0.11}$	387	1.91	$^{+0.11}_{-0.07}$	386	0.93	$^{+0.07}_{-0.07}$	401	2.54	$^{+0.10}_{-0.08}$	381
M7–M7.9	1.87	$^{+0.25}_{-0.13}$	158	3.41	$^{+0.30}_{-0.21}$	153	2.21	$^{+0.18}_{-0.14}$	152	1.02	$^{+0.07}_{-0.07}$	157	2.78	$^{+0.17}_{-0.17}$	145
M8–M8.9	2.19	$^{+0.14}_{-0.18}$	120	3.85	$^{+0.19}_{-0.21}$	108	2.46	$^{+0.14}_{-0.13}$	107	1.12	$^{+0.06}_{-0.10}$	111	3.03	$^{+0.15}_{-0.17}$	100
M9–M9.9	2.35	$^{+0.11}_{-0.10}$	85	4.16	$^{+0.11}_{-0.17}$	61	2.71	$^{+0.09}_{-0.15}$	61	1.19	$^{+0.15}_{-0.07}$	60	3.33	$^{+0.17}_{-0.15}$	68
L0–L0.9	2.41	$^{+0.07}_{-0.07}$	344	4.24	$^{+0.15}_{-0.18}$	307	2.76	$^{+0.15}_{-0.15}$	307	1.24	$^{+0.13}_{-0.18}$	278	3.35	$^{+0.26}_{-0.25}$	320
L1–L1.9	2.45	$^{+0.11}_{-0.10}$	225	4.38	$^{+0.15}_{-0.10}$	175	2.90	$^{+0.13}_{-0.12}$	176	1.32	$^{+0.16}_{-0.19}$	165	3.59	$^{+0.25}_{-0.26}$	201
L2–L2.9	2.41	$^{+0.12}_{-0.09}$	107	4.41	$^{+0.18}_{-0.11}$	90	2.98	$^{+0.11}_{-0.10}$	90	1.49	$^{+0.19}_{-0.22}$	89	3.90	$^{+0.36}_{-0.25}$	99
L3–L3.9	2.51	$^{+0.14}_{-0.18}$	97	4.63	$^{+0.20}_{-0.28}$	78	3.11	$^{+0.13}_{-0.18}$	78	1.58	$^{+0.21}_{-0.24}$	77	4.26	$^{+0.23}_{-0.57}$	94
L4–L4.9	2.68	$^{+0.20}_{-0.20}$	68	4.84	$^{+0.26}_{-0.25}$	51	3.17	$^{+0.15}_{-0.16}$	54	1.65	$^{+0.29}_{-0.31}$	52	4.39	$^{+0.31}_{-0.36}$	72
L5–L5.9	2.83	$^{+0.12}_{-0.23}$	64	5.02	$^{+0.14}_{-0.25}$	51	3.25	$^{+0.10}_{-0.16}$	55	1.75	$^{+0.20}_{-0.26}$	53	4.59	$^{+0.30}_{-0.30}$	74
L6–L6.9	2.96	$^{+0.25}_{-0.35}$	34	5.09	$^{+0.24}_{-0.22}$	28	3.17	$^{+0.15}_{-0.16}$	32	1.59	$^{+0.38}_{-0.19}$	30	4.55	$^{+0.23}_{-0.39}$	43
L7–L7.9	3.07	$^{+0.37}_{-0.23}$	16	5.15	$^{+0.43}_{-0.24}$	12	3.25	$^{+0.16}_{-0.11}$	20	1.82	$^{+0.16}_{-0.17}$	18	4.68	$^{+0.52}_{-0.52}$	23
L8–L8.9	3.45	$^{+0.32}_{-0.49}$	16	5.48	$^{+0.32}_{-0.31}$	14	3.20	$^{+0.23}_{-0.11}$	23	1.86	$^{+0.15}_{-0.24}$	23	4.78	$^{+0.37}_{-0.26}$	26
L9–L9.9	3.60	$^{+0.76}_{-0.37}$	8	5.63	···	6	3.23	$^{+0.27}_{-0.15}$	28	1.67	$^{+0.27}_{-0.21}$	26	4.54	$^{+0.19}_{-0.19}$	33

Table 6.6—Continued

SpT	$i_{P1} - y_{P1}$			$i_{P1} - J_{2MASS}$			$z_{P1} - J_{2MASS}$			$(J - K_S)_{2MASS}$			$y_{P1} - W1$		
	Median (mag)	68% (mag)	N	Median (mag)	68% (mag)	N	Median (mag)	68% (mag)	N	Median (mag)	68% (mag)	N	Median (mag)	68% (mag)	N
T0–T0.9	3.52	···	6	5.66	···	5	3.42	$^{+0.26}_{-0.18}$	13	1.48	$^{+0.14}_{-0.35}$	11	4.29	$^{+0.35}_{-0.36}$	21
T1–T1.9	3.72	···	3	5.85	···	3	3.59	$^{+0.12}_{-0.13}$	14	1.18	$^{+0.38}_{-0.29}$	13	4.10	$^{+0.43}_{-0.42}$	25
T2–T2.9	5.17	···	1	7.43	···	1	3.72	$^{+0.13}_{-0.26}$	21	1.06	$^{+0.27}_{-0.18}$	16	3.83	$^{+0.31}_{-0.36}$	41
T3–T3.9	4.50	···	1	···	···	0	3.82	$^{+0.13}_{-0.18}$	10	0.82	$^{+0.34}_{-0.30}$	7	3.65	$^{+0.50}_{-0.57}$	21
T4–T4.9	···	···	0	···	···	0	4.13	$^{+0.10}_{-0.24}$	21	0.40	$^{+0.04}_{-0.19}$	9	3.07	$^{+0.44}_{-0.20}$	27
T5–T5.9	5.23	···	1	7.75	···	1	4.26	$^{+0.20}_{-0.27}$	27	0.17	···	6	2.92	$^{+0.23}_{-0.12}$	40
T6–T6.9	···	···	0	···	···	0	4.29	$^{+0.15}_{-0.18}$	27	0.16	$^{+0.13}_{-0.18}$	15	3.02	$^{+0.22}_{-0.22}$	49
T7–T7.9	···	···	0	···	···	0	4.38	$^{+0.15}_{-0.20}$	10	0.08	$^{+0.22}_{-0.31}$	7	3.16	$^{+0.39}_{-0.35}$	28
T8–T8.9	···	···	0	···	···	0	4.34	···	4	···	···	0	3.34	$^{+0.60}_{-0.35}$	9
T9–T9.9	···	···	0	···	···	0	4.07	···	1	···	···	0	3.66	···	2

Note. — For each spectral type and color, this table lists the median color and 68% confidence limits followed by the number of objects (N) used to determine the median. Confidence intervals were calculated only when $N \geq 7$.

We construct empirical spectral energy distributions (SEDs) for field ultracool dwarfs using the photometry in our catalog and parallaxes from the literature. Excluding binaries, subdwarfs, and young objects, our catalog contains 234 objects (spectral types M6–T9) with reported parallaxes and $J_{\rm 2MASS}$ photometry with no confusion or contamination flags and errors less than 0.2 mag. We calculate absolute $J_{\rm 2MASS}$ magnitudes for these objects, and determine the weighted mean and rms in bins of one spectral subtype. We then use the median colors relative to $J_{\rm 2MASS}$ from our full catalog (Tables 6.4 and 6.5) to calculate absolute magnitudes for all other bands from $g_{\rm P1}$ to $W3$, adding the rms color for each band in quadrature with the $\rm M_{J_{2MASS}}$ rms magnitude to determine errors. We use our catalog colors rather than directly calculating absolute magnitudes for each band because the colors are derived from a much larger and carefully vetted sample. We present our SEDs for each spectral subtype between M6 and T9 in Table 6.7.

Recently, Deacon et al. (2016, hereinafter D16) published empirical SEDs for the Pan-STARRS1 photometric system for spectral types B8V–M9V. Our two sets of SEDs have only spectral types M6–M9 in common. For these late-M types, the SEDs are consistent within our uncertainties, but we note that our absolute magnitudes are mostly $\approx 0.1 - 0.3$ mag fainter. In Figure 6.9 we compare our PS1 colors for M dwarfs from Table 6.4 to the PS1 colors from D16. The colors are generally quite consistent, although our $g_{\rm P1} - r_{\rm P1}$ colors are $\approx 0.5\sigma - 1\sigma$ bluer and our $z_{\rm P1} - y_{\rm P1}$ colors are $\approx 1\sigma - 2\sigma$ redder than those of D16. The differences in colors are due to the fact that D16 used an earlier processing version (PV2) of PS1 data, and likely also to differences in our input samples (DL16 used ≈500 M dwarfs, while our sample contains over 8000 M dwarfs). We also find a significant blueward turn in the $r_{\rm P1} - i_{\rm P1}$ colors of M9 dwarfs (that continues into the L dwarfs) that D16 do not identify. D16 converted spectral types into absolute magnitudes using bolometric magnitudes and a series of color transformations fitted with splines. In particular, D16 used $g_{\rm P1} - i_{\rm P1}$ as a proxy for spectral type, and this relation does not clearly distinguish M9 dwarfs from M6–M8 dwarfs, so the sudden turn for M9 in $r_{\rm P1} - i_{\rm P1}$ could not be detected by their method.

Table 6.7. Spectral Energy Distributions for Field Ultracool Dwarfs

SpT	N	$M_{g_{P1}}$		$M_{r_{P1}}$		$M_{i_{P1}}$		$M_{z_{P1}}$		$M_{y_{P1}}$		$M_{J_{2MASS}}$		$M_{H_{2MASS}}$		$M_{K_{S},2MASS}$		M_{W1}		M_{W2}		M_{W3}	
		Mean (mag)	σ (mag)	Mean (mag)	σ (mag)	Mean (mag)	σ (mag)	Mean (mag)	σ (mag)	Mean (mag)	σ (mag)	Mean (mag)	σ (mag)	Mean (mag)	σ (mag)	Mean (mag)	σ (mag)	Mean (mag)	σ (mag)	Mean (mag)	σ (mag)	Mean (mag)	σ (mag)
M6–M6.9	30	16.71	0.44	15.37	0.43	13.25	0.34	12.27	0.32	11.76	0.30	10.36	0.30	9.76	0.30	9.43	0.31	9.22	0.30	9.01	0.30	8.72	0.34
M7–M7.9	26	18.11	0.56	16.76	0.50	14.18	0.39	12.98	0.34	12.31	0.31	10.77	0.30	10.14	0.31	9.75	0.31	9.52	0.31	9.31	0.31	8.96	0.33
M8–M8.9	21	19.19	0.59	17.74	0.51	15.00	0.48	13.61	0.45	12.81	0.43	11.15	0.42	10.47	0.43	10.03	0.43	9.78	0.43	9.55	0.44	9.18	0.47
M9–M9.9	9	19.95	0.43	18.14	0.37	15.62	0.39	14.17	0.37	13.23	0.36	11.46	0.34	10.74	0.35	10.27	0.37	9.95	0.37	9.68	0.37	9.24	0.42
L0–L0.9	17	20.33	0.40	18.37	0.31	16.00	0.26	14.52	0.25	13.58	0.23	11.76	0.18	11.00	0.23	10.52	0.24	10.22	0.26	9.94	0.26	9.35	0.32
L1–L1.9	19	20.85	0.78	18.74	0.28	16.41	0.25	14.93	0.23	13.97	0.21	12.03	0.15	11.23	0.21	10.71	0.24	10.36	0.26	10.10	0.26	9.66	0.31
L2–L2.9	12	21.24	···	19.02	0.29	16.73	0.26	15.30	0.24	14.33	0.24	12.32	0.21	11.41	0.25	10.83	0.29	10.43	0.32	10.14	0.33	9.62	0.37
L3–L3.9	8	22.51	···	19.61	0.39	17.40	0.34	15.88	0.31	14.89	0.29	12.77	0.24	11.82	0.29	11.19	0.32	10.66	0.36	10.39	0.38	9.91	0.37
L4–L4.9	8	···	···	20.60	0.56	18.35	0.38	16.68	0.33	15.66	0.32	13.51	0.28	12.45	0.33	11.85	0.40	11.18	0.43	10.84	0.46	10.05	0.44
L5–L5.9	8	···	···	20.74	0.37	18.71	0.33	16.94	0.29	15.87	0.28	13.69	0.25	12.63	0.30	11.94	0.34	11.26	0.34	10.91	0.38	10.13	0.51
L6–L6.9	9	···	···	21.21	0.78	19.27	0.65	17.35	0.62	16.27	0.61	14.18	0.60	13.19	0.62	12.58	0.68	11.85	0.71	11.49	0.75	10.53	0.87
L7–L7.9	7	···	···	···	···	20.09	0.36	18.18	0.26	17.13	0.25	14.94	0.20	13.82	0.31	13.12	0.32	12.42	0.48	11.99	0.57	10.87	1.08
L8–L8.9	10	···	···	22.88	···	20.38	0.39	18.10	0.22	17.04	0.21	14.90	0.13	13.77	0.20	13.04	0.22	12.20	0.28	11.66	0.30	10.66	0.36
L9–L9.9	3	···	···	···	···	20.09	0.79	17.69	0.73	16.57	0.72	14.46	0.71	13.39	0.73	12.79	0.74	11.94	0.74	11.45	0.77	10.48	0.75
T0–T0.9	1	···	···	···	···	20.22	···	17.98	···	16.77	···	14.56	···	13.62	···	13.08	···	12.43	···	11.94	···	11.02	···
T1–T1.9	3	···	···	···	···	21.10	1.14	18.84	0.21	17.45	0.16	15.25	0.12	14.39	0.18	14.07	0.33	13.39	0.38	12.68	0.33	11.26	0.76
T2–T2.9	5	···	···	···	···	21.97	···	18.26	0.23	16.75	0.13	14.54	0.06	13.73	0.15	13.48	0.26	12.94	0.39	12.06	0.33	10.61	0.40
T3–T3.9	2	···	···	···	···	···	···	18.08	0.25	16.50	0.22	14.26	0.16	13.67	0.24	13.44	0.32	12.84	0.61	11.72	0.45	···	···
T4–T4.9	6	···	···	···	···	···	···	18.02	0.39	16.32	0.38	13.89	0.36	13.57	0.40	13.49	0.39	13.31	0.41	11.90	0.39	10.70	···
T5–T5.9	7	···	···	···	···	22.69	···	19.20	0.22	17.43	0.18	14.94	0.12	14.76	0.24	14.77	0.23	14.52	0.25	12.69	0.24	11.37	···
T6–T6.9	11	···	···	···	···	···	···	19.82	0.32	18.06	0.32	15.53	0.27	15.48	0.37	15.37	0.41	15.08	0.35	13.02	0.42	11.61	0.37
T7–T7.9	7	···	···	···	···	···	···	21.17	0.78	19.34	0.81	16.78	0.76	16.70	0.78	16.70	0.93	16.23	0.84	14.11	0.95	12.26	0.76
T8–T8.9	4	···	···	···	···	···	···	21.52	0.52	19.75	0.59	17.18	0.51	17.09	···	···	···	16.58	0.84	14.03	0.92	12.27	0.64
T9–T9.9	1	···	···	···	···	···	···	21.82	···	20.37	···	17.75	···	17.51	···	···	···	16.70	···	13.81	···	11.97	···

Note. — SEDs constructed using parallaxes from the literature to determine absolute J_{2MASS} magnitudes, for which we report the weighted mean and rms for each spectral subtype bin. The number of objects used to determine $M_{J_{2MASS}}$ for each spectral subtype is listed in the second column (N). We use the median colors from our catalog to calculate absolute magnitudes in other bands. Binaries, subdwarfs, and young objects were excluded from these SEDs.

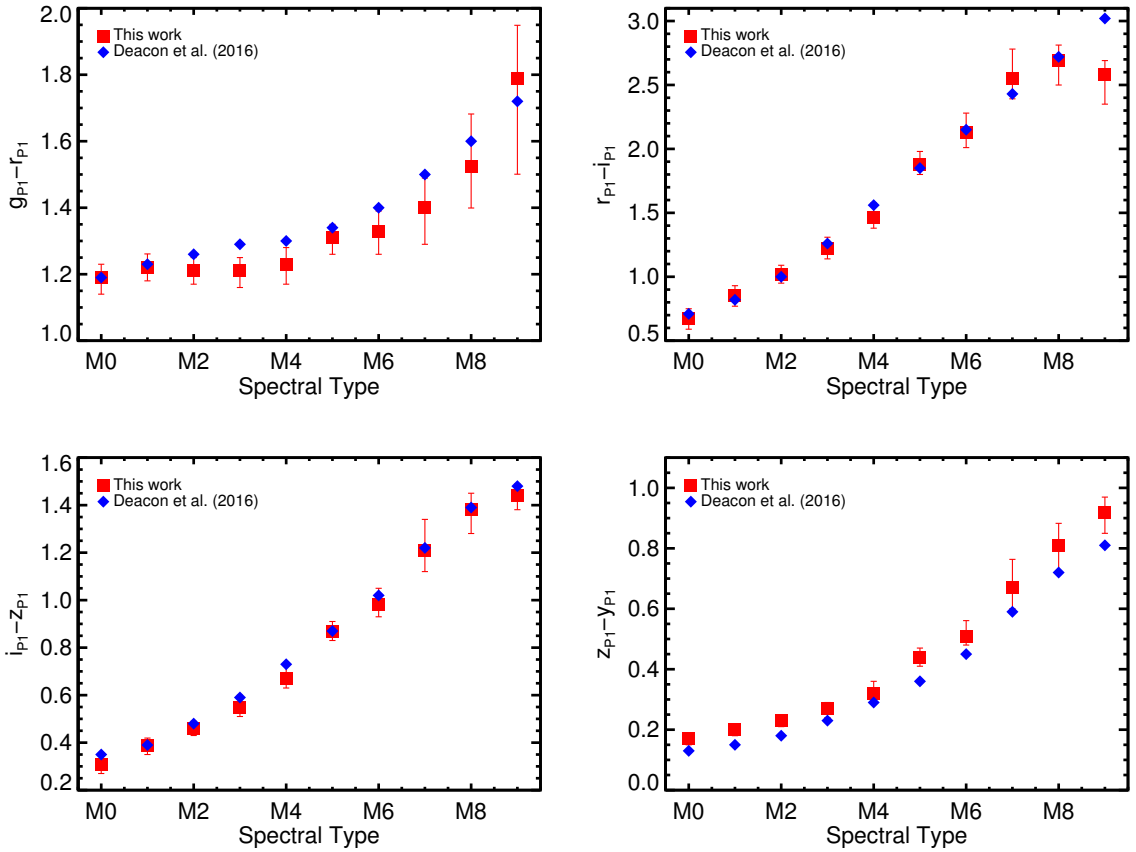

Figure 6.9 The colors of M dwarfs (median and 68% confidence intervals, red squares) as a function of spectral type, compared with the colors derived from the SED templates (blue diamonds) of Deacon et al. (2016). Our colors are generally quite consistent with those of D16, with small variations resulting from D16's use of an earlier processing version of PS1 data (PV2) and differences in our input samples. The blueward turn in $r_{\rm P1}-i_{\rm P1}$ at spectral type M9 was not identified by D16 because of their use of $g_{\rm P1}-i_{\rm P1}$ as a proxy for spectral type, which does not clearly distinguish between the late-M spectral subtypes.

6.4 Proper Motion

Table 6.8 presents our proper motions for 9770 M, L, and T dwarfs based on PS1 astrometry, along with parallaxes (from the literature) or photometric distances, tangential velocities, and proper motions from the literature for comparison. The full table is available for download in electronic form in the online journal. Like Table 6.1, Table 6.8 is arranged in two parts: (1) the late-M, L, and T dwarfs compiled from the literature, followed by (2) the M dwarfs from West et al. (2008). For reference, Table 6.8 also repeats several columns from Table 6.1, including spectral types, gravity classifications, and flags for binaries and young objects.

6.4.1 Method

PS1 database proper motions

The procedure used to calculate the proper motions and errors for the objects in the PS1 database will be described in detail in E. A. Magnier et al. (2017, in prep). Briefly, all detections for an object in all filters were fit simultaneously for proper motion and parallax using iteratively-reweighted least-squares regression with outlier clipping. The detections retained in the fit were then bootstrap-resampled to determine the errors on the proper motion and parallax. For objects having a 2MASS or *Gaia* DR1 counterpart within 1" of the mean PS1 position, the PS1 proper motion calculation includes these positions. (The parallaxes will be presented in E. A. Magnier et al., 2018, in prep). For this paper we also convert the PS1-measured $\mu_\alpha \cos\delta$ and μ_δ to a combined proper motion μ and position angle PA, and we calculate errors for these in a Monte Carlo fashion. To establish a minimum quality for our PS1 proper motions, if either $\mu_\alpha \cos\delta$ or μ_δ for an object has an error greater than 100 mas yr^{-1} and $\mu/\sigma_\mu < 3$, we do not report a proper motion for the object. This rejects large but very uncertain proper motions that may erroneously identify fast-moving objects (e.g., 500 ± 300 mas yr^{-1}), but preserves high-precision measurements of very small proper motions that have a formal S/N < 3 (e.g., 5 ± 3 mas yr^{-1}).

Table 6.8. Positions and Proper Motions of M, L, and T Dwarfs from the Pan-STARRS1 3π Survey (Sample of Columns)

Discovery Name	PS1 Mean Position[d]			PS1 Proper Motion										PS1 $v_{\rm tan}$			
	$\alpha_{\rm J2000}$ (deg)	$\delta_{\rm J2000}$ (deg)	Epoch (MJD)	$\mu_\alpha \cos\delta$ (mas yr^{-1})	err$_{\mu_\alpha \cos\delta}$ (mas yr^{-1})	μ_δ (mas yr^{-1})	err$_{\mu_\delta}$ (mas yr^{-1})	χ^2_ν	$N_{\rm ep}$	Δt (yr)	π (mas)	err$_\pi$ (mas)	dist[e] (pc)	err$_{\rm dist}$ (pc)	$v_{\rm tan}$ (km s^{-1})	$\sigma_{\rm tan}$ (km s^{-1})	References[f] (π; $\mu_{\rm lit}$)
SDSS J000013.54+255418.6	0.056400	25.905389	55326.38	-18.4	5.5	123.1	3.3	1.4	28	15.2	70.80	1.90	14.12	0.38	8.3	0.3	43; 43
SDSS J000112.18+153535.5	0.301175	15.592648	55750.95	137.3	2.2	-181.2	2.8	1.6	34	14.1	···	···	24.34	2.93	26.2	3.2	–; 54
WISEA J000131.93−084126.9	0.383130	-8.690953	55632.76	339.9	2.6	-304.9	3.3	0.7	46	15.8	···	···	···	···	···	···	–; 90
SDSS J000250.98+245413.8	0.712466	24.903795	55309.02	22.4	17.4	-45.6	7.2	1.1	28	15.2	···	···	53.33	6.54	12.8	3.0	–; –
2MASSI J0003422−282241	0.927389	-28.378609	56120.45	285.8	1.5	-142.6	1.3	1.5	67	16.1	25.70	0.93	38.91	1.41	58.9	2.2	131; 131
2MASS J00044144−2058298	1.175450	-20.974698	55862.58	751.9	1.9	91.9	2.5	2.0	74	15.1	···	···	18.94	3.14	68.0	11.3	–; 70
2MASS J00054844−2157196	1.454361	-21.955894	55708.99	709.4	2.2	-122.9	2.5	1.7	66	14.9	···	···	25.43	4.22	86.8	14.4	–; 76
ULAS J000613.24+154020.7	1.555343	15.672398	56032.02	84.7	40.6	-38.5	20.4	0.9	16	3.9	···	···	43.24	5.35	19.1	7.7	–; 74
SDSS J000614.06+160454.5	1.558610	16.081685	55734.32	4.4	4.1	-41.8	3.9	0.7	40	17.2	···	···	103.52	17.46	20.6	4.0	–; 139

[a] Spectral types taken from the literature (Section 6.2.4). When both optical and near-IR types are available, we adopt the optical type for M and L dwarfs and the near-IR type for T dwarfs. Most spectral types have an uncertainty of ±0.5 subtypes; ":" = ±1 subtype; "::" = ±2 or more subtypes. "sd" = subdwarf; "esd" = extreme subdwarf (Gizis 1997).

[b] β, γ, and δ indicate classes of increasingly low gravity based on optical (Kirkpatrick 2005; Cruz et al. 2009) or near-infrared (Gagné et al. 2015c) spectra. FLD-G indicates near-infrared spectral signatures of field-age gravity, INT-G indicates intermediate gravity, and VL-G indicates very low gravity (Allers & Liu 2013a).

[c] Young objects identified by low-gravity classifications or other spectroscopic evidence for youth, membership in star-forming regions or young moving groups, or companionship to a young star (Section 6.2.5).

[d] The mean PS1 position is the position calculated for the weighted mean epoch, in which the epochs are weighted by the rms of the R.A. and Decl. astrometric uncertainties.

[e] Distances were calculated from trigonometric parallaxes when available. If no parallax was available, we calculated photometric distances using $i_{\rm P1}$ magnitudes for spectral types M0–M5 and $W2$ magnitudes (when available) for spectral types M6 and later.

[f] References for spectral type, gravity, and binarity are given in Table 6.1.

[g] Although classified as FLD-G, the spectrum shows hints of intermediate gravity (as described in Aller et al. 2016).

[h] The R.A. and Decl. proper motion components listed in Table 2 of Lodieu et al. (2012b) appear to be reversed. We quote the corrected order here.

References. — (1) Aberasturi et al. (2014), (2) Albert et al. (2011), (3) Aller et al. (2016), (4) Andrei et al. (2011), (5) Artigau et al. (2011), (6) Bardalez Gagliuffi et al. (2014), (7) Baron et al. (2015), (8) Bartlett (2007), (9) Beamín et al. (2013), (10) Béjar et al. (2008), (11) Best et al. (2015), (12) Best et al. (2017b), (13) Bihain et al. (2013), (14) Bouvier et al. (2008), (15) Bouy et al. (2015), (16) Burgasser et al. (2003b), (17) Burgasser et al. (2004), (18) Burgasser et al. (2007), (19) Burgasser et al. (2008a), (20) Burgasser et al. (2008c), (21) Burgasser et al. (2012), (22) Burgasser et al. (2015a), (23) Burgasser et al. (2016), (24) Burningham et al. (2013), (25) Caballero (2007), (26) Cardoso et al. (2015), (27) Casewell et al. (2008), (28) Castro et al. (2013), (29) Castro & Gizis (2016), (30) Costa et al. (2005), (31) Costa et al. (2006), (32) Dahn et al. (2002), (33) Dahn et al. (2008), (34) Deacon et al. (2005), (35) Deacon & Hambly (2007), (36) Deacon et al. (2009), (37) Deacon et al. (2011), (38) Deacon et al. (2012b), (39) Deacon et al. (2014), (40) Deacon et al. (2017b), (41) Dieterich et al. (2014), (42) Dittmann et al. (2014), (43) Dupuy & Liu (2012), (44) Dupuy & Kraus (2013), (45) Dupuy et al. (2015b), (46) Faherty et al. (2009), (47) Faherty et al. (2010), (48) Faherty et al. (2012), (49) Faherty et al. (2016), (50) Finch & Zacharias (2016), (51) Folkes et al. (2012), (52) Forbrich et al. (2016), (53) Gagné et al. (2014b), (54) Gagné et al. (2015b), (55) Gatewood & Coban (2009), (56) Gauza et al. (2015), (57) Gawroński et al. (2017), (58) Gelino et al. (2014), (59) Girard et al. (2011), (60) Gizis et al. (2011a), (61) Gizis et al. (2013), (62) Gizis et al. (2015a), (63) Hambly et al. (2001), (64) Harrington et al. (1993), (65) Henry et al. (2006), (66) Høg et al. (2000), (67) Jameson et al. (2008), (68) Kellogg et al. (2016), (69) Kendall et al. (2004), (70) Kendall et al. (2007a), (71) Kirkpatrick et al. (2010), (72) Kirkpatrick et al. (2011), (73) Kirkpatrick et al. (2014), (74) Lawrence et al. (2012), (75) Leggett et al. (2012), (76) Lépine et al. (2002b), (77) Lépine & Shara (2005), (78) Lépine et al. (2009), (79) Lépine & Gaidos (2011), (80) Liu et al. (2011b), (81) Liu et al. (2016), (82) Lodieu et al. (2005), (83) Lodieu et al. (2006), (84) Lodieu et al. (2012c), (85) Lodieu et al. (2012b), (86) Lodieu et al. (2013), (87) Lodieu (2013), (88) Lodieu et al. (2014), (89) Luhman et al. (2012), (90) Luhman & Sheppard (2014), (91) Luyten (1979), (92) Manjavacas et al. (2013), (93) Marocco et al. (2010), (94) Marocco et al. (2013), (95) Marsh et al. (2013), (96) McCaughrean et al. (2004), (97) Monet et al. (1992), (98) Monet et al. (2003), (99) Muzic et al. (2012), (100) Phan-Bao et al. (2008), (101) Phan-Bao (2011), (102) Pokorny et al. (2004), (103) Qi et al. (2015), (104) Radigan et al. (2008), (105) Reid (2003), (106) Riedel et al. (2014), (107) Roeser et al. (2010), (108) Sahlmann et al. (2014), (109) Sahlmann et al. (2015a), (110) Sahlmann et al. (2016), (111) Salim & Gould (2003), (112) Schilbach et al. (2009), (113) Schmidt et al. (2007), (114) Schmidt et al. (2010), (115) Schneider et al. (2016b), (116) Scholz et al. (2009), (117) Scholz et al. (2014), (118) Schweitzer et al. (1999), (119) Seifahrt et al. (2010), (120) Sheppard & Cushing (2009), (121) Shkolnik et al. (2012), (122) Smart et al. (2013), (123) Smith et al. (2014b), (124) Smith et al. (2014a), (125) Stern et al. (2007), (126) Thompson et al. (2013), (127) Tinney et al. (1995), (128) Tinney (1996), (129) Tinney et al. (2003), (130) van Altena et al. (1995), (131) van Leeuwen (2007a), (132) Vrba et al. (2004), (133) Wang et al. (2014b), (134) Weinberger et al. (2016), (135) West et al. (2008), (136) Wright et al. (2013), (137) Zacharias et al. (2005), (138) Zhang et al. (2009), (139) Zhang et al. (2010).

Note. — This table is available in its entirety in machine-readable form in the online journal. A portion is shown here for guidance regarding its form and content. The full table contains 9888 rows. Columns 2–8 are the same as in Table 6.1, and are repeated here for reference.

PS1 mean positions and epoch

Table 6.8 includes a mean PS1 position and epoch for each object. To determine these, the PS1 astrometric pipeline calculates a weighted mean epoch t_0, in which the epochs are weighted by the rms of the R.A. and Decl. astrometric uncertainties. The mean position (α_0, δ_0) is calculated (in simple terms) by fitting the positions (α, δ) at each epoch t to

$$\begin{aligned} \alpha(t) &= \alpha_0 + \pi p_\alpha(t) + \mu_\alpha(t - t_0)/\cos(\delta) \\ \delta(t) &= \delta_0 + \pi p_\delta(t) + \mu_\delta(t - t_0) \end{aligned} \tag{6.1}$$

where π is the parallax, and p_α and p_δ are the parallax factors in R.A. and Decl., respectively. This is also, by construction, the position at which the covariance with the proper motion is minimized, and is therefore the best position given the set of observations. In cases where the pipeline is unable to fit a proper motion to the data, the mean position coordinates are simply the weighted means of the individual epochs. For objects with an associated 2MASS or *Gaia* DR1 detection, these are included in determining the mean epoch and position.

Our proper motion calculation

The PS1 database builds astronomical objects from individual detections at different epochs by grouping detections within 1" of each other. In cases where two distinct objects are detected within 1" of each other at a single epoch, detections at other epochs are associated with the closer of the two objects (see E. A. Magnier et al., 2017, in prep, for details). This procedure is successful for stationary and slow-moving point sources, but for an object that moved $\gtrsim$1" over the four-year timespan of the PS1 survey, the detections may not all be associated in the PS1 database. In our ultracool catalog, we found that objects with proper motions $\gtrsim$ 200 mas yr^{-1} were often split into two or more "partial objects", identifiable by their proximity on the sky, similar photometry, and astrometric consistency with proper motions from the literature. These partial objects often had significantly

different proper motion measurements but offered no *a priori* way to determine which (if any) of the measurements was correct. This motivated us to recalculate the proper motions for fast-moving objects, using an automated procedure to identify all the detections for an object along its path of motion. While our primary goal was to improve the proper motions of fast-moving objects, we performed the recalculation for all objects of spectral type M6 and later in our catalog.

To determine where to search for detections for each object, we calculated the distance between the PS1 and 2MASS positions and generated a search box for the PS1 data based on the implied proper motion of the distance divided by a baseline of 12 years. We added 4" in quadrature to 5 years times the implied proper motion and used the resulting value for the length of a square search box. We searched the PS1 and 2MASS databases for all detections within this box centered on the PS1 position. In cases where the 2MASS and PS1 positions were more than 2" apart, we also searched around the 2MASS position within a 1" box. Once we identified candidate detections, we determined the path on the sky from the 2MASS position to the PS1 position, and if the 2MASS–PS1 distance was more than 3", we excluded any points that were more than 1" away from the path. For objects in our catalog with no associated 2MASS detection, we used the proper motion from the PS1 database (if available) or the best available proper motion from the literature to predict a 2MASS position by projecting backward 10 years from the PS1 position. For objects with no associated 2MASS detection and no PS1 or literature proper motion, we simply searched in a 4" box around the PS1 position. Finally, we searched the *Gaia* DR1 database for detections within 1" of the PS1 position, and included the astrometry from a *Gaia* match if one was found.

We then calculated proper motions using the method summarized in Section 6.4.1 for objects having at least seven detections (to ensure robust astrometric fits). We applied the same quality standards that we used for the PS1 database proper motions, rejecting those for which $\mu_\alpha \cos\delta$ or μ_δ had an error greater than 100 mas yr^{-1} and $\mu/\sigma_\mu < 3$. Our recalculations produced proper motions for 2376 M6–T9 dwarfs. These included

63 objects that do not have a proper motion in the PS1 database, most of which are moving faster than 200 mas yr^{-1}, demonstrating the success of our method. The largest proper motion for objects in our catalog reported in the PS1 database is 1561 mas yr^{-1}, but our recalculated measurements include 16 objects with greater proper motions, up to a maximum of 3507 mas yr^{-1} (SSSPM J1444−2019). The recalculation was unable to converge on a proper motion fit to the identified detections for 154 objects. Forty-one of the objects for which the recalculation failed do have PS1 database proper motions, but these are mostly poor measurements ($\sigma_\mu \gtrsim 40$ mas yr^{-1}) for faint objects ($y \gtrsim 20$ mag) with relatively few detections ($N \lesssim 10$).

Figure 6.10 compares our recalculated proper motions and errors to the values in the PS1 database. The recalculated proper motions are strongly consistent with the database measurements, and the errors for the recalculated proper motions are lower for 87% of the objects, with a median improvement in precision of 35%. We examined all objects for which the recalculated $\mu_\alpha \cos\delta$ or μ_δ differed by more than three times the error on the corresponding value in the PS1 database, and identified only six cases in which the recalculation produced a result clearly inconsistent with the separation between the PS1 and 2MASS positions or with a literature measurement. In each of these six cases, a nearby object appears to have significantly contaminated the proper motion calculation. We rejected the recalculated values for these six objects. In all other cases of significant discrepancy, the recalculated proper motion was consistent with a value in the literature (except for one object with no literature value), confirming that our recalculation improved the accuracy of these proper motions.

For our catalog (Table 6.8), we adopt the recalculated proper motions by default. We also present mean positions and epochs from our recalculations, which incorporate the 2MASS and *Gaia* DR1 positions used in the calculations. We use the PS1 database proper motions and positions only for the six contaminated recalculations described above as well as 41 cases where our recalculation was unable to fit a proper motion. We also recalculated chip photometry for each object along with the proper motion, but we did not apply the

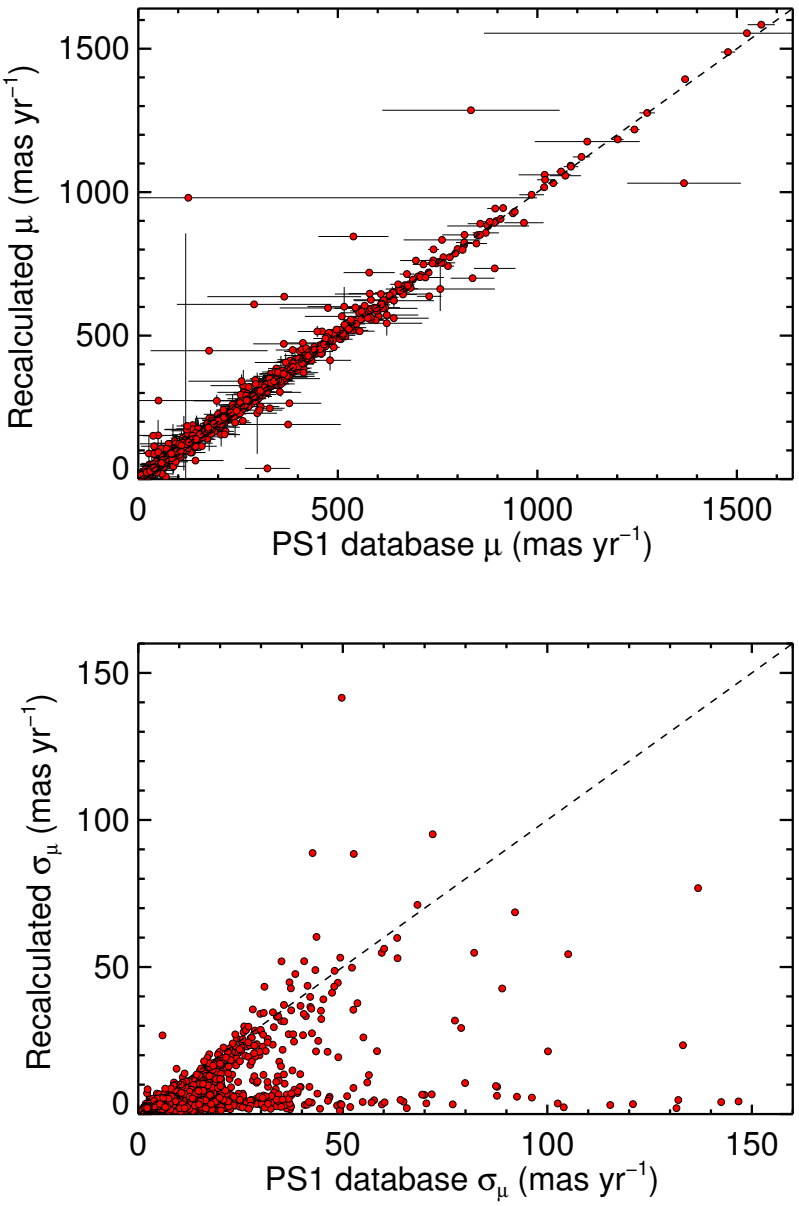

Figure 6.10 Comparison of the recalculated and PS1 database proper motions (*top*) and errors (*bottom*) for the M6–T9 dwarfs in our PS1 ultracool catalog. The dashed lines indicate equal values. The recalculated proper motions are strongly consistent with the database values. In the cases of large discrepancy the recalculated proper motions are consistent with literature values (except for six cases of clear contamination by a nearby object). The errors for the recalculated proper motions are lower for 87% of the objects, with a median reduction of 35%.

rigorous outlier-clipping procedure used for the PS1 database photometry. Thus, we use the database photometry in our catalog by default. We use our recalculated chip photometry in 55 cases where the database reports photometry of insufficient quality (or none at all) but our recalculated photometry meets the quality standards described in Section 6.3.1.

6.4.2 Characteristics

For the remainder of Section 6.4, we restrict our discussion to objects with spectral types M6 and later in order to focus our kinematic analysis on ultracool dwarfs near the Sun. Early-M dwarfs are visible at distances well beyond the solar neighborhood ($\gtrsim$200 pc) where large-scale galactic motions dominate the kinematics, entailing a discussion that is beyond the scope of this paper. We report PS1 proper motions for a total of 2405 M6–T9 dwarfs, including the largest sets of uniformly calculated proper motions for confirmed L dwarfs (1242 objects) and T dwarfs (260 objects) to date. We caution that the proper motions in our catalog do not comprise a clearly defined sample and reflect biases inherited from the programs that discovered the objects (Section 6.2.7), but our proper motions nevertheless serve as a large and illustrative sample of the local ultracool population.

Figure 6.11 shows the time baselines and number of epochs used for the ultracool proper motions in our catalog. Most of our proper motions were calculated using a 2MASS position and have time baselines spanning 13–17 years. Proper motions using only PS1 astrometry have time baselines spanning $1-5$ years (data taken 2009–2014, including during PS1 commissioning). For about one-quarter of our sample (593 objects), a *Gaia* DR1 position was included in our proper motion.

Figures 6.12 and 6.13 show the proper motion distributions for our PS1 ultracool catalog. We find median proper motion components of $\mu_\alpha \cos\delta = -13.4$ mas yr^{-1} and $\mu_\delta = -37.1$ mas yr^{-1}. Our distributions are similar to those found in previous catalogs of ultracool proper motions, including the L dwarf catalog of Schmidt et al. (2010, hereinafter S10), the Brown Dwarf Kinematics Project (BDKP; Faherty et al. 2009, 2012), the BANYAN All-Sky Survey (BASS) Input Sample (Gagné et al. 2015b), and the Late-Type

Extension to MoVeRS (LaTE-MoVeRS; Theissen et al. 2017). Our median proper motion error of 2.9 mas yr^{-1} (Figure 6.13) is a factor of ≈9 smaller than that of S10, ≈5 smaller than BDKP, and ≈3 smaller than BASS and LaTE-MoVeRS. The high precision of the PS1 measurements is a consequence of the astrometric precision of PS1 and the large number of epochs ($N > 20$ for 90% of proper motions), as well as the long time baseline for objects with a 2MASS position.

Figure 6.14 compares our PS1 proper motions to those of S10, BDKP, BASS, and LaTE-MoVeRS, each of which shares more than 350 objects in common with our catalog, as well as other literature sources. We note that the overlaps of our PS1 catalog and the other catalogs are predominantly L dwarfs, with very few T dwarfs in common. We also include a comparison to Motion Verified Red Stars (MoVeRS; Theissen et al. 2016). MoVeRS contains mostly earlier-type M dwarfs and hotter stars and has only 132 ultracool dwarfs in common with our PS1 proper motion catalog (mostly late-M dwarfs), so it does not provide as robust a comparison for our full spectral type range as do the other catalogs. Our proper motions are consistent with all of these large catalogs, within 2σ for ≈95% of objects in common from BASS, MoVeRS, and LaTE-MoVeRS, and for ≈90% of objects in common from BDKP and S10. In addition, we see no systematic offset between our measurements and those from any of the comparison catalogs. We do see a slight offset from the aggregate of other published proper motions (many sources), indicating that proper motions in the literature tend be slightly larger than those from PS1 and the other large catalogs listed here. Nevertheless, 90% of our values are consistent at 3σ or less with these diverse literature sources.

6.4.3 Kinematics

Our catalog includes distances and tangential velocities ($v_{\rm tan}$) for each object with a proper motion (Table 6.8). We calculated distances from parallaxes in the literature (also in Table 6.8) when possible. When no parallax was available, we used $i_{\rm P1}$ photometry and the SED templates from D16 for M0–M5 dwarfs. D16 do not quote uncertainties for their SED templates, so we adopt an uncertainty of 0.2 mag based on the apparent scatter in

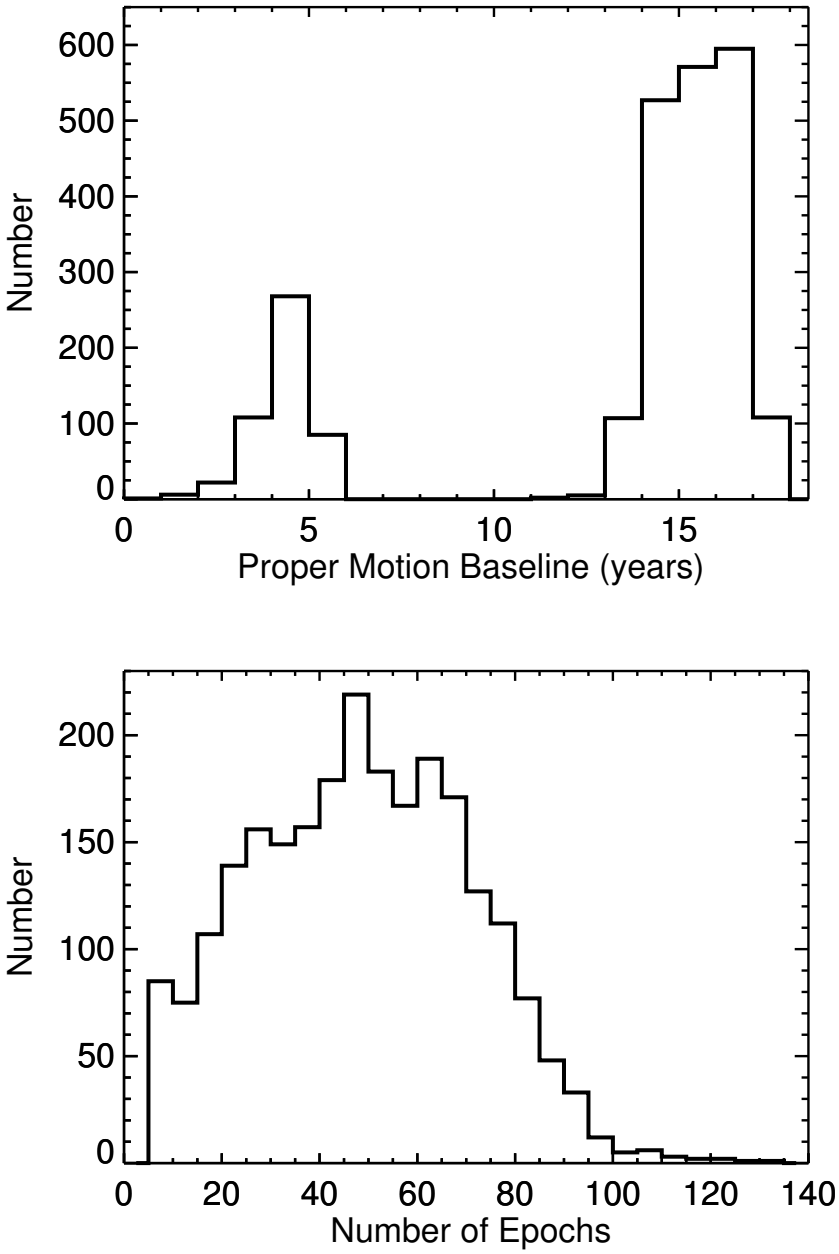

Figure 6.11 Distributions of the time baselines (*top*) and number of epochs (*bottom*) used to calculate the proper motions of the M6–T9 dwarfs in our PS1 ultracool catalog. For most objects (baselines ≈13-17 years) a 2MASS position was used in the motion fit. Baselines less than 10 years indicate that only PS1 astrometry was used. When available (for about one quarter of the objects), a *Gaia* DR1 position was also included. We required a minimum of seven epochs to calculate a proper motion fit.

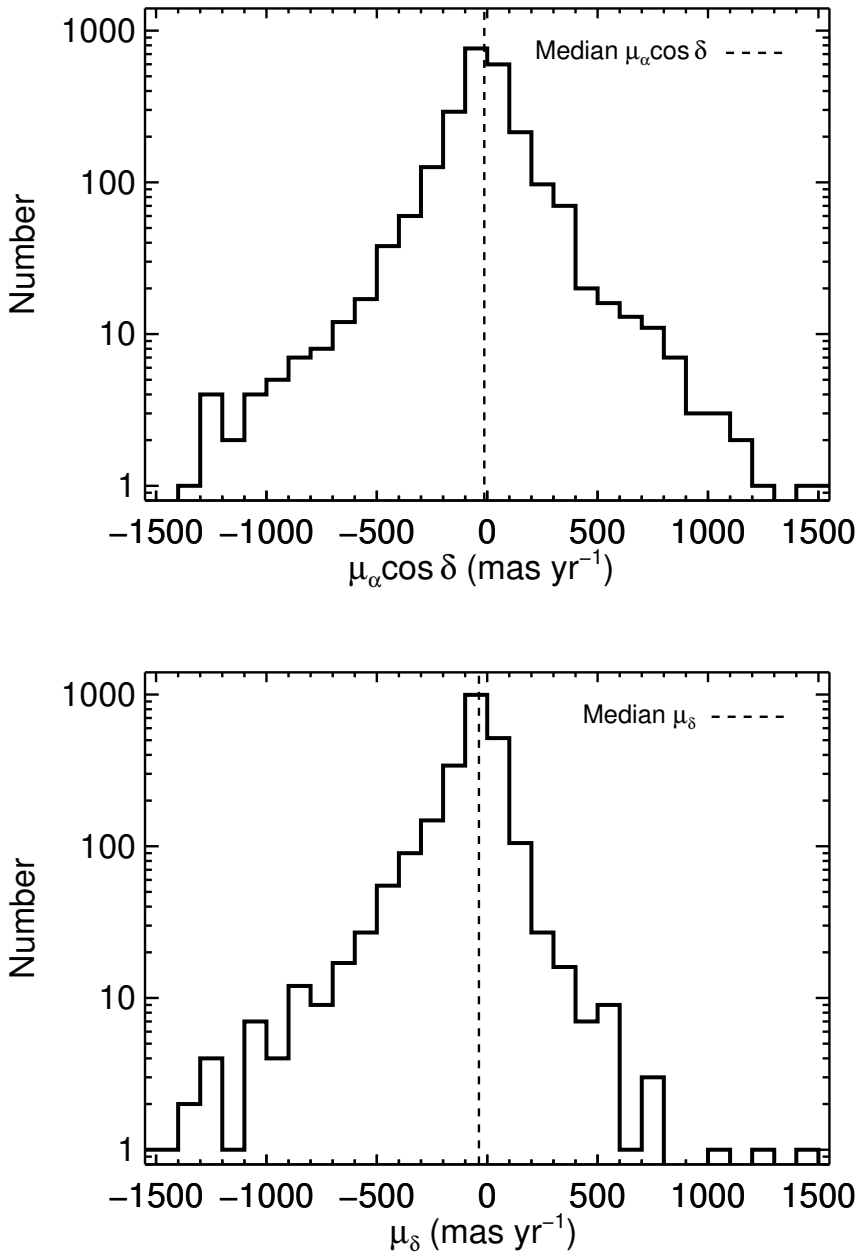

Figure 6.12 Distributions of the R.A. (*top*) and Decl. (*bottom*) proper motion components of the M6–T9 dwarfs in our PS1 ultracool catalog. The vertical dashed lines indicate the median values. The distributions are similar to those found in previous ultracool surveys (S10, BDKP, BASS, and LaTE-MoVeRS).

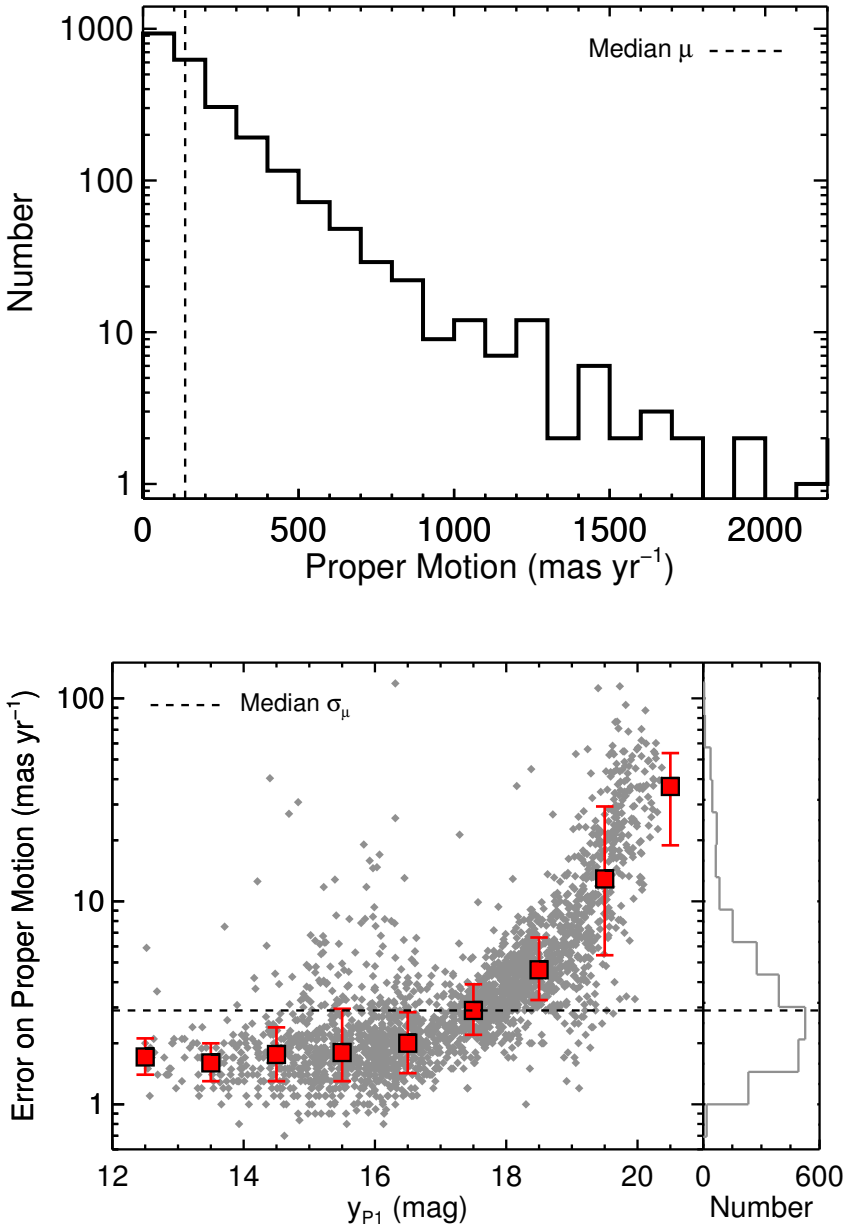

Figure 6.13 Distribution of the total proper motions (*top*) and proper motion errors as a function of $y_{\rm P1}$ (*bottom*) for the M6–T9 dwarfs in our PS1 ultracool catalog. The dashed lines indicate the median values, including a median error of 2.9 mas yr^{-1}. The large red squares indicate median errors for bins of one magnitude in $y_{\rm P1}$, with error bars showing 68% confidence limits. Our errors are ≈9 times smaller than those in S10, ≈5 times smaller than those in BDKP, and ≈3 times smaller than those in BASS and LaTE-MoVeRS.

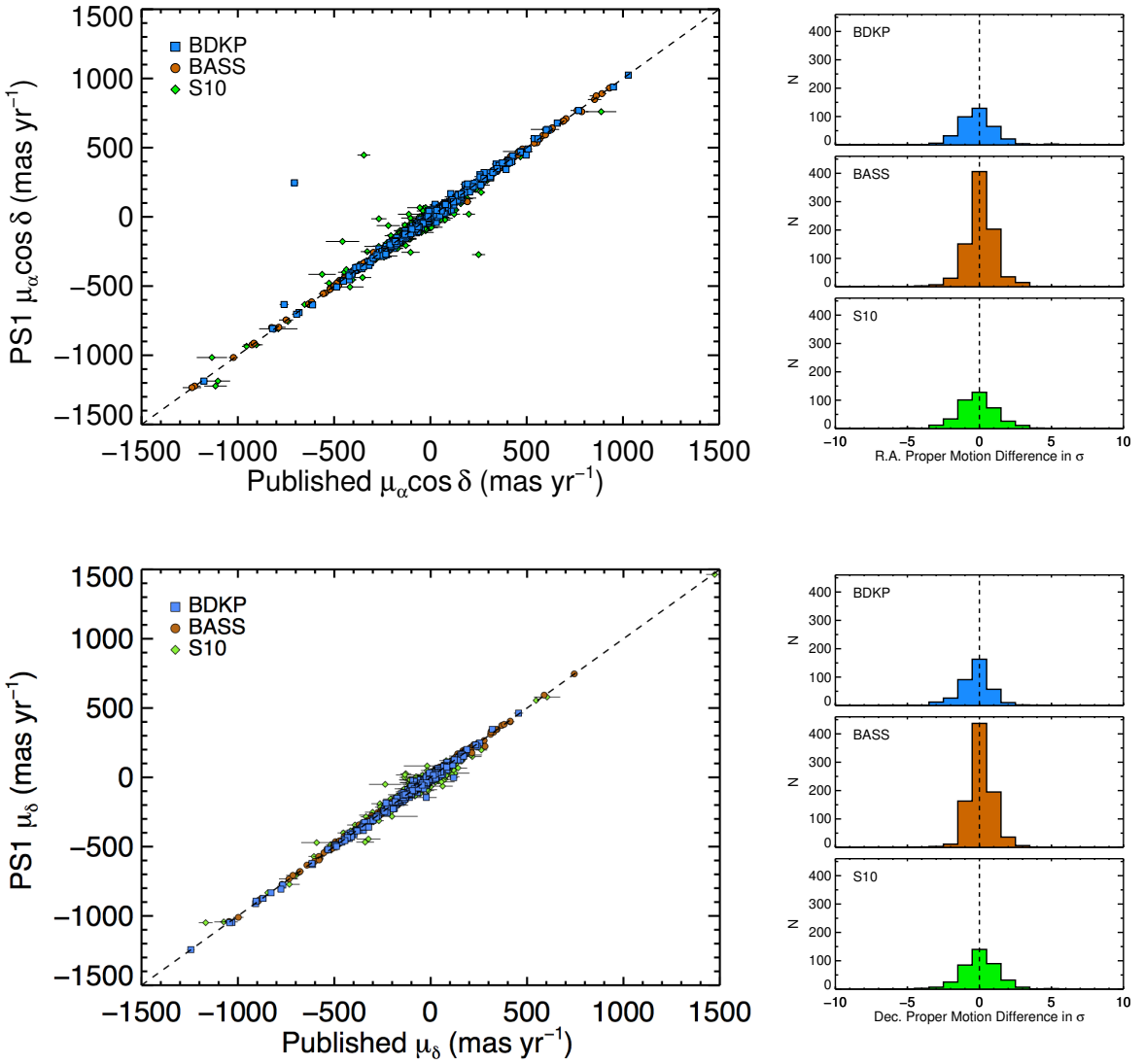

Figure 6.14 *Left*: Comparison of our PS1 proper motions in R.A. (*top*) and Decl. (*bottom*) with other proper motions from the literature, highlighting the large BDKP, BASS, S10, and (on the following page) MoVeRS and LaTE-MoVeRS catalogs. *Right*: Histograms showing differences in R.A. and Decl. proper motions (computed as PS1 value − literature value). ≈95% of are within 2σ of the BASS, MoVeRS, and LaTE-MoVeRS measurements. ≈90% of our proper motions are within 2σ of the BDKP and S10 measurements, and within 3σ of other literature values. The histograms show no systematic offset between our PS1 proper motions and those of the S10, BDKP, BASS, MoVeRS, and LaTE-MoVeRS catalogs, but suggest that other literature sources tend to have slightly larger proper motions.

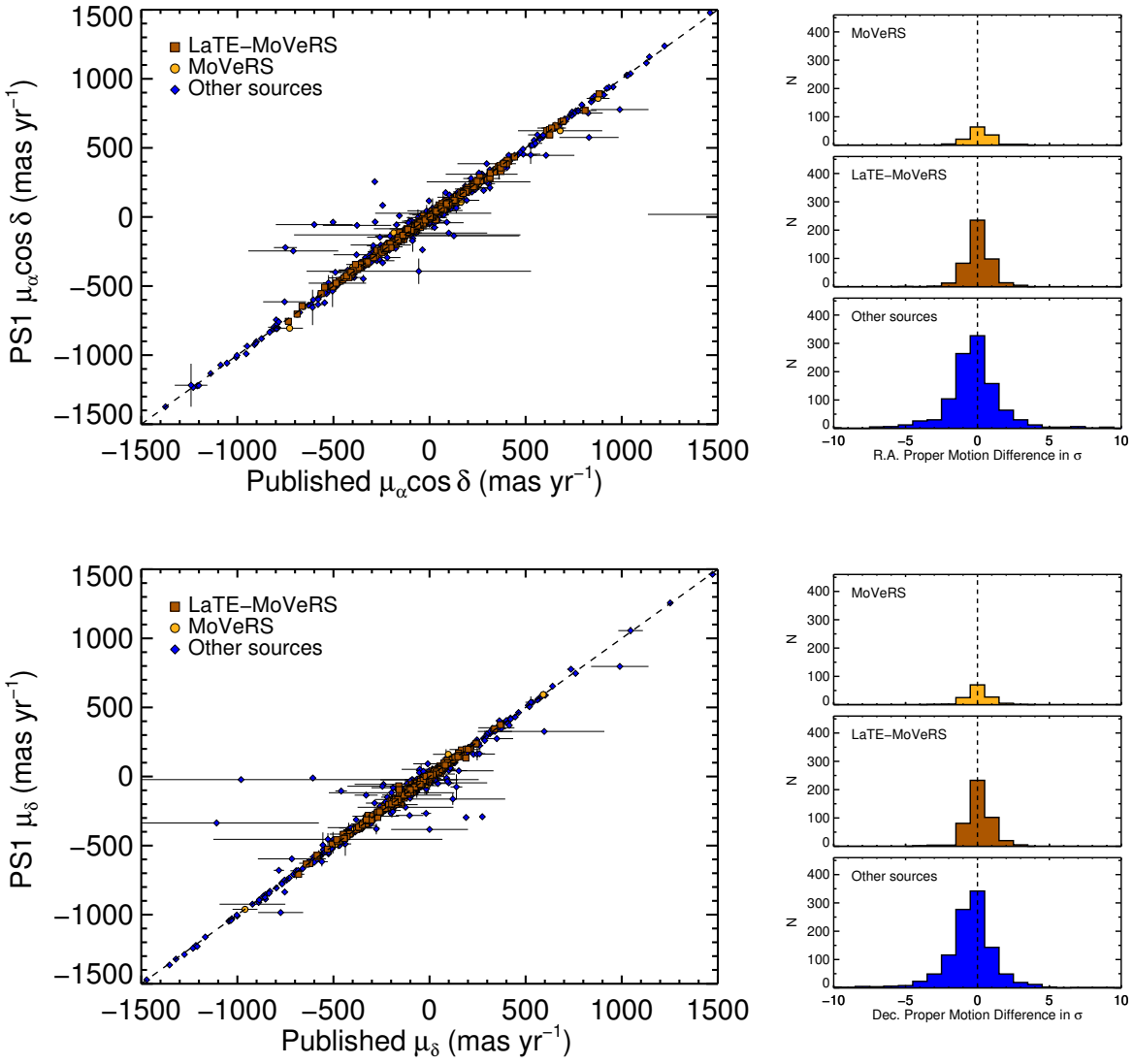

Figure 6.14 continued.

their color transformations, and we add this in quadrature with the photometry errors to determine distance errors. For M6 and later-type dwarfs lacking parallaxes, we use $W2$ photometry with the spectral type-absolute magnitude polynomial and rms from Dupuy & Liu (2012) to calculate photometric distances and errors.

Figure 6.15 shows the distribution of tangential velocities among our single M6–T9 dwarfs, highlighting the young objects (Section 6.2.5) and subdwarfs. Excluding the young objects and subdwarfs, we find a median of $v_{\rm tan} = 29$ km s^{-1} and a dispersion of $\sigma_{\rm tan} = 29$ km s^{-1}, consistent with the $v_{\rm tan} = 26$ km s^{-1} and $\sigma_{\rm tan} = 25$ km s^{-1} found by Faherty et al. (2009, hereinafter F09) for their 20 pc volume-limited ultracool sample and the $v_{\rm tan} = 28$ km s^{-1} and $\sigma_{\rm tan} = 25$ km s^{-1} found by S10 for their L dwarf sample. 90% of our PS1 sample has $v_{\rm tan} < 75$ km s^{-1}, indicating a very high probability of membership in the thin disk population (Dupuy & Liu 2012). 98% of our sample has $v_{\rm tan} < 200$ km s^{-1}, indicating that most of the remaining objects are likely to be in the thick disk population (Dhital et al. 2010; Dupuy & Liu 2012), consistent with the kinematics of the LaTE-MoVeRS sample (Theissen et al. 2017).

Figure 6.15 demonstrates that the young objects and subdwarfs are members of distinct kinematic populations, corroborating Faherty et al. (2012). Almost all young objects have $v_{\rm tan} < 60$ km s^{-1}, with a median of 16 km s^{-1} and dispersion 13 km s^{-1}, slower than the rest of the thin-disk population. On the other hand, all but one subdwarf have $v_{\rm tan} > 60$ km s^{-1} and subdwarfs comprise 85% of the objects with $v_{\rm tan} > 200$ km s^{-1}, extending to much higher velocities than other objects. The high $v_{\rm tan}$ of the subdwarfs implies they are likely to be members of the older thick disk or halo ($v_{\rm tan} > 200$ km s^{-1}) populations, as expected for low-metallicity objects.

F09 and S10 used $(J - K_S)_{\rm 2MASS}$ colors, tangential velocities, and velocity dispersions to identify young populations of late-M and L dwarfs with kinematics distinct from the field population. F09 found that red $(J - K_S)_{\rm 2MASS}$ outliers in their sample have lower $v_{\rm tan}$ and $\sigma_{\rm tan}$, while blue outliers have higher $v_{\rm tan}$ and $\sigma_{\rm tan}$. S10 found evidence that this correlation between $(J - K_S)_{\rm 2MASS}$ and velocity dispersion extends throughout the field

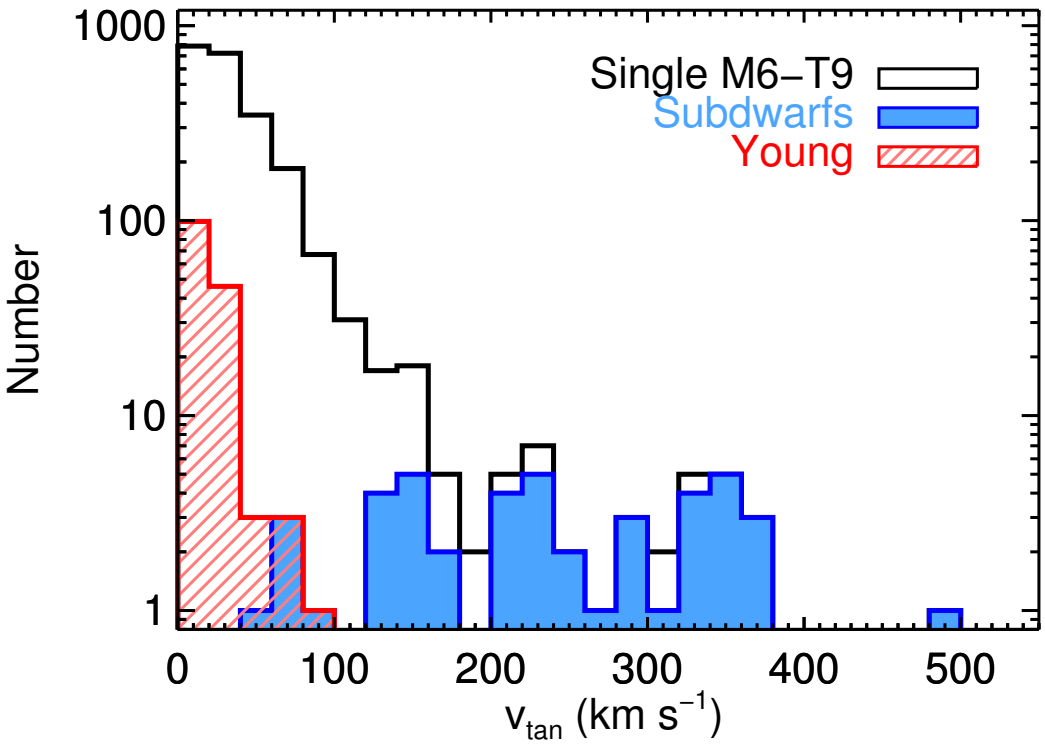

Figure 6.15 Distribution of tangential velocities for the single M6–T9 dwarfs in our catalog (black outline). Over 90% of objects have $v_{\rm tan} < 75$ km s^{-1} indicating membership in the thin disk population (Dupuy & Liu 2012). The solid blue histogram highlights the subdwarfs in our catalog, which have the high $v_{\rm tan}$ values typical of members of the older thick disk and halo populations. The hatched red histogram shows young objects in our catalog, which typically have smaller $v_{\rm tan}$ values than field-age objects.

L dwarf population and is not limited to outliers. Both studies link the reddest objects to young, low-velocity thin disk populations and the bluest objects to older, high-velocity thick disk and halo populations.

To examine the relationship between $v_{\rm tan}$ and color differences in our catalog, we use the $\delta_{J-K_S} = [(J-K_S) - (J-K_S)_{\rm med}]/\sigma_{J-K_S}$ defined by S10, where $(J-K_S)_{\rm med}$ and σ_{J-K_S} are the median and rms $J-K_S$ colors, respectively, for each spectral type. δ_{J-K_S} therefore gives us a spectral type-independent measurement of the extent to which an object's $J-K_S$ color differs from the median, where a negative δ_{J-K_S} value means the object is bluer than the median color. In Figure 6.16, we compare our $v_{\rm tan}$ to δ_{J-K_S} for single M6–T9 dwarfs. We also calculated median $v_{\rm tan}$ values for bins of 1σ in δ_{J-K_S}, excluding subdwarfs and young objects from the medians in order to assess the color dependence of $v_{\rm tan}$ for the generic ultracool field population. We show these median $v_{\rm tan}$ values in Figure 6.16, and we overplot the subdwarfs and young objects for comparison. The blue outliers are mostly subdwarfs with $v_{\rm tan} > 100$ km s^{-1}, while the red outliers are primarily young objects with $v_{\rm tan} < 10$ km s^{-1}, supporting the link between color outliers and age found by F09 and S10. Excluding the subdwarfs and young objects, the field population in our catalog shows a trend toward higher $v_{\rm tan}$ for bluer-than-median objects that is consistent with the $\sigma_{\rm tan}$ trend identified by S10, but we see no correlation between $v_{\rm tan}$ and $J-K_S$ for redder objects.

We explored whether the trend of higher $v_{\rm tan}$ for bluer-than-median objects held true across the full spectral type range of our sample, because color variations in different spectral types will have different physical causes (e.g., different types of atmospheric clouds). We calculated the same median $v_{\rm tan}$ values for narrower ranges of spectral type (M6–M9.5, L0–L3.5, L4–L8.5, L9–T3.5, and T4–T9). Figure 6.17 shows these medians, which make clear that the trend toward higher $v_{\rm tan}$ for bluer field objects is a late-M and L dwarf phenomenon that does not apply to T dwarfs.

We also explored the direct relationship between spectral type and tangential velocity, as any correlation would imply an age trend in ultracool spectral types. Figure 6.18 shows

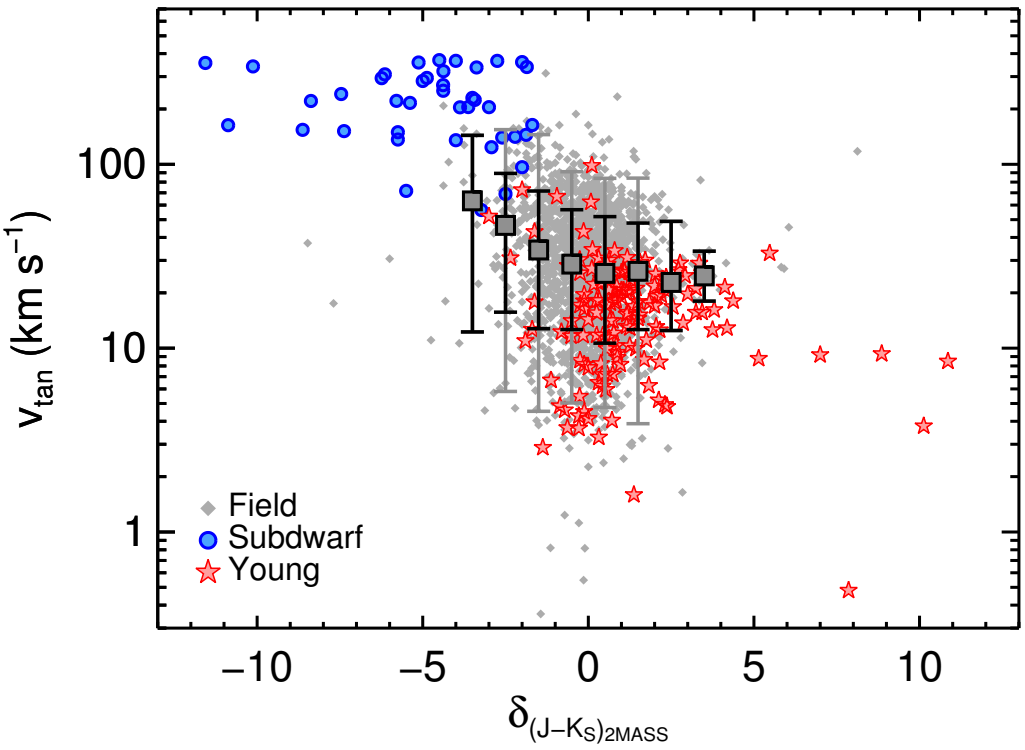

Figure 6.16 Tangential velocity as a function of $\delta_{(J-K_S)_{2\mathrm{MASS}}}$ (the number of standard deviations by which an object's $(J-K_S)_{2\mathrm{MASS}}$ color differs from the median $(J-K_S)_{2\mathrm{MASS}}$ for its spectral type) for single M6–T9 dwarfs. The large gray squares indicate median v_{tan} values for 1σ bins of δ_{J-K_S}, with dark and light error bars marking 68% and 95% confidence intervals, respectively. The medians do not include subdwarfs or young objects, but we overplot these with blue circles and red stars, respectively, for comparison. The blue end of the field population tends toward higher v_{tan}, but there is no correlation with v_{tan} on the red end.

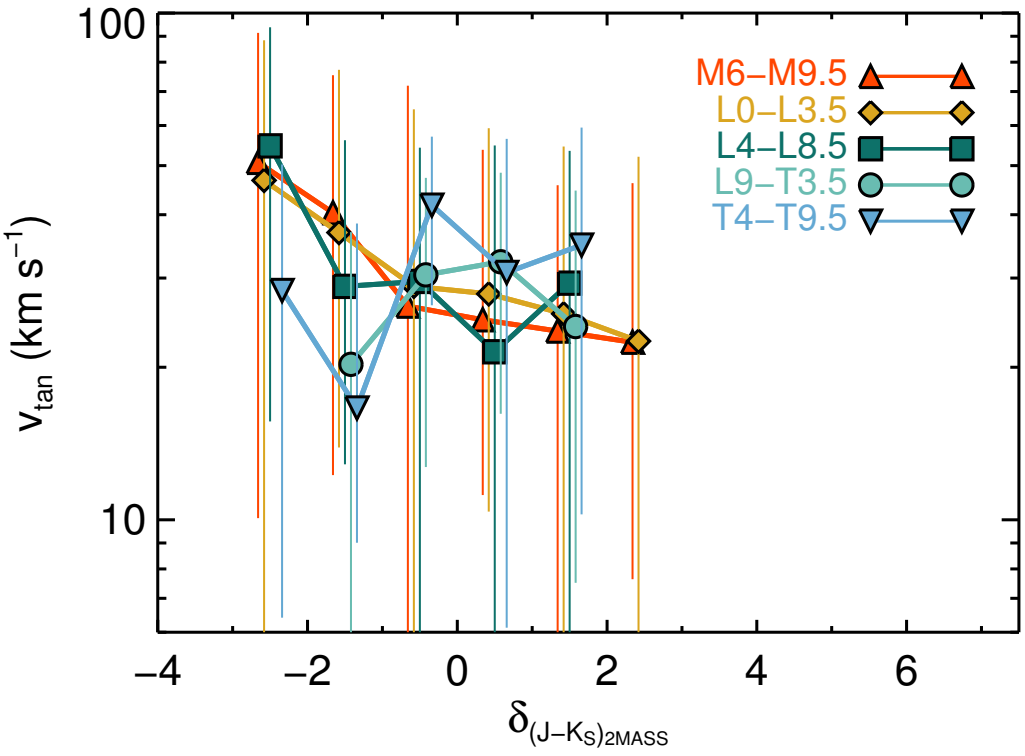

Figure 6.17 Median tangential velocities for 1σ bins of δ_{J-K_S} (same as in Figure 6.16), split into five spectral type ranges (see legend). The δ_{J-K_S} bins are the same for each spectral type range; the median symbols have been offset slightly to improve visibility. The colored lines indicate the 68% confidence intervals for each δ_{J-K_S} bin. The trend toward higher tangential velocities for bluer objects holds true for the late-M and L dwarfs, but not for T dwarfs.

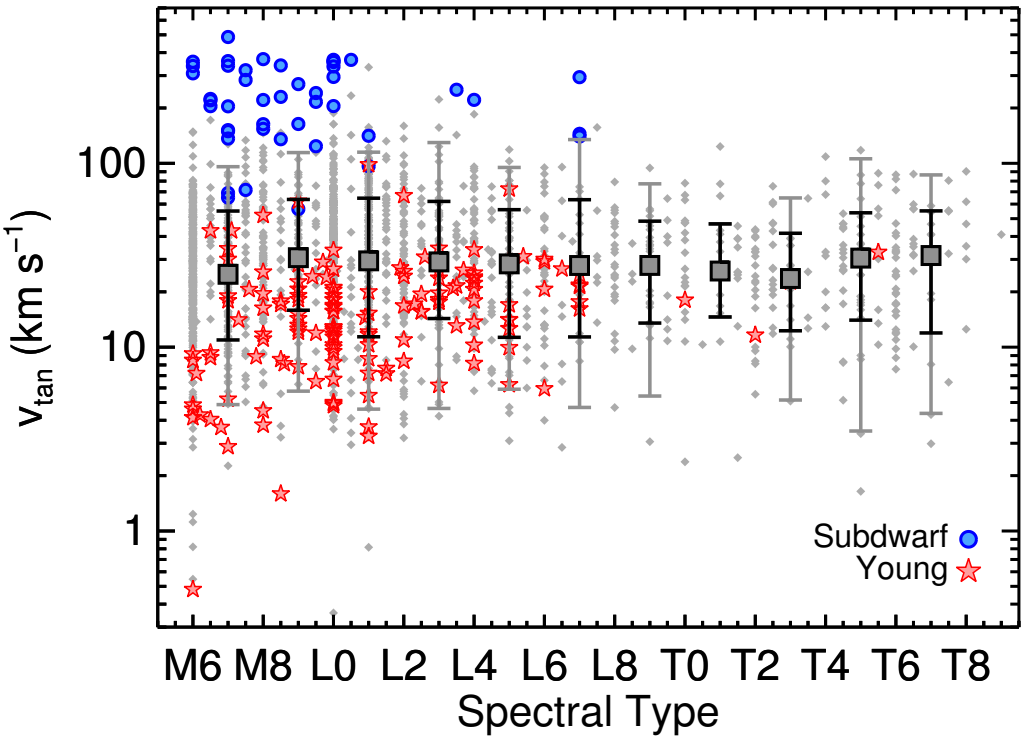

Figure 6.18 Tangential velocity as a function of spectral type for the single M6–T9 dwarfs in our catalog, using the same format as in Figure 6.16. Large gray symbols indicate median tangential velocities for bins of two spectral subtypes, excluding subdwarfs and young objects. We find no correlation between spectral type and tangential velocity in our catalog.

$v_{\rm tan}$ as a function of spectral type. We include median $v_{\rm tan}$ values for bins of two spectral subtypes, excluding subdwarfs and young objects from the medians but overplotting them for reference. We see no evidence for a dependence of $v_{\rm tan}$ on spectral type for ultracool dwarfs.

6.5 A Binary Discovered in PS1

During outlier inspection we discovered a new visual binary. 2MASS J09033514−0637336 (hereinafter 2MASS J0903−0637), first identified and assigned a spectral type of M7 by Cruz

et al. (2003), is clearly resolved in individual r_{P1}, i_{P1}, z_{P1}, and y_{P1} warp images, even though it appears in the PS1 database as a single object (see Section 6.2.6 for a discussion of similar objects). Using the i_{P1} warp images, we measure a difference in flux of 0.10 ± 0.03 mag, separation of $1\farcs14 \pm 0\farcs02$, and position angle of $239\fdg3 \pm 1\fdg0$ for 2MASS J0903−0637. We detect no change in separation or position angle over the four-year span of the PS1 survey. 2MASS J0903−0637 has a proper motion from PS1 of 63.9 ± 3.4 mas yr^{-1}; if one of the two components were actually a stationary background object, we would see the other component move by $\approx 0\farcs25$ in four years, a change in position significantly larger than our measurement uncertainties. We therefore conclude that the components are gravitationally bound. Using the i_{P1} photometry for 2MASS J0903−0637 and the absolute magnitude for M7 dwarfs from D16, and correcting for a binary with the measured 0.10 mag flux ratio, we calculate a photometric distance of 60.9 ± 5.7 pc. This places the projected binary separation at 69.5 ± 6.6 AU, unusually wide for ultracool field binaries (e.g., Duchêne & Kraus 2013). As expected given the small angular separation, the pair is unresolved in 2MASS and *WISE* images, and therefore was not previously identified as a binary. This was a serendipitous discovery, and we have not undertaken a comprehensive search for more binaries that are newly resolved by PS1 for this catalog.

6.6 Summary

We present a catalog of 9888 M, L, and T dwarfs with photometry and proper motions from the Pan-STARRS1 3π Survey. This catalog contains all L and T dwarfs known as of 2015 December that have well-measured photometry in at least one of the five PS1 bands ($g_{P1}r_{P1}i_{P1}z_{P1}y_{P1}$), including 1265 L dwarfs and 352 T dwarfs. The catalog also contains 463 late-M dwarfs chosen to represent the diversity of the nearby population, including low-gravity objects, high proper motion objects, young moving group members, known or suspected binaries, and wide companions to more massive stars, along with a large sample of 7808 field M dwarfs identified by SDSS. We cross-matched our catalog with 2MASS,

AllWISE, and *Gaia* DR1 to obtain photometry spanning 0.55 to 12 μm. We carefully vetted the detections in PS1, 2MASS, and AllWISE to ensure their association with previously identified M, L, and T dwarfs.

We use two types of photometry from PS1 in our catalog: chip photometry (highest accuracy) for most objects and warp photometry (greater depth) for faint, slow-moving objects. We identified a number of false detections (i.e., measurements of background noise) at the warp limiting magnitude for objects in our catalog, and we develop a method for screening warp detections to ensure they are real.

We use the photometry along with parallaxes from the literature to create empirical SEDs for field ultracool dwarfs covering $g_{\rm P1}$ to $W3$ bands. We determine typical colors of M0–T9 dwarfs, and we present numerous color-spectral type and color-color diagrams, along with median colors for each spectral subtype. We separate binaries, young objects, and subdwarfs from the rest of the field population, and we compare the colors of the different groups. Our catalog includes 494 L dwarfs detected in $r_{\rm P1}$, the largest sample of L dwarfs detected in this optical band. $r_{\rm P1}$ L dwarf colors show striking features, including a sharp blueward turn at the M/L transition due to decreasing TiO absorption in $r_{\rm P1}$, and a handful of young objects with colors bluer than the median for their spectral type.

We calculate proper motions for our catalog using multiple-epoch astrometry from PS1 along with 2MASS and *Gaia* when available. Our method allows us to link the epochs of fast-moving objects that are split into more than one "object" in PS1, improving the precision of our proper motions compared to the PS1 database for 87% of the M6 and later dwarfs in our catalog and producing measurements for 63 objects lacking proper motions in PS1. Our catalog contains proper motions for 9770 objects with a median precision of 2.9 mas yr^{-1} (a factor of $\approx$3$-$10 improvement over previous large catalogs), tied to the *Gaia* DR1 reference frame. The catalog includes proper motions for a total of 2405 M6–T9 dwarfs, including 406 objects with no previously published values and 1176 measurements that improve upon previous literature values. Our catalog incorporates the largest set of homogeneous proper motions for L and T dwarfs published to date.

We assess the kinematics of the late-M, L, and T dwarfs in our sample and find evidence that bluer late-M and L dwarfs with field ages (i.e., not subdwarfs) have higher tangential velocities, consistent with the trend toward higher $\sigma_{\rm tan}$ for bluer L dwarfs found by S10. More work is needed using well-defined (i.e., volume-limited) samples with accurate distances to precisely characterize the relationship between colors and kinematics for nearby ultracool dwarfs.

Our catalog is available for download in electronic form via the online journal and from http://www.ifa.hawaii.edu/ wbest/Will_Best/PS1_MLT_Dwarfs.html.

Chapter 7

Towards a Volume-Limited Sample of L and T Dwarfs with 348 Parallaxes from UKIRT

Abstract

We present parallaxes and proper motions for 348 L and T dwarfs measured using the wide-field camera WFCAM on the United Kingdom Infrared Telescope (UKIRT), representing the largest single batch of parallaxes for brown dwarfs to date. Our target list was designed to complete a volume-limited sample of L0–T8 dwarfs out to 25 pc spanning declinations $-30°$ to $+60°$ (68% of the sky). Our parallaxes have a median uncertainty of 3.5 mas. We report the first parallaxes for 219 objects, including the largest sample of T dwarf parallaxes so far (172), and we improve on previous measurements for another 21 objects. Our targets include 104 objects (mostly early-L dwarfs) having *Gaia* DR2 parallax measurements, with which our parallaxes are strongly consistent. We corrected our parallax and proper motions measurements from relative to absolute astrometry using *Gaia* DR2 measurements of field stars in our images. We also present precise J-band photometry for all of our targets. Our measurements enable for the first time population studies using a volume-limited sample of L and T dwarfs defined entirely by parallaxes.

7.1 Introduction

Brown dwarfs are objects more massive than giant planets ($\gtrsim$ 13 $M_{\rm Jup}$; Spiegel et al. 2011) but not massive enough to sustain hydrogen fusion in their cores and become stars ($\lesssim$ 70 $M_{\rm Jup}$; Dupuy & Liu 2017). Brown dwarfs therefore cool as they age, from late-M ($T_{\rm eff} \approx 3000$ K) spectral types through the L, T, and Y (≈ 300 K) types. All along their cooling sequence, brown dwarfs show a surprising diversity of near- and mid-infrared colors, thought to be caused by variations in surface gravity and condensate clouds (e.g., Burrows et al. 2006) or thermo-chemical instabilities (Tremblin et al. 2016). Young ($\lesssim$100 Myr) low-mass brown dwarfs serve as analogs for directly-imaged exoplanets given their overlapping temperature and age ranges. Since exoplanets are far more difficult to observe in the glare of their host stars, young brown dwarfs are vital templates for understanding giant exoplanets.

As the lowest-mass products of star formation, brown dwarfs also hold unique clues about the history of star formation in our galaxy. However, because brown dwarfs cool continuously after formation, their luminosities and temperatures depend on both age and mass, with the result that a younger, less massive brown dwarf can have the same luminosity and temperature (and thus spectral type) as an older, more massive brown dwarf. This observational degeneracy makes evolutionary trends in brown dwarf populations difficult to identify. A well-defined sample of brown dwarfs with precise luminosities would considerably improve our ability to test models of formation, evolution, and atmospheres.

Trigonometric parallaxes provide the most accurate and direct measures of distance, and are therefore vital for measuring luminosities. Parallaxes are also the best means to determine membership in volume-limited samples, long regarded as the gold standard for population studies as they minimize the selection biases inherent in magnitude-limited samples. However, parallax measurements are observationally expensive and therefore relatively scarce for brown dwarfs. While large digital sky surveys such as the Sloan Digital Sky Survey (SDSS; York et al. 2000), Two Micron All Sky Survey (2MASS; Skrutskie et al. 2006), UKIRT Infrared Deep Sky Survey (UKIDSS; Lawrence et al. 2007), Wide-Field

Infrared Survey Explorer (*WISE*; Wright et al. 2010), and the Panoramic Survey Telescope And Rapid Response System (Pan-STARRS1) 3π Survey (PS1; K. C. Chambers et al., 2018, in prep) have discovered more than 2000 L, T, and Y dwarfs, precise parallaxes have previously been measured for fewer than 20% of them, and no complete volume-limited sample spanning all LTY spectral types has been established.

The bulk of ultracool parallax programs to date have targeted extreme or unusual objects. Our Hawaii Infrared Parallax Program (HIPP) has previously observed mostly L/T transition dwarfs (Dupuy & Liu 2012, hereinafter DL12), young ultracool dwarfs (Liu et al. 2016, hereinafter LDA16), and ultracool binaries (DL12; Dupuy & Liu 2017, hereinafter DL17) with WIRCam on the Canada France Hawaii Telescope (CFHT). Tinney et al. (2003) published the first 10 parallaxes for then-newly-discovered T dwarfs, while others have since focused on ultracool subdwarfs (Schilbach et al. 2009) and young L dwarfs (Zapatero Osorio et al. 2014a). Several programs have targeted late-T and Y dwarfs, the coldest substellar objects in the solar neighborhood (Dupuy & Kraus 2013; Marsh et al. 2013; Tinney et al. 2014; Beichman et al. 2014). Very high precision parallax measurements have also constrained the orbital motion of binaries and planetary-mass companions (Sahlmann et al. 2014, 2015a,b; Sahlmann & Lazorenko 2015; Dupuy et al. 2015b, DL17).

Two large parallax programs targeting nearby stars, the Research Consortium On Nearby Stars (RECONS; e.g., Winters et al. 2017; Henry et al. 2018) and the Carnegie program at Las Campanas (Weinberger et al. 2013, 2016) have also observed a handful of ultracool dwarfs, but the optical detectors used for those programs limited them to observing mostly late-M and early-L dwarfs. Most recently, *Gaia* DR2 (Gaia Collaboration et al. 2018) has measured parallaxes for hundreds of L dwarfs, and, but *Gaia*'s optical detectors face the same limitation and have obtained only a handful of parallaxes for L6 and later objects. (We discuss *Gaia*'s ultracool parallaxes in Section 7.6.)

A comprehensive understanding of brown dwarfs requires a large volume-limited sample representing the full population. Parallax programs that have targeted broad swaths of L and T dwarfs include the United States Naval Observatory near-infrared program (USNO-

IR; Vrba et al. 2004), which so far has published preliminary parallaxes for 22 L dwarfs and 18 T dwarfs; the Brown Dwarf Kinematics Project (BDKP; Faherty et al. 2012, 2016), which obtained 88 parallaxes of late-M, L, and T dwarfs; and the ongoing PARallaxes of Southern Extremely Cool Objects (PARSEC; Andrei et al. 2011; Marocco et al. 2013) and NTT PARSEC (NPARSEC; Smart et al. 2013), which have measured over 40 L and T dwarf parallaxes While these programs have contributed substantially to the ultracool parallax census, collectively their results form a patchwork of varying spatial and spectral type coverage. Consequently, the most complete volume-limited sample assembled to date is the 2MASS-based sample of Reid et al. (2008b), comprising 196 late-M, L, and T dwarfs out to 20 pc over 65% of the sky, but complete only for spectral types M9-L6 and using photometric distances for two-thirds of the members. The full-sky 8 pc volume-limited sample of Kirkpatrick et al. (2012) contains only 33 L, T, and Y dwarfs.

We have obtained infrared parallaxes for 348 L and T dwarfs using the United Kingdom Infrared Telescope (UKIRT), with the goal of completing a volume-limited L and T dwarf sample. This paper describes the measurement and validation of our UKIRT parallaxes. We describe our target selection in Section 7.2, and our observations in Section 7.3. In Section 7.4 we describe our data reduction pipeline, and we explain details of our parallax calculations in Section 7.5. We present our results in Section 7.6.

7.2 Target Selection

Our goal is to establish a complete volume-limited sample of L and T dwarfs large enough for robust statistical analysis. In order to do this with confidence, we require a sample defined entirely by parallaxes to avoid the pitfalls that come with photometric distances (e.g., incorrect distances for binaries or spectrally peculiar objects). Figure 7.1 shows the parallactic or photometric distances to known ultracool dwarfs out to 40 pc at the beginning of our observations in 2014 May, and makes clear that at the time there was no parallax-defined volume-limited sample at any spectral type beyond a few parsecs. Historically,

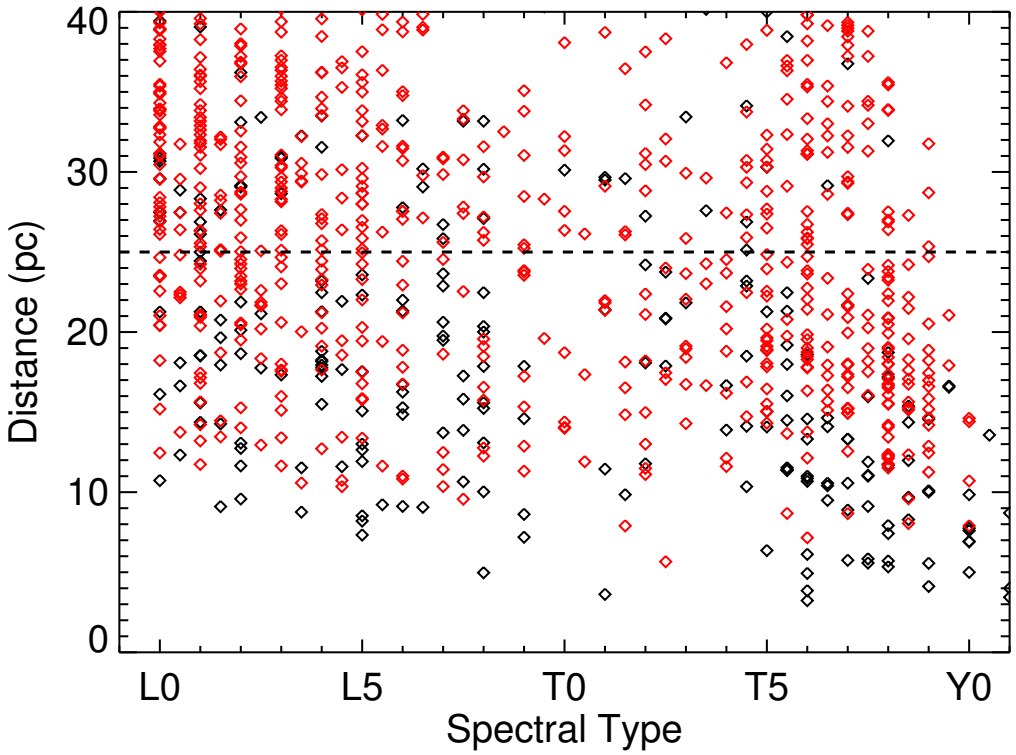

Figure 7.1 The distances of known M9–Y1 dwarfs as a function of spectral type out to 40 pc, as of 2014 May. Black diamonds mark objects with known parallaxes, and red diamonds indicate no parallax measurement (distances are photometric). The black dashed line marks the 25 pc limit of our sample. The parallax census at the time had uneven spectral type coverage and was clearly not volume-limited beyond ≈5 pc.

25 pc has often been used as the boundary of stellar volume-limited samples, including the landmark all-sky Gliese catalog (Gliese & Jahreiss 1991), the Palomar-Michigan State University spectroscopic survey of M dwarfs (Reid et al. 1995), the Nearby Stars project (NStars; Gray et al. 2003), and the RECONS parallax program (e.g., Henry et al. 2006). Space density estimates from Cruz et al. (2007), Metchev et al. (2008), and Day-Jones et al. (2013) indicated that 25 pc would enclose ∼400 L and T dwarfs over roughly half the sky.

The declination boundaries of our target list come from the observing limits of UKIRT and PS1. UKIRT cannot observe north of $\delta = +60°$. PS1 provided the reference catalog we used to calibrate our astrometric measurements (Section 7.4.2), and contributes photometry

and proper motions (Best et al. 2018), so we did not observe farther south than the $\delta = -30°$ limit of PS1.

We identified all spectroscopically confirmed L and T dwarfs in the literature with $-30° \leq \delta \leq 60°$ that lacked a parallax measurement with (error $\leq$ 10%). We selected those having photometric distances based on *WISE* $W2$ photometry and the spectral type-absolute magnitude relations of DL12, or low-quality trigonometric (errors $>$ 10%) distances where available, placing them within 25 pc or at most 1σ beyond 25 pc using the measurement errors from the literature. Many of these objects have spectral types from both optical and near-IR spectra; if both were available, we used the the optical spectral types for L dwarfs and the near-IR spectral types for T dwarfs. One of our eventual targets, 2MASS J00464841+0715177, had an optical spectral type L0:: (Reid et al. 2008b) that was updated to M9 β (Faherty et al. 2016) during the course of our observations. We continued to observe this object and report its parallax in this paper. We also included one target, 2MASSW J0320284−044636, which has an optical spectral type M8 (Cruz et al. 2003) and a near-IR spectral type L0.5 (Wilson et al. 2003). This object has been identified as a spectroscopic binary (Blake et al. 2008) with component spectral types M8.5+T5: (Burgasser et al. 2008a), making it a target of particular interest.

We used the $V/V_{\rm max}$ statistic (Schmidt 1968) to estimate that our targets were ≈85% volume-complete for L0–T6 dwarfs out to 25 pc, with most of the missing objects at low galactic latitudes where few searches for ultracool dwarfs have ventured. At spectral types later than T6, the 25 pc sample of known objects (with and without parallaxes) is expected to be more incomplete due to the limiting magnitude of *WISE* and the limited sky coverage (≈4000 deg^2) UKIDSS, which have discovered most of the known T6+ dwarfs. Most targets become prohibitively faint for near-IR observations from the ground beyond spectral type T8. We decided to retain T6.5–T8 targets brighter than J = 19.2 mag (Section 7.3.2), and discarded fainter and later-type targets. Targets with spectral types ≥T7 are being observed to greater depth for parallaxes with CFHT (e.g., Dupuy & Liu 2012), Magellan (e.g., Tinney et al. 2014), and *Spitzer* (e.g., Dupuy & Kraus 2013; Beichman et al. 2014),

and those results could be combined with ours to form a fairly complete volume-limited sample out ≈20 pc for the latest-type objects.

Our target volume included 97 L0–T8 objects with previously published parallaxes (errors ≤ 10%) placing them within $25 + 1\sigma_{\rm dist}$ pc. For comparison purposes, we retained 24 of those parallax-confirmed objects in our target list, including 7 companions to stars with Hipparcos parallaxes. We eliminated most targets already being observed as part of HIPP at CFHT, but we retained 84 targets known to be on the target lists for other ultracool parallax programs, including PARSEC, NPARSEC, USNO-IR, and a handful from HIPP/CFHT.

Our final target list contained 356 L0–T8 dwarfs. Parallaxes with errors ≤ 10% were published by others for 7 of our targets after our program began, and we continued observing those targets.

7.3 Observations

7.3.1 UKIRT/WFCAM

We used the near-infrared Wide Field Camera (WFCAM; Casali et al. 2007) on UKIRT, the same instrument and telescope that produced the UKIRT Infrared Deep Sky Survey (UKIDSS; Lawrence et al. 2007) and the ongoing UKIRT Hemisphere Survey (UHS; Dye et al. 2018). Marocco et al. (2010) and Smart et al. (2010, 2017) have previously measured 14 parallaxes of mid-T through Y dwarfs, achieving precisions of ≈2–5 mas, demonstrating the potential for UKIRT to measure parallaxes for brighter L and early-T dwarfs.

WFCAM consists of four 2048×2048 Rockwell Hawaii-II (HgCdTe) infrared arrays, each with a field of view of $13\farcm65 \times 13\farcm65$, arranged in a 2×2 grid and spaced by $12\farcm83$. WFCAM has a pixel scale of $0\farcs4$ pixel^{-1}. Based on past the advice of UKIRT staff and challenges with obtaining precise astrometric solutions across wide fields on separated arrays, we only used data from WFCAM's Camera 3 (northeast array).

All UKIRT observations were performed in service (queue) mode, which allowed us obtain good parallax phase coverage by observing every object at different times of the year (when visible) while minimizing disruptions from poor weather. Service mode also facilitated repeating observations at similar airmasses, which enabled us to reduce the impact of differential chromatic refraction (DCR) to an insignificant level (Sections 7.3.2 and 7.5.3). In practice, irregular scheduling due to instrument changes on UKIRT and a non-integrated observing queue (programs from specific institutions had priority on specific nights) meant that some RA ranges received better coverage in different years.

As part of the instrument changes, WFCAM was typically unbolted and removed from the telescope a few times a year. Smart et al. (2010) investigated the impact on astrometry of these remove-replace cycles, and found no systematic effects.

The observations presented in this paper span 2014 May 05 UT through 2018 January 16 UT. Details of observations of all our targets are listed in Table 7.1. Figure 7.2 shows the number of observed epochs and time baselines for our targets.

Table 7.1. Observations

Object	SpT Optical/NIR	$J_{\rm MKO}$ (mag)	FWHM ($''$)	Δairmass	$t_{\rm int}$[a] (s)	$N_{\rm fr}$	$N_{\rm ep}$	Δt (yr)	$N_{\rm ref}$	$N_{\rm cal}$	$N_{\rm abs}$	$\pi_{\rm abs} - \pi_{\rm rel}$ (mas)	References (Disc; SpT)
SDSS J000112.18+153535.5	.../L3.7 INT-G	15.48 ± 0.02	0.79 ± 0.17	0.071	1/5	126	15	3.4	43	29	19	1.6 ± 0.8	48; 33
PSO J001.1277−26.0675	.../T4	16.18 ± 0.02	1.04 ± 0.19	0.019	4/5	86	11	2.4	67	41	20	2.7 ± 0.7	52; 52
WISEPC J000849.76−173922.6	.../T6	16.86 ± 0.02	0.97 ± 0.17	0.017	10	92	11	2.4	80	62	25	3.2 ± 0.5	46; 46
PSO J003.3437−11.7168	.../T4	16.05 ± 0.02	0.86 ± 0.15	0.014	4/5	108	12	2.9	71	50	22	1.7 ± 0.4	52; 52
2MASS J00150206+2959323	.../L7.5pec	16.15 ± 0.02	0.92 ± 0.35	0.041	4/5	120	14	3.4	158	126	67	1.2 ± 0.2	45; 45
2MASSW J0015447+351603	L2/L1.0	13.73 ± 0.02	0.78 ± 0.14	0.058	1/5	105	14	3.1	97	76	61	0.9 ± 0.3	43; 43, 4
PSO J004.1834+23.0741	.../T0	16.52 ± 0.02	0.95 ± 0.33	0.043	4	195	11	3.1	118	87	40	1.2 ± 0.1	6; 6
PSO J004.6359+56.8370	.../T4.5	16.22 ± 0.02	0.90 ± 0.15	0.156	4/5	97	11	2.5	1214	1165	528	0.1 ± 0.1	52; 52
PSO J005.6302−06.8669	.../T3	16.11 ± 0.02	0.85 ± 0.14	0.022	4/5	108	12	3.0	69	45	15	1.6 ± 0.6	52; 52
2MASS J00282091+2249050	.../L7:	15.41 ± 0.03	0.90 ± 0.26	0.058	1/5	104	12	2.2	65	46	27	2.0 ± 0.5	15; 15
2MASSW J0030300−145033	L7/L6: FLD-G	16.49 ± 0.02	0.90 ± 0.14	0.021	6	81	9	2.4	65	48	24	1.1 ± 0.5	43; 43, 51
WISE J003110.04+574936.3	.../L9	14.77 ± 0.02	0.90 ± 0.13	0.021	1/5	89	11	2.3	902	863	559	0.7 ± 0.1	80; 5
PSO J007.9194+33.5961	.../L9	16.38 ± 0.02	0.94 ± 0.30	0.079	6	123	14	3.0	179	155	89	0.9 ± 0.2	6; 6
2MASS J00320509+0219017	L1.5/M9	14.25 ± 0.02	0.82 ± 0.11	0.032	1/5	105	13	3.1	44	27	18	1.4 ± 0.6	71; 71, 83
WISE J004024.88+090054.8	.../T7	16.16 ± 0.02	0.82 ± 0.17	0.118	5	107	12	2.9	87	68	36	1.2 ± 0.2	58; 58
PSO J011.1793−03.7847	.../T2	16.04 ± 0.02	0.86 ± 0.13	0.030	4/5	105	12	2.9	57	37	17	0.7 ± 0.2	52; 52
WISE J004542.56+361139.1	.../T5	15.92 ± 0.02	0.98 ± 0.24	0.108	2/5	144	15	2.9	148	136	85	0.9 ± 0.2	58; 58
2MASS J00464841+0715177	M9 β/L0.9 VL-G	13.82 ± 0.02	0.84 ± 0.12	0.099	1/5	125	15	3.1	50	36	25	0.5 ± 0.4	71; 30, 33
WISEPC J004928.48+044100.1	.../L9	15.77 ± 0.02	0.90 ± 0.20	0.104	2/5	90	12	2.9	57	38	30	1.6 ± 0.4	46; 46
SIPS J0050−1538	L1:/L0.5	13.69 ± 0.02	0.84 ± 0.09	0.033	1/5	77	11	2.4	45	24	22	1.7 ± 0.4	23; 21, 4
2MASSW J0051107−154417	L3.5/L5:	15.18 ± 0.02	0.90 ± 0.15	0.076	1/5	96	11	2.4	43	26	14	1.9 ± 0.5	43; 43, 15

Table 7.1—Continued

Object	SpT Optical/NIR	$J_{\rm MKO}$ (mag)	FWHM ($''$)	Δairmass	$t_{\rm int}$[a] (s)	$N_{\rm fr}$	$N_{\rm ep}$	Δt (yr)	$N_{\rm ref}$	$N_{\rm cal}$	$N_{\rm abs}$	$\pi_{\rm abs} - \pi_{\rm rel}$ (mas)	References (Disc; SpT)
WISEA J010202.11+035541.4	.../L9	16.74 ± 0.02	0.90 ± 0.19	0.024	10	106	12	2.3	66	54	15	1.3 ± 0.4	73; 73
SDSS J011912.22+240331.6	.../T2	17.04 ± 0.02	0.90 ± 0.18	0.060	10	107	12	3.1	168	140	53	1.2 ± 0.2	19; 19
WISEPA J012333.21+414203.9	.../T7	17.00 ± 0.02	0.94 ± 0.23	0.069	20	143	16	3.2	440	395	157	0.3 ± 0.1	46; 46
2MASS J01311838+3801554	L4:/L1.5	14.62 ± 0.02	0.93 ± 0.25	0.077	1/5	122	15	3.2	105	95	58	1.0 ± 0.3	21; 21, 15
WISE J013525.64+171503.4	.../T6	17.10 ± 0.02	0.90 ± 0.18	0.066	10	90	10	2.9	92	75	30	0.7 ± 0.1	58; 58
2MASSW J0135358+120522	L1.5/L0.6	14.35 ± 0.02	0.77 ± 0.11	0.091	1/5	108	12	3.1	52	43	28	1.3 ± 0.4	43; 43, 4
SIMP J013656.5+093347.3	T2/T2.5	13.27 ± 0.02	0.79 ± 0.13	0.103	1/5	84	11	2.7	53	38	22	1.7 ± 0.3	3; 67, 3
PSO J024.4369+09.1360	.../T3.5	16.44 ± 0.02	0.83 ± 0.09	0.097	6	72	9	2.9	75	62	18	0.4 ± 0.6	52; 52
WISEPC J013836.59−032221.2	.../T3	16.13 ± 0.02	1.04 ± 0.28	0.043	4/5	124	18	2.4	56	44	18	0.7 ± 0.4	46; 46
2MASS J01414839−1601196	.../L7:	16.06 ± 0.02	0.91 ± 0.12	0.048	4/5	52	8	2.3	69	46	18	0.9 ± 0.8	45; 45
2MASS J01443536−0716142	L5/L5	14.13 ± 0.02	0.93 ± 0.15	0.052	1/5	142	16	2.4	41	25	18	0.2 ± 0.5	50; 50, 59
WISEPA J015010.86+382724.3	.../T0	15.94 ± 0.02	0.97 ± 0.46	0.121	2/5	117	13	3.1	142	126	78	0.1 ± 0.2	46; 46
ULAS J015024.37+135924.0	.../T7.5	17.81 ± 0.02	0.90 ± 0.22	0.117	60	99	11	3.1	188	166	34	1.3 ± 0.1	16; 16
2MASS J01550354+0950003	L5/L3.2 INT-G	14.73 ± 0.02	0.85 ± 0.14	0.145	1/5	79	10	2.7	52	37	16	2.2 ± 0.4	71; 71, 33
HIP 9269B	.../L6	16.05 ± 0.02	0.88 ± 0.21	0.132	4/5	126	14	3.2	162	146	66	0.4 ± 0.2	27; 27
2MASSW J0205034+125142	L5/L5.5	15.57 ± 0.02	0.84 ± 0.12	0.074	1/5	125	13	2.9	33	28	14	1.8 ± 0.4	43; 43, 15
PSO J031.5651+20.9097	.../T5.5	16.84 ± 0.02	0.91 ± 0.19	0.045	10	112	13	3.1	134	109	37	0.8 ± 0.1	6; 6
2MASSW J0208183+254253	L1/...	13.91 ± 0.02	0.84 ± 0.12	0.065	1/5	99	12	2.8	31	27	16	1.6 ± 0.4	43; 43
2MASSW J0208236+273740	L5/L5	15.65 ± 0.02	0.87 ± 0.18	0.065	1/5	117	13	2.9	88	66	38	0.9 ± 0.1	43; 43, 15
2MASS J02132062+3648506C	.../T3	15.16 ± 0.02	0.87 ± 0.18	0.037	1/5	117	13	2.9	129	112	73	1.2 ± 0.2	28; 28
2MASSI J0213288+444445	L1.5/...	13.39 ± 0.02	0.97 ± 0.33	0.036	1/5	134	16	3.0	200	184	125	0.7 ± 0.1	20; 20

Table 7.1—Continued

Object	SpT Optical/NIR	$J_{\rm MKO}$ (mag)	FWHM ($''$)	Δairmass	$t_{\rm int}$[a] (s)	$N_{\rm fr}$	$N_{\rm ep}$	Δt (yr)	$N_{\rm ref}$	$N_{\rm cal}$	$N_{\rm abs}$	$\pi_{\rm abs} - \pi_{\rm rel}$ (mas)	References (Disc; SpT)
WISEPA J022105.94+384202.9	.../T6.5	17.22 ± 0.02	0.83 ± 0.18	0.048	30	104	12	2.3	476	447	146	0.6 ± 0.1	46; 46
WISEPA J022623.98−021142.8	.../T7	18.42 ± 0.02	1.14 ± 0.30	0.054	60	444	9	2.8	205	178	20	0.5 ± 0.1	46; 46
2MASS J02271036−1624479	L1/L0.5:	13.51 ± 0.02	0.93 ± 0.14	0.051	1/5	78	11	2.3	36	29	15	1.2 ± 0.4	71; 71, 59
2MASSW J0228110+253738	L0:/L0	13.74 ± 0.02	0.83 ± 0.10	0.052	1/5	114	13	2.9	67	55	37	1.1 ± 0.2	83; 20, 83
2MASS J02284243+1639329	L0:/M8.7	13.07 ± 0.02	0.76 ± 0.08	0.065	1/5	115	13	3.0	52	42	21	-0.3 ± 0.4	71; 71, 4
WISE J023038.90−022554.0	.../L8:pec	16.87 ± 0.02	1.11 ± 0.25	0.029	4	176	10	3.0	60	45	17	1.9 ± 0.2	80; 80
WISE J023318.05+303030.5	.../T6	16.53 ± 0.02	0.89 ± 0.26	0.042	4	260	15	3.0	188	163	66	1.0 ± 0.1	58; 58
PSO J041.5426+01.9456	.../L8.5	16.89 ± 0.02	0.92 ± 0.13	0.049	15	107	12	3.0	111	91	37	2.0 ± 0.2	6; 6
WISE J024714.52+372523.5	.../T8	18.01 ± 0.02	0.94 ± 0.21	0.053	60	279	11	2.9	613	589	121	1.1 ± 0.1	58; 58
2MASSI J0251148−035245	L3/L1	12.92 ± 0.02	0.80 ± 0.07	0.020	1/5	89	10	2.9	45	34	19	0.5 ± 0.6	20; 20, 83
PSO J045.3309−23.3226	.../T1	16.64 ± 0.02	0.92 ± 0.19	0.053	10	53	6	2.2	98	70	16	0.8 ± 0.4	52; 52
WISEPA J030533.54+395434.4	.../T6	16.78 ± 0.02	0.87 ± 0.14	0.045	15	106	12	3.1	537	516	223	0.6 ± 0.1	46; 46
WISE J031614.68+382008.0	.../T3	15.89 ± 0.02	0.91 ± 0.18	0.084	2/5	117	13	3.2	292	276	121	2.4 ± 0.1	58; 58
PSO J049.1159+26.8409	.../T2.5	16.17 ± 0.02	0.94 ± 0.16	0.099	4/5	126	14	2.9	140	129	63	1.3 ± 0.2	6; 6
2MASSW J0320284−044636	M8/L0.5	13.16 ± 0.02	0.79 ± 0.10	0.050	1/5	105	12	3.0	58	44	22	1.5 ± 0.4	83; 20, 83
WISEA J032301.86+562558.0	.../L7	15.76 ± 0.02	0.99 ± 0.28	0.154	1/5	76	10	3.2	454	426	84	0.2 ± 0.2	57; 57
SDSS J032553.17+042540.1	.../T5.5	16.03 ± 0.02	0.86 ± 0.10	0.082	2/5	106	13	3.0	87	72	29	1.4 ± 0.3	19; 19
PSO J052.2746+13.3754	.../T3.5	16.24 ± 0.02	0.88 ± 0.15	0.114	5	115	13	3.1	129	110	49	0.5 ± 0.1	52; 52
PSO J052.7214−03.8409	.../L9:	16.26 ± 0.02	0.83 ± 0.12	0.054	5	99	11	3.0	83	70	49	1.3 ± 0.1	6; 6
WISE J033651.90+282628.8	.../T5	16.26 ± 0.02	0.94 ± 0.22	0.139	4/5	116	13	3.1	225	204	100	0.7 ± 0.2	58; 58
2MASSW J0337036−175807	L4.5/L4.3 FLD-G	15.52 ± 0.02	0.93 ± 0.16	0.029	1/5	57	9	3.2	50	34	22	1.5 ± 0.5	43; 43, 33

Table 7.1—Continued

Object	SpT Optical/NIR	$J_{\rm MKO}$ (mag)	FWHM ($''$)	Δairmass	$t_{\rm int}$[a] (s)	$N_{\rm fr}$	$N_{\rm ep}$	Δt (yr)	$N_{\rm ref}$	$N_{\rm cal}$	$N_{\rm abs}$	$\pi_{\rm abs} - \pi_{\rm rel}$ (mas)	References (Disc; SpT)
SDSS J035104.37+481046.8	.../T1:	16.48 ± 0.02	0.86 ± 0.22	0.053	4/5	124	13	3.3	989	949	380	0.8 ± 0.1	19; 19
WISE J040137.21+284951.7	L3/L2.5	13.32 ± 0.02	0.77 ± 0.15	0.149	1/5	107	13	2.9	213	193	115	1.1 ± 0.1	18; 18, 18
WISE J040418.01+412735.6	L2/L2pec	14.02 ± 0.02	0.91 ± 0.18	0.025	1/5	99	11	3.3	148	141	82	0.6 ± 0.2	18; 18, 18
2MASS J04070885+1514565	.../T5	15.67 ± 0.02	0.80 ± 0.14	0.176	2/5	117	13	2.9	153	140	61	1.5 ± 0.2	11; 12
2MASSI J0408290−145033	L2/L4.5	14.15 ± 0.02	0.87 ± 0.09	0.230	1/5	99	10	3.2	56	44	25	0.2 ± 0.3	83; 20, 83
PSO J062.3459+11.1794	.../T3.5	16.18 ± 0.02	0.81 ± 0.09	0.070	4/5	107	12	2.9	152	134	41	0.8 ± 0.2	52; 52
WISE J042417.94+072744.1	.../T7.5	18.33 ± 0.02	0.84 ± 0.12	0.120	60	392	9	2.8	407	390	81	0.7 ± 0.1	58; 58
WISE J043052.92+463331.6	.../T8	19.03 ± 0.03	1.37 ± 0.26	0.030	60	390	9	3.1	2729	2605	137	0.9 ± 0.1	58; 58
PSO J069.7303+04.3834	.../T2	16.38 ± 0.02	0.82 ± 0.06	0.028	6	72	8	2.7	151	140	63	0.6 ± 0.2	52; 52
PSO J070.3773+04.7333	.../T4.5	16.34 ± 0.02	0.82 ± 0.05	0.031	6	70	8	2.7	172	149	77	0.4 ± 0.2	6; 6
PSO J071.8769−12.2713	.../T2:	16.73 ± 0.02	0.79 ± 0.11	0.010	10	77	10	2.1	226	195	63	0.5 ± 0.2	6; 6
2MASS J04474307−1936045	L5:/L4:	15.94 ± 0.02	0.89 ± 0.12	0.102	2/5	71	8	2.1	139	115	58	1.3 ± 0.4	15; 15, 15
WISEPA J044853.29−193548.5	.../T5pec	16.66 ± 0.03	1.00 ± 0.21	0.110	10	99	10	3.2	153	137	60	0.6 ± 0.1	46; 46
2MASSI J0453264−175154	L3:/L2.5 INT-G	15.00 ± 0.02	0.84 ± 0.11	0.087	1/5	72	9	3.2	119	99	59	0.8 ± 0.4	20; 20, 33
WISE J045746.08−020719.2	.../T2	14.63 ± 0.02	0.80 ± 0.16	0.038	1/5	99	12	3.1	157	135	80	0.9 ± 0.1	7; 7
WISEPA J050003.05−122343.2	.../T8	17.89 ± 0.02	0.99 ± 0.33	0.012	30[b]	260	11	3.2	294	269	73	1.2 ± 0.1	46; 46
PSO J076.7092+52.6087	.../T4.5	15.42 ± 0.02	0.95 ± 0.14	0.039	1/5	81	9	3.2	789	728	309	0.4 ± 0.1	6; 6
2MASS J05160945−0445499	.../T5.5	15.54 ± 0.02	0.85 ± 0.11	0.019	2/5	65	12	3.1	224	204	99	1.3 ± 0.2	10; 12
WISE J052126.29+102528.4	.../T7.5	14.86 ± 0.02	0.83 ± 0.10	0.031	1/5	85	10	2.9	404	367	147	1.5 ± 0.1	7; 7
HIP 26653B	.../L1.5	14.64 ± 0.02	0.82 ± 0.14	0.250	1/5	89	11	3.2	452	431	193	0.5 ± 0.1	27; 27
WISEPA J053957.02−103436.5	.../T5.5	17.40 ± 0.02	0.98 ± 0.34	0.022	40	122	13	3.2	587	559	161	0.9 ± 0.1	46; 46

Table 7.1—Continued

Object	SpT Optical/NIR	$J_{\rm MKO}$ (mag)	FWHM ($''$)	Δairmass	$t_{\rm int}$[a] (s)	$N_{\rm fr}$	$N_{\rm ep}$	Δt (yr)	$N_{\rm ref}$	$N_{\rm cal}$	$N_{\rm abs}$	$\pi_{\rm abs} - \pi_{\rm rel}$ (mas)	References (Disc; SpT)
PSO J085.1080−18.0445	.../T5	16.01 ± 0.02	0.94 ± 0.13	0.128	4/5	114	12	3.1	248	230	98	0.7 ± 0.1	52; 52
WISEPA J054231.26−162829.1	.../T6.5	16.30 ± 0.02	0.97 ± 0.20	0.127	6	117	12	3.0	310	273	146	1.2 ± 0.1	46; 46
WISE J054601.19−095947.5	.../T5	15.99 ± 0.02	0.81 ± 0.17	0.021	2/5	106	12	3.0	261	239	43	0.5 ± 0.3	58; 58
WISEA J055007.94+161051.9	.../L2	14.35 ± 0.02	0.74 ± 0.14	0.141	1/5	108	12	2.9	700	663	344	0.6 ± 0.1	47; 47
PSO J087.7749−12.6537	.../L8	16.56 ± 0.02	1.12 ± 0.33	0.019	4	139	11	3.1	350	337	158	0.8 ± 0.1	6; 6
PSO J088.5709−00.1430	.../T4.5	16.08 ± 0.02	0.86 ± 0.14	0.044	4/5	108	12	3.1	548	529	181	1.2 ± 0.1	52; 52
PSO J089.1751−09.4513	.../T5.5	16.46 ± 0.02	0.88 ± 0.11	0.026	10	107	12	3.1	438	409	115	0.9 ± 0.1	52; 52
2MASS J06020638+4043588	.../T4.5	15.28 ± 0.02	0.77 ± 0.09	0.067	1/5	107	12	3.2	558	534	282	0.7 ± 0.1	55; 55
WISEA J060742.13+455037.0	.../L2.5	14.92 ± 0.02	0.79 ± 0.10	0.092	1/5	108	13	3.1	391	362	183	1.1 ± 0.1	47; 47
WISE J061437.73+095135.0	.../T7	16.43 ± 0.02	0.93 ± 0.34	0.010	10	86	13	2.8	1935	1863	651	0.5 ± 0.1	58; 58
2MASS J06143818+3950357	.../L9:	16.55 ± 0.02	0.90 ± 0.21	0.088	4	249	14	3.1	839	800	375	1.3 ± 0.1	65; 65
WISEPA J062309.94−045624.6	.../T8	17.09 ± 0.02	0.92 ± 0.17	0.075	30	107	13	3.0	1322	1288	532	1.7 ± 0.1	46; 46
WISEPA J062542.21+564625.5	.../T6	16.74 ± 0.02	1.01 ± 0.23	0.098	10	43	14	3.3	475	438	176	1.3 ± 0.1	46; 46
WISE J062905.13+241804.9	.../T2	16.34 ± 0.02	0.92 ± 0.33	0.061	4/5	116	14	2.9	1083	1049	370	0.6 ± 0.1	58; 58
WISEA J064750.85−154616.4	.../L9.5	15.14 ± 0.02	0.96 ± 0.17	0.048	1/5	123	14	3.1	850	798	311	0.9 ± 0.1	77; 77
PSO J103.0927+41.4601	.../T0	15.35 ± 0.02	0.97 ± 0.11	0.033	1/5	99	13	3.2	205	187	93	0.6 ± 0.1	5; 5
2MASSI J0652307+471034	L4.5/L6.5	13.37 ± 0.02	0.82 ± 0.15	0.076	1/5	90	12	3.1	144	132	69	1.0 ± 0.2	20; 20, 15
WISEPA J065609.60+420531.0	T2/T3	15.28 ± 0.02	0.82 ± 0.12	0.075	1/5	98	13	3.2	190	178	92	1.2 ± 0.2	46; 67, 46
WISEA J065958.55+171710.9	.../L2	14.74 ± 0.02	0.80 ± 0.13	0.109	1/5	67	13	1.9	672	596	278	0.6 ± 0.1	47; 47
WISEA J071552.38−114532.9	.../L4pec	14.18 ± 0.02	0.85 ± 0.10	0.021	1/5	80	11	3.2	931	879	369	0.4 ± 0.1	47; 47
2MASS J07231462+5727081	L1/L0.2	13.91 ± 0.02	0.87 ± 0.12	0.058	1/5	63	10	2.1	77	65	35	1.3 ± 0.4	71; 71, 4

Table 7.1—Continued

Object	SpT Optical/NIR	$J_{\rm MKO}$ (mag)	FWHM ($''$)	Δairmass	$t_{\rm int}$[a] (s)	$N_{\rm fr}$	$N_{\rm ep}$	Δt (yr)	$N_{\rm ref}$	$N_{\rm cal}$	$N_{\rm abs}$	$\pi_{\rm abs} - \pi_{\rm rel}$ (mas)	References (Disc; SpT)
SDSS J074149.15+235127.5	.../T5	15.90 ± 0.02	0.89 ± 0.18	0.250	2/5	113	12	2.9	229	206	118	1.0 ± 0.1	48; 12
2MASS J07415784+0531568	.../L1.5	14.32 ± 0.02	1.01 ± 0.52	0.074	1/5	108	13	3.0	365	326	166	0.5 ± 0.1	45; 45
SDSS J074201.41+205520.5	.../T5	15.78 ± 0.02	0.92 ± 0.16	0.253	1/5	135	14	3.0	221	199	99	1.1 ± 0.1	48; 12
WISEPA J074457.15+562821.8	.../T8	17.26 ± 0.02	0.92 ± 0.11	0.107	40	90	10	2.2	268	243	79	1.2 ± 0.1	46; 46
PSO J117.0600−01.6779	.../T5.5	16.36 ± 0.02	1.05 ± 0.27	0.058	6	142	16	3.2	578	553	331	0.9 ± 0.1	52; 52
2MASSI J0755480+221218	T6/T5	15.51 ± 0.02	0.92 ± 0.14	0.301	1/5	123	14	3.0	198	170	96	1.2 ± 0.1	8; 9, 12
HIP 38939B	.../T4.5	15.79 ± 0.02	0.99 ± 0.20	0.082	2/5	90	10	3.2	1605	1534	1077	0.6 ± 0.1	25; 25
SDSS J075840.33+324723.4	T3/T2	14.73 ± 0.02	0.81 ± 0.10	0.133	1/5	90	11	2.0	95	75	44	0.3 ± 0.2	48; 67, 12
WISE J080700.23+413026.8	.../L8pec	15.93 ± 0.02	0.82 ± 0.10	0.094	2/5	116	12	2.9	140	122	50	1.5 ± 0.2	80; 80
ULAS J080918.41+212615.2	.../T8	18.58 ± 0.02	0.98 ± 0.18	0.136	60	535	13	3.0	491	461	93	1.1 ± 0.1	17; 17
SDSS J080959.01+443422.2	.../L5.4 INT-G	16.42 ± 0.02	0.90 ± 0.19	0.021	5	135	14	2.1	161	141	62	0.6 ± 0.1	48; 33
ULAS J081110.86+252931.8	.../T7	17.60 ± 0.02	0.80 ± 0.11	0.058	60	139	14	3.0	492	463	78	0.6 ± 0.1	17; 17
WISE J081220.04+402106.2	.../T8	17.95 ± 0.02	0.88 ± 0.13	0.052	60	357	12	2.1	354	332	73	0.7 ± 0.1	58; 58
WISEPA J081958.05−033529.0	T4/T4	14.78 ± 0.02	0.88 ± 0.15	0.026	1/5	125	13	3.1	260	245	163	1.7 ± 0.1	46; 67, 46
2MASSW J0820299+450031	L5/L4.5::	16.24 ± 0.02	0.84 ± 0.12	0.035	4/5	107	12	2.1	147	129	58	0.6 ± 0.1	43; 43, 15
WISEPA J082131.63+144319.3	.../T5.5	16.40 ± 0.02	0.94 ± 0.18	0.042	6	103	12	3.0	211	187	72	0.4 ± 0.1	46; 46
2MASS J08234818+2428577	L3/L1.5	15.00 ± 0.02	0.79 ± 0.09	0.053	1/5	98	13	3.0	109	94	51	1.3 ± 0.2	71; 71, 15
WISEA J082640.45−164031.8	.../L9	15.61 ± 0.02	0.89 ± 0.09	0.042	2/5	80	9	3.0	602	562	344	1.3 ± 0.1	47; 47
2MASSW J0829066+145622	L2/L1.0	14.70 ± 0.02	0.80 ± 0.12	0.050	1/5	89	13	3.0	129	119	63	0.9 ± 0.2	43; 43, 4
PSO J127.5648−11.1861	.../T3	15.71 ± 0.02	0.90 ± 0.16	0.035	2/5	105	11	3.0	389	365	231	1.2 ± 0.1	52; 52
SDSS J083048.80+012831.1	.../T4.5	16.07 ± 0.02	0.88 ± 0.13	0.058	2/5	107	12	3.1	237	215	146	1.0 ± 0.1	48; 12

Table 7.1—Continued

Object	SpT Optical/NIR	$J_{\rm MKO}$ (mag)	FWHM ($''$)	Δairmass	$t_{\rm int}$[a] (s)	$N_{\rm fr}$	$N_{\rm ep}$	Δt (yr)	$N_{\rm ref}$	$N_{\rm cal}$	$N_{\rm abs}$	$\pi_{\rm abs} - \pi_{\rm rel}$ (mas)	References (Disc; SpT)
2MASSW J0832045−012835	L1.5/L1:	14.07 ± 0.02	0.86 ± 0.12	0.070	1/5	99	10	2.2	168	156	118	0.5 ± 0.1	43; 43, 59
2MASS J08355829+0548308	L2:/L1.7	14.49 ± 0.02	0.79 ± 0.09	0.049	1/5	103	13	2.9	150	134	79	1.3 ± 0.1	71; 71, 4
SDSSp J083717.22−000018.3	T0/T1	16.98 ± 0.02	0.93 ± 0.19	0.061	15	141	15	3.1	373	343	135	0.9 ± 0.1	49; 44, 12
PSO J130.7271−06.1732	.../T4.5	15.80 ± 0.02	0.85 ± 0.11	0.031	2/5	135	14	3.2	289	257	155	0.9 ± 0.1	52; 52
SDSS J085234.90+472035.0	.../L9.5:	16.16 ± 0.02	0.89 ± 0.15	0.044	4/5	86	13	3.1	94	82	43	0.8 ± 0.1	48; 48
PSO J133.8016−02.5658	.../T0pec	15.99 ± 0.02	1.01 ± 0.17	0.043	2/5	135	14	3.2	188	166	100	0.8 ± 0.1	6; 6
WISEPA J085716.25+560407.6	.../T8	17.34 ± 0.02	0.79 ± 0.14	0.027	40	116	11	2.1	199	182	33	0.4 ± 0.1	46; 46
SDSSp J085758.45+570851.4	L8/L8:	14.86 ± 0.02	0.81 ± 0.10	0.032	1/5	107	12	3.0	89	68	38	1.6 ± 0.2	34; 44, 34
SDSS J085834.42+325627.7	.../T1	16.36 ± 0.02	0.93 ± 0.34	0.052	4/5	134	14	3.1	109	98	39	1.1 ± 0.2	19; 19
ULAS J085910.69+101017.1	.../T7	17.88 ± 0.02	0.88 ± 0.13	0.033	30	270	9	1.1	277	251	58	0.6 ± 0.1	68; 68
PSO J135.7840+16.9932	.../T0pec	16.41 ± 0.02	0.79 ± 0.10	0.015	6	57	8	1.0	113	86	44	1.5 ± 0.2	6; 6
2MASS J09054654+5623117	L5/L6	15.34 ± 0.02	0.83 ± 0.12	0.025	1/5	81	10	3.0	58	44	17	1.6 ± 0.3	71; 71, 15
PSO J136.5380−14.3267	.../T3.5	16.45 ± 0.02	0.88 ± 0.12	0.101	6	99	11	3.1	249	227	131	0.4 ± 0.1	52; 52
2MASSI J0908380+503208	L5/L9:	14.42 ± 0.02	0.84 ± 0.21	0.025	1/5	89	11	3.1	73	57	31	1.1 ± 0.3	20; 20, 48
Gl 337CD	L8/T0	15.48 ± 0.02	1.15 ± 0.07	0.075	1/5	114	14	3.0	125	96	43	1.4 ± 0.2	82; 82, 12
2MASS J09153413+0422045	L6/...	14.45 ± 0.02	1.18 ± 0.09	0.023	1/5	102	13	2.0	100	72	45	1.6 ± 0.1	71; 71
WISE J092055.40+453856.3	.../L9.5	15.00 ± 0.02	0.82 ± 0.13	0.037	1/5	105	12	3.1	72	53	24	1.7 ± 0.4	58; 5
2MASS J09211410−2104446	L1.5/L4:	12.69 ± 0.02	0.94 ± 0.10	0.087	1/5	90	11	2.1	334	271	141	0.8 ± 0.1	71; 71, 14
SDSS J092308.70+234013.7	L1/L2.3	13.76 ± 0.02	0.92 ± 0.11	0.089	1/5	104	14	3.0	85	65	29	0.3 ± 0.3	72; 72, 4
WISEPC J092906.77+040957.9	.../T6.5	16.86 ± 0.02	0.98 ± 0.45	0.121	15	108	12	2.0	182	163	61	1.5 ± 0.1	46; 46
2MASS J09490860−1545485	.../T2	15.82 ± 0.02	0.89 ± 0.13	0.169	2/5	90	10	2.6	153	121	65	2.0 ± 0.2	81; 12

Table 7.1—Continued

Object	SpT Optical/NIR	$J_{\rm MKO}$ (mag)	FWHM ($''$)	Δairmass	$t_{\rm int}$[a] (s)	$N_{\rm fr}$	$N_{\rm ep}$	Δt (yr)	$N_{\rm ref}$	$N_{\rm cal}$	$N_{\rm abs}$	$\pi_{\rm abs} - \pi_{\rm rel}$ (mas)	References (Disc; SpT)
ULAS J095429.90+062309.6	.../T5	16.62 ± 0.02	0.98 ± 0.16	0.097	4	196	11	3.0	104	82	40	1.2 ± 0.1	76, 17; 17
PSO J149.0341−14.7857	.../L9	15.96 ± 0.02	0.88 ± 0.16	0.186	2/5	81	10	2.6	119	95	58	1.2 ± 0.2	6; 6
PSO J149.1907−19.1730	.../L5pec	15.12 ± 0.02	0.87 ± 0.15	0.206	1/5	72	9	3.7	134	105	64	1.1 ± 0.2	6; 6
2MASS J09593276+4523309	.../L3 γ	15.84 ± 0.02	0.88 ± 0.21	0.073	2/5	106	11	2.6	62	49	19	0.5 ± 0.3	30; 30
SDSS J100711.74+193056.2	.../L8:	16.70 ± 0.02	0.88 ± 0.17	0.116	10	117	14	3.7	106	88	35	0.8 ± 0.1	19; 19
2MASSI J1010148−040649	L6/L6	15.39 ± 0.02	1.00 ± 0.15	0.041	1/5	107	12	3.6	69	54	34	0.5 ± 0.2	20; 20, 45
ULAS J101243.54+102101.7	.../T5.5	16.93 ± 0.02	0.89 ± 0.13	0.132	15	125	14	3.6	112	98	36	0.1 ± 0.1	75; 16
DENIS J1019245−270717	L0.5/M9.5	13.50 ± 0.02	0.85 ± 0.13	0.032	1/5	54	6	3.0	155	115	74	0.8 ± 0.2	62; 62, 42
2MASSI J1029216+162652	L2.5/L2.8	14.22 ± 0.02	0.84 ± 0.13	0.054	1/5	117	13	3.0	25	10	6	2.2 ± 1.1	43; 43, 4
ULAS J102940.52+093514.6	.../T8	17.30 ± 0.02	0.82 ± 0.11	0.171	30	126	14	3.2	115	97	23	1.8 ± 0.1	17; 17
SDSS J103026.78+021306.4	.../L9.5:	17.18 ± 0.02	1.03 ± 0.23	0.088	10	108	12	3.0	128	99	44	0.5 ± 0.1	48; 48
PSO J159.2399−26.3885	.../T1.5	16.59 ± 0.02	1.00 ± 0.13	0.065	10	88	9	2.4	320	260	120	0.8 ± 0.1	6; 6
WISE J103907.73−160002.9	.../T7.5	16.95 ± 0.02	0.96 ± 0.35	0.078	20	106	12	3.6	215	185	67	0.8 ± 0.1	58; 58
SDSS J103931.35+325625.5	.../T1	16.09 ± 0.02	0.99 ± 0.22	0.043	4/5	167	18	3.7	52	36	14	0.2 ± 0.2	19; 19
PSO J160.0416−21.3281	.../T2pec	16.49 ± 0.02	1.02 ± 0.24	0.013	4	117	8	2.4	189	156	93	0.6 ± 0.1	6; 6
2MASS J10430758+2225236	L8/L9:	15.85 ± 0.02	0.90 ± 0.15	0.053	2/5	123	13	3.0	48	36	13	0.2 ± 0.4	21; 21, 15
SDSS J104335.08+121314.1	.../L9	15.89 ± 0.02	0.87 ± 0.12	0.056	2/5	124	13	3.0	65	46	23	2.1 ± 0.1	19; 45
SDSS J104409.43+042937.6	.../L7	15.93 ± 0.02	0.86 ± 0.17	0.061	2/5	113	12	3.7	56	41	19	1.7 ± 0.2	48; 48
SDSS J104842.84+011158.5	L1/L4	12.82 ± 0.02	0.83 ± 0.10	0.069	1/5	112	13	3.6	49	34	16	1.4 ± 0.3	39; 39, 41
WISE J105047.90+505606.2	.../T8	17.90 ± 0.02	0.92 ± 0.15	0.019	30	349	12	2.4	144	120	10	2.1 ± 0.1	58; 58
2MASS J10511900+5613086	L2/L0.8	13.17 ± 0.02	0.81 ± 0.17	0.259	1/5	82	12	3.0	49	14	10	0.6 ± 0.6	71; 71, 4

Table 7.1—Continued

Object	SpT Optical/NIR	$J_{\rm MKO}$ (mag)	FWHM ($''$)	Δairmass	$t_{\rm int}$[a] (s)	$N_{\rm fr}$	$N_{\rm ep}$	Δt (yr)	$N_{\rm ref}$	$N_{\rm cal}$	$N_{\rm abs}$	$\pi_{\rm abs} - \pi_{\rm rel}$ (mas)	References (Disc; SpT)
WISE J105257.95−194250.2	.../T7.5	16.84 ± 0.02	0.97 ± 0.25	0.110	15	107	12	3.6	220	189	86	1.2 ± 0.1	80; 80
2MASS J10595185+3042059	.../T4	16.02 ± 0.02	0.94 ± 0.37	0.040	2/5	81	18	3.7	61	40	25	1.0 ± 0.2	78; 78
2MASS J11000965+4957470	L3.5/L3	15.18 ± 0.02	0.84 ± 0.17	0.027	1/5	117	13	3.0	53	33	14	1.1 ± 0.4	71; 71, 15
2MASSI J1104012+195921	L4/L5.5	14.34 ± 0.02	0.84 ± 0.10	0.068	1/5	88	13	3.7	30	19	15	2.8 ± 0.5	20; 20, 15
Gl 417BC	L4.5/L5: FLD-G	14.46 ± 0.02	0.81 ± 0.12	0.049	1/5	112	13	2.7	66	46	24	1.3 ± 0.4	43; 43, 2
WISEPC J112254.73+255021.5	.../T6	16.26 ± 0.02	0.88 ± 0.14	0.054	4/5	121	13	3.7	63	43	17	-0.0 ± 0.2	46; 46
WISE J112438.12−042149.7	.../T7	16.40 ± 0.02	1.08 ± 0.29	0.042	6	107	12	3.7	79	59	29	0.6 ± 0.1	58; 58
WISEA J114724.10−204021.3	.../L7: red	17.44 ± 0.02	0.99 ± 0.20	0.088	40	62	10	2.7	311	251	55	0.7 ± 0.1	74; 74
2MASS J11533966+5032092	L1:/L0.3	14.04 ± 0.02	0.76 ± 0.09	0.022	1/5	83	12	3.0	53	34	6	0.6 ± 0.4	71; 71, 4
ULAS J115508.39+044502.3	.../T7	18.31 ± 0.02	1.08 ± 0.32	0.056	30	459	9	1.9	163	137	22	-0.3 ± 0.1	17; 17
SDSS J115553.86+055957.5	.../L6.8 FLD-G	15.72 ± 0.02	0.96 ± 0.18	0.094	1/5	97	13	3.7	43	26	19	0.3 ± 0.1	48; 33
SDSS J115700.50+061105.2	.../T1.5	17.06 ± 0.02	0.98 ± 0.36	0.086	10	159	17	3.7	139	114	35	-0.8 ± 0.1	48; 12
DENIS-P J1159+0057	L0/L0.4	14.01 ± 0.02	0.90 ± 0.23	0.095	1/5	106	14	2.0	64	43	36	1.2 ± 0.3	61; 39, 4
PSO J180.1475−28.6160	.../T0	15.97 ± 0.02	1.17 ± 0.41	0.112	2/5	54	6	3.0	127	109	76	0.2 ± 0.4	6; 6
SDSSp J120358.19+001550.3	L3/L5.0	13.90 ± 0.02	0.80 ± 0.16	0.053	1/5	114	14	2.9	62	43	36	2.2 ± 0.2	31; 31, 4
2MASSI J1204303+321259	L0/M9	13.79 ± 0.02	0.82 ± 0.17	0.037	1/5	130	15	2.3	44	31	15	1.4 ± 0.2	20; 20, 83
ULAS J120444.67−015034.9	.../T4.5	16.76 ± 0.02	0.84 ± 0.18	0.035	10	117	13	3.6	101	77	28	0.5 ± 0.1	76, 17; 17
SDSS J120602.51+281328.7	.../T3	16.15 ± 0.02	0.81 ± 0.13	0.044	4/5	131	15	2.8	75	54	26	0.9 ± 0.1	19; 19
SDSS J120747.17+024424.8	L8/T0	15.47 ± 0.02	0.84 ± 0.13	0.051	1/5	125	14	3.6	52	40	28	0.0 ± 0.2	39; 39, 12
2MASSI J1213033−043243	L5/L4.2	14.57 ± 0.02	0.80 ± 0.10	0.025	1/5	106	12	3.6	48	34	27	0.6 ± 0.2	20; 20, 4
SDSS J121951.45+312849.4	.../L8	15.96 ± 0.02	0.80 ± 0.10	0.050	2/5	108	12	3.6	49	34	10	2.2 ± 0.4	19; 19

Table 7.1—Continued

Object	SpT Optical/NIR	$J_{\rm MKO}$ (mag)	FWHM ($''$)	Δairmass	$t_{\rm int}$[a] (s)	$N_{\rm fr}$	$N_{\rm ep}$	Δt (yr)	$N_{\rm ref}$	$N_{\rm cal}$	$N_{\rm abs}$	$\pi_{\rm abs} - \pi_{\rm rel}$ (mas)	References (Disc; SpT)
2MASS J12212770+0257198	L0/M9.7 FLD-G	13.07 ± 0.02	0.76 ± 0.13	0.056	1/5	115	15	2.8	71	48	31	0.7 ± 0.2	71; 71, 33
WISE J122558.86−101345.0	.../T6	16.10 ± 0.02	0.88 ± 0.13	0.026	4/5	106	12	3.6	115	90	47	1.3 ± 0.1	58; 58
2MASS J12312141+4959234	L2/L3.4	14.51 ± 0.02	0.87 ± 0.17	0.027	1/5	111	14	2.3	36	20	4	3.6 ± 1.2	21; 21, 4
2MASS J12314753+0847331	T6/T5.5	15.16 ± 0.02	0.80 ± 0.16	0.055	1/5	107	12	2.9	60	41	24	0.4 ± 0.2	11; 67, 12
2MASS J12321827−0951502	L0/M9.5	13.70 ± 0.02	0.85 ± 0.09	0.048	1/5	108	12	3.6	82	57	33	1.2 ± 0.3	71; 71, 4
NLTT 31450B	.../L6	15.97 ± 0.02	0.78 ± 0.10	NaN	2/5	123	14	3.0	55	38	20	0.8 ± 0.2	27; 27
2MASSW J1246467+402715	L4/L4.0	14.89 ± 0.02	0.72 ± 0.07	0.021	1/5	95	12	2.8	38	24	12	1.5 ± 0.4	43; 43, 4
SDSS J125011.65+392553.9	.../T4	16.15 ± 0.02	0.80 ± 0.12	0.095	4/5	108	11	3.6	71	60	18	2.0 ± 0.1	19; 19
WISE J125015.56+262846.9	.../T6	16.40 ± 0.02	0.78 ± 0.11	0.072	6	117	13	3.6	72	56	30	1.4 ± 0.2	58; 6
WISE J125448.52−072828.4	.../T7	17.26 ± 0.02	0.84 ± 0.13	0.044	20	87	11	2.8	170	133	34	0.9 ± 0.1	80; 80
2MASS J12565688+0146163	L2:/L1.6	14.41 ± 0.02	1.01 ± 0.30	0.065	1/5	71	12	2.8	41	25	18	1.3 ± 0.6	71; 71, 4
WISE J125715.90+400854.2	.../T7	16.88 ± 0.02	0.76 ± 0.08	0.023	20	117	13	3.6	113	94	24	1.6 ± 0.1	58; 58
2MASSW J1300425+191235	L1/L3	12.61 ± 0.02	0.81 ± 0.16	0.094	1/5	93	14	2.8	53	36	21	0.9 ± 0.4	35; 35, 14
ULAS J131610.13+031205.5	.../T3:	16.80 ± 0.02	0.77 ± 0.11	0.026	10	98	11	2.7	120	94	21	0.5 ± 0.1	60; 60
PSO J201.0320+19.1072	.../T3.5	15.60 ± 0.02	1.07 ± 0.22	0.145	1/5	106	13	3.6	39	28	18	-0.2 ± 0.2	24; 24
2MASSW J1326201−272937	L5/L6.6:	15.76 ± 0.03	0.92 ± 0.11	0.016	2/5	80	9	2.1	174	147	70	-1.7 ± 0.3	36; 36, 4
SDSSp J132629.82−003831.5	L8:/L7	16.24 ± 0.02	0.85 ± 0.12	0.071	2/5	77	10	1.9	97	65	24	1.2 ± 0.3	31; 31, 60
PSO J202.1635−03.7660	.../T4.5	16.91 ± 0.02	0.83 ± 0.11	0.071	15	98	11	2.8	166	133	46	0.6 ± 0.1	6; 6
2MASS J13373116+4938367	L0/M8.9	13.72 ± 0.02	0.91 ± 0.20	0.026	1/5	97	11	2.3	38	22	10	2.3 ± 0.7	21; 21, 4
WISE J133750.46+263648.6	.../T5	16.59 ± 0.02	0.86 ± 0.21	0.071	4	147	11	2.8	59	43	6	0.7 ± 0.3	58; 58
2MASSW J1338261+414034	L2.5/L2.4	14.12 ± 0.02	0.78 ± 0.09	0.104	1/5	77	11	2.8	29	20	10	0.5 ± 0.5	43; 43, 4

Table 7.1—Continued

Object	SpT Optical/NIR	$J_{\rm MKO}$ (mag)	FWHM ($''$)	Δairmass	$t_{\rm int}$[a] (s)	$N_{\rm fr}$	$N_{\rm ep}$	Δt (yr)	$N_{\rm ref}$	$N_{\rm cal}$	$N_{\rm abs}$	$\pi_{\rm abs} - \pi_{\rm rel}$ (mas)	References (Disc; SpT)
2MASS J13384944+0437315	L1/L0.0	14.10 ± 0.02	0.84 ± 0.18	0.083	1/5	121	13	3.6	54	40	21	1.8 ± 0.3	71; 71, 4
2MASSW J1343167+394508	L5/L5	15.95 ± 0.02	0.88 ± 0.24	0.097	2/5	97	11	1.7	53	28	12	-0.7 ± 0.5	43; 43, 40
LHS 2803B	.../T5.5	16.25 ± 0.02	0.87 ± 0.12	0.057	4/5	81	9	2.9	103	80	41	-0.8 ± 0.2	26; 26
PSO J207.7496+29.4240	.../T0:pec	17.16 ± 0.02	0.87 ± 0.20	0.086	30	74	12	3.6	136	119	11	0.5 ± 0.1	6; 6
SDSS J135852.68+374711.9	.../T4.5:	16.24 ± 0.02	0.79 ± 0.15	0.093	4/5	95	11	2.8	79	54	17	1.1 ± 0.3	19; 19
SDSS J140023.12+433822.3	.../L7:	16.21 ± 0.02	0.81 ± 0.12	0.060	4/5	99	11	2.8	73	53	17	1.7 ± 0.3	19; 19
2MASSW J1411175+393636	L1.5/L1.5	14.55 ± 0.02	0.76 ± 0.10	0.036	1/5	80	10	2.0	58	38	21	0.7 ± 0.1	43; 43, 4
2MASSW J1412244+163312	L0.5/...	13.83 ± 0.02	0.79 ± 0.06	0.021	1/5	89	10	1.9	45	29	15	1.8 ± 0.3	43; 43
SDSS J141530.05+572428.7	.../T3:	16.55 ± 0.02	0.93 ± 0.13	0.092	6	81	12	2.8	77	66	17	0.9 ± 0.3	19; 19
2MASSW J1421314+182740	L0/M8.9	12.86 ± 0.05	0.95 ± 0.10	0.045	1/5	86	13	2.9	27	18	8	-1.9 ± 0.9	35; 71, 4
2MASS J14283132+5923354	L4/L4.4	14.71 ± 0.02	0.82 ± 0.09	0.108	1/5	106	13	2.9	54	38	18	1.8 ± 0.3	71; 71, 4
VHS J143311.46−083736.3	.../T8	19.05 ± 0.02	1.17 ± 0.20	0.036	60	448	10	2.9	525	472	71	0.4 ± 0.1	54; 54
SDSS J143553.25+112948.6	.../T2:	17.09 ± 0.02	0.87 ± 0.16	0.144	15	89	10	2.0	111	87	39	3.1 ± 0.2	19; 19
WISEPA J143602.19−181421.8	.../T8pec	17.32 ± 0.07	1.14 ± 0.41	0.104	30	108	11	3.0	362	325	74	0.6 ± 0.1	46; 46
WISE J144806.48−253420.3	.../T8	18.94 ± 0.02	1.44 ± 0.45	0.029	60	481	12	2.1	907	841	138	0.1 ± 0.1	80; 80
2MASSW J1448256+103159	L4:/L4.7 FLD-G	14.44 ± 0.02	0.84 ± 0.14	0.090	1/5	133	14	2.9	69	44	25	-0.9 ± 0.2	83; 71, 30
HIP 73169B	.../L2.5	15.93 ± 0.02	0.84 ± 0.10	0.049	2/5	90	10	2.0	116	92	48	-0.5 ± 0.2	27; 27
WISEPC J145715.03+581510.2	T8/T7	16.82 ± 0.02	1.19 ± 0.47	0.073	4	161	9	2.9	69	56	23	0.8 ± 0.3	46; 46, 46
PSO J224.3820+47.4057	.../T7	17.10 ± 0.02	0.88 ± 0.20	0.040	20	91	11	2.9	178	145	43	1.4 ± 0.1	6; 6
HIP 73786B	.../T6:pec	16.59 ± 0.02	0.98 ± 0.25	0.130	4	212	12	2.0	108	79	34	0.8 ± 0.1	75, 64; 64
PSO J226.2599−28.8959	.../T1.5	15.79 ± 0.02	1.04 ± 0.25	0.018	1/5	99	10	3.0	262	218	137	0.2 ± 0.2	24; 24

Table 7.1—Continued

Object	SpT Optical/NIR	$J_{\rm MKO}$ (mag)	FWHM ($''$)	Δairmass	$t_{\rm int}$[a] (s)	$N_{\rm fr}$	$N_{\rm ep}$	Δt (yr)	$N_{\rm ref}$	$N_{\rm cal}$	$N_{\rm abs}$	$\pi_{\rm abs} - \pi_{\rm rel}$ (mas)	References (Disc; SpT)
2MASSW J1506544+132106	L3/L4	13.21 ± 0.02	0.82 ± 0.15	0.122	1/5	135	14	2.8	76	56	33	1.2 ± 0.2	35; 35, 15
SDSS J151240.67+340350.1	L3/L0.7	14.96 ± 0.02	0.88 ± 0.38	0.028	1/5	111	13	2.9	48	37	15	-0.6 ± 0.3	72; 72, 4
2MASSW J1515008+484742	L6/L6	13.96 ± 0.02	0.74 ± 0.11	0.013	1/5	98	11	2.9	55	36	22	1.5 ± 0.3	83; 21, 83
SDSS J151506.11+443648.3	.../L7.5:	16.63 ± 0.02	1.04 ± 0.48	0.025	4	200	11	2.9	79	55	17	0.6 ± 0.1	19; 19
SDSS J151643.01+305344.4	.../T0.5:	16.84 ± 0.03	0.89 ± 0.14	0.111	10	134	15	2.9	127	98	46	0.8 ± 0.1	19; 19
WISE J151721.13+052929.3	.../T8	18.53 ± 0.02	1.04 ± 0.34	0.067	60	502	12	2.0	383	338	71	1.6 ± 0.1	58; 58
SDSS J152039.82+354619.8	.../T0:	15.46 ± 0.02	0.81 ± 0.16	0.066	1/5	107	11	2.0	46	28	21	0.1 ± 0.2	19; 19
SDSS J152103.24+013142.7	.../T3	16.10 ± 0.02	0.96 ± 0.31	0.068	4/5	99	11	2.9	96	80	55	1.0 ± 0.1	48; 60
2MASS J15230657−2347526	.../L2.5	14.07 ± 0.02	0.85 ± 0.11	0.041	1/5	72	9	3.0	323	266	155	0.8 ± 0.2	42; 42
2MASSI J1526140+204341	L7/L5.5	15.42 ± 0.02	0.85 ± 0.28	0.066	1/5	104	12	2.9	50	29	16	1.6 ± 0.5	43; 43, 15
SDSS J153453.33+121949.2	.../L4:	15.28 ± 0.02	0.83 ± 0.14	0.043	1/5	98	12	2.9	84	61	44	0.5 ± 0.2	19; 19
SDSS J154009.36+374230.3	.../L9:	16.35 ± 0.02	1.01 ± 0.23	0.113	6	98	11	2.9	85	57	31	1.2 ± 0.2	19; 19
VHS J154352.78−043909.6	.../T5:	16.45 ± 0.02	0.95 ± 0.30	0.033	6	113	12	2.9	255	213	90	-0.3 ± 0.1	54; 58
WISE J154459.27+584204.5	.../T7.5	18.11 ± 0.02	1.04 ± 0.35	0.109	30	652	12	2.9	226	195	53	0.9 ± 0.1	58; 58
2MASS J15461461+4932114	.../T2.5:	15.65 ± 0.02	0.82 ± 0.15	0.021	1/5	98	11	2.9	60	41	25	1.5 ± 0.4	63; 63
2MASS J15485834−1636018	.../L2:	13.82 ± 0.02	0.79 ± 0.09	0.041	1/5	72	9	3.0	342	270	148	0.8 ± 0.1	42; 42
2MASS J15500845+1455180	L2:/...	14.63 ± 0.02	1.50 ± 0.07	0.070	1/5	92	13	2.0	77	59	32	1.2 ± 0.1	21; 21
SDSS J155120.86+432930.3	L3/L3.1	14.91 ± 0.02	0.91 ± 0.14	0.075	1/5	90	10	2.9	53	44	28	0.4 ± 0.1	72; 72, 4
2MASSW J1615441+355900	L3/L3.6	14.43 ± 0.02	0.80 ± 0.13	0.138	1/5	108	13	2.9	102	72	53	0.9 ± 0.1	43; 43, 4
WISEPA J161705.75+180714.3	T8/T8	17.57 ± 0.02	0.91 ± 0.14	0.067	60	115	12	1.8	254	228	101	0.1 ± 0.1	46; 46, 46
SDSS J161928.31+005011.9	L2/L1.3	14.34 ± 0.02	0.81 ± 0.18	0.059	1/5	95	13	3.0	168	137	109	-0.1 ± 0.1	39; 39, 4

Table 7.1—Continued

Object	SpT Optical/NIR	$J_{\rm MKO}$ (mag)	FWHM ($''$)	Δairmass	$t_{\rm int}$[a] (s)	$N_{\rm fr}$	$N_{\rm ep}$	Δt (yr)	$N_{\rm ref}$	$N_{\rm cal}$	$N_{\rm abs}$	$\pi_{\rm abs} - \pi_{\rm rel}$ (mas)	References (Disc; SpT)
PSO J246.1033−19.6194	.../T2	16.36 ± 0.02	0.89 ± 0.09	0.076	6	99	11	3.0	419	394	82	1.9 ± 0.1	52; 52
WISEPA J162725.64+325525.5	.../T6	16.24 ± 0.02	0.88 ± 0.16	0.125	6	99	10	2.9	146	124	66	0.2 ± 0.2	46; 46
PSO J247.3273+03.5932	T3/T2	15.03 ± 0.02	0.88 ± 0.11	0.074	1/5	86	13	2.9	165	138	95	0.6 ± 0.1	24; 67, 24
SDSS J163022.92+081822.0	.../T5.5	16.16 ± 0.02	0.85 ± 0.16	0.079	4/5	99	11	1.9	229	189	118	0.4 ± 0.1	19; 19
SDSS J163030.53+434404.0	.../L7:	16.54 ± 0.02	0.96 ± 0.17	0.027	4	242	13	2.9	126	106	36	0.7 ± 0.1	48; 48
WISE J163236.47+032927.3	.../T5	16.42 ± 0.02	0.89 ± 0.20	0.072	6	107	12	3.0	299	269	161	-0.0 ± 0.1	58; 58
WISE J163645.56−074325.1	.../T4.5	16.43 ± 0.02	0.84 ± 0.18	0.016	6	90	10	1.9	423	387	198	0.8 ± 0.1	58; 58
2MASS J16452207+3004071	L3/L3.0	15.08 ± 0.02	0.93 ± 0.16	0.044	1/5	117	13	2.0	101	71	56	1.4 ± 0.1	21; 21, 4
WISEPA J164715.59+563208.2	L7/L9pec	16.50 ± 0.02	0.89 ± 0.13	0.153	10	117	11	2.2	193	155	66	1.0 ± 0.1	46; 67, 46
WISEPA J165311.05+444423.9	T8/T8	17.07 ± 0.02	0.81 ± 0.14	0.079	40	87	11	2.9	311	277	79	0.6 ± 0.1	46; 46, 46
2MASS J16573454+1054233	L2/L1.4	14.06 ± 0.02	0.88 ± 0.13	0.050	1/5	108	13	3.1	177	154	103	0.9 ± 0.1	71; 71, 4
WISE J165842.56+510335.0	.../L6pec	14.99 ± 0.02	0.83 ± 0.06	0.171	1/5	63	7	3.1	90	66	44	0.9 ± 0.3	80; 80
WISE J170745.85−174452.5	.../T5:	16.25 ± 0.02	0.90 ± 0.16	0.193	5	97	11	3.0	2019	1952	691	0.8 ± 0.1	58; 58
2MASS J17114559+4028578	.../L5.0	14.94 ± 0.02	0.78 ± 0.12	0.040	1/5	99	11	3.0	126	99	60	1.9 ± 0.1	69; 4
PSO J258.2413+06.7612	.../T0pec	16.04 ± 0.02	0.86 ± 0.14	0.076	4/5	106	11	3.0	475	431	252	0.4 ± 0.1	6; 6
WISE J172134.46+111739.4	.../T6	16.44 ± 0.02	0.92 ± 0.27	0.078	4/5	108	11	3.0	386	346	226	-0.0 ± 0.1	58; 58
PSO J260.9762+04.2354	.../T2.5	16.67 ± 0.02	0.88 ± 0.15	0.115	10	140	15	2.9	986	922	356	0.6 ± 0.1	52; 52
WISEPA J172844.93+571643.6	.../T6	17.42 ± 0.02	0.86 ± 0.12	0.131	40	114	13	3.1	350	305	108	0.9 ± 0.1	46; 46
WISE J173421.02+502349.9	.../T4	16.12 ± 0.02	0.90 ± 0.20	0.021	2/5	108	12	3.0	196	158	101	0.8 ± 0.1	58; 58
WISE J174113.12+132711.9	.../T5	16.91 ± 0.02	1.07 ± 0.30	0.138	4	287	15	2.9	596	558	238	0.8 ± 0.1	58; 58
WISE J174303.71+421150.0	.../T4.5	15.63 ± 0.02	0.96 ± 0.33	0.036	1/5	96	10	3.0	79	59	42	1.3 ± 0.2	58; 58

Table 7.1—Continued

Object	SpT Optical/NIR	$J_{\rm MKO}$ (mag)	FWHM ($''$)	Δairmass	$t_{\rm int}$[a] (s)	$N_{\rm fr}$	$N_{\rm ep}$	Δt (yr)	$N_{\rm ref}$	$N_{\rm cal}$	$N_{\rm abs}$	$\pi_{\rm abs} - \pi_{\rm rel}$ (mas)	References (Disc; SpT)
2MASS J17461199+5034036	L5/L5.7	14.96 ± 0.02	0.85 ± 0.19	0.027	1/5	87	12	3.0	135	108	78	1.4 ± 0.1	71; 71, 4
WISE J174640.78−033818.0	.../T6	17.10 ± 0.02	0.89 ± 0.16	0.109	20	106	12	3.1	2523	2421	479	0.7 ± 0.1	58; 58
SDSS J175024.01+422237.8	.../T2	16.18 ± 0.02	0.93 ± 0.37	0.031	4/5	107	12	3.0	285	243	125	0.8 ± 0.1	48; 12
SDSSp J175032.96+175903.9	T4/T3.5	16.16 ± 0.02	0.93 ± 0.17	0.153	2/5	126	15	3.0	541	499	305	0.3 ± 0.1	34; 67, 12
2MASS J17545447+1649196	T5/T5.5	15.49 ± 0.02	0.92 ± 0.26	0.143	1/5	89	11	3.1	288	268	181	0.5 ± 0.1	29, 13; 67, 29
WISE J175510.28+180320.2	.../T2.5	15.78 ± 0.02	0.86 ± 0.14	0.157	2/5	117	12	2.9	507	477	243	0.5 ± 0.1	58; 6
2MASS J18000116−1559235	.../L4.3	13.29 ± 0.02	0.90 ± 0.14	0.116	1/5	108	10	2.3	252	249	51	0.0 ± 0.2	32, 4; 4
WISEP J180026.60+013453.1	L7.5/L7.5	14.16 ± 0.02	0.85 ± 0.12	0.149	1/5	117	13	2.9	762	725	444	0.1 ± 0.1	37; 38, 37
PSO J272.0887−04.9943	.../T1.5pec	16.98 ± 0.02	0.80 ± 0.15	0.081	15	98	11	2.1	3394	3303	139	0.9 ± 0.1	6; 6
WISE J180901.07+383805.4	.../T7.5	17.38 ± 0.02	0.83 ± 0.10	0.096	40	99	11	2.9	664	623	239	0.8 ± 0.1	56; 58
WISE J180952.53−044812.5	.../T1	15.10 ± 0.02	1.04 ± 0.16	0.072	1/5	89	15	3.3	380	370	72	0.7 ± 0.1	58; 5
WISE J181329.40+283533.3	.../T8	16.92 ± 0.02	0.87 ± 0.22	0.095	20	117	13	3.0	830	790	378	0.8 ± 0.0	58; 58
PSO J276.8234+22.4380	.../L9	16.56 ± 0.02	0.89 ± 0.25	0.083	6	87	10	2.0	751	697	433	0.5 ± 0.1	6; 6
WISE J185101.83+593508.6	.../L9	14.82 ± 0.02	0.81 ± 0.11	0.080	1/5	116	13	2.9	199	175	105	0.8 ± 0.1	80; 6
WISEPA J185215.78+353716.3	.../T7	16.33 ± 0.02	0.89 ± 0.22	0.044	5	121	15	2.8	866	816	473	1.2 ± 0.1	46; 46
2MASS J19010601+4718136	.../T5	15.53 ± 0.02	0.90 ± 0.21	0.051	1/5	127	16	2.8	358	326	233	0.8 ± 0.0	11; 12
WISEPA J190624.75+450808.2	.../T6	15.98 ± 0.02	0.89 ± 0.28	0.057	4/5	143	17	2.8	627	589	364	0.8 ± 0.1	46; 46
DENIS-P J1909081−193748	L1:/...	14.46 ± 0.02	0.82 ± 0.15	0.050	1/5	117	12	2.3	1149	1096	580	0.1 ± 0.1	66; 66
WISE J191915.54+304558.4	.../L9	15.52 ± 0.02	0.84 ± 0.13	0.079	1/5	117	15	2.8	1258	1186	793	0.8 ± 0.1	80; 6
WISE J192841.35+235604.9	.../T6	13.96 ± 0.02	0.90 ± 0.24	0.149	1/5	90	13	2.8	419	407	104	0.9 ± 0.1	58; 58
WISE J195500.42−254013.9	.../T8	17.64 ± 0.02	0.98 ± 0.22	0.047	60	93	13	3.0	1056	978	382	0.5 ± 0.1	58; 58

Table 7.1—Continued

Object	SpT Optical/NIR	$J_{\rm MKO}$ (mag)	FWHM ($''$)	Δairmass	$t_{\rm int}$[a] (s)	$N_{\rm fr}$	$N_{\rm ep}$	Δt (yr)	$N_{\rm ref}$	$N_{\rm cal}$	$N_{\rm abs}$	$\pi_{\rm abs} - \pi_{\rm rel}$ (mas)	References (Disc; SpT)
WISE J200050.19+362950.1	.../T8	15.42 ± 0.02	0.89 ± 0.11	0.106	1/5	81	13	3.0	631	613	331	0.3 ± 0.1	22; 22
2MASS J20025073−0521524	L5 β/L7	15.23 ± 0.02	0.83 ± 0.12	0.076	1/5	114	13	3.4	512	475	272	1.9 ± 0.1	21; 30, 59
WISE J200804.71−083428.5	.../T5.5	16.05 ± 0.02	0.94 ± 0.22	0.070	4/5	116	13	3.4	614	562	285	0.5 ± 0.1	58; 58
WISE J201404.13+042408.5	.../T6.5pec	17.99 ± 0.02	1.06 ± 0.29	0.058	30	1066	11	2.0	1989	1932	572	0.2 ± 0.0	58; 58
SDSS J202820.32+005226.5	L3/L2	14.18 ± 0.02	0.81 ± 0.14	0.039	1/5	171	18	3.2	430	401	280	0.3 ± 0.1	39; 39, 15
WISE J203042.79+074934.7	.../T1.5	14.03 ± 0.02	0.84 ± 0.20	0.057	1/5	116	17	3.0	445	416	293	1.1 ± 0.1	58; 58
UGPS J20480024+503821.9	.../T5	16.38 ± 0.02	0.94 ± 0.15	0.006	5	71	7	1.1	2362	1359	776	0.5 ± 0.1	79; 79
2MASSI J2107316−030733	L0/...	14.12 ± 0.02	0.79 ± 0.08	0.041	1/5	107	12	2.5	194	169	107	0.5 ± 0.1	20; 20
PSO J319.3102−29.6682	.../T0:	15.44 ± 0.02	0.89 ± 0.11	0.054	1/5	51	8	3.2	98	82	42	2.3 ± 0.3	6; 6
WISE J212321.92−261405.1	.../T5.5	17.07 ± 0.02	0.93 ± 0.20	0.014	20	96	11	3.4	241	197	59	0.9 ± 0.1	58; 58
SDSS J212413.89+010000.3	.../T5	15.84 ± 0.02	0.97 ± 0.33	0.066	2/5	134	14	3.5	233	209	122	1.0 ± 0.1	48; 12
2MASSW J2130446−084520	L1.5/M8.3	14.06 ± 0.02	0.83 ± 0.14	0.032	1/5	108	12	3.4	103	86	57	1.0 ± 0.1	44; 44, 4
PSO J323.1320+29.5308	.../T4.5	16.18 ± 0.02	0.85 ± 0.14	0.136	4/5	169	18	3.2	638	595	365	0.5 ± 0.1	52; 52
2MASS J21324898−1452544	.../T4	15.54 ± 0.02	0.89 ± 0.16	0.029	1/5	70	10	3.4	152	108	62	1.0 ± 0.2	59; 59
2MASS J21373742+0808463	L5:/L5	14.64 ± 0.02	0.83 ± 0.15	0.081	1/5	114	15	3.1	140	115	71	0.9 ± 0.2	71; 71, 15
WISE J214706.78−102924.0	.../T7.5	17.37 ± 0.02	1.11 ± 0.43	0.025	40	107	12	3.4	296	241	79	-0.1 ± 0.1	58; 58
PSO J327.1504+22.6612	.../T1.5	16.64 ± 0.02	0.84 ± 0.08	0.126	10	107	12	3.4	388	339	154	0.9 ± 0.1	52; 52
2MASS J21522609+0937575	L6:/...	15.06 ± 0.02	0.92 ± 0.06	0.108	1/5	117	13	3.2	139	116	64	0.7 ± 0.2	70; 71
WISEPC J215751.38+265931.4	.../T7	17.05 ± 0.02	0.82 ± 0.18	0.103	20	133	15	3.4	662	596	242	0.7 ± 0.0	46; 46
2MASS J21580457−1550098	L4:/L5	14.84 ± 0.02	0.84 ± 0.12	0.040	1/5	87	10	3.4	81	65	28	1.3 ± 0.5	44; 44, 59
PSO J330.3214+32.3686	.../T2.5	16.19 ± 0.02	1.13 ± 0.41	0.097	4/5	116	14	3.2	435	397	253	0.6 ± 0.1	6; 6

Table 7.1—Continued

Object	SpT Optical/NIR	$J_{\rm MKO}$ (mag)	FWHM ($''$)	Δairmass	$t_{\rm int}$[a] (s)	$N_{\rm fr}$	$N_{\rm ep}$	Δt (yr)	$N_{\rm ref}$	$N_{\rm cal}$	$N_{\rm abs}$	$\pi_{\rm abs} - \pi_{\rm rel}$ (mas)	References (Disc; SpT)
2MASS J22092183−2711329	.../T2.5	15.54 ± 0.02	0.94 ± 0.23	0.020	1/5	88	12	3.4	128	89	37	0.5 ± 0.1	59; 59
WISEPC J220922.10−273439.5	.../T7	16.60 ± 0.02	1.13 ± 0.29	0.019	4	263	15	3.4	131	107	57	0.6 ± 0.1	46; 46
WISEPC J221354.69+091139.4	.../T7	16.77 ± 0.02	1.01 ± 0.33	0.090	15	143	14	3.0	233	209	74	1.9 ± 0.1	46; 46
2MASS J22153705+2110554	.../T1pec	15.90 ± 0.02	0.89 ± 0.14	0.132	2/5	135	15	3.4	255	224	120	0.5 ± 0.1	40; 40
WISE J222219.93+302601.4	.../L9	16.59 ± 0.02	0.93 ± 0.25	0.138	6	117	12	3.4	328	290	173	0.4 ± 0.1	80; 80
WISEA J223343.53−133140.9	.../T2 (blue)	16.29 ± 0.02	0.94 ± 0.17	0.154	5	108	12	3.4	110	100	48	1.3 ± 0.1	73; 73
WISE J223617.59+510551.9	.../T5	14.43 ± 0.02	0.75 ± 0.09	0.273	1/5	99	11	3.4	1671	1482	827	0.4 ± 0.1	58; 5
WISEPC J223729.53−061434.2	.../T5	17.22 ± 0.02	0.90 ± 0.15	0.043	15	116	13	3.4	173	140	55	0.6 ± 0.1	46; 46
WISEPC J223937.55+161716.2	.../T3	15.97 ± 0.02	0.90 ± 0.28	0.050	2/5	113	14	3.4	146	119	68	1.3 ± 0.1	46; 46
PSO J341.4606−28.7798	.../T4	16.54 ± 0.04	1.13 ± 0.19	0.038	6	60	7	3.4	67	48	29	1.8 ± 0.3	52; 52
2MASS J22490917+3205489	L5/...	15.55 ± 0.02	0.89 ± 0.16	0.067	1/5	116	14	3.4	213	185	111	0.2 ± 0.1	21; 21
WISE J230133.32+021635.0	.../T6.5	16.38 ± 0.02	1.08 ± 0.32	0.061	6	131	14	3.4	87	66	32	1.1 ± 0.1	58; 58
WISEA J230329.45+315022.7	.../T2 (blue)	15.91 ± 0.02	0.92 ± 0.20	0.090	2/5	132	15	3.4	219	188	112	0.8 ± 0.1	73; 73
ULAS J230601.02+130225.0	.../T6.5	17.59 ± 0.02	0.94 ± 0.31	0.166	60	143	17	3.2	245	208	36	0.4 ± 0.1	16; 16
PSO J346.5281−15.9406	.../L7	16.56 ± 0.02	0.99 ± 0.22	0.031	4	215	12	2.4	113	91	45	1.0 ± 0.1	6; 6
SSSPM J2310−1759	L0:/L1:	14.29 ± 0.02	0.85 ± 0.14	0.036	1/5	97	13	3.3	93	58	36	0.7 ± 0.2	53; 21, 59
2MASS J23185497−1301106	.../T5	15.30 ± 0.02	0.94 ± 0.40	0.104	1/5	80	11	3.2	43	34	23	1.1 ± 0.3	59; 59
WISEPC J231939.13−184404.3	.../T7.5	17.55 ± 0.02	0.88 ± 0.12	0.107	30	125	13	3.3	194	169	36	0.8 ± 0.1	46; 46
CFBDS J232304.41−015232.3	.../T6	17.25 ± 0.02	0.86 ± 0.14	0.025	30	117	14	2.4	166	135	32	1.3 ± 0.1	1; 1
2MASS J23254530+4251488	L8/L7.5:	15.42 ± 0.02	0.86 ± 0.21	0.112	1/5	132	15	3.1	301	272	142	1.1 ± 0.1	21; 21, 15
WISEPC J232728.75−273056.5	.../L9	16.50 ± 0.02	1.14 ± 0.15	0.006	4	126	7	3.3	73	52	21	1.0 ± 0.3	46; 46

Table 7.1—Continued

Object	SpT Optical/NIR	$J_{\rm MKO}$ (mag)	FWHM ($''$)	Δairmass	$t_{\rm int}$[a] (s)	$N_{\rm fr}$	$N_{\rm ep}$	Δt (yr)	$N_{\rm ref}$	$N_{\rm cal}$	$N_{\rm abs}$	$\pi_{\rm abs} - \pi_{\rm rel}$ (mas)	References (Disc; SpT)
PSO J353.6355+13.2209	.../L8:	16.59 ± 0.02	0.92 ± 0.26	0.107	4	179	10	2.1	125	97	55	0.8 ± 0.1	6; 6
WISE J233543.79+422255.2	.../T7	17.41 ± 0.02	0.83 ± 0.13	0.026	60	74	10	2.9	851	792	185	0.8 ± 0.1	58; 58
PSO J354.3709+57.7939	.../T2.5	16.40 ± 0.02	1.00 ± 0.24	0.074	6	90	10	3.1	1374	1323	495	0.8 ± 0.1	52; 52
2MASSI J2339101+135230	.../T5	15.82 ± 0.02	0.82 ± 0.15	0.122	2/5	113	14	3.4	113	86	44	2.4 ± 0.2	8; 12
2MASS J23392527+3507165	L3.5/L3.0 FLD-G	15.25 ± 0.02	0.96 ± 0.41	0.032	1/5	120	13	3.4	272	230	114	0.6 ± 0.1	71; 71, 33
ULAS J234228.97+085620.1	.../T6.5	16.41 ± 0.02	0.95 ± 0.28	0.100	6	83	12	3.5	99	82	40	1.6 ± 0.1	75; 58
2MASS J23440624−0733282	L4.5/L6.0	14.74 ± 0.02	0.81 ± 0.10	0.041	1/5	77	11	2.9	40	24	13	-1.2 ± 0.3	44; 44, 4
WISEPC J234841.10−102844.4	.../T7	16.63 ± 0.02	0.88 ± 0.19	0.034	10	102	12	2.9	129	104	22	0.4 ± 0.1	46; 46
PM I23492+3458B	.../L9	16.37 ± 0.02	0.91 ± 0.29	0.132	6	134	15	3.1	246	217	103	0.2 ± 0.1	27; 27
PSO J357.8314+49.6330	.../T0 (blue)	16.44 ± 0.02	0.95 ± 0.23	NaN	6	97	11	2.3	687	638	302	0.6 ± 0.1	6; 6
DENIS J2354599−185221	L2/L2.6:	14.10 ± 0.02	0.86 ± 0.13	0.132	1/5	108	12	3.1	93	62	33	0.5 ± 0.2	62; 62, 4
WISE J235716.49+122741.8	.../T6	16.14 ± 0.02	0.92 ± 0.36	0.170	4/5	113	14	3.4	111	93	48	1.0 ± 0.2	58; 58

Note. — Optical/NIR SpT: for binaries, we list the integrated-light spectral type. Most spectral types have an uncertainty of $\pm$0.5 subtypes; types uncertain by $\pm$1 and $\pm$2 subtypes are denoted by ":" and "::", respectively. $J_{\rm MKO}$: mean photometry measured by our pipeline (Section 7.4.3). FWHM: mean and RMS of the FWHM measured for the parallax target. Δairmass: maximum difference in airmass across all epochs. $N_{\rm fr}$: total number of frames obtained (usually 9 per epoch). $N_{\rm ep}$: number of epochs (i.e., nights) observed. $N_{\rm ref}$: number of stars used for the astrometric reference frame. $N_{\rm cal}$: subset of reference stars used in the absolute astrometric calibration. $N_{\rm abs}$: subset of reference stars used to correct the final parallaxes and proper motions from relative to absolute (Section 7.5.5). $\pi_{\rm abs} - \pi_{\rm rel}$: offset from relative to absolute parallax computed for each field.

[a]Integration times listed as $x/5$ indicate that observations prior to 2016-Feb-01 used x second integrations, while subsequent observations used 5 second integrations.

[b]For its first epoch, WISEPA J050003.05−122343.2 was erroneously observed with $t_{\rm int} = 15$ s and 9 dithers.

References. — (1) Albert et al. (2011), (2) Allers & Liu (2013a), (3) Artigau et al. (2006), (4) Bardalez Gagliuffi et al. (2014), (5) Best et al. (2013), (6) Best et al. (2015), (7) Bihain et al. (2013), (8) Burgasser et al. (2002), (9) Burgasser et al. (2003a), (10) Burgasser et al. (2003d), (11) Burgasser et al. (2004), (12) Burgasser et al. (2006a), (13) Burgasser et al. (2008a), (14) Burgasser et al. (2008b), (15) Burgasser et al. (2010a), (16) Burningham et al. (2010a), (17) Burningham et al. (2013), (18) Castro et al. (2013), (19) Chiu et al. (2006), (20) Cruz et al. (2003), (21) Cruz et al. (2007), (22) Cushing et al. (2014), (23) Deacon et al. (2005), (24) Deacon et al. (2011), (25) Deacon et al. (2012a), (26) Deacon et al. (2012b), (27) Deacon et al. (2014), (28) Deacon et al. (2017b), (29) Faherty et al. (2012), (30) Faherty et al. (2016), (31) Fan et al. (2000), (32) Folkes et al. (2012), (33) Gagné et al. (2015c), (34) Geballe et al. (2002), (35) Gizis et al. (2000b), (36) Gizis (2002), (37) Gizis et al. (2011a), (38) Gizis et al. (2015b), (39) Hawley et al. (2002), (40) Kellogg et al. (2015), (41) Kendall et al. (2004), (42) Kendall et al. (2007a), (43) Kirkpatrick et al. (2000), (44) Kirkpatrick et al. (2008), (45) Kirkpatrick et al. (2010), (46) Kirkpatrick et al. (2011), (47) Kirkpatrick et al. (2014), (48) Knapp et al. (2004), (49) Leggett et al. (2000), (50) Liebert et al. (2003), (51) Liu et al. (2016), (52) Liu et al. (in prep), (53) Lodieu et al. (2002), (54) Lodieu et al. (2012c), (55) Looper et al. (2007), (56) Luhman et al. (2012), (57) Luhman & Sheppard (2014), (58) Mace et al. (2013a), (59) Marocco et al. (2013), (60) Marocco et al. (2015), (61) Martín et al. (1999b), (62) Martín et al. (2010), (63) Metchev et al. (2008), (64) Murray et al. (2011), (65) Muzic et al. (2012), (66) Phan-Bao et al. (2008), (67) Pineda et al. (2016), (68) Pinfield et al. (2008), (69) Radigan et al. (2008), (70) Reid et al. (2006a), (71) Reid et al. (2008b), (72) Schmidt et al. (2010), (73) Schneider et al. (2016a), (74) Schneider et al. (2016b), (75) Scholz (2010a), (76) Scholz et al. (2012), (77) Scholz et al. (2014), (78) Sheppard & Cushing (2009), (79) Smith et al. (2014b), (80) Thompson et al. (2013), (81) Tinney et al. (2005), (82) Wilson et al. (2001), (83) Wilson et al. (2003).

7.3.2 Observing Strategy

Parallaxes require multiple epochs of observations, ideally spread over many months to maximally sample the parallax ellipse of an object. Our initial plan was to observe each target 10 times over two years but not more than five times within any UKIRT observing semester (Feb-Jul or Aug-Nov), to ensure broad coverage of parallax ellipses while extending the time baselines long enough to robustly distinguish parallactic motions from proper motions. The actual completion rate per semester for our program was typically ≈70% because of queue competition, instrument changes, and stretches of poor weather. We therefore needed to extend our observations beyond two years.

We conducted all observations in J-band where most L and T dwarfs are brightest relative to the sky background, and copious (bluer) background stars are available to establish the local astrometric reference frame. Stars and brown dwarfs have different J-band spectra, so images of these objects in the same target field taken at different airmasses will suffer from a different amount of differential chromatic refraction (DCR). This systematic effect can be minimized by observing each target within a narrow range of airmass around transit. DL12 estimate that keeping all observations within an airmass range of 0.07 will limit the effect of DCR to $\lesssim$1 mas for T dwarfs, with an even smaller effect for L dwarfs. A 0.07 airmass range is equivalent to ±1 hour of the meridian for a target at $\delta = -30°$ observed from Maunakea, marking the lowest transit elevation (40°) for our target list. We therefore requested that all of our targets be observed within ±1 hour of transit. In practice, nearly all of our targets were observed at higher elevations and over smaller ranges of airmasses, reducing the impact of DCR to insignificance for our parallaxes (Section 7.5.3).

For most objects, at each epoch we obtained 9 frames using UKIRT's 3×3 large microstepping sequence. Microstepping uses dithers of precise non-integral pixel distances (in this case, exactly $11 + 1/3$ pixels), which can then be interleaved into single "leavstack" images with nominally higher angular resolution. (We ultimately chose to use the individual microstepped frames rather than the leavstacks for our analysis; Section 7.4.1). We selected

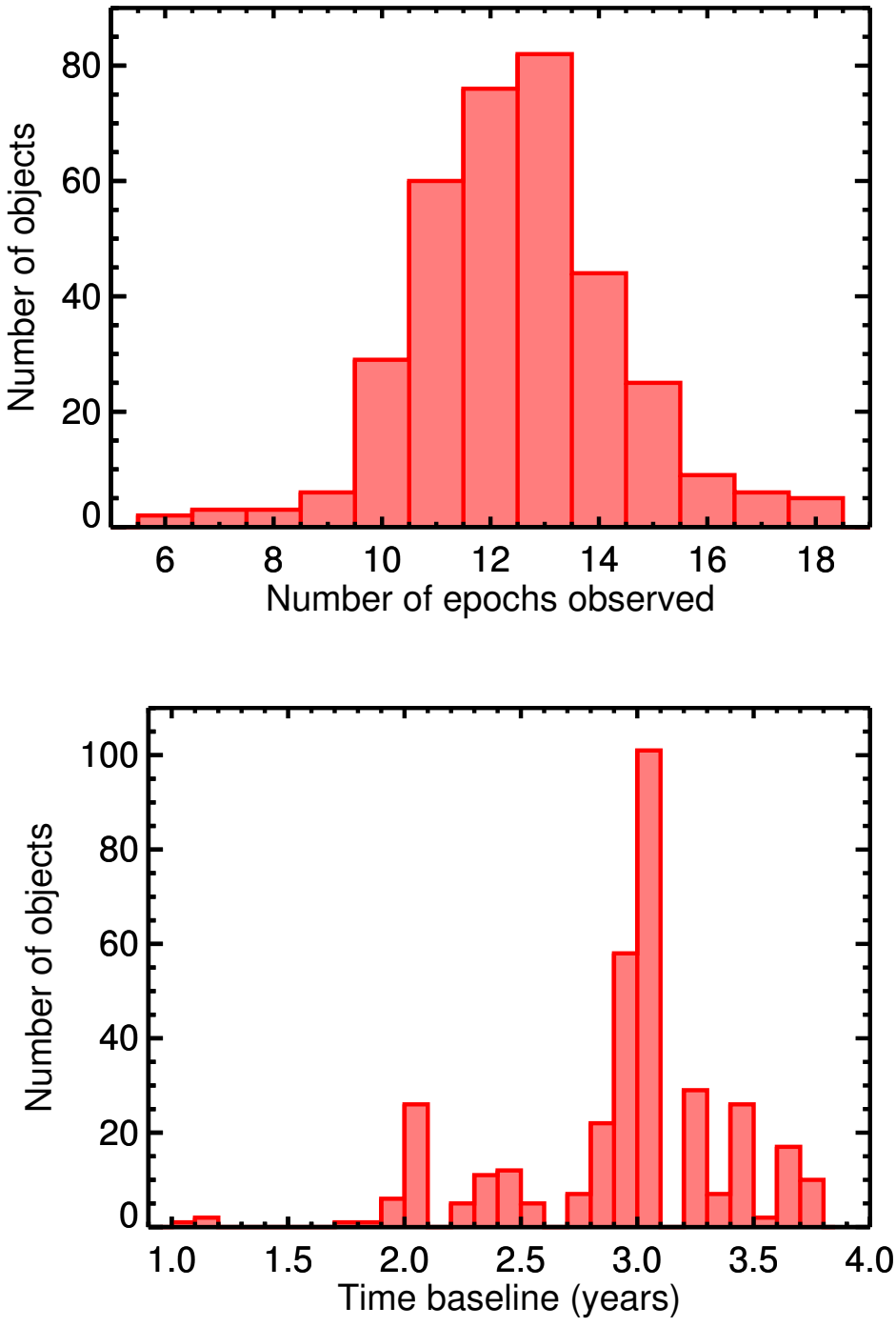

Figure 7.2 Distributions of the number of epochs (*top*) and time baseline (*bottom*) for observations of each target. 97% of targets have at least 8 observations spanning at least 1.7 years, enabling robust parallax measurements.

guide stars and autoguider set-ups that would place our targets on the same WFCAM pixels for every observation to minimize systematic errors. When possible, we placed the base position of the microstep pattern at the center of Camera 3. For 38% of our targets, we needed to use a different base position in order to have a sufficiently bright guide star. For 10 objects, we switched to a brighter guide star after difficulties observing with the first choice of guide star at the first epoch.

We chose integration times long enough to achieve our goal of parallax errors $\leq 10\%$ while sufficiently short to make observing our entire target list feasible. An object at the 25 pc boundary of our sample has a parallax of 40 mas, requiring parallaxes with errors ≤ 4 mas to achieve 10% or better precision. With 10 planned observations per target, we required astrometric uncertainties $\lesssim 12$ mas per epoch. Approximating astrometric precision as seeing divided by photometric S/N, and assuming 0.8" seeing (typical for UKIRT), we required a photometric S/N $\gtrsim \frac{0.8"}{12 \text{ mas}} = 67$ per epoch. We used the WFCAM Integration Time Calculator and J-band photometry for our targets from the literature ($J = 12.0 - 19.2$ mag) to determine the individual exposure times needed to obtain S/N = 40, expected to result in a total S/N = 120 for each epoch's 9-point microstepping sequence. The individual exposure times ranged from 1 to 300 sec, with the faint limit of our target list ($J = 19.2$ mag) determined by the S/N = 40 minimum for 300 sec exposures. In addition, we required that all observations be taken with seeing $\leq 1''$ and in clear or slightly cloudy skies (no more than 0.5 mag of extinction) to ensure that we would detect our targets and ample reference stars in all exposures. The median seeing for our observations was $0.85''$, as measured by the FWHM of our parallax targets (Figure 7.3). Most of our chosen integration times were standard for WFCAM, in the sense that we could use regularly updated facility dark frames with those integration times for calibration. For objects with non-standard integration times, we repeated the 3x3 microstepping sequence with shorter standard integrations to obtain the desired total integration times.

After the first year of observations, we assessed the astrometric precision of our images from and determined that we were reaching our target of $\lesssim$12 mas per epoch only for

exposure times $\gtrsim$4 sec. Therefore, in 2016 February, we raised the minimum integration time for all targets to 5 sec in order to obtain more background stars with sufficient S/N to use as astrometric references, and to better average the astrometric jitter caused by Earth's turbulent atmosphere.

7.4 Data Reduction

We reduced our data using a modified version of the astrometry pipeline developed for WIRCam on CFHT, explained in detail in DL12 and LDA16. Here we summarize the components of the pipeline and describe our modifications for UKIRT/WFCAM data.

7.4.1 CASU pipeline and leavstacks

All data were initially reduced by the WFCAM Cambridge Astronomical Survey Unit (CASU) pipeline (Irwin et al. 2004; Lawrence et al. 2007), which performs dark subtraction, flat fielding, and astrometric and photometric calibration. Our 9-point microstepped frames were then interleaved at CASU to produce leavstack images by reversing the dither offsets to align the frames and placing the images on an interwoven grid such that each 0.4" pixel was represented by a 0.133" pixel centered at the same position. We retrieved the CASU-reduced leavstack images and "flat files" (catalogs of detections) from the WFCAM Science Archive (Hambly et al. 2008). For objects with more than one 9-point sequence of frames at each epoch, the resulting leavstacks were not themselves stacked by the CASU pipeline, and we received more than one leavstack per epoch.

Visual inspection of the leavstack images revealed several problems. In many leavstacks, the point sources were significantly oversampled with large variations in pixel-to-pixel brightness (a known issue that can be addressed by drizzling-type procedures). Many point sources contained brighter pixels in every-third-pixel grids that were offset from the core of the PSF. We also noticed trails of bright pixels extending from point sources in some leavstacks, again in every-third-pixel grids. We learned that the CASU interleaving

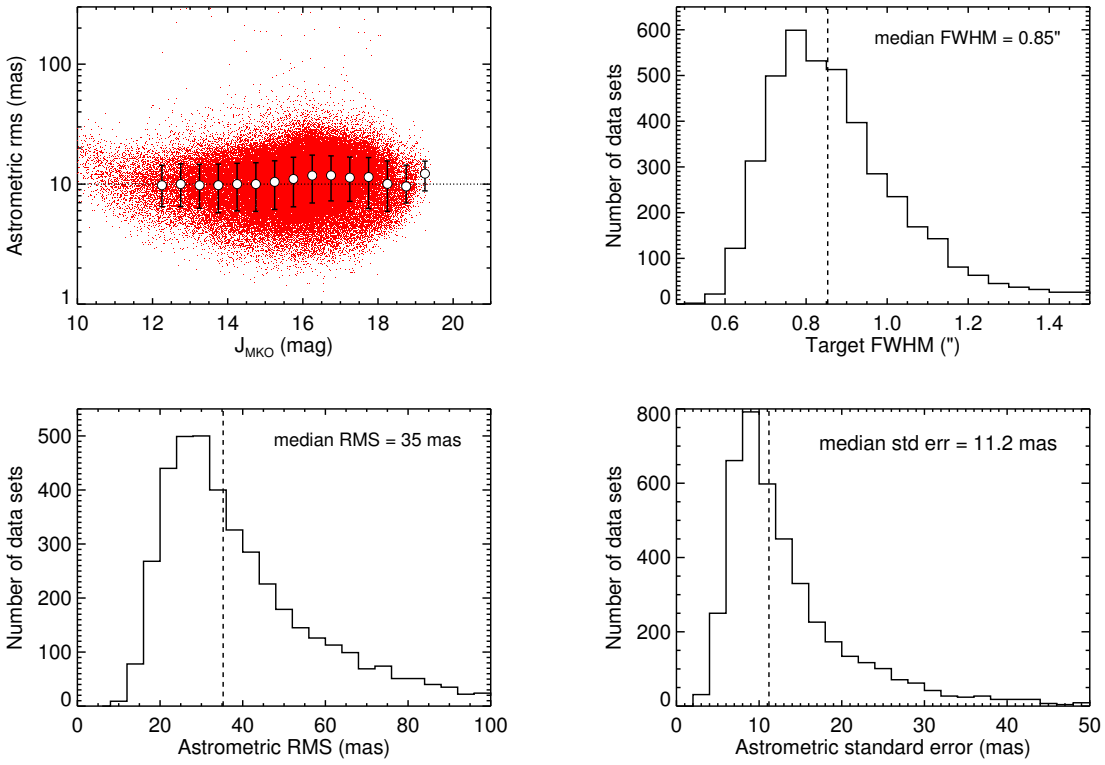

Figure 7.3 *Top left*: RMS of the astrometric measurements of all detections matched across individual frames at each epoch, plotted as a function of $J_{\rm MKO}$. White circles indicate the median and 68% confidence limits for the RMS in bins of 0.5 mag. The RMS increases slightly with $J_{\rm MKO}$ but overall is fairly flat as a function of target brightness, as expected given that we increase the exposure times for fainter targets. *Top right*: Distribution of the FWHM of our parallax targets at each epoch of observation. *Bottom*: Distributions of the per-epoch RMS (*left*) and standard error (*right*) for our parallax targets. The standard errors, which we adopt as our final astrometric uncertainties, are consistent with our goal of $\lesssim$12 mas astrometric precision per epoch.

process performs no alignment of individual objects or removal of outlier pixels, so the success of the interleaving depends entirely on the accuracy of the WFCAM guider and microstepper, which appeared to have been inaccurate for some of our observations. (CASU performs outlier removal on leavstacks taken at different points of larger dither patterns, but our observations did not include such dither sequences.) In addition, the astrometric measurement errors of sources reported in the flat files were implausibly small given the size and appearance of the PSFs in the images. We therefore decided to work directly with the original CASU-detrended images rather than the leavstacks and flat files.

We used the individual pixels from each leavstack to reconstruct its 9 microstepped frames. For observations producing $n > 1$ leavstacks at each epoch, we reconstructed $n \times 9$ individual frames per epoch. We modified the World Coordinate System (WCS) astrometry keywords from the leavstack and flat file FITS headers to compensate for the change in pixel scale from the leavstacks to the individual frames.

7.4.2 Astrometric Measurements

As described in DL12, we extracted (x, y) position measurements from each individual frame using SExtractor v2.19.5 (Bertin & Arnouts 1996), and began the process of associating detections across multiple frames at each epoch by first cross-matching the detections with an external reference catalog. We used PS1 as our reference catalog because its observations (2010 May – 2014 March) preceded ours by only a few years, it is deeper and/or more precise than any other all-sky catalog (2MASS, AllWISE, USNO, *Gaia*), and its astrometry is tied to the *Gaia* DR1 absolute reference frame (Lindegren et al. 2016).

Astrometric Projection

In order to cross-match with PS1, we needed (α, δ) coordinates for the detections in each frame. The WFCAM FITS headers provide initial astrometric solutions that convert the (x, y) positions into (α, δ) coordinates of each detected object. The solutions includes standard World Coordinate System (WCS) linear terms along with a single

cubic term for WFCAM's distortion, which is $\approx 10''$ at the outer edges of the cameras. As described in DL12, our pipeline uses the catalog matching software SCAMP v1.4.4 (Bertin 2006) to improve the astrometric solution for each image and thereby foster better matching of detections across dithers and epochs (Section 7.4.2). However, the astrometric projection used by the WFCAM image headers (zenithal polynomial projection, or ZPN) is incompatible with SCAMP as well as other stages of our pipeline. In addition, we found that the reference pixel in WFCAM header astrometry changed by as much as 75 pixels ($30''$) between some epochs for most targets, making it impossible to create a single astrometric solution uniting multiple observations of a target without modifying the reference pixel and other WCS keywords.

We resolved both of these problems by establishing a single reference pixel for all frames at $(1024, 1024)$, the center of WFCAM Camera 3, and calculating a new tangential (TAN) projection for each frame as the starting point for our astrometric solutions. We used the original ZPN astrometry to calculate the (α, δ) at $(1024, 1024)$, discarded the ZPN astrometric solution, and used SCAMP to calculate a TAN projection with additional higher-order terms by matching our detections to the 2MASS catalog.

Registration of Dithers

The SCAMP solutions gave us (α, δ) coordinates that were sufficiently accurate to cross-match >90% of our detections with PS1 using a $3''$ matching radius. We then calculated more precise astrometric solutions for each frame as described in DL12, associating detections lying within $1''$ of each other across multiple frames at a single epoch. We discarded objects detected in fewer than half of the frames.

We optimally registered the remaining cross-identified objects as in DL12. After obtaining an initial registration solution, we used the IDL routine `robust_sigma.pro` to clip positional measurements more than 3σ discrepant with the mean position in order to eliminate inaccurate measurements or artifacts incorrectly associated with detected objects. After robust clipping, we recalculated a final registration solution. We note that we did not

use the SExtractor-reported positional uncertainties for individual detections to weight the solution.

Distortion Solution for WFCAM

DL12 corrected their astrometry for distortion in CFHT/WIRCam using a third-order polynomial function in x and y applied to all frames. The polynomial was calculated by fitting multiple dithers of a dense star field to the SDSS DR7 catalog. We used the same approach to correct for distortion in WFCAM Camera 3. We calculated a polynomial solution by fitting one epoch of observations (9 dithers) of WISE J174640.78−033818.0 (≈2500 detections per frame) to the PS1 catalog. Figure 7.4 shows the residuals of our fits using first-, second-, and third-order polynomials, clearly indicating that third-order terms are needed to capture the distortion. We also fit fourth- and fifth-order polynomials but found no improvement in the residuals. We therefore adopted our third-order polynomial (presented in Table 7.2) as the distortion solution for WFCAM Camera 3, and we applied this correction to our cross-identified detections at each epoch prior to optimal registration (Section 7.4.2).

We also corrected for differential aberration and refraction caused by the Earth's atmosphere in the same manner as DL12 and DL17.

Astrometric Uncertainties

Cross-matching and registering the detections from each microstepped frame produced mean and RMS (α, δ) measurements for each detection. Figure 7.3 shows the distribution of the combined RMS (adding the RMS for α and δ in quadrature) for our parallax targets at each epoch (median 35 mas), along with the RMS positions of all detections as a function of $J_{\rm MKO}$ magnitude and the distribution of FWHM for our targets at each epoch. The astrometric precision of each per-epoch measurement should scale as $1/\sqrt{N_{\rm frames}}$ (i.e., standard errors on the mean), and we adopt these as our final uncertainties for each epoch. Figure 7.3 also shows the distribution of these standard errors, which are typically 7–12 mas (median

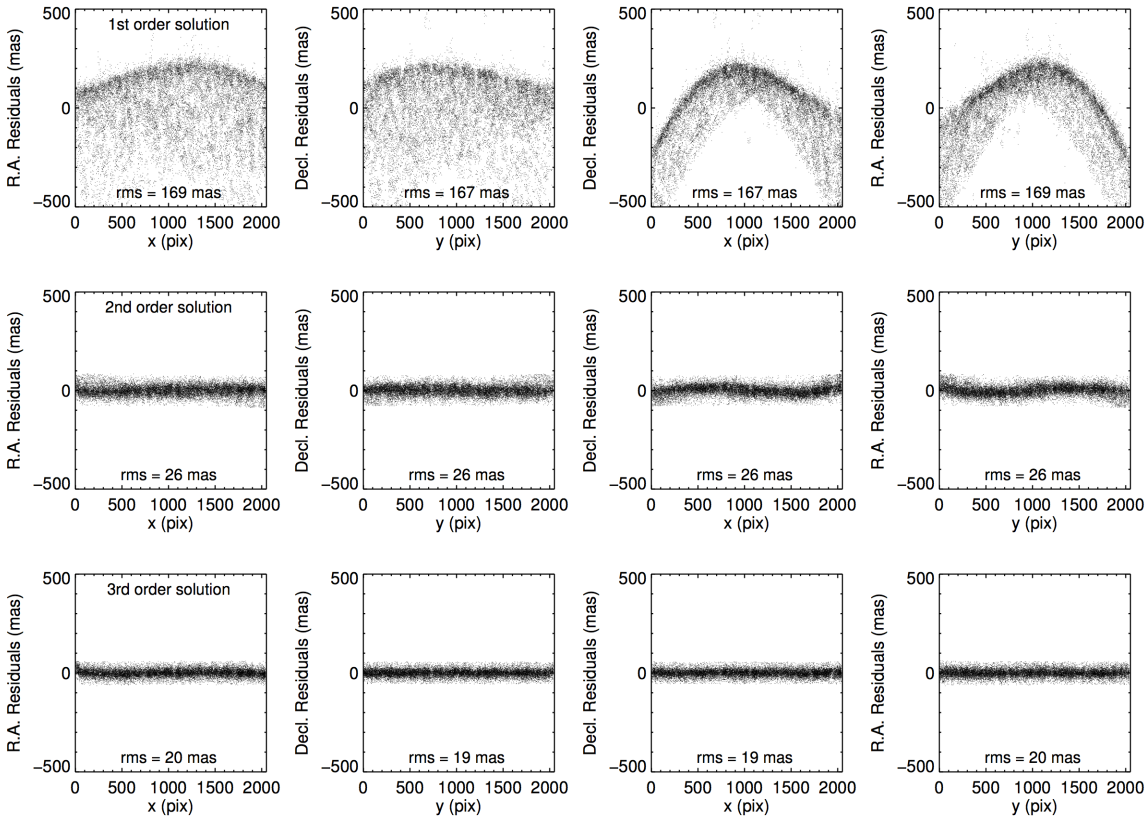

Figure 7.4 Residuals of measured star positions on WFCAM Camera 3 compared with the PS1 catalog after applying linear and higher order distortion corrections for WFCAM, as a function of x and y positions. These plots show residuals for ≈2100 stars in images targeting WISE J174640.78−033818.0 observed over 9 dithers with offsets of ≈9". Second- and third-order terms both reduce the RMS of the residuals. There is no obvious structure in the third-order residuals, and higher-order solutions do not lower the RMS, so our third-order solution is sufficient for WFCAM.

Table 7.2. Distortion Coefficients for WFCAM Northeast Array (Camera 3)

Term	a_{ij}	b_{ij}
x^2	1.486×10^{-7}	4.832×10^{-7}
xy	-2.643×10^{-7}	-2.766×10^{-7}
y^2	5.007×10^{-7}	1.321×10^{-7}
x^3	-6.436×10^{-14}	-6.496×10^{-11}
x^2y	5.640×10^{-11}	-6.172×10^{-11}
xy^2	6.094×10^{-11}	-4.511×10^{-11}
y^3	6.589×10^{-11}	-2.088×10^{-11}

Note. — To use this distortion correction, first define the origin as the central pixel (1024,1024):

$$x' = x - 1024 \qquad y' = y - 1024$$

where x and y are the pixel positions for a detection. Distortion-corrected positions may then be computed as:

$$\begin{aligned} x'' &= x' + a_{20}x'^2 + a_{11}x'y' + a_{02}y'^2 + a_{30}x'^3 + ... \\ y'' &= y' + b_{20}x'^2 + b_{11}x'y' + b_{02}y'^2 + b_{30}x'^3 + ... \end{aligned}$$

11.2 mas). These uncertainties are somewhat larger than those from other red-optical and infrared parallax programs discussed in DL12, but are consistent with our original goal of $\lesssim$12 mas astrometric precision per epoch and sufficient to obtain $\approx$3–4 mas parallax precision with $\approx$10 epochs of observation.

Combining Epochs and Absolute Astrometric Calibration

For each target, we combined our final positions for all detections across all epochs using the method described in DL12, clipping measurements with an R.A. or Decl. RMS greater than 80 mas. We used a $1''$ matching radius to associate objects across epochs, accounting for the proper motions of our targets using measurements from PS1 (Best et al. 2018) or other literature sources. We required objects to be detected in at least $N_{\rm ep} - 2$ epochs (where $N_{\rm ep}$ is the total number observed) to reject transient sources, artifacts, and those whose detectability varied with observing conditions (i.e., very faint objects). We then calibrated the astrometry of the combined positions to the absolute reference frame of PS1 as described in DL12.

7.4.3 Photometry

In addition to (x, y) positions, we also obtained J-band photometry for each detected source in our images from SExtractor via the `MAG_AUTO` and `MAGERR_AUTO` parameters, which we calibrated using the zeropoint magnitudes from the flat file FITS headers. As these zeropoints were measured on leavstack images, we modified them to compensate for the effective factor of 9 decrease in exposure time from the leavstacks to the deleaved frames. Our pipeline thus produced a $J_{\rm MKO}$ magnitude for each detection in each frame. For our parallax targets, we used the IDL routine `resistant_mean.pro` to find an outlier-resistant mean of all measurements retained at each epoch after clipping astrometric outliers. We then calculated the outlier-resistant mean and standard deviation across epochs. We added a systematic uncertainty of 0.015 mag (Hodgkin et al. 2009) (usually the dominant source of error) to the standard deviations of our measurements.

To assess the accuracy of our photometry, we identified the parallax targets with previously published J-band photometry from WFCAM (e.g., UKIDSS), and compared our new measurements to the published values. We found that our J magnitudes were offset from the literature WFCAM magnitudes by 0.059 ± 0.002 mag, so we subtracted this value from our measurements (adding the uncertainties in quadrature) to obtain our final J-band photometry.

7.5 Calculation of Parallaxes

7.5.1 Relative Parallax Solutions

Levenberg-Marquardt Least Squares

Initially, we calculated parallaxes, proper motions, and positions for our targets relative to our pipeline-generated astrometric reference frames using the approach described in DL12. Briefly, DL12 used the Levenberg-Marquardt least squares (LMLS) method, implemented using the IDL package `mpfit`, to fit five parameters to the mean coordinates from each epoch: parallax (π), proper motion ($\mu_\alpha \cos\delta$, μ_δ), and position at the first epoch of observation (α_0, δ_0). With this solution as a starting guess, DL12 then used Markov Chain Monte Carlo (MCMC) to determine the posterior distributions and their uncertainties (typically 1–4 mas for parallaxes). The MCMC trials produced Gaussian-like posteriors, which could be robustly described by means and standard deviations. No automated scheme was employed to mask outlier epochs that were biasing the fits. Rather, each solution was inspected by eye, and in some cases epochs with low S/N or significantly discrepant airmass were removed, with the goal of bringing the reduced chi-squared (χ^2_ν) of the solution closer to 1.

We found that the χ^2_ν of the LMLS best-fit solutions tended to be larger than 1 (Figure 7.5), and visually the astrometric errors on the individual epochs often appeared smaller than the scatter of the measurements about the fit, suggesting the errors were somewhat underestimated. We therefore explored additional methods for calculating astrometric solutions, in order to determine the most accurate parallaxes and proper motions

with uncertainties that fairly represented the precision of our data. First, we used bootstrap resampling to re-calculate parallaxes and proper motions from the individual epochs, using LMLS fitting as before, and determined median parameters and 68% confidence limits from the bootstrap posteriors. Bootstrapping typically yielded parameters consistent with those from the MCMC while increasing both the range and average size of the uncertainties. A handful of the bootstrap solutions yielded very large parallax errors ($\gtrsim$ 10 mas).

Iteratively-Reweighted Least Squares

We then solved for proper motion and parallax following an iteratively reweighted least squares (IRLS) procedure. IRLS has been shown to calculate astrometric solutions and uncertainties consistent with least-squares solutions for well-detected objects in PS1 while minimizing the impact of outlier measurements (E. Magnier et al., 2018, in prep). Briefly, using our LMLS solution as a starting point, IRLS re-weighted the position measurements and repeated the LMLS fit in an iterative fashion. We used Cauchy weights of the form

$$W = \frac{1}{1 + (\frac{X}{2.385})^2} \tag{7.1}$$

where X is the deviation of an α or δ measurement from its best-fit value, normalized by the measurement error, i.e.,

$$X = \frac{\alpha_{\rm meas} - \alpha_{fit}}{\sigma_\alpha} \quad \text{or} \quad X = \frac{\delta_{\rm meas} - \delta_{fit}}{\sigma_\delta}. \tag{7.2}$$

To re-weight, we multiplied our measurement errors by $\frac{1}{\sqrt{W}}$, which effectively multiplied the inverse variance weights used in the LMLS fitting by W. We iterated until all three parameters (π, μ_α, μ_δ) varied by less than a factor of 10^{-3}, capping the number of iterations at 300. In this implementation, IRLS essentially increased the measurement errors of more deviant epochs to bring those errors into concurrence with the scatter of residuals around the best fit.

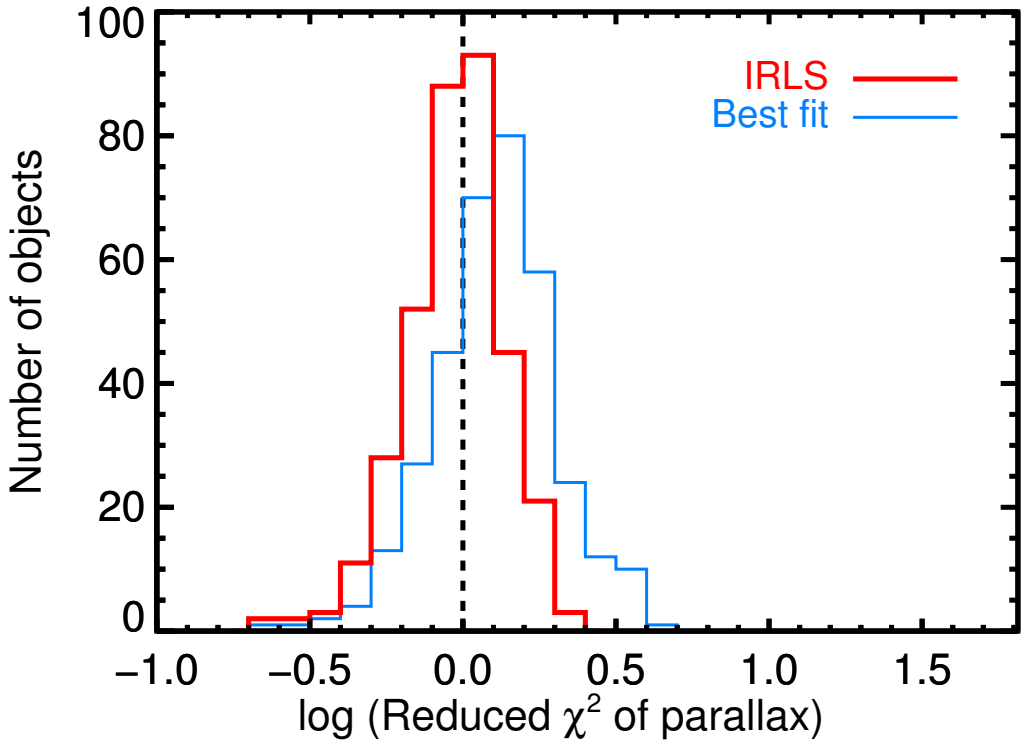

Figure 7.5 The distribution of χ^2_ν for our IRLS solutions (thick red histogram) compared with the same distribution for our LMLS solutions (thin blue histogram). The IRLS χ^2_ν peak strongly near 1 (median = 0.96), indicating that the IRLS-reweighted errors are commensurate with the scatter of measurements around the IRLS solutions. The χ^2_ν for the LMLS solutions peak higher than 1, implying that those uncertainties tend to be underestimated.

Figure 7.5 compares the distribution of χ^2_ν for our astrometric solutions from IRLS to the original LMLS solutions. The χ^2_ν distribution for our IRLS solutions peaks almost exactly at 1 (median = 0.96), indicating that the scatter of data about our parallax and proper motion fits is consistent with the re-weighted astrometric errors at individual epochs for Gaussian-distributed data. The χ^2_ν for the original LMLS solutions peak higher than 1, suggesting that their uncertainties tend to be somewhat underestimated.

After obtaining a final IRLS solution, we re-calculated parallaxes, proper motions, positions, and uncertainties from MCMC trials using the IRLS-determined parameters and re-weighted astrometry as the starting point for the MCMC chains. As another method,

Table 7.3. Comparison of UKIRT Parallaxes to *Gaia* DR2 Parallaxes

Method	*Gaia* σ_π[a]		*Gaia* excess noise[b]	
	χ^2	χ^2_ν	χ^2	χ^2_ν
LMLS	204.1	1.98	152.8	1.48
LMLS + MCMC	126.9	1.23	104.7	1.02
Bootstrap + LMLS	108.8	1.06	90.8	0.88
IRLS	161.0	1.56	126.0	1.22
IRLS + MCMC	109.8	1.07	91.2	0.89
Bootstrap + IRLS	129.4	1.26	105.4	1.02

Note. — For each of the six methods we used to calculate UKIRT parallaxes, this table shows the χ^2 and reduced χ^2 (χ^2_ν) for a 1:1 fit of our parallaxes to *Gaia* DR2's, using two different parameters for *Gaia* parallax uncertainties. There are 104 objects in each fit, resulting in 103 degrees of freedom.

[a]Using standard error of parallax (`e_Plx`) as the parallax uncertainty for *Gaia* DR2 parallaxes.

[b]Using `astrometric_excess_noise` as the parallax uncertainty for *Gaia* DR2 parallaxes.

we bootstrap-resampled the IRLS-reweighted measurements to obtain median parameters and confidence intervals.

In total, we obtained parallax and proper motions solutions for each target using six distinct methods, which are listed in Table 7.3.

Choosing the Final Solution

We compared our UKIRT parallax solutions from all six methods to *Gaia* DR2 parallaxes for the 104 targets in common. We calculated χ^2_ν for a 1:1 fit of our parallaxes to *Gaia*'s. Table 7.3 lists our methods and their χ^2_ν values for this fit. (For this comparison, we corrected our UKIRT parallaxes from relative to absolute astrometry as describe in Section 7.5.5). We note that nearly all of the *Gaia* DR2 parallaxes in this comparison have an `astrometric_excess_noise` parameter larger than the quoted parallax uncertainty, implying that the *Gaia* DR2 uncertainties may be significantly underestimated.

If we conservatively use the `astrometric_excess_noise` values as the *Gaia* parallax uncertainties, we find that several methods have $\chi^2_\nu \lesssim 1$ for the fit with our UKIRT parallaxes (Table 7.3). The two methods with the lowest χ^2_ν are bootstrapping of the original LMLS astrometry and IRLS + MCMC. The parallaxes calculated using these two procedures are very consistent, within 0.5σ for 98% of the targets and within 1.0σ in all cases. However, the uncertainties produced by the two procedures differ significantly (Figure 7.6). IRLS + MCMC typically obtains slightly larger parallax uncertainties than those from the initial IRLS solution (0–2 mas increase for 86% of our targets), while bootstrapping produces errors with a broader range of differences compared to the LMLS uncertainties ($-1-4$ mas increase for 85% of targets).

Considering also that the IRLS solutions have χ^2_ν closer to 1 (Section 7.5.1), we find a preference for IRLS + MCMC over the bootstrapping results. We therefore adopt the IRLS + MCMC parameters and uncertainties as our final solutions. Figure 7.7 shows our data along with the best-fit α and δ parallax curves and residuals for each of our targets. We compare our solutions to *Gaia* DR2 in more detail in Section 7.6.4.

7.5.2 Excluded Epochs

While analyzing the six procedures for obtaining astrometric solutions described in Section 7.5.1, we noted a handful of targets whose parallax confidence limits from bootstrapping were significantly larger than the uncertainties from other procedures, an indication that one or two data points may be significantly biasing those parallax fits. Many of these targets also had an LMLS parallax that differed significantly from a *Gaia* DR2 or literature measurement, and/or parallaxes that varied significantly across the six procedures we tested.

We therefore inspected the per-epoch astrometry and parallax solutions for all targets having (1) $\chi^2_\nu > 2$ from the IRLS fit or (2) one or both confidence limits from IRLS + bootstrapping more than 4 mas greater than the parallax uncertainty from IRLS + MCMC. Five of these targets had 8 or fewer epochs of observations spanning $\leq$2 years, suggesting

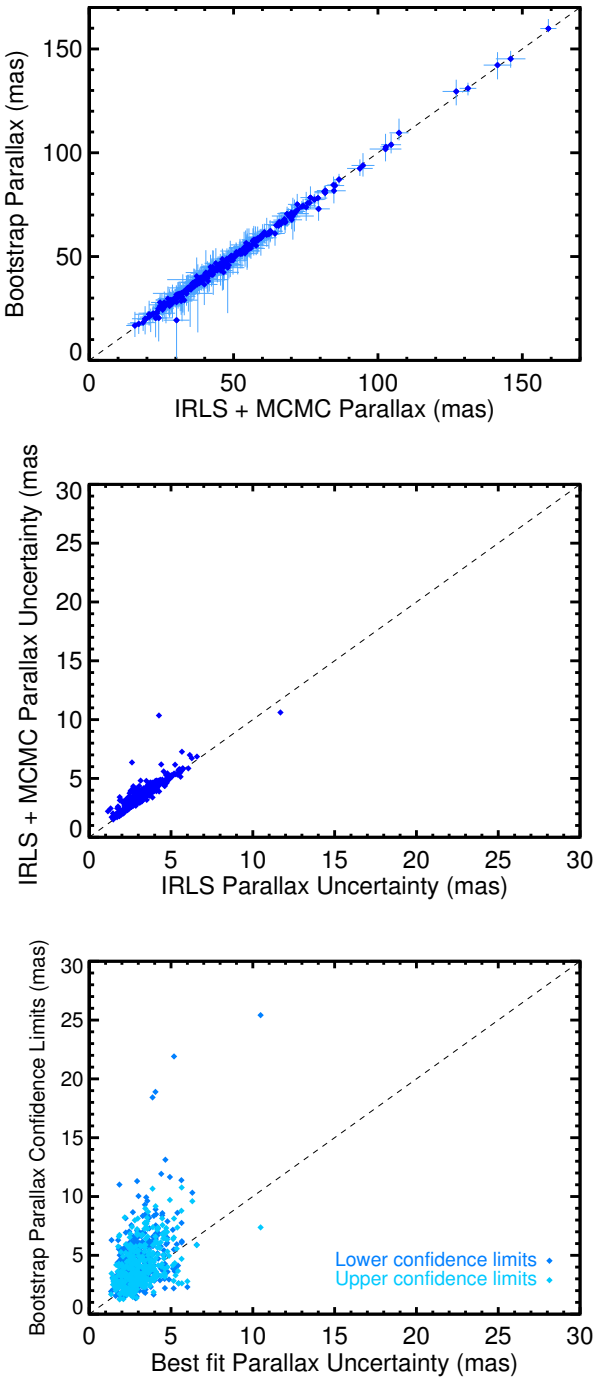

Figure 7.6 *Top*: Comparison of parallaxes from two of our procedures: bootstrapping + LMLS and IRLS + MCMC. The dashed line marks the 1:1 correspondence. The parallaxes from the two methods are all consistent within the uncertainties. However, while the MCMC usually produces slightly larger uncertainties than the IRLS solutions (*middle*), bootstrapping generates a wide range of uncertainties that are often large increases over the LMLS uncertainties(*bottom*).

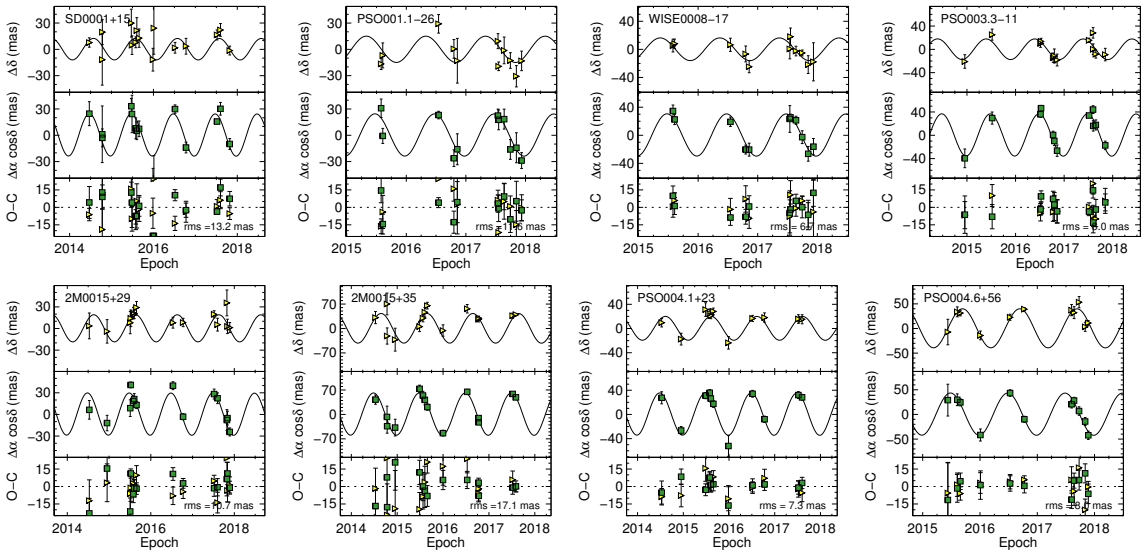

Figure 7.7 Examples of parallax fits and residuals for our targets. For each object, the top and middle panels show relative parallax fits in δ and α after subtracting the best-fit proper motion, as a function of Julian year. The bottom panels show the residuals after subtracting both the proper motion and the parallax.

that more observations are needed to identify possible outliers and securely measure their parallaxes.

For most of the rest of these targets, we found one of two types of outliers among the epochs. The first type was an α or δ measurement at one epoch with an implausibly small uncertainty ($<$2 mas, compared to a median of $\approx$8 mas), likely a statistical consequence of using a small number of dithers ($\leq$9) to compute the RMS. The second type was an α or δ measurement deviating by $\gtrsim$50 mas from the IRLS solution, often carrying a similarly large measurement error. We found that excluding these epochs resolved the problems with the parallax fits, i.e., reduced the χ^2_ν to $\approx$1, lowered the bootstrapping uncertainties into consistency with other procedures, and/or brought the parallax into agreement with the *Gaia* DR2 or literature value.

We also attempted to correct the fits in a more automated fashion by adding a noise floor (up to 4 mas) to the astrometry at each epoch and by clipping epochs with low weights from the IRLS fitting, but neither of these was successful in systematically improving the

parallax fits. We therefore adopted the parallaxes with the epochs excluded by hand for 16 targets.

7.5.3 Differential Chromatic Refraction

Our observation strategy strove to minimize any impact from DCR on our astrometry by observing each target over a narrow airmass range around transit (i.e., minimum airmass; Section 7.3.2). A handful of observations were nevertheless taken at higher airmasses. To assess the impact of these observations, we re-calculated parallaxes after removing observations taken at airmasses more than 0.1 greater than the minimum airmass at which each target was observed. In total this meant we removed 1 epoch from 62 targets (18% of all targets) and two or more epochs from 24 targets (7%). The expected impact of DCR on the measurements of these epochs was ≈2 mas for later T dwarfs at elevation 40° (the lowest elevation for our observations; DL12), and less for earlier-type objects and observations at higher elevations. We found that the parallaxes and proper motions for the objects with removed epochs changed by less than their uncertainties, consistent with the ≈2–5 mas uncertainties for our final parallaxes (Section 7.6), and in general the uncertainties increased slightly as expected when removing 1 or 2 out of ∼10 measurements. The epochs removed due to discrepant airmass also did not correspond systematically to outlier measurements in our data. We conclude that DCR contributes insignificantly to our parallaxes and proper motions and their uncertainties, which are dominated by the variation in position measurements across individual frames. We therefore did not remove the higher-airmass epochs from our final astrometric solutions.

7.5.4 Orbital Motion

Stars and brown dwarfs that are binaries will exhibit orbital motion in addition to parallax and proper motions. Sufficiently precise and frequent astrometric measurements can detect such orbital motion even when a companion is unresolved, and provide useful constraints on the masses of the components (e.g., Sahlmann et al. 2013; Dupuy et al. 2015b). The

≈11 mas precision of our per-epoch astrometry and ≈2–5 mas precision of our parallaxes is insufficient to detect orbital motions that are typically ≈5 mas in amplitude, manifest over multiple-year periods, and alter parallaxes by less than 1 mas (e.g., Dupuy & Liu 2012, 2017). The residuals of our parallax fits shown in Figure 7.7 also revealed no obvious trends suggesting orbital motion. We therefore did not attempt to correct for orbital motion of any of our targets, including known binaries.

7.5.5 Correction to Absolute Parallax and Proper Motion

Up to this point, we have calculated parallaxes and proper motions relative to field objects in our images, most of which are background stars. These reference stars, while more distant, nevertheless have nonzero parallaxes and proper motions. The mean positions of these stars were calibrated to the PS1 absolute reference frame (Section 7.4.2), but individual epochs are still impacted by the parallactic motions of the background stars, which systematically reduce the parallaxes measured for our targets. To convert these relative parallaxes to absolute astrometry, DL12 used Besançon galaxy models (Robin et al. 2003) to estimate the mean parallaxes of field objects in their images and apply this as a correction. LDA16 included proper motions in their conversions from relative to absolute astrometry. Others have used photometry to estimate distances to the reference stars (e.g., Faherty et al. 2012). With the advent of *Gaia* DR2, we can use actual parallax measurements for reference stars in a target's field to determine the correction to absolute astrometry for our UKIRT parallaxes.

For each target in our sample, we cross-matched the set of field stars used for the astrometric reference frame with *Gaia* DR2 using a $1''$ matching radius.

We retained only the "quality" matches, namely those having *Gaia* parallax errors less than 0.5 mas, DR2 parameter `astrometric_excess_noise` = 0, and proper motions less than 20 mas yr^{-1} (faster-moving objects were also excluded from our UKIRT reference frames). These "quality" *Gaia* matches comprised on average 38% of all reference stars and 42% of those with *Gaia* matches (Figure 7.8). We added the 29 μas zero-point offset from Lindegren et al. (2018) to the *Gaia* DR2 parallaxes and the 43 μas systematic noise

floor from Lindegren et al. (2018) in quadrature to the *Gaia* DR2 parallax uncertainties (although the impact of these on our final parallaxes is negligible).

Our pipeline calculates parallaxes and proper motions for all objects (science targets *and* reference stars) matched across at least $N_{\rm ep} - 2$ epochs, so we also have UKIRT relative parallaxes and proper motions for the *Gaia*-matched reference stars. The difference between the *Gaia* and UKIRT parallax for each object, $\pi_{Gaia} - \pi_{\rm UKIRT}$, is the amount of parallax motion we ignore when defining our reference frames For each target, we computed the weighted mean and weighted standard error of $(\pi_{Gaia} - \pi_{\rm UKIRT})$ for all quality reference stars as the correction for turning the relative astrometry into absolute astrometry (Table 7.1). We calculated and applied analogous corrections to our UKIRT relative proper motion measurements, incorporating the 66 μas yr^{-1} noise floor from Lindegren et al. (2018).

We investigated whether we could obtain more accurate astrometric reference frames and parallaxes by using *Gaia* DR2 instead of PS1 as our external reference catalog throughout the reduction process. In theory, this approach might provide more accurate corrections to absolute astrometry, since we would be using the same stars for the reference frames and the correction to absolute astrometry. But we might also lose astrometric precision since PS1 is a deeper catalog with more objects than *Gaia* DR2. We selected fifty targets for which the fractions of reference stars with quality *Gaia* parallaxes spanned the full range for our target list, and ran these fifty objects through our pipeline using *Gaia* DR2 as the reference catalog instead of PS1. The final parallaxes and uncertainties and the corrections to absolute parallaxes were nearly identical whether PS1 or *Gaia* DR2 was used as the reference catalog. We opted to use the deeper PS1 as the external catalog.

7.5.6 Targets with No Astrometric Solution

We were unable to calculate a parallax for 8 of our 356 targets. Six of these were observed at fewer than 6 epochs, making a robust astrometric solution impossible. One target, WISE J033605.05−014350.4, proved to be too faint to be detected in our longest 300 sec frames. For the final target, 2MASS J21371044+1450475, we calculated a parallax of

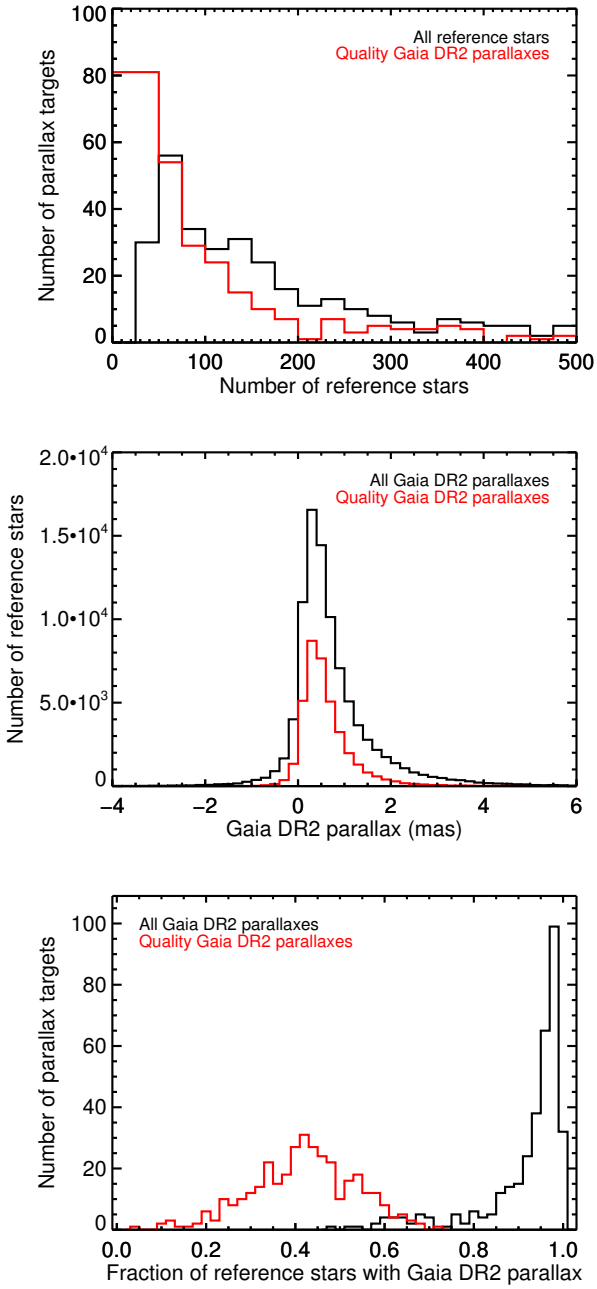

Figure 7.8 *Top*: Distributions of the total number of reference frame stars for each parallax target (black) and the number of reference stars having "quality" *Gaia* DR2 parallaxes (38% of all reference stars; see text for definition). *Middle*: Distributions of all *Gaia* DR2 parallaxes (black) and quality *Gaia* DR2 parallaxes (red; 42% of all *Gaia* parallaxes) for the reference stars. Nearly all quality *Gaia* parallaxes are between −0.5 and 2 mas. *Bottom*: Distribution of the fraction of stars used to build the astrometric references that have a *Gaia* DR2 parallax (black) and a quality *Gaia* DR2 parallax (red). We used only the quality *Gaia* parallaxes to correct our ultracool parallaxes from relative to absolute reference frames.

19.8 ± 19.7 mas using IRLS+MCMC and a wide range of other solutions (including 0 and a negative parallax) using the other methods described in Section 7.5.1. This object is relatively bright at $J_{\rm 2MASS} = 14.13$ mag and has a *Gaia* DR2 parallax of 42.39 ± 0.32 mas, so it should have been a straightforward target for our program. The scatter in our data suggest that several of the epochs were corrupted, but it is unclear which epochs are affected. We therefore do not include 2MASS J21371044+1450475 in our final results.

7.6 Results

We present parallaxes and proper motions for 348 L and T dwarfs in Table 7.4, representing the largest single sample of infrared parallaxes published to date. Figure 7.9 shows the distributions for our absolute parallaxes, parallax uncertainties, and the reduced χ^2 of our final IRLS + MCMC solutions. We achieve a best parallax precision of 1.5 mas, and 97% of our uncertainties are less than 6 mas. Our median precision of 3.5 mas is comparable to the ≈1–4 mas precision of other ground-based infrared parallax observations (LDA16). Our results also improve the parallaxes for 21 objects with previously published values.

Three targets in our sample — ULAS J085910.69+101017.1, PSO J135.0395+32.0845, and UGPS J20480024+503821.9 — have observations spanning only one year. While our solutions for these objects appear to be robust, the parallaxes and proper motions should be regarded as preliminary.

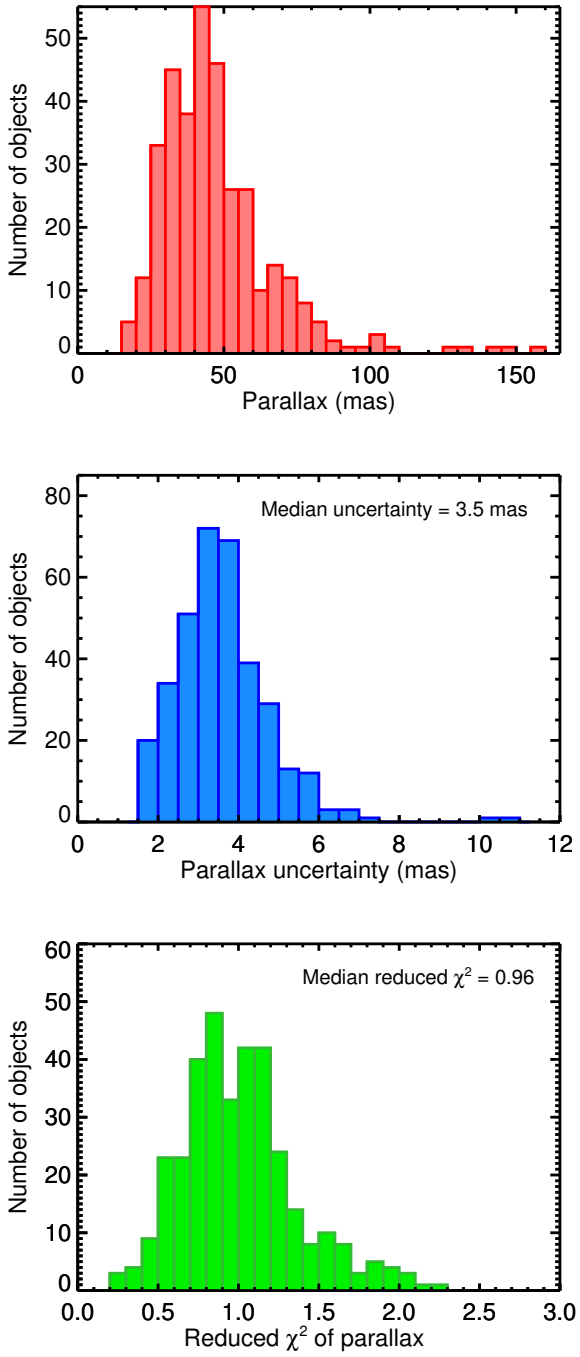

Figure 7.9 Distributions of our final parallaxes (*top*) and uncertainties (*middle*) including the corrections to absolute astrometry, and of the minimum χ^2_ν for our IRLS + MCMC chains (*bottom*). Objects with parallaxes $\geq$ 40 mas are within our target 25 pc volume. 97% of our uncertainties are less than 6 mas, equivalent to a 15% error at 25 pc. Our χ^2_ν distribution peaks strongly near 1 (median = 0.96), indicating that the scatter of data about our best-fit parallaxes is commensurate with the astrometric uncertainties.

Table 7.4. UKIRT/WFCAM Parallaxes and Proper Motions

Object	α_{J2000} (deg)	δ_{J2000} (deg)	Epoch (MJD)	Relative			Absolute			χ^2/dof
				π_{rel} (mas)	$\mu_{\alpha,rel}\cos\delta$ (mas yr^{-1})	$\mu_{\delta,rel}$ (mas yr^{-1})	π_{abs} (mas)	$\mu_{\alpha,abs}\cos\delta$ (mas yr^{-1})	$\mu_{\delta,abs}$ (mas yr^{-1})	
SDSS J000112.18+153535.5	000.3013707	+15.5925657	56829.63	25.7 ± 3.4	123.2 ± 2.1	-175.3 ± 1.9	27.2 ± 3.5	132.5 ± 2.2	-180.3 ± 1.9	26.5/25
PSO J001.1277−26.0675	001.1278586	−26.0676516	57234.57	30.4 ± 4.6	-7.2 ± 4.2	-237.8 ± 3.8	33.1 ± 4.7	-0.9 ± 4.3	-243.7 ± 3.8	26.2/17
WISEPC J000849.76−173922.6	002.2072022	−17.6569863	57234.57	32.8 ± 3.9	-178.0 ± 3.1	-372.5 ± 3.1	36.1 ± 3.9	-171.1 ± 3.1	-373.1 ± 3.1	11.3/17
PSO J003.3437−11.7168	003.3439192	−11.7168434	57007.20	38.7 ± 3.1	209.0 ± 3.2	-17.7 ± 3.0	40.3 ± 3.1	213.7 ± 3.3	-26.7 ± 3.1	20.0/19
2MASS J00150206+2959323	003.7604536	+29.9914289	56850.60	30.4 ± 3.3	372.3 ± 2.2	-225.9 ± 2.3	31.6 ± 3.3	372.5 ± 2.2	-231.8 ± 2.3	23.8/23
2MASSW J0015447+351603	003.9369026	+35.2664116	56850.61	64.8 ± 3.5	47.2 ± 2.8	-255.0 ± 2.7	65.7 ± 3.5	47.2 ± 2.8	-257.8 ± 2.7	23.5/23
PSO J004.1834+23.0741	004.1837991	+23.0741642	56850.60	37.2 ± 3.3	402.5 ± 2.0	66.6 ± 2.4	38.4 ± 3.3	405.4 ± 2.1	61.8 ± 2.5	12.9/17
PSO J004.6359+56.8370	004.6369722	+56.8371228	57183.63	46.4 ± 3.9	376.5 ± 3.2	12.4 ± 2.7	46.5 ± 3.9	375.9 ± 3.2	10.4 ± 2.7	14.0/17
PSO J005.6302−06.8669	005.6302611	−06.8669750	57007.20	29.0 ± 2.9	-111.4 ± 2.2	0.7 ± 2.2	30.6 ± 3.0	-106.7 ± 2.3	-7.2 ± 2.3	9.4/19
2MASS J00282091+2249050	007.0902250	+22.8159638	57201.63	36.0 ± 4.7	559.8 ± 4.0	-427.9 ± 4.0	38.1 ± 4.7	564.4 ± 4.0	-436.8 ± 4.1	17.5/19
2MASSW J0030300−145033	007.6266907	−14.8426999	57212.63	40.0 ± 5.3	249.7 ± 3.4	-36.9 ± 3.2	41.1 ± 5.3	256.1 ± 3.4	-41.7 ± 3.3	15.0/13
WISE J003110.04+574936.3	007.7933510	+57.8267612	57226.63	70.3 ± 5.0	525.4 ± 3.5	-22.1 ± 4.0	71.0 ± 5.0	522.5 ± 3.5	-23.9 ± 4.0	24.0/17
PSO J007.9194+33.5961	007.9194529	+33.5960652	56942.37	44.5 ± 3.8	-19.1 ± 2.3	-14.9 ± 1.9	45.4 ± 3.8	-17.3 ± 2.3	-19.2 ± 1.9	21.8/23
2MASS J00320509+0219017	008.0229029	+02.3158798	56942.38	43.6 ± 3.9	389.7 ± 2.7	-324.1 ± 3.0	44.9 ± 4.0	389.8 ± 2.8	-331.1 ± 3.1	19.8/21
WISE J004024.88+090054.8	010.1037573	+09.0151730	57006.25	70.1 ± 2.7	-55.7 ± 2.8	-54.0 ± 2.3	71.3 ± 2.7	-53.7 ± 2.8	-62.3 ± 2.3	12.5/19
PSO J011.1793−03.7847	011.1795549	−03.7846008	57007.20	37.4 ± 2.7	173.3 ± 2.4	89.5 ± 2.1	38.1 ± 2.7	180.2 ± 2.4	79.0 ± 2.2	23.9/19
WISE J004542.56+361139.1	011.4273264	+36.1940359	56942.37	52.6 ± 5.2	-88.8 ± 2.7	-163.9 ± 3.2	53.4 ± 5.2	-88.0 ± 2.7	-166.1 ± 3.2	26.4/25
2MASS J00464841+0715177	011.7021893	+07.2547383	56942.38	24.0 ± 2.5	84.0 ± 2.5	-55.3 ± 2.5	24.5 ± 2.5	87.4 ± 2.5	-58.8 ± 2.5	19.4/25
WISEPC J004928.48+044100.1	012.3691081	+04.6836509	57006.25	61.1 ± 2.9	296.9 ± 2.9	240.7 ± 2.8	62.6 ± 2.9	307.6 ± 3.0	237.0 ± 2.8	18.7/19
SIPS J0050−1538	012.6008236	−15.6407009	57212.63	35.6 ± 2.3	-231.2 ± 2.7	-488.2 ± 3.7	37.3 ± 2.3	-224.1 ± 2.7	-492.2 ± 3.7	18.5/17

Table 7.4—Continued

Object	$\alpha_{\rm J2000}$ (deg)	$\delta_{\rm J2000}$ (deg)	Epoch (MJD)	Relative			Absolute			χ^2/dof
				$\pi_{\rm rel}$ (mas)	$\mu_{\alpha,{\rm rel}}\cos\delta$ (mas yr^{-1})	$\mu_{\delta,{\rm rel}}$ (mas yr^{-1})	$\pi_{\rm abs}$ (mas)	$\mu_{\alpha,{\rm abs}}\cos\delta$ (mas yr^{-1})	$\mu_{\delta,{\rm abs}}$ (mas yr^{-1})	
2MASSW J0051107−154417	012.7953603	−15.7381327	57234.57	25.7 ± 3.0	51.0 ± 3.6	-39.4 ± 4.2	27.6 ± 3.1	55.0 ± 3.7	-47.6 ± 4.2	20.3/17
WISEA J010202.11+035541.4	015.5093605	+03.9283207	57234.58	38.9 ± 2.8	348.0 ± 2.6	77.7 ± 2.2	40.2 ± 2.8	353.2 ± 2.6	71.0 ± 2.3	9.1/19
SDSS J011912.22+240331.6	019.8017949	+24.0588455	56942.38	27.7 ± 2.9	264.4 ± 1.5	10.3 ± 1.6	28.9 ± 2.9	264.6 ± 1.5	5.5 ± 1.6	15.3/19
WISEPA J012333.21+414203.9	020.8897184	+41.7014371	56942.37	39.0 ± 2.4	600.0 ± 1.3	91.1 ± 1.3	39.3 ± 2.4	601.0 ± 1.3	88.9 ± 1.3	14.2/27
2MASS J01311838+3801554	022.8287834	+38.0319466	56942.37	38.1 ± 4.3	373.2 ± 3.3	-24.6 ± 3.3	39.1 ± 4.3	374.1 ± 3.3	-30.3 ± 3.3	17.7/25
WISE J013525.64+171503.4	023.8564298	+17.2507309	57006.26	46.1 ± 3.5	-366.7 ± 2.6	-239.6 ± 2.5	46.7 ± 3.5	-365.4 ± 2.6	-245.6 ± 2.5	5.9/15
2MASSW J0135358+120522	023.8993049	+12.0876455	56942.38	39.4 ± 2.3	-50.5 ± 3.0	-439.9 ± 2.3	40.7 ± 2.3	-43.7 ± 3.0	-445.9 ± 2.3	19.4/19
SIMP J013656.5+093347.3	024.2409293	+09.5631188	57006.26	157.6 ± 2.8	1231.6 ± 3.2	-8.2 ± 3.0	159.2 ± 2.8	1237.7 ± 3.2	-14.3 ± 3.1	14.7/17
PSO J024.4369+09.1360	024.4369927	+09.1360200	56942.38	25.2 ± 4.4	-55.0 ± 2.8	-140.0 ± 2.3	25.7 ± 4.5	-49.2 ± 2.8	-145.1 ± 2.4	9.8/13
WISEPC J013836.59−032221.2	024.6526800	−03.3730468	57243.60	43.2 ± 2.9	107.5 ± 2.6	-300.1 ± 3.1	43.9 ± 2.9	112.1 ± 2.7	-307.8 ± 3.2	31.6/31
2MASS J01414839−1601196	025.4525864	−16.0218285	57243.60	27.9 ± 5.7	191.3 ± 3.5	60.9 ± 5.5	28.8 ± 5.8	198.2 ± 3.5	55.5 ± 5.5	8.7/11
2MASS J01443536−0716142	026.1492728	−07.2714409	57243.60	81.5 ± 3.7	368.2 ± 4.2	-191.0 ± 4.6	81.7 ± 3.7	372.3 ± 4.2	-200.5 ± 4.6	24.7/27
WISEPA J015010.86+382724.3	027.5469055	+38.4566677	56942.37	39.7 ± 4.6	877.8 ± 2.0	-124.6 ± 2.1	39.8 ± 4.6	878.2 ± 2.1	-125.1 ± 2.1	27.0/21
ULAS J015024.37+135924.0	027.6016599	+13.9900373	56943.45	36.6 ± 2.2	23.1 ± 1.4	26.3 ± 1.5	37.9 ± 2.2	27.8 ± 1.4	20.3 ± 1.5	20.9/17
2MASS J01550354+0950003	028.7662254	+09.8331368	57006.26	36.9 ± 2.7	316.3 ± 2.4	-89.1 ± 3.5	39.0 ± 2.7	323.0 ± 2.5	-94.9 ± 3.5	15.4/15
HIP 9269B	029.7961785	+33.2072799	56942.37	42.9 ± 3.7	242.6 ± 1.7	-348.6 ± 1.9	43.3 ± 3.7	245.7 ± 1.7	-352.7 ± 1.9	18.2/23
2MASSW J0205034+125142	031.2660854	+12.8616813	57007.35	40.7 ± 3.0	360.6 ± 2.3	-16.6 ± 2.6	42.5 ± 3.0	364.6 ± 2.4	-29.5 ± 2.7	16.3/21
PSO J031.5651+20.9097	031.5654555	+20.9097053	56943.46	36.2 ± 2.1	230.9 ± 1.9	-91.0 ± 1.3	37.0 ± 2.2	235.0 ± 1.9	-95.2 ± 1.3	21.3/21
2MASSW J0208183+254253	032.0783863	+25.7146944	57007.35	44.0 ± 5.7	366.8 ± 3.3	-31.1 ± 3.9	45.5 ± 5.7	374.2 ± 3.3	-36.4 ± 3.9	12.4/19
2MASSW J0208236+273740	032.0996673	+27.6273055	57007.35	20.4 ± 2.7	202.9 ± 2.9	-110.1 ± 2.8	21.3 ± 2.7	205.2 ± 2.9	-115.9 ± 2.8	34.0/21

Table 7.4—Continued

Object	$\alpha_{\rm J2000}$ (deg)	$\delta_{\rm J2000}$ (deg)	Epoch (MJD)	Relative			Absolute			χ^2/dof
				$\pi_{\rm rel}$ (mas)	$\mu_{\alpha,{\rm rel}}\cos\delta$ (mas yr^{-1})	$\mu_{\delta,{\rm rel}}$ (mas yr^{-1})	$\pi_{\rm abs}$ (mas)	$\mu_{\alpha,{\rm abs}}\cos\delta$ (mas yr^{-1})	$\mu_{\delta,{\rm abs}}$ (mas yr^{-1})	
2MASS J02132062+3648506C	033.3328651	+36.8106421	57006.33	68.9 ± 3.9	29.0 ± 3.6	54.1 ± 3.7	70.1 ± 3.9	31.2 ± 3.6	50.0 ± 3.7	22.5/21
2MASSI J0213288+444445	033.3697380	+44.7453324	57006.33	53.6 ± 2.6	-60.4 ± 2.5	-146.3 ± 2.9	54.3 ± 2.6	-61.8 ± 2.5	-148.8 ± 2.9	31.7/27
WISEPA J022105.94+384202.9	035.2751534	+38.7010366	57235.62	37.1 ± 2.0	132.6 ± 1.7	-24.3 ± 1.5	37.7 ± 2.0	133.9 ± 1.7	-27.2 ± 1.5	29.9/19
WISEPA J022623.98−021142.8	036.5997005	−02.1954775	56943.41	50.6 ± 2.3	-296.0 ± 1.8	-430.6 ± 1.4	51.1 ± 2.3	-291.8 ± 1.8	-433.5 ± 1.4	14.3/13
2MASS J02271036−1624479	036.7950936	−16.4145056	57243.63	46.3 ± 3.9	431.0 ± 3.6	-306.6 ± 4.7	47.5 ± 4.0	437.3 ± 3.6	-312.0 ± 4.7	8.9/17
2MASSW J0228110+253738	037.0471536	+25.6271447	57007.35	27.6 ± 2.7	239.6 ± 2.8	-29.5 ± 3.1	28.7 ± 2.7	242.3 ± 2.8	-33.1 ± 3.2	24.4/21
2MASS J02284243+1639329	037.1786121	+16.6574328	56943.46	46.8 ± 3.5	392.3 ± 2.6	-434.4 ± 2.4	46.5 ± 3.5	395.8 ± 2.7	-440.1 ± 2.4	15.7/21
WISE J023038.90−022554.0	037.6625898	−02.4315475	56972.43	33.2 ± 3.9	322.6 ± 3.4	63.9 ± 2.8	35.1 ± 3.9	324.4 ± 3.4	56.4 ± 2.9	15.7/15
WISE J023318.05+303030.5	038.3251447	+30.5084746	56943.47	27.2 ± 2.6	-133.7 ± 1.8	-25.5 ± 1.6	28.2 ± 2.6	-132.0 ± 1.8	-29.9 ± 1.6	26.3/25
PSO J041.5426+01.9456	041.5428187	+01.9456058	57007.35	31.2 ± 2.4	40.1 ± 2.0	-71.9 ± 1.5	33.2 ± 2.4	47.6 ± 2.0	-76.8 ± 1.6	21.4/19
WISE J024714.52+372523.5	041.8107256	+37.4229727	56943.48	63.7 ± 2.0	27.0 ± 1.4	-85.5 ± 1.2	64.8 ± 2.0	28.9 ± 1.4	-88.0 ± 1.2	15.6/17
2MASSI J0251148−035245	042.8171720	−03.8876970	57007.34	77.5 ± 3.4	1101.5 ± 3.5	-1842.4 ± 4.2	78.0 ± 3.5	1104.0 ± 3.5	-1847.1 ± 4.2	13.5/15
PSO J045.3309−23.3226	045.3312213	−23.3226648	57262.58	36.4 ± 3.8	230.8 ± 3.2	-115.5 ± 3.9	37.3 ± 3.8	234.3 ± 3.2	-119.2 ± 3.9	10.9/7
WISEPA J030533.54+395434.4	046.3903466	+39.9096730	56943.47	27.2 ± 2.0	271.6 ± 1.5	7.7 ± 1.5	27.8 ± 2.0	273.0 ± 1.5	4.7 ± 1.5	12.6/19
WISE J031614.68+382008.0	049.0611103	+38.3352246	56943.47	31.6 ± 3.3	-95.1 ± 2.3	-306.0 ± 2.2	34.1 ± 3.3	-93.8 ± 2.3	-307.9 ± 2.2	16.8/21
PSO J049.1159+26.8409	049.1161477	+26.8409559	56943.46	32.2 ± 3.1	198.7 ± 2.4	-46.8 ± 1.9	33.5 ± 3.1	201.1 ± 2.4	-52.8 ± 1.9	12.9/23
2MASSW J0320284−044636	050.1172831	−04.7789344	57007.34	47.5 ± 2.8	-245.6 ± 2.6	-520.5 ± 2.9	49.0 ± 2.8	-240.3 ± 2.6	-523.8 ± 3.0	25.9/19
WISEA J032301.86+562558.0	050.7586516	+56.4324589	56943.48	60.6 ± 5.6	319.1 ± 3.3	-274.8 ± 3.4	60.8 ± 5.6	320.1 ± 3.3	-276.3 ± 3.5	3.2/15
SDSS J032553.17+042540.1	051.4711201	+04.4277147	56943.46	42.6 ± 3.2	-182.7 ± 2.6	-69.6 ± 2.4	44.0 ± 3.2	-178.5 ± 2.6	-74.0 ± 2.4	24.7/21
PSO J052.2746+13.3754	052.2748350	+13.3754602	56943.47	43.9 ± 3.0	271.3 ± 2.0	-17.2 ± 2.0	44.3 ± 3.0	273.0 ± 2.0	-20.7 ± 2.0	15.9/21

Table 7.4—Continued

Object	$\alpha_{\rm J2000}$ (deg)	$\delta_{\rm J2000}$ (deg)	Epoch (MJD)	Relative			Absolute			χ^2/dof
				$\pi_{\rm rel}$ (mas)	$\mu_{\alpha,{\rm rel}}\cos\delta$ (mas yr^{-1})	$\mu_{\delta,{\rm rel}}$ (mas yr^{-1})	$\pi_{\rm abs}$ (mas)	$\mu_{\alpha,{\rm abs}}\cos\delta$ (mas yr^{-1})	$\mu_{\delta,{\rm abs}}$ (mas yr^{-1})	
PSO J052.7214−03.8409	052.7213421	−03.8408257	57007.34	55.8 ± 3.5	-145.5 ± 2.4	67.5 ± 2.6	57.1 ± 3.5	-141.0 ± 2.4	64.0 ± 2.7	9.7/17
WISE J033651.90+282628.8	054.2164882	+28.4411852	56943.47	28.1 ± 3.4	103.4 ± 1.8	-174.1 ± 2.2	28.8 ± 3.4	106.9 ± 1.8	-177.1 ± 2.2	17.8/21
2MASSW J0337036−175807	054.2659467	−17.9683114	56943.54	29.2 ± 4.8	194.8 ± 4.1	99.0 ± 4.7	30.7 ± 4.8	200.2 ± 4.1	93.8 ± 4.7	18.6/13
SDSS J035104.37+481046.8	057.7695131	+48.1791914	56943.47	27.7 ± 4.3	288.0 ± 2.7	-192.0 ± 2.5	28.5 ± 4.3	289.2 ± 2.7	-194.4 ± 2.5	15.6/21
WISE J040137.21+284951.7	060.4044875	+28.8309409	57004.40	71.4 ± 3.1	-468.3 ± 2.7	-99.0 ± 3.0	72.5 ± 3.1	-466.1 ± 2.7	-103.7 ± 3.0	27.5/21
WISE J040418.01+412735.6	061.0751033	+41.4594507	56943.50	58.8 ± 4.2	-59.6 ± 3.3	-396.4 ± 3.8	59.4 ± 4.2	-55.9 ± 3.3	-398.2 ± 3.8	14.2/17
2MASS J04070885+1514565	061.7876523	+15.2486446	57004.40	53.8 ± 2.7	208.3 ± 2.4	-122.0 ± 2.0	55.4 ± 2.7	211.8 ± 2.4	-127.5 ± 2.0	21.6/21
2MASSI J0408290−145033	062.1220245	−14.8430855	56943.54	48.7 ± 4.7	194.8 ± 2.8	-108.6 ± 2.6	48.9 ± 4.7	202.8 ± 2.8	-114.4 ± 2.7	7.5/15
PSO J062.3459+11.1794	062.3458943	+11.1794709	57004.40	44.9 ± 2.7	-164.8 ± 2.2	-73.2 ± 2.6	45.7 ± 2.7	-162.8 ± 2.2	-78.0 ± 2.6	16.9/19
WISE J042417.94+072744.1	066.0758146	+07.4609893	57004.40	42.9 ± 1.5	417.9 ± 1.0	-930.6 ± 1.1	43.7 ± 1.5	421.6 ± 1.0	-933.5 ± 1.1	24.2/13
WISE J043052.92+463331.6	067.7222607	+46.5592575	56943.50	80.5 ± 3.5	883.1 ± 2.5	377.4 ± 2.5	81.4 ± 3.5	884.5 ± 2.5	375.4 ± 2.5	14.6/13
PSO J069.7303+04.3834	069.7304549	+04.3835412	57004.43	36.0 ± 5.7	128.1 ± 4.4	12.8 ± 3.4	36.6 ± 5.7	131.7 ± 4.4	10.1 ± 3.4	10.5/11
PSO J070.3773+04.7333	070.3775952	+04.7332319	57004.40	23.1 ± 4.9	211.1 ± 3.1	-102.7 ± 2.9	23.5 ± 4.9	212.5 ± 3.1	-105.7 ± 2.9	12.7/11
PSO J071.8769−12.2713	071.8767937	−12.2713495	57363.42	22.4 ± 3.8	-12.5 ± 2.6	-98.8 ± 2.3	23.0 ± 3.9	-6.3 ± 2.6	-99.1 ± 2.3	28.4/15
2MASS J04474307−1936045	071.9299844	−19.6008537	57363.44	19.4 ± 5.0	83.8 ± 4.2	86.1 ± 4.2	20.7 ± 5.0	87.4 ± 4.2	85.3 ± 4.2	7.9/11
WISEPA J044853.29−193548.5	072.2233578	−19.5958161	56943.54	54.8 ± 3.4	893.6 ± 1.7	759.3 ± 1.8	55.3 ± 3.4	896.8 ± 1.7	758.1 ± 1.8	19.2/15
2MASSI J0453264−175154	073.3605853	−17.8651284	56943.54	36.6 ± 5.7	32.8 ± 4.9	-23.0 ± 3.8	37.4 ± 5.7	34.7 ± 4.9	-24.0 ± 3.9	7.3/13
WISE J045746.08−020719.2	074.4422695	−02.1220912	56972.53	81.1 ± 2.9	89.5 ± 3.0	-103.5 ± 2.1	82.0 ± 2.9	93.0 ± 3.0	-105.2 ± 2.2	12.5/19
WISEPA J050003.05−122343.2	075.0120852	−12.3946716	56943.57	83.3 ± 2.2	-536.2 ± 1.6	490.8 ± 1.9	84.6 ± 2.2	-533.6 ± 1.6	490.5 ± 1.9	16.3/17
PSO J076.7092+52.6087	076.7093806	+52.6085462	56943.54	59.2 ± 5.4	48.1 ± 3.3	-204.0 ± 3.8	59.6 ± 5.4	49.8 ± 3.3	-205.9 ± 3.8	11.1/13

Table 7.4—Continued

Object	$\alpha_{\rm J2000}$ (deg)	$\delta_{\rm J2000}$ (deg)	Epoch (MJD)	Relative			Absolute			χ^2/dof
				$\pi_{\rm rel}$ (mas)	$\mu_{\alpha,{\rm rel}}\cos\delta$ (mas yr^{-1})	$\mu_{\delta,{\rm rel}}$ (mas yr^{-1})	$\pi_{\rm abs}$ (mas)	$\mu_{\alpha,{\rm abs}}\cos\delta$ (mas yr^{-1})	$\mu_{\delta,{\rm abs}}$ (mas yr^{-1})	
2MASS J05160945−0445499	079.0384590	−04.7647454	56972.54	53.0 ± 4.3	-224.7 ± 3.6	-199.9 ± 2.7	54.2 ± 4.3	-222.1 ± 3.6	-202.6 ± 2.7	22.8/19
WISE J052126.29+102528.4	080.3599557	+10.4240671	57004.40	139.7 ± 4.8	213.3 ± 5.2	-413.7 ± 2.8	141.2 ± 4.8	216.0 ± 5.2	-418.2 ± 2.8	8.8/15
HIP 26653B	084.9564067	+52.8993684	56943.54	32.0 ± 3.9	-14.8 ± 2.9	-143.6 ± 2.6	32.5 ± 3.9	-13.1 ± 2.9	-147.1 ± 2.6	16.4/17
WISEPA J053957.02−103436.5	084.9872992	−10.5774011	56943.59	30.1 ± 2.8	-259.5 ± 1.8	-362.4 ± 1.2	31.0 ± 2.8	-258.1 ± 1.8	-363.0 ± 1.2	36.5/21
PSO J085.1080−18.0445	085.1080328	−18.0445030	56943.54	58.5 ± 4.0	-94.9 ± 3.0	-11.8 ± 2.3	59.2 ± 4.0	-94.0 ± 3.0	-10.3 ± 2.3	14.5/19
WISEPA J054231.26−162829.1	085.6301162	−16.4743653	56943.54	60.1 ± 2.6	-221.8 ± 2.5	300.3 ± 2.4	61.3 ± 2.6	-219.3 ± 2.5	299.3 ± 2.4	32.2/19
WISE J054601.19−095947.5	086.5050365	−09.9964717	56972.54	49.9 ± 3.6	-10.1 ± 2.8	-7.6 ± 2.1	50.4 ± 3.6	-7.9 ± 2.8	-8.7 ± 2.1	23.4/19
WISEA J055007.94+161051.9	087.5334793	+16.1807705	57004.44	53.4 ± 2.8	241.5 ± 4.3	-299.5 ± 3.3	53.9 ± 2.8	242.3 ± 4.3	-302.1 ± 3.3	21.1/19
PSO J087.7749−12.6537	087.7748054	−12.6537846	56943.60	33.7 ± 3.4	-140.6 ± 2.7	-58.7 ± 2.2	34.5 ± 3.4	-140.3 ± 2.7	-59.4 ± 2.2	9.3/17
PSO J088.5709−00.1430	088.5710671	−00.1430178	56972.54	30.6 ± 3.4	16.3 ± 1.9	-102.6 ± 2.0	31.7 ± 3.4	16.4 ± 1.9	-103.8 ± 2.0	20.1/19
PSO J089.1751−09.4513	089.1751383	−09.4513835	56943.60	43.4 ± 2.5	-114.2 ± 2.0	-114.6 ± 2.1	44.3 ± 2.5	-112.3 ± 2.0	-115.1 ± 2.1	26.9/19
2MASS J06020638+4043588	090.5279911	+40.7321689	56943.58	64.5 ± 4.2	228.6 ± 2.9	-223.5 ± 2.9	65.1 ± 4.2	229.9 ± 2.9	-225.7 ± 2.9	12.4/19
WISEA J060742.13+455037.0	091.9258308	+45.8429807	56943.59	32.5 ± 3.5	106.0 ± 3.6	-561.4 ± 4.1	33.6 ± 3.5	106.9 ± 3.6	-564.2 ± 4.1	21.3/21
WISE J061437.73+095135.0	093.6578687	+09.8596191	57004.44	56.2 ± 2.0	386.3 ± 1.7	-155.1 ± 1.5	56.7 ± 2.0	387.5 ± 1.7	-156.2 ± 1.5	16.4/21
2MASS J06143818+3950357	093.6590117	+39.8422145	56943.58	42.7 ± 2.6	-32.4 ± 1.7	-261.4 ± 1.8	44.0 ± 2.6	-31.9 ± 1.7	-264.9 ± 1.8	12.7/23
WISEPA J062309.94−045624.6	095.7903446	−04.9398677	56943.60	84.8 ± 1.7	-906.9 ± 1.8	168.8 ± 1.6	86.5 ± 1.7	-906.3 ± 1.8	168.8 ± 1.6	23.8/21
WISEPA J062542.21+564625.5	096.4259985	+56.7737491	56943.61	43.1 ± 3.4	-50.3 ± 2.5	-19.8 ± 2.5	44.4 ± 3.4	-49.9 ± 2.5	-22.3 ± 2.5	37.3/23
WISE J062905.13+241804.9	097.2713799	+24.3008889	57004.44	32.5 ± 3.1	-7.1 ± 2.5	-349.9 ± 2.0	33.0 ± 3.1	-6.4 ± 2.5	-352.6 ± 2.0	30.6/23
WISEA J064750.85−154616.4	101.9621113	−15.7710458	56972.62	46.7 ± 3.9	111.7 ± 3.9	122.1 ± 3.2	47.6 ± 3.9	110.8 ± 3.9	123.2 ± 3.2	24.7/23
PSO J103.0927+41.4601	103.0927246	+41.4600001	56943.64	44.4 ± 3.7	-1.5 ± 2.9	-32.8 ± 2.2	45.1 ± 3.7	-1.7 ± 2.9	-38.2 ± 2.2	13.6/21

Table 7.4—Continued

Object	$\alpha_{\rm J2000}$ (deg)	$\delta_{\rm J2000}$ (deg)	Epoch (MJD)	Relative			Absolute			χ^2/dof
				$\pi_{\rm rel}$ (mas)	$\mu_{\alpha,{\rm rel}}\cos\delta$ (mas yr^{-1})	$\mu_{\delta,{\rm rel}}$ (mas yr^{-1})	$\pi_{\rm abs}$ (mas)	$\mu_{\alpha,{\rm abs}}\cos\delta$ (mas yr^{-1})	$\mu_{\delta,{\rm abs}}$ (mas yr^{-1})	
2MASSI J0652307+471034	103.1273523	+47.1769607	56943.64	106.2 ± 3.3	-121.0 ± 3.2	131.8 ± 3.9	107.2 ± 3.3	-119.6 ± 3.2	128.0 ± 3.9	13.6/19
WISEPA J065609.60+420531.0	104.0406551	+42.0924547	56943.64	61.8 ± 4.1	321.2 ± 4.7	159.5 ± 2.9	63.0 ± 4.1	321.0 ± 4.7	155.5 ± 2.9	17.4/21
WISEA J065958.55+171710.9	104.9941404	+17.2857525	57362.50	36.1 ± 3.7	67.8 ± 7.7	-461.6 ± 5.0	36.7 ± 3.7	67.9 ± 7.7	-463.4 ± 5.0	16.9/21
WISEA J071552.38−114532.9	108.9691643	−11.7595200	56943.64	57.5 ± 3.7	701.8 ± 3.8	-383.4 ± 3.0	57.9 ± 3.7	697.4 ± 3.8	-383.3 ± 3.0	18.2/17
2MASS J07231462+5727081	110.8114812	+57.4512765	56943.64	40.7 ± 3.3	54.8 ± 6.5	-218.3 ± 7.9	42.0 ± 3.3	56.0 ± 6.5	-216.5 ± 7.9	9.6/15
SDSS J074149.15+235127.5	115.4537947	+23.8568550	57004.44	52.0 ± 3.7	-256.6 ± 3.6	-215.2 ± 2.5	53.0 ± 3.7	-257.5 ± 3.6	-220.1 ± 2.5	16.2/19
2MASS J07415784+0531568	115.4910435	+05.5316079	57004.49	35.7 ± 4.4	-7.8 ± 4.4	-220.5 ± 2.2	36.2 ± 4.4	-8.7 ± 4.4	-221.7 ± 2.2	39.1/21
SDSS J074201.41+205520.5	115.5038069	+20.9211147	57004.44	57.3 ± 3.3	-332.7 ± 3.5	-225.3 ± 3.9	58.4 ± 3.3	-334.4 ± 3.5	-226.7 ± 3.9	27.3/23
WISEPA J074457.15+562821.8	116.2389198	+56.4715836	56943.65	66.4 ± 2.1	154.0 ± 2.4	-757.4 ± 2.8	67.6 ± 2.1	156.0 ± 2.4	-762.0 ± 2.8	8.3/15
PSO J117.0600−01.6779	117.0599801	−01.6779513	56943.65	41.8 ± 3.7	-359.5 ± 2.5	-360.2 ± 2.3	42.6 ± 3.7	-360.6 ± 2.5	-360.2 ± 2.3	23.0/27
2MASSI J0755480+221218	118.9497938	+22.2036524	57004.54	57.7 ± 3.3	-21.7 ± 3.7	-260.8 ± 3.0	58.9 ± 3.3	-23.1 ± 3.7	-265.1 ± 3.0	16.2/23
HIP 38939B	119.5073129	−25.6506597	56972.62	55.0 ± 3.6	359.4 ± 2.8	-251.9 ± 2.9	55.6 ± 3.6	357.5 ± 2.8	-250.3 ± 2.9	15.8/15
SDSS J075840.33+324723.4	119.6670764	+32.7886558	56943.64	93.4 ± 4.4	-229.9 ± 6.6	-328.5 ± 4.7	93.7 ± 4.4	-232.1 ± 6.6	-335.6 ± 4.7	11.2/17
WISE J080700.23+413026.8	121.7510482	+41.5070214	57004.62	49.6 ± 3.8	-9.6 ± 2.7	-344.9 ± 3.1	51.1 ± 3.8	-11.2 ± 2.7	-350.6 ± 3.1	22.3/19
ULAS J080918.41+212615.2	122.3264818	+21.4373753	57004.45	27.1 ± 2.5	-170.3 ± 1.3	-113.3 ± 1.3	28.1 ± 2.5	-170.8 ± 1.3	-116.9 ± 1.3	35.1/21
SDSS J080959.01+443422.2	122.4949779	+44.5717858	57362.59	41.8 ± 3.6	-181.5 ± 2.7	-196.9 ± 2.5	42.4 ± 3.6	-181.8 ± 2.7	-203.4 ± 2.5	26.6/23
ULAS J081110.86+252931.8	122.7953952	+25.4918047	57004.55	21.4 ± 2.2	40.2 ± 1.1	-231.9 ± 1.3	22.0 ± 2.2	39.5 ± 1.1	-234.6 ± 1.3	32.4/23
WISE J081220.04+402106.2	123.0842081	+40.3517554	56972.55	32.7 ± 2.0	256.4 ± 1.2	21.8 ± 1.2	33.5 ± 2.0	255.3 ± 1.2	17.8 ± 1.2	25.9/19
WISEPA J081958.05−033529.0	124.9916995	−03.5914101	56972.62	70.0 ± 3.2	-196.4 ± 2.6	-165.7 ± 2.2	71.7 ± 3.3	-198.7 ± 2.6	-166.5 ± 2.2	20.9/21
2MASSW J0820299+450031	125.1240956	+45.0072345	57362.61	30.2 ± 3.6	-120.8 ± 3.0	-310.7 ± 2.1	30.9 ± 3.6	-116.8 ± 3.0	-316.4 ± 2.1	11.3/19

Table 7.4—Continued

Object	$\alpha_{\rm J2000}$ (deg)	$\delta_{\rm J2000}$ (deg)	Epoch (MJD)	Relative			Absolute			χ^2/dof
				$\pi_{\rm rel}$ (mas)	$\mu_{\alpha,{\rm rel}}\cos\delta$ (mas yr^{-1})	$\mu_{\delta,{\rm rel}}$ (mas yr^{-1})	$\pi_{\rm abs}$ (mas)	$\mu_{\alpha,{\rm abs}}\cos\delta$ (mas yr^{-1})	$\mu_{\delta,{\rm abs}}$ (mas yr^{-1})	
WISEPA J082131.63+144319.3	125.3819220	+14.7216843	57004.54	43.3 ± 3.9	-35.4 ± 2.7	-275.5 ± 2.8	43.7 ± 3.9	-36.0 ± 2.7	-279.2 ± 2.8	15.0/19
2MASS J08234818+2428577	125.9500839	+24.4829416	57004.56	41.0 ± 3.6	-159.3 ± 3.6	49.9 ± 2.5	42.3 ± 3.6	-160.5 ± 3.6	43.5 ± 2.5	27.0/21
WISEA J082640.45−164031.8	126.6675828	−16.6748633	56972.62	52.7 ± 4.3	-830.6 ± 4.9	500.4 ± 3.5	54.0 ± 4.3	-833.8 ± 4.9	502.0 ± 3.5	11.2/13
2MASSW J0829066+145622	127.2774580	+14.9385033	57004.56	37.5 ± 3.3	-56.1 ± 3.0	-242.7 ± 3.0	38.4 ± 3.3	-58.8 ± 3.0	-246.3 ± 3.0	17.2/21
PSO J127.5648−11.1861	127.5649719	−11.1860572	56972.62	41.7 ± 3.7	34.4 ± 3.6	-1.9 ± 2.2	42.9 ± 3.7	31.2 ± 3.6	-1.9 ± 2.2	25.6/17
SDSS J083048.80+012831.1	127.7041663	+01.4739429	57004.54	41.7 ± 4.7	186.3 ± 2.7	-360.4 ± 2.6	42.7 ± 4.7	181.6 ± 2.7	-362.2 ± 2.6	14.8/19
2MASSW J0832045−012835	128.0191493	−01.4765885	56972.63	42.3 ± 3.7	63.2 ± 5.4	3.7 ± 5.6	42.8 ± 3.7	57.5 ± 5.4	0.5 ± 5.6	9.7/15
2MASS J08355829+0548308	128.9924780	+05.8085166	57004.56	22.5 ± 2.1	-118.5 ± 2.6	-18.3 ± 3.1	23.9 ± 2.1	-120.5 ± 2.6	-21.1 ± 3.2	29.2/21
SDSSp J083717.22−000018.3	129.3216361	−00.0057419	56972.63	28.9 ± 2.7	-27.1 ± 1.8	-173.9 ± 1.8	29.8 ± 2.7	-30.5 ± 1.8	-175.7 ± 1.8	21.8/25
PSO J130.7271−06.1732	130.7270348	−06.1732514	56972.62	37.4 ± 2.8	-354.9 ± 2.2	-53.9 ± 2.0	38.3 ± 2.8	-357.8 ± 2.2	-54.4 ± 2.0	18.7/23
SDSS J085234.90+472035.0	133.1452429	+47.3415559	56972.65	41.3 ± 3.4	-49.5 ± 2.0	-394.1 ± 1.8	42.2 ± 3.4	-50.6 ± 2.0	-396.5 ± 1.8	25.4/21
PSO J133.8016−02.5658	133.8015009	−02.5656139	56972.62	20.0 ± 3.1	-146.6 ± 2.4	94.9 ± 2.3	20.8 ± 3.1	-150.7 ± 2.4	93.7 ± 2.3	9.5/23
WISEPA J085716.25+560407.6	134.3160465	+56.0685069	57006.55	75.9 ± 2.4	-702.7 ± 3.1	-236.5 ± 3.0	76.3 ± 2.4	-704.1 ± 3.1	-241.6 ± 3.0	17.5/17
SDSSp J085758.45+570851.4	134.4906367	+57.1460407	57004.62	69.7 ± 1.7	-395.5 ± 2.3	-378.1 ± 3.0	71.3 ± 1.8	-396.9 ± 2.3	-380.2 ± 3.0	25.8/19
SDSS J085834.42+325627.7	134.6410460	+32.9412661	57004.62	39.8 ± 3.6	-620.6 ± 2.3	75.7 ± 2.2	40.9 ± 3.6	-623.2 ± 2.3	71.3 ± 2.2	18.3/23
ULAS J085910.69+101017.1[a]	134.7937159	+10.1699656	57362.57	48.0 ± 2.0	-366.3 ± 2.8	-609.7 ± 3.0	48.6 ± 2.0	-369.3 ± 2.8	-612.3 ± 3.0	13.9/13
PSO J135.7840+16.9932	135.7841880	+16.9931982	57362.58	17.7 ± 4.6	34.1 ± 7.4	-24.4 ± 8.5	19.2 ± 4.6	30.3 ± 7.4	-29.8 ± 8.5	16.5/11
2MASS J09054654+5623117	136.4441149	+56.3870772	57004.62	37.3 ± 3.5	19.2 ± 2.2	102.0 ± 4.4	38.9 ± 3.5	13.2 ± 2.3	101.8 ± 4.4	11.1/15
PSO J136.5380−14.3267	136.5379781	−14.3266318	56972.61	37.0 ± 4.1	-236.1 ± 2.8	94.6 ± 3.3	37.4 ± 4.1	-240.8 ± 2.8	96.0 ± 3.3	9.9/17
2MASSI J0908380+503208	137.1558213	+50.5337375	56972.65	94.1 ± 4.0	-418.0 ± 3.4	-459.3 ± 2.9	95.2 ± 4.0	-423.6 ± 3.4	-467.5 ± 2.9	16.4/17

Table 7.4—Continued

Object	$\alpha_{\rm J2000}$ (deg)	$\delta_{\rm J2000}$ (deg)	Epoch (MJD)	Relative			Absolute			χ^2/dof
				$\pi_{\rm rel}$ (mas)	$\mu_{\alpha,{\rm rel}}\cos\delta$ (mas yr^{-1})	$\mu_{\delta,{\rm rel}}$ (mas yr^{-1})	$\pi_{\rm abs}$ (mas)	$\mu_{\alpha,{\rm abs}}\cos\delta$ (mas yr^{-1})	$\mu_{\delta,{\rm abs}}$ (mas yr^{-1})	
Gl 337CD	138.0586692	+14.9955879	57004.54	45.0 ± 3.8	-538.1 ± 3.1	253.9 ± 2.9	46.4 ± 3.8	-542.9 ± 3.1	249.8 ± 3.0	22.1/23
2MASS J09153413+0422045	138.8918805	+04.3680591	57361.60	58.3 ± 3.2	-112.2 ± 4.5	31.6 ± 2.8	59.9 ± 3.2	-116.4 ± 4.5	27.7 ± 2.8	23.5/21
WISE J092055.40+453856.3	140.2307686	+45.6479092	56972.65	77.7 ± 3.9	-79.2 ± 4.1	-844.6 ± 2.4	79.4 ± 3.9	-82.2 ± 4.1	-852.6 ± 2.4	22.4/19
2MASS J09211410−2104446	140.3100121	−21.0829945	57363.60	74.2 ± 4.6	248.9 ± 4.4	-920.6 ± 4.0	75.0 ± 4.6	244.9 ± 4.4	-918.4 ± 4.0	20.4/17
SDSS J092308.70+234013.7	140.7871008	+23.6695165	57004.54	43.5 ± 3.7	260.1 ± 3.1	-368.1 ± 2.7	43.8 ± 3.7	254.9 ± 3.1	-373.5 ± 2.7	18.6/23
WISEPC J092906.77+040957.9	142.2788390	+04.1654744	56972.61	43.7 ± 2.3	526.8 ± 3.0	-465.6 ± 2.8	45.2 ± 2.3	518.6 ± 3.0	-468.6 ± 2.8	22.6/19
2MASS J09490860−1545485	147.2854940	−15.7633959	56787.25	30.9 ± 4.0	-97.8 ± 4.0	8.7 ± 5.3	32.9 ± 4.0	-105.6 ± 4.0	9.5 ± 5.3	15.6/15
ULAS J095429.90+062309.6	148.6239076	+06.3854486	56972.63	39.7 ± 3.2	-508.5 ± 3.0	-425.8 ± 3.2	40.9 ± 3.2	-513.4 ± 3.0	-429.5 ± 3.2	15.7/17
PSO J149.0341−14.7857	149.0341911	−14.7857851	56787.25	64.2 ± 3.4	76.9 ± 4.7	-150.8 ± 4.3	65.4 ± 3.4	74.0 ± 4.7	-150.2 ± 4.3	13.9/15
PSO J149.1907−19.1730	149.1906290	−19.1728114	56787.24	33.9 ± 4.8	-104.9 ± 3.8	33.3 ± 2.9	35.0 ± 4.8	-112.3 ± 3.8	34.2 ± 2.9	18.2/13
2MASS J09593276+4523309	149.8860136	+45.3913276	57146.27	29.7 ± 2.7	-94.5 ± 2.6	-128.0 ± 3.1	30.2 ± 2.8	-105.0 ± 2.6	-138.2 ± 3.1	15.3/17
SDSS J100711.74+193056.2	151.7982947	+19.5156130	56794.28	44.8 ± 2.0	-259.2 ± 1.7	-16.1 ± 1.5	45.6 ± 2.0	-263.2 ± 1.7	-19.4 ± 1.6	25.9/23
2MASSI J1010148−040649	152.5603853	−04.1138580	56794.23	54.5 ± 4.0	-318.3 ± 3.7	-16.3 ± 1.9	55.0 ± 4.0	-324.2 ± 3.7	-17.8 ± 1.9	10.2/19
ULAS J101243.54+102101.7	153.1806583	+10.3494333	56794.28	59.6 ± 1.8	-402.1 ± 1.9	-541.7 ± 1.9	59.7 ± 1.8	-405.7 ± 1.9	-545.9 ± 1.9	26.3/23
DENIS J1019245−270717	154.8490894	−27.1212473	56787.26	47.0 ± 5.8	-636.5 ± 5.9	34.2 ± 7.5	47.8 ± 5.8	-639.7 ± 5.9	33.1 ± 7.5	11.7/7
2MASSI J1029216+162652	157.3418489	+16.4462822	56794.23	55.4 ± 4.2	364.0 ± 3.9	-360.6 ± 4.3	57.5 ± 4.3	357.8 ± 4.0	-367.5 ± 4.5	26.3/21
ULAS J102940.52+093514.6	157.4182502	+09.5872335	56972.64	66.8 ± 1.7	-414.4 ± 2.0	-139.8 ± 1.8	68.6 ± 1.7	-419.3 ± 2.0	-142.5 ± 1.8	39.8/23
SDSS J103026.78+021306.4	157.6119143	+02.2186785	56794.28	19.0 ± 2.8	67.5 ± 4.2	41.2 ± 2.5	19.5 ± 2.8	60.7 ± 4.2	38.5 ± 2.5	8.3/19
PSO J159.2399−26.3885	159.2399416	−26.3884895	57004.64	15.0 ± 3.0	-40.2 ± 2.8	-6.5 ± 3.7	15.7 ± 3.0	-48.2 ± 2.8	-8.1 ± 3.7	14.5/13
WISE J103907.73−160002.9	159.7820771	−16.0008689	56787.26	44.6 ± 2.0	-191.5 ± 2.2	-119.8 ± 2.3	45.3 ± 2.0	-197.4 ± 2.2	-120.4 ± 2.3	36.8/19

Table 7.4—Continued

Object	$\alpha_{\rm J2000}$ (deg)	$\delta_{\rm J2000}$ (deg)	Epoch (MJD)	Relative			Absolute			χ^2/dof
				$\pi_{\rm rel}$ (mas)	$\mu_{\alpha,{\rm rel}}\cos\delta$ (mas yr^{-1})	$\mu_{\delta,{\rm rel}}$ (mas yr^{-1})	$\pi_{\rm abs}$ (mas)	$\mu_{\alpha,{\rm abs}}\cos\delta$ (mas yr^{-1})	$\mu_{\delta,{\rm abs}}$ (mas yr^{-1})	
SDSS J103931.35+325625.5	159.8806045	+32.9400407	56785.28	29.8 ± 3.3	-37.4 ± 2.9	-143.4 ± 2.4	30.0 ± 3.3	-40.9 ± 2.9	-149.9 ± 2.4	38.4/31
PSO J160.0416−21.3281	160.0413740	−21.3280613	57004.64	32.8 ± 4.7	-248.1 ± 4.7	-44.7 ± 3.6	33.4 ± 4.7	-256.3 ± 4.7	-44.8 ± 3.6	14.8/11
2MASS J10430758+2225236	160.7810375	+22.4231944	56794.24	52.3 ± 2.9	-126.2 ± 2.9	-10.5 ± 3.5	52.4 ± 2.9	-131.7 ± 2.9	-11.9 ± 3.5	27.3/21
SDSS J104335.08+121314.1	160.8962861	+12.2198051	56794.24	57.8 ± 3.1	21.5 ± 3.5	-249.8 ± 3.2	59.9 ± 3.1	13.6 ± 3.5	-253.9 ± 3.2	13.2/21
SDSS J104409.43+042937.6	161.0391788	+04.4941699	56794.24	29.1 ± 3.1	-30.1 ± 3.3	94.7 ± 3.0	30.8 ± 3.1	-38.6 ± 3.3	94.0 ± 3.1	10.6/19
SDSS J104842.84+011158.5	162.1766842	+01.1986325	56794.23	66.3 ± 3.4	-443.3 ± 3.2	-229.9 ± 2.4	67.7 ± 3.4	-447.8 ± 3.2	-233.6 ± 2.4	14.2/21
WISE J105047.90+505606.2	162.6987751	+50.9348823	57004.62	43.2 ± 2.2	-434.1 ± 2.0	-57.8 ± 2.2	45.3 ± 2.2	-437.8 ± 2.0	-64.5 ± 2.2	23.1/19
2MASS J10511900+5613086	162.8274920	+56.2177664	56787.25	68.9 ± 3.6	-215.8 ± 3.5	-311.3 ± 4.3	69.5 ± 3.6	-229.2 ± 3.6	-316.7 ± 4.3	8.5/19
WISE J105257.95−194250.2	163.2418669	−19.7142913	56787.26	66.6 ± 2.2	323.9 ± 2.2	-314.5 ± 2.0	67.8 ± 2.2	318.0 ± 2.2	-314.9 ± 2.0	26.7/19
2MASS J10595185+3042059	164.9649399	+30.6992034	56785.28	37.5 ± 3.0	-228.6 ± 2.4	-531.8 ± 2.6	38.6 ± 3.0	-233.1 ± 2.4	-540.2 ± 2.7	24.6/31
2MASS J11000965+4957470	165.0394000	+49.9625025	56787.27	30.6 ± 3.9	-142.8 ± 3.9	-130.7 ± 4.1	31.7 ± 3.9	-149.3 ± 3.9	-135.2 ± 4.1	23.8/21
2MASSI J1104012+195921	166.0056222	+19.9899117	56794.24	48.0 ± 4.8	57.2 ± 4.1	127.2 ± 3.2	50.8 ± 4.8	53.8 ± 4.1	118.6 ± 3.3	21.2/21
Gl 417BC	168.1056064	+35.8029003	57146.29	39.1 ± 3.4	-241.4 ± 3.8	-144.7 ± 3.3	40.4 ± 3.4	-244.3 ± 3.8	-148.8 ± 3.3	11.5/21
WISEPC J112254.73+255021.5	170.7267702	+25.8391012	56794.25	63.0 ± 2.8	-1000.8 ± 3.0	-319.8 ± 3.5	62.9 ± 2.8	-1011.9 ± 3.0	-323.8 ± 3.5	23.7/21
WISE J112438.12−042149.7	171.1582146	−04.3636982	56794.23	56.7 ± 3.4	-562.2 ± 2.4	70.7 ± 3.0	57.3 ± 3.4	-568.8 ± 2.4	69.1 ± 3.0	15.2/19
WISEA J114724.10−204021.3	176.8503475	−20.6726658	57147.32	25.9 ± 2.0	-110.2 ± 1.9	-70.3 ± 2.9	26.7 ± 2.0	-118.2 ± 1.9	-70.7 ± 2.9	22.7/15
2MASS J11533966+5032092	178.4158502	+50.5360849	56787.27	24.9 ± 2.9	77.7 ± 3.4	30.7 ± 3.9	25.5 ± 2.9	80.1 ± 3.4	23.5 ± 4.1	22.5/19
ULAS J115508.39+044502.3	178.7855365	+04.7500025	56794.25	49.5 ± 2.3	490.6 ± 3.0	-525.4 ± 2.5	49.1 ± 2.3	488.1 ± 3.0	-529.0 ± 2.5	20.5/13
SDSS J115553.86+055957.5	178.9728258	+05.9991641	56794.24	46.2 ± 3.9	-445.6 ± 2.9	-62.3 ± 3.3	46.5 ± 3.9	-457.8 ± 2.9	-69.3 ± 3.3	12.9/21
SDSS J115700.50+061105.2	179.2525727	+06.1843196	56794.28	28.0 ± 1.7	112.7 ± 1.6	-121.3 ± 1.6	27.3 ± 1.7	106.8 ± 1.6	-128.1 ± 1.6	34.9/29

Table 7.4—Continued

Object	$\alpha_{\rm J2000}$ (deg)	$\delta_{\rm J2000}$ (deg)	Epoch (MJD)	Relative			Absolute			χ^2/dof
				$\pi_{\rm rel}$ (mas)	$\mu_{\alpha,{\rm rel}}\cos\delta$ (mas yr^{-1})	$\mu_{\delta,{\rm rel}}$ (mas yr^{-1})	$\pi_{\rm abs}$ (mas)	$\mu_{\alpha,{\rm abs}}\cos\delta$ (mas yr^{-1})	$\mu_{\delta,{\rm abs}}$ (mas yr^{-1})	
DENIS-P J1159+0057	179.9105104	+00.9574351	57146.35	34.0 ± 3.7	18.5 ± 5.8	-4.1 ± 5.7	35.2 ± 3.7	17.3 ± 5.8	-9.3 ± 5.7	26.3/23
PSO J180.1475−28.6160	180.1469618	−28.6159943	56787.28	40.5 ± 5.4	-551.7 ± 3.8	-34.3 ± 4.1	40.7 ± 5.4	-561.7 ± 3.8	-36.9 ± 4.1	3.6/7
SDSSp J120358.19+001550.3	180.9873617	+00.2628150	56824.25	64.2 ± 3.5	-1216.4 ± 3.5	-282.3 ± 3.4	66.4 ± 3.5	-1224.2 ± 3.5	-288.4 ± 3.4	17.5/23
2MASSI J1204303+321259	181.1269534	+32.2164505	57007.68	38.8 ± 3.1	80.2 ± 4.2	-23.7 ± 4.7	40.2 ± 3.1	69.4 ± 4.2	-24.2 ± 4.7	25.5/25
ULAS J120444.67−015034.9	181.1855105	−01.8427723	56823.24	27.0 ± 1.7	-395.1 ± 1.2	135.5 ± 1.6	27.5 ± 1.7	-403.8 ± 1.2	130.3 ± 1.6	17.3/21
SDSS J120602.51+281328.7	181.5106251	+28.2244787	56824.25	33.1 ± 2.4	53.7 ± 2.4	-71.1 ± 2.9	34.0 ± 2.4	53.7 ± 2.4	-74.7 ± 2.9	27.7/25
SDSS J120747.17+024424.8	181.9446135	+02.7407923	56824.25	44.8 ± 3.5	-496.0 ± 4.5	129.8 ± 3.3	44.8 ± 3.6	-501.5 ± 4.5	126.6 ± 3.3	18.2/23
2MASSI J1213033−043243	183.2625108	−04.5455650	56824.24	55.7 ± 3.8	-359.6 ± 2.7	-30.6 ± 2.3	56.3 ± 3.8	-380.9 ± 2.7	-33.4 ± 2.4	25.7/19
SDSS J121951.45+312849.4	184.9636201	+31.4804071	56824.26	49.8 ± 3.7	-248.3 ± 3.0	-9.8 ± 2.5	52.0 ± 3.8	-253.4 ± 3.1	-19.4 ± 2.6	16.7/19
2MASS J12212770+0257198	185.3649567	+02.9553712	56824.25	52.2 ± 3.6	-141.6 ± 3.0	-38.1 ± 3.4	52.9 ± 3.6	-144.1 ± 3.0	-43.4 ± 3.5	41.2/25
WISE J122558.86−101345.0	186.4951720	−10.2295571	56824.24	39.9 ± 2.9	-153.9 ± 2.6	-332.7 ± 2.2	41.1 ± 2.9	-158.8 ± 2.6	-335.0 ± 2.2	17.0/19
2MASS J12312141+4959234	187.8389049	+49.9897652	57007.68	24.8 ± 2.8	-39.2 ± 3.8	-31.0 ± 4.5	28.3 ± 3.1	-49.4 ± 3.9	-35.2 ± 4.9	15.5/23
2MASS J12314753+0847331	187.9434323	+08.7884044	56824.25	69.8 ± 3.6	-1177.5 ± 2.8	-1033.8 ± 3.3	70.2 ± 3.6	-1181.7 ± 2.8	-1038.4 ± 3.3	18.5/19
2MASS J12321827−0951502	188.0754524	−09.8644121	56823.24	33.3 ± 4.4	-172.3 ± 2.8	-119.0 ± 2.6	34.5 ± 4.5	-182.5 ± 2.8	-122.8 ± 2.6	21.0/19
NLTT 31450B	189.9549651	+32.1507152	57031.63	26.4 ± 2.5	-23.5 ± 3.0	-183.3 ± 2.7	27.2 ± 2.5	-29.3 ± 3.0	-186.5 ± 2.8	25.2/23
2MASSW J1246467+402715	191.6956827	+40.4537918	56824.26	46.9 ± 5.1	146.2 ± 3.7	-99.3 ± 2.9	48.4 ± 5.1	137.2 ± 3.7	-112.7 ± 3.0	19.6/19
SDSS J125011.65+392553.9	192.5484641	+39.4290963	56824.26	40.8 ± 3.2	-38.0 ± 3.4	-826.2 ± 2.6	42.8 ± 3.2	-42.4 ± 3.4	-830.5 ± 2.6	11.7/17
WISE J125015.56+262846.9	192.5643219	+26.4790478	56824.26	56.1 ± 3.7	-475.6 ± 3.4	-555.2 ± 2.5	57.5 ± 3.7	-484.4 ± 3.4	-557.3 ± 2.5	16.8/21
WISE J125448.52−072828.4	193.7020916	−07.4747280	56824.25	40.3 ± 2.7	6.0 ± 2.7	-129.5 ± 3.0	41.1 ± 2.7	1.3 ± 2.7	-133.7 ± 3.0	21.6/17
2MASS J12565688+0146163	194.2362372	+01.7710925	56824.27	26.8 ± 4.8	-196.5 ± 4.8	-32.5 ± 3.3	28.1 ± 4.9	-210.9 ± 4.8	-40.4 ± 3.4	34.0/19

Table 7.4—Continued

Object	$\alpha_{\rm J2000}$ (deg)	$\delta_{\rm J2000}$ (deg)	Epoch (MJD)	Relative			Absolute			χ^2/dof
				$\pi_{\rm rel}$ (mas)	$\mu_{\alpha,{\rm rel}}\cos\delta$ (mas yr^{-1})	$\mu_{\delta,{\rm rel}}$ (mas yr^{-1})	$\pi_{\rm abs}$ (mas)	$\mu_{\alpha,{\rm abs}}\cos\delta$ (mas yr^{-1})	$\mu_{\delta,{\rm abs}}$ (mas yr^{-1})	
WISE J125715.90+400854.2	194.3167050	+40.1485036	56824.27	55.4 ± 1.8	296.4 ± 1.7	172.7 ± 1.4	57.0 ± 1.8	294.9 ± 1.7	168.0 ± 1.4	21.4/21
2MASSW J1300425+191235	195.1737486	+19.2046425	56824.25	66.6 ± 3.2	-799.2 ± 3.0	-1244.4 ± 3.0	67.5 ± 3.2	-807.4 ± 3.0	-1253.5 ± 3.1	51.0/23
ULAS J131610.13+031205.5	199.0418441	+03.2015253	57146.38	28.5 ± 2.4	-210.2 ± 2.9	-13.5 ± 3.3	29.0 ± 2.4	-221.6 ± 2.9	-19.5 ± 3.3	14.9/17
PSO J201.0320+19.1072	201.0318986	+19.1071568	56824.25	33.7 ± 3.9	-105.2 ± 2.8	-101.2 ± 2.8	33.6 ± 3.9	-114.2 ± 2.8	-101.8 ± 2.8	10.1/21
2MASSW J1326201−272937	201.5819623	−27.4937107	57150.38	56.4 ± 5.9	-357.9 ± 4.7	-22.8 ± 5.7	54.7 ± 5.9	-364.8 ± 4.7	-25.0 ± 5.7	10.3/13
SDSSp J132629.82−003831.5	201.6232796	−00.6425142	56824.24	46.7 ± 2.9	-227.4 ± 4.9	-100.9 ± 5.1	47.9 ± 2.9	-233.4 ± 5.0	-107.7 ± 5.2	8.5/15
PSO J202.1635−03.7660	202.1633230	−03.7659816	56824.24	31.1 ± 2.4	-255.6 ± 2.7	45.2 ± 2.5	31.7 ± 2.4	-263.7 ± 2.7	40.0 ± 2.5	24.4/17
2MASS J13373116+4938367	204.3802355	+49.6438188	57031.68	24.3 ± 4.0	55.6 ± 4.3	73.0 ± 4.0	26.7 ± 4.0	44.2 ± 4.3	69.2 ± 4.2	4.9/17
WISE J133750.46+263648.6	204.4604990	+26.6131963	56824.27	39.7 ± 2.1	126.9 ± 2.1	-275.7 ± 2.8	40.4 ± 2.1	118.0 ± 2.1	-282.4 ± 2.8	6.2/17
2MASSW J1338261+414034	204.6081045	+41.6747591	56824.26	45.0 ± 4.2	-154.5 ± 3.1	-304.7 ± 4.4	45.5 ± 4.2	-161.0 ± 3.2	-313.1 ± 4.5	13.0/17
2MASS J13384944+0437315	204.7064611	+04.6245332	56824.27	27.4 ± 2.9	113.0 ± 2.2	-229.8 ± 2.2	29.2 ± 2.9	104.5 ± 2.2	-234.1 ± 2.2	21.5/21
2MASSW J1343167+394508	205.8173370	+39.7529089	57146.37	30.9 ± 3.4	-322.9 ± 5.8	116.2 ± 4.1	30.2 ± 3.4	-327.8 ± 5.8	109.9 ± 4.1	20.2/17
LHS 2803B	207.0096457	−13.7372689	56822.27	60.4 ± 3.6	-677.9 ± 2.6	-507.5 ± 4.7	59.5 ± 3.6	-686.6 ± 2.6	-514.4 ± 4.7	27.6/13
PSO J207.7496+29.4240	207.7494853	+29.4240075	56824.27	26.8 ± 1.9	-145.9 ± 1.5	-84.0 ± 1.4	27.3 ± 1.9	-148.8 ± 1.5	-89.9 ± 1.4	14.3/19
SDSS J135852.68+374711.9	209.7194523	+37.7852568	56824.26	48.5 ± 3.1	-21.4 ± 2.8	-448.2 ± 2.5	49.6 ± 3.1	-27.0 ± 2.8	-455.7 ± 2.5	20.1/17
SDSS J140023.12+433822.3	210.0953533	+43.6395455	56826.29	39.1 ± 3.2	-233.7 ± 3.0	5.4 ± 3.6	40.8 ± 3.2	-239.8 ± 3.0	0.2 ± 3.7	10.3/17
2MASSW J1411175+393636	212.8174135	+39.6106357	57146.44	29.4 ± 4.2	-918.7 ± 2.8	114.7 ± 4.6	30.1 ± 4.2	-923.8 ± 2.8	108.9 ± 4.6	29.0/15
2MASSW J1412244+163312	213.1021852	+16.5528275	56822.33	27.3 ± 5.9	16.8 ± 7.8	-106.1 ± 9.4	29.0 ± 5.9	5.2 ± 7.8	-112.5 ± 9.4	4.6/15
SDSS J141530.05+572428.7	213.8755345	+57.4068655	56856.25	24.7 ± 3.6	52.5 ± 3.3	-355.0 ± 3.1	25.6 ± 3.6	51.1 ± 3.3	-355.5 ± 3.1	14.3/19
2MASSW J1421314+182740	215.3777646	+18.4605909	56824.28	36.1 ± 6.7	-758.9 ± 7.4	-151.5 ± 8.1	34.2 ± 6.7	-764.5 ± 7.5	-150.2 ± 8.1	21.2/21

Table 7.4—Continued

Object	$\alpha_{\rm J2000}$ (deg)	$\delta_{\rm J2000}$ (deg)	Epoch (MJD)	Relative			Absolute			χ^2/dof
				$\pi_{\rm rel}$ (mas)	$\mu_{\alpha,{\rm rel}}\cos\delta$ (mas yr^{-1})	$\mu_{\delta,{\rm rel}}$ (mas yr^{-1})	$\pi_{\rm abs}$ (mas)	$\mu_{\alpha,{\rm abs}}\cos\delta$ (mas yr^{-1})	$\mu_{\delta,{\rm abs}}$ (mas yr^{-1})	
2MASS J14283132+5923354	217.1289512	+59.3926715	56822.27	42.6 ± 5.6	-197.2 ± 4.5	-123.4 ± 5.0	44.4 ± 5.6	-201.9 ± 4.6	-124.0 ± 5.0	23.2/21
VHS J143311.46−083736.3	218.2973840	−08.6269309	56822.28	61.8 ± 3.6	-291.2 ± 3.6	-213.1 ± 2.6	62.2 ± 3.6	-295.4 ± 3.6	-217.4 ± 2.6	11.0/15
SDSS J143553.25+112948.6	218.9722580	+11.4971986	57145.48	33.3 ± 3.7	104.3 ± 3.2	93.4 ± 2.6	36.4 ± 3.7	100.2 ± 3.2	86.3 ± 2.6	12.4/15
WISEPA J143602.19−181421.8	219.0091334	−18.2394892	56822.32	48.3 ± 4.5	-65.7 ± 2.4	-91.6 ± 2.4	48.9 ± 4.5	-70.8 ± 2.4	-96.1 ± 2.4	34.7/17
WISE J144806.48−253420.3	222.0272126	−25.5733626	57151.40	47.6 ± 3.4	130.3 ± 3.1	-735.0 ± 3.0	47.7 ± 3.4	124.8 ± 3.1	-738.5 ± 3.0	16.2/19
2MASSW J1448256+103159	222.1077952	+10.5326366	56824.28	74.9 ± 4.4	224.7 ± 3.9	-116.7 ± 3.6	74.0 ± 4.4	218.7 ± 3.9	-124.6 ± 3.6	27.4/23
HIP 73169B	224.2973981	−06.3242568	57148.43	27.1 ± 3.5	-264.7 ± 4.9	-75.9 ± 4.4	26.6 ± 3.5	-269.8 ± 4.9	-83.8 ± 4.5	19.2/15
WISEPC J145715.03+581510.2	224.3116319	+58.2527673	56822.28	46.0 ± 5.7	-487.2 ± 5.0	-62.5 ± 4.9	46.8 ± 5.8	-488.5 ± 5.0	-65.8 ± 4.9	13.4/13
PSO J224.3820+47.4057	224.3823151	+47.4055900	56822.37	48.0 ± 2.9	143.9 ± 3.0	-78.3 ± 2.3	49.5 ± 2.9	140.0 ± 3.0	-84.7 ± 2.3	14.9/17
HIP 73786B	226.2391254	+05.6326153	57145.39	55.9 ± 4.3	-596.5 ± 3.5	-497.3 ± 3.3	56.7 ± 4.3	-599.6 ± 3.5	-502.6 ± 3.3	29.7/19
PSO J226.2599−28.8959	226.2601555	−28.8964881	56865.23	37.2 ± 10.6	111.4 ± 5.2	-443.3 ± 4.0	37.4 ± 10.6	105.0 ± 5.2	-443.2 ± 4.0	22.2/15
2MASSW J1506544+132106	226.7220133	+13.3516774	56824.28	83.1 ± 4.1	-1063.9 ± 4.4	-7.9 ± 3.7	84.3 ± 4.1	-1066.8 ± 4.4	-14.3 ± 3.8	26.0/23
SDSS J151240.67+340350.1	228.1704652	+34.0639236	56826.29	41.4 ± 4.6	241.8 ± 3.9	-13.6 ± 4.8	40.8 ± 4.6	233.5 ± 3.9	-13.9 ± 4.9	18.2/21
2MASSW J1515008+484742	228.7479333	+48.8007288	56822.34	103.0 ± 3.5	-936.3 ± 3.0	1465.4 ± 3.5	104.5 ± 3.5	-944.5 ± 3.0	1460.8 ± 3.6	16.8/17
SDSS J151506.11+443648.3	228.7759435	+44.6133722	56826.29	27.2 ± 3.8	98.4 ± 3.4	0.4 ± 3.3	27.8 ± 3.8	92.9 ± 3.4	-5.4 ± 3.3	14.5/17
SDSS J151643.01+305344.4	229.1789687	+30.8957679	56826.29	47.4 ± 2.7	-79.3 ± 3.3	13.2 ± 2.9	48.2 ± 2.7	-82.3 ± 3.3	8.1 ± 2.9	28.8/25
WISE J151721.13+052929.3	229.3379174	+05.4917402	57145.40	44.5 ± 2.1	-61.1 ± 2.6	200.3 ± 2.6	46.1 ± 2.1	-65.6 ± 2.6	196.5 ± 2.6	28.6/19
SDSS J152039.82+354619.8	230.1672960	+35.7709182	57145.44	57.3 ± 4.8	322.4 ± 5.0	-374.1 ± 5.7	57.4 ± 4.8	318.0 ± 5.0	-385.6 ± 5.7	8.6/17
SDSS J152103.24+013142.7	230.2628912	+01.5287613	56824.28	42.4 ± 6.2	-170.5 ± 4.4	50.2 ± 3.9	43.3 ± 6.2	-175.7 ± 4.4	43.4 ± 4.0	22.6/17
2MASS J15230657−2347526	230.7766717	−23.7979978	56856.29	33.0 ± 4.4	-154.4 ± 5.0	-17.3 ± 4.0	33.8 ± 4.4	-159.5 ± 5.0	-20.8 ± 4.0	3.4/13

Table 7.4—Continued

Object	$\alpha_{\rm J2000}$ (deg)	$\delta_{\rm J2000}$ (deg)	Epoch (MJD)	Relative			Absolute			χ^2/dof
				$\pi_{\rm rel}$ (mas)	$\mu_{\alpha,{\rm rel}}\cos\delta$ (mas yr^{-1})	$\mu_{\delta,{\rm rel}}$ (mas yr^{-1})	$\pi_{\rm abs}$ (mas)	$\mu_{\alpha,{\rm abs}}\cos\delta$ (mas yr^{-1})	$\mu_{\delta,{\rm abs}}$ (mas yr^{-1})	
2MASSI J1526140+204341	231.5574453	+20.7264597	56824.28	42.5 ± 5.3	-214.2 ± 4.0	-354.6 ± 3.6	44.1 ± 5.3	-216.2 ± 4.0	-363.0 ± 3.6	14.9/19
SDSS J153453.33+121949.2	233.7227077	+12.3302811	56822.33	46.1 ± 4.1	170.4 ± 3.4	-30.0 ± 5.6	46.7 ± 4.2	166.8 ± 3.4	-46.0 ± 5.7	24.8/19
SDSS J154009.36+374230.3	235.0382475	+37.7072736	56822.34	39.6 ± 4.7	-203.7 ± 5.1	-383.6 ± 5.7	40.8 ± 4.7	-203.4 ± 5.1	-389.0 ± 5.7	17.5/17
VHS J154352.78−043909.6	235.9698923	−04.6526419	56823.35	33.9 ± 4.4	-92.6 ± 3.9	-15.3 ± 3.1	33.6 ± 4.4	-99.0 ± 3.9	-19.7 ± 3.1	10.9/19
WISE J154459.27+584204.5	236.2468757	+58.7007678	56822.28	48.2 ± 1.9	-65.2 ± 1.9	-524.1 ± 1.8	49.1 ± 1.9	-68.5 ± 1.9	-527.4 ± 1.8	24.8/19
2MASS J15461461+4932114	236.5621542	+49.5336232	56822.35	45.0 ± 5.4	162.6 ± 3.3	-672.8 ± 3.7	46.5 ± 5.4	159.2 ± 3.3	-677.4 ± 3.8	19.0/17
2MASS J15485834−1636018	237.2421780	−16.6010180	56856.29	41.5 ± 3.4	-202.3 ± 4.1	-127.1 ± 3.5	42.3 ± 3.4	-212.3 ± 4.1	-129.9 ± 3.5	4.5/13
2MASS J15500845+1455180[b]	237.5357549	+14.9210420	57145.48	23.4 ± 3.0	106.7 ± 4.5	-134.7 ± 4.5	24.7 ± 3.0	102.3 ± 4.5	-136.3 ± 4.5	23.4/21
SDSS J155120.86+432930.3	237.8372079	+43.4916703	56826.29	16.9 ± 3.9	29.4 ± 3.0	-35.4 ± 4.6	17.3 ± 3.9	24.3 ± 3.0	-40.6 ± 4.6	18.9/15
2MASSW J1615441+355900	243.9339126	+35.9811448	56854.38	45.1 ± 3.4	-30.9 ± 3.8	-536.7 ± 4.0	46.0 ± 3.4	-36.0 ± 3.8	-537.0 ± 4.0	24.7/21
WISEPA J161705.75+180714.3	244.2740597	+18.1205790	56855.28	77.9 ± 3.1	101.3 ± 4.5	-34.0 ± 3.1	78.0 ± 3.1	94.2 ± 4.5	-38.9 ± 3.1	8.8/19
SDSS J161928.31+005011.9	244.8682459	+00.8363276	56855.34	35.7 ± 2.8	50.3 ± 3.0	-81.5 ± 4.2	35.7 ± 2.8	45.2 ± 3.0	-85.2 ± 4.2	18.9/21
PSO J246.1033−19.6194	246.1035576	−19.6194839	56856.29	41.6 ± 3.0	126.3 ± 2.4	-118.3 ± 3.7	43.5 ± 3.0	124.5 ± 2.4	-123.1 ± 3.7	15.3/17
WISEPA J162725.64+325525.5	246.8567814	+32.9231383	56854.38	51.9 ± 2.2	-83.2 ± 3.9	-347.4 ± 3.6	52.1 ± 2.2	-87.0 ± 3.9	-350.9 ± 3.6	9.3/15
PSO J247.3273+03.5932	247.3276818	+03.5931022	56830.43	75.9 ± 3.5	227.5 ± 3.1	-151.3 ± 3.9	76.5 ± 3.5	227.0 ± 3.1	-155.2 ± 3.9	22.1/21
SDSS J163022.92+081822.0	247.5953695	+08.3058008	56830.43	44.7 ± 4.7	-56.8 ± 4.5	-100.9 ± 3.6	45.1 ± 4.7	-60.7 ± 4.5	-106.6 ± 3.6	9.9/17
SDSS J163030.53+434404.0	247.6265916	+43.7344671	56857.29	44.0 ± 2.6	-147.0 ± 3.1	37.4 ± 2.7	44.7 ± 2.6	-151.4 ± 3.1	31.4 ± 2.7	21.5/21
WISE J163236.47+032927.3	248.1520916	+03.4910357	56830.43	37.4 ± 3.1	78.8 ± 3.1	49.5 ± 2.9	37.4 ± 3.1	75.8 ± 3.1	45.9 ± 2.9	12.2/19
WISE J163645.56−074325.1	249.1900701	−07.7238141	56856.29	31.7 ± 5.1	-52.7 ± 5.0	-128.8 ± 3.2	32.5 ± 5.1	-55.0 ± 5.0	-133.2 ± 3.2	12.8/15
2MASS J16452207+3004071	251.3416476	+30.0683880	57145.48	35.5 ± 3.9	-83.6 ± 4.7	-63.2 ± 4.1	36.9 ± 3.9	-78.5 ± 4.7	-68.2 ± 4.2	17.7/21

Table 7.4—Continued

Object	$\alpha_{\rm J2000}$ (deg)	$\delta_{\rm J2000}$ (deg)	Epoch (MJD)	Relative			Absolute			χ^2/dof
				$\pi_{\rm rel}$ (mas)	$\mu_{\alpha,{\rm rel}}\cos\delta$ (mas yr^{-1})	$\mu_{\delta,{\rm rel}}$ (mas yr^{-1})	$\pi_{\rm abs}$ (mas)	$\mu_{\alpha,{\rm abs}}\cos\delta$ (mas yr^{-1})	$\mu_{\delta,{\rm abs}}$ (mas yr^{-1})	
WISEPA J164715.59+563208.2	251.8145536	+56.5360303	57145.47	41.8 ± 2.1	-183.2 ± 1.4	247.7 ± 2.6	42.7 ± 2.1	-184.6 ± 1.4	241.0 ± 2.6	32.4/17
WISEPA J165311.05+444423.9	253.2958734	+44.7392400	56854.39	75.1 ± 1.9	-75.6 ± 1.8	-394.4 ± 2.3	75.7 ± 1.9	-76.0 ± 1.8	-398.1 ± 2.3	13.2/17
2MASS J16573454+1054233	254.3936301	+10.9061879	56830.42	41.5 ± 4.0	-90.5 ± 3.5	-91.9 ± 2.5	42.4 ± 4.0	-91.8 ± 3.5	-96.3 ± 2.5	15.3/21
WISE J165842.56+510335.0	254.6768730	+51.0594226	56824.49	29.3 ± 4.5	-280.1 ± 3.8	-285.8 ± 3.9	30.2 ± 4.5	-282.3 ± 3.8	-290.4 ± 3.9	11.8/9
WISE J170745.85−174452.5	256.9413350	−17.7479012	56856.29	78.5 ± 3.2	172.2 ± 2.8	-6.5 ± 3.0	79.2 ± 3.2	169.9 ± 2.8	-9.7 ± 3.0	17.2/17
2MASS J17114559+4028578	257.9415109	+40.4831088	56854.38	44.6 ± 4.3	254.6 ± 4.4	76.7 ± 3.5	46.5 ± 4.3	254.8 ± 4.4	67.2 ± 3.5	15.5/17
PSO J258.2413+06.7612	258.2412066	+06.7611522	56830.42	21.9 ± 3.6	-192.0 ± 2.9	-124.5 ± 3.1	22.2 ± 3.6	-193.6 ± 2.9	-127.0 ± 3.1	12.8/17
WISE J172134.46+111739.4	260.3935007	+11.2944725	56830.43	48.4 ± 4.2	-95.8 ± 3.5	142.5 ± 1.6	48.4 ± 4.2	-97.1 ± 3.5	135.8 ± 1.6	13.5/17
PSO J260.9762+04.2354	260.9761774	+04.2354761	56855.34	31.1 ± 2.4	-211.3 ± 2.2	20.3 ± 1.1	31.8 ± 2.4	-212.9 ± 2.2	15.7 ± 1.1	49.9/25
WISEPA J172844.93+571643.6	262.1875160	+57.2787464	56824.51	38.4 ± 2.5	92.3 ± 1.7	124.4 ± 1.9	39.3 ± 2.5	90.7 ± 1.7	122.5 ± 1.9	25.8/21
WISE J173421.02+502349.9	263.5878380	+50.3977980	56854.38	38.9 ± 3.7	-29.9 ± 2.9	302.9 ± 3.6	39.7 ± 3.7	-30.8 ± 2.9	295.6 ± 3.6	14.7/19
WISE J174113.12+132711.9	265.3047009	+13.4531197	56855.35	25.2 ± 3.2	-44.0 ± 2.8	-193.4 ± 2.4	26.0 ± 3.2	-44.4 ± 2.8	-197.9 ± 2.4	22.8/25
WISE J174303.71+421150.0	265.7655821	+42.1965830	56854.38	53.5 ± 4.2	29.7 ± 3.5	-515.2 ± 6.6	54.8 ± 4.2	30.2 ± 3.5	-519.2 ± 6.6	28.4/15
2MASS J17461199+5034036	266.5517669	+50.5677156	56854.38	44.6 ± 2.7	288.2 ± 4.1	27.4 ± 4.2	45.9 ± 2.7	286.8 ± 4.1	25.7 ± 4.2	9.1/19
WISE J174640.78−033818.0	266.6698128	−03.6383922	56824.50	32.1 ± 2.7	-36.2 ± 2.9	-103.7 ± 2.9	32.8 ± 2.7	-37.9 ± 2.9	-107.1 ± 2.9	17.2/19
SDSS J175024.01+422237.8	267.5991562	+42.3774154	56854.38	31.4 ± 3.4	-43.8 ± 2.9	74.0 ± 3.2	32.2 ± 3.4	-46.2 ± 2.9	71.2 ± 3.2	22.4/19
SDSSp J175032.96+175903.9	267.6381058	+17.9848492	56855.34	44.2 ± 3.0	184.3 ± 2.3	96.2 ± 3.3	44.5 ± 3.0	183.0 ± 2.3	92.0 ± 3.3	31.9/25
2MASS J17545447+1649196	268.7275125	+16.8216271	56830.43	63.9 ± 3.4	108.4 ± 3.5	-148.3 ± 3.9	64.3 ± 3.4	106.8 ± 3.5	-152.6 ± 3.9	16.4/17
WISE J175510.28+180320.2	268.7924675	+18.0557150	56830.43	50.9 ± 4.8	-424.8 ± 2.3	12.2 ± 2.6	51.5 ± 4.8	-425.9 ± 2.3	6.6 ± 2.6	20.5/19
2MASS J18000116−1559235	270.0048566	−15.9912325	57144.56	70.4 ± 5.2	-8.8 ± 3.5	-294.2 ± 3.6	70.5 ± 5.2	-10.8 ± 3.5	-298.0 ± 3.6	7.2/15

Table 7.4—Continued

Object	$\alpha_{\rm J2000}$ (deg)	$\delta_{\rm J2000}$ (deg)	Epoch (MJD)	Relative			Absolute			χ^2/dof
				$\pi_{\rm rel}$ (mas)	$\mu_{\alpha,{\rm rel}}\cos\delta$ (mas yr^{-1})	$\mu_{\delta,{\rm rel}}$ (mas yr^{-1})	$\pi_{\rm abs}$ (mas)	$\mu_{\alpha,{\rm abs}}\cos\delta$ (mas yr^{-1})	$\mu_{\delta,{\rm abs}}$ (mas yr^{-1})	
WISEP J180026.60+013453.1	270.1111322	+01.5809740	56824.49	126.8 ± 4.7	180.3 ± 2.6	-383.1 ± 4.3	126.9 ± 4.7	178.4 ± 2.6	-386.2 ± 4.3	16.9/21
PSO J272.0887−04.9943	272.0888885	−04.9943237	57144.58	41.9 ± 2.0	55.2 ± 2.7	-57.7 ± 3.7	42.8 ± 2.0	53.8 ± 2.7	-61.1 ± 3.7	12.8/17
WISE J180901.07+383805.4	272.2536901	+38.6342599	56824.50	51.6 ± 2.3	-589.0 ± 2.5	-504.8 ± 2.3	52.4 ± 2.3	-590.5 ± 2.5	-506.6 ± 2.3	18.7/17
WISE J180952.53−044812.5	272.4688212	−04.8039786	56824.49	48.6 ± 3.4	-41.2 ± 2.9	-411.4 ± 2.3	49.3 ± 3.4	-42.2 ± 2.9	-416.0 ± 2.3	23.1/25
WISE J181329.40+283533.3	273.3720975	+28.5917470	56783.63	72.9 ± 2.0	-207.4 ± 2.0	-463.0 ± 2.9	73.6 ± 2.0	-208.9 ± 2.0	-468.0 ± 2.9	19.4/21
PSO J276.8234+22.4380	276.8235397	+22.4380635	56783.63	24.6 ± 3.1	69.9 ± 3.2	1.7 ± 5.2	25.1 ± 3.1	68.2 ± 3.2	-2.4 ± 5.2	16.3/15
WISE J185101.83+593508.6	282.7578051	+59.5862574	56821.50	35.0 ± 5.1	35.9 ± 3.5	428.6 ± 5.2	35.8 ± 5.1	36.6 ± 3.5	424.6 ± 5.2	13.7/21
WISEPA J185215.78+353716.3	283.0661081	+35.6208886	56824.50	65.1 ± 2.9	256.1 ± 2.9	-284.2 ± 3.1	66.3 ± 2.9	254.6 ± 2.9	-288.2 ± 3.1	24.2/25
2MASS J19010601+4718136	285.2760048	+47.3056075	56824.50	53.8 ± 4.3	125.7 ± 3.7	413.8 ± 4.1	54.5 ± 4.3	125.1 ± 3.7	410.7 ± 4.1	24.5/27
WISEPA J190624.75+450808.2	286.6031079	+45.1349437	56824.50	53.3 ± 3.0	-21.9 ± 2.6	-348.2 ± 2.8	54.1 ± 3.0	-24.7 ± 2.6	-354.0 ± 2.8	22.7/29
DENIS-P J1909081−193748	287.2840853	−19.6306269	57144.59	49.7 ± 4.8	-32.5 ± 3.6	-150.3 ± 4.2	49.8 ± 4.8	-33.3 ± 3.6	-154.9 ± 4.2	11.0/19
WISE J191915.54+304558.4	289.8153888	+30.7667920	56824.49	45.5 ± 4.1	390.7 ± 3.5	415.6 ± 3.9	46.3 ± 4.1	388.9 ± 3.5	411.5 ± 3.9	24.0/25
WISE J192841.35+235604.9	292.1719242	+23.9349438	56824.49	145.1 ± 5.2	-246.1 ± 3.6	240.8 ± 3.5	146.0 ± 5.2	-247.4 ± 3.6	236.1 ± 3.5	18.1/21
WISE J195500.42−254013.9	298.7521566	−25.6707389	56782.63	43.4 ± 3.9	350.7 ± 2.9	-251.9 ± 3.0	43.9 ± 3.9	350.2 ± 2.9	-260.4 ± 3.0	28.7/21
WISE J200050.19+362950.1	300.2091489	+36.4977043	56785.63	130.8 ± 2.9	3.5 ± 3.3	373.8 ± 4.1	131.2 ± 2.9	1.9 ± 3.3	368.4 ± 4.1	17.9/21
2MASS J20025073−0521524	300.7109117	−05.3650210	56816.60	49.7 ± 3.4	-115.1 ± 2.8	-114.6 ± 2.8	51.6 ± 3.4	-115.5 ± 2.8	-118.6 ± 2.8	18.7/21
WISE J200804.71−083428.5	302.0200048	−08.5747289	56816.60	53.7 ± 3.8	302.7 ± 1.7	-157.2 ± 3.1	54.2 ± 3.8	301.6 ± 1.7	-163.0 ± 3.1	26.8/21
WISE J201404.13+042408.5	303.5164652	+04.4027433	56818.54	45.3 ± 2.4	-610.9 ± 1.7	314.9 ± 1.7	45.5 ± 2.4	-612.4 ± 1.7	310.2 ± 1.7	35.1/17
SDSS J202820.32+005226.5	307.0852312	+00.8740525	56794.63	30.7 ± 2.1	93.4 ± 2.0	-8.8 ± 2.5	31.0 ± 2.1	92.8 ± 2.0	-13.0 ± 2.5	23.4/31
WISE J203042.79+074934.7	307.6791102	+07.8262055	56794.63	101.5 ± 5.7	657.0 ± 3.5	-107.3 ± 2.8	102.6 ± 5.7	658.0 ± 3.5	-114.7 ± 2.8	28.6/29

Table 7.4—Continued

Object	$\alpha_{\rm J2000}$ (deg)	$\delta_{\rm J2000}$ (deg)	Epoch (MJD)	Relative			Absolute			χ^2/dof
				$\pi_{\rm rel}$ (mas)	$\mu_{\alpha,{\rm rel}}\cos\delta$ (mas yr^{-1})	$\mu_{\delta,{\rm rel}}$ (mas yr^{-1})	$\pi_{\rm abs}$ (mas)	$\mu_{\alpha,{\rm abs}}\cos\delta$ (mas yr^{-1})	$\mu_{\delta,{\rm abs}}$ (mas yr^{-1})	
UGPS J20480024+503821.9[a]	312.0014017	+50.6400121	57680.24	31.8 ± 4.6	106.6 ± 15.1	318.6 ± 11.1	32.3 ± 4.6	104.5 ± 15.1	318.4 ± 11.1	6.9/9
2MASSI J2107316−030733	316.8827483	−03.1261029	57163.63	27.3 ± 3.5	147.8 ± 3.7	-17.3 ± 2.7	27.8 ± 3.5	148.5 ± 3.7	-24.3 ± 2.7	22.0/19
PSO J319.3102−29.6682	319.3104547	−29.6683078	56820.56	50.1 ± 6.8	138.3 ± 4.5	-165.7 ± 4.8	52.4 ± 6.8	139.3 ± 4.5	-171.0 ± 4.8	8.9/11
WISE J212321.92−261405.1	320.8412472	−26.2346175	56820.60	39.4 ± 4.7	49.2 ± 2.2	-20.8 ± 2.3	40.3 ± 4.7	51.8 ± 2.2	-26.0 ± 2.3	20.2/17
SDSS J212413.89+010000.3	321.0585791	+01.0010399	56799.63	56.0 ± 3.2	186.1 ± 2.9	268.8 ± 2.0	57.0 ± 3.2	186.2 ± 2.9	262.1 ± 2.0	18.7/23
2MASSW J2130446−084520	322.6875191	−08.7558424	56818.61	38.6 ± 3.6	343.6 ± 3.2	-37.6 ± 2.9	39.6 ± 3.6	349.3 ± 3.2	-40.3 ± 2.9	14.2/19
PSO J323.1320+29.5308	323.1321491	+29.5309855	56794.63	32.7 ± 4.0	138.9 ± 1.7	174.0 ± 1.4	33.1 ± 4.0	137.2 ± 1.7	169.1 ± 1.4	58.9/31
2MASS J21324898−1452544	323.2036912	−14.8824123	56820.60	36.0 ± 4.1	-118.4 ± 4.0	-160.2 ± 4.3	37.0 ± 4.1	-119.8 ± 4.0	-165.9 ± 4.3	12.2/15
2MASS J21373742+0808463	324.4086687	+08.1465724	56794.63	69.7 ± 7.3	684.4 ± 3.4	95.6 ± 2.7	70.6 ± 7.3	683.9 ± 3.4	89.3 ± 2.7	25.3/25
WISE J214706.78−102924.0	326.7784042	−10.4901810	56816.60	44.5 ± 3.8	96.9 ± 2.3	-142.5 ± 2.1	44.4 ± 3.8	96.7 ± 2.3	-147.1 ± 2.1	31.4/19
PSO J327.1504+22.6612	327.1506909	+22.6612320	56818.54	33.7 ± 2.7	320.0 ± 2.3	-140.7 ± 2.7	34.6 ± 2.7	318.5 ± 2.3	-145.1 ± 2.7	15.8/19
2MASS J21522609+0937575	328.1097924	+09.6332595	56794.63	40.2 ± 6.9	261.7 ± 2.6	145.6 ± 2.9	40.9 ± 6.9	260.5 ± 2.6	139.7 ± 2.9	16.1/21
WISEPC J215751.38+265931.4	329.4640895	+26.9919419	56799.63	62.1 ± 2.2	67.6 ± 1.3	-96.0 ± 1.6	62.8 ± 2.2	65.8 ± 1.3	-100.5 ± 1.6	27.8/25
2MASS J21580457−1550098	329.5192967	−15.8362727	56820.59	44.9 ± 5.6	37.0 ± 3.3	-58.2 ± 2.4	46.1 ± 5.6	39.5 ± 3.3	-67.4 ± 2.5	19.4/15
PSO J330.3214+32.3686	330.3215211	+32.3687105	56820.63	30.8 ± 5.4	113.2 ± 2.1	63.0 ± 1.7	31.4 ± 5.4	110.8 ± 2.1	59.5 ± 1.7	21.2/23
2MASS J22092183−2711329	332.3409831	−27.1929764	56821.61	40.3 ± 3.9	-14.9 ± 3.6	-133.8 ± 4.0	40.7 ± 3.9	-7.3 ± 3.6	-137.3 ± 4.0	10.5/19
WISEPC J220922.10−273439.5	332.3412184	−27.5781388	56821.62	71.7 ± 3.8	-765.5 ± 2.0	-433.7 ± 2.2	72.3 ± 3.8	-765.1 ± 2.0	-440.9 ± 2.2	20.1/25
WISEPC J221354.69+091139.4	333.4777299	+09.1942704	56821.63	50.2 ± 3.1	-114.0 ± 1.6	-29.0 ± 1.8	52.0 ± 3.1	-116.2 ± 1.6	-35.4 ± 1.8	24.3/23
2MASS J22153705+2110554	333.9047281	+21.1814062	56821.63	55.4 ± 4.4	48.1 ± 3.0	-180.5 ± 2.4	55.9 ± 4.4	48.8 ± 3.0	-186.3 ± 2.4	20.5/25
WISE J222219.93+302601.4	335.5831307	+30.4339263	56820.63	27.6 ± 3.1	32.1 ± 2.1	219.2 ± 2.2	27.9 ± 3.1	29.8 ± 2.1	215.0 ± 2.2	24.9/19

Table 7.4—Continued

Object	$\alpha_{\rm J2000}$ (deg)	$\delta_{\rm J2000}$ (deg)	Epoch (MJD)	Relative			Absolute			χ^2/dof
				$\pi_{\rm rel}$ (mas)	$\mu_{\alpha,{\rm rel}}\cos\delta$ (mas yr^{-1})	$\mu_{\delta,{\rm rel}}$ (mas yr^{-1})	$\pi_{\rm abs}$ (mas)	$\mu_{\alpha,{\rm abs}}\cos\delta$ (mas yr^{-1})	$\mu_{\delta,{\rm abs}}$ (mas yr^{-1})	
WISEA J223343.53−133140.9	338.4318467	−13.5279614	56821.61	17.5 ± 4.4	315.4 ± 2.2	1.0 ± 2.4	18.7 ± 4.4	318.3 ± 2.2	-5.6 ± 2.4	12.6/19
WISE J223617.59+510551.9	339.0747465	+51.0981336	56824.52	102.4 ± 1.9	710.8 ± 2.1	328.7 ± 2.5	102.8 ± 1.9	708.6 ± 2.1	326.7 ± 2.5	9.5/17
WISEPC J223729.53−061434.2	339.3731137	−06.2427338	56818.61	34.4 ± 2.7	140.7 ± 2.1	108.7 ± 1.8	35.0 ± 2.7	142.8 ± 2.1	103.0 ± 1.8	13.4/21
WISEPC J223937.55+161716.2	339.9069253	+16.2880556	56821.63	41.6 ± 3.0	396.9 ± 2.6	240.2 ± 2.3	42.9 ± 3.0	397.4 ± 2.6	234.5 ± 2.3	34.9/23
PSO J341.4606−28.7798	341.4607624	−28.7797512	56821.62	30.3 ± 10.4	-6.9 ± 4.5	45.9 ± 4.3	32.1 ± 10.4	-6.4 ± 4.5	38.3 ± 4.3	6.1/9
2MASS J22490917+3205489	342.2917998	+32.0962353	56820.63	49.6 ± 3.2	692.6 ± 2.7	-168.9 ± 2.5	49.7 ± 3.2	691.7 ± 2.7	-172.5 ± 2.5	22.9/23
WISE J230133.32+021635.0	345.3888449	+02.2764034	56821.63	50.8 ± 3.8	-70.5 ± 2.7	-89.1 ± 2.7	52.0 ± 3.8	-66.0 ± 2.7	-93.8 ± 2.7	27.6/23
WISEA J230329.45+315022.7	345.8730846	+31.8398585	56820.63	45.7 ± 3.3	240.1 ± 2.1	166.8 ± 2.1	46.5 ± 3.3	237.5 ± 2.1	161.7 ± 2.1	24.2/25
ULAS J230601.02+130225.0	346.5044634	+13.0404050	56818.62	35.4 ± 2.9	69.4 ± 1.3	57.1 ± 1.5	35.8 ± 2.9	69.9 ± 1.3	52.1 ± 1.5	22.3/29
PSO J346.5281−15.9406	346.5283445	−15.9405661	57193.62	22.8 ± 3.5	121.9 ± 2.3	1.4 ± 2.1	23.8 ± 3.5	129.0 ± 2.4	-6.2 ± 2.2	20.9/19
SSSPM J2310−1759	347.5771056	−17.9872371	56865.55	24.8 ± 3.3	8.0 ± 2.6	-297.9 ± 3.2	25.5 ± 3.3	11.4 ± 2.6	-301.4 ± 3.2	17.3/21
2MASS J23185497−1301106	349.7258108	−13.0206266	56821.62	65.4 ± 3.1	-801.6 ± 3.4	-243.4 ± 3.3	66.5 ± 3.2	-796.6 ± 3.4	-248.6 ± 3.4	30.7/17
WISEPC J231939.13−184404.3	349.9132653	−18.7344131	56821.62	84.3 ± 3.1	71.8 ± 1.4	135.5 ± 1.3	85.1 ± 3.1	74.1 ± 1.4	131.3 ± 1.4	16.9/21
CFBDS J232304.41−015232.3	350.7688153	−01.8760522	57193.63	28.9 ± 2.2	91.3 ± 1.5	-53.1 ± 1.6	30.2 ± 2.2	93.3 ± 1.5	-63.4 ± 1.6	21.3/23
2MASS J23254530+4251488	351.4386316	+42.8623430	56820.63	66.8 ± 3.4	-42.2 ± 3.4	-283.4 ± 3.1	67.9 ± 3.4	-43.8 ± 3.4	-286.7 ± 3.1	22.4/25
WISEPC J232728.75−273056.5	351.8702359	−27.5156698	56865.55	54.6 ± 6.1	287.4 ± 3.5	68.1 ± 2.9	55.6 ± 6.1	296.2 ± 3.5	61.6 ± 2.9	9.4/9
PSO J353.6355+13.2209	353.6356872	+13.2209308	57190.61	22.5 ± 6.3	40.6 ± 2.1	-7.8 ± 2.5	23.3 ± 6.3	43.2 ± 2.1	-13.4 ± 2.5	11.1/15
WISE J233543.79+422255.2	353.9324120	+42.3819829	56942.36	35.7 ± 3.1	53.6 ± 1.3	-58.5 ± 1.5	36.4 ± 3.1	52.6 ± 1.3	-60.9 ± 1.5	24.3/15
PSO J354.3709+57.7939	354.3711149	+57.7938735	56942.33	25.3 ± 4.6	28.2 ± 2.8	-132.8 ± 2.8	26.1 ± 4.6	26.1 ± 2.8	-135.0 ± 2.8	15.5/15
2MASSI J2339101+135230	354.7942762	+13.8709324	56821.63	60.3 ± 4.4	370.0 ± 2.0	-979.2 ± 2.8	62.7 ± 4.4	371.6 ± 2.0	-983.4 ± 2.8	24.3/23

Table 7.4—Continued

Object	α_{J2000} (deg)	δ_{J2000} (deg)	Epoch (MJD)	Relative			Absolute			χ^2/dof
				π_{rel} (mas)	$\mu_{\alpha,rel}\cos\delta$ (mas yr^{-1})	$\mu_{\delta,rel}$ (mas yr^{-1})	π_{abs} (mas)	$\mu_{\alpha,abs}\cos\delta$ (mas yr^{-1})	$\mu_{\delta,abs}$ (mas yr^{-1})	
2MASS J23392527+3507165	354.8562798	+35.1211947	56829.62	29.8 ± 4.9	169.5 ± 3.2	-24.9 ± 2.8	30.4 ± 4.9	168.7 ± 3.2	-28.0 ± 2.8	18.2/21
ULAS J234228.97+085620.1	355.6211688	+08.9388573	56818.63	44.6 ± 4.7	256.9 ± 2.4	-49.9 ± 1.6	46.2 ± 4.7	255.3 ± 2.4	-56.5 ± 1.6	26.2/19
2MASS J23440624−0733282	356.0260595	−07.5581715	56943.33	43.1 ± 4.3	-7.1 ± 3.1	-71.0 ± 2.8	41.9 ± 4.3	-4.2 ± 3.1	-74.4 ± 2.8	14.1/17
WISEPC J234841.10−102844.4	357.1720939	−10.4786807	56943.33	67.2 ± 3.9	616.1 ± 2.1	151.7 ± 1.9	67.6 ± 3.9	621.0 ± 2.1	146.2 ± 1.9	13.9/19
PM I23492+3458B	357.3130234	+34.9819202	56941.28	34.1 ± 3.1	-6.7 ± 2.1	-108.9 ± 2.2	34.3 ± 3.1	-7.3 ± 2.1	-112.3 ± 2.2	22.7/25
PSO J357.8314+49.6330	357.8308279	+49.6328181	57226.55	31.9 ± 4.9	-355.6 ± 2.8	-179.5 ± 3.4	32.4 ± 4.9	-357.4 ± 2.8	-182.0 ± 3.4	13.9/17
DENIS J2354599−185221	358.7489233	−18.8729191	56943.33	40.1 ± 3.0	-191.1 ± 2.4	-48.3 ± 2.9	40.7 ± 3.0	-185.4 ± 2.4	-52.7 ± 3.0	11.4/19
WISE J235716.49+122741.8	359.3188514	+12.4609676	56821.63	55.8 ± 4.1	21.3 ± 1.7	-506.4 ± 1.9	56.8 ± 4.1	24.3 ± 1.7	-512.9 ± 1.9	27.4/23

Note. — This table gives all the astrometric parameters derived from our MCMC analysis of the IRLS solution for each target. (α, δ, MJD): coordinates and epoch for our first observation of that target. (π, μ_δ, μ_δ): We list both relative and absolute parallaxes and proper motions. Absolute values include a correction for the mean parallax and proper motion of our reference stars, which includes an additional uncertainty added in quadrature to the relative astrometry's uncertainties (Section 7.5.5). χ^2/dof: the smallest χ^2 among the IRLS + MCMC chain along with the degrees of freedom (dof) for the data set.

[a]Observations for this object span only one year. While our astrometric solution appears to be robust, the parallax and proper motions should be regarded as preliminary.

[b]This known 0.9″ binary (Burgasser et al. 2009a) is resolved in our UKIRT images. Our astrometric solution appears reasonable but should be treated with caution.

7.6.1 Spectral Type Distribution and *Gaia* DR2 Overlap

Figure 7.10 shows the distribution of spectral types among our targets with parallax measurements, highlighting the 104 targets that also have a parallax from *Gaia* DR2. When both optical and near-IR spectral types are available for an object, we use the the optical spectral types for L dwarfs and the near-IR spectral types for T dwarfs. While our UKIRT targets are distributed across L0–T8 types, *Gaia* DR2 is largely limited to earlier spectral types, observing only a few very nearby L6 or later dwarfs. Including the 10 UKIRT wide-companion targets for which *Gaia* has observed the primary star, *Gaia* DR2 provides more precise parallaxes than our measurements for 104 (30%) of our targets, along with two more of our targets (2MASS J09352803−2934596 and 2MASS J21371044+1450475) for which we did not measure a parallax. 86% of the *Gaia* DR2 parallaxes are for spectral types earlier than L7. Our UKIRT measurements include the first and only parallaxes for 219 objects, with spectral types mostly L6 and later. Among these are 172 T dwarfs, comprising the largest sample of T dwarf parallaxes published to date.

7.6.2 Current Parallax Census

We combined the Database of Ultracool Parallaxes (DL12; LDA16) with our new UKIRT results and *Gaia* DR2 parallaxes for known L and T dwarfs to create an updated census of ultracool parallaxes. There are now published parallaxes for over 1000 L, T, and Y dwarfs. Figure 7.11 shows the contributions from our UKIRT program, *Gaia* DR2, and other sources to this parallax census as a function of spectral type, choosing only the most precise measurement when more than one is available for an object. Figure 7.12 incorporates the parallaxes into a near-infrared color-magnitude diagram showing the L and T dwarf population.

With hundreds of new measurements, *Gaia* DR2 now provides the most precise parallaxes for 90% of L0–L5 dwarfs. Beyond L5, ground-based infrared measurements become dominant, with UKIRT now contributing the majority of L8–T7 parallaxes. In particular, we have tripled the number of parallaxes for spectral types L9–T5.5. At these

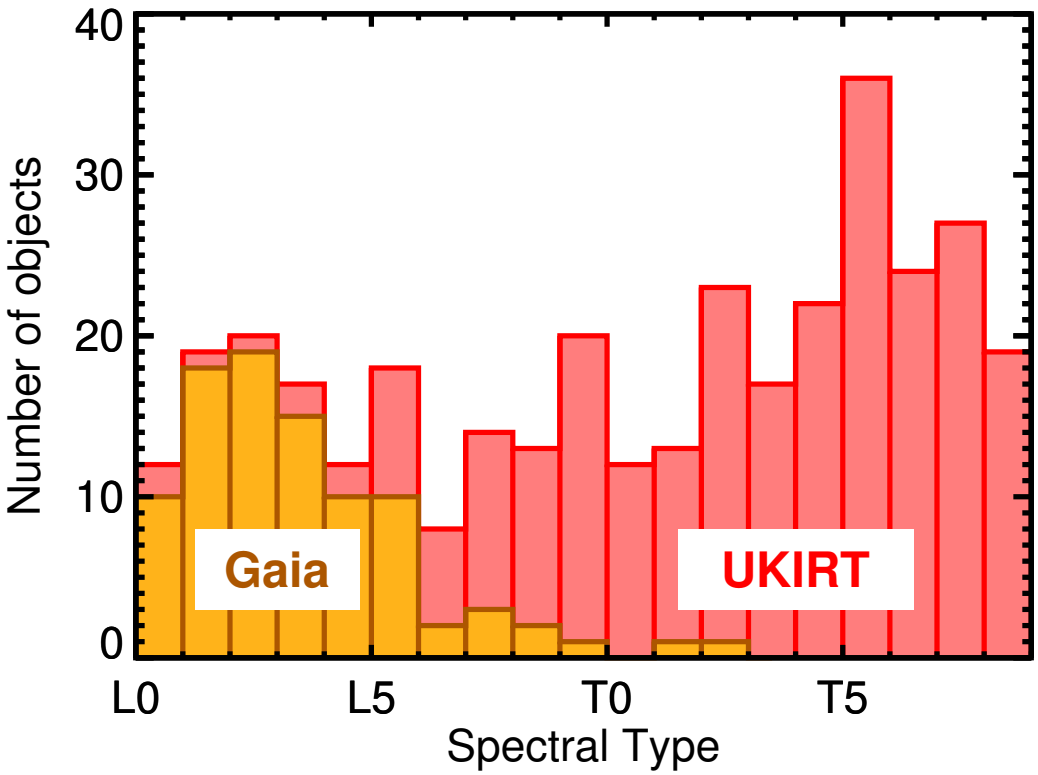

Figure 7.10 Spectral types for all of our 348 UKIRT targets with parallax measurements (red). We highlight the 94 targets that also have parallaxes from *Gaia* DR2 (orange), which primarily have spectral types L0–L5. (*Gaia* DR2 has also measured parallaxes for 10 primary stars of UKIRT wide-companion targets.) UKIRT has obtained the first parallax measurements for 219 targets, which are mostly L6 and later types.

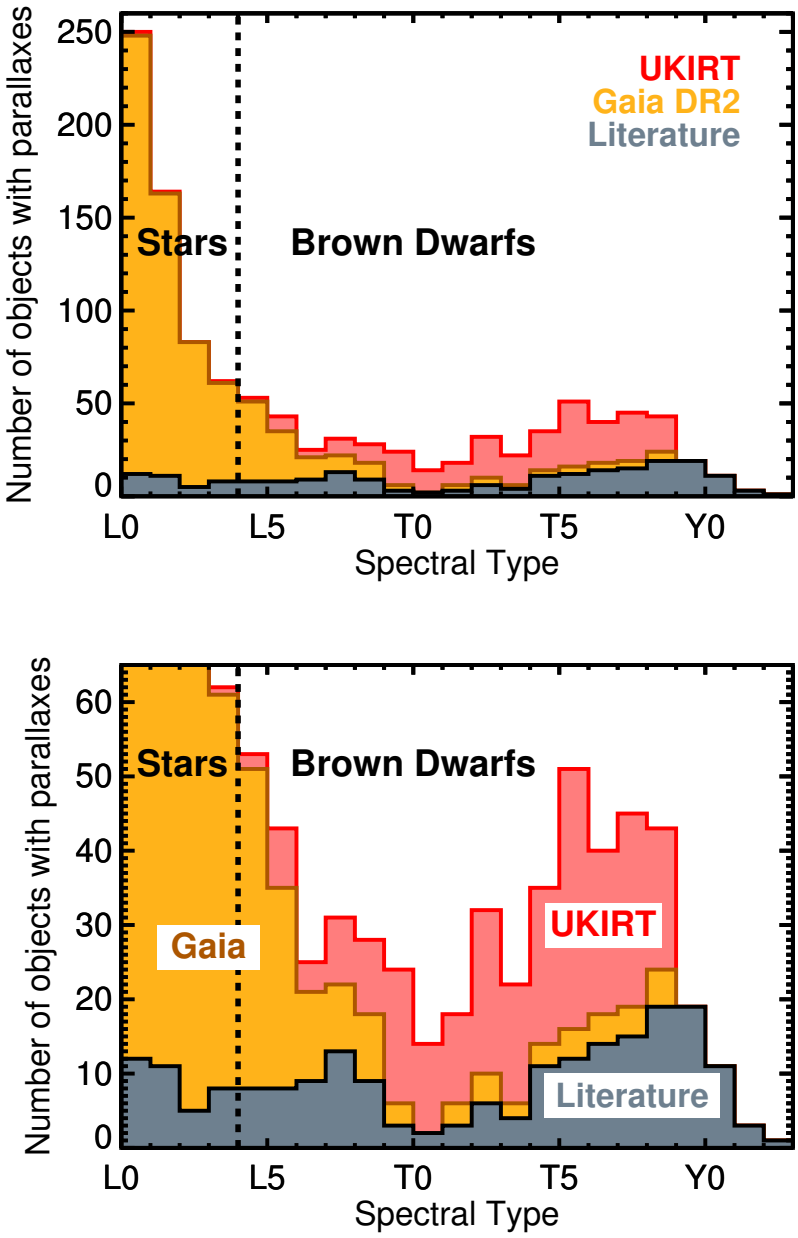

Figure 7.11 *Top*: Distribution of spectral types for all L0 and later dwarfs with parallax measurements, stacking the contributions of parallaxes from UKIRT (red), *Gaia* DR2 (orange), and other literature sources (gray). For objects with more than one parallax, we show only the source of the most precise measurement. The black dashed line at L4 marks the approximate substellar boundary for field-age objects (Dupuy & Liu 2017). *Bottom*: Same plot but with a smaller vertical axis range to highlight spectral types L5 and later. *Gaia* DR2 dominates spectral types L0–L5 but is mostly limited to observing stars. UKIRT is now the largest contributor for brown dwarf spectral types L9–T8 and has also tripled the number of L9–T5.5 parallaxes.

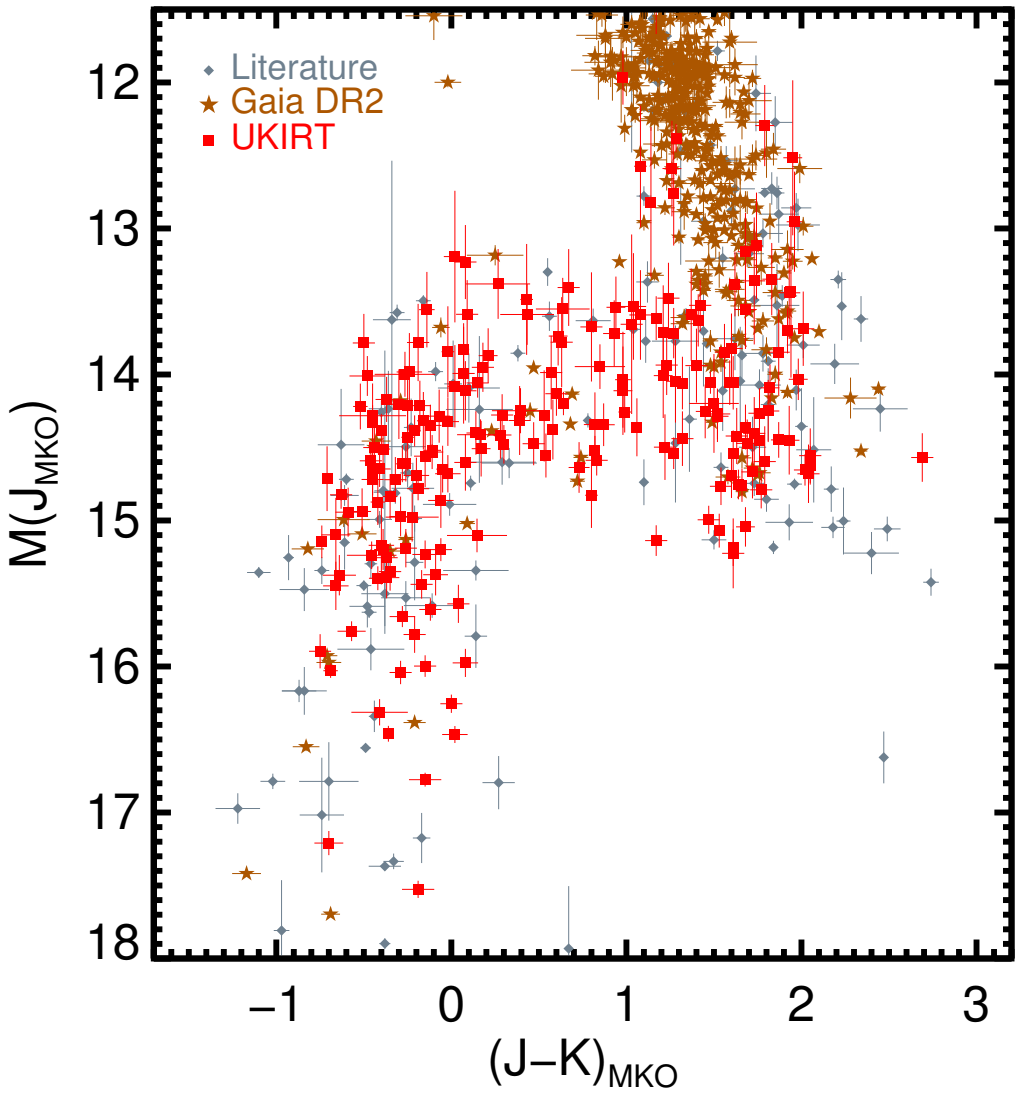

Figure 7.12 M_J vs. $J - K$ (MKO) color-magnitude diagram for ultracool dwarfs with a parallax measurement having error $< 20\%$. We highlight the parallax contributions of UKIRT (red), *Gaia* DR2 (brown), and other literature sources (gray), using only the most precise parallax available for an object. Cooling brown dwarfs move down the L dwarf sequence on the right, from right to left across the L/T transition, and down the later-T dwarf sequence on the left-hand side. Our UKIRT parallaxes have contributed 172 new T dwarf parallaxes, providing a wealth of data for understanding the evolution of these objects.

L/T transition spectral types, evolutionary and atmospheric models struggle to reproduce observed luminosities and effective temperatures for objects with known masses and/or ages (e.g., Dupuy et al. 2009b, 2015b). Our parallaxes provide a wealth of new empirical constraints for L/T transition modeling. For the coolest late-T and Y dwarfs, CFHT (near-IR), Magellan (near-IR), and *Spitzer* (mid-IR) have made most of the parallax measurements.

The mid-L spectral types at which UKIRT/WFCAM and other instruments begin to contribute a large fraction of the parallaxes is remarkably close to the field substellar boundary at ≈L4 (DL17). Earlier spectral types will contain a mixture of very low-mass stars and young brown dwarfs, while later spectral types will be all brown dwarfs. Figure 7.11 makes clear that *Gaia* is largely a stellar survey for the field population, measuring parallaxes for only a handful of field brown dwarfs, while infrared parallax programs will continue to be essential for studies of brown dwarfs in the era of *Gaia*.

7.6.3 Comparison With Literature Parallaxes

For UKIRT targets having parallaxes in the literature, we compare our parallaxes in Figure 7.13. We identify objects from several major ultracool parallax programs, including CFHT, BDKP, PARSEC and NPARSEC, USNO-IR, and Carnegie, as well as companions to stars with *Hipparcos* parallaxes (van Leeuwen 2007b).

We find good agreement for our parallaxes with most values from the literature. The notable exceptions are a handful of parallaxes from BDKP and a Hipparcos parallax for the primary of HIP 73169B (van Leeuwen 2007b). Most of the BDKP parallaxes that differ significantly from ours have large uncertainties ($\gtrsim$10 mas). On the whole, the BDKP parallaxes tend to be larger than ours, a trend also noted by Liu et al. (2016) when comparing BDKP to CFHT parallaxes. The Hipparcos parallax of 36.61 ± 9.38 mas for HIP 73169 has an unusually large uncertainty, and *Gaia* DR2 has measured a parallax of 22.25 ± 0.05 mas for HIP 73169, so the Hipparcos measurement appears to be incorrect.

Our UKIRT measurement of 26.6 ± 3.5 mas for HIP 73169B is much closer to the *Gaia* value for the primary, agreeing at the 1.2σ level.

7.6.4 Comparison With *Gaia* DR2

As described in Section 7.6.1, *Gaia* has measured parallaxes mostly for ultracool dwarfs with spectral types $\leq$L5. All but three of our 104 UKIRT targets with *Gaia* DR2 parallaxes are L dwarfs. Two of the remaining T dwarfs are very nearby and bright: SIMP J013656.57+093347.3 (T2.5; Artigau et al. 2006) at 6 pc and WISE J203042.79+074934.7 (T1.5; Mace et al. 2013a) at 10 pc. In the third case, *Gaia* DR2 measured a parallax for 2MASS J02132062+3648506AB which has a T dwarf companion 2MASS J02132062+3648506C (Deacon et al. 2017b) in our UKIRT sample. We compare our parallaxes with those of *Gaia* DR2 in Figure 7.14, which shows excellent agreement and validates the accuracy of our UKIRT parallaxes.

7.6.5 Parallaxes for Binaries

Our targets included 36 objects known or strongly suspected to be binaries, with separations generally requiring high-angular resolution imaging or high-resolution spectroscopy to resolve. Our reduction pipeline assumed each target was a point source and did not attempt to fit for binary sources in the images. However, it is possible for binaries with separations similar to the seeing during observations ($\approx 0.5''$ on our best nights) to be partially or fully resolved, which could impact the astrometry from those images. We therefore looked for indications of bias in our astrometric solutions for these binaries.

The parallax fits shown in Figure 7.7 for the binaries appear consistent with the fits for single objects. The median χ^2_ν for final IRLS+MCMC solutions for binaries is 1.00, almost exactly the same as the median of 0.96 for all parallax solutions (Section 7.5.1). The χ^2_ν of the 1:1 fit for UKIRT with Gaia for just the 11 binaries in common (Figure 7.14) is 1.28, larger than the $\chi^2_\nu = 1.09$ for all common objects but not enough to imply a significantly

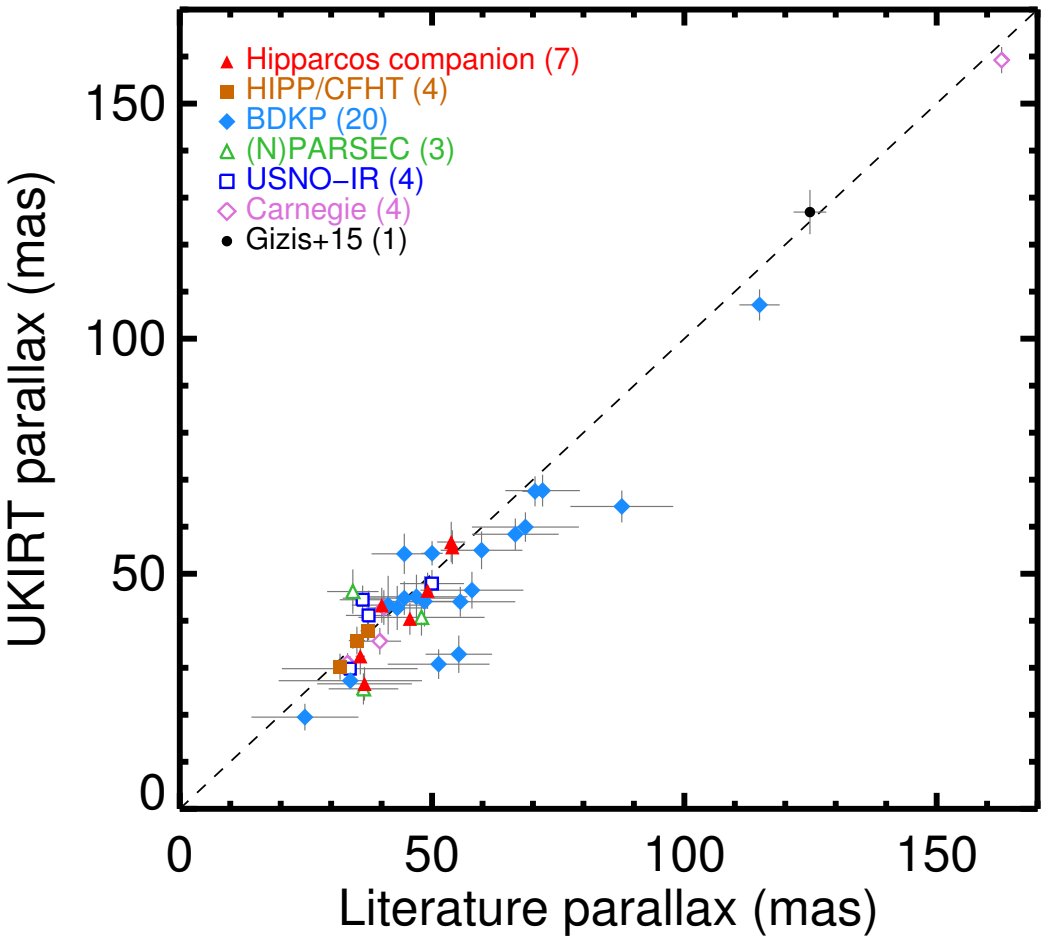

Figure 7.13 Objects measured by UKIRT also having parallax measurements in the literature. Parallaxes from specific programs are identified by color and symbol, with the number of objects in parentheses. Our parallaxes are highly consistent with literature measurements having uncertainties $< 10\%$, most notably those from CFHT and Hipparcos. **References**: Hipparcos: van Leeuwen (2007b); CFHT: Dupuy & Liu (2012), Liu et al. (2016), Dupuy & Liu (2017); BDKP: Faherty et al. (2012, 2016); PARSEC: Andrei et al. (2011), Marocco et al. (2013); NPARSEC: Smart et al. (2013); USNO-IR: Vrba et al. (2004); Carnegie: Weinberger et al. (2013, 2016); Gizis et al. (2015b).

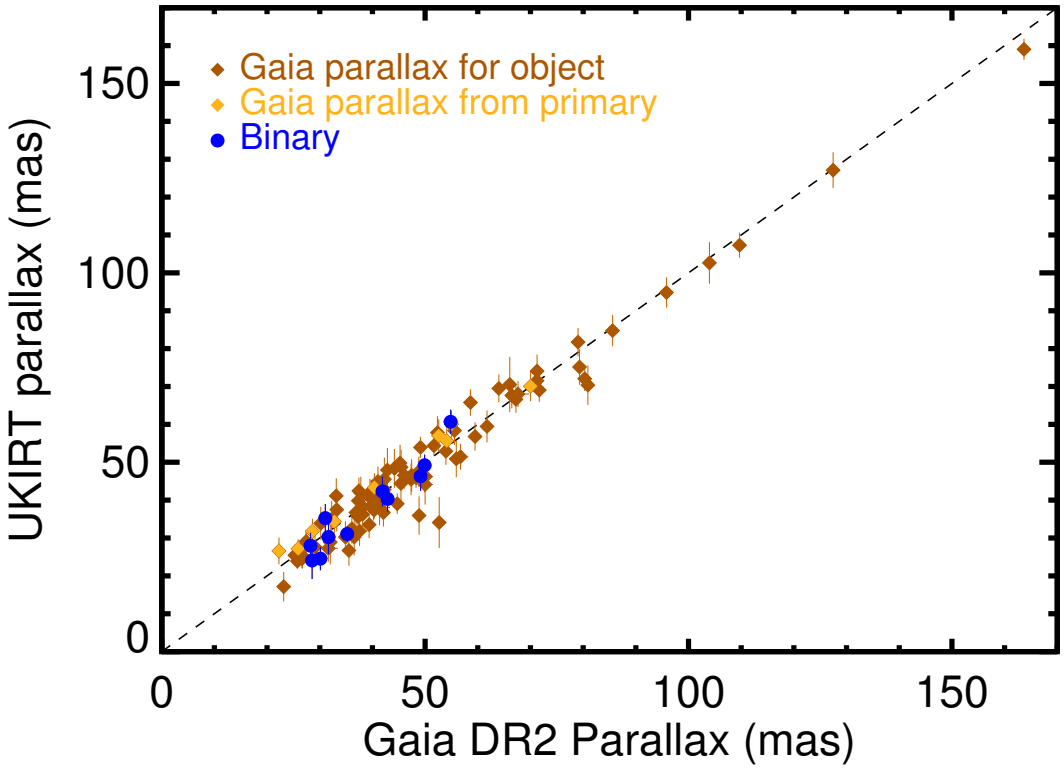

Figure 7.14 Our UKIRT parallaxes compared with *Gaia* DR2 parallaxes for the 104 objects common to both data sets. The dashed line marks the 1:1 correspondence. Orange diamonds indicate wide companions with *Gaia* parallaxes from their host stars. The UKIRT parallaxes agree very well with the *Gaia* DR2 parallaxes, with $\chi^2_\nu = 1.09$ for the 1:1 model. Blue circles mark known binaries. The correspondence between UKIRT and *Gaia* parallaxes for binaries is consistent with the correspondence for all objects, implying that our parallax measurements are not biased by partially resolved targets in our images.

poorer fit. We therefore do not see evidence that our parallaxes for binaries are influenced by non-point source appearance in our images.

There is one possible exception: the 0.9″ L3.5+L4 binary 2MASS J15500845+1455180 (Cruz et al. 2007; Burgasser et al. 2009a), is clearly resolved in our UKIRT images. Our pipeline nevertheless identified and treated 2MASS J15500845+1455180 as a single object at the position of the brighter primary in each frame. The astrometric solution appears to be reasonable with $\chi^2_\nu = 1.12$ and no trends or unusual scatter in the residuals. Our UKIRT parallax of 24.5 ± 3.0 mas differs by 1.8σ from the *Gaia* DR2 parallax of 30.12 ± 0.92 but we note that while *Gaia* has also resolved the system and identifies both objects in DR2, only one component has a parallax, so the *Gaia* DR2 parallax may not yet be reliable. We include our solution in our results but advise using it with caution.

7.7 Summary

We have measured parallaxes, proper motions, and $J_{\rm MKO}$ photometry for 348 ultracool dwarfs with spectral types L0–T8 using astrometry from UKIRT/WFCAM. We observed targets over two-thirds of the sky ($\delta = -30°$ to $+60°$) having photometric distances within 1σ of 25 pc that lacked precise parallax measurements, with the goal of establishing a complete volume-limited sample of L0–T8 dwarfs. These measurements represent the largest set of infrared parallax measurements for ultracool dwarfs published to date, and include 219 objects without a previous parallax measurement. We achieved a median parallax precision of 3.5 mas, comparable to several previous infrared parallax program that targeted far fewer objects.

Our target list shares 104 objects with *Gaia* DR2. Most of these are L0–L5 dwarfs, a demonstration that *Gaia* is a survey of stars; ground-based infrared observations continue to be essential for studies of brown dwarfs. Our parallaxes demonstrate excellent consistency with *Gaia* DR2 measurements.

Our UKIRT parallaxes make possible population studies of L and T dwarfs using, for the first time, a volume-limited sample with several hundred members defined entirely by parallaxes.

Chapter 8

Population Properties of L and T Dwarfs Within 25 pc of the Sun

Abstract

We present the first large volume-limited sample of L0–T8 dwarfs defined entirely by parallaxes, using new measurements from UKIRT/WFCAM along with parallaxes from *Gaia* DR2 and the literature. The sample extends to 25 pc, covers 68% of the sky ($\delta = -30°$ to $+60°$), and has 350 members, ≈4 times larger than the previous largest volume-limited sample of L and T dwarfs. We estimate our volume-limited sample to be ≈90% complete for L0–T4.5 dwarfs and ≈70% complete for T5–T8 dwarfs, the latest-type objects being too faint to be observed at 25 pc by the large sky surveys that have discovered most brown dwarfs. We identify a gap ≈0.5 mag wide in $(J - K)_{\rm MKO}$ colors at spectral type ≈T1 ($T_{\rm eff} \approx 1300$ K), implying a rapid phase of atmospheric evolution in the transition from L to T dwarfs. We apply a Lutz-Kelker correction and the $V/V_{\rm max}$ method to calculate space densities and the luminosity function for our volume-limited sample. We use population synthesis modeling to obtain the best constraints to date on the initial mass function and birth history of L and T dwarfs in the Solar neighborhood. For an IMF of form $dN/dM \propto M^{-\alpha}$ we find $\alpha = -0.46 \pm 0.42$, consistent with most previous estimates for for the field brown dwarf population but lower than estimates for star-forming regions. For a birth rate $b(t) \propto e^{-\beta t}$ we find $\beta = 0.08 \pm 0.12$, the first strong constrain obtained used

population synthesis modeling of the Solar neighborhood. Our volume-limited sample will continue to be a rich source of empirical constraints for studies of local ultracool dwarfs.

8.1 Introduction

Brown dwarfs have masses $\lesssim$70 $M_{\rm Jup}$ (e.g., Saumon & Marley 2008; Dupuy & Liu 2017), insufficient to sustain hydrogen fusion and reach the steady-state luminosity that defines main-sequence stars. Brown dwarfs therefore cool continuously after formation, so their luminosities and temperatures depend on both age and mass. Consequently, a younger, less massive brown dwarf can have the same luminosity and temperature (and thus spectral type) as an older, more massive brown dwarf. This observational degeneracy makes ages and evolutionary trends in the brown dwarf population difficult to identify. The cooling also causes brown dwarf atmospheres to undergo complex chemical transformations. This is particularly true in the L/T transition (spectral types ≈L8–T4), where evolutionary and atmospheric models struggle to reproduce observed luminosities and effective temperatures for L/T objects with known masses and/or ages (e.g., Dupuy et al. 2009b, 2015b). With only a handful of accurate parallax-based luminosities measured for L/T transition dwarfs (Best et al. 2018), we have yet to develop an accurate map for this distinctive evolutionary phase.

Previous modeling established the first estimates of the local low-mass initial mass function (IMF) and formation history (e.g., Allen et al. 2005; Metchev et al. 2008). These studies used the best available space density, luminosity function, binary fraction, and evolutionary models, but were unable to place significant constraints on either the IMF or the birth rate for ultracool dwarfs. In the most recent effort, Marocco et al. (2015) compiled space density estimates across L and T spectral types from several sources. These estimates still can only weakly constrain the substellar IMF ($\Psi(M) \propto M^{-\alpha}$) slope to between $-1 \lesssim \alpha \lesssim 1$ and are significantly hampered by uncertainty in the binary fraction (whose estimates span $5-45\%$ across different surveys; Burgasser et al. 2003c; Maxted &

Jeffries 2005; Burningham et al. 2010a). None of the previous studies produced a constraint on the substellar birth history beyond general agreement with a constant formation rate over the history of the Galaxy.

Volume-limited samples are ideal for population studies, as they minimize the selection biases intrinsic to magnitude-limited samples. Parallaxes provide the most direct measures of distance to nearby objects and are therefore preferred for establishing volume-limited samples in the solar neighborhood. A parallax-defined volume-limited sample of nearby brown dwarfs would enable the best estimates of the underlying mass and age distributions. The most complete volume-limited samples assembled to date are those of Kirkpatrick et al. (2012), whose full-sky 8 pc sample contains only 33 L, T, and Y dwarfs; and Reid et al. (2008b), comprising 196 late-M, L, and T dwarfs out to 20 pc but complete only for spectral types M9–L6 and using photometric distances for two-thirds of the members.

We present here a new volume-limited sample of L and T dwarfs out to 25 pc containing 350 members chosen entirely by parallaxes. Using a near-infrared color-magnitude diagram (CMD) for this sample, we identify a gap in $J-K$ color in the L/T transition (spectral type $\approx$T1). We calculate the most precise estimates for space density and luminosity function for L and T dwarfs to date, and use these to assess the birth history and IMF of the local brown dwarf population.

8.2 A Volume-limited Sample of L and T Dwarfs

8.2.1 Construction

We present the first volume-limited sample of L and T dwarfs chosen entirely by parallaxes out to 25 pc. We use our UKIRT/WFCAM measurements of L0–T8 dwarf parallaxes with $\delta = -30°$ to $+60°$. In addition, we searched the literature for all spectroscopically confirmed objects in the same spectral type and declination ranges as our UKIRT targets having parallax measurements with errors $< 20\%$, including parallaxes from *Gaia* DR2 (Gaia Collaboration et al. 2018). After merging the UKIRT and literature parallax lists

and choosing the most precise parallax available for each object, we removed objects with parallaxes < 40 mas (i.e., distances > 25 pc) to obtain a volume-limited sample. We present our volume-limited sample in Table 8.1. It includes 350 L0–T8 dwarfs and is defined by 152 parallaxes from UKIRT, 125 from *Gaia* DR2, and 73 from other literature sources. Figure 8.1 shows the spectral type distribution of our sample.

Table 8.1. Our volume-limited 25 pc sample of L0–T8 dwarfs

Object	Distance (pc)	Parallax (mas)	Spectral Type[a] (Optical/NIR)	J_{MKO} (mag)	H_{MKO} (mag)	K_{MKO} (mag)	References (Disc; π; SpT; Phot)
SDSS J000013.54+255418.6	14.1 ± 0.4	70.8 ± 1.9	T5/T4.5	14.73 ± 0.03	14.74 ± 0.03	14.82 ± 0.03	85; 50; 121,20; 85
PSO J003.3437−11.7168	24.8 ± 1.9	40.3 ± 3.1	.../T4	16.05 ± 0.02	15.74 ± 0.22	15.76 ± 0.22	97; 8; 97; 8,39
2MASSW J0015447+351603	17.1 ± 0.1	58.6 ± 0.4	L2/L1.0	13.73 ± 0.02	12.96 ± 0.02	12.25 ± 0.02	80; 59; 80,4; 8
PSO J004.6359+56.8370	21.5 ± 1.8	46.5 ± 3.9	.../T4.5	16.22 ± 0.02	...	...	97; 8; 97; 8
2MASS J00282091+2249050	24.2 ± 1.2	41.3 ± 2.0	.../L7:	15.41 ± 0.03	14.55 ± 0.06	13.77 ± 0.06	26; 59; 26; 8
WISE J003110.04+574936.3	14.1 ± 1.0	71.0 ± 5.0	.../L9	14.80 ± 0.01	13.86 ± 0.01	13.21 ± 0.03	147; 8; 6; 6,8
PSO J007.9194+33.5961	22.0 ± 1.8	45.4 ± 3.8	.../L9	16.38 ± 0.02	15.45 ± 0.06	14.66 ± 0.06	7; 8; 7; 8
2MASS J00320509+0219017	24.4 ± 0.3	41.0 ± 0.4	L1.5/M9	14.22 ± 0.00	13.45 ± 0.00	12.80 ± 0.00	129; 59; 129,154; 86
2MASS J00332386−1521309	22.9 ± 0.5	43.6 ± 0.9	L4 β/L1: FLD-G	15.24 ± 0.06	14.28 ± 0.04	13.39 ± 0.04	66; 59; 36,2; 8
2MASS J00345157+0523050	9.5 ± 0.7	105.4 ± 7.5	.../T6.5	15.14 ± 0.00	15.58 ± 0.01	16.07 ± 0.03	19; 53; 20; 32
2MASSW J0036159+182110	8.7 ± 0.0	114.4 ± 0.2	L3.5/L4:	12.30 ± 0.03	11.64 ± 0.03	11.04 ± 0.03	127; 59; 80,85; 85
HD 3651B	11.1 ± 0.0	89.8 ± 0.1	.../T7.5	16.16 ± 0.03	16.68 ± 0.04	16.87 ± 0.05	115; 59; 104; 104
WISE J004024.88+090054.8	14.0 ± 0.5	71.3 ± 2.7	.../T7	16.13 ± 0.01	16.56 ± 0.02	16.55 ± 0.05	107; 8; 107; 86
2MASSW J0045214+163445	15.4 ± 0.1	65.0 ± 0.2	L2 β/L2: VL-G	13.00 ± 0.02	12.14 ± 0.02	11.33 ± 0.02	154; 59; 36,2; 8
WISE J004542.56+361139.1	18.7 ± 1.8	53.4 ± 5.2	.../T5	15.92 ± 0.02	16.13 ± 0.06	16.07 ± 0.06	107; 8; 107; 8
WISEPC J004928.48+044100.1	16.0 ± 0.7	62.6 ± 2.9	.../L9	15.77 ± 0.01	14.80 ± 0.01	14.13 ± 0.01	83; 8; 83; 86
SIPS J0050−1538	24.8 ± 0.1	40.3 ± 0.2	L1:/L0.5	13.69 ± 0.02	13.15 ± 0.03	12.62 ± 0.03	41; 59; 35,4; 8
WISEA J010202.11+035541.4	24.9 ± 1.7	40.2 ± 2.8	.../L9	16.67 ± 0.02	15.75 ± 0.01	15.07 ± 0.01	136; 8; 136; 86
2MASSI J0103320+193536	21.3 ± 3.5	46.9 ± 7.6	L6 β/L6: INT-G	16.16 ± 0.08	14.94 ± 0.06	14.09 ± 0.06	80; 53; 53,2; 53
SDSSp J010752.33+004156.1	15.6 ± 1.1	64.1 ± 4.5	L8/L7pec	15.75 ± 0.03	14.56 ± 0.03	13.58 ± 0.03	61; 152; 75,58; 88
2MASS J01311838+3801554	24.9 ± 0.5	40.2 ± 0.8	L4:/L1.5	14.62 ± 0.02	13.77 ± 0.03	13.03 ± 0.03	35; 59; 35,26; 8

Table 8.1—Continued

Object	Distance (pc)	Parallax (mas)	Spectral Type[a] (Optical/NIR)	$J_{\rm MKO}$ (mag)	$H_{\rm MKO}$ (mag)	$K_{\rm MKO}$ (mag)	References (Disc; π; SpT; Phot)
WISE J013525.64+171503.4	21.4 ± 1.6	46.7 ± 3.5	.../T6	17.10 ± 0.02	17.45 ± 0.06	17.76 ± 0.07	107; 8; 107; 8
SIMP J013656.5+093347.3	6.1 ± 0.0	163.7 ± 0.7	T2/T2.5	13.27 ± 0.02	12.81 ± 0.00	12.59 ± 0.00	3; 59; 121,3; 8,86
WISEPC J013836.59−032221.2	22.8 ± 1.5	43.9 ± 2.9	.../T3	16.13 ± 0.02	15.67 ± 0.06	15.26 ± 0.06	83; 8; 83; 8
2MASSW J0141032+180450	23.6 ± 0.2	42.3 ± 0.3	L1/L4.5	13.83 ± 0.03	13.10 ± 0.03	12.48 ± 0.03	154; 59; 35,154; 8
2MASS J01443536−0716142	12.7 ± 0.1	79.0 ± 0.6	L5/L5	14.13 ± 0.02	13.09 ± 0.02	12.26 ± 0.02	92; 59; 92,111; 8
SDSS J015141.69+124429.6	21.4 ± 1.5	46.7 ± 3.4	.../T1	16.39 ± 0.01	15.60 ± 0.01	15.29 ± 0.01	61; 152; 20; 86
2MASS J01550354+0950003	22.4 ± 0.3	44.7 ± 0.7	L5/L3.2 INT-G	14.73 ± 0.00	13.88 ± 0.00	13.11 ± 0.04	129; 59; 129,58; 86,8
HIP 9269B	24.8 ± 0.0	40.4 ± 0.0	.../L6	16.13 ± 0.02	15.08 ± 0.01	14.30 ± 0.02	45; 59; 45; 45
2MASSW J0205034+125142	23.5 ± 1.7	42.5 ± 3.0	L5/L5.5	15.56 ± 0.01	14.51 ± 0.00	13.64 ± 0.00	80; 8; 80,26; 86
DENIS J020529.0−115925	19.8 ± 0.6	50.6 ± 1.5	L7/L5.5::	14.43 ± 0.05	13.61 ± 0.05	12.99 ± 0.05	47; 40; 79,85; 88
WISEPA J020625.26+264023.6	19.2 ± 0.5	52.1 ± 1.4	.../L8 (red)	16.43 ± 0.11	15.18 ± 0.08	14.50 ± 0.08	83; 96; 96; 8
2MASSW J0208183+254253	23.7 ± 0.4	42.3 ± 0.6	L1/...	13.91 ± 0.02	13.18 ± 0.03	12.57 ± 0.03	80; 59; 80; 8
2MASS J02132062+3648506C	14.3 ± 0.0	70.0 ± 0.2	.../T3	15.16 ± 0.01	14.89 ± 0.02	14.93 ± 0.02	46; 59; 46; 46
2MASSI J0213288+444445	19.3 ± 0.1	51.7 ± 0.4	L1.5/...	13.39 ± 0.02	12.81 ± 0.02	12.19 ± 0.02	33; 59; 33; 8,39
WISEPA J022623.98−021142.8	19.6 ± 0.9	51.1 ± 2.3	.../T7	18.42 ± 0.02	...	...	83; 8; 83; 8
2MASS J02271036−1624479	20.5 ± 0.1	48.8 ± 0.3	L1/L0.5:	13.51 ± 0.02	12.70 ± 0.03	12.13 ± 0.03	129; 59; 129,111; 8
2MASS J02284243+1639329	21.7 ± 0.2	46.0 ± 0.4	L0:/M8.7	13.07 ± 0.02	12.38 ± 0.02	11.80 ± 0.02	129; 59; 129,4; 8
GJ 1048B	21.5 ± 0.1	46.6 ± 0.3	L1/L1	12.66 ± 0.50	12.80 ± 0.08	12.17 ± 0.08	64; 59; 64,64; 53,8
2MASSI J0243137−245329	10.7 ± 0.4	93.6 ± 3.6	T5.5/T6	15.13 ± 0.03	15.39 ± 0.03	15.34 ± 0.03	15; 152; 121,20; 85
WISE J024714.52+372523.5	15.4 ± 0.5	64.8 ± 2.0	.../T8	18.01 ± 0.02	...	...	107; 8; 107; 8
2MASSI J0251148−035245	12.8 ± 0.6	78.0 ± 3.5	L3/L1	12.92 ± 0.02	12.31 ± 0.02	11.64 ± 0.02	33; 8; 33,154; 8,39

Table 8.1—Continued

Object	Distance (pc)	Parallax (mas)	Spectral Type[a] (Optical/NIR)	$J_{\rm MKO}$ (mag)	$H_{\rm MKO}$ (mag)	$K_{\rm MKO}$ (mag)	References (Disc; π; SpT; Phot)
PSO J043.5395+02.3995	7.4 ± 0.8	134.7 ± 14.9	.../T8	16.14 ± 0.12	16.51 ± 0.12	16.84 ± 0.12	94,140; 51; 94; 94
CFBDS J030135.11−161418.0	20.4 ± 1.6	49.1 ± 3.8	.../T7	18.34 ± 0.07	18.99 ± 0.10	18.07 ± 0.06	1; 52; 1; 1
2MASS J03140344+1603056	13.6 ± 0.1	73.4 ± 0.3	L0/L0: FLD-G	12.49 ± 0.02	11.89 ± 0.02	11.21 ± 0.02	129; 59; 129,2; 8
WISEA J032301.86+562558.0	16.4 ± 1.5	60.8 ± 5.6	.../L7	15.76 ± 0.02	14.67 ± 0.06	13.72 ± 0.06	106; 8; 106; 8
SDSS J032553.17+042540.1	22.7 ± 1.6	44.0 ± 3.2	.../T5.5	16.00 ± 0.01	16.26 ± 0.02	16.52 ± 0.04	32; 8; 32; 86
PSO J052.2746+13.3754	22.5 ± 1.5	44.3 ± 3.0	.../T3.5	16.24 ± 0.02	15.97 ± 0.06	15.77 ± 0.06	97; 8; 97; 8
PSO J052.7214−03.8409	17.5 ± 1.1	57.1 ± 3.5	.../L9:	16.26 ± 0.02	15.24 ± 0.02	14.58 ± 0.05	7; 8; 7; 7,8
2MASS J03552337+1133437	9.1 ± 0.1	109.7 ± 0.7	L5 γ/L3: VL-G	13.90 ± 0.03	12.60 ± 0.03	11.46 ± 0.02	128; 59; 36,2; 54
WISE J040137.21+284951.7	12.5 ± 0.0	80.3 ± 0.3	L3/L2.5	13.32 ± 0.02	12.50 ± 0.02	11.80 ± 0.02	31; 59; 31,31; 8
WISE J040418.01+412735.6	16.2 ± 0.1	61.8 ± 0.4	L2/L2pec	14.02 ± 0.02	13.17 ± 0.02	12.34 ± 0.00	31; 59; 31,31; 8,103
2MASS J04070885+1514565	18.1 ± 0.9	55.4 ± 2.7	.../T5	15.67 ± 0.02	15.83 ± 0.06	15.88 ± 0.03	19; 8; 20; 8,86
2MASSI J0408290−145033	22.0 ± 0.2	45.4 ± 0.3	L2/L4.5	14.15 ± 0.02	13.41 ± 0.02	12.80 ± 0.02	154; 59; 33,154; 8
PSO J062.3459+11.1794	21.9 ± 1.3	45.7 ± 2.7	.../T3.5	16.18 ± 0.02	15.73 ± 0.15	15.88 ± 0.02	97; 8; 97; 8,39,86
2MASSI J0415195−093506	5.7 ± 0.1	175.2 ± 1.7	T8/T8	15.34 ± 0.00	15.67 ± 0.01	15.83 ± 0.03	15; 50; 16,20; 85
SDSSp J042348.57−041403.5	13.9 ± 0.2	72.1 ± 1.1	L7.5/T0	14.30 ± 0.03	13.51 ± 0.03	12.96 ± 0.03	61; 50; 33,20; 88
WISE J042417.94+072744.1	22.9 ± 0.8	43.7 ± 1.5	.../T7.5	18.33 ± 0.02	...	...	107; 8; 107; 8
WISE J043052.92+463331.6	12.3 ± 0.5	81.4 ± 3.5	.../T8	19.03 ± 0.03	19.25 ± 0.13	...	107; 8; 107; 8,107
2MASSI J0439010−235308	12.4 ± 0.1	80.8 ± 0.5	L6.5/L6	14.31 ± 0.03	13.44 ± 0.03	12.77 ± 0.02	33; 59; 33,26; 53
WISEPA J044853.29−193548.5	18.1 ± 1.1	55.3 ± 3.4	.../T5pec	16.66 ± 0.03	16.95 ± 0.07	17.30 ± 0.09	83; 8; 83; 8
WISE J045746.08−020719.2	12.2 ± 0.4	82.0 ± 2.9	.../T2	14.63 ± 0.02	14.19 ± 0.00	13.99 ± 0.00	9; 8; 9; 8,86
WISEPA J050003.05−122343.2	11.8 ± 0.3	84.6 ± 2.2	.../T8	17.89 ± 0.02	18.13 ± 0.12	18.08 ± 0.09	83; 8; 83; 8,86

Table 8.1—Continued

Object	Distance (pc)	Parallax (mas)	Spectral Type[a] (Optical/NIR)	$J_{\rm MKO}$ (mag)	$H_{\rm MKO}$ (mag)	$K_{\rm MKO}$ (mag)	References (Disc; π; SpT; Phot)
2MASS J05002100+0330501	13.1 ± 0.1	76.2 ± 0.4	L4/L4.2 FLD-G	13.60 ± 0.02	12.76 ± 0.02	12.04 ± 0.02	129; 59; 129,58; 8
2MASS J05012406−0010452	21.2 ± 0.4	47.1 ± 0.9	L4 γ/L3: VL-G	14.86 ± 0.04	13.76 ± 0.03	12.91 ± 0.04	129; 59; 36,2; 53
PSO J076.7092+52.6087	16.8 ± 1.5	59.6 ± 5.4	.../T4.5	15.44 ± 0.02	15.47 ± 0.02	15.60 ± 0.03	7; 8; 7; 7
2MASS J05160945−0445499	18.4 ± 1.5	54.2 ± 4.3	.../T5.5	15.54 ± 0.02	15.77 ± 0.01	15.79 ± 0.02	18; 8; 20; 8,86
2MASS J05185995−2828372	22.9 ± 0.4	43.7 ± 0.8	L7/T1pec	15.87 ± 0.10	14.86 ± 0.07	14.11 ± 0.07	34; 50; 81,20; 53
WISE J052126.29+102528.4	7.1 ± 0.2	141.2 ± 4.8	.../T7.5	14.86 ± 0.02	15.25 ± 0.06	14.98 ± 0.06	9; 8; 9; 8
2MASSI J0523382−140302	12.8 ± 0.0	78.4 ± 0.2	L2.5/L5	12.97 ± 0.03	12.28 ± 0.03	11.62 ± 0.03	33; 59; 33,154; 39
SDSSp J053951.99−005902.0	12.7 ± 0.1	78.5 ± 0.6	L5/L5	13.85 ± 0.03	13.04 ± 0.03	12.40 ± 0.03	56; 59; 56,85; 87
PSO J085.1080−18.0445	16.9 ± 1.2	59.2 ± 4.0	.../T5	16.01 ± 0.02	...	...	97; 8; 97; 8
WISEPA J054231.26−162829.1	16.3 ± 0.7	61.3 ± 2.6	.../T6.5	16.30 ± 0.02	16.63 ± 0.10	16.76 ± 0.14	83; 8; 83; 8,83
WISE J054601.19−095947.5	19.9 ± 1.4	50.4 ± 3.6	.../T5	15.99 ± 0.02	16.24 ± 0.06	16.43 ± 0.06	107; 8; 107; 8
WISEA J055007.94+161051.9	20.4 ± 0.4	49.1 ± 0.9	.../L2	14.35 ± 0.02	13.57 ± 0.03	12.81 ± 0.03	84; 59; 84; 8
PSO J089.1751−09.4513	22.6 ± 1.2	44.3 ± 2.5	.../T5.5	16.46 ± 0.02	16.57 ± 0.07	16.66 ± 0.07	97; 8; 97; 8
2MASS J05591914−1404488	10.4 ± 0.1	96.6 ± 1.0	T5/T4.5	13.57 ± 0.03	13.64 ± 0.03	13.73 ± 0.03	14; 50; 16,20; 88
2MASS J06020638+4043588	15.4 ± 1.0	65.1 ± 4.2	.../T4.5	15.28 ± 0.02	15.38 ± 0.06	15.40 ± 0.06	101; 8; 101; 8
LSR J0602+3910	11.7 ± 0.0	85.6 ± 0.2	L1/L2: INT-G	12.26 ± 0.02	11.53 ± 0.02	10.84 ± 0.02	133; 59; 133,2; 8
WISEP J060738.65+242953.4	7.3 ± 0.0	136.9 ± 0.7	L8/L9	14.12 ± 0.03	13.12 ± 0.03	12.46 ± 0.02	30; 59; 31,31; 8
Gl 229B	5.8 ± 0.0	173.7 ± 0.1	.../T7pec	14.01 ± 0.05	14.36 ± 0.05	14.36 ± 0.05	118; 59; 20; 89
WISEPA J061135.13−041024.0	21.2 ± 1.4	47.2 ± 3.2	.../T0	15.40 ± 0.01	14.74 ± 0.01	14.29 ± 0.01	83; 62; 83; 62,86
WISE J061437.73+095135.0	17.6 ± 0.6	56.7 ± 2.0	.../T7	16.43 ± 0.02	16.64 ± 0.06	16.49 ± 0.06	107; 8; 107; 8
2MASS J06143818+3950357	22.7 ± 1.3	44.0 ± 2.6	.../L9:	16.55 ± 0.02	15.63 ± 0.06	15.01 ± 0.06	117; 8; 117; 8

Table 8.1—Continued

Object	Distance (pc)	Parallax (mas)	Spectral Type[a] (Optical/NIR)	$J_{\rm MKO}$ (mag)	$H_{\rm MKO}$ (mag)	$K_{\rm MKO}$ (mag)	References (Disc; π; SpT; Phot)
DENIS-P J0615493−010041	21.9 ± 0.1	45.7 ± 0.1	L2:/L1.0	13.70 ± 0.03	13.05 ± 0.03	12.52 ± 0.03	120; 131; 120,4; 8
WISEPA J062309.94−045624.6	11.6 ± 0.2	86.5 ± 1.7	.../T8	17.09 ± 0.02	17.32 ± 0.07	17.24 ± 0.09	83; 8; 83; 8
WISEPA J062542.21+564625.5	22.5 ± 1.7	44.4 ± 3.4	.../T6	16.74 ± 0.02	16.96 ± 0.10	16.96 ± 0.15	83; 8; 83; 8,83
WISE J064205.58+410155.5	15.6 ± 0.3	64.1 ± 1.2	.../L9 (red)	16.15 ± 0.02	15.11 ± 0.01	14.31 ± 0.01	107; 52; 7; 7
WISEA J064750.85−154616.4	21.0 ± 1.7	47.6 ± 3.9	.../L9.5	15.14 ± 0.02	14.35 ± 0.06	13.72 ± 0.06	142; 8; 142; 8,39
DENIS-P J0652197−253450	16.1 ± 0.0	62.0 ± 0.1	L0/M9.2	12.72 ± 0.02	12.09 ± 0.02	11.49 ± 0.02	120; 131; 120,4; 8
PSO J103.0927+41.4601	22.2 ± 1.8	45.1 ± 3.7	.../T0	15.36 ± 0.01	14.51 ± 0.03	13.95 ± 0.03	6; 8; 6; 6
2MASSI J0652307+471034	9.1 ± 0.0	109.7 ± 0.4	L4.5/L6.5	13.37 ± 0.02	12.47 ± 0.02	11.67 ± 0.02	33; 59; 33,26; 8
WISEPA J065609.60+420531.0	15.9 ± 1.0	63.0 ± 4.1	T2/T3	15.28 ± 0.02	14.98 ± 0.06	14.99 ± 0.06	83; 8; 121,83; 8
WISEA J065958.55+171710.9	23.8 ± 0.5	42.1 ± 0.9	.../L2	14.74 ± 0.02	13.83 ± 0.03	13.00 ± 0.03	84; 59; 84; 8,39
2MASS J07003664+3157266	11.3 ± 0.0	88.3 ± 0.3	L3.5/...	12.82 ± 0.02	12.00 ± 0.02	11.29 ± 0.02	148; 59; 148; 53
WISEA J071552.38−114532.9	18.0 ± 0.1	55.6 ± 0.3	.../L4pec	14.18 ± 0.02	13.58 ± 0.05	12.78 ± 0.04	84; 59; 84; 8
DENIS-P J0716478−063037	24.4 ± 0.1	40.9 ± 0.1	L1:/L1.1	13.80 ± 0.00	13.13 ± 0.00	12.56 ± 0.00	120; 131; 120,4; 103
2MASSI J0727182+171001	8.9 ± 0.1	112.5 ± 0.9	T8/T7	15.19 ± 0.03	15.67 ± 0.03	15.69 ± 0.03	15; 50; 16,20; 85
SDSS J074149.15+235127.5	18.9 ± 1.3	53.0 ± 3.7	.../T5	15.89 ± 0.01	16.10 ± 0.02	16.28 ± 0.04	85; 8; 20; 86
SDSS J074201.41+205520.5	17.1 ± 1.0	58.4 ± 3.3	.../T5	15.78 ± 0.02	15.95 ± 0.03	16.06 ± 0.03	85; 8; 20; 85
WISEPA J074457.15+562821.8	14.8 ± 0.5	67.6 ± 2.1	.../T8	17.26 ± 0.02	17.65 ± 0.12	17.70 ± 0.20	83; 8; 83; 8,83
2MASSI J0746425+200032	12.3 ± 0.1	81.1 ± 0.9	L0.5/L1	11.64 ± 0.03	11.01 ± 0.03	10.43 ± 0.03	127; 50; 80,85; 88
PSO J117.0600−01.6779	23.5 ± 2.0	42.6 ± 3.7	.../T5.5	16.36 ± 0.02	16.24 ± 0.05	16.19 ± 0.05	97; 8; 97; 8
DENIS-P J0751164−253043	17.8 ± 0.0	56.3 ± 0.1	L1.5/L1.1	13.10 ± 0.02	12.57 ± 0.02	11.97 ± 0.02	120; 131; 120,4; 8
2MASSI J0755480+221218	17.0 ± 1.0	58.9 ± 3.3	T6/T5	15.48 ± 0.00	15.78 ± 0.01	15.93 ± 0.02	15; 8; 16,20; 86

Table 8.1—Continued

Object	Distance (pc)	Parallax (mas)	Spectral Type[a] (Optical/NIR)	$J_{\rm MKO}$ (mag)	$H_{\rm MKO}$ (mag)	$K_{\rm MKO}$ (mag)	References (Disc; π; SpT; Phot)
HIP 38939B	18.5 ± 0.0	54.1 ± 0.0	.../T4.5	15.79 ± 0.02	16.03 ± 0.08	16.22 ± 0.08	43; 59; 43; 8,43
SDSS J075840.33+324723.4	10.7 ± 0.5	93.7 ± 4.4	T3/T2	14.73 ± 0.02	14.21 ± 0.04	13.90 ± 0.06	85; 8; 121,20; 8,119
SDSS J080531.84+481233.0	21.4 ± 0.4	46.8 ± 1.0	L4/L9:	14.61 ± 0.03	14.01 ± 0.03	13.51 ± 0.03	75; 59; 75,85; 85
WISE J080700.23+413026.8	19.6 ± 1.5	51.1 ± 3.8	.../L8pec	15.93 ± 0.02	14.99 ± 0.06	14.24 ± 0.06	147; 8; 147; 8
SDSS J080959.01+443422.2	23.6 ± 2.0	42.4 ± 3.6	.../L5.4 INT-G	16.42 ± 0.02	15.32 ± 0.06	14.37 ± 0.06	85; 8; 58; 8
DENIS-P J0812316−244442	21.2 ± 0.0	47.3 ± 0.1	L2.5:/L0.9	13.78 ± 0.03	13.00 ± 0.02	12.38 ± 0.02	120; 131; 120,4; 8
WISEPA J081958.05−033529.0	13.9 ± 0.6	71.7 ± 3.3	T4/T4	14.78 ± 0.02	14.59 ± 0.06	14.63 ± 0.06	83; 8; 121,83; 8
WISEPA J082131.63+144319.3	22.9 ± 2.0	43.7 ± 3.9	.../T5.5	16.40 ± 0.02	16.60 ± 0.06	16.32 ± 0.06	83; 8; 83; 8
2MASSI J0825196+211552	10.7 ± 0.1	93.8 ± 1.0	L7.5/L7pec	14.89 ± 0.03	13.81 ± 0.03	12.93 ± 0.03	80; 40; 80,85; 88
WISEA J082640.45−164031.8	18.5 ± 1.5	54.0 ± 4.3	.../L9	15.61 ± 0.02	14.66 ± 0.07	14.09 ± 0.07	84; 8; 84; 8,39
SSSPM J0829−1309	11.6 ± 0.0	85.8 ± 0.2	L2/L2:	12.76 ± 0.03	11.92 ± 0.02	11.28 ± 0.02	137; 131; 98,111; 8
SDSSp J083008.12+482847.4	13.1 ± 0.6	76.4 ± 3.4	L8/L9:	15.22 ± 0.03	14.40 ± 0.03	13.68 ± 0.03	61; 152; 81,61; 88
PSO J127.5648−11.1861	23.3 ± 2.0	42.9 ± 3.7	.../T3	15.71 ± 0.02	15.43 ± 0.05	15.50 ± 0.05	97; 8; 97; 8
SDSS J083048.80+012831.1	23.4 ± 2.6	42.7 ± 4.7	.../T4.5	16.05 ± 0.01	16.25 ± 0.02	16.35 ± 0.04	85; 8; 20; 86
2MASSW J0832045−012835	23.7 ± 0.2	42.2 ± 0.4	L1.5/L1:	14.07 ± 0.02	13.39 ± 0.03	12.69 ± 0.03	80; 59; 80,111; 8
2MASSI J0835425−081923	7.2 ± 0.0	138.6 ± 0.3	L5/L4pec	13.04 ± 0.02	11.99 ± 0.02	11.08 ± 0.02	33; 59; 33,58; 53
2MASSI J0847287−153237	17.6 ± 0.1	56.9 ± 0.3	L2/...	13.42 ± 0.03	12.66 ± 0.03	12.02 ± 0.02	33; 59; 33; 53
SDSS J085234.90+472035.0	23.7 ± 1.9	42.2 ± 3.4	.../L9.5:	16.16 ± 0.02	15.30 ± 0.06	14.64 ± 0.06	85; 8; 85; 8
WISEPA J085716.25+560407.6	13.1 ± 0.4	76.3 ± 2.4	.../T8	17.34 ± 0.02	···	···	83; 8; 83; 8
SDSSp J085758.45+570851.4	14.0 ± 0.2	71.2 ± 1.0	L8/L8:	14.86 ± 0.02	13.89 ± 0.03	12.94 ± 0.03	61; 59; 81,61; 8
SDSS J085834.42+325627.7	24.4 ± 2.1	40.9 ± 3.6	.../T1	16.36 ± 0.02	15.49 ± 0.06	14.73 ± 0.06	32; 8; 32; 8

Table 8.1—Continued

Object	Distance (pc)	Parallax (mas)	Spectral Type[a] (Optical/NIR)	$J_{\rm MKO}$ (mag)	$H_{\rm MKO}$ (mag)	$K_{\rm MKO}$ (mag)	References (Disc; π; SpT; Phot)
ULAS J085910.69+101017.1	20.6 ± 0.8	48.6 ± 2.0	.../T7	17.88 ± 0.02	18.30 ± 0.09	18.29 ± 0.16	122; 8; 122; 8,86
2MASSI J0859254−194926	15.3 ± 1.4	65.4 ± 6.1	L6::/L8	15.42 ± 0.05	14.47 ± 0.04	13.70 ± 0.06	33; 53; 33,147; 53
ULAS J090116.23−030635.0	16.0 ± 0.7	62.6 ± 2.6	.../T7.5	17.89 ± 0.04	18.49 ± 0.13	···	99; 110; 99; 86
2MASS J09054654+5623117	24.8 ± 0.8	40.4 ± 1.2	L5/L6	15.34 ± 0.02	14.37 ± 0.04	13.71 ± 0.04	129; 59; 129,26; 8
2MASSI J0908380+503208	10.4 ± 0.1	95.8 ± 0.7	L5/L9:	14.42 ± 0.02	13.56 ± 0.03	12.93 ± 0.03	33; 59; 33,85; 8
DENIS-P J090957.1−065806	24.9 ± 0.2	40.1 ± 0.3	L0/L0:	13.81 ± 0.02	13.12 ± 0.02	12.50 ± 0.03	48; 59; 81,111; 53
Gl 337CD	20.3 ± 0.1	49.2 ± 0.3	L8/T0	15.48 ± 0.02	14.65 ± 0.08	14.00 ± 0.06	153; 59; 153,20; 8,53
2MASS J09153413+0422045	18.2 ± 0.4	54.8 ± 1.1	L6/...	14.52 ± 0.00	13.63 ± 0.00	12.89 ± 0.00	129; 59; 129; 86
WISE J092055.40+453856.3	12.6 ± 0.6	79.4 ± 3.9	.../L9.5	15.04 ± 0.01	14.19 ± 0.02	13.77 ± 0.01	107; 8; 6; 6
2MASS J09211410−2104446	12.6 ± 0.0	79.3 ± 0.2	L1.5/L4:	12.69 ± 0.02	12.23 ± 0.02	11.66 ± 0.02	129; 59; 129,23; 8
SDSS J092308.70+234013.7	22.8 ± 1.9	43.8 ± 3.7	L1/L2.3	13.76 ± 0.02	13.23 ± 0.02	12.78 ± 0.02	135; 8; 135,4; 8
SDSSp J092615.38+584720.9	22.9 ± 0.6	43.7 ± 1.1	T5/T4.5	15.71 ± 0.07	15.38 ± 0.19	15.53 ± 0.19	61; 50; 121,20; 8
WISEPC J092906.77+040957.9	22.1 ± 1.1	45.2 ± 2.3	.../T6.5	16.87 ± 0.01	17.24 ± 0.01	17.61 ± 0.02	83; 8; 83; 29
2MASSI J0937347+293142	6.1 ± 0.1	163.4 ± 1.8	T7/T6pec	14.29 ± 0.03	14.67 ± 0.03	15.39 ± 0.06	15; 134; 16,20; 85
2MASS J09393548−2448279	5.3 ± 0.1	187.3 ± 4.6	T8/T8	15.61 ± 0.09	15.96 ± 0.09	16.83 ± 0.09	150; 24; 121,20; 90
ULAS J095047.28+011734.3	19.7 ± 0.0	50.8 ± 0.1	.../T8	18.02 ± 0.03	18.40 ± 0.03	18.85 ± 0.07	29; 59; 107; 29
ULAS J095429.90+062309.6	24.5 ± 1.9	40.9 ± 3.2	.../T5	16.60 ± 0.01	16.87 ± 0.01	17.05 ± 0.01	141,29; 8; 29; 29
PSO J149.0341−14.7857	15.3 ± 0.8	65.4 ± 3.4	.../L9	15.99 ± 0.02	15.07 ± 0.01	14.46 ± 0.02	7; 8; 7; 7
G 196-3B	22.5 ± 0.4	44.3 ± 0.8	L3 β/L3: VL-G	14.75 ± 0.05	13.75 ± 0.03	12.74 ± 0.03	126; 59; 36,2; 8
DENIS J1004403−131818	24.6 ± 0.4	40.7 ± 0.7	.../L1:	14.57 ± 0.04	13.94 ± 0.04	13.34 ± 0.04	113; 59; 111; 39
SDSS J100711.74+193056.2	21.9 ± 0.9	45.6 ± 2.0	.../L8:	16.70 ± 0.02	15.87 ± 0.06	15.23 ± 0.06	32; 8; 32; 8

Table 8.1—Continued

Object	Distance (pc)	Parallax (mas)	Spectral Type[a] (Optical/NIR)	J_{MKO} (mag)	H_{MKO} (mag)	K_{MKO} (mag)	References (Disc; π; SpT; Phot)
2MASSI J1010148−040649	18.2 ± 1.3	55.0 ± 4.0	L6/L6	15.39 ± 0.02	14.43 ± 0.04	13.57 ± 0.05	33; 8; 33,82; 8,53
ULAS J101243.54+102101.7	16.8 ± 0.5	59.7 ± 1.8	.../T5.5	16.88 ± 0.01	17.25 ± 0.05	17.45 ± 0.08	138; 8; 27; 86
DENIS J1019245−270717	23.3 ± 0.1	42.8 ± 0.2	L0.5/M9.5	13.50 ± 0.02	12.97 ± 0.02	12.45 ± 0.02	113; 59; 113,78; 8
2MASS J10224821+5825453	18.4 ± 0.1	54.3 ± 0.3	L1 β/L1: FLD-G	13.45 ± 0.03	12.71 ± 0.03	12.14 ± 0.03	129; 59; 36,2; 8
CFBDS J102841.01+565401.9	23.0 ± 0.7	43.4 ± 1.3	.../T8	17.98 ± 0.04	18.38 ± 0.08	18.85 ± 0.09	1; 52; 1; 1
2MASSI J1029216+162652	19.1 ± 0.3	52.3 ± 0.7	L2.5/L2.8	14.22 ± 0.02	13.41 ± 0.02	12.60 ± 0.02	80; 59; 80,4; 8
ULAS J102940.52+093514.6	14.6 ± 0.4	68.6 ± 1.7	.../T8	17.28 ± 0.01	17.63 ± 0.01	17.64 ± 0.02	29; 8; 29; 29
WISE J103907.73−160002.9	22.1 ± 0.9	45.3 ± 2.0	.../T7.5	16.95 ± 0.02	17.36 ± 0.06	17.10 ± 0.07	107; 8; 107; 8
2MASS J10430758+2225236	19.1 ± 1.1	52.4 ± 2.9	L8/L9:	15.85 ± 0.02	14.82 ± 0.04	13.98 ± 0.04	35; 8; 35,26; 8
SDSS J104335.08+121314.1	16.7 ± 0.9	59.9 ± 3.1	.../L9	15.87 ± 0.01	14.91 ± 0.01	14.21 ± 0.01	32; 8; 82; 86
2MASSI J1045240−014957	17.0 ± 0.1	58.7 ± 0.2	L1/L1: FLD-G	13.08 ± 0.00	12.40 ± 0.00	11.78 ± 0.00	65; 59; 65,2; 86
2MASSI J1047538+212423	10.6 ± 0.4	94.7 ± 3.8	T7/T6.5	15.46 ± 0.03	15.83 ± 0.03	16.20 ± 0.03	12; 152; 16,20; 88
SDSS J104842.84+011158.5	15.0 ± 0.0	66.5 ± 0.2	L1/L4	12.80 ± 0.00	12.16 ± 0.00	11.58 ± 0.00	75; 59; 75,77; 86
WISE J105047.90+505606.2	22.1 ± 1.1	45.3 ± 2.2	.../T8	17.94 ± 0.02	18.31 ± 0.03	···	107; 8; 107; 107
2MASS J10511900+5613086	15.6 ± 0.0	64.0 ± 0.2	L2/L0.8	13.17 ± 0.02	12.50 ± 0.02	11.88 ± 0.02	129; 59; 129,4; 8
WISE J105257.95−194250.2	14.7 ± 0.5	67.8 ± 2.2	.../T7.5	16.84 ± 0.02	17.07 ± 0.06	16.99 ± 0.06	147; 8; 147; 8
DENIS-P J1058.7−1548	18.3 ± 0.2	54.7 ± 0.5	L3/L2.2 FLD-G	14.12 ± 0.05	13.29 ± 0.05	12.55 ± 0.05	47; 59; 79,58; 88
2MASSI J1104012+195921	17.9 ± 0.1	55.9 ± 0.4	L4/L5.5	14.34 ± 0.02	13.56 ± 0.03	12.93 ± 0.03	33; 59; 33,26; 8
2MASS J11061197+2754225	20.8 ± 1.3	48.0 ± 3.0	.../T2.5	14.96 ± 0.04	14.20 ± 0.05	13.84 ± 0.05	101; 109; 101; 109
SDSSp J111010.01+011613.1	19.2 ± 0.4	52.1 ± 1.2	.../T5.5	16.16 ± 0.01	16.20 ± 0.02	16.05 ± 0.03	61; 50; 20; 86
Gl 417BC	21.9 ± 0.2	45.6 ± 0.4	L4.5/L5: FLD-G	14.46 ± 0.02	13.55 ± 0.03	12.67 ± 0.03	80; 155; 80,2; 8,53

Table 8.1—Continued

Object	Distance (pc)	Parallax (mas)	Spectral Type[a] (Optical/NIR)	$J_{\rm MKO}$ (mag)	$H_{\rm MKO}$ (mag)	$K_{\rm MKO}$ (mag)	References (Disc; π; SpT; Phot)
2MASS J11145133−2618235	5.6 ± 0.0	179.2 ± 1.4	T8/T7.5	15.52 ± 0.05	15.82 ± 0.05	16.54 ± 0.05	150; 50; 121,20; 91
WISEPC J112254.73+255021.5	15.9 ± 0.7	62.9 ± 2.8	.../T6	16.26 ± 0.02	16.63 ± 0.06	16.63 ± 0.06	83; 8; 83; 8
WISE J112438.12−042149.7	17.5 ± 1.0	57.3 ± 3.4	.../T7	16.40 ± 0.02	16.79 ± 0.06	16.66 ± 0.06	107; 8; 107; 8
ULAS J115508.39+044502.3	20.3 ± 1.0	49.1 ± 2.3	.../T7	18.31 ± 0.02	...	...	29; 8; 29; 8
SDSS J115553.86+055957.5	21.5 ± 1.8	46.5 ± 3.9	.../L6.8 FLD-G	15.72 ± 0.01	14.75 ± 0.01	14.11 ± 0.01	85; 8; 58; 86
PSO J180.1475−28.6160	24.6 ± 3.3	40.7 ± 5.4	.../T0	15.96 ± 0.02	15.15 ± 0.01	14.75 ± 0.05	7; 8; 7; 7,8
SDSSp J120358.19+001550.3	14.9 ± 0.1	67.2 ± 0.6	L3/L5.0	13.93 ± 0.00	13.11 ± 0.00	12.44 ± 0.00	56; 59; 56,4; 86
2MASSI J1204303+321259	24.3 ± 0.2	41.2 ± 0.3	L0/M9	13.79 ± 0.02	13.16 ± 0.03	12.49 ± 0.03	33; 59; 33,154; 8
SDSS J120747.17+024424.8	22.3 ± 1.8	44.8 ± 3.6	L8/T0	15.46 ± 0.01	14.71 ± 0.01	14.19 ± 0.01	75; 8; 75,20; 86
2MASS J12095613−1004008	21.8 ± 0.5	45.8 ± 1.0	T3.5/T3	15.55 ± 0.03	15.24 ± 0.03	15.17 ± 0.03	19; 50; 81,20; 32
2MASSI J1213033−043243	16.8 ± 0.3	59.5 ± 1.0	L5/L4.2	14.57 ± 0.02	13.73 ± 0.03	13.00 ± 0.03	33; 59; 33,4; 8
2MASSI J1217110−031113	11.0 ± 0.3	90.8 ± 2.2	T7/T7.5	15.56 ± 0.03	15.98 ± 0.03	15.92 ± 0.03	12; 149; 16,20; 88
SDSS J121951.45+312849.4	19.2 ± 1.4	52.0 ± 3.8	.../L8	15.96 ± 0.02	15.03 ± 0.01	14.35 ± 0.01	32; 8; 32; 8,86
2MASS J12212770+0257198	18.5 ± 0.1	54.0 ± 0.2	L0/M9.7 FLD-G	13.07 ± 0.00	12.44 ± 0.00	11.91 ± 0.00	129; 59; 129,58; 86
2MASS J12255432−2739466	13.3 ± 0.4	75.1 ± 2.5	T6/T6	14.88 ± 0.03	15.17 ± 0.03	15.28 ± 0.03	12; 149; 16,20; 88
WISE J122558.86−101345.0	24.3 ± 1.7	41.1 ± 2.9	.../T6	16.10 ± 0.02	16.46 ± 0.15	16.47 ± 0.06	107; 8; 107; 8,107
DENIS-P J122813.8−154711	22.3 ± 0.9	44.8 ± 1.8	L5/L6::	14.28 ± 0.05	13.40 ± 0.05	12.71 ± 0.05	47; 50; 79,85; 88
2MASS J12314753+0847331	14.3 ± 0.7	70.2 ± 3.6	T6/T5.5	15.15 ± 0.00	15.46 ± 0.01	15.55 ± 0.02	19; 8; 121,20; 86
2MASSW J1239272+551537	23.6 ± 1.2	42.4 ± 2.1	L5/...	14.62 ± 0.03	13.63 ± 0.03	12.76 ± 0.03	80; 50; 80; 8
2MASSW J1246467+402715	22.6 ± 0.4	44.2 ± 0.8	L4/L4.0	14.89 ± 0.02	14.04 ± 0.04	13.25 ± 0.04	80; 59; 80,4; 8
SDSS J125011.65+392553.9	23.4 ± 1.7	42.8 ± 3.2	.../T4	16.15 ± 0.02	16.24 ± 0.25	16.18 ± 0.25	32; 8; 32; 8,39

Table 8.1—Continued

Object	Distance (pc)	Parallax (mas)	Spectral Type[a] (Optical/NIR)	J_{MKO} (mag)	H_{MKO} (mag)	K_{MKO} (mag)	References (Disc; π; SpT; Phot)
WISE J125015.56+262846.9	17.4 ± 1.1	57.5 ± 3.7	.../T6	16.40 ± 0.01	16.74 ± 0.02	16.79 ± 0.05	107; 8; 7; 86
WISE J125448.52−072828.4	24.3 ± 1.6	41.1 ± 2.7	.../T7	17.30 ± 0.01	17.63 ± 0.03	17.39 ± 0.07	147; 8; 147; 147,8
SDSSp J125453.90−012247.4	11.8 ± 0.3	84.9 ± 1.9	T2/T2	14.67 ± 0.00	14.14 ± 0.00	13.89 ± 0.01	87; 40; 16,20; 86
VHS J125601.92−125723.9 b	12.7 ± 1.0	78.8 ± 6.4	L8::/L7:: VL-G	17.14 ± 0.02	15.78 ± 0.02	14.67 ± 0.01	60; 60; 60,60; 60
WISE J125715.90+400854.2	17.6 ± 0.6	57.0 ± 1.8	.../T7	16.88 ± 0.02	17.12 ± 0.06	17.16 ± 0.07	107; 8; 107; 8
Ross 458C	11.5 ± 0.0	86.9 ± 0.2	.../T8	16.69 ± 0.02	17.01 ± 0.04	16.90 ± 0.06	71; 59; 37; 86
2MASSW J1300425+191235	14.0 ± 0.0	71.7 ± 0.2	L1/L3	12.61 ± 0.02	12.16 ± 0.02	11.60 ± 0.02	63; 59; 63,23; 8
Kelu-1	18.6 ± 0.2	53.8 ± 0.7	L2/L0.5pec	13.23 ± 0.05	12.45 ± 0.05	11.78 ± 0.05	130; 59; 79,146; 91
2MASSI J1305410+204639	19.8 ± 0.3	50.4 ± 0.8	L5/L6.5	15.12 ± 0.05	14.13 ± 0.04	13.34 ± 0.04	33; 59; 72,4; 8
ULAS J131508.42+082627.4	23.4 ± 4.2	42.8 ± 7.7	.../T7.5	18.86 ± 0.04	19.50 ± 0.10	19.60 ± 0.12	122; 110; 122; 50
2MASSI J1315309−264951	18.6 ± 0.4	53.9 ± 1.1	L5.5/L6.7	15.11 ± 0.05	14.14 ± 0.04	13.45 ± 0.04	74; 59; 81,4; 8
2MASSW J1326201−272937	18.3 ± 2.0	54.7 ± 5.9	L5/L6.6:	15.76 ± 0.03	14.83 ± 0.05	13.83 ± 0.05	65; 8; 65,4; 8
SDSSp J132629.82−003831.5	20.9 ± 1.3	47.9 ± 2.9	L8:/L7	16.22 ± 0.01	15.11 ± 0.01	14.17 ± 0.01	56; 8; 56,112; 86
SDSS J133148.92−011651.4	14.9 ± 2.8	67.3 ± 12.6	L6/L6:	15.33 ± 0.01	14.67 ± 0.00	14.05 ± 0.01	75; 111; 75,112; 86
WISE J133750.46+263648.6	24.8 ± 1.3	40.4 ± 2.1	.../T5	16.56 ± 0.02	16.81 ± 0.03	17.02 ± 0.06	107; 8; 107; 86
2MASSW J1338261+414034	21.1 ± 0.1	47.3 ± 0.3	L2.5/L2.4	14.12 ± 0.02	13.38 ± 0.02	12.75 ± 0.02	80; 59; 80,4; 8
SDSSp J134646.45−003150.4	14.6 ± 0.5	68.3 ± 2.3	T7/T6.5	15.64 ± 0.01	15.97 ± 0.01	15.96 ± 0.02	151; 149; 16,20; 86
LHS 2803B	18.2 ± 0.0	55.0 ± 0.1	.../T5.5	16.39 ± 0.02	16.57 ± 0.04	16.90 ± 0.08	44; 59; 44; 44
SDSS J135852.68+374711.9	20.1 ± 1.3	49.6 ± 3.1	.../T4.5:	16.24 ± 0.02	16.49 ± 0.06	16.69 ± 0.06	32; 8; 32; 8
SDSS J140023.12+433822.3	24.5 ± 1.9	40.8 ± 3.2	.../L7:	16.21 ± 0.02	15.21 ± 0.06	14.45 ± 0.06	32; 8; 32; 8
ULAS J141623.94+134836.3	9.3 ± 0.0	107.6 ± 0.3	.../T7.5	17.26 ± 0.02	17.58 ± 0.03	18.43 ± 0.08	139,28; 59; 25; 86,8

Table 8.1—Continued

Object	Distance (pc)	Parallax (mas)	Spectral Type[a] (Optical/NIR)	$J_{\rm MKO}$ (mag)	$H_{\rm MKO}$ (mag)	$K_{\rm MKO}$ (mag)	References (Disc; π; SpT; Phot)
SDSS J141624.08+134826.7	9.3 ± 0.0	107.6 ± 0.3	L6/L6::pec	13.07 ± 0.00	12.50 ± 0.00	12.11 ± 0.00	11; 59; 11,11; 86
2MASSW J1421314+182740	19.0 ± 0.1	52.7 ± 0.3	L0/M8.9	12.86 ± 0.05	12.49 ± 0.02	11.92 ± 0.02	63; 59; 129,4; 8
BD +01 2920B	17.2 ± 0.2	58.2 ± 0.5	.../T8	18.55 ± 0.03	18.96 ± 0.07	17.45 ± 0.22	123; 155; 107; 107,8
2MASS J14283132+5923354	22.0 ± 0.2	45.4 ± 0.5	L4/L4.4	14.71 ± 0.02	13.95 ± 0.03	13.25 ± 0.03	129; 59; 129,4; 8
VHS J143311.46−083736.3	16.1 ± 0.9	62.2 ± 3.6	.../T8	19.05 ± 0.02	19.22 ± 0.14	···	100; 8; 100; 8,100
WISEPA J143602.19−181421.8	20.4 ± 1.9	48.9 ± 4.5	.../T8pec	17.32 ± 0.07	···	···	83; 8; 83; 8
2MASSW J1439284+192915	14.4 ± 0.1	69.6 ± 0.5	L1/...	12.66 ± 0.03	12.05 ± 0.03	11.47 ± 0.03	79; 40; 79; 88
SDSSp J144600.60+002452.0	22.0 ± 1.6	45.5 ± 3.2	L6/L5	15.58 ± 0.01	14.66 ± 0.01	13.92 ± 0.01	61; 152; 75,85; 86
WISE J144806.48−253420.3	21.0 ± 1.5	47.7 ± 3.4	.../T8	18.94 ± 0.02	···	···	147; 8; 147; 8
2MASSW J1448256+103159	14.0 ± 0.1	71.2 ± 0.7	L4:/L4.7 FLD-G	14.42 ± 0.00	13.51 ± 0.00	12.67 ± 0.00	154; 59; 129,55; 86
Gl 564BC	18.2 ± 0.0	54.9 ± 0.1	.../L4:	13.20 ± 0.08	12.42 ± 0.15	11.69 ± 0.04	124; 59; 73; 49
WISEPC J145715.03+581510.2	21.4 ± 2.6	46.8 ± 5.8	T8/T7	16.82 ± 0.02	17.16 ± 0.06	17.22 ± 0.07	83; 8; 83,83; 8
Gliese 570D	5.9 ± 0.0	170.0 ± 0.1	T7/T7.5	14.82 ± 0.05	15.28 ± 0.05	15.52 ± 0.05	13; 59; 16,20; 91
PSO J224.3820+47.4057	20.2 ± 1.2	49.5 ± 2.9	.../T7	17.10 ± 0.02	17.43 ± 0.06	17.06 ± 0.06	7; 8; 7; 8,7
2MASS J15031961+2525196	6.5 ± 0.0	154.9 ± 1.1	T6/T5	13.55 ± 0.03	13.90 ± 0.03	13.99 ± 0.03	17; 59; 16,20; 85
SDSS J150411.63+102718.4	21.7 ± 0.7	46.1 ± 1.5	.../T7	16.51 ± 0.01	16.99 ± 0.05	17.12 ± 0.08	32; 50; 32; 86
HIP 73786B	19.0 ± 0.0	52.6 ± 0.1	.../T6:pec	16.59 ± 0.02	17.05 ± 0.04	17.41 ± 0.09	138,116; 59; 116; 86
2MASSW J1506544+132106	11.7 ± 0.0	85.6 ± 0.3	L3/L4	13.21 ± 0.02	12.46 ± 0.02	11.72 ± 0.02	63; 59; 63,26; 8
2MASSW J1507476−162738	7.4 ± 0.0	135.2 ± 0.3	L5/L5.5	12.70 ± 0.03	11.90 ± 0.03	11.29 ± 0.03	127; 59; 80,85; 88
2MASSW J1515008+484742	9.6 ± 0.3	104.5 ± 3.5	L6/L6	13.96 ± 0.02	13.18 ± 0.02	12.48 ± 0.02	154; 8; 35,154; 8
SDSS J151643.01+305344.4	20.7 ± 1.2	48.2 ± 2.7	.../T0.5:	16.77 ± 0.02	16.00 ± 0.02	15.16 ± 0.01	32; 8; 32; 86

Table 8.1—Continued

Object	Distance (pc)	Parallax (mas)	Spectral Type[a] (Optical/NIR)	$J_{\rm MKO}$ (mag)	$H_{\rm MKO}$ (mag)	$K_{\rm MKO}$ (mag)	References (Disc; π; SpT; Phot)
WISE J151721.13+052929.3	21.7 ± 1.0	46.1 ± 2.1	.../T8	18.53 ± 0.02	18.85 ± 0.15	···	107; 8; 107; 8,86
SDSS J152039.82+354619.8	17.4 ± 1.5	57.4 ± 4.8	.../T0:	15.46 ± 0.02	14.58 ± 0.05	14.01 ± 0.05	32; 8; 32; 8,119
SDSS J152103.24+013142.7	23.1 ± 3.3	43.3 ± 6.2	.../T3	16.10 ± 0.01	15.68 ± 0.01	15.57 ± 0.02	85; 8; 112; 86
Gl 584C	17.9 ± 0.2	56.0 ± 0.8	L8/L8	16.05 ± 0.01	15.08 ± 0.01	14.38 ± 0.01	80; 155; 80,61; 86
2MASSI J1526140+204341	20.0 ± 0.6	50.0 ± 1.5	L7/L5.5	15.42 ± 0.02	14.52 ± 0.04	13.88 ± 0.05	80; 59; 80,26; 8,53
2MASSI J1534498−295227	16.0 ± 0.3	62.4 ± 1.3	T6/T5.5	14.60 ± 0.03	14.74 ± 0.03	14.91 ± 0.03	15; 50; 16,20; 85
SDSS J153453.33+121949.2	20.0 ± 0.7	49.9 ± 1.7	.../L4:	15.28 ± 0.02	14.38 ± 0.04	13.80 ± 0.04	32; 59; 32; 8
DENIS-P J153941.96−052042.4	17.0 ± 0.1	58.8 ± 0.4	L4:/L2	13.84 ± 0.03	13.08 ± 0.03	12.54 ± 0.03	77; 59; 81,77; 53
SDSS J154009.36+374230.3	24.5 ± 2.8	40.8 ± 4.7	.../L9:	16.35 ± 0.02	15.40 ± 0.06	14.62 ± 0.06	32; 8; 32; 8
WISE J154459.27+584204.5	20.4 ± 0.8	49.1 ± 1.9	.../T7.5	18.11 ± 0.02	18.40 ± 0.29	···	107; 8; 107; 8,107
2MASS J15461461+4932114	21.5 ± 2.5	46.5 ± 5.4	.../T2.5:	15.65 ± 0.02	15.35 ± 0.12	15.08 ± 0.06	114; 8; 114; 8,119
2MASSW J1552591+294849	20.4 ± 0.1	49.0 ± 0.2	L0 β/L0: INT-G	13.43 ± 0.03	12.68 ± 0.03	11.99 ± 0.03	154; 59; 36,2; 8
2MASSI J1553022+153236	13.3 ± 0.2	75.1 ± 0.9	.../T7	15.34 ± 0.03	15.76 ± 0.03	15.94 ± 0.03	15; 50; 20; 85
2MASSW J1555157−095605	13.6 ± 0.0	73.7 ± 0.2	L1/L1.6	12.50 ± 0.02	12.06 ± 0.02	11.42 ± 0.02	65; 59; 65,4; 8
2MASS J16150413+1340079	14.6 ± 1.4	68.6 ± 6.4	.../T6	16.32 ± 0.09	16.73 ± 0.10	16.70 ± 0.10	101; 53; 101; 53,8
2MASSW J1615441+355900	20.0 ± 0.1	50.1 ± 0.4	L3/L3.6	14.43 ± 0.02	13.60 ± 0.03	12.91 ± 0.03	80; 59; 80,4; 8
WISEPA J161705.75+180714.3	12.8 ± 0.5	78.0 ± 3.1	T8/T8	17.57 ± 0.02	18.23 ± 0.08	···	83; 8; 83,83; 8,83
SDSSp J162414.37+002915.6	11.0 ± 0.1	90.9 ± 1.2	T6/T6	15.20 ± 0.05	15.48 ± 0.05	15.61 ± 0.05	145; 149; 121,20; 145
PSO J246.1033−19.6194	23.0 ± 1.6	43.5 ± 3.0	.../T2	16.36 ± 0.02	15.87 ± 0.02	15.82 ± 0.02	97; 8; 97; 8,86
WISEPA J162725.64+325525.5	19.2 ± 0.8	52.1 ± 2.2	.../T6	16.24 ± 0.02	16.56 ± 0.06	16.87 ± 0.06	83; 8; 83; 8
SDSS J162838.77+230821.1	13.3 ± 0.2	75.1 ± 0.9	.../T7	16.25 ± 0.03	16.63 ± 0.03	16.72 ± 0.03	32; 50; 32; 32

Table 8.1—Continued

Object	Distance (pc)	Parallax (mas)	Spectral Type[a] (Optical/NIR)	$J_{\rm MKO}$ (mag)	$H_{\rm MKO}$ (mag)	$K_{\rm MKO}$ (mag)	References (Disc; π; SpT; Phot)
PSO J247.3273+03.5932	13.1 ± 0.6	76.5 ± 3.5	T3/T2	15.10 ± 0.01	14.53 ± 0.01	14.28 ± 0.02	42; 8; 121,42; 42
SDSS J163022.92+081822.0	22.2 ± 2.3	45.1 ± 4.7	.../T5.5	16.16 ± 0.02	16.35 ± 0.03	16.41 ± 0.03	32; 8; 32; 32
SDSS J163030.53+434404.0	22.4 ± 1.3	44.7 ± 2.6	.../L7:	16.54 ± 0.02	15.56 ± 0.06	14.77 ± 0.06	85; 8; 85; 8
2MASSW J1632291+190441	15.2 ± 0.5	65.6 ± 2.1	L8/L8	15.77 ± 0.05	14.68 ± 0.05	13.97 ± 0.05	79; 40; 79,20; 88
2MASSW J1645221−131951	11.3 ± 0.0	88.8 ± 0.1	L1.5/...	12.37 ± 0.03	11.71 ± 0.03	11.11 ± 0.03	65; 59; 65; 53
WISEPA J164715.59+563208.2	23.4 ± 1.1	42.7 ± 2.1	L7/L9pec	16.50 ± 0.02	15.41 ± 0.06	14.48 ± 0.06	83; 8; 121,83; 8
WISEPA J165311.05+444423.9	13.2 ± 0.3	75.7 ± 1.9	T8/T8	17.07 ± 0.02	17.59 ± 0.05	17.05 ± 0.07	83; 8; 83,83; 8
2MASS J16573454+1054233	23.9 ± 0.2	41.9 ± 0.3	L2/L1.4	14.06 ± 0.02	13.40 ± 0.03	12.78 ± 0.03	129; 59; 129,4; 8
DENIS-P J170548.38−051645.7	19.0 ± 0.1	52.7 ± 0.3	L0.5/L1: FLD-G	13.23 ± 0.03	12.58 ± 0.02	12.00 ± 0.02	77; 59; 129,2; 53
2MASS J17065487−1314396	19.4 ± 0.2	51.5 ± 0.5	.../L5.0 FLD-G	14.38 ± 0.04	13.68 ± 0.03	13.08 ± 0.03	58; 59; 58; 39
WISE J170745.85−174452.5	12.6 ± 0.5	79.2 ± 3.2	.../T5:	16.35 ± 0.02	17.11 ± 0.03	···	107; 8; 107; 107
WISEPA J171104.60+350036.8	22.4 ± 0.7	44.7 ± 1.3	.../T8	17.63 ± 0.13	18.06 ± 0.14	18.09 ± 0.14	83; 52; 83; 8
2MASS J17114559+4028578	21.1 ± 0.3	47.4 ± 0.6	.../L5.0	14.94 ± 0.02	14.38 ± 0.05	13.78 ± 0.05	125; 59; 4; 8
2MASSI J1721039+334415	16.3 ± 0.1	61.3 ± 0.2	L3/L5:	13.54 ± 0.02	13.03 ± 0.03	12.46 ± 0.02	33; 59; 33,23; 8
WISE J172134.46+111739.4	20.7 ± 1.8	48.4 ± 4.2	.../T6	16.44 ± 0.02	16.70 ± 0.06	16.50 ± 0.07	107; 8; 107; 8
VVV BD001	18.5 ± 0.1	54.0 ± 0.4	.../L5: blue	13.27 ± 0.02	12.67 ± 0.02	12.21 ± 0.03	5; 59; 5; 5,39
2MASS J17312974+2721233	11.9 ± 0.0	83.7 ± 0.1	L0/L0: FLD-G	12.05 ± 0.03	11.45 ± 0.02	10.89 ± 0.02	129; 59; 129,2; 8
DENIS-P J1733423−165449	18.1 ± 0.0	55.3 ± 0.1	L0.5:/L0.9	13.48 ± 0.05	12.87 ± 0.03	12.33 ± 0.03	120; 131; 120,4; 8
2MASS J17392515+2454421	24.0 ± 0.5	41.7 ± 0.9	.../L4	15.73 ± 0.07	14.73 ± 0.05	13.93 ± 0.05	82; 59; 82; 8
WISE J174303.71+421150.0	18.3 ± 1.4	54.8 ± 4.2	.../T4.5	15.63 ± 0.02	15.64 ± 0.06	15.65 ± 0.06	107; 8; 107; 8
DENIS-P J1745346−164053	19.7 ± 0.0	50.9 ± 0.1	L1.5:/L1.3	13.59 ± 0.03	12.95 ± 0.02	12.38 ± 0.02	120; 131; 120,4; 8

Table 8.1—Continued

Object	Distance (pc)	Parallax (mas)	Spectral Type[a] (Optical/NIR)	$J_{\rm MKO}$ (mag)	$H_{\rm MKO}$ (mag)	$K_{\rm MKO}$ (mag)	References (Disc; π; SpT; Phot)
2MASS J17461199+5034036	20.7 ± 0.2	48.3 ± 0.6	L5/L5.7	14.96 ± 0.02	14.13 ± 0.04	13.51 ± 0.04	129; 59; 129,4; 8
2MASS J17502484−0016151	9.2 ± 0.0	108.3 ± 0.3	L5/L5.5	13.21 ± 0.02	12.44 ± 0.02	11.81 ± 0.02	78; 59; 121,78; 53
SDSSp J175032.96+175903.9	22.5 ± 1.5	44.5 ± 3.0	T4/T3.5	16.16 ± 0.02	15.94 ± 0.05	16.02 ± 0.05	61; 8; 121,20; 8,88
2MASS J17545447+1649196	15.6 ± 0.8	64.3 ± 3.4	T5/T5.5	15.49 ± 0.02	15.64 ± 0.13	15.60 ± 0.06	53,22; 8; 121,53; 8,53
WISE J175510.28+180320.2	19.4 ± 1.8	51.5 ± 4.8	.../T2.5	15.82 ± 0.02	15.32 ± 0.02	15.24 ± 0.02	107; 8; 7; 7
SDSS J175805.46+463311.9	14.0 ± 0.0	71.5 ± 0.0	.../T6.5	15.86 ± 0.03	16.20 ± 0.03	16.12 ± 0.03	85; 59; 20; 85
2MASS J18000116−1559235	12.4 ± 0.1	80.9 ± 0.3	.../L4.3	13.29 ± 0.02	12.60 ± 0.03	11.96 ± 0.03	57,4; 59; 4; 8
WISEP J180026.60+013453.1	7.8 ± 0.0	127.4 ± 0.7	L7.5/L7.5	14.16 ± 0.02	13.20 ± 0.03	12.41 ± 0.03	68; 59; 70,68; 8
2MASSI J1807159+501531	14.6 ± 0.0	68.3 ± 0.1	L1.5/L1	12.88 ± 0.02	12.20 ± 0.03	11.58 ± 0.03	33; 59; 33,154; 8
PSO J272.0887−04.9943	23.4 ± 1.1	42.8 ± 2.0	.../T1.5pec	16.98 ± 0.02	16.28 ± 0.04	15.81 ± 0.06	7; 8; 7; 8,7
WISE J180901.07+383805.4	19.1 ± 0.8	52.4 ± 2.3	.../T7.5	17.38 ± 0.02	17.68 ± 0.06	17.30 ± 0.07	105; 8; 107; 8
WISE J180952.53−044812.5	20.3 ± 1.4	49.3 ± 3.4	.../T1	15.15 ± 0.01	14.44 ± 0.05	13.98 ± 0.01	107; 8; 6; 6,8
WISE J181329.40+283533.3	13.6 ± 0.4	73.6 ± 2.0	.../T8	16.92 ± 0.02	17.11 ± 0.06	16.92 ± 0.06	107; 8; 107; 8
2MASS J18212815+1414010	9.4 ± 0.0	106.7 ± 0.2	L4.5pec/L5: FLD-G	13.35 ± 0.02	12.49 ± 0.02	11.62 ± 0.02	102; 132; 102,96; 8
WISE J185101.83+593508.6	20.5 ± 0.3	48.8 ± 0.6	.../L9	14.85 ± 0.01	14.03 ± 0.02	13.45 ± 0.05	147; 59; 7; 6,8
WISEPA J185215.78+353716.3	15.1 ± 0.7	66.3 ± 2.9	.../T7	16.33 ± 0.02	16.72 ± 0.06	16.50 ± 0.06	83; 8; 83; 8
2MASS J19010601+4718136	18.3 ± 1.4	54.5 ± 4.3	.../T5	15.53 ± 0.02	15.65 ± 0.06	15.71 ± 0.06	19; 8; 20; 8
WISEPA J190624.75+450808.2	18.5 ± 1.0	54.1 ± 3.0	.../T6	15.98 ± 0.02	16.37 ± 0.08	16.39 ± 0.06	83; 8; 83; 8
WISEP J190648.47+401106.8	16.8 ± 0.0	59.6 ± 0.1	L1/L1	13.04 ± 0.02	12.33 ± 0.02	11.75 ± 0.02	67; 59; 69,67; 8
DENIS-P J1909081−193748	22.1 ± 0.3	45.2 ± 0.5	L1:/...	14.46 ± 0.02	13.60 ± 0.03	12.90 ± 0.03	120; 59; 120; 8,39
WISE J191915.54+304558.4	21.6 ± 1.9	46.3 ± 4.1	.../L9	15.52 ± 0.02	14.56 ± 0.01	13.96 ± 0.05	147; 8; 7; 7,8

Table 8.1—Continued

Object	Distance (pc)	Parallax (mas)	Spectral Type[a] (Optical/NIR)	$J_{\rm MKO}$ (mag)	$H_{\rm MKO}$ (mag)	$K_{\rm MKO}$ (mag)	References (Disc; π; SpT; Phot)
WISE J192841.35+235604.9	6.8 ± 0.2	146.0 ± 5.2	.../T6	13.96 ± 0.02	14.21 ± 0.06	14.15 ± 0.06	107; 8; 107; 8
WISE J195500.42−254013.9	22.8 ± 2.0	43.9 ± 3.9	.../T8	17.58 ± 0.02	18.00 ± 0.05	···	107; 8; 107; 107
WISE J200050.19+362950.1	7.6 ± 0.2	131.2 ± 2.9	.../T8	15.44 ± 0.01	15.85 ± 0.01	16.13 ± 0.04	38; 8; 38; 38,103
2MASS J20025073−0521524	17.6 ± 0.5	56.7 ± 1.5	L5 β/L7	15.23 ± 0.02	14.38 ± 0.04	13.38 ± 0.04	35; 59; 55,111; 8
Gl 779B	17.7 ± 0.0	56.4 ± 0.1	.../L4.5:	···	14.10 ± 0.14	13.02 ± 0.10	93; 59; 93; 10
WISE J200520.38+542433.9	16.6 ± 0.0	60.4 ± 0.0	.../sdT8	19.64 ± 0.09	19.57 ± 0.08	···	108; 59; 108; 108
WISE J200804.71−083428.5	18.4 ± 1.3	54.2 ± 3.8	.../T5.5	16.05 ± 0.02	16.32 ± 0.06	16.37 ± 0.06	107; 8; 107; 8
WISE J201404.13+042408.5	22.0 ± 1.2	45.5 ± 2.4	.../T6.5pec	17.99 ± 0.02	18.72 ± 0.30	17.97 ± 0.29	107; 8; 107; 8,107
WISE J201920.76−114807.5	13.7 ± 0.3	73.2 ± 1.7	.../T8:	18.09 ± 0.06	18.23 ± 0.07	···	107; 52; 107; 107
WISE J203042.79+074934.7	9.6 ± 0.1	104.0 ± 1.0	.../T1.5	14.05 ± 0.01	13.51 ± 0.04	13.36 ± 0.04	107; 59; 107; 6,8
2MASS J20360316+1051295	23.6 ± 0.2	42.4 ± 0.4	L3/L3.5	13.89 ± 0.03	13.09 ± 0.03	12.42 ± 0.03	129; 59; 129,26; 8
2MASSI J2057540−025230	15.5 ± 0.1	64.5 ± 0.2	L1.5/L2: FLD-G	13.03 ± 0.02	12.30 ± 0.02	11.69 ± 0.03	33; 59; 33,2; 53
2MASSI J2104149−103736	17.2 ± 0.1	58.2 ± 0.4	L2.5/L2	13.78 ± 0.03	13.05 ± 0.02	12.35 ± 0.02	33; 59; 81,26; 8
PSO J318.5338−22.8603	22.2 ± 0.8	45.1 ± 1.7	.../L7: VL-G	17.15 ± 0.04	15.68 ± 0.02	14.41 ± 0.02	95; 96; 95; 95
PSO J319.3102−29.6682	19.1 ± 2.5	52.4 ± 6.8	.../T0:	15.45 ± 0.02	14.65 ± 0.01	14.17 ± 0.05	7; 8; 7; 7,8
WISE J212321.92−261405.1	24.8 ± 2.9	40.3 ± 4.7	.../T5.5	17.07 ± 0.02	17.54 ± 0.07	17.73 ± 0.08	107; 8; 107; 8
SDSS J212413.89+010000.3	17.5 ± 1.0	57.0 ± 3.2	.../T5	15.83 ± 0.01	16.05 ± 0.02	16.09 ± 0.03	85; 8; 20; 86
2MASS J21371044+1450475	23.6 ± 0.2	42.4 ± 0.3	L2/L0.8	14.07 ± 0.02	13.37 ± 0.03	12.80 ± 0.03	129; 59; 129,4; 8
2MASS J21373742+0808463	15.1 ± 0.2	66.1 ± 0.9	L5:/L5	14.64 ± 0.02	13.67 ± 0.03	13.00 ± 0.03	129; 59; 129,26; 8,39
2MASS J21392676+0220226	9.9 ± 0.2	101.5 ± 2.0	T2/T1.5	15.10 ± 0.05	14.27 ± 0.05	13.60 ± 0.05	129,21; 144; 121,20; 8
HN Peg B	18.1 ± 0.0	55.2 ± 0.1	.../T2.5	15.86 ± 0.03	15.40 ± 0.03	15.12 ± 0.03	104; 59; 104; 104

Table 8.1—Continued

Object	Distance (pc)	Parallax (mas)	Spectral Type[a] (Optical/NIR)	J_{MKO} (mag)	H_{MKO} (mag)	K_{MKO} (mag)	References (Disc; π; SpT; Phot)
WISE J214706.78−102924.0	22.5 ± 1.9	44.4 ± 3.8	.../T7.5	17.37 ± 0.02	17.86 ± 0.36	···	107; 8; 107; 8,107
2MASS J21481628+4003593	8.1 ± 0.0	123.3 ± 0.5	L6/L6 FLD-G	14.07 ± 0.03	12.88 ± 0.02	11.73 ± 0.02	102; 59; 102,95; 8
2MASS J21522609+0937575	24.4 ± 4.1	40.9 ± 6.9	L6:/...	15.06 ± 0.02	14.14 ± 0.03	13.32 ± 0.03	128; 8; 129; 8,39
2MASS J21543318+5942187	15.5 ± 0.4	64.7 ± 1.5	.../T5	15.44 ± 0.07	15.70 ± 0.09	15.70 ± 0.09	101; 52; 101; 8
WISEPC J215751.38+265931.4	15.9 ± 0.6	62.8 ± 2.2	.../T7	17.05 ± 0.02	17.49 ± 0.04	17.34 ± 0.06	83; 8; 83; 8
2MASS J21580457−1550098	21.7 ± 2.6	46.1 ± 5.6	L4:/L5	14.84 ± 0.02	13.95 ± 0.04	13.16 ± 0.04	81; 8; 81,111; 8
2MASS J22092183−2711329	24.6 ± 2.3	40.7 ± 3.9	.../T2.5	15.54 ± 0.02	15.20 ± 0.15	15.11 ± 0.15	111; 8; 111; 8,39
WISEPC J220922.10−273439.5	13.8 ± 0.7	72.3 ± 3.8	.../T7	16.60 ± 0.02	16.95 ± 0.06	17.35 ± 0.06	83; 8; 83; 8
WISEPC J221354.69+091139.4	19.2 ± 1.1	52.0 ± 3.1	.../T7	16.77 ± 0.02	17.11 ± 0.06	17.12 ± 0.06	83; 8; 83; 8
2MASS J22153705+2110554	17.9 ± 1.4	55.9 ± 4.4	.../T1pec	15.90 ± 0.02	15.51 ± 0.06	15.17 ± 0.06	76; 8; 76; 8,76
2MASSW J2224438−015852	11.5 ± 0.1	86.6 ± 0.7	L4.5/L3: FLD-G	13.89 ± 0.03	12.84 ± 0.03	11.98 ± 0.03	80; 59; 80,96; 85
WISE J223617.59+510551.9	9.7 ± 0.2	102.8 ± 1.9	.../T5	14.46 ± 0.01	14.62 ± 0.02	14.57 ± 0.05	107; 8; 6; 6,8
2MASSI J2238074+435317	22.7 ± 0.1	44.1 ± 0.2	L1.5/L0.6	13.81 ± 0.03	13.12 ± 0.03	12.53 ± 0.03	33; 59; 33,4; 8
WISEPC J223937.55+161716.2	23.3 ± 1.6	42.9 ± 3.0	.../T3	15.97 ± 0.02	15.57 ± 0.06	15.37 ± 0.06	83; 8; 83; 8
2MASS J22425317+2542573	21.3 ± 0.3	47.0 ± 0.7	L3/...	14.76 ± 0.04	13.82 ± 0.03	13.03 ± 0.03	66; 59; 35; 8
2MASSW J2244316+204343	17.0 ± 0.3	58.7 ± 0.9	L6.5/L6: VL-G	16.38 ± 0.14	15.10 ± 0.07	13.98 ± 0.07	40; 96; 81,2; 8
2MASS J22490917+3205489	20.1 ± 1.3	49.7 ± 3.2	L5/...	15.55 ± 0.02	14.41 ± 0.05	13.57 ± 0.05	35; 8; 35; 8,39
DENIS-P J225210.73−173013.4	16.9 ± 0.2	59.2 ± 0.8	.../L7.5	14.20 ± 0.03	13.41 ± 0.03	12.90 ± 0.02	77; 59; 77; 8
2MASSI J2254188+312349	13.9 ± 0.6	72.0 ± 3.0	T5/T4	15.32 ± 0.05	15.06 ± 0.08	14.99 ± 0.15	15; 109; 121,20; 109
WISE J230133.32+021635.0	19.2 ± 1.4	52.0 ± 3.8	.../T6.5	16.36 ± 0.01	16.70 ± 0.03	16.87 ± 0.05	107; 8; 107; 86
WISEA J230329.45+315022.7	21.5 ± 1.5	46.5 ± 3.3	.../T2 (blue)	15.91 ± 0.02	15.53 ± 0.16	15.52 ± 0.16	136; 8; 136; 8,39

Table 8.1—Continued

Object	Distance (pc)	Parallax (mas)	Spectral Type[a] (Optical/NIR)	J_{MKO} (mag)	H_{MKO} (mag)	K_{MKO} (mag)	References (Disc; π; SpT; Phot)
2MASS J23185497−1301106	15.0 ± 0.7	66.5 ± 3.2	.../T5	15.30 ± 0.02	15.30 ± 0.13	15.13 ± 0.13	111; 8; 111; 8,39
WISEPC J231939.13−184404.3	11.8 ± 0.4	85.1 ± 3.1	.../T7.5	17.56 ± 0.02	17.95 ± 0.05	18.26 ± 0.08	83; 8; 83; 83,8
ULAS J232035.28+144829.8	21.3 ± 1.8	47.0 ± 4.0	.../T5	16.79 ± 0.02	17.14 ± 0.02	17.40 ± 0.02	138; 109; 27; 27
ULAS J232123.79+135454.9	11.9 ± 0.6	84.0 ± 4.0	.../T7.5	16.72 ± 0.03	17.15 ± 0.03	17.16 ± 0.01	138; 109; 27; 27
2MASS J23254530+4251488	14.8 ± 0.5	67.6 ± 2.1	L8/L7.5:	15.42 ± 0.02	14.53 ± 0.05	13.76 ± 0.05	35; 59; 35,26; 8
WISEPC J232728.75−273056.5	18.0 ± 2.0	55.6 ± 6.1	.../L9	16.50 ± 0.02	15.57 ± 0.06	14.89 ± 0.06	83; 8; 83; 8
WISE J233527.07+451140.9	22.7 ± 0.7	44.0 ± 1.4	.../L7pec	16.83 ± 0.03	15.63 ± 0.02	14.65 ± 0.06	147; 96; 96; 7,8
2MASSI J2339101+135230	16.0 ± 1.1	62.7 ± 4.4	.../T5	15.85 ± 0.01	16.06 ± 0.02	16.20 ± 0.04	15; 8; 20; 86
ULAS J234228.97+085620.1	21.6 ± 2.2	46.2 ± 4.7	.../T6.5	16.39 ± 0.01	16.77 ± 0.01	17.10 ± 0.02	138; 8; 107; 29
WISEPC J234841.10−102844.4	14.8 ± 0.8	67.6 ± 3.9	.../T7	16.63 ± 0.02	16.99 ± 0.06	16.84 ± 0.06	83; 8; 83; 8
2MASS J23512200+3010540	24.3 ± 0.8	41.2 ± 1.4	L5.5/L5: FLD-G	15.78 ± 0.10	14.66 ± 0.06	14.00 ± 0.06	82; 96; 82,96; 8
2MASS J23515044−2537367	20.4 ± 0.2	49.1 ± 0.4	L0.5/M8	12.43 ± 0.03	11.79 ± 0.03	11.25 ± 0.03	143; 59; 143,22; 8
2MASSI J2356547−155310	14.5 ± 0.6	69.0 ± 3.0	.../T5.5	15.48 ± 0.03	15.70 ± 0.03	15.73 ± 0.03	15; 53; 20; 85
WISE J235716.49+122741.8	17.6 ± 1.3	56.8 ± 4.1	.../T6	16.10 ± 0.01	16.49 ± 0.03	16.52 ± 0.04	107; 8; 107; 86

Note. — This table lists all spectroscopically confirmed L0–T8 dwarfs having declinations between −30° and +60° and parallax-determined distances less than 25 pc. The table is available in its entirety in machine-readable form in the online journal. A portion is shown here for guidance regarding its form and content. The full table contains 350 rows.

[a]β, γ, and δ indicate classes of increasingly low gravity based on optical (Kirkpatrick 2005; Cruz et al. 2009) or near-infrared (Gagné et al. 2015c; Cruz et al. 2018) spectra. FLD-G indicates near-infrared spectral signatures of field-age gravity, INT-G indicates intermediate gravity, and VL-G indicates very low gravity (Allers & Liu 2013a).

References. — (1) Albert et al. (2011), (2) Allers & Liu (2013a), (3) Artigau et al. (2006), (4) Bardalez Gagliuffi et al. (2014), (5) Beamín et al. (2013), (6) Best et al. (2013), (7) Best et al. (2015), (8) This work, (9) Bihain et al. (2013), (10) Boccaletti et al. (2003), (11) Bowler et al. (2010), (12) Burgasser et al. (1999), (13) Burgasser et al. (2000a), (14) Burgasser et al. (2000b), (15) Burgasser et al. (2002), (16) Burgasser et al. (2003a), (17) Burgasser et al. (2003b), (18) Burgasser et al. (2003d), (19) Burgasser et al. (2004), (20) Burgasser et al. (2006a), (21) Burgasser & McElwain (2006), (22) Burgasser et al. (2008a), (23) Burgasser et al. (2008b), (24) Burgasser et al. (2008c), (25) Burgasser et al. (2010b), (26) Burgasser et al. (2010a), (27) Burningham et al. (2010a), (28) Burningham et al. (2010b), (29) Burningham et al. (2013), (30) Castro & Gizis (2012), (31) Castro et al. (2013), (32) Chiu et al. (2006), (33) Cruz et al. (2003), (34) Cruz et al. (2004), (35) Cruz et al. (2007), (36) Cruz et al. (2009), (37) Cushing et al. (2011), (38) Cushing et al. (2014), (39) Cutri et al. (2003), (40) Dahn et al. (2002), (41) Deacon et al. (2005), (42) Deacon et al. (2011), (43) Deacon et al. (2012a), (44) Deacon et al. (2012b), (45) Deacon et al. (2014), (46) Deacon et al. (2017b), (47) Delfosse et al. (1997), (48) Delfosse et al. (1999), (49) Dupuy et al. (2009c), (50) Dupuy & Liu (2012), (51) Dupuy & Kraus (2013), (52) T. Dupuy (private communication), (53) Faherty et al. (2012), (54) Faherty et al. (2013), (55) Faherty et al. (2016), (56) Fan et al. (2000), (57) Folkes et al. (2012), (58) Gagné et al. (2015c), (59) Gaia Collaboration et al. (2018), (60) Gauza et al. (2015), (61) Geballe et al. (2002), (62) Gelino et al. (2014), (63) Gizis et al. (2000b), (64) Gizis et al. (2001), (65) Gizis (2002), (66) Gizis et al. (2003), (67) Gizis et al. (2011b), (68) Gizis et al. (2011a), (69) Gizis et al. (2013), (70) Gizis et al. (2015b), (71) Goldman et al. (2010), (72) Gomes et al. (2013), (73) Goto et al. (2002), (74) Hall (2002), (75) Hawley et al. (2002), (76) Kellogg et al. (2015), (77) Kendall et al. (2004), (78) Kendall et al. (2007a), (79) Kirkpatrick et al. (1999), (80) Kirkpatrick et al. (2000), (81) Kirkpatrick et al. (2008), (82) Kirkpatrick et al. (2010), (83) Kirkpatrick et al. (2011), (84) Kirkpatrick et al. (2014), (85) Knapp et al. (2004), (86) Lawrence et al. (2012), (87) Leggett et al. (2000), (88) Leggett et al. (2002b), (89) Leggett et al. (2002a), (90) Leggett et al. (2009), (91) Leggett et al. (2010), (92) Liebert et al. (2003), (93) Liu et al. (2002a), (94) Liu et al. (2011b), (95) Liu et al. (2013), (96) Liu et al. (2016), (97) M. Liu et al. (in prep), (98) Lodieu et al. (2005), (99) Lodieu et al. (2007b), (100) Lodieu et al. (2012c), (101) Looper et al. (2007), (102) Looper et al. (2008b), (103) Lucas et al. (2012), (104) Luhman et al. (2007), (105) Luhman et al. (2012), (106) Luhman & Sheppard (2014), (107) Mace et al. (2013a), (108) Mace et al. (2013b), (109) Manjavacas et al. (2013), (110) Marocco et al. (2010), (111) Marocco et al. (2013), (112) Marocco et al. (2015), (113) Martín et al. (2010), (114) Metchev et al. (2008), (115) Mugrauer et al. (2006), (116) Murray et al. (2011), (117) Muzic et al. (2012), (118) Nakajima et al. (1995), (119) Peña Ramírez et al. (2015), (120) Phan-Bao et al. (2008), (121) Pineda et al. (2016), (122) Pinfield et al. (2008), (123) Pinfield et al. (2012), (124) Potter et al. (2002), (125) Radigan et al. (2008), (126) Rebolo et al. (1998), (127) Reid et al. (2000), (128) Reid et al. (2006a), (129) Reid et al. (2008b), (130) Ruiz et al. (1997), (131) Sahlmann et al. (2014), (132) Sahlmann et al. (2016), (133) Salim et al. (2003), (134) Schilbach et al. (2009), (135) Schmidt et al. (2010), (136) Schneider et al. (2016a), (137) Scholz & Meusinger (2002), (138) Scholz (2010a), (139) Scholz (2010b), (140) Scholz et al. (2011), (141) Scholz et al. (2012), (142) Scholz et al. (2014), (143) Seifahrt et al. (2010), (144) Smart et al. (2013), (145) Strauss et al. (1999), (146) Stumpf et al. (2009), (147) Thompson et al. (2013), (148) Thorstensen & Kirkpatrick (2003), (149) Tinney et al. (2003), (150) Tinney et al. (2005), (151) Tsvetanov et al. (2000), (152) Vrba et al. (2004), (153) Wilson et al. (2001), (154) Wilson et al. (2003), (155) van Leeuwen (2007a).

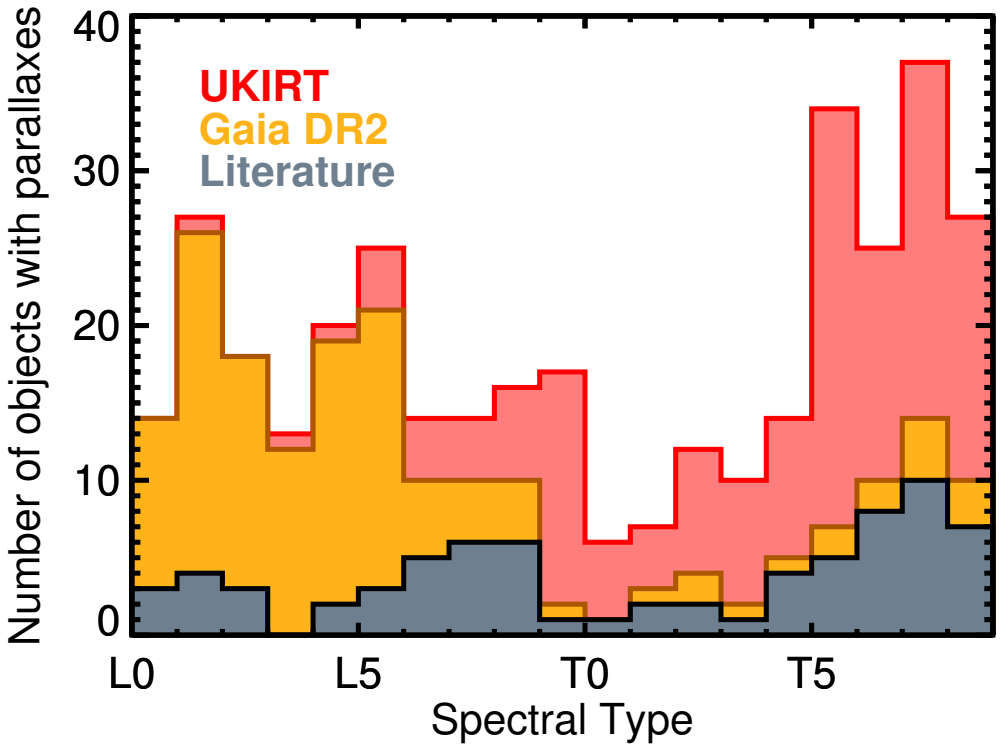

Figure 8.1 Distribution of spectral types for our volume-limited sample, indicating the sources of the parallaxes for sample members: UKIRT (red), *Gaia* DR2 (orange), and other literature sources (gray). For objects with more than one parallax, we use the most precise measurement. (Most of the T dwarf parallaxes from *Gaia* DR2 are actually parallaxes for main sequence stars with T dwarf companions.) The relative scarcity of L/T transition objects (T0–T4) reveals the short timescale for this phase of brown dwarf cooling.

8.2.2 Completeness

We assessed the completeness of our volume-limited sample using the $V/V_{\rm max}$ statistic (Schmidt 1968). In this analysis, V is the volume of space enclosed by a given object in a sample, and $V_{\rm max}$ is the volume of space enclosed by the outer boundary of the sample. $V/V_{\rm max}$ quantifies the position of the object within the sample with a value between 0 and 1. For a sample with uniform spatial distribution, the expectation value is $\langle V/V_{\rm max}\rangle = 0.5$.

Figure 8.2 shows $\langle V/V_{\rm max}\rangle$ as a function of distance for subsets of our volume-limited sample. We calculated error bars using Monte Carlo resampling of the parallax

uncertainties. Our sample has $\langle V/V_{\rm max}\rangle \approx 0.5$ implying completeness out to 16 pc, with decreasing $\langle V/V_{\rm max}\rangle$ at larger distances as expected. At 25 pc, $\langle V/V_{\rm max}\rangle = 0.426$, from which we estimate 85% completeness for our full volume-limited sample. Figure 8.2 also breaks our sample into four spectral type bins, demonstrating that the completeness is ≈90% complete for L0–T4.5 dwarfs and ≈70% for T5–T8 dwarfs at 25 pc. We expected our sample to be less complete for spectral types later than T6 due to the limiting magnitude of *WISE*, the primary source of late-T dwarf discoveries in most of the sky covered by our sample.

8.2.3 Photometry

We used J band for our WFCAM/UKIRT parallax observations, providing us with J photometry on the Mauna Kea Observatories system (MKO; Simons & Tokunaga 2002; Tokunaga et al. 2002) for those objects. For other objects in our volume-limited sample, we use $J_{\rm MKO}$ photometry from the literature, and we use $K_{\rm MKO}$ photometry from the literature for all objects. When MKO photometry was not available for a given band, we calculated synthetic colors using from the SpeX Prism Library (Burgasser et al. 2014) or from the literature, calibrated with observed MKO or 2MASS (Skrutskie et al. 2006) photometry using the approach described in Dupuy & Liu (2012). When no prism spectra were available, we converted 2MASS magnitudes into the MKO system using $\mathrm{M}_{Ks,\rm 2MASS}$ and the polynomials of Dupuy & Liu (2017, Appendix A.2).

8.2.4 Binaries

Binaries and multiples require special consideration in population studies. These systems can be removed from the analysis, or the components can be treated as individual objects; both of these approaches require identification of the binaries/multiples in the sample. Alternatively, the impact of unresolved binaries on the photometry, luminosity, and mass of the sample can be accounted for statistically (e.g., Metchev et al. 2008; Day-Jones et al. 2013). We searched the literature to identify binaries in our volume-limited sample detected

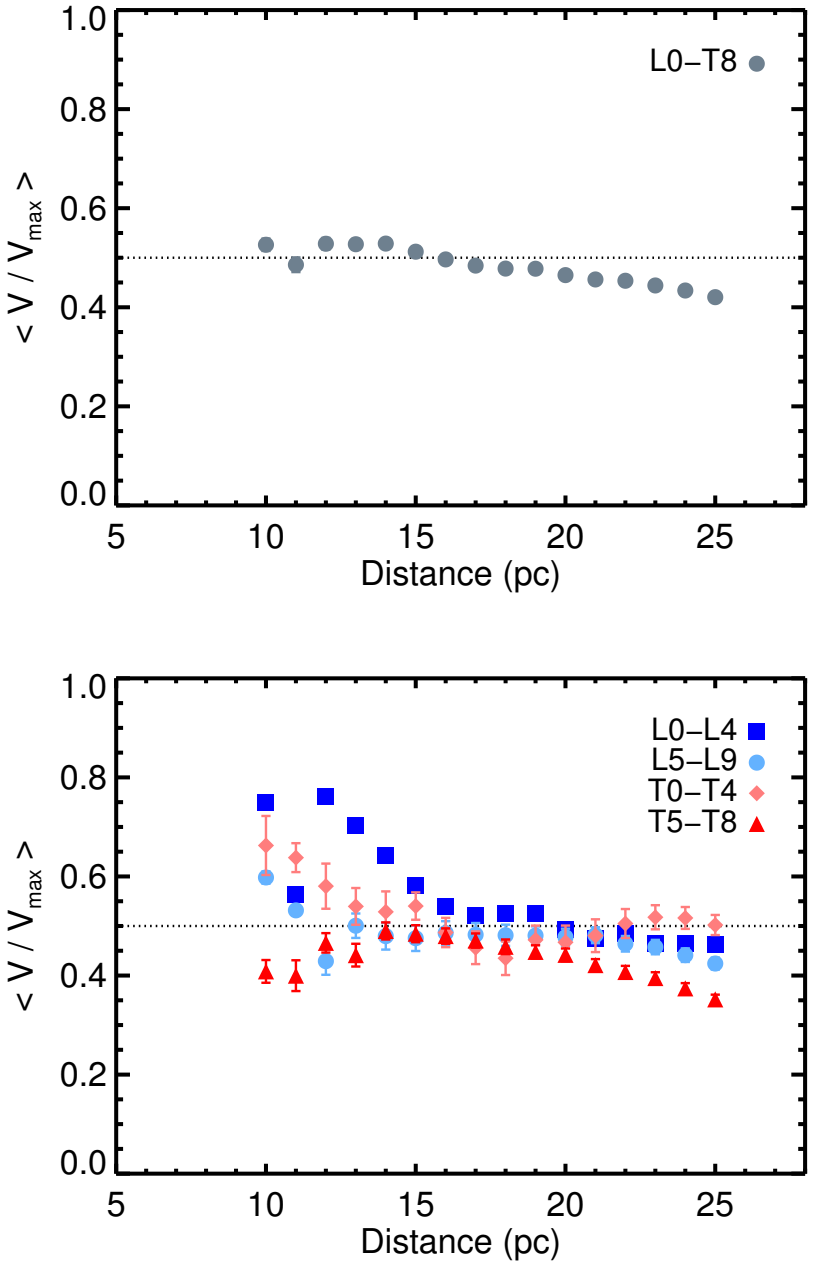

Figure 8.2 $\langle V/V_{\rm max}\rangle$ as a function of limiting distance for our volume-limited sample, for all spectral types in our full sample (L0–T8, *top*) and for four spectral type ranges (*bottom*). Our full sample is complete out to ≈16 pc, and ≈85% complete at 25 pc. The completeness is ≈90% for L0–T4.5 dwarfs, and ≈70% for T5–T8 dwarfs. The lower completeness for later-T dwarfs is expected because T7–T8 dwarfs near 25 pc are too faint to be observed by the large sky surveys that have discovered most nearby brown dwarfs.

via high-angular resolution imaging or radial velocity. Contemporaneously with our parallax observations, we conducted our own high-angular resolution imaging survey of all candidate members of the volume-limited sample lacking previous such observations, using laser guide star adaptive optics on Keck II/NIRC2 (W. Best et al., in preparation).

We removed 40 known binaries from our volume-limited sample, comprising 11% of the full sample. 27 of the binaries have L dwarf primaries, making up 15% of all L dwarfs in the sample. An L-dwarf binary fraction of 15% is consistent with previous estimates (Gizis et al. 2003; Reid et al. 2008a) for binaries resolvable with high-angular resolution imaging ($\gtrsim$1.5 AU), but somewhat lower than the $\approx$24% fraction estimate of (Reid et al. 2006a) that includes L dwarf binaries with smaller separations. It is therefore reasonable to assume that our volume-limited sample contains $\approx$5–10 unresolved binaries (see also Bardalez Gagliuffi et al. 2015), but as the impact of these objects on the space density and luminosity function of the sample would be $\lesssim$3%, we do not explicitly correct for it. For T dwarfs, 13 out of 172 (8%) in our sample are binaries, a fraction consistent with the recent comprehensive assessment of Fontanive et al. (2018).

8.3 A Gap in the L/T Transition

We show the M_J vs. $J-K$ (MKO) CMD for our volume-limited sample in Figure 8.3. We have removed known binaries from our sample in order to present a clean picture of the photometric evolution of cooling brown dwarfs. Our volume-limited CMD features a clear gap at $(J-K)_{\rm MKO} \approx 0.8$–$1.4$ mag. Figure 8.4 shows spectral type vs. $(J-K)_{\rm MKO}$ for our sample, demonstrating that the gap occurs at spectral type $\approx$T1. Figure 8.5 shows the color distribution of the 99 L/T transition dwarfs in our volume-limited sample, computed using Monte Carlo trials to incorporate the uncertainties in the $J-K$ colors. The gap seen in the CMD is clearly a significant feature of the L/T transition.

L/T transition dwarfs simultaneously brighten in J band while dimming in K band as they cool through the transition (e.g., Tinney et al. 2003). This behavior is thought

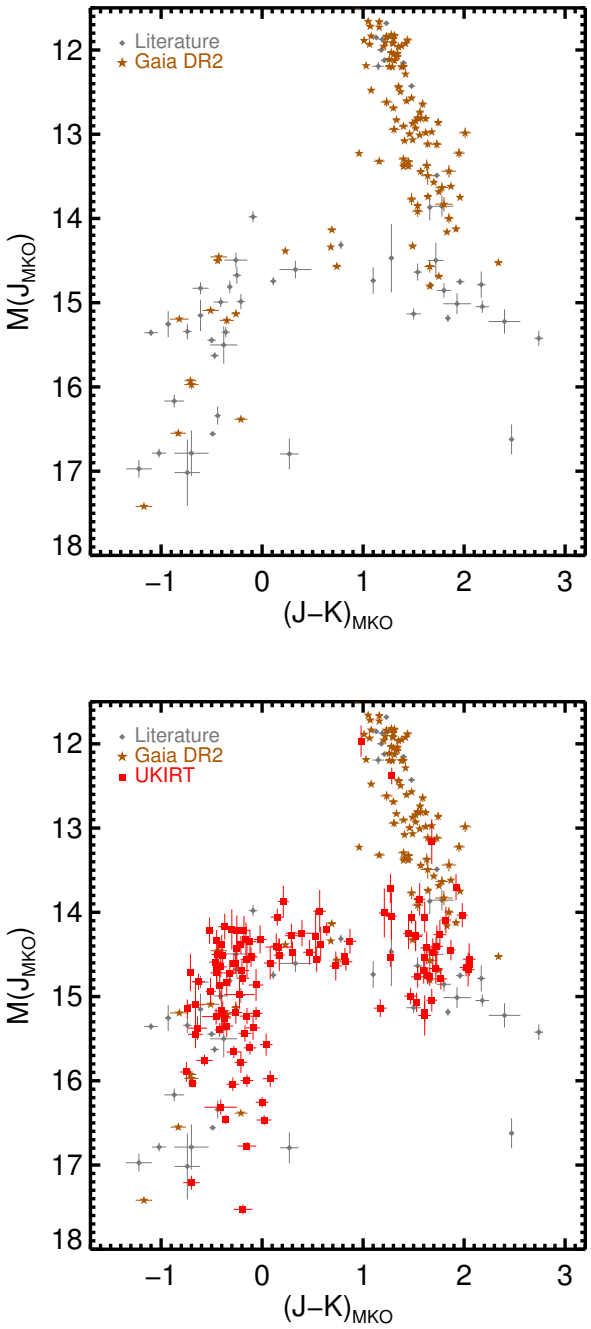

Figure 8.3 M_J vs. $J - K$ (MKO) color-magnitude diagram for our volume-limited sample with binaries removed. We show only objects with parallaxes from *Gaia* DR2 (brown stars) and literature sources (gray diamonds) in the top CMD, and include the UKIRT parallaxes in the bottom CMD. The large gap at ($J - K \approx 1$ mag, $M_J \approx 14.5$ mag) cannot be clearly identified without the UKIRT parallaxes in the bottom CMD. The gap occurs early in the L/T transition and implies a phase of rapid atmospheric evolution as brown dwarfs cool through $T_{\rm eff} \approx 1300$ K (Saumon & Marley 2008).

to be caused by a sudden depletion of clouds formed by one or more condensate species (e.g., Ackerman & Marley 2001; Burrows et al. 2006) or the evolution of thermochemical instabilities (Tremblin et al. 2016). The gap we identify indicates that the distinctive blueward evolution is occurring much more quickly than in other parts of the L/T transition.

The gap is not completely empty, containing a few objects. One type of object that could appear in the gap is an unresolved (and in our Figure 8.3, unrecognized) binary with components of differing spectral types, which individually sit on either side of the gap but whose blended color lies in the gap. We note that PSO J272.0887−04.9943 (Best et al. 2015), which sits at the bottom of the gap in Figure 8.3 ($J - K = 1.09$ mag, $M_J = 15.06$ mag), is a candidate binary based on the peculiar appearance of its near-infrared spectrum and the spectral indices defined by Burgasser et al. (2010a). Other objects in the gap show no evidence of multiplicity, suggesting that $(J - K)_{\rm MKO} \approx 0.8$–$1.4$ mag are rare but not forbidden colors for L/T transition dwarfs.

Deeper magnitude-limited samples will contain a larger proportion of binaries. This provides a natural explanation why the gap has not been discovered until now: previous samples of L/T transition dwarfs were either collections of all known L/T objects with parallaxes (at many distances; e.g., DL12) or volume-limited using photometric distances (e.g., Reid et al. 2008a). The gap is only apparent in a volume-limited sample defined by trigonometric distances.

The "hybrid" evolutionary models of Saumon & Marley (2008, hereinafter SM08) have demonstrated the most success at predicting the mass-luminosity relationship of L/T transition binaries (Dupuy et al. 2015b; Dupuy & Liu 2017). These models predict a pile-up of objects in the L/T transition at $(J - K)_{\rm MKO} \approx 1$ mag, in tension with what we have observed. SM08 attribute their modeled pileup to a slowdown in the cooling of L/T transition dwarfs, as heat trapped by L-dwarf clouds takes time to radiate away when the clouds clear. Our CMD does indicate pile-ups at the corners marking the beginning and end of the L/T transition, i.e., at $((J - K)_{\rm MKO}, M_{J_{\rm MKO}}) \approx (-1.5, 15)$ and $(1.5, 14.5)$ mag, but no strong concentration in the middle. SM08 do predict a paucity of objects at

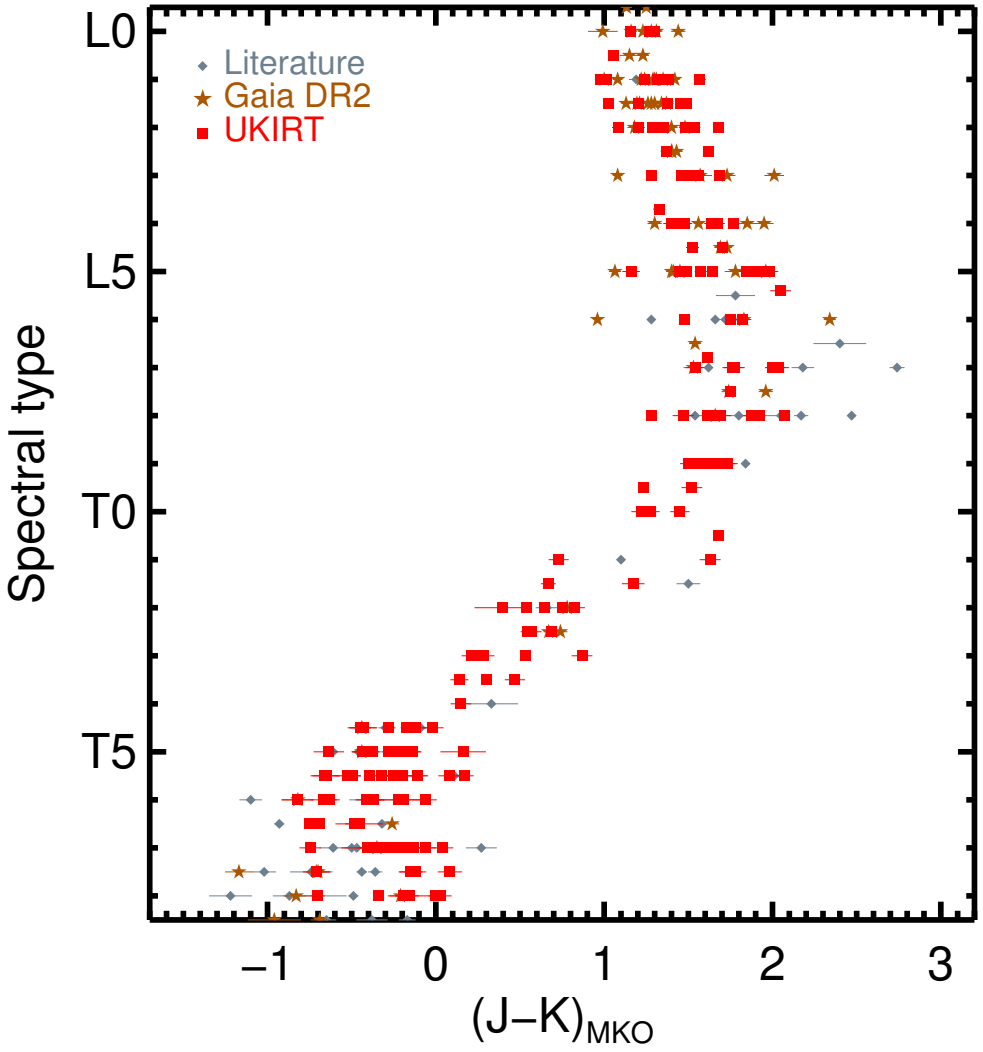

Figure 8.4 Spectral type as a function of $(J-K)_{\rm MKO}$ color for our volume-limited sample. The $J-K \approx 1$ mag gap occurs at spectral type ≈T1.

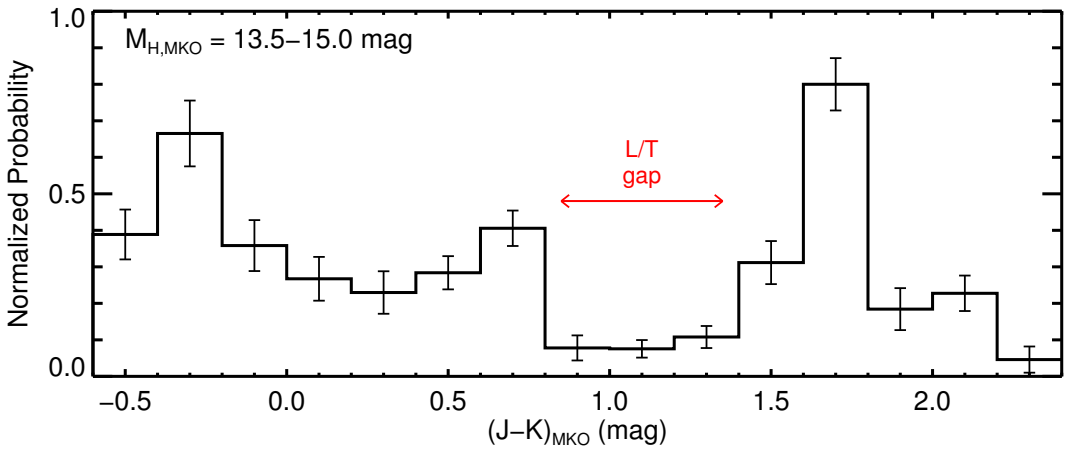

Figure 8.5 The distribution of $(J-K)_{\rm MKO}$ colors for L/T transition dwarfs in our volume-limited sample. We computed the histogram from objects having $13.5 \leq M_{H_{\rm MKO}} \leq 15.0$ mag (we used $M_{H_{\rm MKO}}$ because it is essentially constant across the L/T transition; DL12), sampling their color uncertainties in a Monte Carlo fashion. The error bars are the RMS for each color bin from our Monte Carlo trials. The gap seen in Figure 8.3 is evident. A gap seen previously in at $(J-K)_{\rm MKO} \approx 0.0-0.5$ mag in smaller, less complete samples by DL12 and Best et al. (2015) appears as a shallow deficit in our volume-limited sample, suggesting another slightly accelerated evolutionary phase.

$(J-K)_{\rm MKO} \approx 0.2$–$0.6$ mag, suggesting that the $T_{\rm eff}$ prescription they used for the L/T transition was too cool, since the observed paucity occurs at $(J-K)_{\rm MKO} \approx 0.8$–$1.4$ mag.

Using a much smaller sample of 36 objects, defined by parallaxes but not volume-limited, DL12 tentatively identified a gap at a bluer $(J-K)_{\rm MKO} \approx 0.1$–$0.5$ mag color, along with a pile-up at $(J-K)_{\rm MKO} \approx 1$ mag, similar to the predictions of SM08's hybrid models. Best et al. (2015) found further evidence for this bluer gap in a sample of 70 objects, volume-limited at 25 pc but incomplete and selected in part using photometric distances. Our parallax-defined 25 pc sample now reveals this tentative gap to in fact be a minor underdensity, possibly another phase of accelerated evolution. The samples of DL12 and Best et al. (2015) do show hints of the gap we clearly now identify at $(J-K)_{\rm MKO} \approx 1$ mag, but its significance is not revealed without the large number of early-T dwarf parallaxes provided by our UKIRT observations. These discrepancies with previous models and tentative results demonstrate how essential a complete volume-limited sample is for accurate population analysis.

8.4 Demographics

In Section 8.2 we defined a volume-limited 25-pc sample of L0–T8 dwarfs using a simple parallax cut at 40 mas. Here, we define a statistical volume-limited sample of single L0–T8 dwarfs and correct for Eddington bias and incompleteness in order to accurately quantify the space density and luminosity function of the local single L and T dwarf population. As in Section 8.2, we merged our list of UKIRT parallaxes with all literature parallaxes for spectroscopically confirmed L0–T8 dwarfs in the same declination range as our UKIRT sample ($-30^\circ \leq \delta \leq 60^\circ$). We excluded known binaries (Section 8.2.4) as well as wide companions to main sequence stars identified through common proper motion, obtaining a list of 888 single objects with parallaxes. For objects with more than one parallax, we chose the most precise parallax available. We excluded 11 objects whose best parallax measurement had error $\geq 20\%$.

8.4.1 Eddington Bias

Parallax measurements are not exact, so each object in a parallax-defined sample may in fact lie a little closer or farther than the distance obtained by inverting the parallax. At the boundary of a volume-limited sample, the volume of space outside the sample is larger than the volume inside, so overall the measured distances for more objects will scatter inward than scatter outward, artificially inflating the number of objects in a volume-limited sample. This is a manifestation of the bias that Eddington (1913) identified for data near the boundaries of bins. Lutz & Kelker (1973) realized that the same concept applies to all objects in a parallax-defined sample: on average all objects are slightly farther away than measured, and their luminosities are slightly underestimated by the parallaxes. In the Lutz-Kelker formulation, the size of the bias depends on σ_π/π. The median σ_π/π of our sample is 0.03, and the corresponding Lutz-Kelker correction implies that our parallaxes probe a volume of space $\approx$1% larger than their nominal distances indicate. Since we achieve an uncertainty of $\approx$10% for our space density calculation (Section 8.4.3), Eddington bias is not a significant source of uncertainty, but we nevertheless account for Eddington bias in our sample.

Lutz & Kelker (1973) determined that the distribution of the true parallax π about the measured parallax π_0 is

$$P(\pi|\pi_0) \propto \left(\frac{\pi}{\pi_0}\right)^4 \exp\left(-\frac{(\pi-\pi_0)^2}{2\sigma^2}\right) \tag{8.1}$$

where σ is the standard deviation of π_0 (i.e., the measurement error). The expected value of π from this distribution is

$$\pi = \frac{\pi_0 + \sqrt{(\pi_0^2 - 16\sigma^2)}}{2} \tag{8.2}$$

We corrected the parallaxes in our list to their expected values using Equation (8.2); typical corrections were less than 0.1 mas. We caution that as the Lutz-Kelker correction is a statistical correction for samples of objects, we use our corrected parallaxes only for our

analysis of our volume-limited sample as a whole and do not quote them for individual objects. The effect of the correction was to reduce the membership of our volume-limited sample by ≈3%, confirming that it is not significant relative to our ≈10% uncertainty on the overall space density.

8.4.2 Completeness

We corrected our sample for incompleteness using the $V/V_{\rm max}$ statistic described in Section 8.2.2, with the assumption that L and T dwarfs within 25 pc are distributed uniformly in space. From our list of parallaxes we drew new 25 pc samples in a Monte Carlo fashion, perturbing the parallaxes according to their uncertainties and rejecting the objects with parallaxes < 40 mas. For each Monte Carlo trial, we calculated $\langle V/V_{\rm max}\rangle$ for the entire sample, separately for L and T dwarfs, and for spectral type bins containing ≈20–50 objects (Table 8.2). We divided the number of objects in each spectral type bin by twice the $\langle V/V_{\rm max}\rangle$ for that bin to correct the number of objects for incompleteness and obtain an estimate for space density within 25 pc.

8.4.3 Space Density

We summed the estimates for each spectral type bin to get the total corrected space density for our trial volume-limited samples. To incorporate Poisson errors into our calculations, we replaced the number of objects k in each spectral type bin for each Monte Carlo trial with a number drawn from a Poisson distribution having mean value $k+0.5$ (Metchev et al. 2008). We then computed the mean and standard deviation of the $\langle V/V_{\rm max}\rangle$ corrections and space densities from the Monte Carlo trials to obtain final values, which we list in Table 8.2. The uncertainties on our space densities for single L and T0–T8 dwarfs are $\lesssim$10%, the most precise measurements to date. We note that previous estimates in the literature included binaries, which we do not, but as the binary fraction for L and T dwarfs is $\lesssim$15% (Reid et al. 2008a; Fontanive et al. 2018), the impact is minimal and within their uncertainties. Our $(3.50 \pm 0.31) \times 10^{-3}$ pc^{-3} space density for L dwarfs, as well as our

Table 8.2. Space Density and Completeness of our Volume-Limited Sample

SpT Range	Number	$\langle V/V_{\rm max}\rangle$	Corrected Number	Space Density (10^{-3} objects pc^{-3})
L0 $\leq$ SpT $<$ L3	54.0 ± 7.5	0.493 ± 0.011	54.8 ± 7.5	1.23 ± 0.17
L3 $\leq$ SpT $<$ L6	40.9 ± 6.8	0.394 ± 0.016	52.0 ± 8.4	1.16 ± 0.19
L6 $\leq$ SpT $<$ L9	30.3 ± 5.7	0.42 ± 0.02	36.3 ± 6.8	0.81 ± 0.15
L9 $\leq$ SpT $<$ T2	22.2 ± 4.9	0.47 ± 0.03	23.5 ± 5.2	0.52 ± 0.12
T2 $\leq$ SpT $<$ T4.5	19.2 ± 4.8	0.48 ± 0.04	20.1 ± 4.9	0.45 ± 0.11
T4.5 $\leq$ SpT $<$ T6.5	50.4 ± 7.2	0.41 ± 0.02	61.6 ± 8.7	1.38 ± 0.19
T6.5 $\leq$ SpT $\leq$ T8	60.4 ± 7.8	0.347 ± 0.013	87.1 ± 11.4	1.95 ± 0.26
L0 $\leq$ SpT $<$ T0	136.6 ± 12.1	0.445 ± 0.009	156.4 ± 14.0	3.50 ± 0.31
T0 $\leq$ SpT $\leq$ T8	137.4 ± 11.7	0.397 ± 0.011	177.4 ± 15.7	3.97 ± 0.35
L0 $\leq$ SpT $\leq$ T8	274.0 ± 17.2	0.421 ± 0.006	335.3 ± 21.8	7.50 ± 0.49

Note. — Number of objects and estimates of completeness and space density for our volume-limited sample. Number: Number of objects (mean and standard deviation) in each bin from Monte Carlo trials that resample the parallaxes from their uncertainties. $\langle V/V_{\rm max}\rangle$: Mean $V/V_{\rm max}$ for each bin. A sample with uniform spatial distribution will have $\langle V/V_{\rm max}\rangle = 0.5$. Twice the $\langle V/V_{\rm max}\rangle$ gives an estimate of the volume-completeness of each sample bin (1 = complete). Corrected Number: Number of objects in each bin corrected for incompleteness, i.e., divided by $2 \times \langle V/V_{\rm max}\rangle$. Space Density: Expressed in units of 10^{-3} objects per cubic parsec.

values for bins of L dwarf subclasses, are consistent with previous estimates (Cruz et al. 2007; Reylé et al. 2010; Marocco et al. 2015). For T dwarfs, our estimates are consistent with some previous estimates (Kirkpatrick et al. 2012; Burningham et al. 2013; Marocco et al. 2015). Our overall T dwarf space density of $(3.97 \pm 0.35) \times 10^{-3}$ pc^{-3} is lower than the $\approx (7 \pm 3) \times 10^{-3}$ pc^{-3} estimates of Metchev et al. (2008) and Reylé et al. (2010), with the discrepancy coming at later T6–T8 dwarfs, although our estimates differ by only $\approx 1\sigma$ given the large uncertainties presented in those studies. We note also that our sample is less complete for later-T dwarfs (Figure 8.2) than for earlier spectral types, and it is possible that the $\langle V/V_{\rm max}\rangle$ for these spectral types has underestimated their incompleteness in our sample if there are numerous undiscovered T6–T8 dwarfs $\lesssim$20 pc from the Sun.

8.4.4 Luminosity Function

We calculated bolometric luminosities ($L_{\rm bol}$) for objects on our parallax list using the log ($L_{\rm bol}/L_{\odot}$) vs. $M_{H_{\rm MKO}}$ polynomial from Dupuy & Liu (2017), and converted these to bolometric magnitudes ($M_{\rm bol}$) using $M_{\rm bol,\odot} = 4.74$ mag. The Dupuy & Liu (2017) polynomial is defined for objects with $9.1 \leq M_{H_{\rm MKO}} \leq 17.8$ mag; for fainter objects (there are 4 in our volume-limited sample, all T7.5 or T8 dwarfs) we used the spectral type-based bolometric corrections from Liu et al. (2010) to convert $K_{\rm MKO}$ directly to $M_{\rm bol}$. For objects lacking $K_{\rm MKO}$ photometry (21 in our volume-limited sample), we used $J_{\rm MKO}$ and the corresponding bolometric corrections from Liu et al. (2010). We added the uncertainties from our parallaxes, MKO photometry, and the bolometric corrections in quadrature to obtain uncertainties for our bolometric magnitudes.

To determine the luminosity function for our volume-limited sample, we corrected for incompleteness using the $\langle V/V_{\rm max}\rangle$ statistic and incorporated Poisson errors in the same manner as for space density (Section 8.4.3), using bins of 1 mag in $M_{\rm bol}$ and Monte Carlo trials to calculate uncertainties. We present our completeness-corrected luminosity function in Table 8.3. We plot the luminosity function in Figure 8.6. The mean effect of our correction for Eddington bias (Section 8.4.1) on our luminosity bins was -0.03×10^{-3} objects pc^{-3} per bin. This is less than the uncertainties on the space densities in those bins, indicating that our luminosity function was not significantly impacted by the correction.

8.5 Constraining the IMF and Birth History of Ultracool Dwarfs

8.5.1 Population Models

To constrain the mass and age distributions underlying the observed luminosity function, we turned to forward models of our volume-limited sample. Modeling this population requires the distributions of masses and ages of objects in the sample, from which synthetic objects

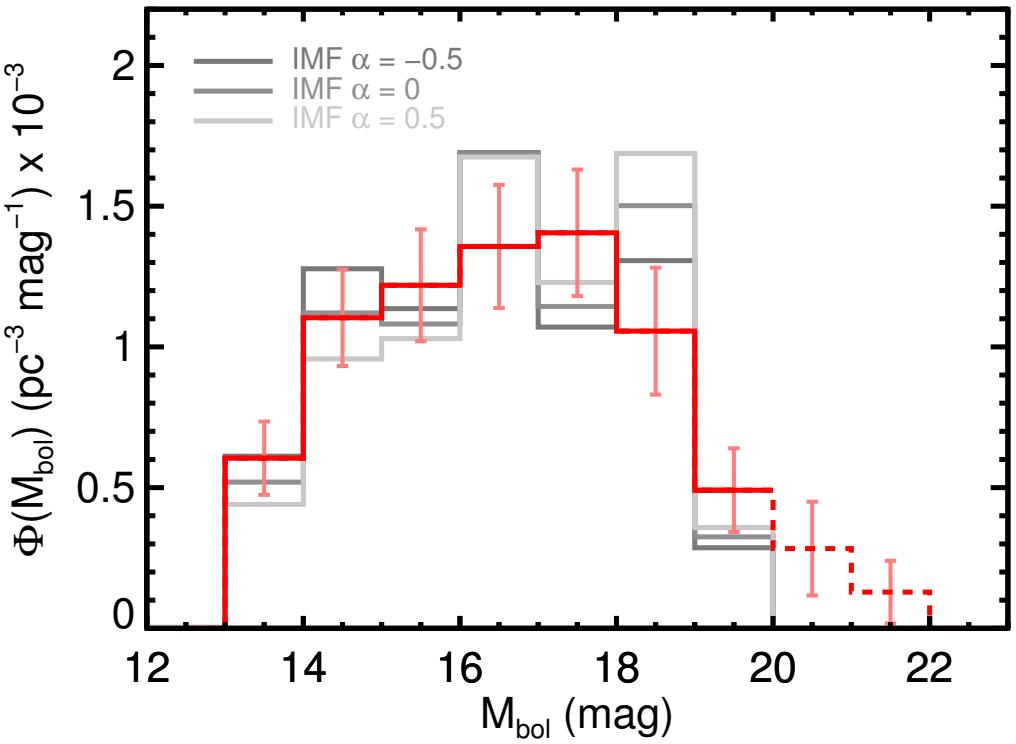

Figure 8.6 The bolometric luminosity function for our volume-limited sample (red), plotted as space density of bins of 1 mag in bolometric magnitude. For context, we also plot in shades of gray three synthetic luminosity functions based on the "hybrid" evolutionary models of Saumon & Marley (2008), assuming an IMF of $dN/dM \propto M^{-\alpha}$ with α equal to -0.5, 0, and 0.5, and a birth rate of $b(t) \propto e^{-\beta t}$ with $\beta = 0$ (Section 8.5). The error bars on our luminosity function are comparable to the differences between the models in some bins, illustrating our ability to constrain model parameters with our volume-limited sample (Section 8.5). The faint-end bins plotted with a dashed line contain fewer than 10 objects (before completeness corrections) and are not used in our comparison with models.

Table 8.3. Luminosity Function for our 25 pc Volume-Limited Sample

$M_{\rm bol}$ (mag)	Number	Space Density (10^{-3} objects pc^{-3})
13.5	27.0 ± 5.8	0.60 ± 0.13
14.5	49.3 ± 7.7	1.10 ± 0.17
15.5	54.5 ± 8.9	1.22 ± 0.20
16.5	60.7 ± 9.8	1.36 ± 0.22
17.5	62.8 ± 10.1	1.41 ± 0.22
18.5	47.2 ± 10.1	1.06 ± 0.23
19.5	21.9 ± 6.6	0.49 ± 0.15
20.5	12.7 ± 7.4	0.28 ± 0.17[a]
21.5	5.8 ± 5.0	0.13 ± 0.11[a]

Note. — The bolometric magnitudes listed are the central values for 1 mag wide bins. The numbers and space densities for each bin have been corrected for incompleteness. The space densities are plotted in Figure 8.6.

[a]Space density based on an uncorrected sample of fewer than 10 objects. We do not use these bins in our comparison with synthetic populations (Section 8.5.2).

are drawn. Each synthetic object's mass and age can then be converted into $L_{\rm bol}$, $T_{\rm eff}$, and other physical properties using evolutionary models. The physical properties can in turn be converted into observables using atmospheric models.

Studies of the stellar IMF normally define the IMF as a power law with form $\xi(M) \equiv dN/d(\log M) \propto M^{-\Gamma}$. This is the form originally used in the seminal work by Salpeter (1955), who determined that $\Gamma = 1.35$ for stars with masses $\geq 1 M_{\odot}$. Previous work on ultracool dwarfs has used the common alternate form

$$\Psi(M) \equiv \frac{dN}{dM} \propto M^{-\alpha} \tag{8.3}$$

so we will also use this form, which is related to the Salpeter form by $\alpha = \Gamma + 1$ (so $\alpha = 2.35$ for super-solar-mass stars). Equation (8.3) can be viewed as the low-mass part of a two-part power law defined by a critical mass M_c, above which the IMF has a Salpeter slope and below which the IMF has a shallower slope (Kroupa et al. 1993). Chabrier (2003) has also shown that an IMF which takes the form of a power law above 1 $M_{\odot}$ and a lognormal distribution below 1 $M_{\odot}$ (defined by a peak mass and a characteristic width) is consistent with the data.

For an age distribution, we use

$$b(t) \propto e^{-\beta t} \tag{8.4}$$

where $t \in [0, 10]$ Gyr is the time since the formation of the Galaxy; hence, the age of an object born at time t is $(10 - t)$ Gyr. This is the most commonly used formulation in previous work (e.g., Allen et al. 2005; Day-Jones et al. 2013). Note that $\beta = 0$ defines a constant birth rate, which is consistent with estimates for the formation history of nearby stars (e.g., Soderblom et al. 1991; Gizis et al. 2002).

Previous modeling of the local ultracool population has produced only poor constraints on the IMF and essentially no constraints on the birth history beyond agreement that brown dwarfs have been forming fairly continuously (at some possibly vary rate) since the birth of the Galaxy ≈10 Gyr ago (e.g., Burgasser 2004a). Allen et al. (2005) found $\alpha = 0.3 \pm 0.6$

for $0.04 < M < 0.1\ M_{\odot}$ using a Bayesian approach, while Metchev et al. (2008) estimated $\alpha \approx 0$ from an analysis of the T dwarf space density. These results are in general agreement with $0 < \alpha < 1$ estimates for substellar objects in young clusters (e.g., Alves de Oliveira et al. 2012, 2013). In contrast, several other studies, primarily focused on T dwarfs, have estimated values of α between -1 and 0 by visually comparing modeled space densities or luminosity functions to empirical data (Pinfield et al. 2008; Reylé et al. 2010; Kirkpatrick et al. 2012; Burningham et al. 2013). However, all of these studies relied on much smaller and usually magnitude-limited samples which produced much larger uncertainties on their space densities and luminosity functions than we have obtained with our 25 pc sample.

8.5.2 Constraints From Our Volume-limited Sample

We constructed synthetic populations with the same volume and space density as our corrected 25 pc sample (Table 8.2) of single objects, oversampled by a factor of 1000. We assigned masses from the power law distribution of Equation (8.3) and ages from the exponential distribution of Equation (8.4). We interpolated the Solar-metallicity "hybrid" evolutionary models of Saumon & Marley (2008, hereinafter SM08), which have to date provided the best matches to measured masses and luminosities for L and early-T dwarfs (Dupuy et al. 2015b; Dupuy & Liu 2017), to obtain $L_{\rm bol}$ and $T_{\rm eff}$ for members of our synthetic populations. We then converted our model $T_{\rm eff}$ values to spectral types by inverting the SpT–$T_{\rm eff}$ relation of Stephens et al. (2009), and we discarded objects with spectral types earlier than L0 or later than T8. We note that the SM08 models have a mass range of 0.002 $M_{\odot}$ to 0.085 $M_{\odot}$, so we could only assign masses to our synthetic objects within these limits. In the models, 0.085 $M_{\odot}$ objects have late-M dwarf temperatures at all ages, and 0.002 $M_{\odot}$ objects have $T_{\rm eff}$ equivalent to spectral types earlier than T8 only for ages < 10 Myr (0.1% of our age range), so this mass range effectively covers the full L0–T8 spectral type range of our 25 pc sample. We then converted the synthetic $L_{\rm bol}$ to $M_{\rm bol}$, binned objects into the same 1 mag $M_{\rm bol}$ bins we used for our volume-limited sample

(Table 8.3), and normalized the bins to match the total space density of our volume-limited sample.

We initially constructed these synthetic populations for $-1 \leq \alpha \leq 1$ in steps of 0.2 and $-0.5 \leq \beta \leq 0.5$ in steps of 0.1. We calculated χ^2 for the fit of our volume-limited luminosity function to those of the model populations. We excluded the bins with $M_{\rm bol} > 20$ mag from our fits because our $M_{\rm bol}$ function contained fewer than 10 objects in these bins, making our space density estimates less robust. This allowed us to identify a single χ^2 minimum near $(\alpha, \beta) = (-0.5, 0.1)$.

We then constructed a finer grid of synthetic populations using $-1.90 \leq \alpha \leq 1.0$ in steps of 0.02 and $-0.70 \leq \beta \leq 0.70$ in steps of 0.02, in order to precisely locate the minimum and discern the surrounding 2-dimensional χ^2 surface. Figure 8.7 shows this χ^2 surface as a contour plot with contours tracing the confidence limits for the (α, β) parameter distribution. The contours clearly constrain the IMF and birth rate exponents. Marginalizing the probability distribution over the fine χ^2 grid for both parameters and integrating each parameter's individual distribution, we obtain $\alpha = -0.46 \pm 0.42$ and $\beta = 0.08 \pm 0.12$ (median and 68% confidence limits, shown in Figure 8.8). These numbers represent the best constraints to date on both parameters, in particular the birth rate for which the only previous analysis found $\beta = -0.13 \pm 0.17$ for masses between 0.072 and 0.1 $M_{\odot}$ (late-M and early-L dwarfs; Deacon & Hambly 2006).

We note a degeneracy between α and β, also seen by Deacon & Hambly (2006), whereby more steeply declining birthrates (higher β) correlate with IMFs that produce fewer of the lowest-mass objects (lower α). This can be explained by the number of low-luminosity objects in our 25 pc sample. Objects with lower luminosities can be older (therefore cooler) or lower-mass brown dwarfs. A population dominated by older objects (high β) therefore should have fewer low-mass objects (low α), or vice versa, in order to maintain consistency with the faint end of our luminosity function.

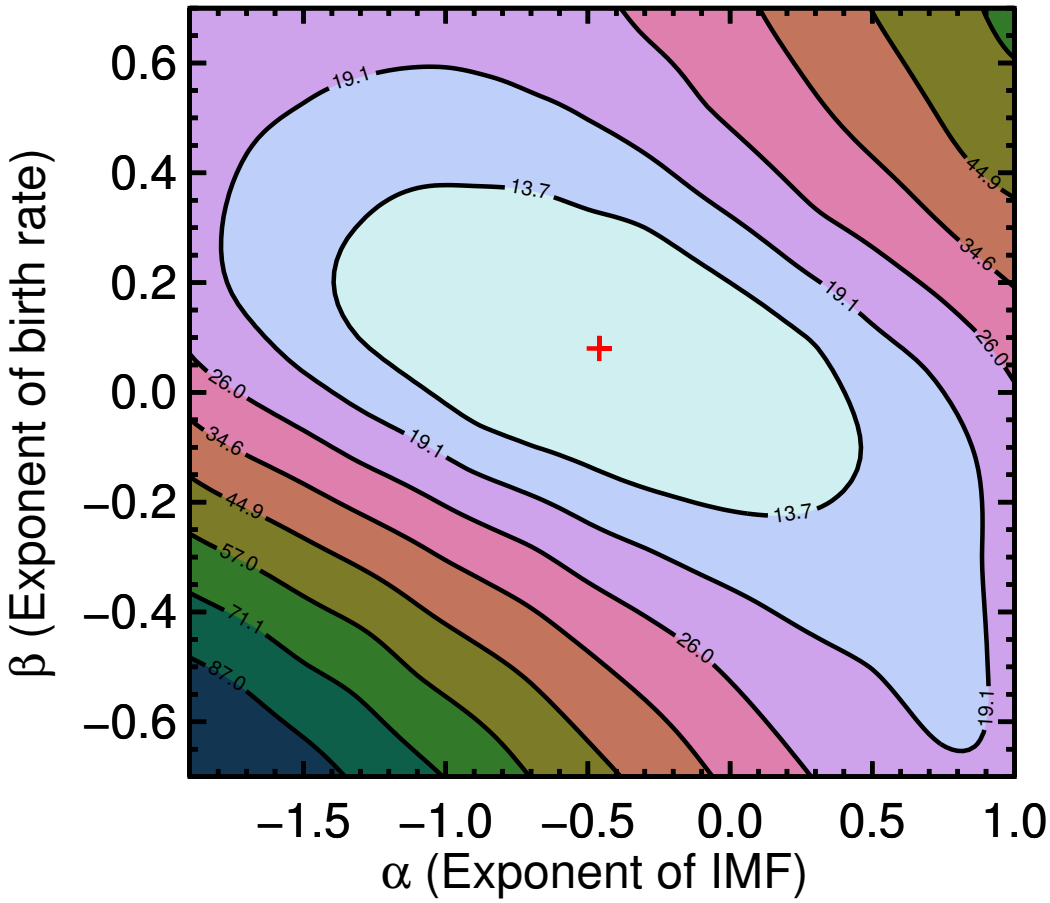

Figure 8.7 Smoothed contour plot representing the χ^2 for fits of our 25 pc luminosity function to those from synthetic populations based on the α (IMF) and β (birth rate) parameters. The red cross at $\alpha = -0.46 \pm 0.42$ and $\beta = 0.08 \pm 0.12$ indicates our best-fit parameters. Contours trace the $1\sigma, 2\sigma, ..., 8\sigma$ confidence limits. The correlation between α and β reflects the constraint of the faint end of our luminosity function.

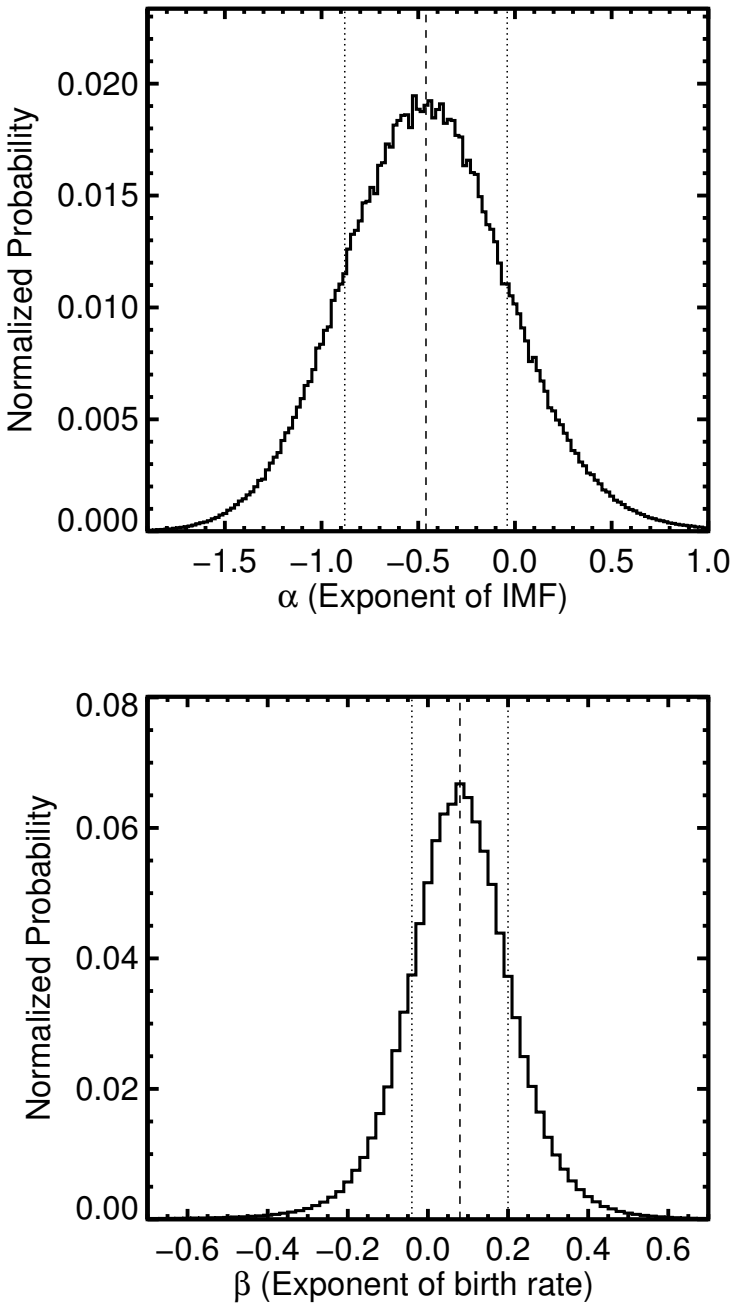

Figure 8.8 Probability distribution functions for the α (IMF, *top*) and β (birth rate, *bottom*) parameters derived from our χ^2 comparison of model luminosity functions to our volume-limited sample. The dashed lines indicate median values ($\alpha = -0.46, \beta = 0.08$), and the dotted lines indicate 68% confidence intervals. Both parameters are clearly constrained by their distributions.

8.5.3 Discussion of IMF and Birth History

We offer a couple of cautionary comments. While our χ^2 analysis provides well-defined constraints on α and β at a single minimum, and the minimum χ^2 of 7.8 for 5 degrees of freedom suggests that our uncertainties are reasonable, our model populations are not well-suited to the luminosity function of our volume-limited sample. Figure 8.9 shows the synthetic luminosity function with our best-fit parameters, which shares the overall morphology of the observed luminosity function but does not match well in several bins. This suggests that alternatives to a single power-law IMF and/or an exponentially-declining birth rate may be better models for the local L and T dwarf population. We note also that the SM08 "hybrid" models predict structure in near-infrared color-magnitude diagrams of the L/T transition that do not match our observations (Section 8.3), which impacts the luminosity functions in the $15 \leq M_{\rm bol} \leq 17$ mag range. Different evolutionary models, or fits to SM08 models that exclude the L/T transition, may provide better matches to our empirical sample, although previous experiments found that changing evolutionary models made little difference to synthetic populations (e.g., Burgasser 2004a).

With those caveats in mind, we compare our results for α and β to previous efforts. Our $\alpha = -0.46 \pm 0.42$ is consistent with the $\alpha = 0.3 \pm 0.6$ estimate of Allen et al. (2005) for stars and brown dwarfs with masses $< 0.1\ M_\odot$ but is clearly on the low end of formal consistency. Our result is also lower than the $\alpha \approx 0$ estimate of Metchev et al. (2008) based on the T dwarf space density. This is naturally explained by our smaller space density estimate for later-T dwarfs, which implies a steeper decline in the IMF toward low-mass brown dwarfs. We find better agreement with the studies estimating $\alpha < 0$ (e.g., Kirkpatrick et al. 2012; Burningham et al. 2013) from T-dwarf space densities consistent with ours, again in tension with our higher value for α. We note that our $\beta = 0.08 \pm 0.12$ is at odds with the age distribution found by Dupuy & Liu (2017, based primarily on late-M and L dwarfs with no objects later than T5), which skews toward younger objects and supports the view that galactic dynamics will gradually excite objects out of the midplane, depleting the Solar neighborhood of older objects (e.g., Robin et al. 2003).

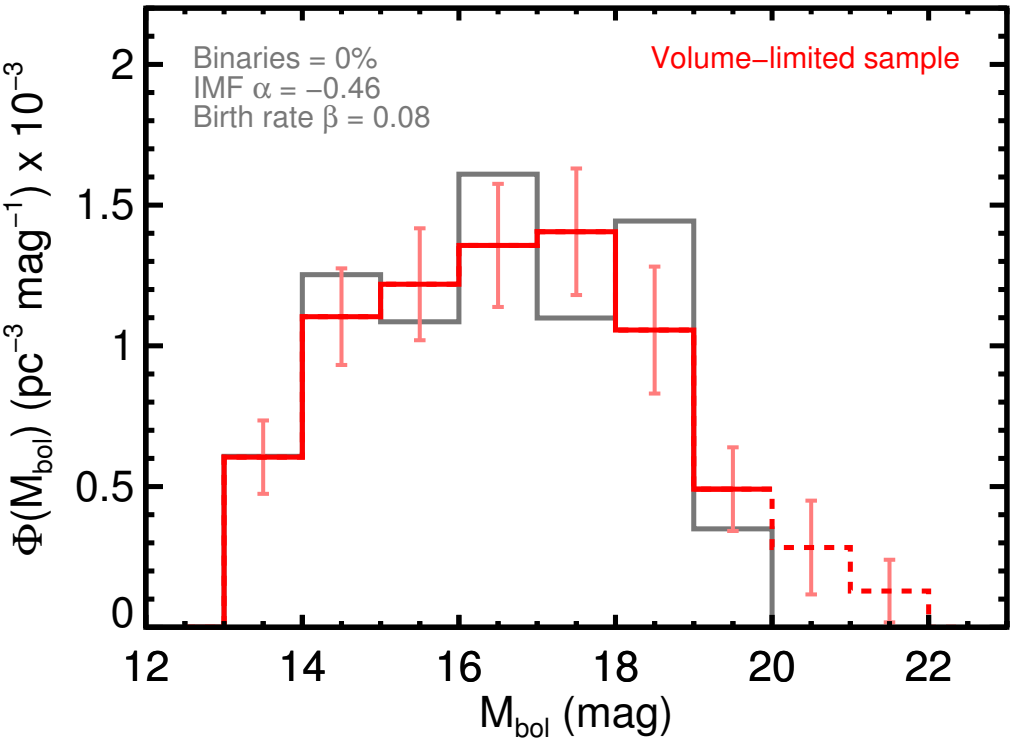

Figure 8.9 Our 25 pc luminosity function for L0–T8 dwarfs (red), compared with the best-fit synthetic luminosity function (gray) from a model population based on an IMF of $dN/dM \propto M^{-0.46}$ and a birth rate $b(t) \propto e^{0.08t}$. The bins with $M_{\rm bol} > 20$ mag (dashed line) were not used in the fit. While the model matches the overall morphology of the empirical luminosity function, the fluctuations of individual bins do not align, indicating that the models do not accurately describe the detailed evolution of the local brown dwarf population.

Studies of star-forming regions and young clusters have mostly found $0 < \alpha < 1$, with constraints tending toward the higher end of that range (e.g., Moraux et al. 2003; Luhman 2004; Alves de Oliveira et al. 2013; Scholz et al. 2013). Our $\alpha = -0.46 \pm 0.42$ therefore adds weight to the argument of Burningham et al. (2013) that the IMF has changed over time, from $\alpha < 0$ for the older field population to $\alpha > 0$ for present-day brown dwarf formation. Further exploration with synthetic populations using narrow ranges of ages may yield more insights into the formation history of the local brown dwarf population.

Chapter 9

Summary

Despite over 1,500 brown dwarf discoveries in the past 20 years, studies of the nearby population have suffered for lack of a large, complete, bias-free sample to provide constraints on evolutionary and atmospheric models. We have now built such a sample.

We first compiled a catalog of 9888 M, L and T dwarfs detected in the Pan-STARRS1 3π Survey (PS1) in order to assess the status of brown dwarf discoveries. We used this catalog to construct empirical SEDs for field ultracool dwarfs spanning $0.5 - 12$ μm. We combined astrometry from PS1, 2MASS, and *Gaia* DR1 to calculate new proper motions for our catalog. We calculated proper motions for 2405 M6–T9 dwarfs, including the largest set of homogeneous proper motions for L and T dwarfs published to date, We used these proper motions to analyze the kinematics of ultracool dwarfs in our catalog , finding evidence that bluer but otherwise generic late-M and L field dwarfs (i.e., not subdwarfs) tend to have tangential velocities higher than those of typical field objects.

We determined that the most significant deficiency in the nearby brown dwarf census was objects in the transition from L to T spectral types (types ≈L8–T4). We conducted a wide-field search using a novel combination of optical and mid-infrared photometry from the Pan-STARRS1 and *WISE* surveys. We discovered 130 M, L, and T dwarfs, including 79 in the L/T transition, the most from any search to date. This filled in the gap in the census of brown dwarfs within 25 pc.

Our search led to several additional discoveries. We identified 10 candidate members of nearby young moving groups (YMG) with spectral types L7–T4.5, including three showing spectroscopic signs of low gravity. If confirmed, any of these would be among the coolest known YMG members and would help to determine the effective temperature at which young brown dwarfs cross the L/T transition. We also discovered eight young M7–L2 dwarfs in the Taurus star-forming region and the Scorpius-Centaurus OB Association. In particular, PSO J060.3200+25.9644 (near-infrared spectral type L1) and PSO J077.1033+24.3809 (L2) in Taurus are among the lowest mass free-floating objects ever discovered, with estimated masses $\approx$6 $M_{\rm Jup}$, and provide further evidence that isolated planetary-mass objects can form as part of normal star-formation processes. Finally, we discovered that the extremely red, low-gravity L7 dwarf 2MASS J11193254−1137466 is a 0.14″ (3.6 au) binary using laser guide star adaptive optics imaging with Keck. 2MASS J11193254−1137466 has previously been identified as a likely member of the young TW Hydrae Association (TWA). At TWA's 10$\pm$3 Myr age and using hot-start evolutionary models, 2MASS J11193254−1137466AB is a pair of $3.7^{+1.2}_{-0.9}$ $M_{\rm Jup}$ brown dwarfs, making it the lowest-mass binary discovered to date.

To complete our volume-limited sample, we measured parallaxes for 348 L and T dwarfs using the wide-field camera WFCAM on the United Kingdom Infrared Telescope (UKIRT), the largest single batch of parallaxes for brown dwarfs to date. We report the first parallaxes for 219 objects, including the largest sample of T dwarf parallaxes so far (172), and we improve on previous measurements for another 21 objects. Our targets include 104 objects (mostly early-L dwarfs) having *Gaia* DR2 parallax measurements, with which our parallaxes are strongly consistent. We constructed a volume-limited sample of L0–T8 dwarfs out to 25 pc covering 68% of the sky. With 356 members, it is four times larger than the previous best sample, $\approx$85% complete, and is the first large brown dwarf sample defined entirely by parallaxes. Using our volume-limited sample, we identified a gap $\approx$ 0.5 mag wide in $J-K$ colors at spectral type $\approx$T1 ($T_{\rm eff} \approx 1300$ K), implying a rapid phase of atmospheric evolution early in the transition from L to T dwarfs.

Using synthetic populations of the solar neighborhood based on evolutionary models, we constrained the initial mass function $dN/dM \propto M^{-\alpha}$ to $\alpha = -0.46 \pm 0.42$ and the birth rate $b(t) \propto e^{-\beta t}$ to $\beta = 0.08 \pm 0.12$, demonstrating the value of our volume-limited sample to provide empirical constraints for the properties of local ultracool dwarfs. Our IMF measurement is consistent with previous estimates and for later T dwarfs in the solar neighborhood but inconsistent with estimates for young objects in nearby star-forming regions, hinting at possible variations of the IMF over the history of galaxy in the substellar regime.

Future Work

Our volume-limited sample, with its precise parallaxes, well-characterized membership, and multi-band photometry, will help to advance substellar population studies of the solar neighborhood into a new era of precision analysis. The χ^2 analysis of the initial mass function and birth history of nearby L and T dwarfs presented in Chapter 8 is the first step. A more through analysis can be achieved using Bayesian analysis and a Monte Carlo Markov Chain approach to explore the IMF and birth history parameter space with greater precision. Such analysis can also include alternate forms for the IMF (e.g., lognormal; Chabrier 2005) and the birth history (e.g., bursts of star formation; Allen et al. 2005) that may better represent the observed luminosity function. Binaries will also be included in the population analysis, for the first time using distributions based on a complete census of the L and T dwarf binaries in a volume-limited sample. In addition, a new generation of evolutionary models is on the horizon, including the recently introduced BHAC15 (Baraffe et al. 2015) and upcoming Sonora models (Marley et al. 2017). These models will include novel treatment of atmospheric properties and the L/T transition that may better reproduce observed spectra and photometry, leading to luminosity functions that more faithfully represent the local population.

In recent years, precise Hubble Space Telescope (HST) data of resolved stellar populations with thousands of members has inspired sophisticated statistical methods

to reconstruct star formation histories by comparing observed color-magnitude diagrams (CMDs) to synthetic CMDs from evolutionary models (e.g., Aparicio & Hidalgo 2009; Weisz et al. 2011). Our volume-limited sample of L and T dwarfs can be combined with the 25 pc volume-limited sample of stars with parallaxes from *Gaia* to produce the first large and complete sample of stars and brown dwarfs in the solar neighborhood. The analytical methods developed for CMDs of higher-mass and evolved stars in nearby galaxies can the be adapted to study the very local population of mostly low-mass stars and brown dwarfs, providing crucial tests for theoretical models of star formation that predict mass functions.

The Transiting Exoplanet Survey Satellite (TESS) will observe ≈900 stars within the 25 pc volume and measure rotation periods yielding gyrochronological age constraints for ≈10% of these (J. van Saders, private communication). The ages of these ≈100 systems will provide a direct comparison for the birth history emerging from CMD analysis, illuminating issues with either the stellar clocks from TESS or the brown dwarf clocks from evolutionary models.

The upcoming Large Synoptic Survey Telescope (LSST, first light in 2020) will dramatically improve optical photometry, proper motions, and variability studies for low-mass stars and brown dwarfs, and will extend parallaxes to much greater distances (≈300 pc). In addition, objects with rare properties (e.g., outlier colors or kinematics) that are not well represented in our volume-limited sample will be more clearly understood using much larger LSST-based samples. Our 25 pc sample enables development of the methods needed to take advantage of the enormously expanded volume-limited sample that LSST will deliver.

Appendix A

Proper Motions of Known Low-Mass Taurus Members

We compiled a catalog of proper motions for low-mass members of Taurus using the Pan-STARRS1 3π (PS1) Survey, Processing Version 3.2 (PV3.2). Photometry and positions from PV3.2 were publically released as part of PS1 DR1 (K. Chambers et al., 2017, in prep), with proper motions and parallaxes planned for a future PS1 release. PS1 astrometry includes Pan-STARRS1 observations from November 2009 to March 2014, as well as detections from 2MASS (October 1997 to November 2000) and *Gaia* DR1 (Epoch 2015.0; Gaia Collaboration et al. 2016a; Lindegren et al. 2016) lying within 1" of the mean PS1 position. PS1 astrometry, including proper motions, is calibrated to the *Gaia* DR1 reference frame.

A full description of the proper motion calculations can be found in E. Magnier et al. (2017, in prep). Briefly, all PS1, 2MASS, and *Gaia* detections for an object were fit simultaneously for position, parallax, and proper motion using iteratively-reweighted least squares regression with outlier clipping. Errors were estimated for each object using a bootstrapping approach, drawing random samples in a Monte Carlo fashion (allowing duplicates) from the set of detections not rejected in the astrometric fit.

To create our catalog, we began with the list of 414 Taurus members from Esplin et al. (2014). Using the 2MASS positions (or WISE positions for the seven objects with no 2MASS

detection), we cross-matched this list with the PS1 database using a 3″ matching radius, and found 363 matches with a proper motion measured by PS1. We supplemented these matches with our two Taurus discoveries presented in the paper. We verified that none of the PS1 sources were identified as quasars, transients, periodic variables, or solar system objects in the PS1 database, and we excluded any objects with poor PSF fits (`psf_qf` < 0.85). To avoid saturation in PS1 we also excluded objects having $i_{\rm P1} < 14.5$ mag or $y_{\rm P1} < 12.5$ mag (corresponding roughly to a spectral type of M3–M4). This left us with 187 members of Taurus having proper motions measured by PS1. Almost every object in the catalog of Esplin et al. (2014) was detected by 2MASS, so the PS1 proper motions have time baselines of ≈14–17 years. Our catalog includes 27 objects with no previously published proper motion and 93 measurements that improve on the best available literature values drawn from NOMAD (Zacharias et al. 2005), PPMXL (Roeser et al. 2010), SDSS DR9 (Ahn et al. 2012), UCAC4 (Zacharias et al. 2013), UKIDSS GCS DR9 (Lawrence et al. 2013), URAT1 (Finch & Zacharias 2016), USNO-B (Monet et al. 2003), and Riaz et al. (2013). It is the largest catalog to date for proper motions of low-mass (spectral types $\gtrsim$ M3) members of Taurus.

We list our proper motions in Table A.1, along with the $i_{\rm P1}$ and $y_{\rm P1}$ photometry, the number of epochs used, the reduced χ^2, and the time baseline for each proper motion fit. We adopt a photometric precision floor of 0.01 mag for the PS1 photometry, following the analysis of Schlafly et al. (2012). The errors reported in the PS1 database are formal errors that do not include systematics, and are often smaller than 0.01 mag. We do not report photometry with errors larger than 0.2 mag. Figure A.1 shows the proper motion errors as a function of the $y_{\rm P1}$ magnitude of each source, and indicates that most of the errors are $\lesssim$5 mas yr^{-1}.

In Figure A.2 we plot the reduced χ^2 for the proper motion fits as a function of $y_{\rm P1}$. Most of our proper motion fits have $\chi^2_\nu > 1$, suggesting that the astrometric uncertainties

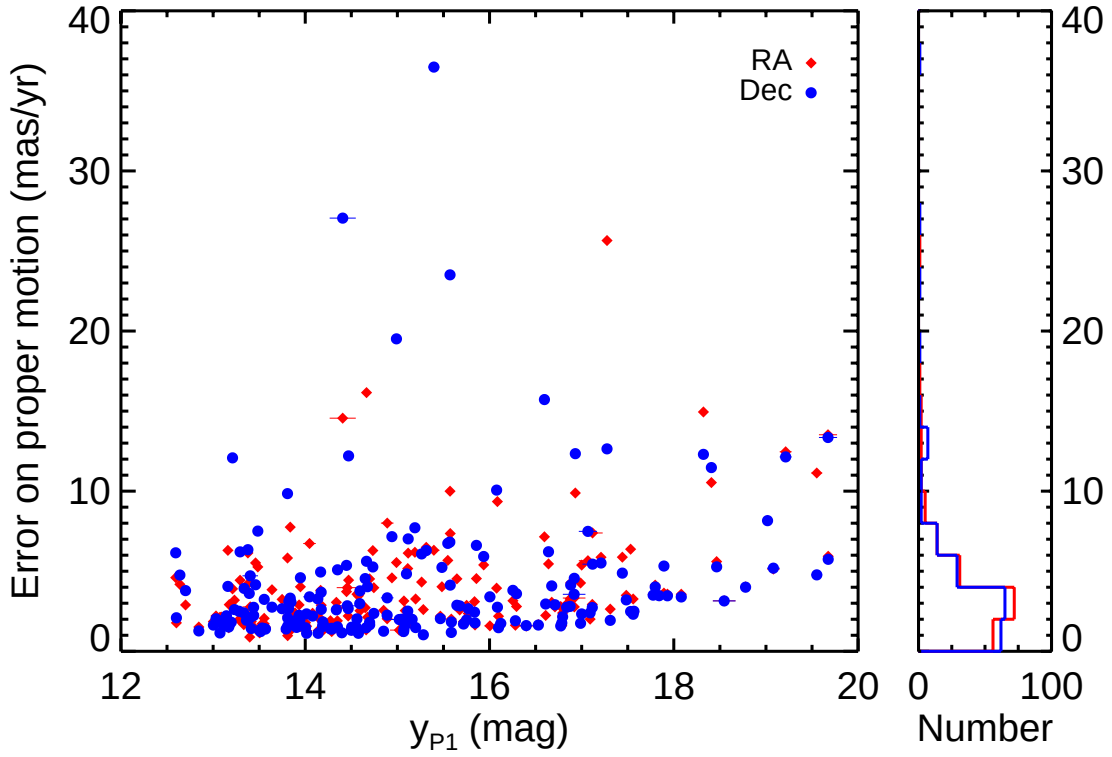

Figure A.1 Errors on our $\mu_\alpha \cos\delta$ (red diamonds) and μ_δ (blue dots) as a function of $y_{\rm P1}$ for known Taurus members that are not saturated in PS1. The histogram on the right shows the distributions of the errors. Most errors are $\lesssim$5 mas yr^{-1}.

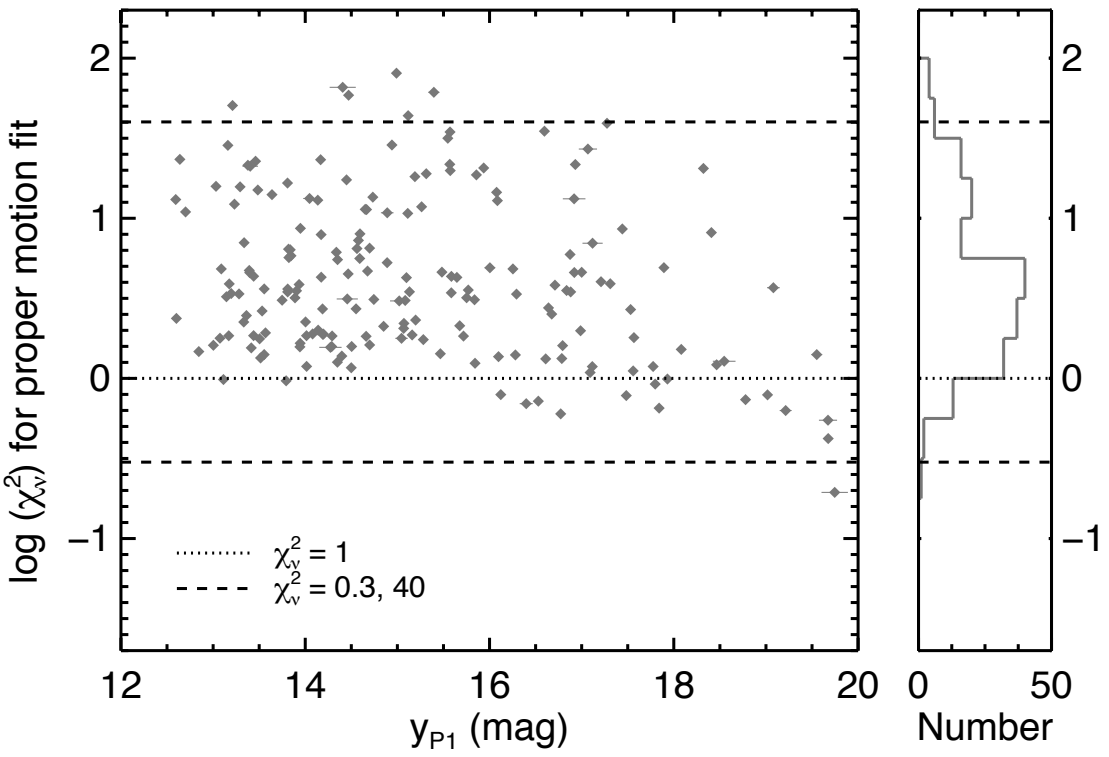

Figure A.2 Reduced χ^2 for our proper motions as a function of $y_{\rm P1}$ for known Taurus members that are not saturated in PS1. The histogram on the right shows the distribution of χ^2_ν. The two dashed lines mark $\chi^2_\nu = 0.3$ and $\chi^2_\nu = 40$, values between which we regard our proper motion fits and errors as reliable (Figure A.3). The dotted line marks $\chi^2_\nu = 1$. The fact that most of the fits have $\chi^2_\nu > 1$ suggests that our estimates for the PS1 astrometric errors are small compared to the scatter in positions between epochs.

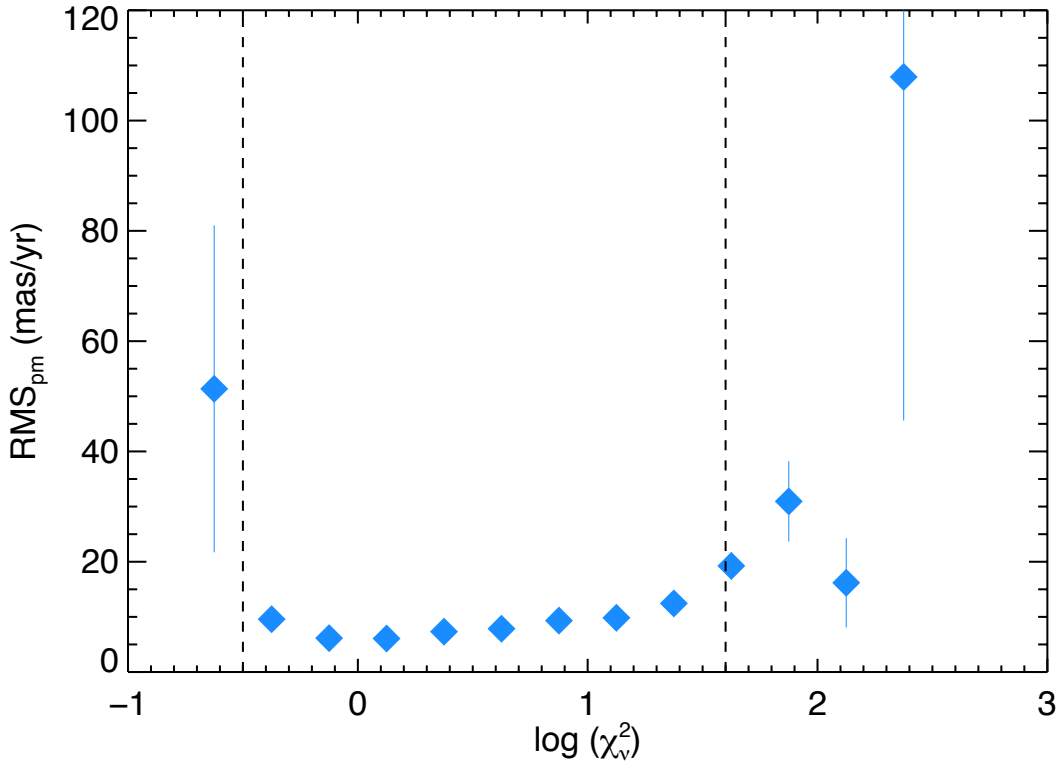

Figure A.3 The rms of PS1 proper motions of well-detected objects in a 0.5 deg^2 patch of sky near Taurus, for bins of 0.25 in $\log(\chi^2_\nu)$. More than 97% of the proper motions in this patch of sky are less than 50 mas yr^{-1}. The low rms for proper motions with $-0.5 < \log(\chi^2_\nu) < 1.6$ (between the vertical dashed black lines), i.e., $0.3 < \chi^2_\nu < 40$, implies that those proper motion measurements are reliable, while measurements with larger or smaller χ^2_ν are less reliable.

of the individual PS1 epochs are small compared to the scatter in R.A. and Dec. of the epochs. The proper motion errors may therefore be underestimated (by a factor of ≈2).

To assess the reliability of our proper motions, we calculated proper motions and χ^2_ν for objects in a 0.5 deg^2 patch of sky near Taurus ($80^\circ < \alpha < 81^\circ$, $5.5^\circ < \delta < 6.0^\circ$), in which more than 97% of objects have proper motions less than 50 mas yr^{-1}. We used all 8,962 objects in this patch meeting the same criteria as our Taurus catalog and also having $y_{\rm P1} < 19.75$ mag to match the faintness limit of our Taurus catalog. Because the proper motions of this sample are small, the rms of the proper motions gives us an estimate of the quality of the measurements. Figure A.3 shows that proper motions measurements with $0.3 < \chi^2_\nu < 40$ had rms $\approx 5 - 15$ mas yr^{-1}, while proper motions with larger or smaller χ^2_ν had significantly greater spread. We therefore adopted these χ^2_ν values as the limits between which we regard our proper motions as reliable measurements. Table A.1 separates our Taurus proper motions into those we regard as reliable (all but 5 of the objects) and unreliable. We report all of our proper motions for completeness, but when $\chi^2_\nu \leq 0.3$ or $\chi^2_\nu \geq 40$ the proper motions should be treated with caution.

Using the reliable proper motions and inverse variance weighting, we calculate a weighted mean proper motion for Taurus of ($\mu_\alpha \cos\delta = 7.6 \pm 0.2$, $\mu_\delta = -17.4 \pm 0.2$ mas yr^{-1}), with a weighted rms of 4.9 mas yr^{-1} in R.A. and 6.4 mas yr^{-1} in Dec. We compare this to the catalog of brighter Taurus members compiled by Ducourant et al. (2005, hereinafter D05), whose proper motions were similarly calculated using optical and 2MASS data and whose time baselines range from 10 to more than 100 years. Using the proper motions from the full D05 Taurus catalog, we calculate a weighted mean proper motion of ($7.9 \pm 1.1, -20.5 \pm 1.0$ mas yr^{-1}). We note a ≈3 mas yr^{-1} discrepancy with the mean proper motion for our Taurus list, which is likely due to differences in the astrometric reference frames used for the two samples. The Pan-STARRS1 PV3.2 astrometry is tied to the *Gaia* DR1 reference frame, while the D05 proper motions use data from many sources with different astrometric reference frames. Only ten Taurus objects in the D05 catalog are not saturated in PS1 and have reliable proper motions, preventing a robust object-by-object

comparison of the PS1 proper motions with those from D05. The ten shared objects mostly have proper motions from the two catalogs that are consistent within errors.

Table A.1. Proper Motions of Taurus Members

Name	Photometry			Proper Motion				
	$i_{\rm P1}$ (mag)	$z_{\rm P1}$ (mag)	$y_{\rm P1}$ (mag)	$\mu_\alpha \cos\delta$ (mas yr^{-1})	μ_δ (mas yr^{-1})	χ^2_ν	$N_{\rm ep}$	Δt (yr)
Reliable fits: $0.3 < \chi^2_\nu < 40$								
PSO J060.3200+25.9644	21.61 ± 0.04	20.06 ± 0.02	19.02 ± 0.02	19.0 ± 8.2	-38.1 ± 8.2	0.8	43	17.2
2MASS J04034997+2620382	16.27 ± 0.01	15.28 ± 0.01	14.73 ± 0.01	15.6 ± 6.3	-16.0 ± 5.3	14	62	15.1
2MASS J04064443+2540182	15.67 ± 0.01	14.68 ± 0.01	14.14 ± 0.01	12.4 ± 1.3	-15.5 ± 1.1	2.0	87	15.2
2MASS J04080782+2807280	15.19 ± 0.01	14.34 ± 0.01	13.91 ± 0.01	2.6 ± 1.5	-7.7 ± 1.5	3.5	91	17.2
2MASS J04102834+2051507	16.90 ± 0.01	15.87 ± 0.01	15.28 ± 0.01	-2.3 ± 2.6	-7.3 ± 1.0	1.7	69	17.2
2MASS J04105425+2501266	20.00 ± 0.03	19.74 ± 0.07	18.78 ± 0.04	9.2 ± 4.0	-15.7 ± 4.0	0.7	34	17.2
2MASS J04135328+2811233	20.37 ± 0.03	18.33 ± 0.01	16.93 ± 0.01	13.3 ± 9.9	-39.8 ± 12.3	22	45	17.2
2MASS J04135737+2918193	14.81 ± 0.08	14.79 ± 0.06	14.66 ± 0.01	5.9 ± 1.3	-26.4 ± 1.5	1.8	64	17.2
2MASS J04141760+2806096	15.14 ± 0.02	14.26 ± 0.02	13.64 ± 0.01	7.7 ± 3.8	-24.6 ± 2.8	14	67	17.2
2MASS J04142626+2806032	19.07 ± 0.05	17.21 ± 0.05	16.29 ± 0.03	8.1 ± 2.8	-18.4 ± 3.6	3.4	41	17.2
2MASS J04142639+2805597	16.51 ± 0.01	15.10 ± 0.01	14.17 ± 0.02	8.3 ± 2.9	-20.2 ± 2.6	4.3	63	17.2
2MASS J04143054+2805147	15.79 ± 0.03	14.63 ± 0.04	13.81 ± 0.04	11.8 ± 2.2	-19.5 ± 1.6	3.6	61	17.2
2MASS J04144158+2809583	···	20.76 ± 0.12	19.68 ± 0.05	-4.7 ± 5.9	-5.6 ± 5.7	0.4	15	15.9
2MASS J04151471+2800096	19.77 ± 0.01	18.07 ± 0.02	17.09 ± 0.01	15.5 ± 2.0	-24.3 ± 2.4	1.1	50	17.2
2MASS J04152409+2910434	17.90 ± 0.01	16.45 ± 0.01	15.59 ± 0.01	12.3 ± 1.8	-9.0 ± 1.8	4.3	60	17.2
2MASS J04153566+2847417	19.81 ± 0.02	18.62 ± 0.03	17.89 ± 0.01	8.1 ± 3.6	-29.6 ± 5.3	4.9	45	17.2
2MASS J04154131+2915078	16.09 ± 0.01	14.96 ± 0.01	14.34 ± 0.01	3.9 ± 3.1	-13.2 ± 2.6	6.1	59	17.2

Table A.1—Continued

Name	Photometry			Proper Motion				
	$i_{\rm P1}$ (mag)	$z_{\rm P1}$ (mag)	$y_{\rm P1}$ (mag)	$\mu_\alpha \cos\delta$ (mas yr^{-1})	μ_δ (mas yr^{-1})	χ^2_ν	$N_{\rm ep}$	Δt (yr)
2MASS J04154269+2909558	16.96 ± 0.01	15.50 ± 0.01	14.65 ± 0.01	13.9 ± 2.7	-1.5 ± 4.5	11	39	17.2
2MASS J04154807+2911331	20.61 ± 0.03	18.86 ± 0.01	17.84 ± 0.02	11.7 ± 3.5	-14.0 ± 3.5	0.7	35	17.2
2MASS J04155799+2746175	14.90 ± 0.01	13.83 ± 0.03	13.36 ± 0.03	9.9 ± 1.9	-23.2 ± 1.9	2.5	60	17.2
2MASS J04161210+2756385	15.50 ± 0.06	14.12 ± 0.01	13.55 ± 0.01	7.3 ± 2.1	-24.8 ± 1.4	1.4	71	17.2
2MASS J04161885+2752155	16.36 ± 0.01	15.09 ± 0.01	14.35 ± 0.01	5.0 ± 1.9	-24.2 ± 1.5	1.3	72	17.2
2MASS J04162725+2053091	14.96 ± 0.01	14.03 ± 0.01	13.50 ± 0.01	2.1 ± 1.2	-10.2 ± 1.3	1.8	98	17.2
2MASS J04163048+3037053	16.43 ± 0.01	15.53 ± 0.01	15.07 ± 0.01	6.6 ± 1.3	-6.2 ± 1.2	2.1	86	17.0
2MASS J04163911+2858491	16.42 ± 0.01	15.24 ± 0.01	14.45 ± 0.01	17.8 ± 3.7	-4.2 ± 5.4	17	56	17.2
2MASS J04181710+2828419	17.71 ± 0.01	16.14 ± 0.01	15.19 ± 0.01	16.2 ± 6.2	-19.1 ± 7.7	18	61	17.2
2MASS J04182909+2826191	···	···	19.55 ± 0.06	11.8 ± 11.1	-21.7 ± 4.8	1.4	13	15.9
2MASS J04183030+2743208	14.86 ± 0.01	···	13.33 ± 0.01	9.1 ± 1.7	-29.2 ± 2.4	2.2	48	17.2
2MASS J04183203+2831153	21.20 ± 0.07	19.38 ± 0.05	18.55 ± 0.12	11.0 ± 3.2	-19.3 ± 3.1	1.3	61	17.2
2MASS J04183444+2830302	···	19.80 ± 0.02	18.08 ± 0.03	9.9 ± 3.6	-22.7 ± 3.4	1.5	31	17.2
2MASS J04184023+2824245	21.16 ± 0.03	19.03 ± 0.03	17.44 ± 0.01	2.7 ± 5.9	-31.8 ± 4.9	8.6	54	17.2
2MASS J04184250+2818498	16.92 ± 0.01	15.52 ± 0.01	14.59 ± 0.01	8.2 ± 2.5	-13.1 ± 3.8	8.0	73	17.2
2MASS J04185115+2814332	17.75 ± 0.01	16.42 ± 0.01	15.65 ± 0.01	11.7 ± 4.5	-27.9 ± 2.9	4.3	87	17.2
2MASS J04185147+2820264	16.68 ± 0.03	15.54 ± 0.03	14.94 ± 0.02	2.3 ± 4.6	-6.0 ± 7.2	29	87	17.2
2MASS J04190126+2802487	20.96 ± 0.04	19.51 ± 0.01	18.46 ± 0.01	7.1 ± 5.6	-28.4 ± 5.3	1.2	53	17.2
2MASS J04190197+2822332	16.41 ± 0.01	15.02 ± 0.01	14.17 ± 0.01	-2.6 ± 3.8	-21.3 ± 4.9	23	83	17.2
2MASS J04194148+2716070	18.03 ± 0.04	17.33 ± 0.03	16.87 ± 0.03	29.0 ± 3.3	-19.3 ± 2.8	5.9	78	17.2

Table A.1—Continued

Name	Photometry			Proper Motion				
	$i_{\rm P1}$ (mag)	$z_{\rm P1}$ (mag)	$y_{\rm P1}$ (mag)	$\mu_\alpha \cos\delta$ (mas yr^{-1})	μ_δ (mas yr^{-1})	χ^2_ν	$N_{\rm ep}$	Δt (yr)
2MASS J04201611+2821325	17.25 ± 0.01	15.98 ± 0.01	15.26 ± 0.01	3.2 ± 4.3	-31.1 ± 6.1	12	73	17.2
2MASS J04202144+2813491	19.41 ± 0.02	18.54 ± 0.08	18.32 ± 0.02	-17.1 ± 14.9	5.2 ± 12.3	20	60	17.2
2MASS J04202555+2700355	16.39 ± 0.01	15.24 ± 0.01	14.58 ± 0.01	18.5 ± 3.5	-14.9 ± 1.1	7.3	82	17.2
2MASS J04202583+2819237	18.37 ± 0.01	17.09 ± 0.05	16.60 ± 0.03	25.2 ± 7.2	-36.6 ± 15.7	35	77	17.2
2MASS J04210795+2702204	18.21 ± 0.01	15.70 ± 0.01	14.89 ± 0.07	11.5 ± 8.0	-7.0 ± 3.3	11	69	17.2
2MASS J04213459+2701388	15.74 ± 0.01	14.47 ± 0.01	13.75 ± 0.01	8.1 ± 3.2	-13.5 ± 2.7	3.1	64	17.2
2MASS J04213965+2649143	16.27 ± 0.01	15.05 ± 0.01	14.35 ± 0.01	14.7 ± 2.7	-13.2 ± 5.1	5.5	68	17.2
2MASS J04214013+2814224	14.84 ± 0.01	13.86 ± 0.01	13.34 ± 0.01	13.5 ± 2.1	-25.3 ± 3.9	7.0	84	17.2
2MASS J04214631+2659296	18.11 ± 0.01	16.70 ± 0.01	15.84 ± 0.01	12.1 ± 1.6	-18.5 ± 1.8	1.2	73	17.2
2MASS J04215450+2652315	20.78 ± 0.02	18.87 ± 0.01	17.78 ± 0.02	12.0 ± 3.5	-9.5 ± 3.5	1.2	57	17.2
2MASS J04215482+2642372	15.34 ± 0.01	14.36 ± 0.01	13.84 ± 0.01	19.2 ± 7.8	-15.9 ± 3.3	6.4	63	17.2
2MASS J04215851+1520145	15.69 ± 0.01	15.05 ± 0.02	14.59 ± 0.01	-2.2 ± 3.6	2.2 ± 3.0	5.6	69	17.2
2MASS J04220069+2657324	18.50 ± 0.04	17.90 ± 0.02	17.12 ± 0.11	-11.3 ± 7.4	-12.8 ± 5.4	7.0	52	17.2
2MASS J04221332+1934392	16.93 ± 0.01	15.52 ± 0.01	14.70 ± 0.01	8.7 ± 2.1	-8.8 ± 1.7	1.6	90	17.2
2MASS J04221568+2657060	16.26 ± 0.01	15.85 ± 0.01	15.48 ± 0.01	10.6 ± 4.0	-4.0 ± 5.2	4.6	74	17.2
2MASS J04221644+2549118	17.07 ± 0.01	15.61 ± 0.01	14.85 ± 0.01	15.9 ± 2.6	-22.4 ± 1.3	2.1	79	17.2
2MASS J04221675+2654570	15.13 ± 0.07	···	14.14 ± 0.03	12.7 ± 2.1	-14.6 ± 3.3	13	79	17.2
2MASS J04223075+1526310	18.11 ± 0.01	16.85 ± 0.01	16.12 ± 0.01	1.3 ± 1.8	-3.5 ± 1.7	0.8	62	17.1
2MASS J04224786+2645530	15.36 ± 0.02	14.74 ± 0.13	14.27 ± 0.12	12.2 ± 1.9	-16.7 ± 1.4	1.6	54	17.2
2MASS J04230607+2801194	15.55 ± 0.01	14.45 ± 0.01	13.81 ± 0.01	11.5 ± 1.0	-25.2 ± 2.1	3.5	64	17.2

Table A.1—Continued

Name	Photometry			Proper Motion				
	$i_{\rm P1}$ (mag)	$z_{\rm P1}$ (mag)	$y_{\rm P1}$ (mag)	$\mu_\alpha \cos\delta$ (mas yr^{-1})	μ_δ (mas yr^{-1})	χ^2_ν	$N_{\rm ep}$	Δt (yr)
2MASS J04230776+2805573	16.34 ± 0.03	15.37 ± 0.01	15.04 ± 0.07	9.8 ± 1.2	-26.2 ± 2.0	1.8	78	17.2
2MASS J04231822+2641156	17.57 ± 0.01	16.10 ± 0.01	15.16 ± 0.01	14.9 ± 1.7	-13.1 ± 2.0	1.9	53	17.2
2MASS J04233539+2503026	14.76 ± 0.01	13.43 ± 0.01	12.64 ± 0.02	11.2 ± 4.2	-15.3 ± 4.8	23	69	17.2
2MASS J04233573+2502596	20.19 ± 0.02	18.40 ± 0.02	17.21 ± 0.01	1.4 ± 5.9	-31.9 ± 5.5	4.0	34	17.2
2MASS J04242090+2630511	16.99 ± 0.01	15.75 ± 0.01	15.07 ± 0.01	12.0 ± 3.1	-25.9 ± 1.4	2.2	47	17.1
2MASS J04242646+2649503	16.28 ± 0.01	15.15 ± 0.01	14.50 ± 0.01	10.9 ± 1.4	-18.3 ± 1.3	1.2	64	17.1
2MASS J04245021+2641006	15.60 ± 0.01	14.51 ± 0.01	13.94 ± 0.01	9.3 ± 1.5	-13.4 ± 1.6	1.7	65	17.2
2MASS J04251550+2829275	14.64 ± 0.01	13.48 ± 0.01	12.84 ± 0.01	10.2 ± 1.5	-23.6 ± 1.3	1.5	72	17.2
2MASS J04262939+2624137	17.02 ± 0.01	15.83 ± 0.01	15.08 ± 0.01	6.2 ± 2.5	-14.8 ± 1.6	3.1	74	17.1
2MASS J04263055+2443558	19.51 ± 0.02	17.70 ± 0.01	16.67 ± 0.01	10.2 ± 3.1	-15.3 ± 4.1	2.5	56	17.1
2MASS J04264449+2756433	15.89 ± 0.01	14.77 ± 0.01	14.17 ± 0.01	4.5 ± 2.0	-30.4 ± 3.7	7.9	102	17.2
2MASS J04265732+2606284	14.95 ± 0.01	13.80 ± 0.01	13.09 ± 0.01	-1.6 ± 2.1	-16.3 ± 1.9	4.8	79	17.1
2MASS J04270266+2605304	20.03 ± 0.04	19.06 ± 0.03	18.41 ± 0.03	3.9 ± 10.5	-27.0 ± 11.5	8.1	47	16.0
2MASS J04270739+2215037	15.49 ± 0.01	14.39 ± 0.01	13.79 ± 0.01	7.9 ± 1.3	-15.3 ± 1.4	1.0	73	17.2
2MASS J04272799+2612052	20.34 ± 0.02	18.58 ± 0.03	17.57 ± 0.01	-0.9 ± 2.5	-25.6 ± 2.5	1.8	59	17.2
2MASS J04274538+2357243	19.27 ± 0.01	17.75 ± 0.01	16.84 ± 0.01	9.3 ± 2.9	-12.6 ± 2.7	3.5	62	17.2
2MASS J04275730+2619183	17.60 ± 0.08	16.66 ± 0.04	15.94 ± 0.04	-6.4 ± 5.4	8.1 ± 5.9	21	73	17.2
2MASS J04284199+1533535	15.46 ± 0.01	14.63 ± 0.01	14.20 ± 0.01	1.1 ± 1.3	-15.1 ± 1.6	1.9	68	17.2
2MASS J04284263+2714039	15.33 ± 0.01	14.45 ± 0.01	13.85 ± 0.01	2.5 ± 1.3	-15.7 ± 3.1	5.8	71	17.2
2MASS J04285053+1844361	14.65 ± 0.01	13.46 ± 0.01	12.70 ± 0.01	9.3 ± 2.9	-9.0 ± 3.8	11	89	17.2

Table A.1—Continued

Name	Photometry			Proper Motion				
	$i_{\rm P1}$ (mag)	$z_{\rm P1}$ (mag)	$y_{\rm P1}$ (mag)	$\mu_\alpha \cos\delta$ (mas yr^{-1})	μ_δ (mas yr^{-1})	χ^2_ν	$N_{\rm ep}$	Δt (yr)
2MASS J04290068+2755033	17.99 ± 0.01	16.55 ± 0.01	15.72 ± 0.01	8.7 ± 1.9	-25.2 ± 1.7	1.8	57	17.2
2MASS J04290498+2649073	18.01 ± 0.01	17.14 ± 0.02	16.64 ± 0.02	12.2 ± 5.5	-9.4 ± 6.2	2.8	69	17.2
2MASS J04292165+2701259	15.67 ± 0.01	14.18 ± 0.01	13.17 ± 0.02	3.9 ± 1.5	-18.9 ± 1.5	1.8	83	17.2
2MASS J04293008+2439550	18.71 ± 0.04	17.92 ± 0.10	16.92 ± 0.12	18.9 ± 3.3	-29.4 ± 3.6	13	71	17.1
2MASS J04294568+2630468	16.31 ± 0.01	15.05 ± 0.01	14.29 ± 0.01	7.4 ± 1.2	-23.0 ± 1.4	1.6	65	17.2
2MASS J04295422+1754041	15.98 ± 0.03	15.18 ± 0.05	14.46 ± 0.11	8.8 ± 4.0	-19.5 ± 2.8	3.1	70	17.2
2MASS J04295950+2433078	16.00 ± 0.07	14.51 ± 0.01	14.01 ± 0.03	10.0 ± 1.6	-15.5 ± 2.3	1.8	66	17.1
2MASS J04300724+2608207	19.24 ± 0.01	17.70 ± 0.01	16.78 ± 0.01	4.4 ± 1.6	-19.4 ± 1.8	1.3	63	17.2
2MASS J04302365+2359129	19.25 ± 0.01	17.70 ± 0.01	16.79 ± 0.01	1.2 ± 2.4	-16.3 ± 2.2	1.6	55	17.2
2MASS J04305171+2441475	16.63 ± 0.01	15.71 ± 0.01	15.11 ± 0.04	1.8 ± 5.2	-16.5 ± 2.5	11	74	17.1
2MASS J04305718+2556394	18.55 ± 0.01	17.10 ± 0.01	16.28 ± 0.01	12.6 ± 1.6	-21.4 ± 1.9	1.4	71	17.2
2MASS J04311907+2335047	17.86 ± 0.01	16.35 ± 0.01	15.47 ± 0.01	6.4 ± 2.2	-9.8 ± 2.0	1.4	58	15.2
2MASS J04312405+1800215	15.46 ± 0.01	14.18 ± 0.01	13.39 ± 0.01	13.9 ± 4.3	-8.8 ± 3.6	4.7	62	15.2
2MASS J04312669+2703188	19.25 ± 0.01	17.69 ± 0.02	16.77 ± 0.01	16.7 ± 2.8	-17.3 ± 1.6	0.6	42	17.2
2MASS J04313407+1808049	19.56 ± 0.03	18.37 ± 0.14	17.27 ± 0.03	-79.0 ± 25.7	-28.5 ± 12.6	39	36	15.2
2MASS J04313613+1813432	16.81 ± 0.02	16.19 ± 0.03	15.57 ± 0.03	21.5 ± 6.9	-18.2 ± 6.8	22	57	15.2
2MASS J04313747+1812244	17.71 ± 0.10	17.36 ± 0.03	17.07 ± 0.10	14.8 ± 5.7	-22.6 ± 7.5	27	64	15.2
2MASS J04314644+2506236	15.13 ± 0.01	14.13 ± 0.01	13.57 ± 0.01	11.3 ± 1.5	-27.8 ± 1.4	1.9	50	17.2
2MASS J04315968+1821305	16.10 ± 0.02	15.08 ± 0.15	14.05 ± 0.07	5.2 ± 6.7	-23.1 ± 3.4	13	80	14.2
2MASS J04320329+2528078	15.07 ± 0.01	13.91 ± 0.01	13.28 ± 0.01	2.8 ± 2.0	-17.9 ± 2.5	3.4	44	17.1

Table A.1—Continued

Name	Photometry			Proper Motion				
	$i_{\rm P1}$ (mag)	$z_{\rm P1}$ (mag)	$y_{\rm P1}$ (mag)	$\mu_\alpha \cos\delta$ (mas yr^{-1})	μ_δ (mas yr^{-1})	χ^2_ν	$N_{\rm ep}$	Δt (yr)
2MASS J04321540+2428597	14.69 ± 0.02	13.32 ± 0.09	12.59 ± 0.04	14.2 ± 4.6	-8.3 ± 6.1	13	69	17.1
2MASS J04321786+2422149	15.13 ± 0.01	13.93 ± 0.01	13.23 ± 0.01	-1.0 ± 3.2	-16.9 ± 2.6	12	76	17.2
2MASS J04322210+1827426	14.61 ± 0.01	13.69 ± 0.01	13.20 ± 0.01	16.3 ± 1.8	-20.3 ± 1.8	3.4	81	14.3
2MASS J04322329+2403013	16.29 ± 0.02	14.85 ± 0.01	14.08 ± 0.01	6.6 ± 2.4	-18.8 ± 2.2	1.9	69	17.2
2MASS J04322415+2251083	14.55 ± 0.01	13.64 ± 0.01	13.11 ± 0.01	10.8 ± 1.6	-19.9 ± 1.6	1.0	58	14.3
2MASS J04323205+2257266	···	20.05 ± 0.11	19.08 ± 0.07	13.5 ± 5.1	-7.1 ± 5.2	3.7	18	13.3
2MASS J04324938+2253082	15.37 ± 0.16	13.89 ± 0.01	13.16 ± 0.01	18.8 ± 6.3	-18.8 ± 4.1	29	78	14.3
2MASS J04325026+2422115	20.85 ± 0.03	18.56 ± 0.02	17.12 ± 0.02	1.8 ± 2.9	-18.1 ± 2.7	1.2	41	17.2
2MASS J04325119+1730092	19.08 ± 0.02	17.43 ± 0.01	16.53 ± 0.01	12.6 ± 1.7	-20.8 ± 1.6	0.7	61	17.3
2MASS J04330197+2421000	14.56 ± 0.01	13.32 ± 0.01	12.60 ± 0.01	4.9 ± 1.8	-19.1 ± 2.1	2.4	51	17.2
2MASS J04330781+2616066	16.40 ± 0.01	14.89 ± 0.01	14.00 ± 0.01	9.0 ± 1.8	-16.0 ± 1.5	2.3	74	17.2
2MASS J04330945+2246487	17.51 ± 0.02	15.98 ± 0.01	15.20 ± 0.01	-0.6 ± 3.3	-16.8 ± 1.5	2.3	67	16.2
2MASS J04331435+2614235	18.61 ± 0.01	17.52 ± 0.02	16.88 ± 0.01	9.7 ± 4.3	-10.4 ± 4.1	3.5	61	17.2
2MASS J04331907+2246342	15.71 ± 0.04	14.64 ± 0.01	13.89 ± 0.05	7.0 ± 2.4	-18.7 ± 1.9	3.2	74	16.2
2MASS J04332621+2245293	15.93 ± 0.01	14.70 ± 0.01	13.93 ± 0.01	8.0 ± 2.9	-12.4 ± 2.2	3.9	69	16.2
2MASS J04332789+1758436	17.90 ± 0.03	17.19 ± 0.03	16.40 ± 0.07	11.5 ± 1.6	-14.9 ± 1.6	0.7	76	17.3
2MASS J04333905+2227207	16.04 ± 0.01	15.53 ± 0.02	15.10 ± 0.01	6.3 ± 1.9	-10.3 ± 4.8	4.3	77	16.2
2MASS J04334291+2526470	19.29 ± 0.01	17.61 ± 0.01	16.61 ± 0.01	6.0 ± 2.2	-24.5 ± 3.0	1.3	43	17.2
2MASS J04334465+2615005	15.98 ± 0.02	14.92 ± 0.05	13.82 ± 0.03	1.8 ± 2.9	-17.1 ± 2.7	6.4	104	17.2
2MASS J04335245+2612548	20.78 ± 0.02	19.03 ± 0.02	17.93 ± 0.02	9.0 ± 3.6	-15.9 ± 3.5	1.0	73	17.2

Table A.1—Continued

Name	Photometry			Proper Motion				
	$i_{\rm P1}$ (mag)	$z_{\rm P1}$ (mag)	$y_{\rm P1}$ (mag)	$\mu_\alpha \cos\delta$ (mas yr^{-1})	μ_δ (mas yr^{-1})	χ^2_ν	$N_{\rm ep}$	Δt (yr)
2MASS J04340619+2418508	17.99 ± 0.01	16.57 ± 0.01	15.75 ± 0.01	8.1 ± 2.9	-19.9 ± 2.0	3.2	53	17.2
2MASS J04341527+2250309	18.78 ± 0.01	17.09 ± 0.01	16.09 ± 0.01	17.5 ± 9.3	-12.4 ± 2.8	13	45	16.2
2MASS J04344544+2308027	16.14 ± 0.01	15.03 ± 0.01	14.40 ± 0.01	9.7 ± 1.2	-16.1 ± 1.2	1.4	82	16.3
2MASS J04345973+2807017	19.39 ± 0.02	18.22 ± 0.01	17.48 ± 0.01	7.0 ± 3.5	-15.6 ± 3.2	0.8	37	17.1
2MASS J04350850+2311398	15.73 ± 0.01	14.63 ± 0.01	14.01 ± 0.01	9.4 ± 1.3	-19.8 ± 1.1	1.2	89	16.3
2MASS J04354093+2411087	14.85 ± 0.02	14.12 ± 0.04	13.29 ± 0.03	10.9 ± 4.4	-7.7 ± 6.2	16	74	17.2
2MASS J04354183+2234115	16.26 ± 0.01	15.15 ± 0.01	14.50 ± 0.01	9.6 ± 1.3	-16.1 ± 1.5	1.6	88	16.3
2MASS J04354203+2252226	14.68 ± 0.01	13.59 ± 0.01	13.00 ± 0.01	8.4 ± 1.9	-13.0 ± 1.6	1.6	71	16.3
2MASS J04354526+2737130	19.65 ± 0.01	17.94 ± 0.01	16.99 ± 0.01	8.7 ± 4.3	-24.7 ± 1.7	2.0	57	15.2
2MASS J04355143+2249119	20.23 ± 0.01	18.55 ± 0.01	17.53 ± 0.02	20.7 ± 6.4	-14.3 ± 2.5	2.7	59	16.3
2MASS J04355209+2255039	14.78 ± 0.01	13.74 ± 0.01	13.14 ± 0.01	5.9 ± 1.9	-4.4 ± 2.2	3.2	71	16.3
2MASS J04355760+2253574	18.57 ± 0.01	17.55 ± 0.01	17.00 ± 0.02	20.0 ± 5.4	-12.6 ± 2.3	4.6	69	16.3
2MASS J04355949+2238291	17.21 ± 0.03	16.73 ± 0.02	16.25 ± 0.01	13.8 ± 3.2	-14.0 ± 3.8	4.8	89	16.3
2MASS J04361030+2159364	19.19 ± 0.01	17.65 ± 0.02	16.71 ± 0.01	7.7 ± 2.8	-21.9 ± 2.9	3.8	70	16.3
2MASS J04361038+2259560	18.33 ± 0.01	16.79 ± 0.01	15.84 ± 0.01	12.6 ± 3.1	-15.1 ± 2.4	3.1	64	16.3
2MASS J04362151+2351165	16.02 ± 0.01	15.05 ± 0.01	14.55 ± 0.01	-0.4 ± 1.2	-16.7 ± 1.5	2.7	54	16.3
2MASS J04363248+2421395	15.57 ± 0.01	14.24 ± 0.01	13.41 ± 0.01	12.3 ± 1.9	-10.0 ± 1.4	1.6	58	14.3
2MASS J04363893+2258119	18.02 ± 0.01	16.48 ± 0.01	15.55 ± 0.01	13.3 ± 5.7	-24.9 ± 6.7	32	62	16.3
2MASS J04373705+2331080	···	20.75 ± 0.03	19.67 ± 0.10	15.9 ± 13.5	-54.8 ± 13.4	0.6	16	15.0
2MASS J04374333+3056563	15.99 ± 0.01	15.09 ± 0.01	14.56 ± 0.01	6.4 ± 3.6	-10.6 ± 2.0	6.5	81	15.1

Table A.1—Continued

Name	Photometry			Proper Motion				
	$i_{\rm P1}$ (mag)	$z_{\rm P1}$ (mag)	$y_{\rm P1}$ (mag)	$\mu_\alpha \cos\delta$ (mas yr^{-1})	μ_δ (mas yr^{-1})	χ^2_ν	$N_{\rm ep}$	Δt (yr)
2MASS J04375670+2546229	17.21 ± 0.06	16.46 ± 0.07	16.00 ± 0.06	-4.6 ± 1.6	7.6 ± 3.4	4.9	62	16.2
2MASS J04380083+2558572	15.79 ± 0.01	14.34 ± 0.01	13.49 ± 0.01	-9.0 ± 5.3	-35.6 ± 7.5	15	77	16.2
2MASS J04380191+2519266	16.87 ± 0.01	16.07 ± 0.02	15.57 ± 0.01	29.6 ± 10.0	-45.3 ± 23.5	35	78	16.2
2MASS J04381486+2611399	18.98 ± 0.01	17.66 ± 0.01	16.92 ± 0.01	9.5 ± 2.8	-17.0 ± 4.6	4.6	77	16.2
2MASS J04381630+2326402	14.50 ± 0.01	13.65 ± 0.01	13.18 ± 0.01	8.6 ± 2.9	-16.2 ± 1.7	3.9	69	16.2
2MASS J04382134+2609137	···	14.88 ± 0.07	13.82 ± 0.01	21.8 ± 2.9	-17.1 ± 3.1	5.7	54	16.2
2MASS J04384725+1737260	15.57 ± 0.01	14.67 ± 0.01	14.19 ± 0.01	6.0 ± 1.5	-19.7 ± 1.8	1.9	76	17.2
2MASS J04385859+2336351	14.99 ± 0.01	14.00 ± 0.01	13.44 ± 0.01	11.1 ± 1.5	-20.3 ± 2.7	1.8	62	16.3
2MASS J04385871+2323595	15.60 ± 0.01	14.53 ± 0.01	13.94 ± 0.01	5.3 ± 1.7	-20.0 ± 2.0	1.6	70	16.3
2MASS J04390396+2544264	16.74 ± 0.02	15.29 ± 0.01	14.47 ± 0.01	5.2 ± 2.2	-25.9 ± 2.7	4.5	66	16.3
2MASS J04390525+2337450	14.92 ± 0.02	14.57 ± 0.01	14.66 ± 0.02	31.8 ± 16.2	-31.5 ± 5.6	11	77	16.3
2MASS J04390637+2334179	15.20 ± 0.01	14.11 ± 0.01	13.51 ± 0.01	4.5 ± 1.2	-20.4 ± 1.2	1.3	67	16.3
2MASS J04394748+2601407	17.54 ± 0.02	15.79 ± 0.01	14.68 ± 0.01	3.5 ± 2.1	-11.1 ± 4.0	4.7	56	16.3
2MASS J04400067+2358211	15.70 ± 0.01	14.57 ± 0.01	13.95 ± 0.01	-7.8 ± 4.0	-37.2 ± 4.6	8.7	64	16.3
2MASS J04400174+2556292	18.99 ± 0.01	17.25 ± 0.01	16.08 ± 0.02	2.3 ± 3.9	3.9 ± 10.1	15	46	16.3
2MASS J04400800+2605253	18.34 ± 0.01	16.66 ± 0.01	15.68 ± 0.01	-2.2 ± 2.6	-11.4 ± 2.8	2.1	47	16.3
2MASS J04403979+2519061	15.89 ± 0.01	14.59 ± 0.01	13.81 ± 0.01	-0.1 ± 5.8	-8.2 ± 9.8	17	89	16.3
2MASS J04410826+2556074	16.98 ± 0.02	16.25 ± 0.03	15.86 ± 0.04	4.9 ± 4.5	-16.2 ± 6.6	19	69	16.3
2MASS J04411078+2555116	17.90 ± 0.07	16.31 ± 0.07	15.57 ± 0.04	-11.8 ± 7.4	-25.9 ± 4.1	20	68	16.3
2MASS J04413882+2556267	15.09 ± 0.02	14.21 ± 0.02	13.46 ± 0.05	0.0 ± 5.5	-27.4 ± 4.2	23	79	16.3

Table A.1—Continued

Name	Photometry			Proper Motion				
	$i_{\rm P1}$ (mag)	$z_{\rm P1}$ (mag)	$y_{\rm P1}$ (mag)	$\mu_\alpha \cos\delta$ (mas yr^{-1})	μ_δ (mas yr^{-1})	χ^2_ν	$N_{\rm ep}$	Δt (yr)
2MASS J04414489+2301513	18.37 ± 0.01	16.96 ± 0.01	16.10 ± 0.01	6.9 ± 2.2	-19.9 ± 1.5	1.4	59	16.2
2MASS J04414825+2534304	17.81 ± 0.02	16.82 ± 0.01	15.77 ± 0.02	10.9 ± 2.4	-16.6 ± 2.7	3.6	69	16.3
2MASS J04422101+2520343	14.61 ± 0.01	13.60 ± 0.01	13.03 ± 0.01	4.6 ± 2.2	-18.3 ± 2.0	16	64	16.3
2MASS J04440164+1621324	16.64 ± 0.01	15.52 ± 0.01	14.89 ± 0.01	11.3 ± 2.0	-21.0 ± 2.3	5.3	85	17.2
2MASS J04442713+2512164	14.95 ± 0.03	13.91 ± 0.08	13.53 ± 0.04	4.2 ± 1.7	-15.3 ± 1.5	2.6	84	16.2
2MASS J04480632+1551251	17.47 ± 0.01	16.31 ± 0.01	15.59 ± 0.01	13.8 ± 2.0	-19.0 ± 1.2	3.4	71	17.2
2MASS J04484189+1703374	17.09 ± 0.01	15.84 ± 0.01	15.13 ± 0.01	3.8 ± 1.8	-14.8 ± 2.0	3.5	76	17.2
2MASS J04485745+2913521	14.97 ± 0.01	13.94 ± 0.01	13.38 ± 0.01	12.9 ± 6.1	-17.5 ± 6.3	21	71	17.1
2MASS J04485789+2913548	16.59 ± 0.01	15.73 ± 0.04	15.31 ± 0.01	8.7 ± 6.5	-24.0 ± 6.3	19	70	17.1
2MASS J04520668+3047175	19.42 ± 0.02	18.21 ± 0.03	17.31 ± 0.01	9.2 ± 2.6	-31.6 ± 1.9	3.9	65	17.0
2MASS J04520970+3037454	16.02 ± 0.03	15.40 ± 0.05	15.02 ± 0.10	1.9 ± 1.3	-29.8 ± 2.0	3.0	82	17.0
2MASS J04552333+3027366	16.55 ± 0.01	15.38 ± 0.01	14.70 ± 0.01	-6.1 ± 4.5	-23.6 ± 1.8	6.5	71	17.0
2MASS J04554046+3039057	15.63 ± 0.01	14.70 ± 0.01	14.19 ± 0.01	5.0 ± 1.6	-22.9 ± 1.5	2.7	73	17.0
2MASS J04554801+3028050	16.45 ± 0.01	15.37 ± 0.01	14.74 ± 0.01	4.2 ± 4.0	-22.9 ± 2.4	3.1	69	17.0
2MASS J04554969+3019400	15.93 ± 0.01	14.88 ± 0.01	14.29 ± 0.01	5.8 ± 1.7	-22.5 ± 1.4	1.8	49	17.0
2MASS J04555288+3006523	14.51 ± 0.01	13.61 ± 0.01	13.07 ± 0.01	10.8 ± 2.1	-8.7 ± 1.1	1.8	53	16.9
2MASS J04555636+3049374	14.79 ± 0.01	13.88 ± 0.01	13.40 ± 0.01	5.9 ± 0.9	-23.6 ± 2.1	4.6	77	17.0
2MASS J04574903+3015195	20.54 ± 0.03	18.82 ± 0.02	17.80 ± 0.01	-5.2 ± 4.1	-24.1 ± 4.0	0.9	48	17.0
2MASS J04591661+2840468	18.14 ± 0.01	17.54 ± 0.08	17.56 ± 0.02	3.1 ± 3.3	3.1 ± 2.3	1.1	48	17.0
2MASS J05052286+2531312	14.86 ± 0.12	13.71 ± 0.07	13.40 ± 0.08	-0.2 ± 2.8	-17.9 ± 4.7	21	79	14.9

Table A.1—Continued

Name	Photometry			Proper Motion				
	i_{P1} (mag)	z_{P1} (mag)	y_{P1} (mag)	$\mu_\alpha \cos\delta$ (mas yr^{-1})	μ_δ (mas yr^{-1})	χ^2_ν	N_{ep}	Δt (yr)
2MASS J05064662+2104296	14.90 ± 0.01	13.95 ± 0.01	13.44 ± 0.01	8.6 ± 2.3	-18.2 ± 2.2	4.3	53	17.1
2MASS J05073903+2311068	14.75 ± 0.01	14.08 ± 0.01	13.55 ± 0.01	6.5 ± 1.7	-17.4 ± 3.2	3.6	36	17.2
PSO J077.1033+24.3809	21.62 ± 0.10	20.18 ± 0.05	19.21 ± 0.06	14.1 ± 12.5	-27.1 ± 12.1	0.6	27	16.0
Unreliable fits: $\chi^2_\nu \leq 0.3$ or $\chi^2_\nu \geq 40$								
2MASS J04141188+2811535	16.76 ± 0.05	15.78 ± 0.03	14.99 ± 0.01	11.8 ± 5.5	-25.0 ± 19.5	81	53	17.2
2MASS J04174955+2813318	15.70 ± 0.02	15.00 ± 0.01	14.47 ± 0.01	-6.0 ± 4.4	-3.3 ± 12.2	59	90	17.2
2MASS J04180796+2826036	15.14 ± 0.01	13.91 ± 0.01	13.21 ± 0.01	15.0 ± 3.9	1.1 ± 12.1	51	87	17.2
2MASS J04185813+2812234	17.16 ± 0.02	16.04 ± 0.08	15.40 ± 0.06	25.4 ± 6.3	-81.7 ± 36.5	61	97	17.2
2MASS J04292373+2433002	15.51 ± 0.04	14.93 ± 0.10	14.41 ± 0.14	-23.6 ± 14.6	68.5 ± 27.1	66	71	17.1
WISE J043835.50+261041.9	16.20 ± 0.04	15.69 ± 0.07	15.12 ± 0.02	2.2 ± 6.1	-21.7 ± 7.0	44	65	5.1[a]
2MASS J04391389+2553208	···	···	19.75 ± 0.14	-2.0 ± 462.7	-5.4 ± 65.0	0.2	7	15.0

Note. — The objects in this table are taken from the catalog of Esplin et al. (2014), except for PSO J060.3200+25.9644 and PSO J077.1033+24.3809 which are new discoveries presented in this paper. We adopt a photometric precision floor of 0.01 mag for the PS1 photometry, following the analysis of Schlafly et al. (2012). The errors reported in the PS1 database are formal errors that do not include systematics, and are often smaller.

[a]This object does not have a 2MASS detection.

Appendix B

Proper Motions of Known Low-Mass Upper Scorpius Members

We calculated proper motions for 482 members of Upper Sco from the lists of Luhman & Mamajek (2012), Dawson et al. (2014), Rizzuto et al. (2015), and this paper, that met the same selection criteria we used for Taurus members in Appendix A. Our catalog comprises the largest set of proper motions for low-mass (spectral types $\gtrsim$ M3) members of Upper Sco published to date. It includes 40 objects for which no proper motion has previously been published, and 266 that improve on existing literature values, which were drawn from NOMAD (Zacharias et al. 2005), PPMXL (Roeser et al. 2010), SDSS DR9 (Ahn et al. 2012), UCAC4 (Zacharias et al. 2013), UKIDSS GCS DR9 (Lawrence et al. 2013), USNO-B (Monet et al. 2003), Dawson et al. (2011), Lodieu et al. (2007a, 2013), and Lodieu (2013). We list our proper motions, number of epochs used, reduced χ^2, and time baseline for each proper motion fit in Table B.1.

Figure B.1 shows the distribution of errors for our Upper Sco proper motions as a function of the $y_{\rm P1}$ magnitude of each source. As with our Taurus sample (Appendix A), most of the errors are $\lesssim$5 mas yr^{-1}. Figure B.2 shows the reduced χ^2 for the proper motion

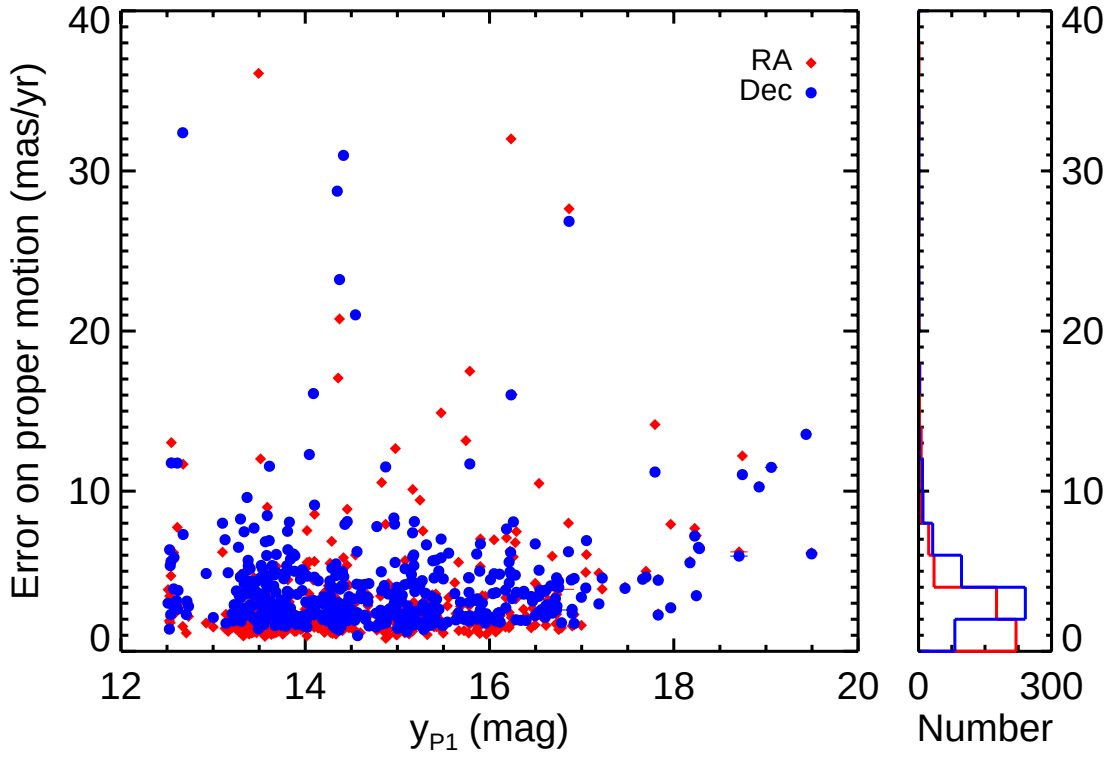

Figure B.1 Errors on our $\mu_\alpha \cos\delta$ and μ_δ as a function of $y_{\rm P1}$ for known Upper Sco members that are not saturated in PS1, using the same format as Figure A.1. Most errors are $\lesssim$5 mas yr^{-1}.

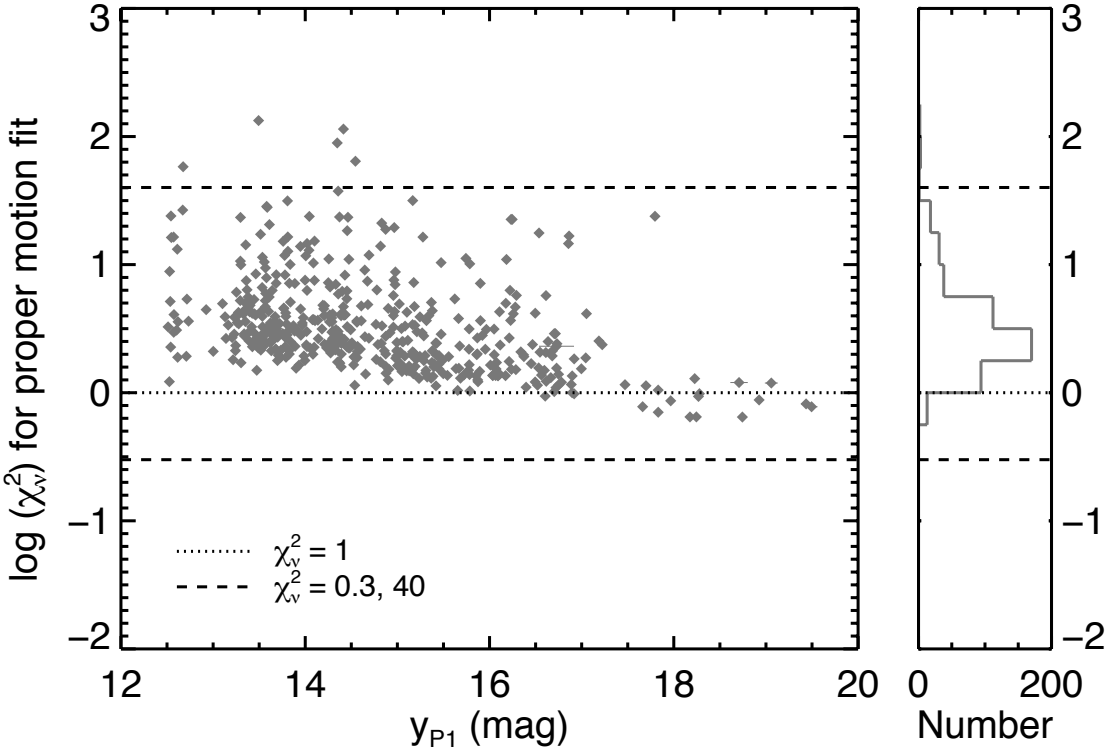

Figure B.2 Reduced χ^2 for our proper motion fits as a function of $y_{\rm P1}$ for known Upper Sco members that are not saturated in PS1, using the same format as Figure A.2. The two dashed lines mark $\chi^2_\nu = 0.3$ and $\chi^2_\nu = 40$, values between which we regard our proper motion fits and errors as reliable (Appendix A). The dotted line marks $\chi^2_\nu = 1$. As in Taurus, most of the proper motion fits have $\chi^2_\nu > 1$.

fits as a function of $y_{\rm P1}$. Again like Taurus, most of our proper motion fits have $\chi^2_\nu > 1$, implying that the proper motion errors may be underestimated (by a factor of $\approx$2).

Using the reliable fits from our Upper Sco list, we calculate a weighted mean proper motion for Upper Sco of ($\mu_\alpha \cos\delta = -8.5 \pm 0.1,\ \mu_\delta = -19.6 \pm 0.1$ mas yr^{-1}), with a weighted rms of 4.3 mas yr^{-1} in R.A. and 5.6 mas yr^{-1} in Dec. We compare our proper motions to those listed in Pecaut et al. (2012, hereinafter P12) for F stars in Upper Sco, which were determined by Hipparcos (van Leeuwen 2007a) or Tycho-2 (Høg et al. 2000). These stars are all saturated in PS1, so we are not able to measure accurate proper motions using PS1 data and compare them directly to the P12 proper motions. For the P12 Upper Sco catalog, we calculate a weighted mean proper motion of ($-11.5 \pm 0.3, -25.0 \pm 0.2$ mas yr^{-1}). We also cross-matched the P12 objects with the UCAC4 catalog (Zacharias et al. 2013), and using those proper motions obtained a weighted mean of ($-9.9 \pm 0.2, -21.6 \pm 0.2$ mas yr^{-1}). The source of the discrepancy between these two mean proper motion vectors for Upper Sco and our determination from PS1 PV3.2 is unclear, and may indicate a difference in the bulk motions of higher mass stars (from P12) and low mass stars and brown dwarfs (our catalog) in Upper Sco.

Table B.1. Proper Motions of Upper Scorpius Members

Name	Photometry			Proper Motion				
	i_{P1} (mag)	z_{P1} (mag)	y_{P1} (mag)	$\mu_\alpha \cos\delta$ (mas yr^{-1})	μ_δ (mas yr^{-1})	χ^2_ν	N_{ep}	Δt (yr)
Reliable fits: $0.3 < \chi^2_\nu < 40$								
2MASS J15350863−2532397	17.98 ± 0.01	16.86 ± 0.01	16.28 ± 0.01	-10.2 ± 6.8	-13.5 ± 4.8	4.7	47	16.5
2MASS J15355111−2021008	18.73 ± 0.01	17.32 ± 0.01	16.50 ± 0.01	-11.2 ± 1.6	-17.6 ± 2.2	1.2	38	16.6
2MASS J15411302−2308161	18.14 ± 0.01	17.02 ± 0.01	16.40 ± 0.01	-12.1 ± 2.2	-22.8 ± 1.9	1.1	48	15.3
2MASS J15420830−2621138	16.83 ± 0.01	15.85 ± 0.01	15.32 ± 0.01	-10.9 ± 3.3	-16.8 ± 6.6	3.7	53	15.7
2MASS J15423609−2108428	18.39 ± 0.01	17.02 ± 0.01	16.22 ± 0.01	-11.1 ± 6.3	-13.5 ± 5.0	6.3	37	16.6
2MASS J15433947−2535549	20.47 ± 0.03	18.85 ± 0.02	17.83 ± 0.02	-15.9 ± 4.5	-16.6 ± 4.4	0.7	41	15.3
2MASS J15442275−2136092	18.29 ± 0.01	17.23 ± 0.01	16.60 ± 0.01	-13.2 ± 2.2	-28.2 ± 2.1	0.9	52	16.6
2MASS J15453662−2510493	17.85 ± 0.01	16.70 ± 0.01	16.05 ± 0.01	-10.9 ± 1.8	-20.2 ± 2.1	2.0	55	15.7
2MASS J15465432−2556520	15.93 ± 0.01	14.93 ± 0.01	14.40 ± 0.01	-11.3 ± 1.9	-15.3 ± 4.1	4.2	64	15.7
2MASS J15470494−2137403	15.55 ± 0.01	14.68 ± 0.01	14.21 ± 0.01	-5.9 ± 3.7	-8.5 ± 3.3	4.0	51	16.6
2MASS J15472282−2139141	20.13 ± 0.02	18.72 ± 0.02	17.83 ± 0.03	-9.2 ± 2.3	-21.1 ± 2.3	1.0	45	16.6
2MASS J15472572−2609185	17.22 ± 0.02	16.10 ± 0.01	15.45 ± 0.01	-13.2 ± 2.0	-27.5 ± 2.6	2.0	54	15.3
2MASS J15480057−1815003	18.72 ± 0.01	17.38 ± 0.01	16.62 ± 0.01	-10.8 ± 2.3	-21.7 ± 2.3	1.2	37	15.9
PSO J237.1470−23.1489	18.69 ± 0.01	17.41 ± 0.01	16.61 ± 0.01	-11.4 ± 2.8	-19.7 ± 2.8	2.1	34	16.6
2MASS J15490414−2120150	17.14 ± 0.01	16.03 ± 0.01	15.43 ± 0.01	-6.6 ± 2.2	-8.5 ± 2.5	2.0	59	16.6
2MASS J15490803−2839550	16.39 ± 0.01	15.49 ± 0.01	15.02 ± 0.01	-20.4 ± 3.2	-18.2 ± 1.9	4.9	67	15.7
2MASS J15491602−2547146	15.92 ± 0.01	14.97 ± 0.01	14.49 ± 0.01	-21.2 ± 1.8	-18.0 ± 2.3	2.3	47	15.3

Table B.1—Continued

Name	Photometry			Proper Motion				
	$i_{\rm P1}$ (mag)	$z_{\rm P1}$ (mag)	$y_{\rm P1}$ (mag)	$\mu_\alpha \cos\delta$ (mas yr^{-1})	μ_δ (mas yr^{-1})	χ^2_ν	$N_{\rm ep}$	Δt (yr)
2MASS J15492260−2146574	14.61 ± 0.01	13.87 ± 0.01	13.49 ± 0.01	-17.1 ± 1.6	-18.2 ± 1.4	2.2	66	16.6
2MASS J15492909−2815384	16.01 ± 0.01	15.03 ± 0.01	14.47 ± 0.01	-15.9 ± 1.5	-22.4 ± 3.4	2.2	54	15.3
2MASS J15493660−2815141	16.31 ± 0.01	15.35 ± 0.01	14.86 ± 0.01	-14.5 ± 1.2	-14.9 ± 4.1	2.1	66	15.7
2MASS J15493784−2514102	18.73 ± 0.01	17.38 ± 0.01	16.60 ± 0.01	-22.8 ± 2.0	-26.0 ± 3.7	1.5	45	15.7
2MASS J15495069−2233511	17.51 ± 0.01	16.20 ± 0.01	15.47 ± 0.01	24.4 ± 14.9	-13.6 ± 5.8	10	54	16.1
2MASS J15495733−2201256	16.69 ± 0.01	15.59 ± 0.01	14.98 ± 0.01	-9.1 ± 12.7	-18.5 ± 2.6	8.8	59	16.6
2MASS J15501958−2805237	17.78 ± 0.01	16.70 ± 0.01	16.11 ± 0.01	-14.6 ± 1.4	-16.3 ± 4.8	4.3	71	15.7
2MASS J15511870−2145235	14.76 ± 0.01	13.98 ± 0.01	13.57 ± 0.01	-10.6 ± 2.3	-19.6 ± 4.7	9.4	60	16.6
2MASS J15514032−2146103	14.70 ± 0.01	13.88 ± 0.01	13.45 ± 0.01	-13.1 ± 2.9	-17.1 ± 2.0	4.1	58	16.6
2MASS J15514709−2113234	16.44 ± 0.08	15.61 ± 0.07	15.32 ± 0.01	-9.6 ± 1.0	-15.3 ± 1.6	1.3	70	16.6
2MASS J15514758−2329332	18.31 ± 0.01	16.96 ± 0.01	16.17 ± 0.01	-11.5 ± 1.5	-16.8 ± 3.8	1.4	45	16.6
2MASS J15521088−2125372	17.22 ± 0.01	16.90 ± 0.12	16.73 ± 0.19	-9.9 ± 3.9	-16.1 ± 2.6	2.3	64	16.6
2MASS J15522255−2313361	17.33 ± 0.01	16.11 ± 0.01	15.45 ± 0.01	-16.5 ± 1.5	-17.8 ± 5.0	1.7	55	16.6
2MASS J15524857−2621453	16.25 ± 0.01	15.30 ± 0.01	14.78 ± 0.01	-16.0 ± 1.3	-13.9 ± 7.8	6.3	46	15.7
2MASS J15530132−2114135	14.78 ± 0.01	13.93 ± 0.01	13.47 ± 0.01	-9.5 ± 1.5	-20.8 ± 1.9	1.5	59	16.3
2MASS J15541998−2135428	19.00 ± 0.01	17.56 ± 0.01	16.70 ± 0.01	-7.3 ± 3.0	-24.1 ± 2.7	1.0	42	16.3
2MASS J15543065−2536054	18.67 ± 0.01	17.41 ± 0.01	16.73 ± 0.01	-10.6 ± 2.3	-19.0 ± 4.6	1.6	47	15.7
2MASS J15543190−2221564	17.95 ± 0.01	16.65 ± 0.01	15.92 ± 0.01	-18.3 ± 3.5	-18.5 ± 3.0	2.8	38	16.6
2MASS J15544486−2843078	17.16 ± 0.01	16.15 ± 0.01	15.62 ± 0.01	-21.1 ± 4.3	-31.7 ± 3.6	5.4	64	15.1
2MASS J15550531−2117402	15.52 ± 0.01	14.59 ± 0.01	14.08 ± 0.01	-10.8 ± 1.7	-18.1 ± 2.6	3.7	50	16.3

Table B.1—Continued

Name	Photometry			Proper Motion				
	$i_{\rm P1}$ (mag)	$z_{\rm P1}$ (mag)	$y_{\rm P1}$ (mag)	$\mu_\alpha \cos\delta$ (mas yr^{-1})	μ_δ (mas yr^{-1})	χ^2_ν	$N_{\rm ep}$	Δt (yr)
2MASS J15551960−2751207	17.45 ± 0.01	16.30 ± 0.01	15.64 ± 0.01	-17.7 ± 2.3	-33.9 ± 2.0	1.5	56	15.1
2MASS J15552561−1817484	15.69 ± 0.01	14.56 ± 0.01	13.95 ± 0.01	-8.2 ± 1.4	-20.2 ± 1.7	2.8	73	16.6
2MASS J15553243−2308171	15.57 ± 0.01	15.12 ± 0.02	14.87 ± 0.01	35.9 ± 7.9	31.8 ± 11.5	19	57	16.6
2MASS J15555600−2045187	16.99 ± 0.01	16.13 ± 0.05	15.37 ± 0.01	-11.2 ± 1.6	-24.4 ± 1.6	1.3	60	16.1
2MASS J15560104−2338081	17.18 ± 0.01	16.04 ± 0.01	15.43 ± 0.01	-13.6 ± 1.5	-20.0 ± 3.2	2.4	75	16.6
2MASS J15560497−2106461	17.82 ± 0.01	16.52 ± 0.01	15.77 ± 0.01	-13.8 ± 1.1	-16.9 ± 4.6	1.5	50	16.6
2MASS J15561216−2354076	···	···	12.51 ± 0.02	-19.7 ± 3.9	-30.0 ± 3.0	3.3	28	15.7
2MASS J15561978−2423288	16.26 ± 0.01	15.32 ± 0.01	14.83 ± 0.01	-3.1 ± 10.5	-19.0 ± 3.8	21	76	15.7
2MASS J15562060−2336099	···	···	12.62 ± 0.01	-12.1 ± 3.1	-14.2 ± 3.8	3.6	64	16.6
2MASS J15563425−2003332	14.63 ± 0.01	13.73 ± 0.01	13.26 ± 0.01	-11.3 ± 1.9	-17.9 ± 2.8	3.5	51	16.6
2MASS J15570641−2206060	14.93 ± 0.01	14.06 ± 0.01	13.65 ± 0.01	-11.3 ± 2.9	-17.1 ± 2.8	3.0	50	15.7
2MASS J15571279−2343465	16.64 ± 0.01	15.59 ± 0.01	14.99 ± 0.01	-11.9 ± 1.4	-15.7 ± 2.2	2.5	52	15.7
2MASS J15572343−2924290	18.30 ± 0.01	17.08 ± 0.01	16.37 ± 0.01	-17.9 ± 2.6	-29.1 ± 3.6	2.0	39	15.1
2MASS J15572692−2715094	16.45 ± 0.01	15.57 ± 0.01	15.11 ± 0.01	-21.5 ± 1.8	-48.6 ± 2.8	2.6	62	14.9
2MASS J15572849−2219051	15.37 ± 0.01	14.48 ± 0.01	14.01 ± 0.01	-16.0 ± 5.2	-14.6 ± 3.1	12	51	14.6
2MASS J15572919−2215237	16.00 ± 0.01	15.22 ± 0.01	14.82 ± 0.01	-29.4 ± 3.5	-8.1 ± 2.6	14	53	14.6
2MASS J15572986−2258438	14.77 ± 0.01	13.94 ± 0.01	13.51 ± 0.01	-26.4 ± 12.0	-11.2 ± 4.6	17	73	14.6
2MASS J15573718−2245251	15.65 ± 0.01	15.06 ± 0.01	14.77 ± 0.01	-9.8 ± 1.6	-12.0 ± 1.5	1.8	65	14.1
2MASS J15574250−2226055	14.73 ± 0.01	14.03 ± 0.01	13.67 ± 0.01	-13.2 ± 1.5	-21.0 ± 2.7	3.2	53	14.6
2MASS J15574757−2444121	15.66 ± 0.01	14.81 ± 0.01	14.40 ± 0.01	-12.7 ± 1.3	-19.1 ± 5.0	2.6	62	15.7

Table B.1—Continued

Name	Photometry			Proper Motion				
	$i_{\rm P1}$ (mag)	$z_{\rm P1}$ (mag)	$y_{\rm P1}$ (mag)	$\mu_\alpha \cos\delta$ (mas yr^{-1})	μ_δ (mas yr^{-1})	χ^2_ν	$N_{\rm ep}$	Δt (yr)
2MASS J15581571−2021368	14.66 ± 0.01	13.81 ± 0.01	13.39 ± 0.01	-11.1 ± 2.0	-21.5 ± 2.9	4.4	63	15.7
2MASS J15581884−1915448	···	···	12.57 ± 0.01	-8.2 ± 2.3	-16.7 ± 3.9	3.0	76	15.7
2MASS J15582337−2151588	15.19 ± 0.01	14.25 ± 0.01	13.73 ± 0.01	-7.5 ± 2.2	-19.1 ± 3.2	2.1	57	15.1
2MASS J15582376−2721435	15.96 ± 0.01	15.04 ± 0.01	14.56 ± 0.01	-6.4 ± 2.1	-22.9 ± 2.3	1.9	66	15.1
2MASS J15582981−2310077	14.96 ± 0.01	14.08 ± 0.01	13.67 ± 0.01	-9.4 ± 1.5	-18.0 ± 4.9	3.6	66	15.7
2MASS J15583162−2402538	16.07 ± 0.03	15.16 ± 0.01	14.65 ± 0.01	-13.5 ± 4.2	-21.1 ± 4.2	9.1	45	15.1
2MASS J15583598−2348136	15.88 ± 0.01	14.96 ± 0.01	14.46 ± 0.01	-10.3 ± 3.0	-24.2 ± 2.4	23	68	15.1
2MASS J15584813−2141338	16.49 ± 0.01	15.51 ± 0.01	15.00 ± 0.01	-21.9 ± 1.7	-30.0 ± 4.0	2.1	45	15.7
PSO J239.7015−23.2665	20.88 ± 0.05	19.26 ± 0.01	18.24 ± 0.02	-0.1 ± 7.2	-23.0 ± 3.5	0.7	38	15.7
2MASS J15590193−2616329	14.84 ± 0.01	13.97 ± 0.01	13.52 ± 0.01	-13.7 ± 1.2	-17.1 ± 5.4	2.8	50	16.5
2MASS J15591135−2338002	17.89 ± 0.01	16.66 ± 0.01	15.97 ± 0.01	-11.0 ± 1.1	-20.9 ± 2.3	3.1	56	14.6
2MASS J15591244−2236502	15.64 ± 0.01	14.73 ± 0.01	14.21 ± 0.01	-10.7 ± 2.1	-16.7 ± 2.9	4.8	60	14.6
2MASS J15591513−2840411	15.58 ± 0.01	14.79 ± 0.01	14.39 ± 0.01	-13.9 ± 2.2	-16.5 ± 2.2	4.0	61	16.5
2MASS J15592591−2305081	15.64 ± 0.01	14.58 ± 0.01	14.01 ± 0.01	-9.1 ± 1.6	-27.3 ± 1.9	2.4	60	15.1
2MASS J15594366−2014396	17.93 ± 0.01	16.63 ± 0.01	15.87 ± 0.01	-11.9 ± 2.3	-24.0 ± 2.0	2.0	54	15.1
2MASS J15594439−1928191	18.37 ± 0.01	17.02 ± 0.01	16.25 ± 0.01	-23.6 ± 16.0	-20.2 ± 3.3	23	41	15.1
2MASS J15594802−2227162	17.80 ± 0.01	16.56 ± 0.01	15.85 ± 0.01	-9.8 ± 2.0	-16.3 ± 3.2	1.4	57	15.7
2MASS J15594970−2301576	15.74 ± 0.01	14.78 ± 0.01	14.25 ± 0.01	-5.7 ± 1.9	-21.4 ± 1.9	2.2	68	15.1
2MASS J15595868−1836520	16.83 ± 0.01	15.67 ± 0.01	15.05 ± 0.01	-7.6 ± 3.0	-16.9 ± 1.8	1.5	61	15.7
2MASS J16000713−2224066	15.86 ± 0.01	15.17 ± 0.01	14.83 ± 0.01	-26.4 ± 2.1	-3.2 ± 1.7	3.3	55	15.7

Table B.1—Continued

Name	Photometry			Proper Motion				
	$i_{\rm P1}$ (mag)	$z_{\rm P1}$ (mag)	$y_{\rm P1}$ (mag)	$\mu_\alpha \cos\delta$ (mas yr^{-1})	μ_δ (mas yr^{-1})	χ^2_ν	$N_{\rm ep}$	Δt (yr)
2MASS J16001610−1726071	18.04 ± 0.01	16.78 ± 0.01	16.07 ± 0.01	-8.5 ± 1.2	-10.6 ± 1.9	1.4	84	16.7
2MASS J16001730−2236504	···	···	12.61 ± 0.04	-16.4 ± 7.7	-30.0 ± 11.8	13	40	15.7
2MASS J16001944−2256287	18.33 ± 0.01	17.00 ± 0.01	16.24 ± 0.01	-11.0 ± 2.1	-19.2 ± 4.8	1.5	56	15.7
2MASS J16002323−2329595	18.40 ± 0.02	17.04 ± 0.01	16.23 ± 0.02	51.4 ± 32.0	-46.1 ± 16.0	23	36	15.7
2MASS J16002631−2259412	15.31 ± 0.01	14.32 ± 0.01	13.78 ± 0.01	-10.0 ± 1.8	-23.5 ± 2.0	2.7	69	15.1
2MASS J16002669−2056316	16.45 ± 0.01	15.50 ± 0.01	14.97 ± 0.01	-3.4 ± 3.1	-11.1 ± 5.5	7.0	75	15.7
2MASS J16003023−2334457	15.85 ± 0.01	14.83 ± 0.01	14.30 ± 0.01	-10.8 ± 1.1	-15.6 ± 2.7	2.7	57	15.7
2MASS J16004318−2229143	19.17 ± 0.01	17.77 ± 0.01	17.00 ± 0.01	-10.8 ± 1.6	-17.2 ± 3.4	1.5	54	15.7
2MASS J16005065−1927502	15.71 ± 0.01	14.61 ± 0.02	13.95 ± 0.01	-4.2 ± 2.1	-18.1 ± 2.2	4.5	69	15.1
2MASS J16005265−2812087	16.65 ± 0.01	15.66 ± 0.01	15.10 ± 0.01	-6.8 ± 1.6	-28.8 ± 1.6	1.5	73	15.9
2MASS J16010605−2215246	14.90 ± 0.01	14.12 ± 0.01	13.70 ± 0.01	-8.1 ± 1.9	-29.2 ± 2.8	2.7	57	15.1
2MASS J16011915−2306394	16.86 ± 0.01	15.78 ± 0.01	15.19 ± 0.01	-16.6 ± 2.3	-27.9 ± 3.7	3.4	50	15.1
2MASS J16012238−2708194	18.80 ± 0.01	17.38 ± 0.01	16.55 ± 0.01	-6.7 ± 2.4	-20.1 ± 3.8	2.1	58	16.5
2MASS J16012902−2509069	···	···	12.67 ± 0.01	-10.9 ± 1.6	-100.6 ± 32.4	27	69	16.5
2MASS J16014157−2111380	15.88 ± 0.02	14.89 ± 0.04	14.38 ± 0.01	-10.2 ± 1.4	-17.5 ± 2.2	1.7	76	16.5
2MASS J16014528−2138551	18.91 ± 0.01	17.64 ± 0.01	16.92 ± 0.01	-6.3 ± 2.3	-10.4 ± 1.7	1.8	64	16.5
2MASS J16014769−2441011	16.85 ± 0.01	15.89 ± 0.01	15.38 ± 0.01	-7.9 ± 1.7	-15.7 ± 5.7	2.1	46	16.5
2MASS J16014955−2351082	15.64 ± 0.01	14.76 ± 0.01	14.30 ± 0.01	-10.4 ± 1.9	-19.3 ± 1.7	4.1	54	16.5
2MASS J16015498−2131230	16.22 ± 0.01	15.23 ± 0.01	14.69 ± 0.01	-14.6 ± 3.4	-23.2 ± 1.6	12	66	16.0
2MASS J16015976−1952202	15.29 ± 0.01	14.36 ± 0.01	13.89 ± 0.01	-15.3 ± 2.0	-27.8 ± 2.2	3.1	66	16.0

Table B.1—Continued

Name	Photometry			Proper Motion				
	$i_{\rm P1}$ (mag)	$z_{\rm P1}$ (mag)	$y_{\rm P1}$ (mag)	$\mu_\alpha \cos\delta$ (mas yr^{-1})	μ_δ (mas yr^{-1})	χ^2_ν	$N_{\rm ep}$	Δt (yr)
2MASS J16020287−2236139	14.77 ± 0.01	14.32 ± 0.01	14.10 ± 0.01	-22.0 ± 8.6	-50.3 ± 9.1	15	50	16.5
2MASS J16020429−2050425	16.05 ± 0.01	14.98 ± 0.01	14.38 ± 0.01	-5.1 ± 1.6	-18.0 ± 3.9	2.8	79	16.5
2MASS J16021096−2007495	15.16 ± 0.01	14.28 ± 0.01	13.83 ± 0.01	-6.0 ± 1.6	-13.9 ± 3.6	3.1	78	16.5
2MASS J16021489−2438325	14.93 ± 0.01	14.01 ± 0.01	13.52 ± 0.01	-16.8 ± 1.5	-34.8 ± 2.9	2.4	41	15.9
2MASS J16022357−2259332	14.89 ± 0.01	13.91 ± 0.01	13.38 ± 0.01	-10.8 ± 2.0	-17.2 ± 5.1	2.9	56	16.5
2MASS J16022616−2002403	14.65 ± 0.01	13.79 ± 0.01	13.34 ± 0.01	-6.9 ± 1.1	-14.2 ± 7.5	4.4	83	16.5
2MASS J16023185−2132340	15.65 ± 0.01	14.73 ± 0.01	14.20 ± 0.01	-7.2 ± 3.6	-16.6 ± 3.4	4.5	39	16.5
2MASS J16023227−2200486	16.57 ± 0.01	15.48 ± 0.01	14.88 ± 0.01	-10.4 ± 1.5	-20.2 ± 1.8	1.4	64	16.0
2MASS J16023418−2200354	16.25 ± 0.01	15.02 ± 0.01	14.37 ± 0.01	-11.9 ± 1.7	-22.9 ± 1.3	1.7	70	16.0
2MASS J16023587−2320170	···	···	12.53 ± 0.01	-10.8 ± 3.4	-27.7 ± 6.3	8.8	39	16.5
2MASS J16024142−2248419	16.20 ± 0.01	15.17 ± 0.01	14.56 ± 0.01	-10.9 ± 2.0	-20.1 ± 6.2	3.6	42	16.5
2MASS J16024152−2138245	15.05 ± 0.01	14.22 ± 0.01	13.72 ± 0.01	-11.7 ± 1.6	-13.9 ± 2.8	3.5	71	16.5
2MASS J16024448−2543323	14.68 ± 0.01	13.93 ± 0.01	13.57 ± 0.01	-12.5 ± 3.3	-16.2 ± 4.2	5.9	75	16.5
2MASS J16024544−1930377	15.08 ± 0.01	14.12 ± 0.01	13.60 ± 0.01	-6.7 ± 1.1	-14.9 ± 2.6	3.0	87	16.0
2MASS J16024546−1946034	15.25 ± 0.01	14.65 ± 0.01	14.33 ± 0.01	-3.5 ± 1.1	6.5 ± 5.5	3.1	95	16.5
2MASS J16024575−2304509	15.35 ± 0.01	14.38 ± 0.01	13.87 ± 0.01	-21.3 ± 1.8	-26.6 ± 6.1	3.3	56	16.5
2MASS J16025116−2401502	15.67 ± 0.01	14.65 ± 0.01	14.04 ± 0.01	-16.5 ± 5.6	-10.1 ± 12.3	24	46	16.5
2MASS J16025214−2121296	18.52 ± 0.01	17.10 ± 0.02	16.34 ± 0.01	-5.4 ± 1.9	-17.6 ± 1.9	2.1	54	16.5
2MASS J16025529−1922431	16.06 ± 0.01	14.95 ± 0.01	14.33 ± 0.01	-11.0 ± 1.8	-19.5 ± 1.5	2.2	97	16.0
2MASS J16030161−2207523	15.70 ± 0.01	14.78 ± 0.01	14.27 ± 0.01	-9.1 ± 2.1	-18.7 ± 4.4	4.1	51	16.5

Table B.1—Continued

Name	Photometry			Proper Motion				
	$i_{\rm P1}$ (mag)	$z_{\rm P1}$ (mag)	$y_{\rm P1}$ (mag)	$\mu_\alpha \cos\delta$ (mas yr^{-1})	μ_δ (mas yr^{-1})	χ^2_ν	$N_{\rm ep}$	Δt (yr)
2MASS J16031329−2112569	14.98 ± 0.01	14.12 ± 0.01	13.62 ± 0.01	-9.5 ± 1.9	-19.3 ± 3.1	3.3	83	16.5
2MASS J16031491−2234454	14.59 ± 0.01	13.62 ± 0.01	13.13 ± 0.01	-9.7 ± 1.4	-19.0 ± 7.0	3.9	51	16.5
2MASS J16032625−2155378	15.46 ± 0.01	14.56 ± 0.01	14.05 ± 0.01	-11.3 ± 1.5	-19.1 ± 2.9	2.2	67	16.5
2MASS J16032940−1955038	14.62 ± 0.01	13.81 ± 0.01	13.39 ± 0.01	-3.9 ± 1.1	-12.8 ± 2.8	5.2	93	16.5
2MASS J16033471−1829303	15.54 ± 0.01	14.56 ± 0.01	14.02 ± 0.01	-7.0 ± 1.0	-16.5 ± 1.5	2.3	84	16.5
2MASS J16034030−2335237	14.79 ± 0.01	14.01 ± 0.01	13.61 ± 0.01	-10.2 ± 2.9	-16.9 ± 6.9	5.6	51	16.5
2MASS J16035175−2140154	14.57 ± 0.01	13.55 ± 0.01	13.00 ± 0.01	-9.3 ± 1.5	-24.4 ± 2.1	2.1	70	16.0
2MASS J16035404−2509393	14.91 ± 0.01	14.08 ± 0.01	13.64 ± 0.01	-10.5 ± 2.0	-21.9 ± 5.4	6.3	61	16.5
2MASS J16035652−2357250	16.51 ± 0.01	15.59 ± 0.01	15.08 ± 0.01	-8.6 ± 1.1	-16.1 ± 4.2	1.9	47	16.5
2MASS J16041792−1941505	16.65 ± 0.01	15.47 ± 0.01	14.91 ± 0.01	-5.7 ± 1.4	-16.2 ± 2.2	1.5	78	16.5
2MASS J16042796−1904337	14.77 ± 0.01	13.93 ± 0.01	13.46 ± 0.01	-1.8 ± 1.7	-16.9 ± 4.4	8.5	78	16.5
2MASS J16043565−1948302	15.02 ± 0.01	14.10 ± 0.01	13.58 ± 0.01	-9.1 ± 1.7	-21.8 ± 2.3	3.2	70	15.9
2MASS J16044026−2254323	18.00 ± 0.01	16.72 ± 0.01	16.18 ± 0.04	-10.6 ± 3.3	-17.4 ± 2.7	5.0	49	16.5
2MASS J16044068−1946538	16.56 ± 0.01	15.53 ± 0.01	14.96 ± 0.01	-5.8 ± 1.9	-14.8 ± 3.5	5.7	91	16.5
2MASS J16044075−1936525	17.04 ± 0.01	15.84 ± 0.01	15.15 ± 0.01	-8.7 ± 2.9	-16.5 ± 4.8	2.0	74	16.5
2MASS J16044303−2318258	17.14 ± 0.01	15.98 ± 0.01	15.31 ± 0.01	-8.7 ± 1.5	-17.9 ± 2.4	1.5	88	16.5
2MASS J16044930−2045581	19.21 ± 0.01	17.76 ± 0.01	16.90 ± 0.01	-6.0 ± 1.6	-16.9 ± 2.4	1.4	47	16.5
2MASS J16044997−2038353	14.86 ± 0.01	13.90 ± 0.01	13.40 ± 0.01	-6.9 ± 2.0	-16.1 ± 5.2	4.8	74	16.5
2MASS J16045199−2224108	17.85 ± 0.01	16.44 ± 0.01	15.65 ± 0.01	-9.1 ± 2.1	-20.4 ± 2.1	1.0	52	15.9
2MASS J16045379−2002271	16.38 ± 0.01	15.40 ± 0.01	14.87 ± 0.01	-7.8 ± 0.8	-16.1 ± 2.0	1.6	81	16.5

Table B.1—Continued

Name	Photometry			Proper Motion				
	$i_{\rm P1}$ (mag)	$z_{\rm P1}$ (mag)	$y_{\rm P1}$ (mag)	$\mu_\alpha \cos\delta$ (mas yr^{-1})	μ_δ (mas yr^{-1})	χ^2_ν	$N_{\rm ep}$	Δt (yr)
2MASS J16045581−2307438	17.38 ± 0.01	16.14 ± 0.01	15.42 ± 0.01	-6.4 ± 3.6	-18.2 ± 5.7	2.4	72	16.5
2MASS J16045716−2104160	15.07 ± 0.01	14.27 ± 0.01	13.84 ± 0.01	-7.5 ± 2.2	-19.5 ± 5.8	2.5	67	16.5
2MASS J16050231−1941554	15.14 ± 0.01	14.32 ± 0.01	13.89 ± 0.01	-7.2 ± 2.3	-14.8 ± 6.0	7.1	79	16.5
2MASS J16050474−1956274	···	···	12.54 ± 0.01	-0.7 ± 4.7	-17.4 ± 5.6	24	81	16.5
2MASS J16051403−2406524	16.16 ± 0.01	15.01 ± 0.01	14.39 ± 0.01	-12.0 ± 1.4	-24.1 ± 1.7	1.6	80	16.0
2MASS J16051615−1938310	15.03 ± 0.01	14.21 ± 0.01	13.80 ± 0.01	-6.0 ± 2.3	-18.3 ± 5.3	3.4	59	16.5
2MASS J16052556−2035397	15.05 ± 0.01	14.09 ± 0.01	13.57 ± 0.01	-5.8 ± 3.2	-33.3 ± 6.8	4.7	71	16.5
2MASS J16052787−2115510	15.87 ± 0.01	15.00 ± 0.01	14.51 ± 0.01	-7.2 ± 1.8	-14.1 ± 2.6	2.5	85	16.5
2MASS J16053077−2246200	17.18 ± 0.01	16.03 ± 0.01	15.38 ± 0.01	-12.1 ± 3.0	-21.9 ± 2.2	2.1	71	15.1
2MASS J16053128−1926240	15.35 ± 0.01	14.43 ± 0.01	13.93 ± 0.01	-8.4 ± 2.1	-21.1 ± 1.7	1.6	64	15.1
2MASS J16053215−1933159	15.49 ± 0.01	14.67 ± 0.01	14.28 ± 0.01	-7.4 ± 1.2	-15.6 ± 3.4	2.0	57	15.7
2MASS J16054416−2155054	14.91 ± 0.01	13.94 ± 0.01	13.40 ± 0.01	-14.0 ± 2.0	-36.0 ± 4.4	4.3	67	15.1
2MASS J16054565−1948353	15.49 ± 0.01	14.61 ± 0.01	14.14 ± 0.01	-7.5 ± 1.4	-15.4 ± 4.4	2.6	64	15.7
2MASS J16054778−1945263	14.88 ± 0.01	14.05 ± 0.01	13.63 ± 0.01	-5.2 ± 1.1	-13.6 ± 4.8	2.9	76	15.7
2MASS J16055407−1818443	16.78 ± 0.01	15.64 ± 0.01	15.00 ± 0.01	-4.8 ± 2.0	-14.7 ± 1.4	1.6	68	15.7
2MASS J16055409−1818488	21.26 ± 0.10	19.66 ± 0.03	18.71 ± 0.09	-16.2 ± 6.2	-31.7 ± 5.9	1.2	15	14.1
2MASS J16060374−2219298	20.55 ± 0.04	18.94 ± 0.02	17.97 ± 0.01	7.4 ± 7.9	-13.3 ± 2.7	0.9	36	15.7
2MASS J16060391−2056443	17.34 ± 0.01	16.02 ± 0.01	15.27 ± 0.01	-8.6 ± 2.1	-20.0 ± 4.4	2.9	62	15.1
2MASS J16060629−2335133	20.70 ± 0.04	19.23 ± 0.01	18.28 ± 0.01	-7.5 ± 6.5	-18.1 ± 6.4	1.0	31	15.1
2MASS J16061144−1935405	15.82 ± 0.03	14.96 ± 0.01	14.32 ± 0.01	-4.7 ± 3.4	-13.1 ± 1.7	2.4	65	15.7

Table B.1—Continued

Name	Photometry			Proper Motion				
	$i_{\rm P1}$ (mag)	$z_{\rm P1}$ (mag)	$y_{\rm P1}$ (mag)	$\mu_\alpha \cos\delta$ (mas yr^{-1})	μ_δ (mas yr^{-1})	χ^2_ν	$N_{\rm ep}$	Δt (yr)
2MASS J16061199−1935331	15.05 ± 0.01	14.05 ± 0.01	13.50 ± 0.01	-6.0 ± 1.7	-15.0 ± 1.7	2.2	62	15.7
2MASS J16061935−1923326	15.20 ± 0.01	14.31 ± 0.01	13.84 ± 0.01	-4.1 ± 2.8	-25.2 ± 2.7	5.1	71	15.1
2MASS J16062277−2011243	14.61 ± 0.01	13.84 ± 0.01	13.42 ± 0.01	-8.1 ± 3.3	-15.3 ± 2.9	4.2	80	15.7
2MASS J16062389−1941165	14.77 ± 0.01	13.82 ± 0.01	13.30 ± 0.01	-6.0 ± 1.2	-21.9 ± 1.9	1.7	78	15.1
2MASS J16062637−2306113	16.08 ± 0.01	15.17 ± 0.01	14.69 ± 0.01	-5.8 ± 2.3	-14.2 ± 4.2	2.7	74	15.7
2MASS J16062860−2043317	14.65 ± 0.01	13.71 ± 0.01	13.16 ± 0.01	-12.4 ± 1.2	-13.3 ± 4.9	3.4	87	15.7
2MASS J16062870−2856580	16.54 ± 0.01	15.57 ± 0.01	15.04 ± 0.01	-3.9 ± 1.7	-19.4 ± 1.7	1.7	72	15.9
2MASS J16063210−2020538	15.87 ± 0.01	14.95 ± 0.01	14.46 ± 0.01	-19.5 ± 8.9	-9.6 ± 8.1	18	75	15.8
2MASS J16063461−2255043	14.72 ± 0.01	13.86 ± 0.01	13.39 ± 0.01	-10.0 ± 1.6	-21.0 ± 2.4	2.5	51	15.9
2MASS J16063539−2516510	15.26 ± 0.01	14.41 ± 0.01	13.97 ± 0.01	-9.6 ± 1.4	-20.6 ± 5.1	3.5	53	16.5
2MASS J16063922−2248340	15.09 ± 0.01	14.24 ± 0.01	13.78 ± 0.01	-4.0 ± 2.3	-25.8 ± 4.9	12	77	16.4
2MASS J16064102−2455489	15.70 ± 0.01	14.89 ± 0.01	14.41 ± 0.01	-10.3 ± 1.8	-20.0 ± 4.1	4.7	64	16.5
2MASS J16064266−1851140	18.26 ± 0.01	16.86 ± 0.01	16.04 ± 0.01	-7.4 ± 2.1	-20.8 ± 2.1	1.4	47	15.9
2MASS J16064818−2230400	19.06 ± 0.01	17.61 ± 0.01	16.75 ± 0.01	-8.0 ± 1.4	-16.3 ± 4.0	1.2	42	16.4
2MASS J16065018−2309539	14.57 ± 0.01	13.74 ± 0.01	13.29 ± 0.01	-7.0 ± 1.9	-22.4 ± 2.4	5.2	74	16.4
2MASS J16070009−2043102	14.50 ± 0.01	13.70 ± 0.01	13.25 ± 0.01	-7.9 ± 1.4	-20.7 ± 3.8	6.1	76	15.7
2MASS J16070051−2206362	···	13.05 ± 0.01	12.71 ± 0.01	-12.2 ± 1.1	-19.9 ± 2.3	1.9	92	15.7
2MASS J16070169−2028579	16.67 ± 0.01	15.74 ± 0.01	15.04 ± 0.01	-8.5 ± 2.2	-24.7 ± 3.1	3.2	70	15.1
2MASS J16070474−2015557	15.14 ± 0.01	14.32 ± 0.01	13.88 ± 0.01	-5.0 ± 1.2	-14.7 ± 5.0	3.0	84	15.7
2MASS J16070700−2515127	14.51 ± 0.01	13.76 ± 0.01	13.37 ± 0.01	-11.6 ± 2.2	-16.7 ± 9.6	6.4	48	16.5

Table B.1—Continued

Name	Photometry			Proper Motion				
	$i_{\rm P1}$ (mag)	$z_{\rm P1}$ (mag)	$y_{\rm P1}$ (mag)	$\mu_\alpha \cos\delta$ (mas yr^{-1})	μ_δ (mas yr^{-1})	χ^2_ν	$N_{\rm ep}$	Δt (yr)
2MASS J16070873−1927341	14.71 ± 0.01	13.95 ± 0.01	13.51 ± 0.01	-9.0 ± 2.4	-14.3 ± 2.0	4.3	75	15.7
2MASS J16071007−1917046	15.64 ± 0.01	14.66 ± 0.01	14.14 ± 0.01	-13.6 ± 2.0	-23.7 ± 3.1	3.7	81	15.1
2MASS J16071348−2106016	15.35 ± 0.01	14.41 ± 0.01	13.89 ± 0.01	-10.0 ± 1.3	-24.6 ± 2.2	2.3	85	15.1
2MASS J16071478−2321011	···	19.81 ± 0.01	18.74 ± 0.02	0.2 ± 12.2	-16.3 ± 11.0	0.7	17	14.3
2MASS J16071750−1820348	18.95 ± 0.01	17.48 ± 0.01	16.72 ± 0.04	-4.5 ± 2.6	-21.1 ± 3.3	2.9	50	15.7
2MASS J16072240−2011581	15.75 ± 0.01	14.76 ± 0.01	14.19 ± 0.01	-7.2 ± 1.9	-25.8 ± 2.0	4.8	85	15.1
2MASS J16072382−2211018	19.51 ± 0.02	17.93 ± 0.01	17.05 ± 0.01	-19.5 ± 6.0	-21.7 ± 6.9	4.1	53	15.7
2MASS J16072641−2144169	17.98 ± 0.01	16.85 ± 0.01	16.21 ± 0.01	-9.2 ± 2.4	-20.7 ± 4.3	2.7	62	15.1
2MASS J16072754−2018344	15.76 ± 0.01	14.66 ± 0.01	14.04 ± 0.01	-6.2 ± 3.6	-23.6 ± 2.3	13	70	15.1
2MASS J16072853−2407543	···	···	12.55 ± 0.01	-3.2 ± 13.0	-20.8 ± 11.8	16	62	16.5
2MASS J16073556−2027134	15.80 ± 0.01	14.92 ± 0.01	14.43 ± 0.01	-8.2 ± 1.5	-22.8 ± 2.7	2.6	64	15.1
2MASS J16073799−2242468	···	19.99 ± 0.02	18.93 ± 0.03	-14.4 ± 10.3	-16.5 ± 10.3	0.9	36	14.8
2MASS J16074036−2357019	16.88 ± 0.01	15.80 ± 0.01	15.21 ± 0.01	-7.0 ± 1.8	-20.3 ± 2.5	3.0	73	15.7
2MASS J16074200−2107302	15.12 ± 0.01	14.23 ± 0.01	13.77 ± 0.01	-4.7 ± 2.2	-14.4 ± 4.5	4.5	82	15.7
2MASS J16074522−2222574	15.30 ± 0.01	14.41 ± 0.01	13.91 ± 0.01	-9.7 ± 1.4	-11.9 ± 3.6	3.1	73	15.7
2MASS J16075039−2221021	15.18 ± 0.01	14.27 ± 0.01	13.79 ± 0.01	-8.3 ± 2.8	-19.9 ± 3.1	4.2	70	15.1
2MASS J16075567−2443267	16.75 ± 0.01	15.78 ± 0.01	15.28 ± 0.01	-8.2 ± 7.5	-17.1 ± 2.9	16	60	16.5
2MASS J16075850−2039485	16.88 ± 0.01	15.78 ± 0.01	15.18 ± 0.01	-4.6 ± 3.1	-22.6 ± 6.0	7.2	85	15.7
2MASS J16080051−2040289	15.27 ± 0.01	14.33 ± 0.01	13.81 ± 0.01	-0.7 ± 4.5	-28.2 ± 6.3	13	84	15.1
2MASS J16080217−2259057	15.15 ± 0.01	14.18 ± 0.01	13.68 ± 0.01	-8.4 ± 1.2	-14.8 ± 3.7	2.2	62	15.7

Table B.1—Continued

Name	Photometry			Proper Motion				
	$i_{\rm P1}$ (mag)	$z_{\rm P1}$ (mag)	$y_{\rm P1}$ (mag)	$\mu_\alpha \cos\delta$ (mas yr^{-1})	μ_δ (mas yr^{-1})	χ^2_ν	$N_{\rm ep}$	Δt (yr)
2MASS J16080245−2531392	14.61 ± 0.01	13.75 ± 0.01	13.28 ± 0.01	-14.8 ± 2.7	-17.8 ± 3.5	4.1	57	16.5
2MASS J16080370−1812385	16.78 ± 0.01	16.10 ± 0.01	15.79 ± 0.01	34.8 ± 17.5	17.1 ± 11.7	10	65	15.7
2MASS J16080745−2345055	17.93 ± 0.01	16.74 ± 0.01	16.05 ± 0.01	-5.0 ± 7.0	-17.7 ± 4.8	3.1	63	15.7
2MASS J16081081−2229428	15.62 ± 0.01	14.61 ± 0.01	14.08 ± 0.01	-4.4 ± 2.1	-20.7 ± 3.2	2.0	68	15.7
2MASS J16081758−2348508	16.66 ± 0.01	15.64 ± 0.01	15.08 ± 0.02	-6.5 ± 5.7	-18.9 ± 5.2	3.3	57	15.7
2MASS J16081843−2232248	20.92 ± 0.04	19.26 ± 0.02	18.18 ± 0.01	-11.7 ± 5.6	-26.7 ± 5.5	0.7	46	15.1
2MASS J16082096−1832197	17.66 ± 0.01	16.52 ± 0.01	15.87 ± 0.01	-15.6 ± 1.6	-18.3 ± 3.3	2.7	57	15.7
2MASS J16082229−2217029	15.96 ± 0.01	15.00 ± 0.01	14.47 ± 0.01	-19.1 ± 4.1	-25.9 ± 1.9	11	53	15.7
2MASS J16082751−1949047	14.52 ± 0.01	13.61 ± 0.01	13.10 ± 0.01	10.7 ± 6.2	-6.2 ± 8.0	5.0	74	15.7
2MASS J16082847−2315103	20.03 ± 0.02	18.43 ± 0.01	17.47 ± 0.01	-8.6 ± 4.0	-30.8 ± 3.9	1.2	41	15.1
2MASS J16083048−2335109	19.08 ± 0.01	17.58 ± 0.01	16.75 ± 0.01	-12.3 ± 4.1	-18.7 ± 4.4	1.4	45	15.7
2MASS J16083455−2211559	15.36 ± 0.01	14.47 ± 0.01	13.97 ± 0.01	-9.8 ± 1.7	-18.7 ± 3.8	3.4	81	15.7
2MASS J16083659−1802497	16.26 ± 0.01	15.10 ± 0.01	14.42 ± 0.01	-5.4 ± 1.5	-17.7 ± 4.7	4.1	88	15.7
2MASS J16084171−1856107	15.46 ± 0.01	14.38 ± 0.01	13.79 ± 0.01	-6.5 ± 1.5	-18.6 ± 1.6	1.9	73	15.1
2MASS J16084565−2430000	14.73 ± 0.01	13.93 ± 0.01	13.54 ± 0.01	-10.6 ± 1.4	-14.3 ± 5.2	3.3	75	16.5
2MASS J16084744−2235477	20.14 ± 0.02	18.56 ± 0.01	17.66 ± 0.01	0.1 ± 4.5	-27.3 ± 4.5	0.8	46	15.1
2MASS J16084836−2341209	15.43 ± 0.01	14.46 ± 0.01	13.98 ± 0.01	-9.4 ± 2.3	-17.6 ± 4.9	3.9	72	15.7
2MASS J16085871−2449363	14.86 ± 0.01	14.08 ± 0.01	13.68 ± 0.01	-10.0 ± 1.8	-15.4 ± 4.9	7.2	82	16.5
2MASS J16090002−1908368	14.75 ± 0.01	13.87 ± 0.01	13.43 ± 0.01	-4.9 ± 1.2	-19.2 ± 3.8	2.3	74	15.7
2MASS J16090051−2745194	14.95 ± 0.01	14.04 ± 0.01	13.53 ± 0.01	-14.0 ± 3.0	-17.8 ± 3.2	3.9	58	16.5

Table B.1—Continued

Name	Photometry			Proper Motion				
	$i_{\rm P1}$ (mag)	$z_{\rm P1}$ (mag)	$y_{\rm P1}$ (mag)	$\mu_\alpha \cos\delta$ (mas yr^{-1})	μ_δ (mas yr^{-1})	χ^2_ν	$N_{\rm ep}$	Δt (yr)
2MASS J16090071−2029086	17.83 ± 0.01	16.63 ± 0.01	15.95 ± 0.01	-4.5 ± 3.4	-22.4 ± 1.8	2.2	46	15.7
2MASS J16090168−2740521	16.21 ± 0.01	15.08 ± 0.01	14.46 ± 0.01	-11.3 ± 2.2	-24.4 ± 2.1	2.3	68	15.9
2MASS J16090197−2151225	17.15 ± 0.01	15.96 ± 0.01	15.29 ± 0.01	-8.1 ± 2.7	-15.9 ± 2.7	2.8	59	15.7
2MASS J16090407−2417588	15.01 ± 0.01	13.86 ± 0.01	13.35 ± 0.02	-8.4 ± 2.1	-25.6 ± 3.6	14	74	16.0
2MASS J16090451−2224523	16.60 ± 0.01	15.37 ± 0.01	14.65 ± 0.01	-6.1 ± 2.1	-16.5 ± 2.0	1.4	68	15.1
2MASS J16090776−2339545	15.04 ± 0.01	14.09 ± 0.01	13.56 ± 0.01	-8.4 ± 2.1	-26.7 ± 1.9	2.4	77	15.1
2MASS J16090884−2217466	15.74 ± 0.01	14.82 ± 0.01	14.36 ± 0.01	-15.9 ± 1.7	-26.0 ± 3.0	3.0	73	15.7
2MASS J16091580−1937063	15.03 ± 0.01	14.22 ± 0.01	13.78 ± 0.01	-3.2 ± 1.6	-13.5 ± 2.0	2.3	77	15.7
2MASS J16091689−2341324	14.74 ± 0.01	13.83 ± 0.01	13.38 ± 0.01	-15.2 ± 2.7	-15.2 ± 5.7	5.6	72	15.7
2MASS J16091837−2007349	16.40 ± 0.01	15.23 ± 0.01	14.61 ± 0.01	-11.7 ± 3.4	-25.6 ± 3.3	3.6	47	15.1
2MASS J16092054−1926318	16.32 ± 0.03	15.21 ± 0.01	14.61 ± 0.01	-9.5 ± 3.3	-18.6 ± 3.6	4.8	58	15.7
2MASS J16092136−2139342	15.11 ± 0.01	14.12 ± 0.02	13.58 ± 0.01	-10.2 ± 4.7	-6.3 ± 6.0	28	64	15.1
2MASS J16092619−2403030	14.94 ± 0.01	14.09 ± 0.01	13.66 ± 0.01	-8.0 ± 1.1	-18.6 ± 4.1	2.6	77	16.5
2MASS J16092938−2343121	17.83 ± 0.01	16.57 ± 0.01	15.87 ± 0.01	-8.3 ± 1.4	-16.1 ± 2.0	1.3	59	15.7
2MASS J16093019−2059536	17.30 ± 0.01	16.17 ± 0.01	15.56 ± 0.01	-5.8 ± 3.4	-13.7 ± 6.1	1.9	63	15.7
2MASS J16093245−2405593	16.11 ± 0.01	15.05 ± 0.01	14.43 ± 0.01	-4.8 ± 1.9	-17.5 ± 7.9	8.3	74	16.5
2MASS J16093558−1828232	14.62 ± 0.01	13.81 ± 0.01	13.38 ± 0.01	-2.6 ± 1.4	-14.7 ± 5.3	4.6	90	15.7
2MASS J16093706−2052529	15.82 ± 0.01	14.90 ± 0.01	14.39 ± 0.01	-5.9 ± 1.6	-15.4 ± 2.3	2.0	83	15.1
2MASS J16094634−2255335	14.71 ± 0.01	13.87 ± 0.01	13.44 ± 0.01	-7.1 ± 4.6	-15.1 ± 7.7	5.3	70	15.7
2MASS J16095060−1848521	18.73 ± 0.01	17.25 ± 0.01	16.37 ± 0.01	-6.0 ± 3.6	-20.6 ± 3.7	1.9	41	15.1

Table B.1—Continued

Name	Photometry			Proper Motion				
	$i_{\rm P1}$ (mag)	$z_{\rm P1}$ (mag)	$y_{\rm P1}$ (mag)	$\mu_\alpha \cos\delta$ (mas yr^{-1})	μ_δ (mas yr^{-1})	χ^2_ν	$N_{\rm ep}$	Δt (yr)
2MASS J16095107−2722418	16.72 ± 0.01	15.58 ± 0.01	14.92 ± 0.01	-11.1 ± 3.9	-20.1 ± 2.7	2.9	64	16.5
2MASS J16095217−2136277	16.11 ± 0.01	14.91 ± 0.01	14.23 ± 0.01	-5.1 ± 1.7	-27.4 ± 2.2	2.2	61	15.1
2MASS J16095287−2441535	14.77 ± 0.01	13.86 ± 0.01	13.35 ± 0.01	-7.2 ± 1.7	-26.6 ± 2.6	3.6	63	16.0
2MASS J16095307−1948169	16.04 ± 0.01	14.94 ± 0.01	14.33 ± 0.01	-3.7 ± 2.2	-10.6 ± 4.7	7.0	61	15.1
2MASS J16095361−1754474	15.50 ± 0.01	14.56 ± 0.01	14.11 ± 0.01	-8.3 ± 2.8	-17.3 ± 2.6	3.7	81	15.7
2MASS J16095695−2212027	16.69 ± 0.01	15.69 ± 0.01	15.13 ± 0.01	-6.8 ± 1.1	-17.4 ± 4.2	1.5	73	15.7
2MASS J16095852−2345186	16.09 ± 0.01	14.92 ± 0.01	14.26 ± 0.01	-7.2 ± 2.2	-25.2 ± 2.4	11	87	15.1
2MASS J16095990−2155424	17.54 ± 0.01	16.45 ± 0.01	15.86 ± 0.01	-7.4 ± 1.3	-16.4 ± 6.1	2.0	77	15.7
2MASS J16100129−2152243	15.82 ± 0.01	14.78 ± 0.01	14.18 ± 0.01	-0.7 ± 1.7	-25.0 ± 2.3	3.1	79	15.1
2MASS J16100394−2728479	14.65 ± 0.01	13.85 ± 0.01	13.44 ± 0.01	-7.7 ± 1.2	-14.9 ± 3.5	2.9	68	16.5
2MASS J16100541−1919362	17.93 ± 0.01	16.66 ± 0.03	15.90 ± 0.02	0.5 ± 5.3	-13.4 ± 2.6	7.1	49	15.7
2MASS J16100608−2127440	19.16 ± 0.02	17.61 ± 0.01	16.73 ± 0.01	-6.1 ± 3.6	-19.1 ± 2.8	2.4	46	15.7
2MASS J16100753−1810568	16.16 ± 0.01	14.99 ± 0.01	14.35 ± 0.01	-4.2 ± 1.6	-22.2 ± 1.8	1.7	76	15.1
2MASS J16101100−1946040	15.09 ± 0.01	14.22 ± 0.01	13.77 ± 0.01	-9.3 ± 1.2	-15.5 ± 2.6	4.6	89	15.7
2MASS J16101191−2101550	16.81 ± 0.01	15.72 ± 0.01	15.06 ± 0.01	-5.6 ± 1.7	-19.4 ± 1.9	2.5	79	15.1
2MASS J16101316−2856308	17.53 ± 0.01	16.34 ± 0.01	15.68 ± 0.01	-15.0 ± 2.8	-15.2 ± 3.1	1.3	51	16.5
2MASS J16101445−1951377	···	···	12.61 ± 0.01	-2.3 ± 2.9	-15.3 ± 2.6	1.9	46	15.7
2MASS J16101888−2502325	14.90 ± 0.01	14.02 ± 0.01	13.59 ± 0.02	-28.4 ± 9.0	-30.8 ± 8.5	28	46	16.5
2MASS J16101942−2331089	16.66 ± 0.01	15.67 ± 0.01	15.13 ± 0.01	-5.1 ± 1.2	-13.6 ± 2.3	1.6	62	15.7
2MASS J16102087−2331556	14.76 ± 0.01	13.86 ± 0.01	13.35 ± 0.01	-13.5 ± 2.1	-24.2 ± 3.6	5.0	76	15.1

Table B.1—Continued

Name	Photometry			Proper Motion				
	$i_{\rm P1}$ (mag)	$z_{\rm P1}$ (mag)	$y_{\rm P1}$ (mag)	$\mu_\alpha \cos\delta$ (mas yr^{-1})	μ_δ (mas yr^{-1})	χ^2_ν	$N_{\rm ep}$	Δt (yr)
2MASS J16102564−2411250	18.81 ± 0.01	17.46 ± 0.01	16.68 ± 0.01	-16.2 ± 5.9	-20.2 ± 2.4	1.9	51	16.0
2MASS J16102819−1910444	15.90 ± 0.01	14.93 ± 0.01	14.40 ± 0.01	-6.8 ± 2.4	-11.1 ± 1.9	6.2	80	15.7
2MASS J16102988−2403497	15.65 ± 0.01	14.82 ± 0.01	14.36 ± 0.01	-7.2 ± 3.1	-21.4 ± 2.3	5.9	66	16.0
2MASS J16103008−1839065	14.86 ± 0.01	13.86 ± 0.01	13.28 ± 0.01	-5.8 ± 1.2	-19.2 ± 2.8	3.4	86	15.7
2MASS J16103014−2315167	18.10 ± 0.01	16.83 ± 0.01	16.09 ± 0.01	-6.3 ± 2.0	-29.7 ± 2.0	1.4	64	15.1
2MASS J16103525−2029168	15.73 ± 0.01	14.74 ± 0.01	14.21 ± 0.01	-8.1 ± 1.2	-16.7 ± 3.1	2.4	74	15.7
2MASS J16103876−1829235	17.66 ± 0.01	16.46 ± 0.01	15.72 ± 0.01	-4.0 ± 1.3	-12.9 ± 2.0	1.4	67	15.7
2MASS J16104636−1840598	15.50 ± 0.01	14.58 ± 0.01	14.01 ± 0.01	-0.2 ± 2.7	-24.6 ± 2.2	3.0	82	15.1
2MASS J16104714−2239492	19.75 ± 0.02	18.13 ± 0.01	17.22 ± 0.01	-4.3 ± 3.9	-17.0 ± 4.6	2.4	50	15.7
2MASS J16104996−2212515	15.95 ± 0.01	14.89 ± 0.01	14.28 ± 0.01	-5.0 ± 1.5	-18.7 ± 2.8	2.4	54	15.7
2MASS J16105429−2309108	15.84 ± 0.01	14.92 ± 0.01	14.45 ± 0.01	-21.7 ± 3.2	-35.6 ± 3.0	5.4	78	15.1
2MASS J16105499−2126139	16.05 ± 0.01	14.98 ± 0.01	14.36 ± 0.01	22.8 ± 17.1	-11.6 ± 2.9	37	71	15.1
2MASS J16105728−2359540	15.58 ± 0.01	14.72 ± 0.01	14.27 ± 0.01	-11.4 ± 5.5	-12.9 ± 4.0	6.7	70	16.5
2MASS J16110142−1924489	16.44 ± 0.01	15.44 ± 0.01	14.87 ± 0.01	-4.9 ± 1.7	-14.6 ± 1.8	2.0	83	15.1
2MASS J16110212−2335504	14.63 ± 0.01	13.80 ± 0.01	13.34 ± 0.01	-5.7 ± 1.5	-20.5 ± 4.2	2.9	64	15.7
2MASS J16110360−2426429	18.98 ± 0.01	17.46 ± 0.01	16.61 ± 0.01	-9.1 ± 1.6	-24.4 ± 3.8	5.7	55	14.6
2MASS J16110737−2228501	15.51 ± 0.01	14.43 ± 0.01	13.83 ± 0.01	-3.4 ± 2.0	-18.9 ± 2.0	2.0	73	15.1
2MASS J16111095−1933320	15.08 ± 0.01	14.19 ± 0.01	13.72 ± 0.01	-1.6 ± 1.4	-18.0 ± 1.8	2.9	83	15.7
2MASS J16111237−1927374	16.01 ± 0.01	14.93 ± 0.01	14.31 ± 0.01	-0.8 ± 1.5	-17.0 ± 1.6	2.6	81	15.7
2MASS J16111687−2639331	14.79 ± 0.01	14.00 ± 0.01	13.62 ± 0.01	-7.0 ± 1.5	-20.1 ± 2.3	3.5	57	14.6

Table B.1—Continued

Name	Photometry			Proper Motion				
	$i_{\rm P1}$ (mag)	$z_{\rm P1}$ (mag)	$y_{\rm P1}$ (mag)	$\mu_\alpha \cos\delta$ (mas yr^{-1})	μ_δ (mas yr^{-1})	χ^2_ν	$N_{\rm ep}$	Δt (yr)
2MASS J16111711−2217173	17.96 ± 0.01	16.73 ± 0.01	16.04 ± 0.01	-2.9 ± 1.4	-14.7 ± 3.6	1.4	62	15.7
2MASS J16111744−2441203	···	···	12.73 ± 0.01	-7.9 ± 2.2	-18.6 ± 2.8	3.6	59	14.6
2MASS J16111820−1803585	16.04 ± 0.01	14.93 ± 0.01	14.32 ± 0.01	-9.7 ± 1.6	-17.7 ± 2.6	2.8	76	15.1
2MASS J16111907−2319202	15.67 ± 0.01	15.15 ± 0.10	13.71 ± 0.03	-8.1 ± 1.4	-23.9 ± 2.1	2.0	74	15.1
2MASS J16111935−1905080	17.49 ± 0.01	16.21 ± 0.01	15.47 ± 0.01	-2.9 ± 1.5	-17.3 ± 7.0	2.9	37	15.7
2MASS J16112023−1847554	15.96 ± 0.01	14.89 ± 0.01	14.32 ± 0.01	-1.4 ± 1.7	-18.6 ± 2.6	2.9	81	15.1
2MASS J16112479−2655461	18.50 ± 0.01	17.24 ± 0.01	16.52 ± 0.01	-12.9 ± 2.4	-17.6 ± 2.4	1.1	50	14.6
2MASS J16112630−2340059	16.48 ± 0.01	15.51 ± 0.01	14.96 ± 0.01	-7.1 ± 2.4	-13.6 ± 8.3	7.6	74	15.7
2MASS J16112939−1942246	15.14 ± 0.01	14.22 ± 0.01	13.67 ± 0.01	-4.3 ± 1.2	-19.4 ± 4.8	3.0	76	15.7
2MASS J16112959−1900292	17.37 ± 0.01	16.11 ± 0.01	15.39 ± 0.01	-5.4 ± 1.8	-18.5 ± 2.8	1.3	48	15.7
2MASS J16113180−2237082	15.79 ± 0.01	14.83 ± 0.01	14.29 ± 0.01	-4.8 ± 1.9	-17.2 ± 5.2	3.0	82	15.7
2MASS J16113363−1914003	···	···	12.57 ± 0.01	-12.9 ± 6.2	-16.3 ± 2.8	16	83	15.7
2MASS J16113470−2219442	16.35 ± 0.01	15.37 ± 0.01	14.83 ± 0.01	-7.6 ± 1.5	-16.3 ± 5.0	2.4	81	15.7
2MASS J16113761−2346147	14.81 ± 0.01	14.00 ± 0.01	13.56 ± 0.01	-7.9 ± 0.9	-18.3 ± 3.4	2.5	83	15.7
2MASS J16113837−2307072	17.00 ± 0.01	15.95 ± 0.01	15.34 ± 0.01	-6.5 ± 3.0	-21.4 ± 2.3	4.0	82	15.7
2MASS J16114040−2311347	15.62 ± 0.01	14.63 ± 0.01	14.09 ± 0.01	-15.2 ± 4.4	-51.4 ± 16.1	10	77	15.7
2MASS J16114353−2527073	14.69 ± 0.01	13.74 ± 0.01	13.23 ± 0.01	-13.6 ± 1.9	-29.5 ± 2.8	3.9	48	15.9
2MASS J16114530−2254329	15.99 ± 0.01	14.95 ± 0.01	14.36 ± 0.01	-6.7 ± 1.7	-27.4 ± 2.2	2.4	83	15.1
2MASS J16114534−1928132	16.08 ± 0.01	15.02 ± 0.01	14.44 ± 0.01	-7.6 ± 3.0	-14.7 ± 2.7	4.1	56	15.7
2MASS J16114612−1907429	15.28 ± 0.01	14.31 ± 0.01	13.79 ± 0.01	-7.0 ± 2.0	-27.5 ± 2.7	3.9	75	15.1

Table B.1—Continued

Name	Photometry			Proper Motion				
	$i_{\rm P1}$ (mag)	$z_{\rm P1}$ (mag)	$y_{\rm P1}$ (mag)	$\mu_\alpha \cos\delta$ (mas yr^{-1})	μ_δ (mas yr^{-1})	χ^2_ν	$N_{\rm ep}$	Δt (yr)
2MASS J16114735−2242062	16.45 ± 0.01	15.47 ± 0.01	14.97 ± 0.01	-6.8 ± 3.0	-9.7 ± 7.9	4.3	64	15.7
2MASS J16114920−1947431	14.66 ± 0.01	13.76 ± 0.01	13.28 ± 0.01	-9.1 ± 1.5	-18.0 ± 6.5	4.2	67	15.7
2MASS J16115436−2157025	18.50 ± 0.01	17.04 ± 0.01	16.18 ± 0.01	-2.2 ± 7.1	-10.0 ± 7.6	11	40	15.7
2MASS J16115439−2236491	17.59 ± 0.01	16.49 ± 0.01	15.89 ± 0.01	-8.4 ± 1.1	-12.2 ± 5.0	1.5	68	15.7
2MASS J16115737−2215066	16.78 ± 0.01	15.80 ± 0.01	15.23 ± 0.01	-8.8 ± 1.6	-16.4 ± 1.8	1.3	73	15.1
2MASS J16121016−2758305	18.94 ± 0.02	17.63 ± 0.01	16.86 ± 0.02	32.5 ± 27.6	24.4 ± 26.9	17	42	16.5
2MASS J16121043−1932275	15.29 ± 0.01	14.30 ± 0.01	13.76 ± 0.01	-5.8 ± 1.1	-13.6 ± 1.6	2.9	78	15.7
2MASS J16121185−2047267	17.14 ± 0.01	15.95 ± 0.01	15.29 ± 0.01	-6.6 ± 1.7	-22.2 ± 1.4	1.8	74	15.7
2MASS J16121492−2218038	15.05 ± 0.01	14.22 ± 0.01	13.78 ± 0.01	-5.2 ± 2.4	-18.7 ± 4.7	8.3	67	15.7
2MASS J16121609−2344248	16.11 ± 0.01	15.18 ± 0.01	14.68 ± 0.01	-15.4 ± 2.8	-15.4 ± 3.1	4.9	67	15.7
2MASS J16121723−2839082	14.75 ± 0.01	13.94 ± 0.01	13.54 ± 0.01	-2.6 ± 4.6	-15.7 ± 2.5	11	62	16.5
2MASS J16122737−2009596	15.70 ± 0.01	14.68 ± 0.01	14.10 ± 0.01	-8.3 ± 1.5	-23.8 ± 2.7	2.3	73	15.1
2MASS J16122764−2156407	···	20.33 ± 0.02	19.44 ± 0.06	-5.2 ± 13.6	-19.8 ± 13.5	0.8	17	14.8
2MASS J16122768−2406485	15.94 ± 0.01	14.95 ± 0.01	14.39 ± 0.01	-6.7 ± 1.9	-23.9 ± 1.6	2.4	68	16.0
2MASS J16122895−2159358	···	20.32 ± 0.04	19.06 ± 0.07	-33.1 ± 83.4	-36.8 ± 11.5	1.2	14	13.9
2MASS J16123458−2458341	14.96 ± 0.01	13.98 ± 0.01	13.46 ± 0.01	-8.3 ± 3.1	-25.0 ± 4.3	4.0	67	15.9
2MASS J16123759−2349234	16.93 ± 0.01	15.93 ± 0.01	15.37 ± 0.01	-6.8 ± 1.7	-26.5 ± 2.2	1.7	69	15.1
2MASS J16124374−2308231	14.59 ± 0.01	13.79 ± 0.01	13.33 ± 0.01	-8.3 ± 1.0	-23.6 ± 4.8	4.1	77	15.7
2MASS J16124506−2305303	16.56 ± 0.01	15.57 ± 0.01	14.99 ± 0.01	-8.8 ± 1.0	-24.2 ± 3.3	2.1	70	15.7
2MASS J16124692−2338408	17.00 ± 0.01	15.87 ± 0.01	15.24 ± 0.01	-8.8 ± 2.7	-19.3 ± 1.6	1.9	69	15.1

Table B.1—Continued

Name	Photometry			Proper Motion				
	$i_{\rm P1}$ (mag)	$z_{\rm P1}$ (mag)	$y_{\rm P1}$ (mag)	$\mu_\alpha \cos\delta$ (mas yr^{-1})	μ_δ (mas yr^{-1})	χ^2_ν	$N_{\rm ep}$	Δt (yr)
2MASS J16124726−1903531	16.06 ± 0.01	15.01 ± 0.01	14.45 ± 0.01	-2.2 ± 5.4	-29.2 ± 3.0	6.2	62	15.1
2MASS J16125528−2226542	15.15 ± 0.01	14.28 ± 0.01	13.81 ± 0.01	-14.6 ± 4.9	-23.0 ± 3.5	16	71	15.1
2MASS J16130232−2124283	···	20.63 ± 0.04	19.50 ± 0.06	-9.0 ± 6.2	-23.3 ± 6.1	0.8	24	14.8
2MASS J16130235−1904450	17.72 ± 0.02	16.60 ± 0.02	15.79 ± 0.02	-10.8 ± 2.1	-18.0 ± 2.2	1.0	52	15.1
2MASS J16130306−1929319	16.72 ± 0.01	15.64 ± 0.01	15.03 ± 0.01	-9.7 ± 1.5	-25.3 ± 1.7	1.7	71	15.1
2MASS J16130762−1703524	16.74 ± 0.01	15.73 ± 0.01	15.17 ± 0.01	-22.6 ± 10.1	-4.9 ± 5.9	32	68	15.2
2MASS J16130996−1904269	14.52 ± 0.03	13.68 ± 0.01	13.23 ± 0.01	-5.5 ± 1.6	-17.3 ± 2.9	2.9	67	15.7
2MASS J16131082−2313514	15.23 ± 0.01	14.36 ± 0.01	13.90 ± 0.01	-13.9 ± 1.3	-33.2 ± 1.7	1.6	71	15.1
2MASS J16131211−2305031	17.55 ± 0.01	16.35 ± 0.01	15.68 ± 0.01	-6.0 ± 2.1	-24.5 ± 2.1	2.3	69	15.1
2MASS J16132665−2230348	16.97 ± 0.01	15.80 ± 0.01	15.18 ± 0.01	-3.9 ± 2.2	-17.6 ± 5.3	2.0	48	15.7
2MASS J16132809−1924524	16.22 ± 0.01	15.14 ± 0.01	14.53 ± 0.01	-3.9 ± 1.3	-19.8 ± 3.3	1.9	77	15.7
2MASS J16133476−2328156	16.40 ± 0.01	15.49 ± 0.01	14.98 ± 0.01	-5.9 ± 1.1	-14.9 ± 2.7	1.9	75	15.7
2MASS J16133647−2327353	15.05 ± 0.01	14.12 ± 0.01	13.63 ± 0.01	-10.0 ± 1.2	-24.5 ± 2.2	2.1	74	15.1
2MASS J16133834−2158518	14.58 ± 0.01	13.79 ± 0.01	13.36 ± 0.01	-1.5 ± 3.9	-11.7 ± 2.5	7.5	58	15.7
2MASS J16133840−2443309	···	13.09 ± 0.01	12.72 ± 0.01	-12.2 ± 3.0	-15.9 ± 3.1	5.4	64	16.5
2MASS J16134045−2233156	16.02 ± 0.01	14.99 ± 0.01	14.42 ± 0.01	-2.5 ± 1.8	-23.6 ± 2.1	4.0	64	15.1
2MASS J16134079−2219459	18.60 ± 0.01	17.25 ± 0.01	16.47 ± 0.01	-2.7 ± 2.7	-20.7 ± 3.1	2.4	43	15.1
2MASS J16134264−2301279	16.98 ± 0.01	15.91 ± 0.01	15.31 ± 0.01	-5.3 ± 1.6	-14.8 ± 3.6	1.4	84	15.7
2MASS J16134490−2434143	···	···	12.58 ± 0.01	-6.5 ± 2.4	-19.2 ± 5.9	4.1	55	16.5
2MASS J16134880−2509006	16.84 ± 0.01	15.75 ± 0.01	15.19 ± 0.01	-5.3 ± 1.9	-18.3 ± 3.8	1.6	70	16.5

Table B.1—Continued

Name	Photometry			Proper Motion				
	$i_{\rm P1}$ (mag)	$z_{\rm P1}$ (mag)	$y_{\rm P1}$ (mag)	$\mu_\alpha \cos\delta$ (mas yr^{-1})	μ_δ (mas yr^{-1})	χ^2_ν	$N_{\rm ep}$	Δt (yr)
2MASS J16135765−2053447	17.18 ± 0.01	16.12 ± 0.01	15.54 ± 0.01	-22.8 ± 2.8	-30.4 ± 1.8	1.4	56	15.1
2MASS J16140514−2042017	18.04 ± 0.02	16.79 ± 0.01	16.09 ± 0.01	-9.4 ± 2.4	-18.8 ± 2.4	1.4	56	15.1
2MASS J16141352−2244578	15.03 ± 0.01	14.22 ± 0.01	13.81 ± 0.01	-10.8 ± 7.5	-13.8 ± 7.5	31	70	15.7
2MASS J16141484−2427081	15.66 ± 0.01	14.58 ± 0.01	14.00 ± 0.01	0.5 ± 2.6	-20.1 ± 2.3	7.6	71	16.5
2MASS J16141974−2428404	17.13 ± 0.01	16.01 ± 0.01	15.37 ± 0.01	-9.9 ± 2.8	-15.0 ± 3.4	5.1	49	16.5
2MASS J16142144−2339146	18.53 ± 0.01	17.31 ± 0.01	16.64 ± 0.01	-16.0 ± 3.2	-15.9 ± 2.9	2.5	51	15.1
2MASS J16142312−2219338	14.82 ± 0.01	13.86 ± 0.01	13.30 ± 0.01	-2.8 ± 3.3	-19.6 ± 3.4	10	56	15.7
2MASS J16142478−1733329	18.86 ± 0.01	17.47 ± 0.01	16.68 ± 0.01	-11.1 ± 2.5	-22.0 ± 2.7	2.1	45	15.2
2MASS J16143287−2242133	17.81 ± 0.01	16.57 ± 0.01	15.90 ± 0.01	-4.4 ± 7.0	-18.7 ± 6.7	3.7	53	15.7
2MASS J16143751−1858240	14.92 ± 0.01	14.27 ± 0.01	13.95 ± 0.01	-20.6 ± 2.2	-33.9 ± 4.5	14	75	15.7
2MASS J16144169−2351058	20.96 ± 0.05	19.29 ± 0.01	18.23 ± 0.03	-15.6 ± 7.7	-16.2 ± 7.2	1.3	30	15.1
2MASS J16145258−2017133	19.59 ± 0.02	18.07 ± 0.01	17.19 ± 0.01	-1.2 ± 4.9	-16.6 ± 3.0	2.5	51	15.7
2MASS J16145392−2504305	14.94 ± 0.01	14.09 ± 0.01	13.64 ± 0.01	-5.2 ± 1.5	-22.0 ± 4.0	2.5	51	16.5
2MASS J16145928−2459308	14.80 ± 0.01	13.99 ± 0.01	13.55 ± 0.01	-7.3 ± 1.9	-17.8 ± 1.7	2.8	45	16.5
2MASS J16150524−2459351	15.63 ± 0.01	14.64 ± 0.01	14.09 ± 0.01	-5.4 ± 1.9	-21.2 ± 2.3	3.7	57	15.9
2MASS J16150702−2535528	17.63 ± 0.01	16.44 ± 0.01	15.78 ± 0.01	-9.0 ± 1.7	-17.3 ± 1.9	1.4	73	15.9
2MASS J16150891−2345048	14.89 ± 0.01	14.08 ± 0.01	13.68 ± 0.01	-9.3 ± 2.0	-17.4 ± 2.4	3.5	58	15.7
2MASS J16151116−2420153	17.43 ± 0.01	16.39 ± 0.01	15.78 ± 0.01	-7.9 ± 1.9	-12.1 ± 4.6	1.7	52	16.5
2MASS J16151239−2420091	15.97 ± 0.01	15.06 ± 0.01	14.57 ± 0.01	-14.0 ± 2.1	-19.3 ± 2.4	2.1	53	15.9
2MASS J16151361−2304261	18.30 ± 0.01	17.11 ± 0.01	16.45 ± 0.01	-14.4 ± 1.5	-17.2 ± 3.4	1.7	56	15.7

Table B.1—Continued

Name	Photometry			Proper Motion				
	$i_{\rm P1}$ (mag)	$z_{\rm P1}$ (mag)	$y_{\rm P1}$ (mag)	$\mu_\alpha \cos\delta$ (mas yr^{-1})	μ_δ (mas yr^{-1})	χ^2_ν	$N_{\rm ep}$	Δt (yr)
2MASS J16151602−2345103	15.31 ± 0.01	14.36 ± 0.01	13.83 ± 0.01	-6.8 ± 3.1	-17.4 ± 8.1	7.1	56	15.7
2MASS J16151667−2340462	20.44 ± 0.03	18.71 ± 0.01	17.70 ± 0.01	-8.0 ± 5.0	-19.5 ± 4.6	1.1	35	15.1
2MASS J16152009−2333545	16.24 ± 0.01	15.15 ± 0.01	14.53 ± 0.01	-2.3 ± 2.1	-20.9 ± 2.0	1.7	61	15.1
2MASS J16152750−2627281	14.76 ± 0.01	14.01 ± 0.01	13.60 ± 0.01	-3.6 ± 2.5	-15.6 ± 2.8	4.3	51	16.5
2MASS J16152819−2315439	15.88 ± 0.01	15.04 ± 0.01	14.60 ± 0.01	-13.5 ± 1.2	-24.5 ± 4.2	2.2	79	15.7
2MASS J16153648−2315175	16.92 ± 0.01	15.98 ± 0.01	15.49 ± 0.01	-7.9 ± 1.6	-23.3 ± 1.6	1.8	54	15.1
2MASS J16153844−2341558	14.93 ± 0.01	14.11 ± 0.01	13.69 ± 0.01	-7.9 ± 5.3	-12.2 ± 6.0	8.3	86	15.7
2MASS J16153866−2240371	15.51 ± 0.01	14.57 ± 0.01	14.10 ± 0.01	-10.1 ± 5.6	-17.1 ± 4.6	7.5	60	15.7
2MASS J16153913−1917005	15.13 ± 0.01	14.04 ± 0.01	13.42 ± 0.01	-2.8 ± 1.1	-22.4 ± 2.2	3.3	89	15.1
2MASS J16155507−2444365	16.92 ± 0.01	15.73 ± 0.01	15.05 ± 0.01	-9.6 ± 2.4	-25.2 ± 3.5	2.5	49	15.9
2MASS J16155926−2329363	14.94 ± 0.01	14.11 ± 0.01	13.69 ± 0.01	-10.4 ± 1.4	-16.3 ± 2.6	3.2	78	15.7
2MASS J16160080−2214192	14.72 ± 0.01	13.80 ± 0.01	13.34 ± 0.01	-6.3 ± 1.5	-16.0 ± 2.2	2.8	57	15.7
2MASS J16161183−2316268	15.60 ± 0.01	14.70 ± 0.01	14.25 ± 0.01	-11.0 ± 1.6	-24.1 ± 2.3	2.4	61	15.1
2MASS J16161948−2405301	15.63 ± 0.01	14.75 ± 0.01	14.29 ± 0.01	-9.2 ± 1.7	-20.4 ± 2.1	3.6	70	15.9
2MASS J16162399−2408301	16.16 ± 0.01	15.20 ± 0.01	14.67 ± 0.01	-10.4 ± 3.5	-18.1 ± 3.4	7.4	64	15.9
2MASS J16162531−2412057	16.60 ± 0.01	15.65 ± 0.02	15.03 ± 0.01	-8.1 ± 1.3	-13.2 ± 3.3	1.6	62	16.5
2MASS J16162598−2112227	17.36 ± 0.01	16.33 ± 0.01	15.78 ± 0.01	-11.7 ± 2.8	-8.5 ± 3.1	3.1	51	15.7
2MASS J16163068−2512201	15.95 ± 0.01	14.96 ± 0.01	14.46 ± 0.01	-8.2 ± 1.7	-16.2 ± 1.9	3.3	65	15.9
2MASS J16163226−2205201	16.81 ± 0.01	15.76 ± 0.01	15.20 ± 0.01	-3.7 ± 2.3	-17.8 ± 2.4	1.8	43	15.1
2MASS J16163343−2327210	15.23 ± 0.01	14.27 ± 0.01	13.76 ± 0.01	-15.9 ± 3.2	-19.2 ± 2.2	15	84	15.1

Table B.1—Continued

Name	Photometry			Proper Motion				
	$i_{\rm P1}$ (mag)	$z_{\rm P1}$ (mag)	$y_{\rm P1}$ (mag)	$\mu_\alpha \cos\delta$ (mas yr^{-1})	μ_δ (mas yr^{-1})	χ^2_ν	$N_{\rm ep}$	Δt (yr)
2MASS J16163345−2521505	···	···	12.60 ± 0.01	-6.8 ± 2.8	-20.5 ± 3.1	3.1	56	16.5
2MASS J16163503−2057551	15.28 ± 0.01	14.27 ± 0.01	13.73 ± 0.01	-6.6 ± 1.3	-24.4 ± 1.7	1.9	74	15.1
2MASS J16164539−2333413	16.82 ± 0.01	15.82 ± 0.01	15.30 ± 0.01	-13.2 ± 1.5	-29.9 ± 1.8	1.9	102	15.1
2MASS J16165158−2048537	14.77 ± 0.01	13.95 ± 0.01	13.53 ± 0.01	-5.4 ± 2.6	-15.3 ± 2.7	6.6	59	15.7
2MASS J16165430−2459590	14.56 ± 0.01	13.75 ± 0.01	13.30 ± 0.01	-8.2 ± 2.9	-14.8 ± 8.3	23	67	16.5
2MASS J16170606−2225414	14.79 ± 0.01	13.98 ± 0.01	13.58 ± 0.01	-7.5 ± 2.3	-0.6 ± 4.5	7.9	58	15.1
2MASS J16171901−2137129	16.69 ± 0.01	15.63 ± 0.01	15.03 ± 0.01	-3.6 ± 1.5	-21.2 ± 1.9	2.1	76	15.1
2MASS J16172505−2350380	17.09 ± 0.01	16.01 ± 0.01	15.40 ± 0.01	-4.5 ± 1.5	-16.9 ± 4.6	1.7	58	15.7
2MASS J16173103−2050469	16.49 ± 0.01	15.31 ± 0.01	14.65 ± 0.01	-5.9 ± 2.1	-23.6 ± 2.3	2.7	68	15.1
2MASS J16173236−2040362	18.06 ± 0.01	16.85 ± 0.01	16.11 ± 0.01	-1.2 ± 2.2	-14.3 ± 2.4	1.4	55	15.1
2MASS J16173786−2119159	14.96 ± 0.01	14.11 ± 0.01	13.68 ± 0.01	-12.3 ± 1.2	-20.4 ± 2.7	2.2	65	15.7
2MASS J16174366−2111552	17.11 ± 0.01	16.30 ± 0.01	15.87 ± 0.01	-7.7 ± 2.3	-8.5 ± 2.3	1.2	55	15.1
2MASS J16174539−2353360	17.53 ± 0.01	16.33 ± 0.01	15.66 ± 0.01	-7.1 ± 5.6	-29.6 ± 2.4	3.8	55	15.9
2MASS J16174583−2414436	16.72 ± 0.01	15.72 ± 0.01	15.16 ± 0.01	-2.5 ± 1.3	-20.0 ± 1.8	3.4	57	16.5
2MASS J16181201−2413326	15.82 ± 0.01	14.81 ± 0.01	14.26 ± 0.01	-6.2 ± 2.1	-11.3 ± 2.7	3.6	67	15.9
2MASS J16181568−2347084	16.24 ± 0.01	15.00 ± 0.01	14.29 ± 0.01	-27.4 ± 6.9	-28.6 ± 2.1	3.8	73	15.7
2MASS J16181600−2437266	14.79 ± 0.01	13.78 ± 0.01	13.24 ± 0.01	-4.2 ± 1.6	-17.8 ± 2.1	2.1	57	15.9
2MASS J16181618−2619080	15.41 ± 0.01	14.41 ± 0.01	13.84 ± 0.01	-18.5 ± 3.5	-22.7 ± 2.0	10	70	15.9
2MASS J16181904−2028479	15.35 ± 0.01	14.36 ± 0.01	13.82 ± 0.01	-1.4 ± 1.7	-20.6 ± 1.8	2.1	78	15.1
2MASS J16182082−2401502	18.46 ± 0.01	17.24 ± 0.01	16.56 ± 0.01	-9.3 ± 2.2	-23.6 ± 2.6	1.4	54	15.9

Table B.1—Continued

Name	Photometry			Proper Motion				
	$i_{\rm P1}$ (mag)	$z_{\rm P1}$ (mag)	$y_{\rm P1}$ (mag)	$\mu_\alpha \cos\delta$ (mas yr^{-1})	μ_δ (mas yr^{-1})	χ^2_ν	$N_{\rm ep}$	Δt (yr)
2MASS J16182501−2338106	17.23 ± 0.01	16.08 ± 0.01	15.45 ± 0.01	-7.0 ± 2.0	-25.1 ± 1.8	1.5	78	15.1
2MASS J16183317−2517504	16.21 ± 0.01	15.07 ± 0.02	14.37 ± 0.01	39.1 ± 20.8	30.7 ± 23.2	24	62	16.5
2MASS J16183618−2425333	14.82 ± 0.01	13.97 ± 0.01	13.52 ± 0.01	-1.3 ± 2.8	-15.8 ± 3.3	2.2	69	16.5
2MASS J16184074−2209482	17.22 ± 0.01	16.05 ± 0.01	15.38 ± 0.01	-11.3 ± 3.5	-21.9 ± 2.4	4.4	50	15.7
2MASS J16184955−2541499	19.11 ± 0.01	17.82 ± 0.01	17.04 ± 0.01	-4.0 ± 4.9	-14.1 ± 4.0	1.9	55	16.5
2MASS J16185037−2424319	16.84 ± 0.01	15.77 ± 0.01	15.16 ± 0.01	-6.6 ± 1.9	-27.0 ± 1.6	1.5	57	15.9
2MASS J16185430−2346075	18.88 ± 0.01	17.65 ± 0.01	16.92 ± 0.01	-6.0 ± 1.6	-15.5 ± 4.5	1.0	46	15.7
2MASS J16190341−2344085	17.98 ± 0.01	16.72 ± 0.01	16.01 ± 0.01	-6.7 ± 1.4	-24.3 ± 4.5	1.6	61	15.7
2MASS J16190474−2307526	16.21 ± 0.01	15.14 ± 0.01	14.56 ± 0.01	2.6 ± 3.1	-27.7 ± 4.2	3.6	52	15.1
2MASS J16191521−2417241	15.22 ± 0.01	14.24 ± 0.01	13.70 ± 0.01	-14.1 ± 1.2	-15.3 ± 2.8	1.8	59	16.5
2MASS J16191646−2347235	18.95 ± 0.01	17.58 ± 0.01	16.78 ± 0.01	-7.6 ± 1.5	-14.3 ± 1.8	1.2	75	15.7
2MASS J16192634−2412444	16.93 ± 0.01	15.80 ± 0.01	15.18 ± 0.01	-9.7 ± 2.0	-8.9 ± 8.1	4.7	62	16.5
2MASS J16192988−2440469	18.39 ± 0.01	16.90 ± 0.01	16.07 ± 0.01	-7.4 ± 1.2	-24.4 ± 3.7	1.5	59	16.5
2MASS J16192992−2425540	14.63 ± 0.01	13.70 ± 0.01	13.21 ± 0.01	-7.3 ± 1.5	-23.6 ± 2.3	2.7	77	15.9
2MASS J16193976−2145349	16.58 ± 0.01	15.43 ± 0.01	14.77 ± 0.01	-5.1 ± 1.6	-22.7 ± 2.4	3.4	59	15.1
2MASS J16194210−2504323	18.87 ± 0.01	17.58 ± 0.01	16.86 ± 0.01	-15.7 ± 8.0	-12.5 ± 6.2	15	62	16.5
2MASS J16194309−2216175	14.73 ± 0.01	13.99 ± 0.01	13.62 ± 0.01	-15.0 ± 3.4	-18.8 ± 4.1	2.5	70	15.7
2MASS J16194836−2212519	···	···	12.53 ± 0.01	-6.5 ± 1.8	-14.6 ± 5.4	5.2	77	15.7
2MASS J16195143−2241332	18.28 ± 0.01	16.99 ± 0.01	16.21 ± 0.01	-5.3 ± 1.5	-13.2 ± 5.6	1.8	51	15.7
2MASS J16195827−2832276	20.98 ± 0.04	19.37 ± 0.02	18.27 ± 0.03	-17.7 ± 6.5	-19.9 ± 6.5	0.9	49	15.7

Table B.1—Continued

Name	Photometry			Proper Motion				
	$i_{\rm P1}$ (mag)	$z_{\rm P1}$ (mag)	$y_{\rm P1}$ (mag)	$\mu_\alpha \cos\delta$ (mas yr^{-1})	μ_δ (mas yr^{-1})	χ^2_ν	$N_{\rm ep}$	Δt (yr)
2MASS J16200757−2359150	16.76 ± 0.01	15.55 ± 0.01	14.87 ± 0.01	-14.4 ± 3.7	-22.7 ± 2.0	2.8	63	14.4
2MASS J16201318−2425014	16.25 ± 0.01	15.49 ± 0.01	15.10 ± 0.01	-3.7 ± 2.0	-5.8 ± 1.2	4.2	61	14.8
2MASS J16202128−2120289	16.65 ± 0.01	15.55 ± 0.01	14.90 ± 0.01	-5.6 ± 1.0	-16.6 ± 3.6	1.3	67	15.7
2MASS J16202163−2005348	14.94 ± 0.01	14.03 ± 0.01	13.56 ± 0.01	-16.5 ± 2.8	-23.9 ± 3.6	10	76	15.1
2MASS J16202523−2316033	17.89 ± 0.01	16.72 ± 0.01	16.08 ± 0.01	-9.5 ± 1.3	-20.3 ± 2.0	1.7	60	15.7
2MASS J16203456−2430205	18.93 ± 0.01	17.26 ± 0.01	16.29 ± 0.01	8.0 ± 7.5	-18.7 ± 3.7	5.7	38	14.2
2MASS J16204144−2425491	18.44 ± 0.01	17.08 ± 0.01	16.29 ± 0.01	-11.8 ± 3.3	-15.2 ± 2.0	1.5	60	14.8
2MASS J16210222−2358395	18.87 ± 0.01	17.51 ± 0.01	16.70 ± 0.01	-7.4 ± 2.6	-16.7 ± 3.0	2.9	54	15.7
2MASS J16211563−2436117	14.54 ± 0.01	13.95 ± 0.01	13.67 ± 0.01	-27.7 ± 1.8	-15.9 ± 1.6	3.9	64	15.5
2MASS J16211920−2425525	15.75 ± 0.01	14.66 ± 0.01	14.00 ± 0.01	-0.5 ± 1.6	-14.5 ± 1.6	1.8	70	15.1
2MASS J16212488−2426145	16.17 ± 0.01	15.15 ± 0.01	14.57 ± 0.01	-6.5 ± 2.4	-17.3 ± 1.0	2.3	74	15.5
2MASS J16212953−2529431	···	···	12.54 ± 0.01	-5.1 ± 2.1	-18.8 ± 2.3	2.3	77	15.5
2MASS J16212961−2129038	15.02 ± 0.01	14.07 ± 0.01	13.61 ± 0.01	-3.1 ± 3.0	-18.7 ± 11.6	21	71	15.7
2MASS J16213591−2355035	17.65 ± 0.01	16.40 ± 0.01	15.67 ± 0.01	-9.6 ± 1.3	-17.8 ± 2.2	1.6	72	15.7
2MASS J16214853−2517266	···	···	12.53 ± 0.01	-8.1 ± 1.9	-20.0 ± 1.4	1.2	58	16.8
2MASS J16215975−2706366	14.68 ± 0.01	13.91 ± 0.01	13.51 ± 0.01	-9.0 ± 1.6	-22.1 ± 2.2	2.5	66	16.2
2MASS J16221693−1825131	···	···	17.80 ± 0.04	-25.9 ± 14.2	-0.6 ± 11.2	24	14	14.3
2MASS J16222160−2217307	16.56 ± 0.01	15.51 ± 0.01	14.96 ± 0.01	-22.7 ± 3.3	-18.6 ± 2.6	4.0	66	15.1
2MASS J16222521−2405139	18.27 ± 0.01	17.00 ± 0.01	16.23 ± 0.01	-13.9 ± 1.7	-3.4 ± 6.2	3.7	62	16.8
2MASS J16223834−2541017	18.50 ± 0.01	17.28 ± 0.03	16.53 ± 0.02	-8.8 ± 4.0	-13.0 ± 3.4	1.6	59	16.8

Table B.1—Continued

Name	Photometry			Proper Motion				
	$i_{\rm P1}$ (mag)	$z_{\rm P1}$ (mag)	$y_{\rm P1}$ (mag)	$\mu_\alpha \cos\delta$ (mas yr^{-1})	μ_δ (mas yr^{-1})	χ^2_ν	$N_{\rm ep}$	Δt (yr)
2MASS J16224385−1951057	16.63 ± 0.01	15.14 ± 0.01	14.25 ± 0.01	3.2 ± 4.1	-21.4 ± 2.9	7.2	51	15.7
2MASS J16230646−2528419	19.09 ± 0.01	17.71 ± 0.01	16.90 ± 0.01	-14.9 ± 2.6	-24.4 ± 2.6	1.0	50	16.0
2MASS J16232202−2609553	18.88 ± 0.02	17.66 ± 0.01	16.89 ± 0.03	-6.8 ± 2.6	-18.5 ± 4.5	1.2	49	16.8
2MASS J16235155−2317270	17.43 ± 0.01	16.07 ± 0.01	15.24 ± 0.01	-14.1 ± 9.4	-26.7 ± 4.1	3.9	59	15.7
2MASS J16235470−2438319	17.23 ± 0.01	15.94 ± 0.01	15.17 ± 0.01	-2.2 ± 2.7	-17.0 ± 4.3	1.4	61	16.8
2MASS J16250277−3006556	18.31 ± 0.01	17.14 ± 0.01	16.50 ± 0.01	-7.0 ± 4.2	-22.3 ± 6.7	4.2	50	16.5
2MASS J16252860−1658509	17.44 ± 0.01	16.14 ± 0.01	15.40 ± 0.01	-6.3 ± 3.2	-8.5 ± 2.5	1.6	63	16.7
2MASS J16252969−2214543	16.52 ± 0.01	15.42 ± 0.01	14.82 ± 0.01	-5.9 ± 2.0	-15.7 ± 1.8	1.7	51	15.7
2MASS J16253274−2611386	14.63 ± 0.01	13.76 ± 0.01	13.30 ± 0.01	-7.1 ± 4.8	-14.6 ± 4.6	11	90	16.5
2MASS J16253672−2224285	17.03 ± 0.01	15.88 ± 0.01	15.16 ± 0.01	-5.2 ± 2.7	-15.8 ± 7.4	2.1	47	15.7
2MASS J16254322−2230026	15.98 ± 0.01	15.02 ± 0.01	14.49 ± 0.01	-5.9 ± 3.1	-18.2 ± 2.3	3.1	58	15.7
2MASS J16254808−2154195	14.63 ± 0.01	13.87 ± 0.01	13.46 ± 0.01	-9.4 ± 2.4	-18.6 ± 3.6	2.6	72	15.7
2MASS J16255066−2155454	17.24 ± 0.01	16.26 ± 0.01	15.74 ± 0.01	-16.1 ± 13.2	-24.1 ± 2.2	11	66	15.7
2MASS J16260625−2334030	16.90 ± 0.01	15.69 ± 0.01	14.96 ± 0.01	2.0 ± 2.7	-31.9 ± 3.5	3.3	80	15.3
2MASS J16263026−2336551	17.68 ± 0.03	16.27 ± 0.01	15.50 ± 0.04	-3.5 ± 1.1	-16.9 ± 4.5	1.4	55	15.7
2MASS J16263276−2622589	14.50 ± 0.01	13.49 ± 0.01	12.92 ± 0.01	-6.8 ± 1.8	-27.2 ± 4.9	4.5	53	15.1
2MASS J16265619−2213519	16.84 ± 0.01	15.72 ± 0.01	15.05 ± 0.01	-7.9 ± 1.8	-20.6 ± 2.3	1.6	62	15.3
2MASS J16270217−2542346	18.98 ± 0.01	17.59 ± 0.01	16.72 ± 0.01	-10.2 ± 1.7	-13.0 ± 2.7	1.1	32	15.7
2MASS J16270942−2148457	16.30 ± 0.01	15.22 ± 0.03	14.79 ± 0.02	-8.7 ± 1.7	-18.4 ± 1.7	2.4	70	15.7
2MASS J16272034−2844302	18.47 ± 0.01	17.31 ± 0.04	16.54 ± 0.01	-30.5 ± 10.5	-34.7 ± 5.1	18	57	15.3

Table B.1—Continued

Name	Photometry			Proper Motion				
	$i_{\rm P1}$ (mag)	$z_{\rm P1}$ (mag)	$y_{\rm P1}$ (mag)	$\mu_\alpha \cos\delta$ (mas yr^{-1})	μ_δ (mas yr^{-1})	χ^2_ν	$N_{\rm ep}$	Δt (yr)
2MASS J16272553−2138036	15.10 ± 0.01	14.24 ± 0.01	13.80 ± 0.01	-7.6 ± 1.3	-17.7 ± 3.7	2.8	69	15.7
2MASS J16274799−2457134	17.47 ± 0.01	16.19 ± 0.01	15.42 ± 0.01	-6.7 ± 1.8	-21.6 ± 1.9	1.1	64	15.3
2MASS J16281808−2428358	16.61 ± 0.01	15.30 ± 0.01	14.54 ± 0.01	-3.5 ± 1.3	-25.2 ± 1.9	1.1	62	15.7
2MASS J16284703−2428138	16.65 ± 0.04	15.81 ± 0.01	15.19 ± 0.02	-6.6 ± 1.6	-18.5 ± 1.9	1.9	58	15.7
2MASS J16292211−1742091	15.41 ± 0.01	14.49 ± 0.01	14.02 ± 0.01	-25.0 ± 7.5	-22.3 ± 2.2	6.3	61	16.7
2MASS J16293624−2456527	16.51 ± 0.01	15.52 ± 0.01	14.90 ± 0.01	-12.8 ± 4.2	-19.5 ± 2.6	4.6	80	15.7
2MASS J16293662−1708413	14.83 ± 0.01	13.94 ± 0.01	13.47 ± 0.01	-2.3 ± 1.2	-19.5 ± 3.7	2.5	75	16.7
2MASS J16293934−1614570	14.54 ± 0.01	13.89 ± 0.01	13.57 ± 0.01	-26.2 ± 2.4	-6.0 ± 2.2	5.2	72	16.7
2MASS J16294879−2137086	15.50 ± 0.01	14.55 ± 0.01	14.02 ± 0.01	-4.0 ± 5.5	-17.6 ± 4.7	15	64	15.7
2MASS J16302673−2359087	16.07 ± 0.01	14.95 ± 0.02	14.30 ± 0.01	-1.5 ± 1.8	-24.4 ± 4.0	3.0	61	15.1
2MASS J16303390−2428062	14.72 ± 0.01	13.76 ± 0.01	13.22 ± 0.01	-4.3 ± 1.7	-19.3 ± 1.9	1.8	63	15.1
2MASS J16305349−2424538	15.69 ± 0.01	14.61 ± 0.01	13.99 ± 0.01	-1.6 ± 2.1	-21.9 ± 1.6	1.9	79	16.1
2MASS J16310240−2408431	14.73 ± 0.01	13.78 ± 0.01	13.24 ± 0.01	0.9 ± 1.8	-22.0 ± 2.1	2.3	69	16.1
2MASS J16313519−2542261	18.41 ± 0.01	17.05 ± 0.01	16.26 ± 0.01	-11.8 ± 5.9	-18.7 ± 8.1	4.1	43	14.6
2MASS J16320136−2237081	17.70 ± 0.01	16.50 ± 0.01	15.78 ± 0.01	-5.1 ± 2.3	-17.2 ± 3.7	2.2	55	16.0
2MASS J16324221−2316562	14.66 ± 0.01	13.66 ± 0.01	13.14 ± 0.01	-16.6 ± 2.3	-34.1 ± 1.7	2.7	62	16.2
2MASS J16324727−2059375	16.55 ± 0.01	15.53 ± 0.02	14.97 ± 0.01	-12.4 ± 8.0	-17.3 ± 3.0	19	65	16.6
2MASS J16332000−2741076	17.80 ± 0.01	16.71 ± 0.01	16.12 ± 0.01	-13.2 ± 2.2	-17.8 ± 1.8	2.4	54	16.5
2MASS J16342850−2201119	16.81 ± 0.01	15.64 ± 0.01	14.99 ± 0.01	-8.9 ± 1.8	-25.8 ± 2.2	1.9	62	16.1
2MASS J16370753−2432395	19.35 ± 0.01	17.69 ± 0.01	16.67 ± 0.01	-2.9 ± 2.4	-13.6 ± 4.1	1.3	50	16.5

Table B.1—Continued

Name	Photometry			Proper Motion				
	$i_{\rm P1}$ (mag)	$z_{\rm P1}$ (mag)	$y_{\rm P1}$ (mag)	$\mu_\alpha \cos\delta$ (mas yr^{-1})	μ_δ (mas yr^{-1})	χ^2_ν	$N_{\rm ep}$	Δt (yr)
Unreliable fits: $\chi^2_\nu \leq 0.3$ or $\chi^2_\nu \geq 40$								
2MASS J16002535−2644060	16.03 ± 0.01	15.09 ± 0.01	14.54 ± 0.01	-23.2 ± 6.0	19.9 ± 21.0	64	64	15.9
2MASS J16070211−2019387	15.74 ± 0.02	14.82 ± 0.04	14.35 ± 0.04	102.4 ± 41.2	48.9 ± 28.7	89	79	15.7
2MASS J16090405−1934000	14.85 ± 0.02	14.02 ± 0.03	13.49 ± 0.01	-70.2 ± 36.1	95.5 ± 54.7	130	65	15.7
2MASS J16125723−2428013	15.80 ± 0.01	14.89 ± 0.01	14.41 ± 0.01	-8.5 ± 5.8	1.0 ± 31.0	110	70	16.5
2MASS J16273320−2821097	···	···	12.67 ± 0.01	-17.2 ± 11.7	-9.8 ± 7.3	58	65	15.7

Note. — The objects in this table are taken from the catalogs of Luhman & Mamajek (2012), Dawson et al. (2014), and Rizzuto et al. (2015), except for PSO J237.1470−23.1489 and PSO J239.7015−23.2665 which are new discoveries presented in this paper. We adopt a photometric precision floor of 0.01 mag for the PS1 photometry, following the analysis of Schlafly et al. (2012). The errors reported in the PS1 database are formal errors that do not include systematics, and are often smaller.

Appendix C

A New SpeX Prism Spectrum for the L0 Field Standard

We identified a wavelength offset in the spectrum of 2MASS J03454316+2540233 (hereinafter 2MASS J0345+2540) publically available from the SpeX Prism Library[1]. 2MASS J0345+2540 is the field L0 spectral standard for both optical (Kirkpatrick et al. 1999) and near-infrared (Kirkpatrick et al. 2010) wavelengths. The spectrum, first published in Burgasser & McElwain (2006, hereinafter BM06), is shifted ≈0.01 μm toward longer wavelengths (Figure C.1). The offset is insignificant when visually compared to other spectra over the full 0.8–2.5 μm range of SpeX prism spectra, but is large enough to impact calculations of the Allers & Liu (2013a) gravity-sensitive spectral indices that use ≈0.02 μm-wide J-band absorption features (Section 4.4.3). The offset is equivalent to a velocity of ≈2,400 km s^{-1}, two orders of magnitude larger than the radial velocities typical of nearby late-M and early-L dwarfs (Burgasser et al. 2015b), so the offset is almost certainly due to a wavelength calibration error.

To obtain a spectrum for 2MASS J0345+2540 with an accurate wavelength calibration, we observed the object on 2016 February 03 UT with IRTF/SpeX in prism mode, using the 0.5" slit. Conditions were clear. Observations were made at an airmass of 1.01 and comprised six exposures of 120 sec using an ABBA nodding pattern. Immediately

[1]http://pono.ucsd.edu/∼adam/browndwarfs/spexprism

after we observed the A0V star HD 19600 for telluric calibration. We reduced the 2MASS J0345+2540 spectrum using Spextool v. 4.0 in standard fashion. The final spectrum has a mean S/N of 115 in J band (1.20–1.31 μm). Figure C.1 shows our spectrum compared with the BM06 spectrum for 2MASS J0345+2540 and the SpeX Prism Library spectrum for the L0 dwarf 2MASS J02281101+2537380 (Burgasser et al. 2008a). The redward offset on the BM06 spectrum is evident in the J-band absorption features. We therefore used our new spectrum for 2MASS J0345+2540 in our analysis (Sections 4.4.2 and 4.4.3).

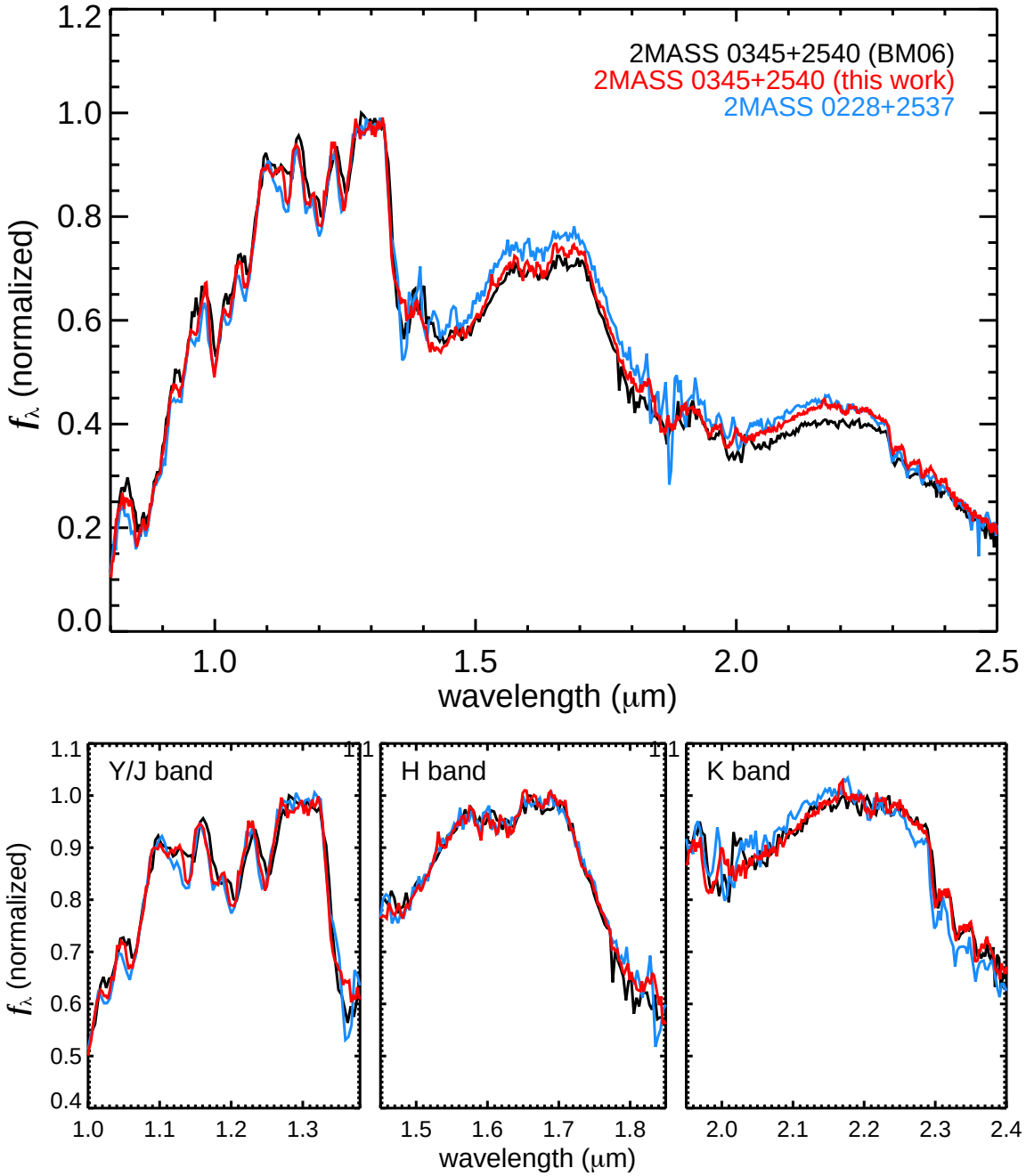

Figure C.1 *Top*: The SpeX Prism Library spectra for the L0 field standard 2MASS J0345+2540 (Burgasser & McElwain 2006, BM06, black) and the L0 dwarf 2MASS J0228+2537 (Burgasser et al. 2008a, blue), compared with our new SpeX prism spectrum for 2MASS J0345+2540 (red). *Bottom*: The same three spectra normalized and plotted separately for Y/J, H, and K bands to compare the spectral shapes in each band. The offset of the BM06 2MASS J0345+2540 spectrum towards longer wavelengths is evident in the J-band absorption features. We use our new spectrum for 2MASS J0345+2540 for analysis in this paper.

References

Abazajian, K., Adelman-McCarthy, J. K., Agüeros, M. A., et al. 2003, AJ, 126, 2081

Aberasturi, M., Burgasser, A. J., Mora, A., et al. 2014, AJ, 148, 129

Aberasturi, M., Solano, E., & Martín, E. L. 2011, A&A, 534, L7

Ackerman, A. S., & Marley, M. S. 2001, ApJ, 556, 872

Aganze, C., Burgasser, A. J., Faherty, J. K., et al. 2016, AJ, 151, 46

Ahn, C. P., Alexandroff, R., Allende Prieto, C., et al. 2012, ApJS, 203, 21

Albert, L., Artigau, E., Delorme, P., et al. 2011, AJ, 141, 203

Allard, F., Hauschildt, P. H., Alexander, D. R., Tamanai, A., & Schweitzer, A. 2001, ApJ, 556, 357

Allen, P. R. 2007, ApJ, 668, 492

Allen, P. R., Burgasser, A. J., Faherty, J. K., & Kirkpatrick, J. D. 2012, AJ, 144, 62

Allen, P. R., Koerner, D. W., McElwain, M. W., Cruz, K. L., & Reid, I. N. 2007, AJ, 133, 971

Allen, P. R., Koerner, D. W., Reid, I. N., & Trilling, D. E. 2005, ApJ, 625, 385

Aller, K. M., Kraus, A. L., Liu, M. C., et al. 2013, ApJ, 773, 63

Aller, K. M., Liu, M. C., Magnier, E. A., et al. 2016, ApJ, 821, 120

Allers, K. N., Gallimore, J. F., Liu, M. C., & Dupuy, T. J. 2016, ApJ, 819, 133

Allers, K. N., & Liu, M. C. 2013a, ApJ, 772, 79

Allers, K. N., & Liu, M. C. 2013b, in Brown Dwarfs Come of Age, Mem. S.A.It., 84, 1089

Allers, K. N., Liu, M. C., Dupuy, T. J., & Cushing, M. C. 2010, ApJ, 715, 561

Allers, K. N., Liu, M. C., Shkolnik, E. L., et al. 2009, ApJ, 697, 824

Alves de Oliveira, C., Moraux, E., Bouvier, J., & Bouy, H. 2012, A&A, 539, 151

Alves de Oliveira, C., Moraux, E., Bouvier, J., et al. 2013, A&A, 549, 123

Andrei, A. H., Smart, R. L., Penna, J. L., et al. 2011, AJ, 141, 54

Andrews, S. M., Rosenfeld, K. A., Kraus, A. L., & Wilner, D. J. 2013, ApJ, 771, 129

Apai, D., Radigan, J., Buenzli, E., et al. 2013, ApJ, 768, 121

Aparicio, A., & Hidalgo, S. L. 2009, AJ, 138, 558

Artigau, E., Bouchard, S., Doyon, R., & Lafreniere, D. 2009, ApJ, 701, 1534

Artigau, E., Doyon, R., Lafreniere, D., et al. 2006, ApJL, 651, L57

Artigau, E., Lafreniere, D., Doyon, R., et al. 2011, ApJ, 739, 48

Bailer-Jones, C. A. L. 2004, A&A, 419, 703

Baraffe, I., Homeier, D., Allard, F., & Chabrier, G. 2015, A&A, 577, A42

Bardalez Gagliuffi, D. C., Gelino, C. R., & Burgasser, A. J. 2015, AJ, 150, 163

Bardalez Gagliuffi, D. C., Burgasser, A. J., Gelino, C. R., et al. 2014, ApJ, 794, 143

Barman, T. S., Macintosh, B., Konopacky, Q. M., & Marois, C. 2011, ApJ, 733, 65

Baron, F., Lafreniere, D., Artigau, E., et al. 2015, ApJ, 802, 37

Barrado Y Navascués, D., Zapatero Osorio, M. R., Martín, E. L., et al. 2002, A&A, 393, L85

Bartlett, J. L. 2007, PhD thesis, ProQuest Dissertations and Theses, AAT 3239972, University of Virginia

Basri, G. 2000, ARAA, 38, 485

Basri, G., Mohanty, S., Allard, F., et al. 2000, ApJ, 538, 363

Basri, G., & Reiners, A. 2006, AJ, 132, 663

Beamín, J. C., Minniti, D., Gromadzki, M., et al. 2013, A&A, 557, L8

Becklin, E. E., & Zuckerman, B. 1988, Nature, 336, 656

Beichman, C., Gelino, C. R., Kirkpatrick, J. D., et al. 2014, ApJ, 783, 68

Béjar, V. J. S., Zapatero Osorio, M. R., Pérez Garrido, A., et al. 2008, ApJL, 673, L185

Bell, C. P. M., Mamajek, E. E., & Naylor, T. 2015, MNRAS, 454, 593

Bernard, E. J., Ferguson, A. M. N., Schlafly, E. F., et al. 2014, MNRAS, 442, 2999

Bertin, E. 2006, in ASP Conf. Ser., 351, Astronomical Data Analysis Software and Systems XV, ed. C. Gabriel, C. Arviset, D. Ponz, & E. Solano, San Francisco, CA, 112

Bertin, E., & Arnouts, S. 1996, A&AS, 117, 393

Bessell, M. S. 1991, AJ, 101, 662

Best, W. M. J., Liu, M. C., Dupuy, T. J., & Magnier, E. A. 2017a, ApJL, 843, L4

Best, W. M. J., Liu, M. C., Magnier, E. A., et al. 2013, ApJ, 777, 84

—. 2015, ApJ, 814, 118

—. 2017b, ApJ, 837, 95

Best, W. M. J., Magnier, E. A., Liu, M. C., et al. 2018, ApJS, 234, 1

Bihain, G., Rebolo, R., Béjar, V. J. S., et al. 2006, A&A, 458, 805

Bihain, G., Rebolo, R., Zapatero Osorio, M. R., Béjar, V. J. S., & Caballero, J. A. 2010, A&A, 519, 93

Bihain, G., Scholz, R.-D., Storm, J., & Schnurr, O. 2013, A&A, 557, 43

Blake, C. H., Charbonneau, D., White, R. J., et al. 2008, ApJ, 678, L125

Boccaletti, A., Chauvin, G., Lagrange, A. M., & Marchis, F. 2003, A&A, 410, 283

Bochanski, J. J., Hawley, S. L., Covey, K. R., et al. 2010, AJ, 139, 2679

Boeshaar, P. C. 1976, PhD thesis, Ph.D. thesis, Ohio State University, Ohio State University, Columbus.

Boss, A. P. 1997, Science, 276, 1836

Boudreault, S., & Lodieu, N. 2013, MNRAS, 434, 142

Bouvier, J., Kendall, T., Meeus, G., et al. 2008, A&A, 481, 661

Bouy, H., Brandner, W., Martín, E. L., et al. 2003, AJ, 126, 1526

Bouy, H., Martín, E. L., Brandner, W., & Bouvier, J. 2005, AJ, 129, 511

Bouy, H., Duchêne, G., Köhler, R., et al. 2004, A&A, 423, 341

Bouy, H., Bertin, E., Sarro, L. M., et al. 2015, A&A, 577, A148

Bowler, B. P., & Hillenbrand, L. A. 2015, ApJL, 811, L30

Bowler, B. P., Liu, M. C., & Dupuy, T. J. 2010, ApJ, 710, 45

Bowler, B. P., Liu, M. C., Kraus, A. L., & Mann, A. W. 2014, ApJ, 784, 65

Bowler, B. P., Liu, M. C., Kraus, A. L., Mann, A. W., & Ireland, M. J. 2011, ApJ, 743, 148

Bryja, C., Humphreys, R. M., & Jones, T. J. 1994, AJ, 107, 246

Bryja, C., Jones, T. J., Humphreys, R. M., et al. 1992, ApJL, 388, L23

Buenzli, E., Apai, D., Morley, C. V., et al. 2012, ApJL, 760, L31

Burgasser, A. J. 2004a, ApJS, 155, 191

—. 2004b, ApJL, 614, L73

—. 2007a, ApJ, 659, 655

—. 2007b, AJ, 134, 1330

Burgasser, A. J., Cruz, K. L., Cushing, M. C., et al. 2010a, ApJ, 710, 1142

Burgasser, A. J., Cruz, K. L., & Kirkpatrick, J. D. 2007, ApJ, 657, 494

Burgasser, A. J., Dhital, S., & West, A. A. 2009a, AJ, 138, 1563

Burgasser, A. J., Geballe, T. R., Leggett, S. K., Kirkpatrick, J. D., & Golimowski, D. A. 2006a, ApJ, 637, 1067

Burgasser, A. J., & Kirkpatrick, J. D. 2006, ApJ, 645, 1485

Burgasser, A. J., Kirkpatrick, J. D., Cruz, K. L., et al. 2006b, ApJS, 166, 585

Burgasser, A. J., Kirkpatrick, J. D., Liebert, J., & Burrows, A. S. 2003a, ApJ, 594, 510

Burgasser, A. J., Kirkpatrick, J. D., & Lowrance, P. J. 2005a, AJ, 129, 2849

Burgasser, A. J., Kirkpatrick, J. D., McElwain, M. W., et al. 2003b, AJ, 125, 850

Burgasser, A. J., Kirkpatrick, J. D., Reid, I. N., et al. 2003c, ApJ, 586, 512

Burgasser, A. J., Liu, M. C., Ireland, M. J., Cruz, K. L., & Dupuy, T. J. 2008a, ApJ, 681, 579

Burgasser, A. J., Looper, D. L., Kirkpatrick, J. D., Cruz, K. L., & Swift, B. J. 2008b, ApJ, 674, 451

Burgasser, A. J., Looper, D. L., & Rayner, J. T. 2010b, AJ, 139, 2448

Burgasser, A. J., Luk, C., Dhital, S., et al. 2012, ApJ, 757, 110

Burgasser, A. J., & McElwain, M. W. 2006, AJ, 131, 1007

Burgasser, A. J., McElwain, M. W., & Kirkpatrick, J. D. 2003d, AJ, 126, 2487

Burgasser, A. J., McElwain, M. W., Kirkpatrick, J. D., et al. 2004, AJ, 127, 2856

Burgasser, A. J., Reid, I. N., Leggett, S. K., et al. 2005b, ApJL, 634, L177

Burgasser, A. J., Sitarski, B. N., Gelino, C. R., Logsdon, S. E., & Perrin, M. D. 2011a, ApJ, 739, 49

Burgasser, A. J., Tinney, C. G., Cushing, M. C., et al. 2008c, ApJL, 689, L53

Burgasser, A. J., Witte, S., Helling, C., et al. 2009b, ApJ, 697, 148

Burgasser, A. J., Kirkpatrick, J. D., Brown, M. E., et al. 1999, ApJ, 522, L65

Burgasser, A. J., Kirkpatrick, J. D., Cutri, R. M., et al. 2000a, ApJ, 531, L57

Burgasser, A. J., Wilson, J. C., Kirkpatrick, J. D., et al. 2000b, AJ, 120, 1100

Burgasser, A. J., Kirkpatrick, J. D., Brown, M. E., et al. 2002, ApJ, 564, 421

Burgasser, A. J., Kirkpatrick, J. D., Burrows, A. S., et al. 2003e, ApJ, 592, 1186

Burgasser, A. J., Cushing, M. C., Kirkpatrick, J. D., et al. 2011b, ApJ, 735, 116

Burgasser, A. J., Gillon, M., Faherty, J. K., et al. 2014, ApJ, 785, 48

Burgasser, A. J., Gillon, M., Melis, C., et al. 2015a, AJ, 149, 104

Burgasser, A. J., Logsdon, S. E., Gagné, J., et al. 2015b, ApJS, 220, 18

Burgasser, A. J., Lopez, M. A., Mamajek, E. E., et al. 2016, ApJ, 820, 32

Burningham, B., Pinfield, D. J., Lucas, P. W., et al. 2010a, MNRAS, 406, 1885

Burningham, B., Leggett, S. K., Lucas, P. W., et al. 2010b, MNRAS, 404, 1952

Burningham, B., Lucas, P. W., Leggett, S. K., et al. 2011, MNRASL, 414, L90

Burningham, B., Cardoso, C. V., Smith, L., et al. 2013, MNRAS, 433, 457

Burrows, A. S., Hubbard, W. B., Lunine, J. I., & Liebert, J. 2001, Rev Mod Phys, 73, 719

Burrows, A. S., Sudarsky, D., & Hubeny, I. 2006, ApJ, 640, 1063

Burrows, A. S., Marley, M. S., Hubbard, W. B., et al. 1997, ApJ, 491, 856

Caballero, J. A. 2007, ApJ, 667, 520

Cardoso, C. V., Burningham, B., Smart, R. L., et al. 2015, MNRAS, 450, 2486

Carrasco, J. M., Evans, D. W., Montegriffo, P., et al. 2016, A&A, 595, A7

Casali, M., Adamson, A., Alves de Oliveira, C., et al. 2007, A&A, 467, 777

Casewell, S. L., Jameson, R. F., & Burleigh, M. R. 2008, MNRAS, 390, 1517

Castro, P. J., & Gizis, J. E. 2012, ApJ, 746, 3

—. 2016, ApJ, 816, 78

Castro, P. J., Gizis, J. E., Harris, H. C., et al. 2013, ApJ, 776, 126

Chabrier, G. 2003, PASP, 115, 763

—. 2005, The Initial Mass Function 50 years later. Edited by E. Corbelli and F. Palle, 327, 41

Chabrier, G., Baraffe, I., Allard, F., & Hauschildt, P. 2000, ApJ, 542, 464

Chabrier, G., Johansen, A., Janson, M., & Rafikov, R. 2014, in Protostars and Planets VI, ed. H. Beuther, R. Klessen, C. P. Dullemond, & T. Henning, University of Arizona Press, Tucson, 619–642

Chambers, K. C., Magnier, E. A., Metcalfe, N., et al. 2018, in preparation, arXiv:1612.05560

Chiu, K., Fan, X., Leggett, S. K., et al. 2006, AJ, 131, 2722

Chiu, K., Liu, M. C., Jiang, L., et al. 2008, MNRASL, 385, L53

Close, L. M., Potter, D., Brandner, W., et al. 2002a, ApJ, 566, 1095

Close, L. M., Siegler, N., Freed, M., & Biller, B. A. 2003, ApJ, 587, 407

Close, L. M., Siegler, N., Potter, D., Brandner, W., & Liebert, J. 2002b, ApJL, 567, L53

Cohen, M., Wheaton, W. A., & Megeath, S. T. 2003, AJ, 126, 1090

Costa, E., Méndez, R. A., Jao, W. C., et al. 2005, AJ, 130, 337

—. 2006, AJ, 132, 1234

Crifo, F., Phan-Bao, N., Delfosse, X., et al. 2005, A&A, 441, 653

Cross, N. J. G., Collins, R. S., Mann, R. G., et al. 2012, A&A, 548, 119

Cruz, K. L., Burgasser, A. J., Reid, I. N., & Liebert, J. 2004, ApJL, 604, L61

Cruz, K. L., Kirkpatrick, J. D., & Burgasser, A. J. 2009, AJ, 137, 3345

Cruz, K. L., Núñez, A., Burgasser, A. J., et al. 2018, AJ, 155, 34

Cruz, K. L., & Reid, I. N. 2002, AJ, 123, 2828

Cruz, K. L., Reid, I. N., Liebert, J., Kirkpatrick, J. D., & Lowrance, P. J. 2003, AJ, 126, 2421

Cruz, K. L., Reid, I. N., Kirkpatrick, J. D., et al. 2007, AJ, 133, 439

Cushing, M. C., Kirkpatrick, J. D., Gelino, C. R., et al. 2014, AJ, 147, 113

Cushing, M. C., Rayner, J. T., & Vacca, W. D. 2005, ApJ, 623, 1115

Cushing, M. C., & Vacca, W. D. 2006, AJ, 131, 1797

Cushing, M. C., Vacca, W. D., & Rayner, J. T. 2004, PASP, 116, 362

Cushing, M. C., Marley, M. S., Saumon, D., et al. 2008, ApJ, 678, 1372

Cushing, M. C., Kirkpatrick, J. D., Gelino, C. R., et al. 2011, ApJ, 743, 50

Cutri, R. M., Skrutskie, M. F., Van Dyk, S., et al. 2003, yCat, II/246, 0

—. 2006, Explanatory Supplement to the 2MASS All Sky Data Release (IPAC/California Institute of Technology)

Cutri, R. M., Wright, E. L., Conrow, T., et al. 2012, yCat, II/311, 0

—. 2014, yCat, II/328, 0

Daemgen, S., Bonavita, M., Jayawardhana, R., Lafreniere, D., & Janson, M. 2015, ApJ, 799, 155

Dahn, C. C., Liebert, J., & Harrington, R. S. 1986, AJ, 91, 621

Dahn, C. C., Harris, H. C., Vrba, F. J., et al. 2002, AJ, 124, 1170

Dahn, C. C., Harris, H. C., Levine, S. E., et al. 2008, ApJ, 686, 548

Danilov, V. M., & Loktin, A. V. 2015, Astrophysical Bulletin, 70, 414

Davenport, J. R. A., Ivezić, Ž., Becker, A. C., et al. 2014, MNRAS, 440, 3430

Dawson, P., Scholz, A., & Ray, T. P. 2011, MNRAS, 418, 1231

Dawson, P., Scholz, A., Ray, T. P., et al. 2013, MNRAS, 429, 903

—. 2014, MNRAS, 442, 1586

Day-Jones, A. C., Marocco, F., Pinfield, D. J., et al. 2013, MNRAS, 430, 1171

de Bruijne, J. H. J. 1999, MNRAS, 310, 585

de Zeeuw, P. T., Hoogerwerf, R., de Bruijne, J. H. J., Brown, A. G. A., & Blaauw, A. 1999, AJ, 117, 354

Deacon, N. R., & Hambly, N. C. 2006, MNRAS, 371, 1722

—. 2007, A&A, 468, 163

Deacon, N. R., Hambly, N. C., & Cooke, J. A. 2005, A&A, 435, 363

Deacon, N. R., Hambly, N. C., King, R. R., & McCaughrean, M. J. 2009, MNRAS, 394, 857

Deacon, N. R., Liu, M. C., Magnier, E. A., et al. 2011, AJ, 142, 77

—. 2012a, ApJ, 755, 94

—. 2012b, ApJ, 757, 100

—. 2014, ApJ, 792, 119

Deacon, N. R., Kraus, A. L., Mann, A. W., et al. 2016, MNRAS, 455, 4212

Deacon, N. R., Magnier, E. A., Best, W. M. J., et al. 2017a, MNRAS, 468, 3499

Deacon, N. R., Magnier, E. A., Liu, M. C., et al. 2017b, MNRAS, 467, 1126

Delfosse, X., Tinney, C. G., Forveille, T., et al. 1999, A&AS, 135, 41

—. 1997, A&A, 327, L25

Delorme, P., Willott, C. J., Forveille, T., et al. 2008, A&A, 484, 469

Dhital, S., West, A. A., Stassun, K. G., & Bochanski, J. J. 2010, AJ, 139, 2566

Dieterich, S. B., Henry, T. J., Jao, W.-C., et al. 2014, AJ, 147, 94

Diolaiti, E., Bendinelli, O., Bonaccini, D., et al. 2000, A&AS, 147, 335

Dittmann, J. A., Irwin, J. M., Charbonneau, D., & Berta-Thompson, Z. K. 2014, ApJ, 784, 156

Dobbie, P. D., Kenyon, F., Jameson, R. F., et al. 2002, MNRAS, 329, 543

Duchêne, G., & Kraus, A. 2013, ARAA, 51, 269

Ducourant, C., Teixeira, R., Périé, J. P., et al. 2005, A&A, 438, 769

Dupuy, T. J., Forbrich, J., Rizzuto, A., et al. 2016, ApJ, 827, 23

Dupuy, T. J., & Kraus, A. L. 2013, Science, 341, 1492

Dupuy, T. J., & Liu, M. C. 2011, ApJ, 733, 122

—. 2012, ApJS, 201, 19

—. 2017, ApJS, 231, 15

Dupuy, T. J., Liu, M. C., & Bowler, B. P. 2009a, ApJ, 706, 328

Dupuy, T. J., Liu, M. C., Bowler, B. P., et al. 2010, ApJ, 721, 1725

Dupuy, T. J., Liu, M. C., & Ireland, M. J. 2009b, ApJ, 699, 168

—. 2009c, ApJ, 692, 729

—. 2014, ApJ, 790, 133

Dupuy, T. J., Liu, M. C., & Leggett, S. K. 2015a, ApJ, 803, 102

Dupuy, T. J., Liu, M. C., Leggett, S. K., et al. 2015b, ApJ, 805, 56

Dye, S., Lawrence, A., Read, M. A., et al. 2018, MNRAS, 473, 5113

Eddington, A. S. 1913, MNRAS, 73, 359

Enoch, M. L., Brown, M. E., & Burgasser, A. J. 2003, AJ, 126, 1006

Epchtein, N., Deul, E., Derriere, S., et al. 1999, A&A, 349, 236

Esplin, T. L., Luhman, K. L., & Mamajek, E. E. 2014, ApJ, 784, 126

Faherty, J. K., Burgasser, A. J., Cruz, K. L., et al. 2009, AJ, 137, 1

Faherty, J. K., Burgasser, A. J., West, A. A., et al. 2010, AJ, 139, 176

Faherty, J. K., Rice, E. L., Cruz, K. L., Mamajek, E. E., & Núñez, A. 2013, AJ, 145, 2

Faherty, J. K., Burgasser, A. J., Walter, F. M., et al. 2012, ApJ, 752, 56

Faherty, J. K., Riedel, A. R., Cruz, K. L., et al. 2016, ApJS, 225, 10

Fan, X., Knapp, G. R., Strauss, M. A., et al. 2000, AJ, 119, 928

Festin, L. 1998, MNRAS, 298, L34

Finch, C. T., & Zacharias, N. 2016, AJ, 151, 160

Folkes, S. L., Pinfield, D. J., Jones, H. R. A., et al. 2012, MNRAS, 427, 3280

Fontanive, C., Biller, B. A., Bonavita, M., & Allers, K. N. 2018, MNRAS, 479, 2702

Forbrich, J., Dupuy, T. J., Reid, M. J., et al. 2016, ApJ, 827, 22

Forveille, T., Beuzit, J. L., Delorme, P., et al. 2005, A&A, 435, L5

Freed, M., Close, L. M., & Siegler, N. 2003, ApJ, 584, 453

Gagné, J., Burgasser, A. J., Faherty, J. K., et al. 2015a, ApJL, 808, L20

Gagné, J., Lafreniere, D., Doyon, R., et al. 2014a, ApJL, 792, L17

Gagné, J., Lafreniere, D., Doyon, R., Malo, L., & Artigau, E. 2014b, ApJ, 783, 121

—. 2015b, ApJ, 798, 73

Gagné, J., Faherty, J. K., Cruz, K. L., et al. 2015c, ApJS, 219, 33

Gagné, J., Faherty, J. K., Mamajek, E. E., et al. 2017, ApJS, 228, 18

Gaia Collaboration, Prusti, T., de Bruijne, J. H. J., et al. 2016a, A&A, 595, A1

Gaia Collaboration, Brown, A. G. A., Vallenari, A., et al. 2016b, A&A, 595, A2

—. 2018, A&A, 616, A1

Gatewood, G., & Coban, L. 2009, AJ, 137, 402

Gauza, B., Bejar, V. J. S., Pérez Garrido, A., et al. 2015, ApJ, 804, 96

Gauza, B., Béjar, V. J. S., Rebolo, R., et al. 2012, MNRAS, 427, 2457

Gawroński, M. P., Goździewski, K., & Katarzyński, K. 2017, MNRAS, 466, 4211

Geballe, T. R., Knapp, G. R., Leggett, S. K., et al. 2002, ApJ, 564, 466

Geißler, K., Metchev, S. A., Kirkpatrick, J. D., Berriman, G. B., & Looper, D. L. 2011, ApJ, 732, 56

Gelino, C. R., Kirkpatrick, J. D., Cushing, M. C., et al. 2011, AJ, 142, 57

Gelino, C. R., Smart, R. L., Marocco, F., et al. 2014, AJ, 148, 6

Giampapa, M. S., & Liebert, J. 1986, ApJ, 305, 784

Giclas, H. L., Burnham, R., & Thomas, N. G. 1967, Bulletin / Lowell Observatory ; no. 138, 7

Gillon, M., Jehin, E., Lederer, S. M., et al. 2016, Nature, 533, 221

Gilmore, G., Reid, I. N., & Hewett, P. 1985, MNRAS, 213, 257

Girard, T. M., van Altena, W. F., Zacharias, N., et al. 2011, AJ, 142, 15

Gizis, J. E. 1997, AJ, 113, 806

—. 2002, ApJ, 575, 484

Gizis, J. E., Allers, K. N., Liu, M. C., et al. 2015a, ApJ, 799, 203

Gizis, J. E., Burgasser, A. J., Berger, E., et al. 2013, ApJ, 779, 172

Gizis, J. E., Burgasser, A. J., Faherty, J. K., Castro, P. J., & Shara, M. M. 2011a, AJ, 142, 171

Gizis, J. E., Burgasser, A. J., & Vrba, F. J. 2015b, AJ, 150, 179

Gizis, J. E., Kirkpatrick, J. D., & Wilson, J. C. 2001, AJ, 121, 2185

Gizis, J. E., Monet, D. G., Reid, I. N., Kirkpatrick, J. D., & Burgasser, A. J. 2000a, MNRAS, 311, 385

Gizis, J. E., Monet, D. G., Reid, I. N., et al. 2000b, AJ, 120, 1085

Gizis, J. E., & Reid, I. N. 1997, PASP, 109, 849

Gizis, J. E., Reid, I. N., & Hawley, S. L. 2002, AJ, 123, 3356

Gizis, J. E., Reid, I. N., Knapp, G. R., et al. 2003, AJ, 125, 3302

Gizis, J. E., Troup, N. W., & Burgasser, A. J. 2011b, ApJL, 736, L34

Gizis, J. E., Faherty, J. K., Liu, M. C., et al. 2012, AJ, 144, 94

Gliese, W. 1957, Astron. Rechen-Institut, 8, 1

Gliese, W., & Jahreiss, H. 1991, On: The Astronomical Data Center CD-ROM: Selected Astronomical Catalogs

—. 1995, VizieR On-line Data Catalog: V/70A. Originally published in: Astron. Rechen-Institut, 5070, 0

Goldman, B., Marsat, S., Henning, T., Clemens, C., & Greiner, J. 2010, MNRAS, 405, 1140

Goldman, B., Cushing, M. C., Marley, M. S., et al. 2008, A&A, 487, 277

Goldman, B., Röser, S., Schilbach, E., et al. 2013, A&A, 559, A43

Golimowski, D. A., Leggett, S. K., Marley, M. S., et al. 2004, AJ, 127, 3516

Gomes, J. I., Pinfield, D. J., Marocco, F., et al. 2013, MNRAS, 431, 2745

Goto, M., Kobayashi, N., Terada, H., et al. 2002, ApJ, 567, L59

Gray, R. O., Corbally, C. J., Garrison, R. F., McFadden, M. T., & Robinson, P. E. 2003, AJ, 126, 2048

Green, G. M., Schlafly, E. F., Finkbeiner, D. P., et al. 2014, ApJ, 783, 114

Guieu, S., Dougados, C., Monin, J.-L., Magnier, E. A., & Martín, E. L. 2006, A&A, 446, 485

Hall, P. B. 2002, ApJL, 564, L89

Hambly, N. C., MacGillivray, H. T., Read, M. A., et al. 2001, MNRAS, 326, 1279

Hambly, N. C., Collins, R. S., Cross, N. J. G., et al. 2008, MNRAS, 384, 637

Harrington, R. S., Dahn, C. C., Kallarakal, V. V., et al. 1993, AJ, 105, 1571

Hawley, S. L., Covey, K. R., Knapp, G. R., et al. 2002, AJ, 123, 3409

Henry, T. J., Jao, W.-C., Subasavage, J. P., et al. 2006, AJ, 132, 2360

Henry, T. J., & Kirkpatrick, J. D. 1990, ApJL, 354, L29

Henry, T. J., Subasavage, J. P., Brown, M. A., et al. 2004, AJ, 128, 2460

Henry, T. J., Jao, W.-C., Winters, J. G., et al. 2018, AJ, 155, 265

Hewett, P. C., Warren, S. J., Leggett, S. K., & Hodgkin, S. T. 2006, MNRAS, 367, 454

Hodgkin, S. T., Irwin, M. J., Hewett, P. C., & Warren, S. J. 2009, MNRAS, 394, 675

Høg, E., Fabricius, C., Makarov, V. V., et al. 2000, A&A, 355, L27

Hogan, E., Jameson, R. F., Casewell, S. L., Osbourne, S. L., & Hambly, N. C. 2008, MNRAS, 388, 495

Huelamo, N., Ivanov, V. D., Kurtev, R., et al. 2015, A&A, 578, A1

Irwin, M., McMahon, R. G., & Reid, I. N. 1991, MNRAS, 252, 61P

Irwin, M. J., Lewis, J., Hodgkin, S., et al. 2004, Proc SPIE, 5493, 411

Ivezić, Ž., Tyson, J. A., Abel, B., et al. 2008, arXiv.org, 0805.2366v4

Jameson, R. F., Casewell, S. L., Bannister, N. P., et al. 2008, MNRAS, 384, 1399

Kaiser, N., Burgett, W., Chambers, K. C., et al. 2010, Proc SPIE, 7733, 77330E

Kellogg, K., Metchev, S. A., Gagné, J., & Faherty, J. 2016, ApJL, 821, L15

Kellogg, K., Metchev, S. A., Geißler, K., et al. 2015, AJ, 150, 182

Kendall, T. R., Delfosse, X., Martín, E. L., & Forveille, T. 2004, A&A, 416, L17

Kendall, T. R., Jones, H. R. A., Pinfield, D. J., et al. 2007a, MNRAS, 374, 445

Kendall, T. R., Mauron, N., Azzopardi, M., & Gigoyan, K. 2003, A&A, 403, 929

Kendall, T. R., Tamura, M., Tinney, C. G., et al. 2007b, A&A, 466, 1059

Kenyon, S. J., Gómez, M., & Whitney, B. A. 2008, in Handbook of Star Forming Regions: Vol. I, The Northern Sky, ed. B. Reipurth (San Francisco: ASP Mongraph Publications), 405

Khandrika, H., Burgasser, A. J., Melis, C., et al. 2013, AJ, 145, 71

Kirkpatrick, J. D. 2005, ARAA, 43, 195

Kirkpatrick, J. D., Barman, T. S., Burgasser, A. J., et al. 2006, ApJ, 639, 1120

Kirkpatrick, J. D., Beichman, C. A., & Skrutskie, M. F. 1997a, ApJ, 476, 311

Kirkpatrick, J. D., Dahn, C. C., Monet, D. G., et al. 2001a, AJ, 121, 3235

Kirkpatrick, J. D., Henry, T. J., & Irwin, M. J. 1997b, AJ, 113, 1421

Kirkpatrick, J. D., Henry, T. J., & Liebert, J. 1993, ApJ, 406, 701

Kirkpatrick, J. D., Henry, T. J., & McCarthy, D. W. J. 1991, ApJS, 77, 417

Kirkpatrick, J. D., Henry, T. J., & Simons, D. A. 1995, AJ, 109, 797

Kirkpatrick, J. D., Liebert, J., Cruz, K. L., Gizis, J. E., & Reid, I. N. 2001b, PASP, 113, 814

Kirkpatrick, J. D., McGraw, J. T., Hess, T. R., Liebert, J., & McCarthy, D. W. J. 1994, ApJS, 94, 749

Kirkpatrick, J. D., Reid, I. N., Liebert, J., et al. 1999, ApJ, 519, 802

—. 2000, AJ, 120, 447

Kirkpatrick, J. D., Cruz, K. L., Barman, T. S., et al. 2008, ApJ, 689, 1295

Kirkpatrick, J. D., Looper, D. L., Burgasser, A. J., et al. 2010, ApJS, 190, 100

Kirkpatrick, J. D., Cushing, M. C., Gelino, C. R., et al. 2011, ApJS, 197, 19

Kirkpatrick, J. D., Gelino, C. R., Cushing, M. C., et al. 2012, ApJ, 753, 156

Kirkpatrick, J. D., Schneider, A. C., Fajardo-Acosta, S., et al. 2014, ApJ, 783, 122

Kirkpatrick, J. D., Kellogg, K., Schneider, A. C., et al. 2016, ApJS, 224, 36

Knapp, G. R., Leggett, S. K., Fan, X., et al. 2004, AJ, 127, 3553

Koen, C. 2013, MNRAS, 428, 2824

Koen, C., Tanabé, T., Tamura, M., & Kusakabe, N. 2005, MNRAS, 362, 727

Koerner, D. W., Kirkpatrick, J. D., McElwain, M. W., & Bonaventura, N. R. 1999, ApJL, 526, L25

Konopacky, Q. M., Ghez, A. M., Barman, T. S., et al. 2010, ApJ, 711, 1087

Kouwenhoven, M. B. N., Goodwin, S. P., Parker, R. J., et al. 2010, MNRAS, 404, 1835

Kraus, A. L., & Hillenbrand, L. A. 2009a, ApJ, 704, 531

—. 2009b, ApJ, 703, 1511

Kroupa, P., Tout, C. A., & Gilmore, G. 1993, MNRAS, 262, 545

Lachapelle, F.-R., Lafreniere, D., Gagné, J., et al. 2015, ApJ, 802, 61

Lafreniere, D., Jayawardhana, R., & van Kerkwijk, M. H. 2008, ApJ, 689, L153

Law, N. M., Hodgkin, S. T., & Mackay, C. D. 2006, MNRAS, 368, 1917

Lawrence, A., Warren, S. J., Almaini, O., et al. 2007, MNRAS, 379, 1599

—. 2012, yCat, II/314, 0

—. 2013, yCat, II/319, 0

Leggett, S. K. 1992, ApJS, 82, 351

Leggett, S. K., Allard, F., Berriman, G., Dahn, C. C., & Hauschildt, P. H. 1996, ApJS, 104, 117

Leggett, S. K., Hauschildt, P. H., Allard, F., Geballe, T. R., & Baron, E. 2002a, MNRAS, 332, 78

Leggett, S. K., Morley, C. V., Marley, M. S., & Saumon, D. 2015, ApJ, 799, 37

Leggett, S. K., Tremblin, P., Esplin, T. L., Luhman, K. L., & Morley, C. V. 2017, ApJ, 842, 118

Leggett, S. K., Geballe, T. R., Fan, X., et al. 2000, ApJL, 536, L35

Leggett, S. K., Golimowski, D. A., Fan, X., et al. 2002b, ApJ, 564, 452

Leggett, S. K., Cushing, M. C., Saumon, D., et al. 2009, ApJ, 695, 1517

Leggett, S. K., Burningham, B., Saumon, D., et al. 2010, ApJ, 710, 1627

Leggett, S. K., Saumon, D., Marley, M. S., et al. 2012, ApJ, 748, 74

Leinert, C., Weitzel, N., Richichi, A., Eckart, A., & Tacconi-Garman, L. E. 1994, A&A, 291, L47

Lépine, S. 2005, AJ, 130, 1680

Lépine, S., & Bongiorno, B. 2007, AJ, 133, 889

Lépine, S., & Gaidos, E. 2011, AJ, 142, 138

Lépine, S., Rich, R. M., Neill, J. D., Caulet, A., & Shara, M. M. 2002a, ApJL, 581, L47

Lépine, S., Rich, R. M., & Shara, M. M. 2003a, ApJL, 591, L49

—. 2003b, AJ, 125, 1598

Lépine, S., & Shara, M. M. 2005, AJ, 129, 1483

Lépine, S., Shara, M. M., & Rich, R. M. 2002b, AJ, 124, 1190

—. 2003c, ApJL, 585, L69

Lépine, S., Thorstensen, J. R., Shara, M. M., & Rich, R. M. 2009, AJ, 137, 4109

Liebert, J., Dahn, C. C., Gresham, M., & Strittmatter, P. A. 1979, ApJ, 233, 226

Liebert, J., & Gizis, J. E. 2006, PASP, 118, 659

Liebert, J., Kirkpatrick, J. D., Cruz, K. L., et al. 2003, AJ, 125, 343

Limoges, M. M., Lépine, S., & Bergeron, P. 2013, AJ, 145, 136

Lindegren, L., Lammers, U., Bastian, U., et al. 2016, A&A, 595, A4

Lindegren, L., Hernández, J., Bombrun, A., et al. 2018, A&A, 616, A2

Liu, M. C., Dupuy, T. J., & Allers, K. N. 2016, ApJ, 833, 96

Liu, M. C., Dupuy, T. J., Bowler, B. P., Leggett, S. K., & Best, W. M. J. 2012, ApJ, 758, 57

Liu, M. C., Dupuy, T. J., & Ireland, M. J. 2008, ApJ, 689, 436

Liu, M. C., Dupuy, T. J., & Leggett, S. K. 2010, ApJ, 722, 311

Liu, M. C., Fischer, D. A., Graham, J. R., et al. 2002a, ApJ, 571, 519

Liu, M. C., & Leggett, S. K. 2005, ApJ, 634, 616

Liu, M. C., Leggett, S. K., Golimowski, D. A., et al. 2006, ApJ, 647, 1393

Liu, M. C., Wainscoat, R. J., Martín, E. L., Barris, B., & Tonry, J. L. 2002b, ApJL, 568, L107

Liu, M. C., Delorme, P., Dupuy, T. J., et al. 2011a, ApJ, 740, 108

Liu, M. C., Deacon, N. R., Magnier, E. A., et al. 2011b, ApJL, 740, L32

Liu, M. C., Magnier, E. A., Deacon, N. R., et al. 2013, ApJL, 777, L20

Lodieu, N. 2013, MNRAS, 431, 3222

Lodieu, N., Boudreault, S., & Béjar, V. J. S. 2014, MNRAS, 445, 3908

Lodieu, N., Deacon, N. R., & Hambly, N. C. 2012a, MNRAS, 422, 1495

Lodieu, N., Dobbie, P. D., Cross, N. J. G., et al. 2013, MNRAS, 435, 2474

Lodieu, N., Dobbie, P. D., & Hambly, N. C. 2011, A&A, 527, 24

Lodieu, N., Espinoza Contreras, M., Zapatero Osorio, M. R., et al. 2012b, A&A, 542, 105

Lodieu, N., Hambly, N. C., & Jameson, R. F. 2006, MNRAS, 373, 95

Lodieu, N., Hambly, N. C., Jameson, R. F., & Hodgkin, S. T. 2008, MNRAS, 383, 1385

Lodieu, N., Hambly, N. C., Jameson, R. F., et al. 2007a, MNRAS, 374, 372

Lodieu, N., Scholz, R.-D., & McCaughrean, M. J. 2002, A&A, 389, L20

Lodieu, N., Scholz, R.-D., McCaughrean, M. J., et al. 2005, A&A, 440, 1061

Lodieu, N., Zapatero Osorio, M. R., Martín, E. L., Solano, E., & Aberasturi, M. 2010, ApJL, 708, L107

Lodieu, N., Zapatero Osorio, M. R., Rebolo, R., Martín, E. L., & Hambly, N. C. 2009, A&A, 505, 1115

Lodieu, N., Pinfield, D. J., Leggett, S. K., et al. 2007b, MNRAS, 379, 1423

Lodieu, N., Burningham, B., Day-Jones, A. C., et al. 2012c, A&A, 548, 53

Looper, D. L. 2011, PhD thesis, ProQuest Dissertations and Theses, AAT 3572607, University of Hawai'i at Manoa

Looper, D. L., Gelino, C. R., Burgasser, A. J., & Kirkpatrick, J. D. 2008a, ApJ, 685, 1183

Looper, D. L., Kirkpatrick, J. D., & Burgasser, A. J. 2007, AJ, 134, 1162

Looper, D. L., Kirkpatrick, J. D., Cutri, R. M., et al. 2008b, ApJ, 686, 528

Loutrel, N. P., Luhman, K. L., Lowrance, P. J., & Bochanski, J. J. 2011, ApJ, 739, 81

Lucas, P. W., Tinney, C. G., Burningham, B., et al. 2010, MNRASL, 408, L56

Lucas, P. W., Hoare, M. G., Longmore, A., et al. 2012, yCat, II/316, 0

Luhman, K. L. 2004, ApJ, 617, 1216

—. 2006, ApJ, 645, 676

—. 2013, ApJL, 767, L1

—. 2014, ApJL, 786, L18

Luhman, K. L., Burgasser, A. J., & Bochanski, J. J. 2011, ApJL, 730, L9

Luhman, K. L., & Mamajek, E. E. 2012, ApJ, 758, 31

Luhman, K. L., Mamajek, E. E., Allen, P. R., & Cruz, K. L. 2009, ApJ, 703, 399

Luhman, K. L., & Sheppard, S. S. 2014, ApJ, 787, 126

Luhman, K. L., Stauffer, J. R., Muench, A. A., et al. 2003, ApJ, 593, 1093

Luhman, K. L., Wilson, J. C., Brandner, W., et al. 2006, ApJ, 649, 894

Luhman, K. L., Patten, B. M., Marengo, M., et al. 2007, ApJ, 654, 570

Luhman, K. L., Allen, L. E., Allen, P. R., et al. 2008, ApJ, 675, 1375

Luhman, K. L., Loutrel, N. P., McCurdy, N. S., et al. 2012, ApJ, 760, 152

Lutz, T. E., & Kelker, D. H. 1973, PASP, 85, 573

Luyten, W. J. 1979, A Catalogue of Stars with Proper Motions Exceeding 0.2" Annually (NLTT Catalogue) (Minneapolis: Univ. Minnesota)

Mace, G. N. 2014, PhD thesis, ProQuest Dissertations and Theses, AAT 3621230, University of California, Los Angeles

Mace, G. N., Kirkpatrick, J. D., Cushing, M. C., et al. 2013a, ApJS, 205, 6

—. 2013b, ApJ, 777, 36

Magnier, E. A. 2006, in The Advanced Maui Optical and Space Surveillance Technologies Conference, ed. S. Ryan, Red Hook, NY: Curran Associates, 455

Magnier, E. A. 2007, in ASP Conf. Ser., 364, The Future of Photometric, Spectrophotometric and Polarimetric Standardization, ed. C. Sterken, San Francisco, CA, 153

Magnier, E. A., Liu, M. C., Monet, D. G., & Chambers, K. C. 2008, in IAU Symp. 248, A Giant Step: From Milli- to Micro-arcsecond Astrometry, ed. W. J. Jin, I. Platais, & M. A. C. Perryman, Cambridge: Cambridge Univ. Press, 553–559

Magnier, E. A., Schlafly, E., Finkbeiner, D., et al. 2013, ApJS, 205, 20

Magnier, E. A., Schlafly, E. F., Finkbeiner, D. P., et al. 2018, in preparation, arXiv:1612.05242

Makarov, V. V., & Urban, S. 2000, MNRAS, 317, 289

Malo, L., Doyon, R., Lafreniere, D., et al. 2013, ApJ, 762, 88

Manjavacas, E., Goldman, B., Reffert, S., & Henning, T. 2013, A&A, 560, 52

Marley, M. S., Saumon, D., Fortney, J. J., et al. 2017, AAS, 230, 315.07

Marley, M. S., Saumon, D., & Goldblatt, C. 2010, ApJL, 723, L117

Marocco, F., Smart, R. L., Jones, H. R. A., et al. 2010, A&A, 524, 38

Marocco, F., Andrei, A. H., Smart, R. L., et al. 2013, AJ, 146, 161

Marocco, F., Jones, H. R. A., Day-Jones, A. C., et al. 2015, MNRAS, 449, 3651

Marsh, K. A., Wright, E. L., Kirkpatrick, J. D., et al. 2013, ApJ, 762, 119

Marshall, J. L. 2008, AJ, 135, 1000

Martín, E. L., Basri, G., Gallegos, J. E., et al. 1998a, ApJL, 499, L61

Martín, E. L., Basri, G., Zapatero Osorio, M. R., Rebolo, R., & García López, R. J. 1998b, ApJL, 507, L41

Martín, E. L., Brandner, W., & Basri, G. 1999a, Science, 283, 1718

Martín, E. L., Brandner, W., Bouvier, J., et al. 2000, ApJ, 543, 299

Martín, E. L., Delfosse, X., Basri, G., et al. 1999b, AJ, 118, 2466

Martín, E. L., Delfosse, X., & Guieu, S. 2004, AJ, 127, 449

Martín, E. L., Rebolo, R., & Magazzu, A. 1994, ApJ, 436, 262

Martín, E. L., Rebolo, R., & Zapatero Osorio, M. R. 1996, ApJ, 469, 706

Martín, E. L., Phan-Bao, N., Bessell, M., et al. 2010, A&A, 517, 53

Mathews, G. S., Williams, J. P., Ménard, F., et al. 2012, ApJ, 745, 23

Matsuoka, Y., Peterson, B. A., Murata, K. L., et al. 2011, AJ, 142, 64

Maxted, P. F. L., & Jeffries, R. D. 2005, MNRASL, 362, L45

McCarthy, M. F., Bertiau, F. C., & Treanor, P. J. 1964, Ricerche Astronomiche, 6, 571

McCaughrean, M. J., Close, L. M., Scholz, R.-D., et al. 2004, A&A, 413, 1029

McCaughrean, M. J., Scholz, R.-D., & Lodieu, N. 2002, A&A, 390, L27

McElwain, M. W., & Burgasser, A. J. 2006, AJ, 132, 2074

McGovern, M. R., Kirkpatrick, J. D., McLean, I. S., et al. 2004, ApJ, 600, 1020

Melis, C., Reid, M. J., Mioduszewski, A. J., Stauffer, J. R., & Bower, G. C. 2014, Science, 345, 1029

Metchev, S. A., & Hillenbrand, L. A. 2006, ApJ, 651, 1166

Metchev, S. A., Kirkpatrick, J. D., Berriman, G. B., & Looper, D. L. 2008, ApJ, 676, 1281

Mohanty, S., & Basri, G. 2003, ApJ, 583, 451

Monet, D. G., Dahn, C. C., Vrba, F. J., et al. 1992, AJ, 103, 638

Monet, D. G., Levine, S. E., Canzian, B., et al. 2003, AJ, 125, 984

Montagnier, G., Ségransan, D., Beuzit, J. L., et al. 2006, A&A, 460, L19

Moraux, E., Bouvier, J., Stauffer, J. R., & Cuillandre, J. C. 2003, A&A, 400, 891

Mugrauer, M., Seifahrt, A., Neuhäuser, R., & Mazeh, T. 2006, MNRASL, 373, L31

Murphy, S. J., Lawson, W. A., & Bento, J. 2015, MNRAS, 453, 2220

Murray, D. N., Burningham, B., Jones, H. R. A., et al. 2011, MNRAS, 414, 575

Muzic, K., Radigan, J., Jayawardhana, R., et al. 2012, AJ, 144, 180

Nakajima, T., Oppenheimer, B. R., Kulkarni, S. R., et al. 1995, Nature, 378, 463

Naud, M.-E., Artigau, E., Malo, L., et al. 2014, ApJ, 787, 5

Noll, K. S., Geballe, T. R., Leggett, S. K., & Marley, M. S. 2000, ApJL, 541, L75

Pecaut, M. J., Mamajek, E. E., & Bubar, E. J. 2012, ApJ, 746, 154

Peña Ramírez, K., Zapatero Osorio, M. R., & Béjar, V. J. S. 2015, A&A, 574, A118

Phan-Bao, N. 2011, Astronomische Nachrichten, 332, 668

Phan-Bao, N., & Bessell, M. S. 2006, A&A, 446, 515

Phan-Bao, N., Guibert, J., Crifo, F., et al. 2001, A&A, 380, 590

Phan-Bao, N., Bessell, M. S., Martín, E. L., et al. 2006, MNRASL, 366, L40

—. 2008, MNRAS, 383, 831

Pineda, J. S., Hallinan, G., Kirkpatrick, J. D., et al. 2016, ApJ, 826, 73

Pinfield, D. J., Dobbie, P. D., Jameson, R. F., et al. 2003, MNRAS, 342, 1241

Pinfield, D. J., Burningham, B., Tamura, M., et al. 2008, MNRAS, 390, 304

Pinfield, D. J., Burningham, B., Lodieu, N., et al. 2012, MNRAS, 422, 1922

Pokorny, R. S., Jones, H. R. A., Hambly, N. C., & Pinfield, D. J. 2004, A&A, 421, 763

Potter, D., Martín, E. L., Cushing, M. C., et al. 2002, ApJ, 567, L133

Preibisch, T., & Mamajek, E. 2008, in Handbook of Star Forming Regions: Vol. II, The Southern Sky, ed. B. Reipurth (San Francisco: ASP Mongraph Publications), 235

Preibisch, T., & Zinnecker, H. 1999, AJ, 117, 2381

Probst, R. G., & Liebert, J. 1983, ApJ, 274, 245

Qi, Z., Yu, Y., Bucciarelli, B., et al. 2015, AJ, 150, 137

Quanz, S. P., Goldman, B., Henning, T., et al. 2010, ApJ, 708, 770

Radigan, J., Jayawardhana, R., Lafreniere, D., et al. 2012, ApJ, 750, 105

—. 2013, ApJ, 778, 36

Radigan, J., Lafreniere, D., Jayawardhana, R., & Artigau, E. 2014, ApJ, 793, 75

Radigan, J., Lafreniere, D., Jayawardhana, R., & Doyon, R. 2008, ApJ, 689, 471

Rayner, J. T., Cushing, M. C., & Vacca, W. D. 2009, ApJS, 185, 289

Rayner, J. T., Toomey, D. W., Onaka, P. M., et al. 2003, PASP, 115, 362

Rebolo, R., Zapatero Osorio, M. R., Madruga, S., et al. 1998, Science, 282, 1309

Rebull, L. M., Padgett, D. L., McCabe, C. E., et al. 2010, ApJS, 186, 259

Reid, I. N. 2003, AJ, 126, 2449

Reid, I. N., & Cruz, K. L. 2002, AJ, 123, 2806

Reid, I. N., Cruz, K. L., & Allen, P. R. 2007, AJ, 133, 2825

Reid, I. N., Cruz, K. L., Burgasser, A. J., & Liu, M. C. 2008a, AJ, 135, 580

Reid, I. N., Cruz, K. L., Kirkpatrick, J. D., et al. 2008b, AJ, 136, 1290

Reid, I. N., & Gilmore, G. 1981, MNRAS, 196, 15P

Reid, I. N., & Gizis, J. E. 2005, PASP, 117, 676

Reid, I. N., Gizis, J. E., & Hawley, S. L. 2002a, AJ, 124, 2721

Reid, I. N., Gizis, J. E., Kirkpatrick, J. D., & Koerner, D. W. 2001, AJ, 121, 489

Reid, I. N., Hawley, S. L., & Gizis, J. E. 1995, AJ, 110, 1838

Reid, I. N., Kirkpatrick, J. D., Gizis, J. E., et al. 2000, AJ, 119, 369

Reid, I. N., Kirkpatrick, J. D., Liebert, J., et al. 2002b, AJ, 124, 519

Reid, I. N., Lewitus, E., Allen, P. R., Cruz, K. L., & Burgasser, A. J. 2006a, AJ, 132, 891

Reid, I. N., Lewitus, E., Burgasser, A. J., & Cruz, K. L. 2006b, ApJ, 639, 1114

Reid, I. N., & Walkowicz, L. M. 2006, PASP, 118, 671

Reid, I. N., Cruz, K. L., Laurie, S. P., et al. 2003a, AJ, 125, 354

Reid, I. N., Cruz, K. L., Allen, P., et al. 2003b, AJ, 126, 3007

—. 2004, AJ, 128, 463

Reiners, A., & Basri, G. 2006, AJ, 131, 1806

—. 2008, ApJ, 684, 1390

Reipurth, B., & Clarke, C. 2001, AJ, 122, 432

Reipurth, B., & Mikkola, S. 2015, AJ, 149, 145

Reylé, C., & Robin, A. C. 2004, A&A, 421, 643

Reylé, C., Delorme, P., Willott, C. J., et al. 2010, A&A, 522, A112

Riaz, B., Martín, E. L., Petr-Gotzens, M. G., & Monin, J.-L. 2013, A&A, 559, A109

Rice, E. L., Faherty, J. K., & Cruz, K. L. 2010, ApJL, 715, L165

Riedel, A. R., Blunt, S. C., Lambrides, E. L., et al. 2017, AJ, 153, 95

Riedel, A. R., Finch, C. T., Henry, T. J., et al. 2014, AJ, 147, 85

Rizzuto, A. C., Ireland, M. J., & Kraus, A. L. 2015, MNRAS, 448, 2737

Robin, A. C., Reylé, C., Derriere, S., & Picaud, S. 2003, A&A, 409, 523

Rockenfeller, B., Bailer-Jones, C. A. L., & Mundt, R. 2006, A&A, 448, 1111

Rodono, M., Ciatti, F., & Vittone, A. 1980, AJ, 85, 298

Rodriguez, D. R., Zuckerman, B., Kastner, J. H., et al. 2013, ApJ, 774, 101

Roeser, S., Demleitner, M., & Schilbach, E. 2010, AJ, 139, 2440

Ruiz, M. T., Leggett, S. K., & Allard, F. 1997, ApJL, 491, L107

Ruiz, M. T., Wischnjewsky, M., Rojo, P. M., & Gonzalez, L. E. 2001, ApJS, 133, 119

Sahlmann, J., & Lazorenko, P. F. 2015, MNRASL, 453, L103

Sahlmann, J., Lazorenko, P. F., Bouy, H., et al. 2016, MNRAS, 455, 357

Sahlmann, J., Lazorenko, P. F., Ségransan, D., et al. 2014, A&A, 565, A20

—. 2015a, A&A, 577, A15

—. 2013, A&A, 556, 133

Sahlmann, J., Burgasser, A. J., Martín, E. L., et al. 2015b, A&A, 579, A61

Salim, S., & Gould, A. 2003, ApJ, 582, 1011

Salim, S., Lépine, S., Rich, R. M., & Shara, M. M. 2003, ApJL, 586, L149

Salpeter, E. E. 1955, ApJ, 121, 161

Sarro, L. M., Bouy, H., Berihuete, A., et al. 2014, A&A, 563, A45

Saumon, D., & Marley, M. S. 2008, ApJ, 689, 1327

Schilbach, E., Röser, S., & Scholz, R.-D. 2009, A&A, 493, L27

Schlafly, E. F., & Finkbeiner, D. P. 2011, ApJ, 737, 103

Schlafly, E. F., Finkbeiner, D. P., Juric, M., et al. 2012, ApJ, 756, 158

Schlafly, E. F., Green, G., Finkbeiner, D. P., et al. 2014, ApJ, 789, 15

Schlieder, J. E., Bonnefoy, M., Herbst, T. M., et al. 2014, ApJ, 783, 27

Schmidt, M. 1968, Astrophysical Journal, 151, 393

Schmidt, S. J., Cruz, K. L., Bongiorno, B. J., Liebert, J., & Reid, I. N. 2007, AJ, 133, 2258

Schmidt, S. J., Hawley, S. L., West, A. A., et al. 2015, AJ, 149, 158

Schmidt, S. J., West, A. A., Hawley, S. L., & Pineda, J. S. 2010, AJ, 139, 1808

Schneider, A. C., Cushing, M. C., Kirkpatrick, J. D., et al. 2014, AJ, 147, 34

Schneider, A. C., Greco, J., Cushing, M. C., et al. 2016a, ApJ, 817, 112

Schneider, A. C., Melis, C., Song, I., & Zuckerman, B. 2011, ApJ, 743, 109

Schneider, A. C., Windsor, J., Cushing, M. C., Kirkpatrick, J. D., & Wright, E. L. 2016b, ApJL, 822, L1

Schneider, D. P., Greenstein, J. L., Schmidt, M., & Gunn, J. E. 1991, AJ, 102, 1180

Schneider, D. P., Knapp, G. R., Hawley, S. L., et al. 2002, AJ, 123, 458

Scholz, A., Geers, V., Clark, P., Jayawardhana, R., & Muzic, K. 2013, ApJ, 775, 138

Scholz, R.-D. 2010a, A&A, 515, 92

—. 2010b, A&A, 510, L8

—. 2014, A&A, 561, 113

Scholz, R.-D., Bihain, G., Schnurr, O., & Storm, J. 2011, A&A, 532, L5

—. 2012, A&A, 541, 163

Scholz, R.-D., Bihain, G., & Storm, J. 2014, A&A, 567, A43

Scholz, R.-D., Lehmann, I., Matute, I., & Zinnecker, H. 2004a, A&A, 425, 519

Scholz, R.-D., Lodieu, N., & McCaughrean, M. J. 2004b, A&A, 428, L25

Scholz, R.-D., & Meusinger, H. 2002, MNRAS, 336, L49

Scholz, R.-D., Meusinger, H., & Jahreiss, H. 2001, A&A, 374, L12

Scholz, R.-D., Storm, J., Knapp, G. R., & Zinnecker, H. 2009, A&A, 494, 949

Schweitzer, A., Scholz, R.-D., Stauffer, J., Irwin, M., & McCaughrean, M. J. 1999, A&A, 350, L62

Seifahrt, A., Reiners, A., Almaghrbi, K. A. M., & Basri, G. 2010, A&A, 512, A37

Service, M., Lu, J. R., Campbell, R., et al. 2016, PASP, 128, 095004

Sheppard, S. S., & Cushing, M. C. 2009, AJ, 137, 304

Shkolnik, E. L., Anglada-Escudé, G., Liu, M. C., et al. 2012, ApJ, 758, 56

Shkolnik, E. L., Liu, M. C., & Reid, I. N. 2009, ApJ, 699, 649

Siegler, N., Close, L. M., Burgasser, A. J., et al. 2007, AJ, 133, 2320

Siegler, N., Close, L. M., Cruz, K. L., Martín, E. L., & Reid, I. N. 2005, ApJ, 621, 1023

Siegler, N., Close, L. M., Mamajek, E. E., & Freed, M. 2003, ApJ, 598, 1265

Silvestri, N. M., Lemagie, M. P., Hawley, S. L., et al. 2007, AJ, 134, 741

Simons, D. A., & Tokunaga, A. T. 2002, PASP, 114, 169

Sivarani, T., Lépine, S., Kembhavi, A. K., & Gupchup, J. 2009, ApJL, 694, L140

Skrutskie, M. F., Cutri, R. M., Stiening, R., et al. 2006, AJ, 131, 1163

Skrzypek, N., Warren, S. J., Faherty, J. K., et al. 2015, A&A, 574, A78

Slesnick, C. L., Carpenter, J. M., Hillenbrand, L. A., & Mamajek, E. E. 2006, AJ, 132, 2665

Slesnick, C. L., Hillenbrand, L. A., & Carpenter, J. M. 2008, ApJ, 688, 377

Smart, R. L., Jones, H. R. A., Lattanzi, M. G., et al. 2010, A&A, 511, 30

Smart, R. L., Tinney, C. G., Bucciarelli, B., et al. 2013, MNRAS, 433, 2054

Smart, R. L., Apai, D., Kirkpatrick, J. D., et al. 2017, MNRAS, 468, 3764

Smith, L., Lucas, P. W., Burningham, B., et al. 2014a, MNRAS, 437, 3603

Smith, L., Lucas, P. W., Bunce, R., et al. 2014b, MNRAS, 443, 2327

Soderblom, D. R., Duncan, D. K., & Johnson, D. R. H. 1991, Astrophysical Journal, 375, 722

Spiegel, D. S., Burrows, A. S., & Milsom, J. A. 2011, ApJ, 727, 57

Stamatellos, D., & Whitworth, A. P. 2009, MNRAS, 392, 413

Stauffer, J. R., Schild, R., Barrado y Navascués, D., et al. 1998a, ApJ, 504, 805

Stauffer, J. R., Schultz, G., & Kirkpatrick, J. D. 1998b, ApJ, 499, L199

Steele, I. A., & Jameson, R. F. 1995, MNRAS, 272, 630

Stephens, D. C., & Leggett, S. K. 2004, PASP, 116, 9

Stephens, D. C., Leggett, S. K., Cushing, M. C., et al. 2009, ApJ, 702, 154

Stern, D., Kirkpatrick, J. D., Allen, L. E., et al. 2007, ApJ, 663, 677

Stone, J. M., Skemer, A. J., Kratter, K. M., et al. 2016, ApJL, 818, L12

Strauss, M. A., Fan, X., Gunn, J. E., et al. 1999, ApJL, 522, L61

Stumpf, M. B., Brandner, W., Bouy, H., Henning, T., & Hippler, S. 2010, A&A, 516, 37

Stumpf, M. B., Brandner, W., Köhler, R., Bouy, H., & Henning, T. 2009, AIP Conference Proceedings, 1094, 561

Stumpf, M. B., Geißler, K., Bouy, H., et al. 2011, A&A, 525, 123

Theissen, C. A., & West, A. A. 2014, ApJ, 794, 146

Theissen, C. A., West, A. A., & Dhital, S. 2016, AJ, 151, 41

Theissen, C. A., West, A. A., Shippee, G., Burgasser, A. J., & Schmidt, S. J. 2017, AJ, 153, 92

Thompson, M. A., Kirkpatrick, J. D., Mace, G. N., et al. 2013, PASP, 125, 809

Thorstensen, J. R., & Kirkpatrick, J. D. 2003, PASP, 115, 1207

Tinney, C. G. 1993a, ApJ, 414, 279

—. 1993b, AJ, 105, 1169

—. 1996, MNRAS, 281, 644

Tinney, C. G., Burgasser, A. J., & Kirkpatrick, J. D. 2003, AJ, 126, 975

Tinney, C. G., Burgasser, A. J., Kirkpatrick, J. D., & McElwain, M. W. 2005, AJ, 130, 2326

Tinney, C. G., Delfosse, X., Forveille, T., & Allard, F. 1998, A&A, 338, 1066

Tinney, C. G., Faherty, J. K., Kirkpatrick, J. D., et al. 2014, ApJ, 796, 39

Tinney, C. G., Mould, J. R., & Reid, I. N. 1993, AJ, 105, 1045

Tinney, C. G., Reid, I. N., Gizis, J. E., & Mould, J. R. 1995, AJ, 110, 3014

Todorov, K., Luhman, K. L., & McLeod, K. K. 2010, ApJL, 714, L84

Tokunaga, A. T., Simons, D. A., & Vacca, W. D. 2002, PASP, 114, 180

Tonry, J. L., Stubbs, C. W., Lykke, K. R., et al. 2012, ApJ, 750, 99

Torres, C. A. O., Quast, G. R., Melo, C. H. F., & Sterzik, M. F. 2008, in Handbook of Star Forming Regions, Volume II, The Southern Sky, ed. B. Reipurth (San Francisco: ASP), 757

Tremblin, P., Amundsen, D. S., Chabrier, G., et al. 2016, ApJL, 817, L19

Tsuji, T. 2005, ApJ, 621, 1033

Tsvetanov, Z. I., Golimowski, D. A., Zheng, W., et al. 2000, ApJL, 531, L61

Vacca, W. D., Cushing, M. C., & Rayner, J. T. 2003, PASP, 115, 389

van Altena, W. F., Lee, J. T., & Hoffleit, E. D., eds. 1995, The General Catalogue of Trigonometric [Stellar] Parallaxes (New Haven, CT: Yale University Observatory)

van Biesbroeck, G. 1961, AJ, 66, 528

van Dam, M. A., Bouchez, A. H., Le Mignant, D., et al. 2006, PASP, 118, 310

van Leeuwen, F. 2007a, A&A, 474, 653

van Leeuwen, F., ed. 2007b, Hipparcos, the New Reduction of the Raw Data: ASSL, Vol. 350 (Dordrecht: Springer)

Vrba, F. J., Henden, A. A., Luginbuhl, C. B., et al. 2004, AJ, 127, 2948

Wang, P. F., Chen, W. P., Lin, C. C., et al. 2014a, ApJ, 784, 57

Wang, Y., Jones, H. R. A., Smart, R. L., et al. 2014b, PASP, 126, 15

Webb, R. A., Zuckerman, B., Platais, I., et al. 1999, ApJL, 512, L63

Weights, D. J., Lucas, P. W., Roche, P. F., Pinfield, D. J., & Riddick, F. 2009, MNRAS, 392, 817

Weinberger, A. J., Anglada-Escudé, G., & Boss, A. P. 2013, ApJ, 767, 96

Weinberger, A. J., Boss, A. P., Keiser, S. A., et al. 2016, AJ, 152, 24

Weisz, D. R., Dalcanton, J. J., Williams, B. F., et al. 2011, ApJ, 739, 5

West, A. A., Hawley, S. L., Bochanski, J. J., et al. 2008, AJ, 135, 785

West, A. A., Morgan, D. P., Bochanski, J. J., et al. 2011, AJ, 141, 97

Wielen, R. 1977, A&A, 60, 263

Wilson, J. C., Kirkpatrick, J. D., Gizis, J. E., et al. 2001, AJ, 122, 1989

Wilson, J. C., Miller, N. A., Gizis, J. E., et al. 2003, in IAU Symp. 211, Brown Dwarfs, ed. E. L. Martín (San Francisco: ASP), 197

Winters, J. G., Sevrinsky, R. A., Jao, W.-C., et al. 2017, AJ, 153, 14

Wizinowich, P. L., Le Mignant, D., Bouchez, A. H., et al. 2006, PASP, 118, 297

Wright, E. L., Eisenhardt, P. R. M., Mainzer, A. K., et al. 2010, AJ, 140, 1868

Wright, E. L., Skrutskie, M. F., Kirkpatrick, J. D., et al. 2013, AJ, 145, 84

York, D. G., Adelman, J., Anderson, J. E. J., et al. 2000, AJ, 120, 1579

Zacharias, N., Finch, C. T., Girard, T. M., et al. 2013, AJ, 145, 44

Zacharias, N., Monet, D. G., Levine, S. E., et al. 2005, yCat, I/297, 0

Zapatero Osorio, M. R., Béjar, V. J. S., Martín, E. L., et al. 2000, Science, 290, 103

Zapatero Osorio, M. R., Béjar, V. J. S., Miles-Páez, P. A., et al. 2014a, A&A, 568, 6

Zapatero Osorio, M. R., Béjar, V. J. S., Rebolo, R., Martín, E. L., & Basri, G. 1999, ApJL, 524, L115

Zapatero Osorio, M. R., Rebolo, R., Martín, E. L., et al. 1997, ApJL, 491, L81

Zapatero Osorio, M. R., Gálvez-Ortiz, M. C., Bihain, G., et al. 2014b, A&A, 568, 77

Zapatero Osorio, M. R., Béjar, V. J. S., Martín, E. L., et al. 2014c, A&A, 572, A67

Zhang, Z. H., Pokorny, R. S., Jones, H. R. A., et al. 2009, A&A, 497, 619

Zhang, Z. H., Pinfield, D. J., Day-Jones, A. C., et al. 2010, MNRAS, 404, 1817

Zhang, Z. H., Pinfield, D. J., Burningham, B., et al. 2013, MNRAS, 434, 1005

Zuckerman, B., & Song, I. 2004, ARAA, 42, 685

Zuckerman, B., Song, I., & Bessell, M. S. 2004, ApJ, 613, L65

Zuckerman, B., Song, I., Bessell, M. S., & Webb, R. A. 2001, ApJ, 562, L87